

Advances in
**Planar Lipid Bilayers
and Liposomes**

Volume 8



PREFACE

Volume 8 is the next one in our series on both planar lipid bilayers and spherical liposomes. The results show that this research field, based on a historic perspective of the lipid bilayer concept and its experimental realization as well as on spherical liposomes, is growing and getting more intertwined with many new exciting interdisciplinary areas. Many of the contributing authors collaborated in the past with late Prof. H. Ti Tien, the founding editor of this book series, whose fourth anniversary of his untimely and painful death we just commemorated in May 2008. Prof. H. Ti Tien had a great vision about the practical impact of supported BLMs (Bilayer Lipid Membranes) for new molecular electronic devices as well as for biosensors development. On reading the chapters published in this volume, we can see how correct his predictions and how relevant his contributions into this scientific field have been. His life-long research was focused and dedicated to the studies of planar lipid bilayers and their applications.

The original work of late Prof. H. Ti Tien and his colleagues from the early 1960s based on the description of mundane soap bubbles, followed by “black holes” in soap films, and ending with an invisible “black” lipid membrane, made from lipid extracts of cows’ brains, has come since that time very far in the work represented by many researchers worldwide. The reconstituted structure (6–9 nm thick) was created just like a cell membrane; separating two aqueous solutions. A biological membrane represents a selectively permeable barrier through which a lot of material transport takes place. This process is usually accomplished in many ways, for example, by simple diffusion (passive transport), by facilitated diffusion, or by active transport. The self-assembled lipid bilayer is in a dynamic and liquid–crystalline state. A functional biomembrane should be considered from the molecular point of view as well as from the electronic point of view. It can support both ion and electron transport, and it is also the site of cellular activities because it functions as a “device” for either energy conversion or signal transduction. Such a system, as we can assume, must act as some kind of a transducer capable of gathering information, processing it, and then delivering a response based on this information.

In Volume 8 of the *Advances* series on planar lipid membranes and liposomes, many contributors from all over the world describe their interesting research results in these both reconstituted systems, namely, planar BLMs and spherical liposomes. We continue in our endeavor started by late Prof. H. Ti Tien to invite newcomers from a broad spectrum of this interdisciplinary field to write a chapter for the *Advances* series, but at the same time we also provide enough space to well-established and experienced researchers in this area of research. Volume 8 of the *Advances* series on planar lipid membranes and liposomes continues to include invited chapters on a broad range of topics, starting from theoretical research to specific studies and experimental methods, but also refers to practical applications in many areas.

We, the editor and the editorial board of this *Advances* series, express our gratitude to every author who contributed his/her chapter for this new volume and in that way honored the legacy of late Prof. H. Ti Tien. Their hard work and many new ideas are appreciated by all members of the scientific community working in this exciting new field.

We will continue to do our best to invite more contributors from all over the world to submit their respective chapters about their latest research results to this *Advances* series. In the upcoming volumes of this series, we plan to dedicate each volume to both topics: planar lipid bilayers and spherical liposomes because it is very exciting and stimulating to follow up at the same time the progress achieved in both research areas. We keep in mind the broader goal for the further development of this interdisciplinary field worldwide. In this way we can honor the leading idea of late Prof. H. Ti Tien in establishing this book series. All chapters in this volume have one feature in common: further exploring theoretically and experimentally the planar lipid bilayer systems and spherical liposomes.

We plan to continue in our very interesting and at the same time challenging work of this *Advances* series with Elsevier. We feel that this is the best way to pay a high tribute to late Prof. H. Ti Tien, who called himself a scientific missionary. He continued to spread all over the world during his life as a scientist the latest results of his own experimental work on BLMs and also his vision for further development of this exciting research discipline in the last four decades or so.

Angelica Leitmannova Liu
(Editor)

CONTRIBUTORS

Angela Agostano

Dip. di Chimica, Università di Bari, Via Orabona 4, 70126 Bari, Italy

IPCF-CNR, sez. Bari, Via Orabona 4, 70126 Bari, Italy

Aleš Ambrožič

Department of Rheumatology, University Medical Centre, Vodnikova 62, SI-1000 Ljubljana, Slovenia

Vincent Ball

Institut National de la Santé et de la Recherche Médicale, Unité Mixte de Recherche 595,11 rue Humann, 67085 Strasbourg, France

Centre National de la Recherche Scientifique, Unité Propre 22-Institut Charles Sadron, 23 rue du Loess, BP84074, F-67034 Strasbourg Cedex 2

Klemen Bohinc

Laboratory of Physics, Faculty of Electrical Engineering, University of Ljubljana, Ljubljana, Slovenia

Faculty of Health Studies, University of Ljubljana, Ljubljana, Slovenia

Borut Božič

Department of Rheumatology, University Medical Centre, Vodnikova 62, SI-1000 Ljubljana, Slovenia

Lucia Catucci

Dip. di Chimica, Università di Bari, Via Orabona 4, 70126 Bari, Italy

IPCF-CNR, sez. Bari, Via Orabona 4, 70126 Bari, Italy

Saša Čučnik

Department of Rheumatology, University Medical Centre, Vodnikova 62, SI-1000 Ljubljana, Slovenia

Mojca Frank

Department of Rheumatology, University Medical Centre, Vodnikova 62, SI-1000 Ljubljana, Slovenia

Sara Ghassemifar

Department of Physiology and Health Science, Ball State University, 2000 University Ave., Muncie, IN 47306, USA

Talitha Hampton

Department of Chemical Engineering, University of Alabama in Huntsville, AL 35899, USA

Aleš Iglič

Laboratory of Physics, Faculty of Electrical Engineering, University of Ljubljana, Ljubljana, Slovenia

Marie Kelly-Worden

Department of Physiology and Health Science, Ball State University, 2000 University Ave., Muncie, IN 47306, USA

Veronika Kralj-Iglič

Laboratory of Clinical Biophysics, Faculty of Medicine, University of Ljubljana, Ljubljana, Slovenia

Tanja Kveder

Department of Rheumatology, University Medical Centre, Vodnikova 62, SI-1000 Ljubljana, Slovenia

Angela Leitmannova Liu

Membrane Biophysics Laboratory, Department of Physiology, 2201 Biomedical and Physical Sciences Building, Michigan State University, East Lansing, MI 48824, USA

Centre for Interface Sciences, Department of Microelectronics, Faculty of Electrical Engineering & Information Technology, Slovak University of Technology, Bratislava, Slovak Republic

Valery V. Malev

Institute of Cytology of the Russian Academy of Sciences, 194064 Saint-Petersburg, Russia

Department of Chemistry, Saint-Petersburg State University, 198504 Petergof, Russia

Marc Michel

Centre National de la Recherche Scientifique, Unité Propre 22-Institut Charles Sadron, 23 rue du Loess, BP84074, F-67034 Strasbourg Cedex 2

Francesco Milano

IPCF-CNR, sez. Bari, Via Orabona 4, 70126 Bari, Italy

Helmut Möhwald

Max Planck Institut for Colloids and interfaces, D-14424 Potsdam, Germany

Olga S. Ostroumova

Institute of Cytology of the Russian Academy of Sciences, 194064 Saint-Petersburg, Russia

Janez Pavlič

College of Health Studies, University of Ljubljana, Poljanska 26, SI-1000 Ljubljana, Slovenia

Laboratory of Physics, Faculty of Electrical Engineering, University of Ljubljana, Trzaska 25, SI-1000 Ljubljana, Slovenia

Blaž Rozman

Department of Rheumatology, University Medical Centre, Vodnikova 62, SI-1000 Ljubljana, Slovenia

Pierre Schaaf

Centre National de la Recherche Scientifique, Unité Propre 22-Institut Charles Sadron, 23 rue du Loess, BP84074, F-67034 Strasbourg Cedex 2

Ludmila V. Schagina

Institute of Cytology of the Russian Academy of Sciences, 194064 Saint-Petersburg, Russia

Tomaž Slivnik

Laboratory of Physics, Faculty of Electrical Engineering, University of Ljubljana, Ljubljana, Slovenia

Snežna Sodin-Šemrl

Department of Rheumatology, University Medical Centre, Vodnikova 62, SI-1000 Ljubljana, Slovenia

Vid Šuštar

Laboratory of Clinical Biophysics, Faculty of Medicine, University of Ljubljana, Lipiceva 2, SI-1000 Ljubljana, Slovenia

Jon Y. Takemoto

Department of Biology, Utah State University, Logan, UT 84322-5305, USA

Massimo Trotta

IPCF-CNR, sez. Bari, Via Orabona 4, 70126 Bari, Italy

Andrea Ventrella

Dip. di Chimica, Università di Bari, Via Orabona 4, 70126 Bari, Italy

Jean-Claude Voegel

Institut National de la Santé et de la Recherche Médicale, Unité Mixte de Recherche 595, 11 rue Humann, 67085 Strasbourg, France

Centre National de la Recherche Scientifique, Unité Propre 22-Institut Charles Sadron, 23 rue du Loess, BP84074, F-67034 Strasbourg Cedex 2

Dmitry V. Volodkin

Institut National de la Santé et de la Recherche Médicale, Unité Mixte de Recherche 595, 11 rue Humann, 67085 Strasbourg, France

Max Planck Institut for Colloids and interfaces, D-14424 Potsdam, Germany

Alexander G. Volkov

Department of Chemistry and Biochemistry, Oakwood University, Huntsville, AL 35896, USA

Jian-Shan Ye

School of Chemistry and Chemical Engineering, South China University of Technology, Wushan, Guangzhou 510640, P. R. China

LIPOSOME EMBEDDING INTO POLYELECTROLYTE MULTILAYERS: A NEW WAY TO CREATE DRUG RESERVOIRS AT SOLID-LIQUID INTERFACES

Dmitry V. Volodkin,^{1,3} Marc Michel,² Pierre Schaaf,² Jean-Claude Voegel,^{1,2} Helmut Möhwald,³ and Vincent Ball,^{1,2,*}

Contents

1. Introduction	2
2. Vesicle Adhesion Followed by Supported Bilayer Formation (SLB) Versus Vesicle Adhesion without Rupture (SV)	3
2.1. Formation of SLB from Vesicles	3
2.2. Controlled Deposition of Stable Vesicles on Surfaces	8
3. Embedding on Vesicles in PEM Films	8
4. Applications of PEM Films Loaded with Vesicles and Future Developments	15
5. Conclusions	20
References	20

Abstract

This review is aimed to describe recent progress in the immobilization of lipid vesicles on solid surfaces but also their embedding in quasi two-dimensional films made from polyelectrolyte multilayers (PEMs). Owing to their impermeability to small molecules and to proteins in particular and macromolecules in general, such immobilized reservoirs could achieve great interest in the performance of confined chemical reactions as well as in the development of controlled release systems. The results of the first experiments showing the proof of concept of vesicle embedding in polyelectrolyte multilayers will be presented.

* Corresponding author. Tel.: +33 3 90 24 32 58;
E-mail address: vincent.ball@medecine.u-strasbg.fr.

¹ Institut National de la Santé et de la Recherche Médicale, Unité Mixte de Recherche 595, 11 rue Humann, 67085 Strasbourg, France

² Centre National de la Recherche Scientifique, Unité Propre 22-Institut Charles Sadron, 23 rue du Loess, BP84074, F-67034 Strasbourg Cedex 2

³ Max Planck Institut for Colloids and interfaces, D-14424 Potsdam, Germany

1. INTRODUCTION

Lipid vesicles, so-called liposomes, made of a self-closed lipid bilayer, are explored for more than 40 years as possible drug delivery vehicles [1, 2] with a lot of promises and a lot of deceptions [3]. Nevertheless, some formulations have been FDA approved and a strong research activity continues in this field in parallel with other drug delivery strategies, notably the use of core shell polymeric particles [4] or micelles made from block copolymers [5]. The lipid vesicle field seems to be “boosted” by the use of liposomes containing cationic lipids as gene transfer agents, so-called lipoplexes [6]. The injection of drug loaded vesicles leads usually, in the case of unprotected vesicles, to a rapid clearance by the reticuloendothelial system [7]. This problem has mostly been solved by the use of so-called sterically stabilized liposomes, in which some of the lipids have been modified with poly(ethylene glycol) chains [2,3]. In addition to their biomedical applications, vesicles appear quite attractive for many physical investigations aiming to understand the physics of cell membranes. Indeed, they are relatively easy to prepare, particularly if one uses the so-called extrusion method [8] or ultrasound [9]. It is also possible and more and more frequent to work with giant vesicles [10] (of unilamellar or multilamellar nature), which can be “micromanipulated” under an optical microscope [11] and subjected to different physical forces [12]. This research aims to understand the fundamentals of cell fusion processes [13] as well as to improve relevant drug delivery processes such as electroporation [14].

Quite more Recently, vesicles have been used to functionalize surfaces. The first aim was to circumvent the inherent difficulties of the Langmuir and Langmuir Blodgett deposition methods to produce supported lipid bilayers (SLB). Indeed, to have at disposition a flat equivalent of a biological membrane, with incorporated membrane proteins and keeping the native dynamics of the lipid bilayer, offers the possibility to investigate the inherently complicated cell fusion processes with the tools of surface chemistry [15]. These planar lipid bilayers can also be used as biosensing films when properly functionalized [16,17]. But depending on the nature of the substrate surface and the physicochemical conditions in the vesicle solution, the final state may not be a flat lipid bilayer but a state in which the vesicles are immobilized in an intact or slightly deformed state. This is not necessarily a drawback and opens the route to a method leading to surface immobilized drug reservoirs. Several strategies for that have been described in the recent literature, based mainly on covalent binding [18,19] of the vesicles to the surface or the use of biospecific interactions [20–24]. These strategies are highly efficient but need a high investment in terms of covalent modification of part of the lipids used to form the vesicles.

Hence, we found it beneficial to use less “demanding” vesicle immobilization methods based on a noncovalent modification of lipid vesicles. In order to increase the lifetime of the vesicles and to trigger a controlled drug release with an external stimuli, the immobilized vesicles need to be stabilized; they do not have to fuse upon adhesion on the substrate to form SLB with a subsequent and instantaneous drug release. This led to the idea of immobilizing vesicles in gels or in polyelectrolyte multilayer (PEM) films. Why trying to immobilize vesicles into PEM films and not

hollow capsules made from PEM films around a sacrificial colloid [25] (which are known to have better mechanical properties and improved stability with respect to liposomes)? The answer to this question is straightforward: just because the lipid barrier is highly impermeable even to low molecular mass molecules—a family to which most drugs belong to. This offers a great advantage despite the inherent lack of mechanical stability of the lipid bilayers.

The aim of this review is essentially to describe the progress in surface vesicle immobilization in the last three years, with an emphasis on embedding vesicles into PEM films, which under certain physicochemical conditions display the same rheological behavior as gels [26], as will be discussed later. But to reach this goal, we will, in the first part, briefly describe vesicle adhesion and its spreading on solid surfaces, which has to be avoided if one wants intact vesicle deposition. This will help to understand that the intrinsic instability of vesicles needs to increase their rigidity in order to reach the state of intact (or slightly deformed) surface adherent vesicles, which can be further embedded in a PEM film or in a gel. Embedding vesicles into PEM films, their characterization, and particularly the study of their molecular integrity will be the subjects of the second part of this review. The last part will describe some applications of PEM-embedded vesicles as surface immobilized chemical reactors and as potential systems for stimuli triggered drug release films. Some clues will also be given to improve system stability. In particular, the use of vesicles made from block copolymers will be suggested.

2. VESICLE ADHESION FOLLOWED BY SUPPORTED BILAYER FORMATION (SLB) VERSUS VESICLE ADHESION WITHOUT RUPTURE (SV)

2.1. Formation of SLB from Vesicles

The formation of SLB was first reported by McConnell and colleagues [27], about 23 years ago, while using lipid modified surfaces as cell stimulating substrates. This pioneering finding immediately raised great enthusiasm, and fundamental research was devoted to understand the mechanism of bilayer formation from vesicles initially suspended in solution [28]. SLB can also be formed on hydrophilic surfaces already modified with a lipid monolayer [29,30]. Of particular interest was the finding that the lipid bilayer is separated from the solid substrate (in that case glass beads) by a water layer of around 2 nm thickness [31].

The most useful biophysical techniques for these investigations were found to be optical techniques based on an evanescent field at the substrate–solution interface such as total internal reflection fluorescence microscopy and fluorescence recovery after photobleaching using fluorescent lipids as probes [29,32] as well as surface plasmon resonance spectroscopy [33]. The implantation of the quartz crystal microbalance with monitoring of dissipation (QCM-D), a sensor based on evanescent acoustic waves generated by the shear motion of a piezoelectric quartz crystal [34], to measurements in solution [35,36] has provided a very convenient tool to follow the vesicle adhesion process *in situ* and in real time. These experiments show that vesicle adhesion followed

by a rupture, leading to SLB films, can be easily distinguished from the vesicle adhesion without rupture, leading to supported vesicles (SV) (Fig. 1). This last technique, in combination with atomic force microscopy (AFM), provided the major information allowing to follow the fate of a vesicular suspension in contact with a solid substrate in given conditions. AFM confirms the presence of a homogeneous SLB, often with some small defects [37] from the height difference between a disk consisting of a deposited bilayer and the uncovered substrate, whereas QCM-D allows a real time monitoring of the deposition process with a time resolution that can be better than 1 s. Note that the AFM should be interpreted with great care because one can never exclude that the tip will not induce some vesicle rupture [37].

From all these studies using a combination of QCM-D, to follow *in situ* the vesicle deposition kinetics, and AFM, it appeared that the major control parameters for vesicle deposition are as follows:

- (i) The surface chemistry of the substrate [38]. For instance vesicles made from POPC (1-palmitoyl-2-oleoyl-*sn*-glycero-3-phosphocholine) having an average diameter of 30 nm, form an SLB on SiO_2 and Si_3N_4 covered quartz crystals, whereas under the same experimental conditions (10 mM Tris buffer, pH 8 with 100 mM NaCl, temperature fixed at 295 K) SV were obtained on gold [39], platinum, and TiO_2 covered surfaces [38, 40]. The case of mica surfaces seems to be intermediate: large unilamellar vesicles obtained by the extrusion method through calibrated filters lead to the formation of SLBs [37]

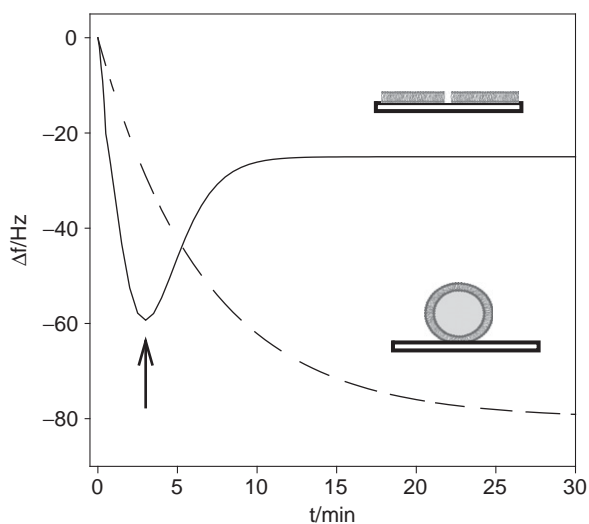


Figure 1 Typical frequency change curves obtained by QCM-D upon adhesion of lipid vesicles to solid—liquid interfaces: (solid line) vesicle adhesion followed by their rupture (starting at the position of the vertical arrow) yielding a supported lipid bilayer (SLB) versus (dashed line) vesicle adhesion without rupture yielding a film of supported vesicles (SV). This figure is inspired by Ref. [38]. For simplicity the dissipation curves versus time are not represented: they display a maximum in the case of SLB formation and a slight and continuous increase in the case of SV deposition. The inserted cartoons show the final state of the substrate in both situations. The gray color represents the interior of the supported vesicle.

whereas small unilamellar vesicles obtained by sonication always lead to SV, as long as the buffer solution contains no Ca^{2+} ions.

- (ii) The temperature [38, 41]. In particular small temperature changes above or below the main phase transition temperature of the used lipid can play a determinant role. Monte Carlo simulations [42] have suggested that the activation energy for vesicle rupture should be of the order of 5 kcal mol^{-1} , hence around $2 k_{\text{B}}T$ (where k_{B} is the Boltzmann constant and T the thermodynamic temperature). Anyway, the importance of the temperature in accelerating the transition from the supported adherent vesicle regime to the rupture and SLB regime clearly demonstrates that the formation of SLB is a thermally activated process.
- (iii) The vesicle size [40]. It appears that the frequency shift associated with vesicle deposition without rupture increases linearly with the vesicle size, which can be expected on the basis of single scaling arguments and remembering that the QCM-D technique measures not only the frequency shift associated with the surface bound lipid but also that due to the contribution of bound water: the mass of a vesicle scales as R^3 (where R is the vesicle radius) whereas the surface occupied by a vesicle scales as R^2 (neglecting the small vesicle deformation effect upon adhesion). Hence the mass per unit area, which leads to a frequency change measured by QCM-D, scales as R ; as found experimentally. On the other hand, when the vesicle adhesion leads to SLB, hence on silica, it is the frequency decrease at the minimum of the frequency versus time curves (see Fig. 1), which scales linearly with the average vesicle size. This point corresponds to the transition of the bound vesicles to their rupture and the formation of SLB. The fact that the frequency starts to increase at that time (and the dissipation decreases, not shown in Fig. 1), is due to the release of bound water after vesicle rupture. It hence appears that each SLB formation process is kinetically preceded by the deposition of a supported vesicle layer. For reasons of a too low vesicle density or too low available activation energy, these adherent vesicles may not rupture and/or fuse to form a supported lipid bilayer.
- (iv) The difference in the ionic strength between the internal aqueous lumen of the vesicles and the external solution, hence the osmotic pressure. In the case, where vesicle adhesion leads to SV, hence on gold and platinum, the osmotic pressure seems to be of little influence on the adhesion process: even if the ionic strength outside the vesicles is 300 mM (the internal ionic strength being equal to 100 mM in NaCl), the vesicles do not rupture [38]. On the other hand, when the vesicle rupture occurs, hence on SiO_2 , the increase in ionic strength in the external solution displaces the minimum in the frequency versus time curves to lower times, meaning that the rupture of the adherent vesicles is accelerated and facilitated from a thermodynamic point of view.
- (v) The chemical composition of the lipids: on suprasil quartz and on silicon plates (both cleaned with boiling butanol and methanol and the detergent Hellmanex at 2% w/v) POPC vesicles of around 75–90 nm diameter yielded SLB, whereas vesicles of the same size made from *Escherichia coli* lipids (containing around 85 mol% phosphatidylethanolamine, 10 mol% phosphatidylglycerol and 5 mol% cardiolipin, the two last head groups being negatively charged) yielded SV film [32] as long as no calcium was present in the buffer. At the same time the

adhesion of calcium promoted the deposition of SLB. The presence of either cationic or anionic lipids in presence of an excess fraction of zwitterionic lipids is of great importance for the quality of the bilayer formed by vesicle fusion: below the phase transition temperature cationic lipids like 1,2-dimyristoyl-3-trimethylammonium-propane (DMTAP) decrease the mutual repulsion between the phosphate groups of 1,2-dimyristoyl-*sn*-glycero-3-phosphocholine (DMPC) which is not the case when DMTAP is replaced by a negatively charged lipid. As a result, in presence of DMTAP, the bilayer appears defect free in the gel state (below the main phase transition temperature) which is not the case in presence of pure zwitterionic DMPC [43].

- (vi) The presence of calcium ions in solution, which act in favor of SLB formation, be it for small unilamellar or large unilamellar vesicles, even in case where the vesicles carry zwitterionic head groups [37]. This finding appeared quite surprising at first glance because it is not expected that Ca^{2+} would have the ability to form trans-bilayer complexes in the case of a bilayer containing no negatively charged lipid head groups. It is well known, however, that Ca^{2+} induces such aggregation [44] and also some phase separation in bilayers containing a mixture of neutral and negatively charged lipids [45]. Hence to interpret the data with lipids containing zwitterionic head groups, it has been postulated that Ca^{2+} modifies the bending modulus of the lipid bilayer [37].

The influence of all these parameters has been reviewed recently [46] and it has to be recognized that the situation is pretty complicated because of the interplay between all the parameters listed above. It appears also, as predicted from theoretical arguments, that the stability or rupture of adherent vesicles relies on a subtle balance between adhesion energy and the energy needed to change the vesicle curvature [47, 48]. To summarize, when the absolute value of the adhesion energy is too high with respect to the elastic energy of the membrane (governed by its bending rigidity and its bending modulus associated with the bilayer's Gaussian curvature), the vesicle is destabilized and it ruptures to form SLB. Note however, that the overall process is very complex, since there is good experimental evidence for an auto-catalytic formation of SLB as soon as some bilayer islands are present on the surface: at the edge of such a disk, not all hydrophobic tails of the lipids are shielded from water. Such defects in the lipid bilayer may disappear, with a subsequent decrease in the free energy of the whole system (buffer + lipid + surface of the solid substrate) by inducing the rupture of intact vesicles coming in close contact with such a defect through a diffusion process. Experimental findings of vesicle rupture when they interact with solid surface were made by Reviakine and Brisson [37].

One can hence operate in one direction or the other, and more accurately predict the fate of a given type of vesicles, on a given kind of substrate, in given conditions; provided an accurate knowledge of the surface energy of the vesicle and the substrate is given. Such a state of knowledge has not been yet reached even if substantial progress has been made [46].

At first glance, it seems that the occurrence of SLB formation is favored in the case where the adsorption substrate is highly hydrophilic, above the main phase transition temperature of the used lipid (or lipid mixture), when the vesicle size is superior to a

critical radius below which adhesion can not occur and when the electrostatic interactions between the substrate and the vesicles are not too strongly repulsive.

To make a complicated story short, and to simplify at the extreme, to deposit SLB from a solution containing lipid vesicles, one has to favor the vesicle adhesion: the released free energy due to adhesion has to overcome the positive cost of elastic energy. The opposite holds when one wants to end up with the SV state.

At present, SLB have been deposited on hydrophilic glass substrates [49–51] but also on films of carbon nanotubes [52] as well as on PEM films (PEMs) [53–55]. These PEM films are made by alternating deposition of polycations and polyanions on solid substrates (Fig. 2) of any kind of shape [56–58] (so-called layer-by-layer technique). The driving force for their build up relies on charge overcompensation upon deposition of the last layer. Such film deposition offers great versatility concerning the choice of the adsorption substrate as well as the chosen polyelectrolytes and also offers a fine control over the film thickness and properties as mechanical or permeability properties [59–61]. It has also been demonstrated that films of controlled thickness can be deposited in a layer-by-layer manner by just using polymers bearing complementary functionalities, like hydrogen bond donor-acceptors [62] or biospecific interactions [63]. The aim behind the deposition of compact, and if possible impermeable SLB on PEM films is evident: it is to isolate different parts of the films and to create reservoirs for different active molecules. This is a particularly promising approach in the case where the different compartments of the PEM film, separated by the lipid barrier are highly hydrated as is the case for PEM films that grow exponentially with the number of deposited layer pairs [57].

The SLB films obtained from vesicle adhesion, rupture, and fusion can be patterned [64] and used to implement various biosensors, which offers a wide range of potential applications. The fact that it is possible to deposit vesicles

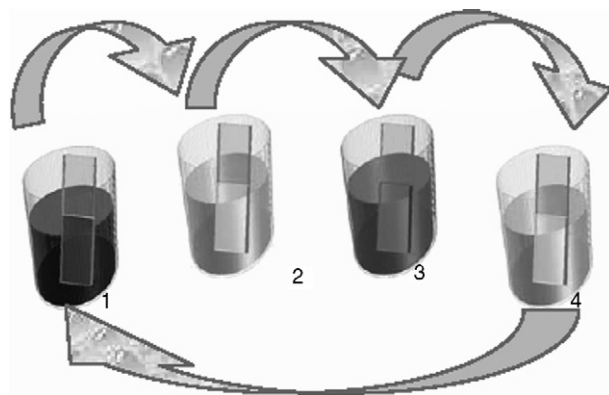


Figure 2 Schematics showing the deposition method of a PEM film. Step 1: adsorption of polyelectrolyte A (either a polycation or a polyanion). Step 2: rinse with buffer solution to remove the excess of solution A as well as the weakly bound polyelectrolyte A. Step 3: adsorption of polyelectrolyte B (either a polyanion or a polycation) whose electrostatic charge is of opposite sign to that of A. Step 4: rinse with buffer solution to remove the excess of solution B as well as the weakly bound B polyelectrolyte. The repetition of Steps 1–4 results in the deposition of an $(A-B)_n$ PEM film made of n layer pairs.

at interfaces without inducing their rupture also presents great potential because a vesicle by itself is impermeable to most charged solutes and to all solutes having a molecular mass higher than around 400 g mol^{-1} . If one needs to implement some specific permeability for biosensing applications, one can just incorporate the membrane protein specifically designed to allow the transport of the targeted solute [65].

2.2. Controlled Deposition of Stable Vesicles on Surfaces

From the preceding paragraphs, it appears that successful deposition of intact vesicles relies on minimization of the interaction between the lipid molecules and the adhesion substrate. Nevertheless some adhesion is necessary. It is hence advisable to minimize the number of strong interaction sites between the vesicles and the adhesion substrate. To that aim, vesicles have been designed which contain a small fraction of functionalized lipids that can interact strongly either covalently (for instance via lipids containing thiol moieties in their polar head groups, [18]) or through biospecific interaction (for instance base pairing between complementary single stranded DNA molecules) [20–24,66,67]. The approach presented by the group of Boxer [20] is fascinating because it uses a planar patterned bilayer containing a different kind of binding oligonucleotide in each corral. Fluorescent vesicles (either containing an encapsulated dye or carrying a fraction of fluorescently labeled lipids) containing the complementary antisense oligonucleotides to the oligonucleotides already on the surface, are then brought in contact with it. This allows a highly efficient vesicle sorting [20]. In addition the vesicles remain mobile (with diffusion coefficients of about $1 \mu\text{m}^2\text{s}^{-1}$) in each individual corral on the patterned surface and the trapped vesicles preserve their molecular integrity upon individual collisions in each corral.

All these vesicle immobilization strategies on solid, homogeneous or patterned surfaces have been extensively reviewed recently [68]. We will hence no longer focus on this kind of strategies. They offer the advantage of specificity but lack from the necessity to modify part of their lipid molecules with covalent chemistry before the self-assembly in vesicles.

3. EMBEDDING ON VESICLES IN PEM FILMS

To deposit vesicles on surfaces, preferentially on surfaces coated with PEMs, owing to their previously described advantages, the vesicles need to be stabilized. Indeed our preliminary experience has shown that negatively charged vesicles made from 91% POPC (w/w), 4.5% POPG (w/w) and 4.5 mol% (w/w) of cholesterol (CL) (or POPC/POPG/CL vesicles) undergo frequent fusion and rupture when deposited on a PEI-(PGA-PAH)₃ multilayer film [69]. PEI is poly(ethylene imine), PGA is poly(-L-glutamic acid), and PAH is poly(allylamine hydrochloride) (PAH). Many strategies have been designed in the literature in order to increase the stability of lipid vesicles. These methods have been reviewed recently [70]. Four categories of modifications of the lipid surface or hydrophobic region of the lipid bilayer have been described:

- (i) The polymerization of hydrophobic monomers which are solubilized inside the hydrophobic part of the lipid bilayer yielding a polymer network [65].
- (ii) The use of lipids comprising hydrophilic polymerisable groups, such as an organoalkoxysilane [71–72]. Upon contact with water, these moieties spontaneously undergo a polycondensation reaction leading to the formation of a thin silica layer around the vesicles increasing their stability and allowing their incorporation in PEM films.
- (iii) The incorporation and subsequent polymerization of a triblock copolymer comprising polymerizable extremities [73].
- (iv) The coating with a polyelectrolyte monolayer [74–79] or multilayer [80].
- (v) The use of chemically modified lipids [81]: this strategy is reminiscent of that used for producing sterically stabilized vesicles. It needs some covalent chemistry but it offers the advantage of stability with respect to strategy (iv).

Stabilization by polyelectrolyte coating seems to be attractive due to simplicity and a wide range of polyelectrolytes may provide vesicles with versatile properties. Indeed, it has been demonstrated that polycations adsorbed on the surface of negatively charged vesicles may be displaced from their surface through an increase in the salt concentration or through an exchange process in which a polyanion having more affinity with the adsorbed polycation than the polycation itself has for the vesicles [75]. In addition, the adsorption of the polycation can induce the displacement of the negatively charged cardiolipin from the internal leaflet to the outer leaflet (by a so-called polycation induced “flip-flop” mechanism) in order to increase the electrostatic interactions with the polycation. This was observed for vesicles from a mixture of 1,2 dipalmitoyl-*sn*-glycero-3-phosphatidyl choline (DDPC) and negatively charged cardiolipin. The “flip-flop” depends on the phase state of the lipids and will only occur when the lipid mixture is in the liquid crystalline or fluid phase. Differential scanning calorimetry (DSC) experiments have shown that the adsorption of the polycation induces some lateral segregation between the neutral DPPC and the negatively charged cardiolipin. Finally, it was elegantly demonstrated, by using fluorescently labelled lipids whose fluorescence is quenched upon polycation adsorption, that the polycation can be removed upon an increase in the ionic strength of the solution or by adding some negatively charged polyacrylic acid in the solution [75]. When the fraction of negatively charged lipids is above 30%, the adsorption of the polycation will disrupt the lipid bilayer as followed by conductometry [74,75]. As anticipated, all these complications can be suppressed when the polycation is modified on 2% of its 4-vinylpyridine groups with hexadecyl chains. The hydrophobic pending chains of the polycation will then partition in the hydrophobic bilayer and increase the stability of the vesicles [75].

This study, as well as that by Ge et al. [76] inspired our studies aimed to embed lipid vesicles in “exponentially” growing PEM films. The thickness of such films increases exponentially with the number of deposited layer pairs [57]. We selected these kinds of PEM films rather than the more common linearly growing ones in order to embed the deposited large unilamellar vesicles (diameter: 100–200 nm) by the additional deposition of only a small number of layer pairs. Indeed, in the case of films made from PGA and PAH the film thickness reaches about 1 μm after the

deposition of only 10 layer pairs in presence of 10 mM Tris buffer at pH 7.4 and with 100 mM NaCl [82].

Ge *et al.* have shown that the coating of negatively charged vesicles with PAH impeded the sodium dodecyl sulfate induced micellization of the vesicles [76]. Simultaneously to our trial to embed nonruptured vesicles in PEM films, we also tried to optimize the vesicle coating by Poly-[(L-D)lysine] (this notation means that we used both poly-L-lysine and poly-D-lysine, or shortly PLL and PDL). Hence it is possible, as already described in the case of poly-4-vinyl pyridine and copolymers thereof (namely poly(*N*-ethyl-4-vinylpyridinium bromide)) [75], that the adsorption of the polycation on the negatively charged vesicles may induce not only some vesicle rupture, segregation, and adsorption induced “flip-flop” phenomena, but also some vesicle aggregation. As working parameters for optimization of the vesicle coating with PLL, we investigated the influence of [78]:

- (i) The molecular mass of PLL. We have found that PLL of high molecular mass (viscosimetric averaged molecular mass of 280 kg mol^{-1} , or 28 kg mol^{-1}) can be adsorbed on unilamellar vesicles made from 1,2-Dipalmitoyl-*sn*-Glycero-3-Phosphocholine (DPPC), 1,2-Dipalmitoyl-*sn*-Glycero-3-[Phospho-*rac*-(1-glycerol)], Sodium Salt (DPPG), and CL (80/10/10 in weight %, respectively) or let us name the vesicles DPPC/DPPG/CL vesicles. Adsorption leads to no vesicle aggregation provided the PLL/DPPG ratio is significantly higher than 0.7. The ratio 0.7 corresponds to the maximum position of the cupola-like aggregation profile that is slightly different from the expected position (0.5) when all the negative lipid charges in the outer leaflet of the bilayer should be in contact with positively charged amino groups (experiments were performed at pH 7.5). The difference could be attributed to charge inversion leading to partial exposure of PLL charges to the outer solution. At a PLL/DPPG ratio close to 0.7, strong aggregation is found. These aggregates are micron sized and surprisingly monodisperse, as found by others [83,84]. Such a peculiar aggregation phenomenon may be due to the presence of regions on vesicle surfaces with a lack of charge overcompensation, which strongly increases the probability of intervesicle bridging. It nevertheless does not explain the homogeneity of the obtained aggregates. Theoretical studies have demonstrated that such a “uniform” dispersion of aggregates may be due to compensation between long range repulsive and short range attractive forces [85]. By using low molecular mass PLL (2 kg mol^{-1} in viscosimetric molecular mass) we have found strong aggregation whatever the PLL/DPPG ratio [78]. Hence we focused our studies aimed to embed protected vesicles in PEM films, to vesicles protected with PLL of high molecular mass. It also appeared that vesicles coated with PLL of 280 kg mol^{-1} were difficult to separate from the excess of PLL in solution. Hence our embedding studies were done with the 28 kg mol^{-1} PLL.
- (ii) The mixing order between PLL and the vesicles as well as the hydrodynamic conditions under which the mixing is done. To reduce the occurrence of aggregation the liposome solution had to be dropped into the PLL solution. This is well known from colloidal stability studies. In addition strong magnetic agitation (950 rpm) improved the vesicle coating by PLL, suggesting that in

order to reduce the probability of aggregation, the adsorption, and hence the transport of PLL to the vesicle surface has to be fast [78]. Note that we checked that the fast agitation does not lead to vesicle rupture. This was done by encapsulation of 5(6)-carboxyfluorescein (CF) in the vesicles.

In all our studies, we found that PLL coating only slightly increased the hydrodynamic radius of the vesicles, the more so the higher the molecular mass of the used PLL. In addition, DSC experiments allowed to check that the DPPC/DPPG/CL vesicles displayed the same main phase transition temperature in the uncoated and PLL coated state (the transition peak appears nevertheless broader in the presence of PLL than for uncoated vesicles [78]). This strongly suggests that the adsorption of PLL does not induce phase separation in the lipid bilayer, as was previously observed when the protecting polycation was poly(*N*-ethyl-4-vinylpyridinium bromide [75]). The phenomena occurring to the vesicles in a PLL containing solution are summarized in Fig. 3.

Let us consider what happened when uncoated or PLL coated vesicles are in contact with PEM film or are embedded into the film architecture (Fig. 4). Our initial study demonstrated that the adhesion of POPC/POPG/CL vesicles covered with a layer of poly-(*D*-lysine) (viscosimetric molecular mass: 27.2 kg mol^{-1}) leads to

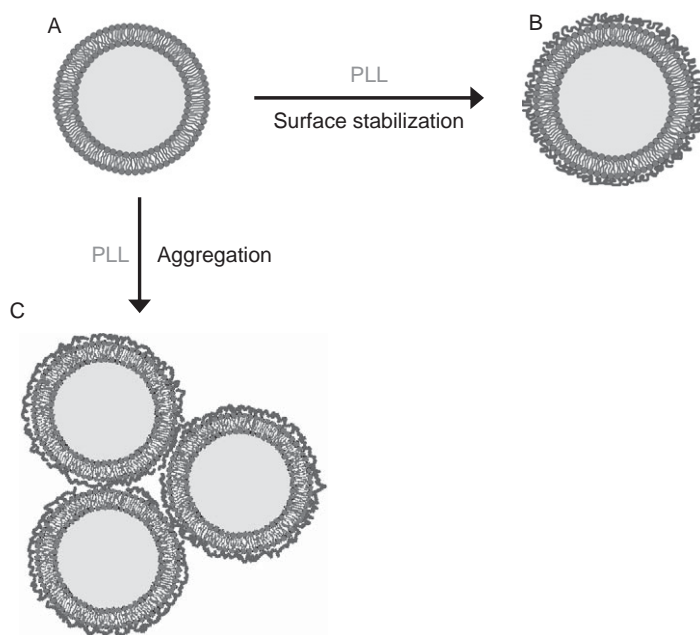


Figure 3 Scheme illustrating the possible events when lipid vesicles (carrying negatively charged lipid headgroups) are dropped in a PLL containing solution. Pathway A–B: formation of a PLL monolayer on the surface of the negatively charged vesicles. Pathway A–C: formation of vesicle aggregates induced by PLL adsorption and interparticle bridging. See reference [78] for additional details and experimental illustrations of pathways A–B and A–C. The gray color represents the interior of the vesicle.

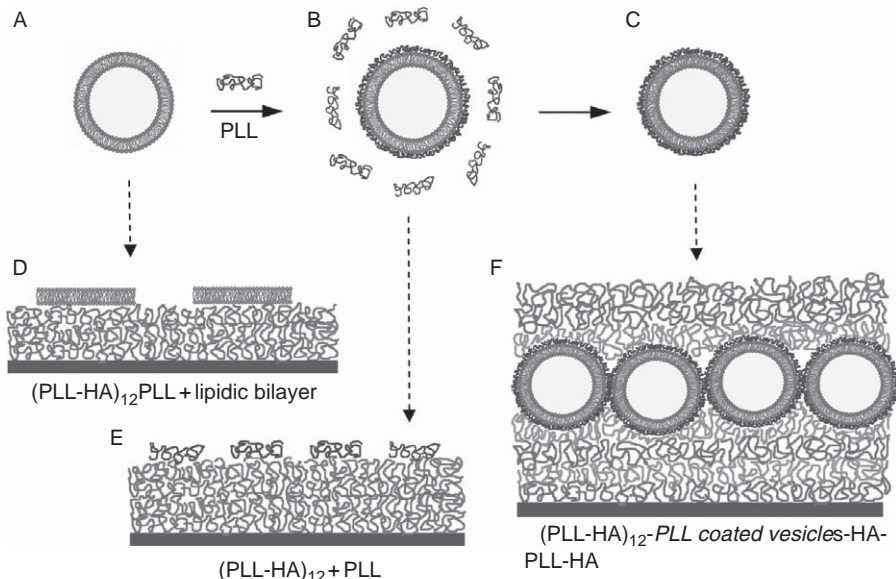


Figure 4 Scheme of vesicle stabilization by PLL coating (A–B) followed by separation of well-covered single vesicles from excess of nonbound PLL (B–C). Native vesicles are disrupted upon adsorption on $(\text{PLL-HA})_{12}$ -PLL film forming lipid bilayer (A–D). Free (non-bound with vesicles) PLL is preferably adsorbed on a $(\text{PLL-HA})_{12}$ film compared to PLL covered vesicles (B–E). Liposome-containing film $(\text{PLL-HA})_{12}$ -PLL coated vesicles-HA-PLL-HA is formed by adsorption of PLL coated vesicles on $(\text{PLL-HA})_{12}$ film followed by additional coating with HA-PLL-HA layers (C–F). See also reference [86] for additional details.

adsorption without rupture of the vesicles on a PEI-(PGA-PAH)_2 -PGA PEM film and the possibility to further embed them to yield a PEI-(PGA-PAH)_2 -PGA-PDL coated vesicles-(PGA-PLL)₂ architecture [69]. The same finding has been made for $(\text{PLL-HA})_{12}$ -PLL coated vesicles-(HA-PLL)-HA films when DPPC/DPPG/CL vesicles were used (Fig. 5) [86].

Unstabilized vesicles, i.e. without PLL coating, were adherent on a PEI-(PGA-PLL)_2 film, but after embedding under two PLL-PGA pairs of layers, significant vesicle fusion and spreading was observed by AFM (data not shown, see Fig. 3 of Ref. [69]). In addition, the QCM-D curves of deposition of PDL-covered vesicle was markedly different compared to that of the unprotected vesicles. These curves were in agreement with vesicle deposition without rupture, leading to SV, and with vesicle adsorption followed by rupture, leading probably to a film containing both SLB and SV (data not shown: see Fig. 2 of Ref. [69]).

The fact that no apparent fusion of the vesicles appeared on the AFM pictures (acquired in the contact mode and after film drying) does not prove that the embedded vesicles keep their structural integrity. To assess this question we used our experience acquired about the permeability of the PEI-(PGA-PAH)_n films with respect to ferrocyanide anions [59, 87]. We have demonstrated by means of cyclic voltammetry that such films, irrespective of the nature of the last deposited layer

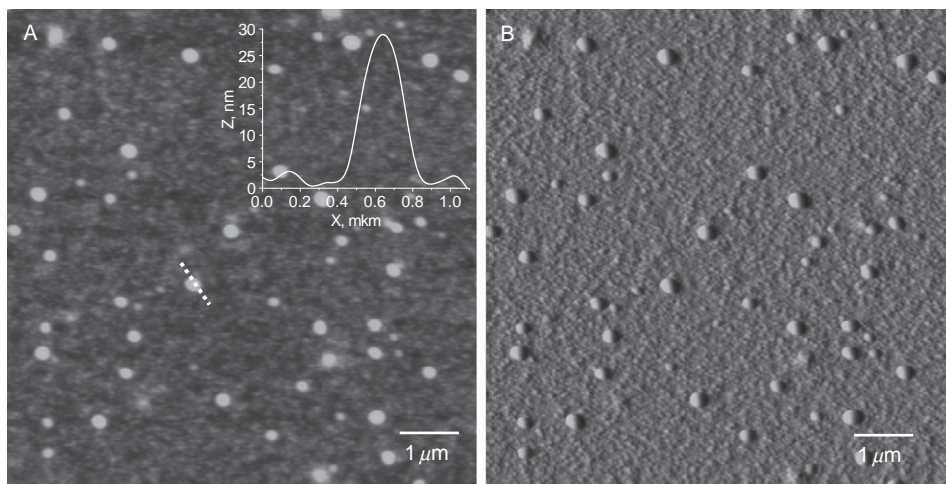


Figure 5 AFM images of a liposome-containing film (HA-PLL)₁₂-PLL coated vesicles-HA-PLL-HA (A – height and B – deflection images). The films were imaged in the dry state with the contact mode. The inset displays the height distribution along the dashed line in part A (from Ref. [86]).

(either PAH or PGA) present a high permeability towards $\text{Fe}(\text{CN})_6^{4-}$ and that the ions present in the film are not removed upon washing with the buffer (these multivalent ions can be quantitatively removed, however, when the film is put in contact with polyanions which can diffuse into the film, leading to an ion exchange process). Hence we loaded large unilamellar vesicles (the composition of which is the same as in our previous study [69]) with a 1 mM $\text{K}_4\text{Fe}(\text{CN})_6$ solution. The non-encapsulated ions were removed by dialysis before protecting the vesicles by adsorption of a PDL layer. Then the PDL-covered vesicles filled with ions were entrapped in a PGA-PAH based PEM film. The whole PEI-(PGA-PAH)₂-PGA-PDL coated vesicles-(PGA-PAH)₂ film was deposited by spray deposition [88] on a gold working electrode in order to speed up the deposition process. Indeed, we wanted to follow the release kinetics of the encapsulated redox probe immediately after the deposition of the last capping layer. Some additional experimental precautions had to be taken and the lipid concentration had to be optimized to deposit the vesicles by spraying without inducing their rupture. These experimental details can be found in the original paper [89]. It was then observed (Fig. 6) that after an initial lag phase of about one hour, where no signal, due to ferrocyanide oxidation or ferricyanide reduction, could be detected, the Faradaic currents progressively increased to reach a plateau after about 12 h. This, in addition to control experiments [89], was a proof that the vesicles kept their structural integrity, at least immediately after their deposition and embedding into the PGA-PAH PEM film [89].

Later on we tested the integrity of DPPC/DPPG/CL vesicles covered with PLL and embedded into a PEM made from PLL and hyaluronic acid (HA). It was found that the vesicle encapsulated CF was not released at all from the liposomes as long as the temperature of the solution in contact with the film was kept lower than the

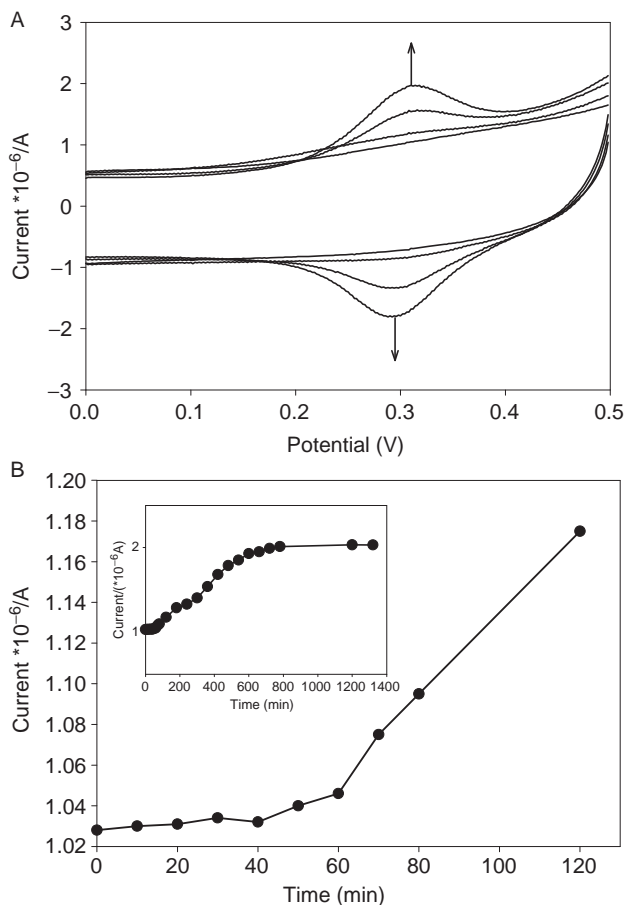


Figure 6 Cyclic voltammety experiments on PEI-(PGA-PAH)₂-PGA-PDL coated vesicles-(PGA-PAH)₂ films sprayed onto the surface of a working gold electrode. These experiments were aimed to demonstrate the molecular integrity of the embedded vesicles. The vesicles contained ferrocyanide ions at a concentration of 1 mM. (A) evolution of the electrochemical signal with time (each signal corresponds to: 0 h, 1 h, 6 h, and 12 h from the bottom to the top curve). (B) plot of the evolution of the maximum of the oxidation current observed at around 300 mV/SCE for short contact time between the modified electrode and the buffer. Inset: evolution of the current intensity over a time period of about 23 h [89].

main phase transition temperature of the lipid mixture (41°C) [86]. Fig. 7A and B show the green dots of CF-containing vesicles adsorbed and embedded into PLL/HA film, respectively. The difference between the two kinds of experiments may be due to the nature of the lipids—the unsaturated POPC/POPG mixture, which is in the liquid crystalline versus the saturated DPPC/DPPG which is in the gel state at ambient temperature. But the nature of the probe, $\text{Fe}(\text{CN})_6^{4-}$ versus CF, as well as a change in the PEM film composition and structure may also contribute to explain the difference. Anyway, in both studies, the vesicles were found not to be leaky immediately after their incorporation into the PEM film. This offers a lot of

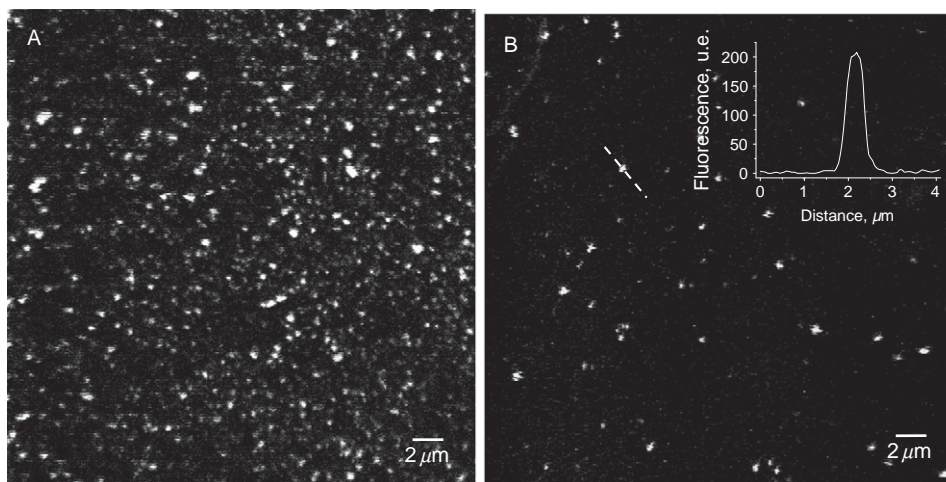


Figure 7 Confocal laser scanning microscopy images of $(\text{PLL-HA})_{12}\text{-PLL}$ coated vesicles (A) and additionally the same film coated with HA-PLL-HA, yielding a $(\text{PLL-HA})_{12}\text{-PLL}$ coated vesicles-HA-PLL-HA film (B). The inset in the image B is a fluorescence profile for the section depicted with a dashed line. See Ref. [86] for additional details.

opportunities for controlled drug release experiments, as will be described in the last chapter of this review.

We were also able to demonstrate that it is possible to embed two layers of PDL protected vesicles into such $(\text{PGA-PAH})_n$ films and that the ferrocyanide release kinetics was qualitatively the same in the case where the film contained two strata or one stratum of embedded vesicles [89].

4. APPLICATIONS OF PEM FILMS LOADED WITH VESICLES AND FUTURE DEVELOPMENTS

A lot of research has been devoted to investigate liposomes as chemical reactors owing to their impermeability to most of the solutes [64,90,91], even low molecular weight hydrophilic molecules, with the notable exception of water and small amphiphilic molecules which present a partition coefficient between the water and lipid phase. Indeed, the biological cell is a (very) complex chemical reactor in which the permeability for given solutes is due to the presence of membrane proteins and membrane embedded molecular motors which, as in the case of the Ca-ATPase, allow diffusion of species against their concentration gradient. Some synthetic systems have now been designed to mimic such complicated events [92]. In the very elegant report by the group of Montemagno, the vesicles containing Ca-ATPase were entrapped in a silica matrix which provided mechanical stability to the chemical reactor [92].

We have demonstrated the possibility to use giant liposomes containing encapsulated Ca^{2+} ions and alkaline phosphatase (ALP), as a reactor able to produce calcium phosphate in the internal lumen of the giant vesicles through the diffusion of paranitrophenylphosphate (PNP) through the lipid bilayer coupled with its ALP catalyzed hydrolysis to produce paranitrophenol and phosphate ions [93]. Hence through the production of $\text{H}_2\text{PO}_4^-/\text{HPO}_4^{2-}$, which are not able to diffuse out of the liposome in opposition to the amphiphilic PNP, the saturation of the intravesicular solution with respect to the different calcium phosphates progressively increases. This leads finally to nucleation and crystal growth. The growth of calcium phosphates, most probably poorly crystalline hydroxyapatite, was located exclusively in the internal aqueous compartment of the giant liposomes [93]. We then tried to develop this concept further by confining the calcium-phosphate reactors inside the PEMs, made from PGA and PAH as in our previous work [69,89]. To this aim, we used large unilamellar POPC/POPG/CL vesicles. These vesicles contained ALP, Ca^{2+} , and spermine (which was shown to accelerate the nucleation and/or crystal growth). All these active constituents were removed [94] from their external aqueous compartment before the vesicles were stabilized by a PDL layer. These stabilized and potentially active chemical reactors were then embedded (by a layer-by-layer deposition method) in PEM films leading to the architecture $\text{PEI}-(\text{PGA}-\text{PAH})_2-[\text{PDL}-\text{ALP containing vesicles}]-(\text{PGA}-\text{PAH})_2$ (Fig. 8). The major challenge was to check that the initially encapsulated ALP still remained in the internal aqueous compartment of the vesicles after the purification steps (aimed to hydrolyze the nonencapsulated polypeptide chains and to complex the nonencapsulated Ca^{2+} ions with ethylenediamine tetraacetic acid). This was checked by means of scanning near field optical microscopy [95] using a mixture of vesicles containing labeled ALP and vesicles with unlabeled ALP [94]. The comparison of the topographical and the fluorescence images allowed to ascertain that most of the fluorescence originated from the interior of the vesicles and hence from the encapsulated ALP (Fig. 9A).

Having demonstrated previously that the substrate of ALP of interest, namely PNP, is able to diffuse in exponentially growing PEM films [96], we then put the $\text{PEI}-(\text{PGA}-\text{PAH})_2-[\text{PDL}-\text{ALP containing vesicles}]-(\text{PGA}-\text{PAH})_2$ PEM in contact with a PNP solution and followed the hydrolysis-precipitation process *in situ* by means of infrared spectroscopy in the attenuated total reflection mode (Fig. 9B). After 18 h of contact between the $\text{PEI}-(\text{PGA}-\text{PAH})_2-[\text{PDL}-\text{ALP containing vesicles}]-(\text{PGA}-\text{PAH})_2$ PEM and the PNP solution, some characteristic bands appear in the infrared spectrum. These bands are very close to those expected in the presence of hydroxyapatite. Unfortunately, there was not enough inorganic material to characterize it by means of X-ray diffraction and to ascertain the presence of hydroxyapatite. However, a selective dissolution of the organic counterpart of the composite film with the aid of 0.1 M hypochlorite solutions at pH 10, allowed to confirm the presence of inorganic platelets whose lateral size was compatible with the diameter distribution of the initially embedded liposomes [94].

In the next study aimed to demonstrate the usefulness of stabilized vesicles embedded in PEM films; we focused on PEM films made from PLL and HA. It appears that $(\text{PLL}-\text{HA})_n$ films are better suited than the previously used $\text{PEI}-(\text{PGA}-\text{PAH})_n$ films. This is due to the difference in interaction between the vesicles and

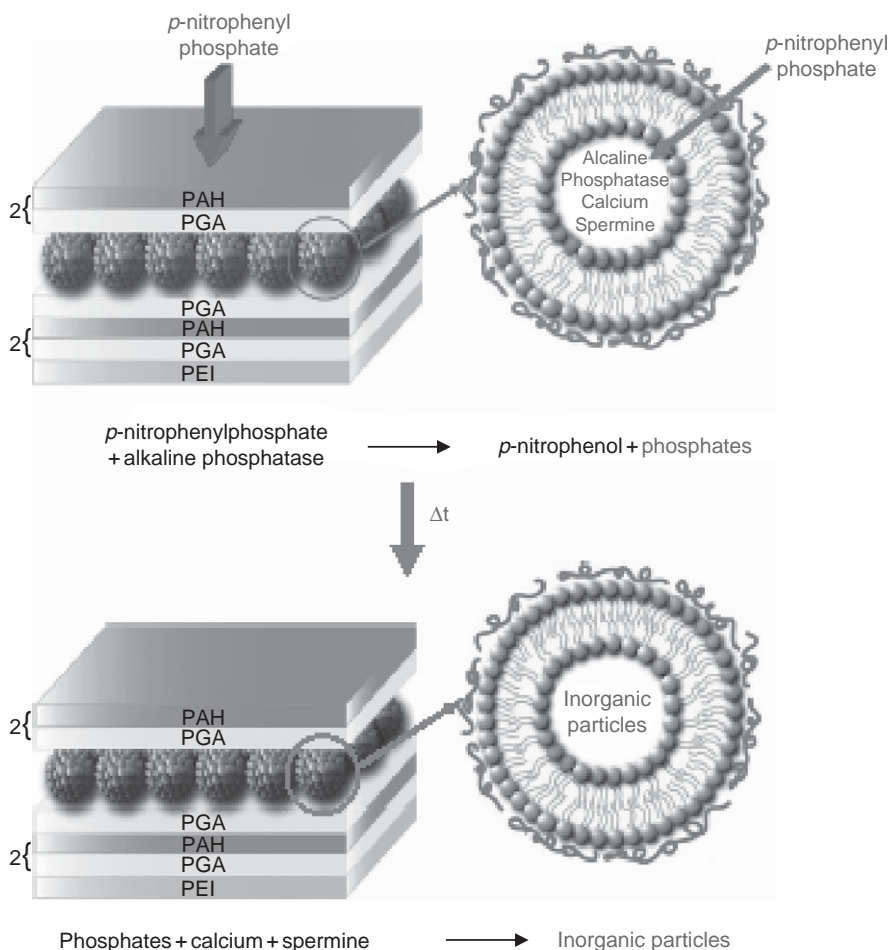


Figure 8 Scheme showing embedded PLL coated vesicles containing the enzyme ALP, calcium, and spermine and put in contact with a solution of paranitrophenyl phosphate (PNP). After a time duration Δt , allowing for the diffusion of PNP in the PEM film and across the lipid bilayers, the supersaturation in the vesicles increases leading to the precipitation of calcium phosphates in the vesicles. Inspired from Ref. [94].

their protective PLL layer with respect to the interaction between the PLL molecules and the last deposited polyanion of the multilayer film (manuscript in preparation). It has been demonstrated that PLL interacts stronger with PGA than with the negatively charged vesicles, leading to some PLL adsorption instead of PLL-vesicle adhesion in the case of the PEI-(PGA-PAH)₂-PGA film. In the case of the (PLL-HA)₁₂ film, the interaction of PLL (28 kg mol⁻¹) with HA is comparable to the interactions between PLL and the negatively charged vesicles leading to better adsorption of PLL coated vesicles on (PLL-HA)₁₂ film.

These considerations point to the intrinsic difficulty to find the optimal combination of the polyelectrolytes (including its composition and molecular mass) and

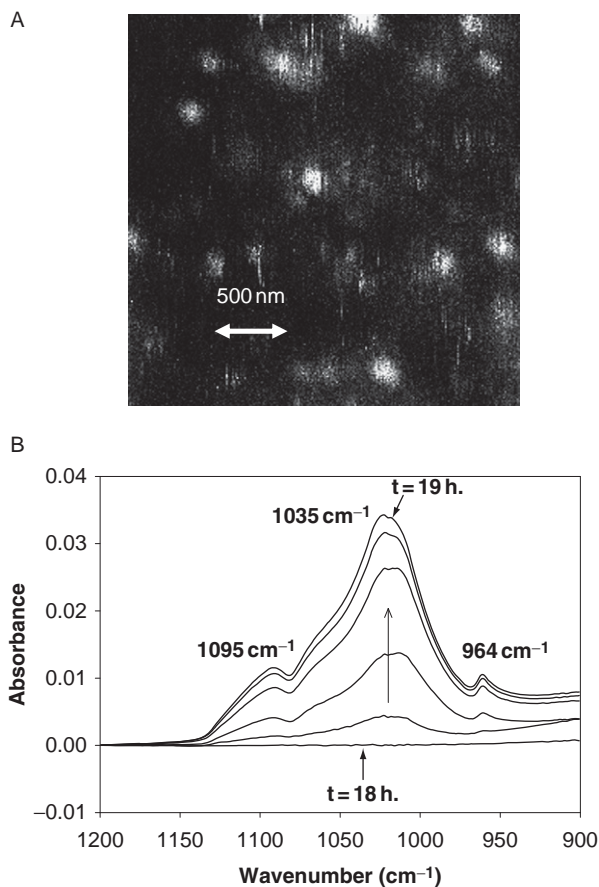


Figure 9 (A) Scanning near field image in the fluorescence detection mode of a PEI-(PGA-PAH)₂-PGA-PDL coated vesicles-(PGA-PAH)₂ film where part of the embedded vesicles contain rhodamine B labeled ALP. (B) Mineralization kinetics of calcium phosphates in a PEI-(PGA-PAH)₂-PGA-PDL coated vesicles-(PGA-PAH)₂ film deposited on a ZnSe crystal used to acquire the infrared spectra in the totally attenuated reflection mode (ATR-FTIR). The PNP solution was put in contact with the film and the ATRFTIR spectra were regularly acquired. Bands attributed to hydroxyapatite appear only after 18 h of reaction. See Ref. [94] for additional details.

the nature of the multilayer film used to embed intact vesicles. Fortunately the knowledge of the interactions leading to the growth of PEM films has made huge progress [97, 98]. Since it was found impossible to embed PLL coated vesicles in linearly growing PEM films made from poly-4-styrene sulfonate (PSS) and PAH, which is a linearly growing PEM film, and since we had success with (PLL-HA)_n as well as with (PGA-PAH)_n films, whose thickness is growing exponentially with the number *n* of deposited layer pairs, we assume that the exponential nature of the PEM film growth is a prerequisite to successfully embed intact lipid vesicles. The fact that intact vesicles can be embedded in exponentially growing PEM films, might well be due to the weakness of the interactions between their constituents (polycations and

polyanions) as well as their high water content (the volume fraction of water in the $(\text{PLL-HA})_n$ films is of the order of 0.7, based on the refractive index of the film calculated from optical waveguide lightmode spectroscopy [99]).

Now let us come back on the embedding of PLL coated vesicles in $(\text{PLL-HA})_n$ films. We have found by fluorescence measurement in the supernatant in contact with the film that a great fraction (around 70%) of the initially deposited vesicles undergoes desorption upon embedding under additional HA-PLL-HA layers [86], which was found by analysis of fluorescent marker encapsulated in the embedded vesicles and was confirmed by confocal laser scanning microscopy [Fig. 7B]. This situation is reminiscent on that observed upon protein embedding [100] in PEM films. In our case, no further desorption is observed when two HA-PLL pairs of layers are deposited on top of the embedded vesicles. This means that a stable situation can be achieved when the adsorbed vesicles are covered with HA-PLL-HA layers reaching an embedded state. At present, we are improving the vesicle embedding by keeping the same approach for embedding (polyelectrolyte stabilizing shell and gel-like HA/PLL film form the perfect matrix to immobilize vesicles) but increase the interaction vesicle-PLL and PLL-outer HA layer of PEM film by strong avidin-biotin chemistry.

In addition, as has already been demonstrated in the case of PEI-(PGA-PAH)_n films, multiple strata of vesicles can be deposited, leading to an increase of the total fluorescence due to the encapsulated dye which is a linear function of the number of embedding steps [86]. Finally, when DPPC/DPPG/CL vesicles containing CF and protected with a PLL layer (PLL having a molecular mass of 28 kg mol^{-1}) are incorporated in a $(\text{PLL-HA})_{12}\text{-PLL coated vesicle-(HA-PLL)-HA}$ film, no CF release is found as long as the solution in contact with the film is kept at a temperature below the main phase transition of the lipid bilayer (41°C). However at 45°C the encapsulated dye is released quantitatively in about half an hour (Fig. 10).

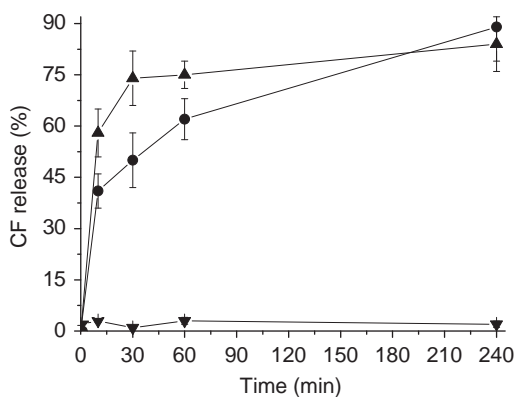


Figure 10 Time evolution of the cumulative CF release from vesicles embedded inside a $(\text{PLL-HA})_{12}\text{-PLL coated vesicle-HA-PLL-HA}$ film architecture, when the film is maintained at ambient temperature (\blacktriangledown) or heated and maintained at 45°C (\blacktriangle). These release kinetics are compared to the release kinetics obtained for the same PLL covered vesicles in aqueous solution at 45°C (\bullet). The data points correspond to the average over three experiments and the error bars correspond to the standard deviation. See Ref. [86] for additional details.

This last finding opens the route for preparing thin PEM films containing vesicles able to release encapsulated drugs in a controlled manner. As other stimuli to release the molecules encapsulated in immobilized vesicles, we plan to apply mechanical stresses in a direction parallel or perpendicular to the plane of a stratified PEM containing vesicles in its lower counterpart. This film will then be covered by a linearly growing capping layer that will act as diffusion barrier impeding any drug release in the absence of lateral forces. But as soon as the resulting strain will be higher than a critical value, pores will open in the capping layer allowing drug release [101] (provided the vesicles in the underlying exponential compartment are leaky: this leakage could be induced by a temperature increase as already described).

In the next future, we plan to apply ultrasound treatment and/or magnetic field to the film containing vesicles to trigger controlled drug delivery. Such vesicle-containing films could be modified with materials sensitive to these stimuli. Owing to some difficulties of the vesicle embedding process, which is mainly due to the coating of the vesicles with PLL and PLL interaction to the PEM film, we plan to use vesicles made from triblock copolymers, which are intrinsically more “rigid” than lipid vesicles or to polymerize acrylic monomers inside of the hydrophobic region of the bilayer.

5. CONCLUSIONS

In this review we have first explained the origin of the difference between SLB formation and deposition of SV when a suspension of lipid vesicles is brought in contact with a solid substrate. To deposit intact vesicles one has to either reduce the vesicle adhesion to single points, using covalent immobilization between some lipids from the vesicles and chemical groups on the substrate, or use biospecific interactions (for instance by pairing of complementary single stranded oligonucleotides). We have also demonstrated that a controlled adsorption of polyelectrolytes on the surface of vesicles containing a small fraction of charged lipids allows their adsorption without rupture (but nevertheless with some small deformation) and their subsequent embedding in PEM films. The best PEM films seems to be those displaying an exponential growth of their thickness with respect to the number of deposited layer pairs, certainly because of their high degree of hydration. Such embedded vesicles can be used as confined submicron sized chemical reactors as well as controlled release systems, for example in future “biopatches.”

REFERENCES

- [1] D.D. Lasic, Novel applications of liposomes, *Trends Biotechnol.* 16 (1998) 307–321.
- [2] D.D. Lasic, D. Papahadjopoulos, *Medical Applications of Liposomes*, Elsevier Science, Amsterdam, 1998.
- [3] Y. Barenholz, Liposome application: Problems and prospects, *Curr. Opin. Colloid Interface Sci.* 6 (2001) 66–77.

- [4] A.V. Kabanov, V.P. Chekhonin, V.Y.u. Alakhov, E.V. Batrakova, A.S. Lebedev, N.S. Melik-Nubarov, S.A. Arzhakov, A.V. Levashov, G.V. Morozov, E.S. Severin, V.A. Kabanov, The neuroleptic activity of haloperidol increases after its solubilization in surfactant micelles. Micelles as microcontainers for drug targeting, *FEBS Lett.* 258 (1989) 343–345.
- [5] K. Kataoka, A. Harada, Y. Nagasaki, Block copolymer micelles for drug delivery: Design, characterization and biological significance, *Adv. Drug Deliv. Rev.* 47 (2001) 113–131.
- [6] P.L. Felgner, T.R. Gadek, M. Holen, R. Roman, H.W. Chan, M. Wenz, J.P. Northrop, G. M. Ringold, M. Danielsen, Lipofectin: A highly efficient, lipid-mediated DNA transfection procedure, *Proc. Natl. Acad. Sci. USA* 84 (1987) 7413–7417.
- [7] J. Sunamoto, *Physical Chemistry of Biological Interfaces*, Marcel Dekker, New York, (2000), pp. 307–358.
- [8] L.D. Mayer, M.J. Hope, P.R. Cullis, Vesicles of variable sizes produced by a rapid extrusion procedure, *Biochim. Biophys. Acta* 858 (1986) 161–168.
- [9] Y. Barenholz, D. Gibbes, B.J. Litman, J. Goll, T.E. Thomson, F.D. Carlson, A single method for the preparation of homogeneous phospholipid vesicles, *Biochemistry* 16 (1977) 2806–2810.
- [10] M.I. Angelova, D.C. Dimitrov, Liposome electroformation, *Faraday Discuss* 81 (1986) 303–311.
- [11] N. Fa, C.M. Marques, E. Mendes, A.P. Schröder, Rheology of giant vesicles: A micropipette study, *Phys. Rev. Lett.* 92 (2004) art 108103.
- [12] R. Dimova, K.A. Riske, S. Aranda, N. Bezlyepkina, R.L. Knorr, R. Lipowsky, Giant vesicles in electric fields, *Soft Matter* 3 (2007) 817–827.
- [13] D.J. Estes, S.R. Lopez, A.O. Fuller, M. Mayer, Triggering and visualizing the aggregation and fusion of lipid membranes in microfluidic chambers, *Biophys. J.* 91 (2006) 233–243.
- [14] M. Golzio, J. Tessié, M.P. Rols, Direct visualization at the single-cell level of electrically mediated gene delivery, *Proc. Natl. Acad. Sci. USA* 99 (2002) 1292–1297.
- [15] E. Sackmann, Supported membranes: Scientific and practical applications, *Science* 271 (1996) 43–48.
- [16] J.J. Ramsden, P. Schneider, Membrane insertion and antibody recognition of a glycosylphosphatidylinositol-anchored protein: An optical study, *Biochemistry* 32 (1993) 523–529.
- [17] E.L. Schmid, T.A. Keller, Z. Dienes, H. Vogel, Reversible oriented surface immobilization of functional proteins on oxide surfaces, *Anal. Chem.* 69 (1997) 1979–1985.
- [18] D. Xu, Q. Cheng, Surface-bound lipid vesicles encapsulating redox species for amperometric biosensing of pore-forming bacterial toxins, *J. Amer. Chem. Soc.* 124 (2002) 14314–14315.
- [19] A.N. Chifen, R. Förch, W. Knoll, P.J. Cameron, H.L. Khor, T.L. Williams, A.T.A. Jenkins, Attachment and phospholipase A₂-induced lysis of phospholipid bilayer vesicles to plasma-polymerized maleic anhydride/SiO₂ multilayers, *Langmuir* 23 (2007) 6294–6298.
- [20] C. Yoshina-Ishii, S.G. Boxer, Arrays of mobile tethered vesicles on supported lipid bilayers, *J. Amer. Chem. Soc.* 125 (2003) 3696–3697.
- [21] C. Yoshina-Ishii, G.P. Miller, M.L. Kraft, E.T. Kool, S.G. Boxer, General method for modification of liposomes for encoded assembly on supported bilayers, *J. Amer. Chem. Soc.* 127 (2005) 1356–1357.
- [22] B. Städler, D. Falconnet, I. Pfeiffer, F. Höök, J. Vörös, Micropatterning of DNA-tagged vesicles, *Langmuir* 20 (2004) 11348–11354.
- [23] I. Pfeiffer, F. Höök, Bivalent cholesterol based coupling of oligonucleotides to lipid membrane assemblies, *J. Amer. Chem. Soc.* 126 (2004) 10224–10225.
- [24] H. Brochu, P. Vermette, Liposome layers characterized by quartz crystal microbalance measurements and multirelease delivery, *Langmuir* 23 (2007) 7679–7686.
- [25] E. Donath, G.B. Sukhorukov, F. Caruso, S.A. Davis, H. Möhwald, Novel hollow polymer shells by colloid-templated assembly of polyelectrolytes, *Angew. Chem. Int. Ed.* 37 (1998) 2201–2205.
- [26] D. Collin, P.h. Lavalley, J.M. Garza, J.C. Voegel, P. Schaaf, P.h. Martinoty, Mechanical properties of cross-linked hyaluronic acid/poly(L-lysine) multilayer films, *Macromolecules* 37 (2004) 10195–10198.
- [27] A.A. Brian, H.M. McConnell, Allogeneic stimulation of cytotoxic T cells by supported planar membranes, *Proc. Natl. Acad. Sci. USA* 81 (1984) 6159–6163.
- [28] L.K. Tamm, H.M. McConnell, Supported phospholipid bilayers, *Biophys. J.* 47 (1985) 105–113.

- [29] E. Kalb, S. Frey, L.K. Tamm, Formation of supported planar bilayers by fusion of vesicles to supported phospholipid monolayers, *Biochim. Biophys. Acta* 1103 (1992) 307–316.
- [30] T. Baumgart, M. Kreiter, H. Lauer, R. Naumann, G. Jung, A. Jonckzyk, A. Offenhäuser, W. Knoll, Fusion of small unilamellar vesicles onto laterally mixed self-assembled monolayers of thiolipopeptides, *J. Colloid Interface Sci.* 258 (2003) 298–309.
- [31] T.M. Bayerl, M. Bloom, Physical properties of single phospholipid bilayers adsorbed to micro glass beads, *Biophys. J.* 58 (1990) 357–362.
- [48] S. M. Jackson, M. D. Reboiras, I. G. Lyle, M. N. Jones, The mechanism of phospholipid adsorption from vesicle dispersions onto glass surfaces, *Colloids Surf.* 27 (1987) 325–340.
- [32] P. Nollert, H. Kiefer, F. Jähnig, Lipid vesicle adsorption versus formation of planar bilayers on solid surfaces, *Biophys. J.* 69 (1995) 1447–1455.
- [33] Z. Salamon, D. Huang, W.A. Cramer, G. Tollin, Coupled plasmon-waveguide resonance spectroscopy studies of the cytochrome b6/f/plastocyanin system in supported lipid bilayer membranes, *Biophys. J.* 75 (1998) 1874–1895.
- [34] G. Sauerbrey, Verwendung von Schwingquarzen zur Wägung dünner Schichten und zur Mikrowägung, *Z. Phys.* 155 (1959) 206–222.
- [35] M.V. Voinova, M. Rodahl, M. Jonson, B. Kasemo, *Phys. Scr.* 59 (1999) 391.
- [36] D. Johannsmann, Viscoelastic analysis of organic thin films on quartz resonators, *Macromol. Chem. Phys.* 200 (1999) 501–516.
- [37] I. Reviakine, A.R. Brisson, Formation of supported phospholipid bilayers from unilamellar vesicles investigated by atomic force microscopy, *Langmuir* 16 (2000) 1806–1815.
- [38] E. Reimhult, F. Höök, B. Kasemo, Intact vesicle adsorption and supported biomembrane formation from vesicles in solution: Influence of surface chemistry, vesicle size, temperature, and osmotic pressure, *Langmuir* 19 (2003) 1681–1691.
- [39] S. Sofou, J.L. Thomas, Stable adsorption of lipid vesicles on modified gold surfaces, *Mat. Res. Symp. Proc.* 705 (2002) 171–176.
- [40] E. Reimhult, F. Höök, B. Kasemo, Vesicle adsorption on SiO₂ and TiO₂: Dependence on vesicle size, *J. Chem. Phys.* 117 (2002) 7401–7404.
- [41] B. Seantier, C. Breffa, O. Félix, G. Decher, In situ investigations of the formation of mixed supported lipid bilayers close to the phase transition temperature, *Nano Lett.* 4 (2004) 5–10.
- [42] K. Dimitrievski, E. Reimhult, B. Kasemo, V.P. Zhdanov, Simulations of temperature dependence of the formation of a supported lipid bilayer via vesicle adsorption, *Colloids Surf. B* 39 (2004) 77–86.
- [43] L. Zhang, T.A. Spurlin, A.A. Gewirth, S. Granick, Electrostatic stitching in gel-phase supported phospholipid bilayers, *J. Phys. Chem. B* 110 (2006) 33–35.
- [44] J. Wilschut, N. Düzgünes, D. Papahadjopoulos, Calcium/magnesium specificity in membrane fusion: Kinetics of aggregation and fusion of phosphatidylserine vesicles and the role of bilayer curvature, *Biochemistry* 20 (1981) 3126–3133.
- [45] D.E. Leckband, C.A. Helm, J.N. Israelachvili, Role of calcium in the adhesion and fusion of bilayers, *Biochemistry* 32 (1993) 1127–1140.
- [46] R.P. Richter, R. Bérat, A.R. Brisson, Formation of solid supported lipid bilayers: An integrated view, *Langmuir* 22 (2006) 3497–3505.
- [47] U. Seifert, R. Lipowsky, Adhesion of vesicles, *Phys. Rev. A* 42 (1990) 4768–4771.
- [48] A. Efremov, J.C. Mauro, S. Raghavan, Macroscopic model of phospholipid vesicle spreading and rupture, *Langmuir* 20 (2004) 5724–5731.
- [49] S.M. Jackson, M.D. Reboiras, I.G. Lyle, M.N. Jones, The mechanism of phospholipid adsorption from vesicle dispersions onto glass surfaces, *Colloids Surf.* 27 (1987) 325–340.
- [50] J. Salafsky, J.T. Groves, S. Boxer, Architecture and Function of membrane proteins in planar supported bilayers: A study with photosynthetic reaction centers, *Biochemistry* 35 (1996) 14773–14781.
- [51] P.S. Cremer, S.G. Boxer, Formation and spreading of lipid bilayers on planar glass supports, *J. Phys. Chem. B* 103 (1999) 2554–2559.
- [52] J. Gagner, H. Johnson, E. Watkins, Q. Li, M. Terrones, J. Majewski, Carbon nanotube supported single phospholipid bilayer, *Langmuir* 22 (2006) 10909–10911.

- [53] C. Delajon, T. Gutberlet, R. Steitz, H. Möhwald, R. Krastev, Formation of polyelectrolyte multilayer architectures with embedded DMPC studied in situ by neutron reflectometry, *Langmuir* 21 (2005) 8514.
- [54] G. Köhler, S.E. Moya, S. Leporatti, C. Bitterlich, E. Donath, Stability and fusion of lipid layers on polyelectrolyte multilayer supports studied by colloidal force spectroscopy, *Eur. Biophys. J.* 36 (2007) 337–347.
- [55] A.M. Pilbat, Z. Szegletes, Z. Kóta, V. Ball, P. Schaaf, J.C. Voegel, B. Szalontai, Phospholipid bilayers as biomembrane-like barriers in layer-by-layer polyelectrolyte films, *Langmuir* 23 (2007) 8236–8242.
- [56] G. Decher, Fuzzy nanoassemblies: Toward layered polymeric multicomposites, *277 Science* (1997) 1232–1237.
- [57] N. Benkirane-Jessel, P.h. Lavallo, V. Ball, J. Ogier, B. Senger, C. Picart, P. Schaaf, J.C. Voegel, G. Decher, G. Polyelectrolyte multilayer films—A general approach to (bio) functional coatings, *In Macromolecular Engineering*, Vol. 2, (K. Matyjaszewski, Y. Gnanou, and L. Leibler, Eds.), 2007 pp. 1249–1305.
- [58] K. Ariga, J.P. Hill, Q. Ji, Layer-by-Layer assembly as a versatile bottom-up nanofabrication technique for exploratory research and realistic application, *Phys. Chem. Chem. Phys.* 9 (2007) 2319–2340.
- [59] T. Fahrat, J.B. Schlenoff, Ion transport and equilibria in polyelectrolyte multilayers, *Langmuir* 17 (2001) 1184–1192.
- [60] E. Hübsch, G. Fleith, J. Fatisson, P. Labbe, J.C. Voegel, P. Schaaf, V. Ball, Multivalent ion/polyelectrolyte exchange processes in exponentially growing multilayers, *Langmuir* 21 (2005) 3664–3669.
- [61] T. Noguchi, J.I. Anzai, Redox properties of the ferricyanide ion on electrodes coated with layer-by-layer thin films composed of polysaccharide and poly(allylamine), *Langmuir* 22 (2006) 2870–2875.
- [62] S.A. Sukhishvili, S. Granick, Layered, erasable, ultrathin polymer films, *J. Amer. Chem. Soc.* 122 (2000) 9550–9551.
- [63] H. Inoue, K. Sato, J.I. Anzai, Disintegration of layer-by-layer assemblies composed of 2-imino-biotin-labelled poly(ethylene imine) and avidin, *Biomacromolecules* 6 (2005) 27–29.
- [64] J.T. Groves, N. Ulman, S.G. Boxer, Micropatterning fluid lipid bilayers on solid supports, *275 Science* (1997) 651–653.
- [65] A. Graff, M. Winterhalter, W. Meier, Nanoreactors from polymer stabilized liposomes, *Langmuir* 17 (2001) 919–923.
- [66] B. Chaize, M. Nguyen, T. Ruyschaert, V. Le Berre, E. Trévisiol, A.M. Caminade, J.P. Majoral, G. Pratviel, B. Meunier, M. Winterhalter, D. Fournier, Microstructured liposome array, *Bioconjug. Chem.* 17 (2006) 245–247.
- [67] T. Stora, Z. Dienes, H. Vogel, C. Duschl, Histidine-tagged amphiphiles for the reversible formation of lipid bilayer aggregates on chelator functionalized gold surfaces, *Langmuir* 16 (2000) 5471–5478.
- [68] S.M. Christensen, D. Stamou, Surface-based lipid vesicle reactor systems: Fabrication and applications, *Soft Matter* 3 (2007) 828–836.
- [69] M. Michel, D. Vautier, J.C. Voegel, P. Schaaf, V. Ball, Layer-by-layer self assembled polyelectrolyte multilayers with embedded phospholipid vesicles, *Langmuir* 20 (2004) 4835–4839.
- [70] T. Ruyschaert, M. Germain, J.F. Pereira da Silva Gomes, D. Fournier, G.B. Sukhorukov, W. Meier, M. Winterhalter, Liposome-based nanocapsules, *IEEE Trans. Nanobioscience* 3 (2004) 49–55.
- [71] K. Katagiri, R. Hamasaki, K. Ariga, J.I. Kikuchi, Layer-by-layer self-assembling of liposomal «cerasome» on substrates, *Langmuir* 18 (2002) 6709–6711.
- [72] K. Katagiri, R. Hamasaki, K. Ariga, J.I. Kikuchi, Layered paving of vesicular nanoparticles formed with cerasome as a bioinspired organic-inorganic hybrid, *J. Am. Chem. Soc.* 124 (2002) 7892–7893.
- [73] T. Ruyschaert, A.F.P. Sonnen, T. Haefele, W. Meier, M. Winterhalter, D. Fournier, Hybrid Nanocapsules: Interactions of ABA block copolymers with liposomes, *J. Am. Chem. Soc.* 127 (2005) 6242–6247.

- [74] A.A. Yaroslavov, E.A. Kiseliova, O.Y. Udalykh, V.A. Kabanov, Integrity of mixed liposomes contacting a polycation depends on the negatively charged lipid content, *Langmuir* 14 (1998) 5160–5163.
- [75] V.A. Kabanov, A.A. Yaroslavov, What happens to negatively charged lipid vesicles upon interacting with polycation species? *J. Control. Release* 78 (2002) 267–271.
- [76] L. Ge, H. Möhwald, J. Li, Phospholipid liposomes stabilized by the coverage of polyelectrolyte, *Colloids Surf. A* 221 (2003) 49–53.
- [77] F. Quemeneur, A. Rammal, M. Rinaudo, B. Pépin-Donat, Large and giant vesicles “decorated” with chitosan: Effects of pH, salt or glucose stress, and surface adhesion, *Biomacromolecules* 8 (2007) 2512–2519.
- [78] D. Volodkin, V. Ball, P. Schaaf, J.C. Voegel, H. Möhwald, Complexation of phosphocholine liposomes with polylysine. Stabilization by surface coverage versus aggregation, *Biochim. Biophys. Acta* 1768 (2007) 280–290.
- [79] D. Volodkin, H. Möhwald, J.C. Voegel, V. Ball, Stabilization of negatively charged liposomes by polylysine surface coating. Drug release study, *J. Control. Release* 117 (2007) 111–120.
- [80] M. Germain, S. Grube, V. Carrière, H. Richard-Foy, M. Winterhalter, D. Fournier, Composite Nanocapsules: Lipid vesicles covered with several layers of cross-linked polyelectrolytes, *Adv. Mater* (2006) 2868–2871.
- [81] F. Vial, S. Rabhi, C. Tribet, Association of octyl-modified poly(acrylic acid) onto unilamellar vesicles of lipids and kinetics of vesicles disruption, *Langmuir* 21 (2005) 853–862.
- [82] F. Boulmedais, V. Ball, P. Schwinte, B. Frisch, J.C. Voegel, P. Schaaf, Buildup of exponentially growing multilayer polypeptide films with internal secondary structure, *Langmuir* 19 (2003) 440–445.
- [83] S. Sennato, F. Bordi, C. Cametti, On the phase diagram of reentrant condensation in polyelectrolyte-liposome complexation, *J. Chem. Phys.* 121 (2004) 4936–4940.
- [84] S. Sennato, F. Bordi, C. Cametti, A. Di Biasio, M. Diociauti, Polyelectrolyte-liposome complexes: An equilibrium cluster phase close to the isoelectric condition, *Colloids Surf. A* (2005) 270–271, 138–147.
- [85] J. Groeneveld, W.K. Kegel, Anomalous large equilibrium clusters of colloids, *J. Phys. Chem. B* 105 (2001) 11702–11709.
- [86] D. Volodkin, Y. Arntz, P. Schaaf, H. Möhwald, J. C. Voegel, V. Ball, Composite polyelectrolyte films containing multiple strata of intact liposomes: Stability and triggered dye release, *Soft Matter* 4 (2008) 122–130.
- [87] M. Schönhoff, V. Ball, A. Bausch, C. Déjugnat, N. Delorme, K. Glinel, R. von Klitzing, R. Steitz, Hydration and internal properties of polyelectrolyte multilayers, *Colloids Surf. A* 303 (2007) 14–29.
- [88] A. Izquierdo, S.S. Ono, J.C. Voegel, P. Schaaf, G. Decher, Dipping versus spraying: Exploring the deposition conditions for speeding-up layer-by-layer assembly, *Langmuir* 21 (2005) 7558–7567.
- [89] M. Michel, A. Izquierdo, G. Decher, J.C. Voegel, P. Schaaf, V. Ball, Layer by layer self-assembled polyelectrolyte multilayers with embedded phospholipid vesicles obtained by spraying: Integrity of the vesicles, *Langmuir* 21 (2005) 7854–7859.
- [90] P. Walde, S. Ichikawa, Enzymes inside lipid vesicles: Preparation, reactivity and applications, *Biomol. Eng.* 18 (2001) 143–177.
- [91] M. Yoshimoto, S. Wang, K. Fukunaga, P. Walde, R. Kuboi, K. Nakao, Preparation and characterization of reactive and stable glucose oxidase-containing liposomes modulated with detergent, *Biotechnol. Bioeng.* 81 (2003) 695–704.
- [92] T.J.M. Luo, R. Zoong, E. Lan, B. Dunn, C. Montemagno, Photo-induced proton gradients and ATP biosynthesis produced by vesicles encapsulated in a silica matrix, *Nat. Mat.* 4 (2005) 220–224.
- [93] M. Michel, M. Winterhalter, L. Darbois, J. Hemmerlé, J.C. Voegel, P. Schaaf, V. Ball, Giant liposome microreactors for controlled production of calcium phosphate crystals, *Langmuir* 20 (2004) 6127–6133.

- [94] M. Michel, Y. Arntz, G. Fleith, J. Toquant, Y. Haikel, J.C. Voegel, P. Schaaf, V. Ball, Layer-by-layer self-assembled polyelectrolyte multilayers with embedded liposomes: Immobilized sub-micronic reactors for mineralization, *Langmuir* 22 (2006) 2358–2364.
- [95] E. Betzig, R.J. Chichester, Single molecules observed by near-field scanning optical microscopy, *Science* 262 (1993) 1422–1425.
- [96] L. Derbal, H. Lesot, J.C. Voegel, V. Ball, Incorporation of alkaline phosphatase into layer-by-layer polyelectrolyte films on the surface of Affi gel heparin particles: Physicochemical characterization and evaluation of the enzyme stability, *Biomacromolecules* 4 (2003) 1255–1263.
- [97] S.A. Sukhishvili, E. Kharlampieva, V. Izumrudov, Where polyelectrolyte multilayers and polyelectrolyte complexes meet, *Macromolecules* 39 (2006) 8873–8881.
- [98] N. Laugel, C. Betscha, M. Winterhalter, J.C. Voegel, P. Schaaf, V. Ball, Relationship between the growth regime of polyelectrolyte multilayers and the polyanion/polycation complexation enthalpy, *J. Phys. Chem. B* 110 (2006) 19443–19449.
- [99] C. Picart, P.h. Lavalle, P. Hubert, F.J.G. Cuisinier, G. Decher, P. Schaaf, J.C. Voegel, Buildup mechanism for poly-(L-lysine)/hyaluronic acid films onto a solid surface, *Langmuir* 17 (2001) 7414–7424.
- [100] Y. Lvov, K. Ariga, I. Ichinose, T. Kunitake, Assembly of multicomponent protein films by means of electrostatic layer-by-layer adsorption, *J. Amer. Chem. Soc.* 117 (1995) 6117–6123.
- [101] D. Mertz, J. Hemmerlé, J. Mutterer, S. Ollivier, J.C. Voegel, P. Schaaf, P.h. Lavalle, Mechanically responding nanovalves based on polyelectrolyte multilayers, *Nano Lett.* 7 (2007) 657–662.

LIPID ENVIRONMENTAL MODULATION OF ACTIVITY OF PHOTOSYNTHETIC MEMBRANE PROTEINS

Lucia Catucci,^{1,2,*} Andrea Ventrella,¹ Francesco Milano,² Massimo Trotta,² and Angela Agostano^{1,2}

Contents

1. Introduction	28
1.1. PSII Structure	29
1.2. Bacterial RC Structure	30
1.3. Photosynthetic Membrane Lipids	31
2. Lipid Content under Osmotic Stress in Higher Plants and in Photosynthetic Bacteria	34
2.1. Studies on Higher Plants (<i>Spinacia oleracea</i> L.)	35
2.2. Studies on Photosynthetic Bacteria (<i>R. sphaeroides</i>)	38
3. Analysis of the Lipids Directly Surrounding Spinach PSII and their Effects on PSII Organization and Activity	39
3.1. Analysis of the Lipids Directly Surrounding PSII	39
3.2. Effects of Phospholipids on PSII Organization and Activity	41
4. Effect of Phospholipids on the Energetic and Dynamics of the Quinone Acceptor Complex in Bacterial Reaction Centres	42
4.1. Electron Transfer Reactions in Bacterial RCs	44
4.2. RC Reconstitution in Artificial Lipid Bilayers (Liposomes)	45
4.3. The Free Energy Change for the $D^+Q_A^-Q_B \rightarrow D^+Q_AQ_B^-$ Electron Transfer	46
4.4. Quinone Exchange at Q_B -site Modulated by the Lipid Environment	48
4.5. Phospholipid Affinity towards Photosynthetic RC	49
4.6. Protein Dynamics and Charge Compensating Effects in Lipid Membranes	50
4.7. Free Energy Change of the $D^*Q_A \rightarrow D^+Q_A^-$ Electron Transfer	51
References	53

Abstract

In this chapter, studies on the influence of lipid environment on photosynthetic protein organization and functionality are reported. The study was carried out on two organisms representing different evolutionary levels: higher plants (spinach) and photosynthetic

* Corresponding author. Tel.: +39 0805443443;

E-mail address: catucci@chimica.uniba.it

¹ Dip. di Chimica, Università di Bari, Via Orabona 4, 70126 Bari, Italy

² IPCF-CNR, sez. Bari, Via Orabona 4, 70126 Bari, Italy

bacteria (*Rhodobacter sphaeroides*). In particular in the first part investigations on the influence of hyperosmotic stress on the lipid content in spinach at different plant organization levels (whole leaves, protoplasts, cells) and in *R. sphaeroides* (cells and sphaeroplasts) are reported. In the second part instead the chapter focuses on the effect of the lipid environment on PSII and bacterial reaction center (RC) activity. The main results can be summarized as follows:

- Hyperosmotic stress causes changes in the membrane lipid content for both spinach and *R. sphaeroides*; in particular a significant CL increment is observed for both species.
- The analysis of the lipids from PSII enriched membranes and from *R. sphaeroides* membranes is discussed; in particular CL structures are obtained by ESI-MS studies.
- The addition of exogenous phospholipids PG and CL better preserves PSII complexes from thermal inactivation, as indicated by Fluorescence Emission, RLS and OER measurements.
- The lipid environment has a deep impact on the quinone acceptor complex properties of *R. sphaeroides* RC. In particular, charge recombination kinetics show that specific phospholipids are responsible for the stabilization of the charge-separated state $D^+Q_B^-$.
- Endogenous and exogenous negatively charged phospholipids (like PG, CL, PI, and PS) can increase the lifetime of the charge-separated state of a factor of 3–5 with respect to zwitterionic phospholipids, mainly destabilizing the Q_A^- state.
- The slow component of the electron transfer reaction $D^+Q_A^-Q_B \rightarrow D^+Q_AQ_B^-$ is slower in PG proteoliposomes than in detergent and PC vesicles, and hence charge compensation effects are deduced to be faster in PC than in PG environment.

1. INTRODUCTION

Lipids represent a class of biological compounds that are fundamental for life: in fact, they are the basic constituents of biological membranes, which provide division into compartments and permeability barriers to the biological cells and cell organelles, regulating the flux of metabolites and solutes, and in which important energetic conversion processes can occur, such as respiration and photosynthesis. Furthermore, membrane lipids are necessary not only to sustain and embed the proteins that are an essential part of the biological membranes, but also for the interactions between membrane lipids and membrane protein complexes, especially in respiration and photosynthesis energy transduction chain complexes [1–4].

Photosynthesis is a crucial biochemical process in which carbohydrates are synthesized from carbon dioxide and an electron donor (water in case of higher plants and algae), by using light energy, in order to overcome the high energetic barrier associated to this thermodynamically unfavorable reaction.

In higher plants and algae, the photosynthetic reactions occurring through the thylakoid membrane, inside the chloroplasts, are called “light reactions”; the protein complexes involved in these reactions are PSII, PSI, and cytochrome b_6f complex [5–7]. These membrane complexes collaborate so as to convert the light energy, harvested by efficient LHCI and LHCII, into the chemical and electrochemical energy needed for the so-called dark reactions, which are carried out in the stroma

and bring about the production of carbohydrates. PSII is specialized in converting light energy into the electrochemical energy needed for the water oxidation and the reduction of a plastoquinone to plastoquinol. After this first redox step, an electron transfer chain takes place, reducing NADP^+ to NADPH at the PSI level and forming a trans-thylakoid membrane gradient for the ATP synthesis. Therefore, it can be asserted that at the thylakoid membrane level, the light energy is converted into chemical energy, contained in the high energy bond molecules NADPH and ATP. These latter are used in the “dark reactions” to form highly energetic carbohydrates.

In addition to higher plants and algae, another class of organisms capable of photosynthetic growth are the photosynthetic bacteria. Among these only cyanobacteria, which contain two different photosystems (PSI and PSII), can carry out oxygenic photosynthesis and are an important component of phytoplanktons in seas and lakes. All other photosynthetic bacteria can carry out only anoxygenic photosynthesis and contain a single photosystem, which is simply termed reaction center (RC). These organisms occupy a small ecological niche in the biosphere, but have played a fundamental role in the discovery of the molecular details in the complex mechanism of solar light conversion into metabolic energy. Photosynthetic bacteria can be classified on several basis. If distinguished on the basis of their photosystems, they can be either PSI or PSII-like, as previously mentioned. In this chapter the attention is paid to the latter kind and particularly to the two nonsulphur bacteria *Blastochloris viridis* (formerly *Rhodospseudomonas viridis*) and *Rhodobacter sphaeroides* (*R. sphaeroides*). The atomic structure of the RC from *R. sphaeroides* is available and the one obtained for *Blastochloris viridis* (*B. viridis*) as first crystallized membrane protein helped scientists fetch Nobel Prize in Chemistry in 1988 (see http://nobelprize.org/nobel_prizes/chemistry/laureates/1988/). On the other side, the RC from *R. sphaeroides* is simpler and therefore it has been possible to engineer a large number of point mutations.

1.1. PSII Structure

In higher plants, PSII is a large supramolecular pigment–protein complex (Fig. 1) responsible for oxidation of water into oxygen, carried out by converting light energy into the electrochemical energy needed for the next photosynthetic steps. It is embedded in the lipid matrix of the thylakoid membrane inside the chloroplasts and it is made of more than 25 protein subunits [6, 7]. At least nine of them interact and are necessary in reducing plastoquinone to plastoquinol and in the evolution of oxygen; the main subunits are represented by D1, D2, the cytochrome b_{559} dimer, CP47, and CP43. The D1 and D2 subunits each weighting about 40 kDa and each consisting of five transmembrane helices, coordinate both the manganese cluster of PSII and all the electron-transfer components [8]. CP43 and CP47 subunits are located close to RC, each consisting of six transmembrane helices and binding 14 and 16 chlorophyll *a* molecules [9], respectively, and thus acting like intrinsic light-harvesting proteins. The three extrinsic polypeptides having molecular masses 33, 23, and 17 kDa represent the OEC together with the manganese cluster. Other subunits act as antenna to harvest light in cooperation with the extrinsic, peripheral LHClI antenna complex, which binds about 50–65% of the total content of chlorophylls *a* and *b* and other pigments such as carotenoids [5, 6]. Therefore,

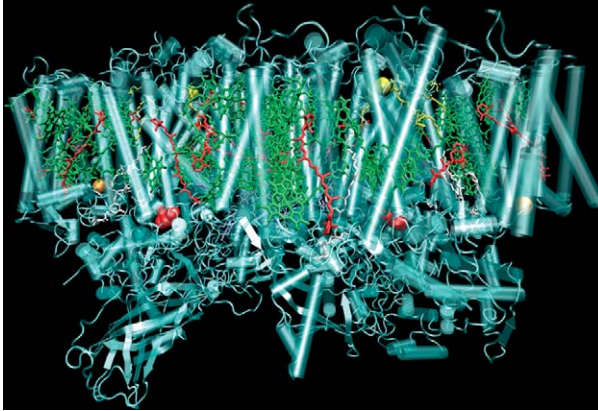


Figure 1 Crystal structure of PSII from *Thermosynechococcus elongatus*, PDB entry code 2AXT. The image was constructed using the VMD program (<http://www.ks.uiuc.edu/Research/vmd>). The protein scaffolding is visualized as cartoon, the cofactors as liquorice, and the metallic ions as Van der Waals spheres.

light energy is transferred to the PSII reaction center, thanks to all these pigments working as light collectors.

In the last years the methods for the extraction and purification of PSII complexes from higher plants, and for its stabilization in suitable suspension buffers have been optimized and it is commonly known that PSII can exist, *in vivo*, both in a monomeric and in a dimeric aggregation state [1,10,11]. It is reported that both these states are active, and some evidences show that the dimeric form in spinach could be more active and efficient [12].

1.2. Bacterial RC Structure

The photosynthetic RC from *R. sphaeroides* (Fig. 2) is a protein–pigment complex consisting of three polypeptides named L, H, and M, forming the scaffolding in which 10 cofactors are noncovalently bound. The protein spans the plasmatic membrane of the bacterium with a unique orientation between the periplasmic (outer space trapped between the plasmatic membrane and the cell wall) and cytoplasmic space. The highly hydrophobic subunits L and M are related by a c_2 symmetry axis and are almost immersed in the bilayer; each subunit is composed of five transmembrane (TM) helices denominated with letters from A to E that are oriented perpendicularly with respect to the membrane surface. The H subunit is mainly globular, protruding in the cytoplasm and contains an alpha helix that anchors it to the rest of the protein. The cofactors are arranged in two symmetrical branches denominated A and B. Starting from the periplasm and moving towards the cytoplasm we found two bacteriochlorophyll molecules organized in a dimer (D), two monomeric bacteriochlorophylls, two monomeric bacteriopheophytins, and two ubiquinone-10 in two distinct pockets denominated Q_A and Q_B . A non-heme Fe^{2+} ion sits between the two quinones.

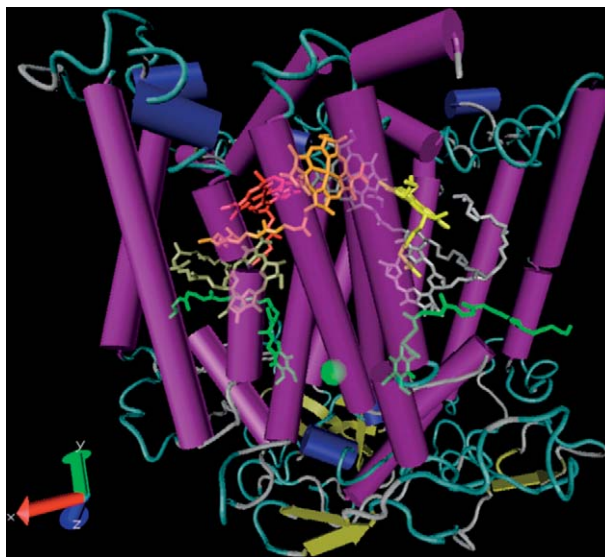


Figure 2 Crystal structure of RC from *R. sphaeroides*, PDB entry code 4RCR. The image was constructed using the VMD program. The protein scaffolding is visualized as cartoon, the cofactors as licorice, and the metallic ions as Van der Waals spheres.

The pigments present in RCs generate a rather rich absorption spectra covering the interval from 250 to 860 nm (up to 960 nm in *B. viridis*). These peaks are mainly attributed to the bacteriochlorins' Soret band at 366 nm, the bacteriopheophytins' Q_X and Q_Y transitions at 540 and 760 nm, respectively, the bacteriochlorophylls' Q_X and Q_Y transitions at 600 and 800 nm, and an extra band due to the excitonic coupling of the bacteriochlorophyll dimer at 860 nm. Several changes occur at the absorption spectra when the reaction center is illuminated, i.e. when it is in its charge-separated state. The most relevant change is registered at 860 nm, where the peak associated to the dimer is bleached under intense illumination.

1.3. Photosynthetic Membrane Lipids

The activity of intrinsic proteins, and in particular photosynthetic ones, can be influenced by several factors, such as temperature, pH, ionic strength, and so on. The biophysical and biochemical properties of intrinsic membrane proteins can also be strongly dependent on their lipid environment: specific protein–lipid interactions are suggested to be crucial for the structural and functional integrity of many prokaryotic and eukaryotic membrane proteins [13].

This also appears to be true for photosynthetic proteins both from higher plants and bacteria. The photosynthetic apparatus of *R. sphaeroides* is located in special compartments of the plasmatic membrane, called ICM, whose phospholipid composition, under phototropic conditions, consists of three major components: PC,

PE, PG with minor amounts of CL. The glycolipid SQDG and the ornithine lipid are also found [14]. PG is a lipid common to *R. sphaeroides*, *Rhodobacter capsulatus*, *Rhodospseudomonas palustris*, *Rhodospseudomonas gelatinosa*, *Rhodospirillum rubrum*, green bacteria, and chloroplasts.

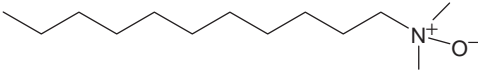
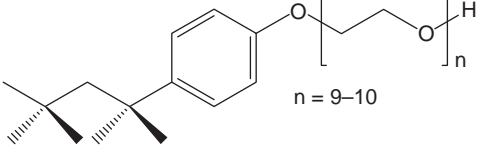
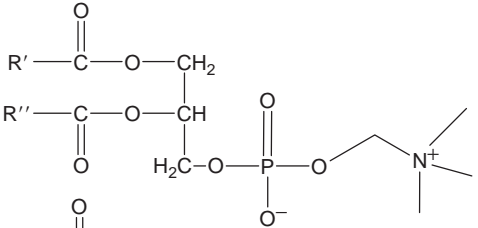
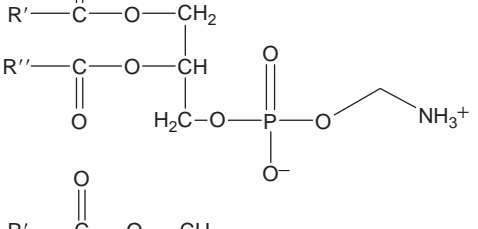
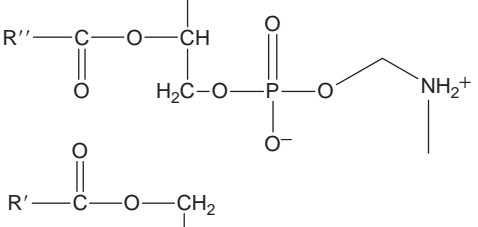
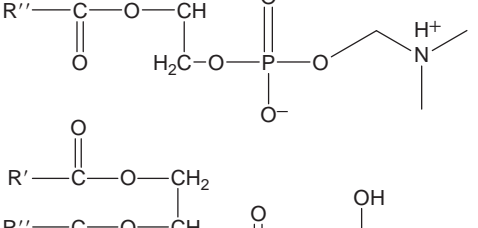
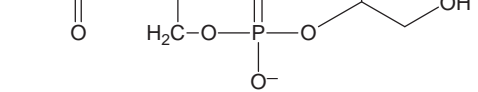
In contrast to the high quantity of phospholipids present in most of the cell membranes, plastid (such as chloroplast) membranes are characterized by the presence of a large amount of glycolipids: sulfolipids and galactolipids. The major part of plastid membrane glycolipids is constituted of galactolipids, which are neutral; they are 80% of the thylakoid membrane glycerolipids, and MGDG represents the main part (50%), DGDG being the remaining percent. These galactolipids are characterized by a very high content of polyunsaturated fatty acids: in some species linolenic acid (18:3) represents up to 95% of the total fatty acids. The sulfolipid SQDG constitutes about 7–15% of total plastid lipids, while phospholipids are only the remaining minor percentage, PG being the major plastid phospholipid. To do some evaluations, in spinach PG is about 7–10% of the total glycerolipid of thylakoids and of the envelope outer and inner membranes [15].

It is reported that PG can be directly involved in the spinach PSII complex dimerization process [1]; also the CL, whose structure can be considered as a PG dimer, resulted to be surprisingly abundant in the purified PSII complexes: its content was found to be double in PSII dimers with respect to monomers, this indicating a possible role played by CL in the PSII complexes stabilization [16].

The debate about the functions that CL can have with respect to membrane intrinsic proteins is still open: it is widely reported that CL is strictly required by mitochondrial and bacterial bioenergetic complexes, but also that the concentration and the acyl composition of this phospholipid can influence respiratory chain complexes functionality [17]. It is widely accepted that all proteins involved in the oxidative phosphorylation interact with CL; for example, removing of the CL causes the respiratory protein cytochrome *c* oxidase to be inactivated [18]. Furthermore, it is reported that the stability and functions of mitochondrial carrier proteins can be preserved by adding exogenous CL during the protein isolation and purification procedures [19]. Also the reaction center of the photosynthetic bacteria interacts with CL, as reported in the case of *R. sphaeroides*. Recently, a specific binding of CL has been evidenced by X-ray structures on the cytoplasmic side in contact with all three subunits of the RC from *R. sphaeroides* [20–22]. The RC structure reported by Camara-Artigas *et al.* [23] shows that CL binds somewhat closer to the Q_A than to the Q_B-site, although the difference is not too large (1M3X entry code in the Protein Data Bank). The shortest distances (oxygen to oxygen) from CL to Q_A and Q_B are about 17 Å and 20 Å, respectively. It is noteworthy to remark that the edge to edge distance between CL and PC in this structure (about 25 Å), does not differ very much from those of CL to Q_A and CL to Q_B.

In higher plants and in particular in chloroplasts, the knowledge of the CL functions is still quite poor, even if recently some attention has been directed to the lipid composition of membrane fraction increasingly enriched in PSII complexes [16,24,25]. Table 1 lists the membrane lipids that are mainly mentioned in this chapter.

Table 1 Lipid structures

Solubilizing molecule	Structural formula
Lauryl-dimethyl amino- <i>N</i> -oxide (LDAO)	
Triton X-100	
1,2-diacyl- <i>sn</i> -glycerol-3-phosphoryl choline	
1,2-diacyl- <i>sn</i> -glycerol-3-phosphoryl ethanolamine	
1,2-diacyl- <i>sn</i> -glycerol-3-phosphoryl <i>N</i> , methyl ethanolamine	
1,2-diacyl- <i>sn</i> -glycerol-3-phosphoryl <i>N,N</i> dimethyl ethanolamine	
1,2-diacyl- <i>sn</i> -glycerol-3-phosphoryl glycerol	

(continued)

Table 1 (continued)

Solubilizing molecule	Structural formula
1,2-diacyl-sn-glycerol-3-phosphoryl inositol	
1,2-diacyl-sn-glycerol-3-phosphoryl serine	
Monogalactosyldiacylglycerol (MGDG)	
Digalactosyldiacylglycerol (DGDG)	

2. LIPID CONTENT UNDER OSMOTIC STRESS IN HIGHER PLANTS AND IN PHOTOSYNTHETIC BACTERIA

The importance of lipids in the photosynthetic organisms can be evidently noticed when these organisms undergo several kinds of stress: for example, plants experience a wide range of environmental changes, which can be determined both by biotic stress (bacteria, viruses, fungi and parasites) and by abiotic stress (salinity,

extreme temperature, drought). All the stress factors can affect and negatively influence a plant growth rate, in a way which generally depends on the stress time: one of the most important and interesting abiotic factors limiting the productivity of crop plants is certainly salt stress. In the genetic engineering field, it is interesting to study the molecular elements involved in hyperosmotic stress responses, in order to find strategies to obtain salt tolerant plants [26]. These kind of transgenic salt-tolerant plants could also be useful because often they are found to be tolerant also to other stresses including chilling, freezing, heat and drought [27].

When plants undergo osmotic stress, they react by means of survival strategies, monitoring the external environment, and transferring the appropriate signals inside in order to adapt; as widely reported, the response can vary depending on different biological organization levels (cell, tissue, organ and whole plant level) [26]. However, the responses to osmotic stress can be different and can consist in the change of several biochemical parameters: for example the synthesis of stress hormones or of proteins specialized in prevention of denaturation and oxidative damage can occur [28, 29] in plants under hyperosmotic stress, but also changes in the ionic fluxes and synthesis of osmolites (sugar and amino acid derivatives) are likely to happen in order to regulate osmotic pressure and turgor, as reported in the literature [28].

Another kind of response can consist in molecular signalling, and some evidences indicate that phospholipids can be used as informational elements by the plant cells, thus confirming the importance of lipids for the nature, not only as fundamental constituent of the biological membranes [30]. Plant cells contain a variety of phospholipid-based signalling pathways including Phospholipase C (PLC), D (PLD), A_2 (PLA_2) and new pathways involving the formation of phosphatidylinositol 3,5-bisphosphate ($PI(3,5)P_2$) [30–32]. Furthermore, it has been reported that the osmotic shock can cause some microorganisms to modify their membrane lipid composition. In fact, the increasing of CL levels has been observed both for microorganisms exposed to hypotonic medium (*Halobacterium salinarium*) and for microorganisms exposed to high salt concentration (*R. sphaeroides*) [13, 33].

During the studies focused on the effect of hyperosmotic conditions on the lipid composition in plants and *R. sphaeroides*, we found the following main points:

1. Spinach (*Spinacia oleracea* L.): Hyperosmotic stress induces changes in the phospholipid content depending on the different plant organization levels studied (whole leaves, protoplasts, cells). In particular an increment of the total phospholipid content was observed in stressed whole leaves showing a salt stimulated phospholipid biosynthesis.
2. Photosynthetic bacteria (*R. sphaeroides*): Hyperosmotic stress does not induce the plasmatic membrane lipids to change their relative amounts at all the osmolite concentrations studied, but CL increases its content of two-three times after the hyperosmotic stress with all the osmolites tested. It was observed that NaCl had more evident effect on CL amount variation than KCl and sucrose.

2.1. Studies on Higher Plants (*Spinacia oleracea* L.)

Recently, we investigated the lipid response under osmotic stress conditions for different plant organization levels: whole leaves, freshly prepared protoplasmic suspension, and mesophyll cells obtained by reformation of the cell wall from protoplast suspension [24].

As it has been written previously, the plant organisms can respond to hyperosmotic conditions, by changing their lipid composition, this depending on the organization level considered: it has been observed by means of TLC measurements that in spinach whole leaves the higher NaCl concentration caused an increment in all phospholipid contents which are found to be proportional to salt concentration; furthermore, in the stressed samples a further lipid has been observed, migrating just below PI, identifiable as a phosphatidylinositol 3,5-biphosphate isomer, as it has been reported for several plant species undergoing hyperosmotic stress [32, 34]. At the same time it has been noticed that the increase of this band is accompanied by the decrease in the PI content, at higher NaCl concentration: this is in accordance with the assumption of an interconversion of PI in its phosphorylated form under osmotic shock and a key role of this PI isomer in osmo-signalling pathway in plant [32, 34].

2.1.1. Whole Leaves

The main lipid components of spinach leaves were identified as glycolipids MGDG, DGDG and SQDG and phospholipids CL, PE, PG and PI. Blue molybdenum staining allowed identifying PC and PS, which comigrate with DGDG and SQDG, respectively. The analysis also evidenced an increase of all phospholipid content proportional to salt concentration. The total lipid extract yield for the samples exposed to hyperosmotic stress results almost two-fold of that relative to non-treated samples, indicating a biosynthesis of phospholipids in stimulated plant cells. In fact it has been reported that stimulated cells with certain agonist, such as salts, induced hydrolysis and/or phosphorylation of some phospholipids with consequent second messenger production, which are utilized not only in the osmo-signalling pathway but also in the phospholipid biosynthesis [30].

Time course of the lipid content under a fixed hyperosmotic stress (NaCl 1.5 M), showed that phospholipid content increases at all incubation time explored reaching maxima values by 2 h. For example, in Fig. 3A it is possible to observe the normalized lipid values after 1 h of leaves incubation with NaCl 1.5 M. PG, which showed greater content than other lipids in the course of the overall experiment, redoubled its content by 1 h of osmotic shock. Only CL continued to increase its amount during an overnight incubation, overtaking also the PG content. An increase of CL content at PG expense under osmotic shock has been observed for extreme halophilic archaeon [35]; moreover, similar increasing of CL response to long incubation time in hyperosmotic medium have been reported for photosynthetic *R. sphaeroides* cells [13] suggesting that this lipid would help to sustain the cell bioenergetic system contributing to render the ATP synthesis more efficient.

2.1.2. Protoplasts

In protoplasts it was evidenced an increase of PG, PC and PI in stressed sample and, conversely to leaves, a decrease of CL and PE. Selective changes in lipid content and in biophysical properties of plant membranes have been reported for maize protoplast under osmotic shock [36]. In particular a loss of phospholipids, mainly those containing unsaturated fatty acyl chains, and a concomitant increase in neutral lipids such as triacylglycerols have been documented.

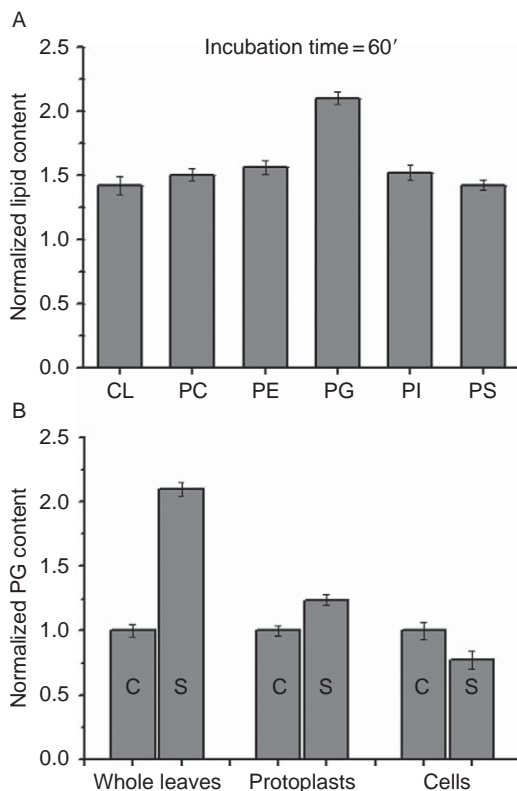


Figure 3 (A) Video densitometric analyses of phospholipid contents in whole spinach leaves in the presence of 1.5 M NaCl obtained from TLC profiles after 60-min incubation time. Values are normalized with respect to control samples (in the absence of NaCl). (B) Video densitometric analyses of PG contents in whole leaves, protoplasts, and cells in absence (C = control samples) and presence (S = shocked samples) of 1.5 M NaCl after 60-min incubation time. Values are obtained from TLC profiles and normalized with respect to the control samples.

2.1.3. Cells

After few days protoplasts synthesized the cell wall [37]. It is noteworthy a decrease in PG content when these cells were exposed to osmotic stress: this behavior, which was opposite to that observed for stressed leaves and protoplasts, underlined that hyperosmotic stress induces changes in the phospholipid content depending on the different plant organization levels studied.

The data summarized in Fig. 3B underline that hyperosmotic stress induces changes in the phospholipid content depending on the different plant organization levels studied. In particular an increment of the total phospholipid content was observed in stressed whole leaves showing a salt stimulated phospholipid biosynthesis. Different responses to osmotic shock were reported for the other systems.

The main variations were recorded for PG, which increased in stressed leaves and freshly isolated protoplasts while it decreased in stressed cells. These results suggest an important role of phospholipids, in particular of PG, in the osmotic stress response.

2.2. Studies on Photosynthetic Bacteria (*R. sphaeroides*)

In accordance with the data previously reported for whole leaves, whole cells and protoplasts, we studied the effect of the hyperosmotic stress on the lipid composition of R-26 strain *R. sphaeroides* cells [13]. Fundamentally, TLC measurements allowed to estimate the lipid contents as functions of incubation time and of incubation solution osmolarity, evaluating also the influence of changing the osmolite (NaCl, KCl and sucrose were used). As a result it was observed that all the plasmatic membrane lipids kept their relative amounts not altered after the maximum incubation time (more than 24 h) and at all the osmolite concentrations studied. Only CL, which represented the 1% of the total lipid extract, showed a completely different behavior increasing its content of two–three times after the hyperosmotic stress with all the osmolites tested. In such a case it can be concluded that neosynthesis of CL occurred under the hyperosmotic stress conditions tested. For a fixed incubation time, the CL amount was found to increase with the osmolite concentration, reaching a maximum (at 400 mM for NaCl). Moreover, it was observed that NaCl had a more evident effect on CL amount variation than KCl and sucrose; the CL content maximum was observed at 400 mM NaCl concentration.

The whole lipid extract was also analysed by ESI-MS, in order to get structural information about the lipid acyl chains; in particular, bicharged ions $[M-2H]^{2-}$ (indicating the molecular ion after losing two protons) at m/z 714.5 and 728.5 were attributed to two specific CLs deprived of two protons. More precisely, 714.5 m/z was attributed to CL having one C16 and one C18 acyl chains; the one at 728.5 m/z was considered due to CL with two C18 acyl chains. Mass-mass spectrometry showed the presence of the C18:1 fatty acid in the molecule generating 728.5 m/z and of C16:0 and C18:1 for the parent ion at 714.5 m/z . These two CL structures can be considered as the dimeric counterparts for the PG (36:2) and PG (34:1) which were present in the spectrum of the total lipid extract at m/z 773.5 and at m/z 747.5, respectively.

As for the *R. sphaeroides* cells, the effect of the external osmolarity was tested also on *R. sphaeroides* sphaeroplasts, obtained from the bacterial cells by disrupting the cell wall as reported in the literature [38]. Several reports assert that in some microorganisms the removing of the cell wall can affect the plasma membrane composition; for instance, in *Staphylococcus aureus* the disruption of the cell wall by lytic enzymes brought about an increase in CL amount [39]. In the case of *R. sphaeroides*, our results showed that the neosynthesis of CL induced by hyperosmotic conditions is only in part connected to the cell wall lysis (carried out by the bacterium) and that this phenomenon can also occur in sphaeroplasts. In particular, we observed that the CL content of sphaeroplasts is higher than that of intact cells and that the CL amount in sphaeroplasts significantly increases after osmotic stress becoming 10 times higher than in the control. The extent of CL increase in sphaeroplasts in the presence of external 400 mM NaCl was found to be higher than for intact cells as it can be observed in Fig. 4, suggesting that the capability of *R. sphaeroides* to neosynthesize CL seems to be increased after removing the cell wall.

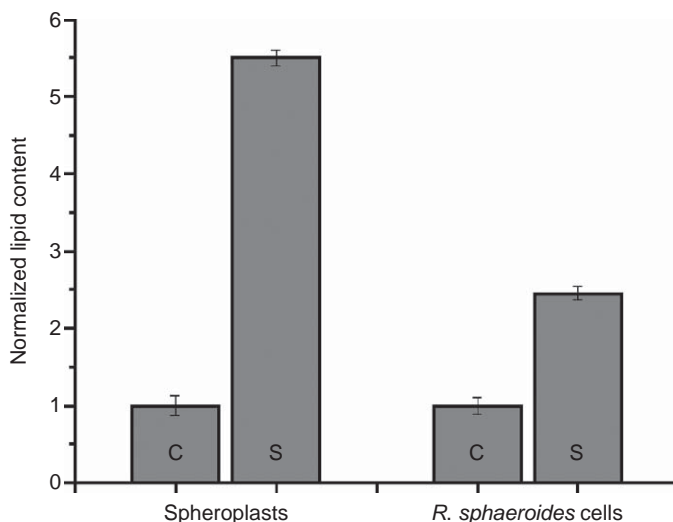


Figure 4 Video densitometric analysis of CL contents in *R. sphaeroides* cells and spheroplasts in the absence (C = control samples) and in the presence (S = shocked samples) of 400 mM NaCl after 60-min incubation time is reported. Values are obtained from TLC profiles and normalized with respect to the control samples.

3. ANALYSIS OF THE LIPIDS DIRECTLY SURROUNDING SPINACH PSII AND THEIR EFFECTS ON PSII ORGANIZATION AND ACTIVITY

During our research work focused on the analysis and characterization of the lipids directly surrounding the PSII and on the effects of particular phospholipids on PSII activity, we found the following main points:

1. CL amount per RC found in PSII dimers is higher than in PSII monomers.
2. Among the lipids directly surrounding the PSII dimer, CLs were found and characterized by ESI-MS, showing that the species have all C18 chains and variable saturation degrees.
3. The addition of exogenous phospholipids PG and CL seemed to better preserve PSII complexes from thermal inactivation, in particular in the presence of CL.

3.1. Analysis of the Lipids Directly Surrounding PSII

The importance of CL has been reported also in the maintenance of superstructural complexes of PSII of higher plants. TLC lipid analysis of different spinach membrane fractions progressively enriched in PSII (thylakoids, PSII enriched membrane fractions called BBYs, OG-cores, and PSII dimer and monomer complexes) showed that in addition to glycolipids (MGDG and DGDG), among phospholipids CL was enriched in the OG-core, monomer and dimer samples with respect to chloroplasts

and thylakoids. In particular, TLC calibration allowed estimating a CL content, which was double in PSII dimers with respect to PSII monomers counterpart, emphasizing the hypothesis that this particular phospholipid could be involved in maintaining the functional and structural properties of the PSII complexes. This result was very interesting because it was the first experimental evidence of the presence of CL in the thylakoid membrane of the spinach chloroplasts [40].

As it has been previously asserted, CL can be considered as the dimeric counterpart of PG, which has been found to be very important for the bacterial RC and for the PSII complexes. In fact, Barber *et al.* reported that PG is involved in PSII dimerization processes, as observed by PSII dimer reconstitution experiment. In particular, it has been found that PG (34:4) is crucial in stabilizing the PSII dimer structures [41–44] especially when it brings trans-hexadecanoic fatty acid (C16:1 Δ 3tr) [1, 45].

Furthermore, recently Loll *et al.* reported the crystal structure of PSII at 3.0 Å resolution [46], evidencing that one PG molecule is present within the protein scaffold at the interface between the D1 and the CP43 subunits [1,45,47]. As a further information, one of the possible binding site of PG to PSII was supposed to be on the D1 subunit, between aminoacid residues 27 and 225 [48]. It has also to be considered that the dimerization of LHCI and trimerization of LHCII proteins require the presence of PG [3, 48–52], in accordance for instance with the recent crystal structure of pea LHCII trimers, in which a PG molecule has been found at the interface between two monomers [51]. All these data confirm the structure-stabilizing role of PG with respect to the membrane protein complexes, and in particular with respect to the photosynthetic complexes.

To gain more information about the lipid compositions in the spinach PSII enriched membrane fractions, we carried out lipid analyses by means of ESI-MS [25]. As a result it was found that the qualitative lipid composition is kept not altered throughout the different PSII containing membrane fractions and in particular from BBYs to PSII dimer lipid extracts, even if the relative lipid amounts vary. In particular, observing the BBY lipid extract, a family of molecular ions $[M-H]^-$ (indicating the molecular ion after losing one proton) attributable to PA having one C16 and one C18 chains and variable saturation degrees, was found at 667.6 m/z (PA (34:4)). Commonly PA is not present in the lipid extract from animal tissues, but it is present in significant content in plants, as a product of phospholipase D; this presence has been considered either as an artifact caused by experimental conditions or as the effect of plant specific cellular responses caused by wounding or osmotic stress conditions [42–47 BBA].

Intense $[M-H]^-$ signals were observed at 741.8 m/z and 815.3 m/z and attributed to PG (34:4) and SQDG (34:3) respectively while, $[M-H]^-$ signals at 833.4 and 837.4 m/z were assigned to phosphatidylinositol (PI) (34:2) and PI (34:0), respectively.

A bicharged peak cluster at 723.0 m/z was then assigned to bicharged molecular ions of CLs ($[M-2H]^{2-}$) with C18 chains and variable saturation degrees.

In the PSII dimer lipid extract, the same lipid composition was observed, even if the intensity of PG signal was found to be remarkably increased with respect to the other peaks, thus confirming the strict connection between this phospholipid and the PSII complexes, in accordance with the data in the literature [1–4, 48].

Actually, an intense signal at 741.8 m/z was attributed to PG (34:4) after the loss of one proton, this structure being compatible with the trans-hexadecanoic fatty acid (C16:13tr) composition reported to be fundamental for PSII complexes [1]. In the PSII dimer extract, bicharged CL ions were found to generate the cluster at 719.4 m/z , giving rise to the hypothesis that the species having all C18 chains and twelve unsaturations could be more strictly connected to the protein complex.

It was interesting that the CL found in association with PSII had all C18 acyl chains, although the other lipids observed in the extracts brought both C16 and C18 chains; nevertheless a low intensity $[M-H]^-$ signal at 765.4 m/z was attributed to a PG (36:6), which is the precursor of the CLs observed. This confirmed that CL has characteristics which are specific and different from the other phospholipids directly surrounding the PSII complexes.

In order to obtain more information about the structure of the CL found in association with PSII, this lipid was isolated and purified from BBY lipid extracts by means of preparative TLC; then, the purified CL was analysed by high resolution ESI-MS, using also mass-mass analyses. As a result a $[M-H]^{2-}$ peak cluster was observed at 721.4713 m/z and attributed to bicharged molecular ions generated by a family of CLs after the loss of two protons; CL, in fact, is a unique phospholipid with a dimeric structure, having four acyl groups and potentially carrying two negative charges.

Daughter-fragment spectra (MS-MS analysis) of these molecular species were obtained and then analysed. The analysis evidenced that the mass signals were attributable to CLs having all C18 chains and twelve, eleven, ten, nine and eight unsaturations; the most intense signal was due to CL having ten total unsaturations.

For mitochondria and *R. sphaeroides* membranes, heterogeneity in the CL molecular species has been already reported [53]. Furthermore, for mitochondrial membranes the presence of CL bringing a significant higher proportion of C18 acyl chains has been documented [53]. It is likely that these structural peculiarities make the CL particularly suitable in creating contacts between different units in the protein quaternary structure, playing a functional role with respect to several membrane protein systems. This assertion is in accordance with the crystallographic evidences of the CL-improved interactions between different units in protein complexes like cytochrome *c* oxidase and the bacterial RC [22]. Moreover, the absence of buried or tightly bound CLs in the 3 Å structure of PSII dimers obtained by Loll *et al.* [34] suggests that CL could be located at the interface between PSII complexes, stabilizing the formation of supercomplexes [25].

3.2. Effects of Phospholipids on PSII Organization and Activity

Further studies were carried out by our research group in order to obtain preliminary information about the influence of phospholipids on PSII structural organization and activity: RLS, Fluorescence and OER measurements were performed on PSII monomers in the absence or in the presence of exogenous CL, PG or PA at 25 °C, as summarized in Table 2. In the RLS experiments it was observed that the phospholipid addition to PSII brought about an increment in the RLS peak, which was more evident with CL, this giving rise to the assumption that phospholipids, and in particular CL enhance a PSII aggregation process [1,54,55]. In fact, RLS is a very

Table 2 Values of fluorescence emission intensity (I_e) at 683 nm, RLS intensity (I_{RLS}) at 522 nm, and OER percentage preservation for PSII samples in the absence or in the presence of phospholipids CL, PG, and PA

	I_e (a.u.)	I_{RLS} (a.u.)	OER pres (%)
PSII	302.08	321.08	17.82
+ CL	170.02	803.83	36.19
+ PG	237.68	549	26.80
+ PA	203.69	810.53	0

sensitive and selective technique in probing the aggregative processes involving chromophores since the signal increases with the increasing of the coupling among them [56, 57].

These results were confirmed by the fluorescence measurements, in which the phospholipid addition to PSII caused a decrement of the fluorescence emission peak at 683 nm, thus indicating that phospholipids favour a chlorophyll *a* quenching [58–60] related to a PSII aggregative process. In fact, it has been reported that chlorophyll *a* fluorescence quenching happens in the presence of aggregates, as in the case of LHCII complexes [61]. Even in the fluorescence experiments the CL was found to give more remarked and evident effects than the other lipids studied.

OER measurements were carried out by studying the effect of adding exogenous PG, CL or PA to PSII before thermal inactivation (at 40 °C). In fact, in the photosynthesis the oxygen evolution is a very heat-sensitive process and it has been reported that the dissociation of the 33-KDa extrinsic subunit, could be the main responsible for the thermal inactivation, even at moderately high temperature (40 °C). This dissociation could depend upon conformational changes in the secondary structure of the 33-KDa subunit, bringing about the loss in oxygen evolution efficiency [62–68]. According to the PSII monomer OER percentage preservation values, obtained after 2 min of incubation at 40 °C, the addition of exogenous phospholipids seemed to better preserve PSII complexes from thermal inactivation, in particular in the presence of CL, except for PA, which completely inactivated the PSII oxygen evolution. This last finding could indicate that the presence of PA could cause PSII unspecific and non-functional aggregation processes. The particular PSII-stabilizing effect of CL against thermal inactivation, instead, could be due to the formation of active PSII aggregates, in accordance with the higher OER values reported for PSII dimers and for PSII aggregates obtained in lipid vesicles with respect to PSII monomers [12,42,69].

4. EFFECT OF PHOSPHOLIPIDS ON THE ENERGETIC AND DYNAMICS OF THE QUINONE ACCEPTOR COMPLEX IN BACTERIAL REACTION CENTRES

After massive studies of bacterial RC in detergent solution since its first isolation, back in the 1971 by G. Feher [70], in recent years more and more attention is given to the role played by native membrane lipids.

Several X-ray crystal structures of RCs from *R. sphaeroides* deposited in the Protein Data Bank (PDB) since 1999 contain one or more modelled lipids, the most occurring being a molecule of CL attached to the intramembrane surface of the M subunit. The position of the CL is interesting since its head-group engages in a network of protein–lipid bond interactions, some of which involve water molecules, that connects the C and E helices of the M subunit in a region where interdigitation with the D helix causes them to split apart; it also provides connections to the cytoplasmic end of the TM helix of the H-polypeptide. It has been found that the thermal stability of the protein is compromised when a point mutation weakens the binding of CL, indicating that this phospholipid plays a role in providing structural support at a potential weak point of the protein scaffold [22]. Since the lipid environment has a deep impact on the energetics of the acceptor quinone complex, it is interesting also to observe the position of the CL with respect to the Q_A and Q_B binding sites.

The natural environment in which bacterial RCs are embedded (ICM) is not suitable for detailed investigations of its physicochemical properties because of its great complexity. A commonly used strategy is the isolation and purification of the protein with the use of detergent and in particular LDAO. This procedure, anyway introduces several changes in the protein structure and functionality. In particular, the RCs are embedded in the native lipid bilayer in such a way that the hydrophobic tails of the lipids lay on the protein surface; on the other hand, in detergent, the hydrophobic tails are inserted into the protein like needles with the polar heads facing the aqueous solution. The discontinuity of the micelle system with the aqueous bulk phase makes an environment deeply different from the bilayer in which the RC are physiologically immersed and where the hydrophobic electron/proton carrier ubiquinone-10 is located, and where it can freely diffuse in a large space.

A more convenient approach is the RC reconstitution in liposomes since in such systems the native environment can be restored preserving the protein integrity. Moreover, the bilayer lipid composition and the lipid/protein molar ratio can be easily controlled so that the influence of individual parameters on the RC properties can be studied.

During our research work focused on the study of the response of the bacterial RC on the lipid environment, with particular emphasis on charge transfer reactions, we found the following main points:

1. The most reliable procedure for protein reconstitution is the so-called micelle-to-vesicle transition method using size exclusion chromatography for the detergent removal.
2. The lipid environment modulates the interaction with other membrane component such as the lipophilic electron carrier ubiquinone-10.
3. The binding of individual phospholipid molecules, rather than a complete bilayer environment, is responsible for the stabilization of the charge-separated state $D^+Q_B^-$ (see the following paragraph on “[Electron transfer reactions in bacterial RCs](#)”). The protein can “sense” the presence of a phospholipid even through a micelle of detergent such as Triton X-100.

4. Negatively charged phospholipids (either native like PG and CL or exogenous like PI and PS) can increase the lifetime of the charge-separated state of a factor of 3–5 compared to that found with zwitterionic phospholipids. The main reason for the prolonged lifetime of the charge-separated state is a rising of the Q_A^- energy level rather than a decrease of Q_B^- .
5. The slow component of the electron transfer reaction $D^+Q_A^-Q_B \rightarrow D^+Q_AQ_B^-$ is slower in PG proteoliposomes compared to values found in detergent and PC vesicles indicating that charge compensation effects are faster in PC than in PG environment. PG and CL added to PC bilayer decreased both the forward electron transfer $D^+Q_A^-Q_B \rightarrow D^+Q_AQ_B^-$ and the charge recombination $D^+(Q_AQ_B)^- \rightarrow D(Q_AQ_B)$. The rate constants as a function of relative PG or CL concentration follow a Michaelis–Menten type mechanism between bound and free anionic phospholipid.

To improve the understanding of the results reported later, it is useful to focus on the electron transfer processes occurring inside the bacterial RC.

4.1. Electron Transfer Reactions in Bacterial RCs

Upon light excitation, the bacteriochlorophyll dimer reaches the S1 excited state and transfers an electron to the adjacent bacteriopheophytin in the A branch within 3 ps. The electron then moves to the quinone in the Q_A pocket within 200 ps and finally reaches the quinone in the Q_B pocket after about 0.1 ms (Fig. 5). In isolated RC, the quinone Q_B can be easily removed [71], so after light excitation the

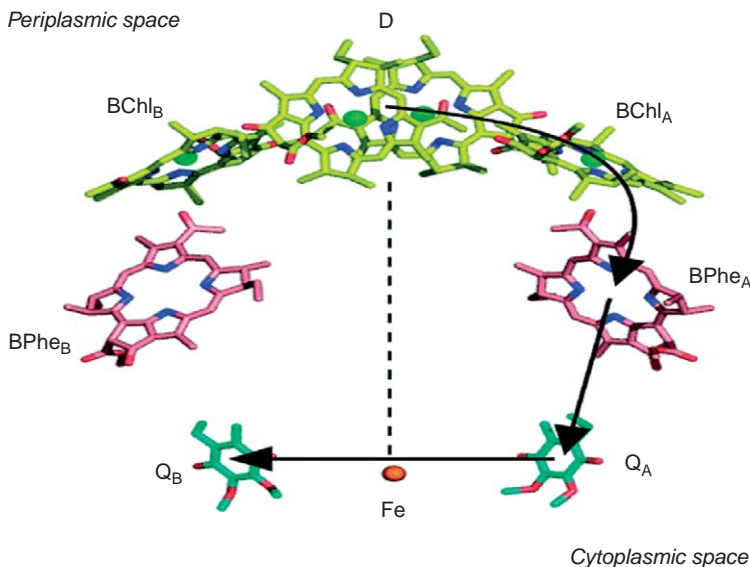


Figure 5 Cofactor arrangement in *R. sphaeroides* RCs (modified from <http://www.bris.ac.uk/biochemistry/research/mrj.html>).

$D^+Q_A^-$ state is formed, which undergoes to a charge recombination (CR) reaction with a characteristic rate constant $k_F = k_{AD} \sim 8 \text{ s}^{-1}$. The Q_B functionality can be restored by adding the ubiquinone-10 or other quinone analogs which can function as final electron acceptors. The photo-produced state $D^+Q_B^-$ recombines with a lifetime of about one to several seconds, depending on the chemical nature of the quinone and on the environment surrounding the RC.

The back reaction can be followed spectrophotometrically at several wavelengths (e.g., 430, 600, and 860 nm) and the forward electron transfer from Q_A^- to Q_B can be tracked at 771 nm where the bacteriochlorins undergo to electrochromic shifts due to the charge movement.

There are two possible routes for the electron transfer from Q_B^- to D^+ : one is the direct charge recombination with rate constant k_{BD} ; the other is through thermal repopulation of Q_A^- . Immediately after the formation of the $D^+Q_AQ_B^-$ state, the electron rapidly equilibrates between the two final acceptors with an equilibrium constant $L_{AB} = k_{AB}/k_{BA}$. When the Q_B -pockets are fully occupied, the charge recombination reaction is also monoexponential with a phenomenological rate constant:

$$k_D = (k_{AD} + k_{BD}L_{AB})(1/(1 + L_{AB})) \sim k_{AD}(1/(1 + L_{AB})) \quad (1)$$

The approximation holds because the direct recombination reaction from the $D^+Q_AQ_B^-$ state has a negligible kinetic constant ($k_{BD} < 0.1 \text{ s}^{-1}$).

The above equation was written assuming that the measured rate constant results from a weighted mean of k_{AD} and k_{BD} , the weight being the relative population of each state in a given moment. The phenomenological rate constant hence reflects the equilibrium constant L_{AB} , and is a measure of the free energy difference between the states $D^+Q_AQ_B^-$ and $D^+Q_A^-Q_B$.

The situation is more complex in presence of a subsaturating quinone concentration: in this case only a fraction of the Q_B -sites can be filled and the decay may have different time courses that will be discussed later.

4.2. RC Reconstitution in Artificial Lipid Bilayers (Liposomes)

After isolation and purification in detergent, RC can be readily reconstituted in lipid bilayer by using the so-called micelle-to-vesicle transition method as detailed in [72]. With this procedure, the lipid composition, the lipid to protein ratio and the size of ubiquinone-10 pool can be easily controlled.

Several properties of the RC change upon insertion in liposomes. The first is a rearrangement of the protein scaffolding which reflects also on cofactors and especially on the electronic distribution of the primary donor cation radical $D^{+\bullet}$. This can be evidenced by the position of its absorption band that is found in the region 850–870 nm: in lipid environment the band is generally found at longer wavelengths indicating a higher electronic coupling of the bacteriochlorophylls macrocycles [73]. Electron Nuclear Double Resonance (ENDOR) spectra of $D^{+\bullet}$ recorded for RCs in detergent and liposomes as well as for the more native

environment chromatophores show that the latter two environments are very close to each other while the spectrum recorded in detergent shows minor but noticeable differences.

A close inspection of the difference between chromatophores and detergent reveals the same peaks found in chromatophores and liposomes plus some additional peaks attributed to the so-called second state in which moieties of the BChl forming the dimer have a different orientation [72]. This finding, due to the presence of different dimer conformations, can be ascribed to the less rigid constraints imposed to the protein scaffolding by the detergent in the protein-detergent complex. These changes, induced by the isolation procedure, appear to be fully reversible upon reconstitution of RC in liposomes. The coincidence of the ENDOR spectra recorded in liposomes and chromatophores demonstrate that these reconstituted systems are reliable membrane-mimicking environments.

4.3. The Free Energy Change for the $D^+Q_A^-Q_B \rightarrow D^+Q_AQ_B^-$ Electron Transfer

While the differences found at the dimer side are not very large, the different solubilizing environments (direct micelles, reverse micelles, and proteoliposomes) induce deeper modifications on the energetics and kinetics of the primary and secondary quinones.

The reaction scheme depicted in Fig. 6 shows the kinetic constants for the set of the final electron acceptors reactions. The reactions take place in the neutral state (lower row) and in the charge-separated state generated in RC following the absorption of a photon in absence of an exogenous electron donor (upper row).

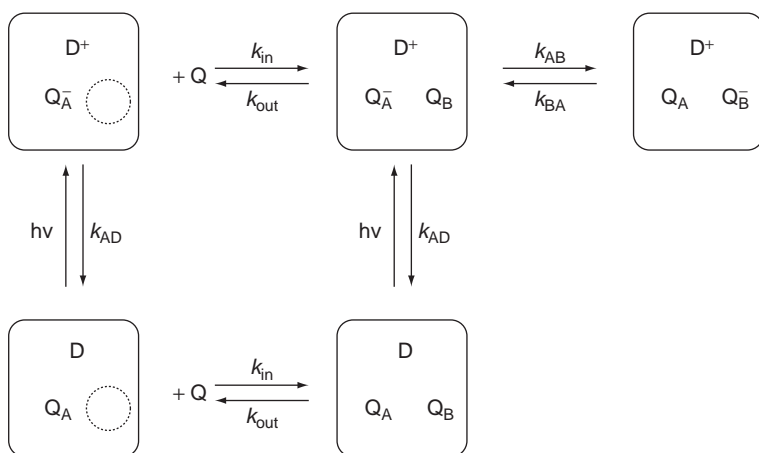


Figure 6 The kinetic scheme for reaction centers in the presence of quinone association and dissociation (quinone exchange), both in the dark and in the charge-separated state. The constants in the scheme are defined in the text. The direct recombination route from $D^+Q_AQ_B^-$ is not shown as its constant is negligible compared with the others. k_{in} and k_{out} are assumed to be independent of the redox state of Q_A .

Several descriptions of the scheme are available, the most detailed of which was given by Shinkarev and Wraight [74].

A closer look to the scheme reveals that the charge recombination reaction results from more than one elementary reaction: the electron hopping back and forth between Q_A and Q_B described by the kinetic constants k_{AB} and k_{BA} , occurring in the millisecond timescale; the secondary quinone binding and unbinding to the Q_B -site (*exchange reaction*) described by the kinetic constants k_{in} and k_{out} which can occur several times during the charge recombination process in the fast exchange regime, or can be frozen in the slow exchange regime; the true charge recombination reaction described by k_{AD} .

The influence played by the surrounding reflects on k_{in} , k_{out} , the kinetic constants of secondary quinone binding, and on free energy difference between the $D^+Q_AQ_B^-$ and $D^+Q_A^-Q_B$ states measured by L_{AB} .

The latter can be evidenced in the presence of a large quinone pool, when the Q_B -site is fully occupied and the exchange reaction can be neglected. As mentioned earlier, in this case the charge recombination follows a monoexponential decay with rate constant k_D , and from Eq. (1) it is possible to calculate the equilibrium constant L_{AB} for the electron transfer between Q_A^- and Q_B .

Figure 7 shows the time course of the charge recombination reaction of RCs embedded in different systems, after excitation with a laser pulse. It is immediately evident that the charge-separated state has a longer lifetime in liposome systems (PC, PE, PG, chromatophores) compared to detergents (LDAO, Triton X-100). Furthermore, within the liposome systems, the negatively charged phospholipid PG brings about a further increase of the charge-separated state lifetime with respect to the zwitterionic PC and PE. Similar kinetics can be observed using other,

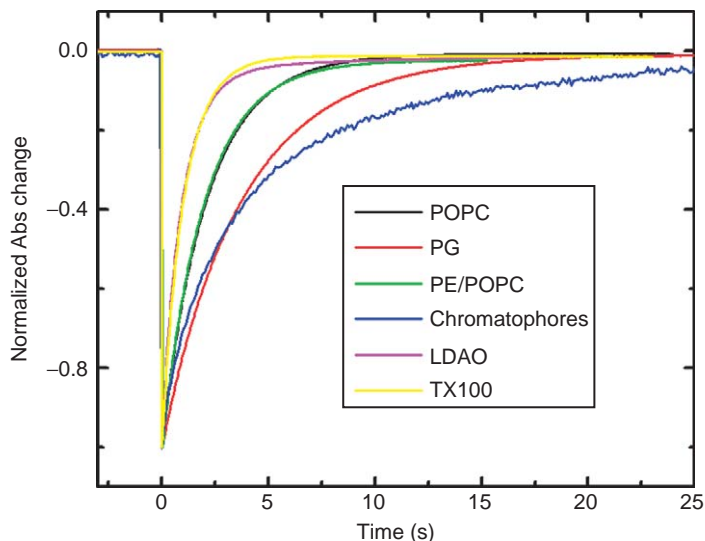


Figure 7 Flash induced charge recombination reaction for RCs incorporated in different systems. The light pulse was taken as reference time.

non-physiologic negatively charged phospholipids like PS or PI. The chromatophores, containing the three phospholipids PE, PC and PG in the ratio 2:1:1, show a kinetic similar to that of PG. This result indicates that the RC reconstitution in liposomes restores an environment structurally and functionally similar to that of the native membrane and underlines the peculiar role of negatively charged phospholipids in stabilizing the charge-separated state. Such stabilization, important for the optimum functioning of the RC *in vivo*, is realized by increasing the energetic gap between the $D^+Q_AQ_B^-$ and $D^+Q_A^-Q_B$ states. Whether this increase is realizing destabilizing Q_A^- or stabilizing Q_B^- will be discussed in a subsequent paragraph.

4.4. Quinone Exchange at Q_B -site Modulated by the Lipid Environment

As already mentioned, another property influenced by the RC solubilizing environment is the dynamic of quinone uptake and release at the Q_B -site. Such kinetic property is efficiently described by comparing the quinone release constant k_{out} with the charge recombination rate constant k_{AD} . In particular, when $k_{out} \ll k_{AD}$ the quinone exchange is slow compared to the charge recombination reaction, and, when subsaturating quinone concentration is present, the RC population can be clearly divided in two groups: those who have the Q_B -site occupied at the moment of the light excitation, and those who have the Q_B -site empty. In this case, found for instance in LDAO micelles, the charge-separated state decays following a biexponential function [71] with a fast phase of constant $k_F = k_{AD}$ and a slow phase of constant $k_S = k_D$ given by Eq. (1). Since the quinone uptake and release can be neglected during the charge recombination reaction, the relative amplitude of the slow phase results proportional to the Q_B -site occupancy: adding increasing quinone concentrations to Q_B -depleted RC, only the relative amplitudes of the two phases changes and not the rate constants. The situation is different in Triton X-100 micelles where the slow phase of the biexponential function describing the charge recombination reaction decays with a constant k_S that depends on the concentration of added quinone ranging from 2.7 to 1.1 s^{-1} . In this case the condition $k_{out}/k_{AD} > 1$ is realized, and the quinone uptake and release take place during the charge recombination reaction resulting in a fast exchange at the Q_B -site [75]. A similar behavior was found by Agostiano *et al.* [76] for RC solubilized in phospholipid reverse micelles with a bulk phase of hexane where the unbound ubiquinone-10 is highly soluble. The decay had a $k_F = k_{AD}$ and a slow phase with a constant k_S decreasing from 3 to 1 s^{-1} and a relative amplitude increasing up to 1.0 for $400 \leq Q/RC \leq 7000$.

In the case of PC proteoliposomes the decay of the charge-separated state can be also fitted by the sum of two exponentials with a fast phase of constant $k_F = k_{AD}$ and a slow phase of constant k_S decreasing from 1.5 to 0.5 s^{-1} when the Q/RC ratio is increased from 0.1 to 10 indicating a much higher affinity of ubiquinone-10 to the Q_B -site. Using the asymptotic k_S value in the equilibrium constant, L_{AB} is found to be 15.6.

The experimental decay curves of the charge separated state obtained at different Q/RC ratio can be used to obtain the unknown kinetic constants by solving

numerically the set of differential equations associated to the kinetic scheme using a fourth order Runge–Kutta method and minimizing the square-root difference between the simulated and experimental traces by using the “simple search method” [77] with a tolerance of 10^{-4} . From the best fit values of $k_{\text{in}} = 7.2 \cdot 10^7 \text{ M}^{-1} \text{ s}^{-1}$ and $k_{\text{out}} = 40 \text{ s}^{-1}$ were obtained, giving $K_{\text{B}} = 1.8 \cdot 10^6 \text{ M}^{-1}$ and $k_{\text{out}}/k_{\text{AD}} = 4.8$, which indicate respectively a very high affinity of ubiquinone-10 for the Q_{B} -site (it binds to the pocket almost quantitatively) and a relatively fast exchange regime.

The main issue arising from all these observations is the different behavior of the quinone exchange passing from direct micelles to proteoliposomes. The difference between these two solubilizing environments is their organization with the enzyme. RC-LDAO complexes have been characterized [78, 79] by Small Angle Neutron Scattering (SANS). The complex is formed by a toroidally-shaped micelle surrounding the most hydrophobic part (LM core) of the protein. In these complexes the detergent around the protein is organized with the chain perpendicular to the protein surface with its terminal part sticking into the protein. This reduces the hydrophobic portion of the detergent in which free quinone can diffuse ($\sim 1500 \text{ \AA}^3$) [78]. Moreover, crystallographic data [80] show that the detergent itself is located into the channel in which the quinone isoprenoid chain sits into the enzyme. This explains the slow exchange process of the quinone at its binding site. On the other side, the dimension of Triton X-100 micelles [81] are larger than those formed by LDAO, allowing a larger quinone pool size as well as a higher ligand mobility.

4.5. Phospholipid Affinity towards Photosynthetic RC

The rate constant of the charge recombination (and that of interquinone electron transfer as we will see later) can be used to monitor the affinity of different lipids to attach to the RC. The RC protein was embedded in intact PC bilayer vesicles in which different amounts of PG or CL phospholipids were also incorporated, and the rate constants of the CR in the liposome of mixed lipids were measured. Starting from pure PC vesicle, the rate CR k_{S} decreased gradually with increasing amount of PG in the vesicle, and reached a minimum level observed in pure PG. About 300 PG/RC can be determined for the 50% change in the PG/PC/RC vesicles, while $\Delta G^{\circ}(Q_{\text{A}}^{-}Q_{\text{B}} \rightarrow Q_{\text{A}}Q_{\text{B}}^{-})$ changed from -76.9 to -88.5 meV.

We carried out the same experiment with CL, and its effect upon incorporation into PC liposome is more complex than observed with PG. The change of rate constant of the back reaction seems to follow two distinct titration phases: the first indicates a very tight association of CL with RC and the second refers to a much looser attachment between CL and RC. Unfortunately, no single component CL vesicles with RC could be prepared, therefore the exact evaluation of the data awaits for further investigations.

The rate constants as a function of relative PG concentration follow Michaelis–Menten type mechanism indicating establishment of equilibrium between bound and free PG in both cases. CL has somewhat different behavior. The titration curve suggests two types of binding sites to the RCs. The high affinity site is close to stoichiometric ratio, and the other site becomes effective at higher concentration range. The strong binding site can be easily saturated and remains saturated even

after different preparation processes. The low affinity binding site requires about 300 CL/RC for half-saturation. It is important to note that care must be taken when liposomes are prepared from CL. First, the concentration of CL in the bacterial membrane is smaller than that of PC and PG. Higher concentration of CL can help us to understand the effect of anionic phospholipids in charge stabilization, but has not much physiological significance. Second, CL/RC intact vesicular system can not be made from pure CL.

Anionic lipids (CL and PG), can form contact surfaces between monomers of membrane proteins and contribute to production of multimers. Although the dimer formation of RCs of *R. sphaeroides in vivo* membranes is still questionable, recent crystallographic data suggest that CL facilitates molecular contacts in dimers of RCs [82] and stabilization of cytochrome c oxidase [83]. PG and CL seem also to be involved in the stabilization of PSII dimers and aggregates, respectively [1, 25]. Change of the electrostatic effects due to alteration of surface contacts is indicative of modified electron transfer parameters that was also proved by the effect of phase transition of DMPC/RC vesicles [84].

4.6. Protein Dynamics and Charge Compensating Effects in Lipid Membranes

There are increasing amounts of evidences that after light excitation the formation of the donor-acceptor charge pair, $D^+Q_A^-$, and the forward electron transfer from Q_A^- to the Q_B , induces charge compensating relaxation rearrangements accompanying conformation movements within the protein. Different conformation states were identified after crystallization of the RCs under dark and light conditions [85, 86].

The optical difference spectra of $D^+Q_A^-/PQ_A$ and/or $D^+Q_B^-/DQ_B$ reflect the electrochromic response of the BPheo absorption due to the different local electrostatic field around the $BPheo_L$ and $BPheo_M$. The electron transfer induces rearrangements of partial charges and/or hydrogen bonding networks within the protein [87], and might be kinetically gated by these conformational rearrangements [88]. Probably, the second electron transfer is also affected by structural reorganization of the protein [89].

The light induced difference absorption spectra of $DQ_A/D^+Q_A^-$ and $DQ_B/D^+Q_B^-$ have characteristic zero crossover points at around 745 nm for Q_B^- and 752.5 nm for the Q_A^- , and minimum and maximum absorption changes at lower and higher wavelengths [90]. From the kinetics of flash-induced absorption change followed at 771 nm of the RCs incorporated into different systems several component could be observed. The rates of the fastest phase, $k_{AB(1)_{fast}}$, for the LDAO, PC and PG samples were $16,800\text{ s}^{-1}$ ($\tau = 59\text{ }\mu\text{s}$), $15,500\text{ s}^{-1}$ ($\tau = 64\text{ }\mu\text{s}$) and $16,700\text{ s}^{-1}$ ($\tau = 60\text{ }\mu\text{s}$), respectively. A slower component of a few hundreds of microseconds related to the interquinone electron transfer was also resolved ($k_{AB(1)_{slow}}$). This phase is characteristic to the charge relaxation within the protein induced by the charge separation and the forward electron transfer, and may reflect the protonation of the characteristic amino acid residues of the protein. It can serve as a kinetic limitation of the overall electron transport between Q_A^- and Q_B . Our

measurements clearly indicate that both the PC and PG lipid environments modify both the size (amplitude) and the rate of this conformation movement. In PC, the rate of the overall electron transport increased by a factor of 1.3 compared to that of the LDAO (increased from 3100 to 4100 s⁻¹). This is in good agreement with the value reported by Taly *et al.* [84]. In PG, however, we measured a rate constant of 710 s⁻¹, which is significantly (4.4 times) smaller than that in LDAO.

The transient absorption signal of RCs in PC and PG liposomes at 771 nm fits the biphasic model of the first electron transfer [91]. This finding is consistent with earlier results that transient absorption change at 398 nm associated with the Q_A⁻ to Q_B electron transfer did not show components of 2–40 μs lifetimes if Q_A and Q_B was reconstituted with UQ₁₀ [92]. The observed lifetimes of the fast phase with few tens of microseconds do not differ significantly in LDAO, PC, and PG in our experiments. This is not the case with the slow component that includes the effect of charge relaxation.

Our results indicate that the charge compensation effects are somewhat larger and significantly faster in PC than in PG environment. These processes include possible rearrangements of hydrogen bonding network, i.e., protonation state of amino acid side chains including GluL212 and water molecules, and change in the van der Waals contacts within the protein with accompanying conformational movements. The change of the electrostatics on the surface of the protein in the close vicinity of the quinones and in the surrounding hydrogen bonding network, may alter the pK_a values of key amino acids and the redox midpoint potential of Q_A/Q_A⁻ and/or Q_B/Q_B⁻, essentially. Consequently, the kinetics and the energetics of the first and second electron transfer may also change.

4.7. Free Energy Change of the D⁺Q_A → D⁺Q_A⁻ Electron Transfer

The larger lifetime of the D⁺Q_AQ_B⁻ state reflects a larger L_{AB} equilibrium constant, but charge recombination experiments cannot reveal if the larger energy difference between the quinones is due to a rise of Q_A⁻ or a decrease of Q_B⁻. For this purpose, it is possible to carry a redox titration of the Q_A/Q_A⁻ couple, or to perform delayed luminescence measurements. In this latter technique, the fluorescence of D⁺, generated by a laser pulse, is measured at 920 nm as a function of time. During the lifetime of D⁺Q_A⁻, a small fraction of proteins decays through the D⁺Q_A state rather than by charge recombination, so the time course of this “delayed fluorescence” resembles that of the charge recombination itself. The probability of decaying through the D⁺Q_A state depends on the equilibrium constant for the reaction, D⁺Q_A ⇌ D⁺Q_A⁻ so the total energy emitted as delayed fluorescence is a measure of the relevant ΔG [93].

Investigation of several systems were reported by Nagy *et al.* [94]: RCs incorporated into Triton X-100, TX, detergent micelles without and with addition of PC, PG, and CL lipids together with DL emission from intact RC/lipid vesicles of single PC and PG components. After addition of PC to the TX/RC system, ΔG^o(D⁺ → Q_A⁻) (the standard free energy change of the D⁺/D⁺ → Q_A/Q_A⁻ electron transport) does not change significantly in good agreement with recent results of Rinyu *et al.* [95]: Δ(ΔG^o(D⁺ → Q_A⁻))_{TX/PC} = (ΔG^o(D⁺ → Q_A⁻))_{TX}

$-(\Delta G^\circ(D^* \rightarrow Q_A^-))_{TX+PC} = 2.3$ meV, which is well within the experimental error of about ± 3.3 meV. However, the free energy change is more pronounced if PG, or CL is added to the TX/RC solution: $\Delta(\Delta G^\circ(D^* \rightarrow Q_A^-))_{TX/PG} = 40.3$ meV and $\Delta(\Delta G^\circ(D^* \rightarrow Q_A^-))_{TX/CL} = 55.3$ meV. Moreover, when the RC is incorporated in vesicle made of single phospholipid, the amplitude of the delayed luminescence increases with respect to that of the TX/RC system: $\Delta(\Delta G^\circ(D^* \rightarrow Q_A^-))_{PC} = 29.3$ meV and $\Delta(\Delta G^\circ(D^* \rightarrow Q_A^-))_{PG} = 46.1$ meV.

Additional and large (20 meV) decrease was noted upon addition of PG to the PC/RC system, in contrast to CL, which did not modify the free energy level of the Q_A/Q_A^- redox couple measured in PC vesicle.

It is possible to calculate the value of $\Delta G^\circ(D^* \rightarrow Q_B^-)$ by the sum of $\Delta G^\circ(Q_A^-Q_B \rightarrow Q_AQ_B^-)$ and $\Delta G^\circ(D^* \rightarrow Q_A^-)$. For the systems TX/RC and liposomes made of PC and PG the $\Delta G^\circ(D^* \rightarrow Q_A^-)$ values are -947 , -921 , and -904 meV, respectively, while the $\Delta G^\circ(Q_A^-Q_B \rightarrow Q_AQ_B^-)$ values are -48 , -77 , and -89 meV. Interestingly, the values of $\Delta G^\circ(D^* \rightarrow Q_B^-)$ calculated for the three systems are -995 , -998 , and -993 meV, within the experimental error of the measurement. The effect of the phospholipids on the quinones is therefore mainly exerted on Q_A . This is rather surprising since in the published structure of RC crystallized with attached CL and PC, these lipids are almost equidistant from Q_A and Q_B . Both CL and PC bind to specific surface groups of the protein, but several weaker binding sites, which can loose their bound lipids during the purification procedure, may be present. The PC is a zwitterionic lipid, and the positive and negative charges, unlike in LDAO, are far from each other. Therefore, they can interact differently with the RC. Introduction of positive or negative charges or both of them can modify the binding interaction of the anionic lipid if PC is present.

The tertiary structure of the photosynthetic RCs is stabilized primarily by efficient atomic packing and helix dipole interactions [96]. The polar interactions, salt bridges, and hydrogen bonding interactions among the subunits do not play a significant role in the intramembrane structure; the coupling between the interhelical connections outside the membrane spanning regions, however, can be more important. PC binds close to one of this region interconnecting the L-D, and L-de helices (L-D is a transmembrane helix, and L-de is parallel to the membrane surface). This extended hydrogen bonding network involving the amino acid side chains as well as peptide bonding nitrogen and oxygen atoms, also in the M subunits close to the amino terminus of this subunit is very sensitive to the electrostatics of the protein surface. Note, that the shortest distance between the PC and the nearby amino acid, ValL220, is 4.12 Å only. Camera-Artigas *et al.* [23] discussed the possible effect of PC on the electrostatics of the BPheo in the inactive branch of the RC. In addition to this possible interaction, the effect of PC on Q_B , through the rearrangement of the hydrogen bonding network cannot be excluded. Q_A and Q_B , together with the iron-cluster, work as a structural and functional unit, called as “acceptor quinone complex” [87, 95]. Because of the extended hydrogen bonding network, it is expected that change in the Q_B electrostatics modify the function of the Q_A side, as well. Similar consideration can be drawn for the other phospholipids (CL and PG) used in our experiments.

REFERENCES

- [1] O. Kruse, B. Hankamer, C. Konczak, C. Gerle, E. Morris, A. Radunz, G.H. Schmid, J. Barber, Phosphatidylglycerol is involved in the dimerization of photosystem II, *J. Biol. Chem.* 275 (2000) 6509–6514.
- [2] S. Nussberger, K. Dorr, D.N. Wang, W. Kuhlbrandt, Lipid–protein interactions in crystals of plant light-harvesting complex, *J. Mol. Biol.* 234 (1993) 347–356.
- [3] S. Hobe, S. Prytulla, W. Kuhlbrandt, H. Paulsen, Trimerization and crystallization of reconstituted light-harvesting chlorophyll a/b complex, *Embo. J.* 13 (1994) 3423–3429.
- [4] A. Corcelli, M. Colella, G. Mascolo, F.P. Fanizzi, M. Kates, A novel glycolipid and phospholipid in the purple membrane, *Biochemistry* 39 (2000) 3318–3326.
- [5] H. Dau, K. Sauer, Exciton equilibration and Photosystem II exciton dynamics—A fluorescence study on Photosystem II membrane particles of spinach, *Biochim. Biophys. Acta.* 1273 (1996) 175–190.
- [6] B. Hankamer, J. Barber, E.J. Boekema, Structure and Membrane Organization of Photosystem II in Green Plants, *Annu. Rev. Plant. Physiol. Plant. Mol. Biol.* 48 (1997) 641–671.
- [7] J. Barber, Photosystem two, *Biochim. Biophys. Acta.* 1365 (1998) 269–277.
- [8] J. Barber, Photosystem II: A multisubunit membrane protein that oxidises water, *Curr. Opin. Struct. Biol.* 12 (2002) 523–530.
- [9] K.N. Ferreira, T.M. Iverson, K. Maghlaoui, J. Barber, S. Iwata, Architecture of the photosynthetic oxygen-evolving center, *Science* 303 (2004) 1831–1838.
- [10] G.F. Peter, J.P. Thornber, Biochemical evidence that the higher plant Photosystem II core complex is organized as a dimer, *Plant. Cell. Physiol.* 32 (1991) 1237–1250.
- [11] J.P. Dekker, M. Germano, H. van Roon, E.J. Boekema, Photosystem II solubilizes as a monomer by mild detergent treatment of unstacked thylakoid membranes, *Photosynth. Res.* 72 (2002) 203–210.
- [12] L. Catucci, W. Dörner, J. Nield, B. Hankamer, I. Vass, J. Barber, Isolation and characterisation of oxygen evolving Photosystem II core complexes from spinach in the presence of glycine betaine, in: G. Garab(Ed.), *Photosynthesis: Mechanisms and Effects*, Kluwer, Dordrecht, The Netherlands, (1998) pp. 973–976.
- [13] L. Catucci, N. Depalo, V.M. Lattanzio, A. Agostiano, A. Corcelli, Neosynthesis of cardiolipin in *Rhodobacter sphaeroides* under osmotic stress, *Biochemistry* 43 (2004) 15066–15072.
- [14] C. Benning, J.T. Beatty, R.C. Prince, C.R. Somerville, The sulfolipid sulfoquinovosyldiacylglycerol is not required for photosynthetic electron transport in *Rhodobacter sphaeroides* but enhances growth under phosphate limitation, *Proc. Natl. Acad. Sci. USA* 90 (1993) 1561–1565.
- [15] J. Joyard, E. Maréchal, C. Miège, M.A. Block, A.J. Dorne, R. Douce, Structure, distribution and biosynthesis of glycerolipids from higher plant chloroplasts, in: P.A. Siegenthaler, N. Murata (Eds.), *Lipids in Photosynthesis: Structure, Function and Genetics*, Kluwer, Dordrecht, The Netherlands, (1998) pp. 21–52.
- [16] N. Depalo, L. Catucci, A. Mallardi, A. Corcelli, A. Agostiano, Enrichment of cardiolipin content throughout the purification procedure of photosystem II, *Bioelectrochemistry* 63 (2004) 103–106.
- [17] P. Vreken, F. Valianpour, L.G. Nijtmans, L.A. Grivell, B. Plecko, R.J. Wanders, P.G. Barth, Defective remodeling of cardiolipin and phosphatidylglycerol in Barth syndrome, *Biochem. Biophys. Res. Commun.* 279 (2000) 378–382.
- [18] B. Gomez Jr., N.C. Robinson, Phospholipase digestion of bound cardiolipin reversibly inactivates bovine cytochrome bc1, *Biochemistry* 38 (1999) 9031–9038.
- [19] F. Palmieri, C. Indiveri, F. Bisaccia, V. Iacobazzi, Mitochondrial metabolite carrier proteins: Purification, reconstitution, and transport studies, *Methods. Enzymol.* 260 (1995) 349–369.
- [20] K.E. McAuley, P.K. Fyfe, J.P. Ridge, N.W. Isaacs, R.J. Cogdell, M.R. Jones, Structural details of an interaction between cardiolipin and an integral membrane protein, *Proc. Natl. Acad. Sci. USA* 96 (1999) 14706–14711.
- [21] A. Camara-Artigas, D. Brune, J.P. Allen, Interactions between lipids and bacterial reaction centers determined by protein crystallography, *Proc. Natl. Acad. Sci. USA* 99 (2002) 11055–11060.

- [22] P.K. Fyfe, N.W. Isaacs, R.J. Cogdell, M.R. Jones, Disruption of a specific molecular interaction with a bound lipid affects the thermal stability of the purple bacterial reaction centre, *Biochim. Biophys. Acta – Bioenerget.* 1608 (2004) 11–22.
- [23] A. Camara-Artigas, D. Brune, J.P. Allen, Interactions between lipids and bacterial reaction centers determined by protein crystallography, *Proc. Natl. Acad. Sci. USA* 99 (2002) 11055–11060.
- [24] L. Bavaro, L. Catucci, N. Depalo, A. Ventrella, A. Corcelli, A. Agostiano, Lipid content in higher plants under osmotic stress, *Bioelectrochemistry* 70 (2007) 12–17.
- [25] A. Ventrella, L. Catucci, G. Mascolo, A. Corcelli, A. Agostiano, Isolation and characterization of lipids strictly associated to PSII complexes: Focus on cardiolipin structural and functional role, *Biochim. Biophys. Acta.* 1768 (2007) 1620–1627.
- [26] O. Borsani, V. Valpuesta, M.A. Botella, Developing salt tolerant plants in a new century: A molecular biology approach, *Plant cell, Tissue Organ Cult.* 73 (2003) 101–115.
- [27] J.K. Zhu, Plant salt tolerance, *Trends Plant Sci.* 6 (2001) 66–71.
- [28] P.M. Hasegawa, R.A. Bressan, J.K. Zhu, H.J. Bohnert, Plant Cellular and Molecular Responses to High Salinity, *Annu. Rev. Plant. Physiol. Plant. Mol. Biol.* 51 (2000) 463–499.
- [29] J.K. Zhu, Genetic analysis of plant salt tolerance using Arabidopsis, *Plant Physiol.* 124 (2000) 941–948.
- [30] T. Munnik, R.F. Irvine, A. Musgrave, Phospholipid signalling in plants, *Biochim. Biophys. Acta.* 1389 (1998) 222–272.
- [31] T. Munnik, Phosphatidic acid: An emerging plant lipid second messenger, *Trends Plant Sci.* 6 (2001) 227–233.
- [32] T. Balla, Inositol-lipid binding motifs: Signal integrators through protein–lipid and protein–protein interactions, *J. Cell. Sci.* 118 (2005) 2093–2104.
- [33] S. Lobasso, P. Lopalco, V.M. Lattanzio, A. Corcelli, Osmotic shock induces the presence of glycardiolipin in the purple membrane of *Halobacterium salinarum*, *J. Lipid. Res.* 44 (2003) 2120–2126.
- [34] H.J. Meijer, C.P. Berrie, C. Iurisci, N. Divecha, A. Musgrave, T. Munnik, Identification of a new polyphosphoinositide in plants, phosphatidylinositol 5-monophosphate (PtdIns5P), and its accumulation upon osmotic stress, *Biochem. J.* 360 (2001) 491–498.
- [35] P. Lopalco, S. Lobasso, F. Babudri, A. Corcelli, Osmotic shock stimulates *de novo* synthesis of two cardiolipins in an extreme halophilic archaeon, *J. Lipid. Res.* 45 (2004) 194–201.
- [36] V. Furtula, I.A. Khan, E.A. Nothnagel, Selective osmotic effect on diffusion of plasma membrane lipids in maize protoplasts, *Proc. Natl. Acad. Sci. USA* 87 (1990) 6532–6536.
- [37] E. Balestri, F. Cinelli, Isolation and cell wall regeneration of protoplasts from *Posidonia oceanica* and *Cymodocea nodosa*, *Aquatic Bot.* 70 (2001) 237–242.
- [38] M.H. Jacobs, A.J. Driessen, W.N. Konings, Characterization of a binding protein-dependent glutamate transport system of *Rhodobacter sphaeroides*, *J. Bacteriol.* 177 (1995) 1812–1816.
- [39] Y. Kanemasa, T. Yoshioka, H. Hayashi, Alteration of the phospholipid composition of *Staphylococcus aureus* cultured in medium containing NaCl, *Biochim. Biophys. Acta.* 280 (1972) 444–450.
- [40] H.A. Schwertner, J.B. Biale, Lipid composition of plant mitochondria and of chloroplasts, *J. Lipid. Res.* 14 (1973) 235–242.
- [41] M. Fragata, E.K. Nenonene, V. Maire, I.S. Gabashvili, Structure of the phosphatidylglycerol-photosystem II complex studied by FT-IR spectroscopy, *J. Mol. Struct.* 405 (1997) 151–158.
- [42] M. Fragata, A. Menikh, E.K. Nenonene, Functional and structural aspects of the thylakoid lipids in oxygen evolution in photosystem II, *Trends Photochem. Photobiol.* 3 (1994) 201–210.
- [43] A. Tremolieres, P. Dainese, R. Bassi, Heterogenous lipid distribution among chlorophyll-binding proteins of photosystem II in maize mesophyll chloroplasts, *Eur. J. Biochem.* 221 (1994) 721–730.
- [44] G. Li, P.F. Knowles, D.J. Murphy, I. Nishida, D. Marsh, Spin-label ESR studies of lipid-protein interactions in thylakoid membranes, *Biochemistry* 28 (1989) 7446–7452.
- [45] O. Kruse, G.H. Schmid, The role of phosphatidylglycerol as a functional effector and membrane anchor of the D1-core peptide from photosystem II-particles of the cyanobacterium *Oscillatoria chalybea*, *Z. Naturforsch. [C]* 50 (1995) 380–390.

- [46] B. Loll, J. Kern, W. Saenger, A. Zouni, J. Biesiadka, Towards complete cofactor arrangement in the 3.0 Å resolution structure of photosystem II, *Nature* 438 (2005) 1040–1044.
- [47] B. Loll, J. Kern, W. Saenger, A. Zouni, J. Biesiadka, Lipids in photosystem II: Interactions with protein and cofactors, *Biochim. Biophys. Acta.* 1767 (2007) 509–519.
- [48] J. Garnier, B. Wu, J. Maroc, D. Guyon, A. Tremolieres, Restoration of both an oligomeric form of the light-harvesting antenna CP11 and a fluorescence state II-state I transition by Δ^3 -trans-hexadecenoic acid-containing phosphatidylglycerol, in cells of a mutant of *Chlamydomonas reinhardtii*, *Biochim. Biophys. Acta.* 1020 (1990) 153–162.
- [49] V.H. Schmid, K.V. Cammarata, B.U. Bruns, G.W. Schmidt, *In vitro* reconstitution of the photosystem I light-harvesting complex LHCl-730: Heterodimerization is required for antenna pigment organization, *Proc. Natl. Acad. Sci. USA* 94 (1997) 7667–7672.
- [50] A. Nilsson, D. Stys, T. Drakenberg, M.D. Spangfort, S. Forsen, J.F. Allen, Phosphorylation controls the three-dimensional structure of plant light harvesting complex II, *J. Biol. Chem.* 272 (1997) 18350–18357.
- [51] Z. Liu, H. Yan, K. Wang, T. Kuang, J. Zhang, L. Gui, X. An, W. Chang, Crystal structure of spinach major light-harvesting complex at 2.72 Å resolution, *Nature* 428 (2004) 287–292.
- [52] S. Nussberger, K. Dorr, D.N. Wang, W. Kuhlbrandt, Lipid-protein interactions in crystals of plant light-harvesting complex, *J. Mol. Biol.* 234 (1993) 347–356.
- [53] M. Schlame, K. Beyer, M. Hayer-Hartl, M. Klingenberg, Molecular species of cardiolipin in relation to other mitochondrial phospholipids. Is there an acyl specificity of the interaction between cardiolipin and the ADP/ATP carrier? *Eur. J. Biochem.* 199 (1991) 459–466.
- [54] P. Doty, R.F. Steiner, Light scattering and spectrometry of colloidal solutions, *J. Chem. Phys.* 18 (1950) 1211–1220.
- [55] V. Militello, V. Vetri, M. Leone, Conformational changes involved in thermal aggregation processes of bovine serum albumin, *Biophys. Chem.* 105 (2003) 133–141.
- [56] R.F. Pasternack, P.J. Collings, Resonance light scattering: A new technique for studying chromophore aggregation, *Science* 269 (1995) 935–939.
- [57] J.C. de Paula, J.H. Robblee, R.F. Pasternack, Aggregation of chlorophyll a probed by resonance light scattering spectroscopy, *Biophys. J.* 68 (1995) 335–341.
- [58] B.D. Hsu, J.Y. Lee, Fluorescence quenching by plastoquinone in an oxygen-evolving photosystem-II-enriched preparation, *J. Photochem. Photobiol. B* 30 (1995) 57–61.
- [59] O. Björkman, B. Demming, Photon yield of O₂ evolution and chlorophyll fluorescence characteristics at 77 K among vascular plants of diverse origins, *Planta* 170 (1987) 489–504.
- [60] F. Franck, P. Juneau, R. Popovic, Resolution of the Photosystem I and Photosystem II contributions to chlorophyll fluorescence of intact leaves at room temperature, *Biochim. Biophys. Acta.* 1556 (2002) 239–246.
- [61] W. Grudzinski, Z. Krupa, M. Garstka, W. Maksymiec, T.E. Swartz, W.I. Gruszecki, Conformational rearrangements in light-harvesting complex II accompanying light-induced chlorophyll a fluorescence quenching, *Biochim. Biophys. Acta.* 1554 (2002) 108–117.
- [62] J.J. Pueyo, M. Alfonso, C. Andres, R. Picorel, Increased tolerance to thermal inactivation of oxygen evolution in spinach Photosystem II membranes by substitution of the extrinsic 33-kDa protein by its homologue from a thermophilic cyanobacterium, *Biochim. Biophys. Acta.* 1554 (2002) 29–35.
- [63] S. Katoh, A. San Pietro, Ascorbate-supported NADP photoreduction by heated *Euglena* chloroplasts, *Arch. Biochem. Biophys.* 122 (1967) 144–152.
- [64] T. Yamashita, W.L. Butler, Inhibition of chloroplasts by UV-irradiation and heat-treatment, *Plant. Physiol.* 43 (1968) 2037–2040.
- [65] N. Lydakis-Simantiris, R.S. Hutchison, S.D. Betts, B.A. Barry, C.F. Yocum, Manganese stabilizing protein of photosystem II is a thermostable, natively unfolded polypeptide, *Biochemistry* 38 (1999) 404–414.
- [66] T. Shutova, K. Irrgang, V.V. Klimov, G. Renger, Is the manganese stabilizing 33 kDa protein of photosystem II attaining a “natively unfolded” or “molten globule” structure in solution? *FEBS. Lett.* 467 (2000) 137–140.

- [67] R.S. Hutchison, S.D. Betts, C.F. Yocum, B.A. Barry, Conformational changes in the extrinsic manganese stabilizing protein can occur upon binding to the photosystem II reaction center: An isotope editing and FT-IR study, *Biochemistry* 37 (1998) 5643–5653.
- [68] I. Enami, M. Kamo, H. Ohta, S. Takahashi, T. Miura, M. Kusayanagi, S. Tanabe, A. Kamei, A. Motoki, M. Hirano, T. Tomo, K. Satoh, Intramolecular cross-linking of the extrinsic 33-kDa protein leads to loss of oxygen evolution but not its ability of binding to photosystem II and stabilization of the manganese cluster, *J. Biol. Chem.* 273 (1998) 4629–4634.
- [69] E.K. Nénonéné, M. Fragata, Interaction of photosystem II proteins with non-aggregated membranes constituted of phosphatidylglycerol and the electrically neutral phosphatidylcholine enhances the oxygen-evolving activity, *Chem. Phys. Lipids* 91 (1998) 97–107.
- [70] G. Feher, Some chemical and physical properties of a bacterial reaction center particle and its primary photochemical reactants, *Photochem. Photobiol.* 14 (1971) 373–388.
- [71] M.Y. Okamura, R.A. Isaacson, G. Feher, The primary acceptor in bacterial photosynthesis: The obligatory role of ubiquinone in photoactive reaction centres of *Rp. sphaeroides*, *Proc. Natl. Acad. Sci. USA* 72 (1975) 3491–3495.
- [72] M. Trotta, F. Milano, L. Nagy, A. Agostiano, Response of membrane protein to the environment: The case of photosynthetic Reaction Centre, *Mater. Sci. Eng. C* 22 (2002) 263–267.
- [73] F. Muh, J. Rautter, W. Lubitz, Two distinct conformations of the primary electron donor in reaction centers from *Rhodobacter sphaeroides* revealed by ENDOR/TRIPLE-spectroscopy, *Biochemistry* 36 (1997) 4155–4162.
- [74] V.P. Shinkarev, C.A. Wraight, Electron and proton transfer in the acceptor quinone complex of reaction centres of phototrophic bacteria, in: J. Deisenhofer, J.R. Norris (Eds.), *The Photosynthetic Reaction Center*, Academic Press, San Diego, CA, (1993) pp. 193–255.
- [75] C.A. Wraight, R.R. Stein, Bacterial Reaction Center as a model for PSII: Turnover of the secondary acceptor quinone, in: AI, I.Y.e. (Ed.), *Oxygen Evolving System of Photosynthesis*, Academic Press, Tokyo, (1983) pp. 383–392.
- [76] A. Agostiano, L. Catucci, G. Colafemmina, M. Della Monica, G. Palazzo, M. Giustini, A. Mallardi, Charge recombination of photosynthetic reaction centres in different membrane models, *Gaz. Chim. Ital.* 125 (1995) 615–622.
- [77] J.C. Lagarias, J.A. Reeds, M.H. Wright, P.E. Wright, Convergence Properties of the Nelder-Mead Simplex Method in Low Dimensions, *SIAM J. Optimization* 9 (1998) 112–147.
- [78] M. Roth, A. Lewitt-Bentley, H. Michel, J. Deisenhofer, R. Huber, D. Oesterhelt, Detergent structure in crystals of a bacterial photosynthetic reaction centre, *Nature* 340 (1989) 656–662.
- [79] M. Roth, B. Arnoux, A. Ducruix, F. Reiss-Husson, Structure of the detergent phase and protein-detergent interactions in crystals of the wild-type (strain Y) *Rhodobacter sphaeroides*, *Biochemistry* 30 (1991) 9403–9413.
- [80] C.R. Lancaster, H. Michel, The coupling of light-induced electron transfer and proton uptake as derived from crystal structures of reaction centres from *Rhodospseudomonas viridis* modified at the binding site of the secondary quinone QB, *Structure* 5 (1997) 1339–1359.
- [81] P. Gast, P.W. Hemelrijk, H.J. Van Gorkom, A.J. Hoff, The association of different detergents with the photosynthetic Reaction Centre protein from *Rhodobacter sphaeroides* R26 and the effects on its photochemistry, *Eur. J. Biochem.* 239 (1996) 805–809.
- [82] G. Katona, U. Andreasson, E.M. Landau, L.E. Andreasson, R. Neutze, Lipidic cubic phase crystal structure of the photosynthetic reaction centre from *Rhodobacter sphaeroides* at 2.35 Å resolution, *J. Mol. Biol.* 331 (2003) 681–692.
- [83] S. Yoshikawa, K. Shinzawa-Itoh, T. Tsukihara, Crystal Structure of Bovine Heart Cytochrome c Oxidase at 2.8 Å Resolution, *J. Bioenerget. Biomembranes* 30 (1998) 7–14.
- [84] A. Taly, L. Baciou, P. Sebban, The DMPC lipid phase transition influences differently the first and the second electron transfer reactions in bacterial reaction centers, *FEBS. Lett.* 532 (2002) 91–96.
- [85] M.H. Stowell, T.M. McPhillips, D.C. Rees, S.M. Soltis, E.C. Abresch, G. Feher, Light-induced structural changes in photosynthetic reaction center: Implications for mechanism of electron-proton transfer, *Science* 276 (1997) 812.

- [86] G. Fritsch, J. Koepke, R. Diem, A. Kuglstatter, L. Baciou, Charge separation induces conformational changes in the photosynthetic reaction centre of purple bacteria, *Acta. Crystallogr. D* 58 (2002) 1660–1663.
- [87] P. Sebban, P. Maroti, M. Schiffer, D.K. Hanson, Electrostatic dominoes: Long distance propagation of mutational effects in photosynthetic reaction centers of *Rhodobacter capsulatus*, *Biochemistry* 34 (1995) 8390–8397.
- [88] M.Y. Okamura, M.L. Paddock, M.S. Graige, G. Feher, Proton and electron transfer in bacterial reaction centers, *Biochim. Biophys. Acta.* 1458 (2000) 148–163.
- [89] L. Nagy, V. Kiss, V. Brumfeld, S. Malkin, Thermal and structural changes of photosynthetic reaction centers characterized by photoacoustic detection with a broad frequency band hydrophone, *Photochem. Photobiol.* 74 (2001) 81–87.
- [90] J. Lavergne, C. Matthews, N. Ginet, Electron and proton transfer on the acceptor side of the reaction center in chromatophores of *Rhodobacter capsulatus*: Evidence for direct protonation of the semiquinone state of QB, *Biochemistry* 38 (1999) 4542–4552.
- [91] D.M. Tiede, J. Vazquez, J. Cordova, P.A. Marone, Time-resolved electrochromism associated with the formation of quinone anions in the *Rhodobacter sphaeroides* R26 reaction center, *Biochemistry* 35 (1996) 10763–10775.
- [92] J. Li, D. Gilroy, D.M. Tiede, M.R. Gunner, Kinetic phases in the electron transfer from P+QA-QB to P+QAQB- and the associated processes in *Rhodobacter sphaeroides* R-26 reaction centers, *Biochemistry* 37 (1998) 2818–2829.
- [93] H. Arata, W.W. Parson, Delayed fluorescence from *Rhodospseudomonas sphaeroides* reaction centers. Enthalpy and free energy changes accompanying electron transfer from P-870 to quinones, *Biochim. Biophys. Acta.* 638 (1981) 201–209.
- [94] L. Nagy, F. Milano, M. Dorogi, A. Agostiano, G. Laczko, K. Szebenyi, G. Varo, M. Trotta, P. Maroti, Protein/lipid interaction in the bacterial photosynthetic reaction center: Phosphatidylcholine and phosphatidylglycerol modify the free energy levels of the quinones, *Biochemistry* 43 (2004) 12913–12923.
- [95] L. Rinyu, E.W. Martin, E. Takahashi, P. Maroti, C. Wraight, Modulation of the free energy of the primary quinone acceptor (Q_A) in Reaction Centers from *Rhodobacter sphaeroides*: Contribution from the protein and the protein–lipid (cardiolipin) interactions, *Biochimica. Biophys. Acta – Bioenerget.* 1655 (2004) 93–101.
- [96] T.O. Yeates, H. Komiya, D.C. Rees, J.P. Allen, G. Feher, Structure of the reaction center from *Rhodobacter sphaeroides* R-26: Membrane–protein interactions, *Proc. Natl. Acad. Sci. USA* 84 (1987) 6438–6442.

VOLTAGE-DEPENDENT ION CHANNELS INDUCED BY CYCLIC LIPODEPSIPEPTIDES IN PLANAR LIPID BILAYERS: STRUCTURE, PROPERTIES, AND RESEMBLANCE TO NATIVE CHANNELS

Valery V. Malev,^{1,2} Olga S. Ostroumova,¹ Jon Y. Takemoto,³ and Ludmila V. Schagina^{1,*}

Contents

1. Introduction and Biological Aspects	60
2. Syringomycin E: Structure and Variations	61
3. Mechanism of Action of SRE	62
3.1. Physiological Studies	62
3.2. Studies Using Yeast	63
3.3. Studies with Erythrocytes	64
4. Channels Formed by Syringomycins in Artificial Lipid Bilayers	64
4.1. Small and Large Channels: Their Selectivity, Sizes, and Cluster Formation	65
4.2. Conductance of Small and Large SRE Channels	70
4.3. Comparisons of Multi- and Single-Channel Measurements with SRE-Modified Bilayers	74
4.4. Gating Charge of SRE Channels	79
4.5. Changes in a Mean Number of Small Channels in Channel Clusters	86
4.6. Influence of Dipole-Modifying Agents on Cluster Synchronization	91
4.7. Influence of Polymers on SRE Channel-Forming Activity	94
5. Summary and Conclusions	100
Acknowledgments	101
References	101

Abstract

The syringomycins (SRs) are cyclic lipodepsipeptides produced by the phytopathogenic bacterium *Pseudomonas syringae* pv. *syringae*. Discovered and described during the

* Corresponding author. Tel.: +7 (812) 2972460; Fax: +7 (812) 2970341;
E-mail address: lvschag@mail.cytspb.rssi.ru.

¹ Institute of Cytology of the Russian Academy of Sciences, 194064 Saint-Petersburg, Russia;
E-mail address: elchem@rbcmail.ru.

² Department of Chemistry, Saint-Petersburg State University, 198504 Petergof, Russia

³ Department of Biology, Utah State University, Logan, UT 84322-5305, USA;
E-mail address: jon@biology.usu.edu.

1980s and 1990s, the effects of the SRs on plant cells and inhibition of fungal and yeast growth are due to specific interactions with membrane lipids of target cells. Using one-side addition of SRs to a system consisting of a bilayer lipid membrane and two aqueous compartments, researchers have shown that the SRs form anion selective channels that possess unique and highly reproducible voltage sensitive properties. Moreover, SRs form two types of ion channels, namely “small” and “large,” that differ several-fold in their conductance. These initial findings generated interest in the SRs to (1) consider development of the SRs as antifungal agents, and (2) use SR channels as mechanistic models for native ion channels. Follow-up kinetic studies were conducted on the opening/closure of ion channels formed by the most abundant form of the SRs, syringomycin E (SRE). It was established that SRE’s channel activities and properties depend on several factors, including the surface charge and composition of membranes, the ionic strength of bathing solutions, and the concentration of membrane modifying agents. Estimations of the inner radius of SRE channels and their anion selectivity showed that the large channels are clusters of synchronously functioning small ones and both clustered and nonclustered single channels have similar radii. Determinations of the gating charge of the SRE channels showed that they are asymmetrical lipid pores stabilized by lipopeptide molecules. The involvement of membrane lipids in the channel structure provides explanations for the dependencies of SRE channel properties on the earlier-mentioned factors, and a model is proposed that features the influence of a dipolar membrane potential on the gating charge of SRE channels. More recent studies have focused on the effects of actin on SRE channel-forming activity. Activity is induced if SRE and actin species are added to opposite sides of the lipid membrane but absent when added on the same side. The observed actin influence is explained as the consequence of changing the bilayer structure with one-side cooperative sorption of actin molecules. As actin is a major component of the cytoskeleton, the sensitivity of cells (fungi, yeasts, and human erythrocytes) to SRs may be modulated by intracellular actin. Other recent studies have been devoted to the properties of the large SRE channel clusters. It was established that the number of small channels synchronously working in such clusters depends on the transmembrane potential, whereas the lifetimes of the small and large channels are not dependent on this parameter. The dependence on electrical potential is altered with addition of dipole-modifying agents. Overall, the resemblance of the properties of the SRE channels with those of natural ion channels suggests their value as models for investigating ion channel structure, regulation, and function.

1. INTRODUCTION AND BIOLOGICAL ASPECTS

Pseudomonas bacteria are well known for producing a diverse array of secondary metabolites [1]. A well studied group of such metabolites are the cyclic lipodepsipeptides (CLPs) (also abbreviated LDPs) that are produced by *Pseudomonas syringae* pv. *syringae* (Pss) [2,3]. Pss is a widespread plant epiphyte that grows on the aerial surfaces of many plants [4]. Its success on plants may be partly due to capabilities for killing or suppressing other microbes, allowing it to effectively compete for nutrients and space. Moreover, Pss is a virulent opportunist on compromised host plants and consequently associated with a variety of necrotic plant

diseases [5]. Historically, the Pss CLPs themselves have been implicated as major virulence factors that cause particular plant diseases. An expanded view is that they are primarily microbial antagonists during epiphytic growth, and at higher concentrations and when Pss begins to overwhelm its compromised hosts—they are phytotoxic as well.

The Pss CLPs are divided into two groups on the basis of their structural differences [2,3,6]. They are the small CLPs (MW 1100–1300) and the large CLPs (MW 2200–2500). The former display potent fungicidal properties—particularly against yeasts such as *Saccharomyces cerevisiae* [7], and the latter are mainly bactericidal—particularly against Gram-positive bacteria [8,9] although certain members are also antifungal. At concentrations that exceed their effective antimicrobial activities, both kinds of CLPs cause necroses of plant tissues, and the larger CLPs generally being more effective in this regard [7,10]. Members of the small CLPs are often termed the syringomycins and the large CLPs are commonly called the syringopeptins.

The fungicidal and bactericidal activities of the Pss CLPs are not confined to plant associated microbes. They also kill several human pathogenic microbes [7–9, 11]. These include some of the most significant infectious microbes of humans: *Candida albicans*, *Cryptococcus neoformans*, *Aspergillus fumigatus*, *Staphylococcus aureus*, *Enterococcus faecalis*, *Listeria monocytogenes*, and *Streptococcus pyogenes*. In addition, certain syringopeptins (e.g., SP508A and SP25A) inhibit *Mycobacterium smegmatis*, which is a commonly used surrogate for the tuberculosis bacillus, *Mycobacterium tuberculosis*. A report that the small CLP syringomycin is also inhibitory to *M. smegmatis* has been published [12]. These findings suggest that the Pss CLPs are potential lead drug compounds for combating human infectious diseases.

2. SYRINGOMYCIN E: STRUCTURE AND VARIATIONS

Among the small CLPs, the best studied in terms of mechanism of action is (SRE). It is the subject of most of the mechanism of action studies described in this review. Its structure is shown in Fig. 1.

It is composed of nine amino acids with the C-terminus 4-chlorothreonine ester linked to the N-terminus serine [13,14]. The N-terminus serine is N-acylated to 3-OH dodecanoic acid. The closest analogs, syringomycins A₁ and G, vary in the length of the 3-OH acyl chain with 10 and 14 carbons, respectively. The syringotoxins, syringostatins, and pseudomycins are structurally more distant [13–16]. All of the syringomycin analogs (close and distant) possess the structural motif dehydroaminobutanoic acid- β -OH aspartic acid-4-chlorothreonine-serine-3-OH acyl chain, and it is the structural signature for this and additional members of this family of lipopeptides.

The kind of syringomycin analog produced is often related to the specificity of the bacterium for its plant host. For example, SRE and SRs A₁, and G are typically produced by Pss strains isolated from stone fruits and grasses [13,14], and Pss strains from citrus produce the syringotoxins [15]. The syringostatins were extracted from a

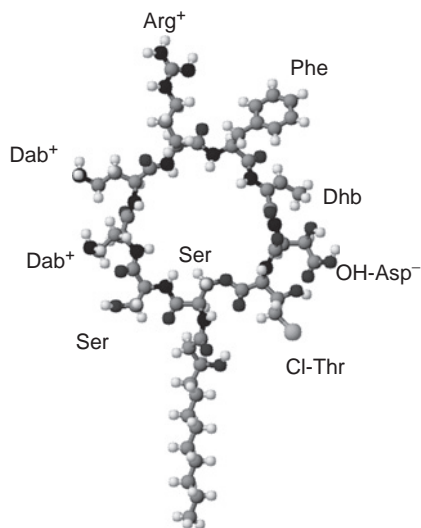


Figure 1 The zwitterionic form of syringomycin E. Arg⁺, arginine; OH-Asp⁻, 3-hydroxiaspartic acid; Dab, 2,4-diaminobutyric acid; Dhb, dehydro-2-aminobutyric acid; Cl-Thr, 4-chlorothreonine; ser, serine; Phe, phenylalanine.

Pss isolate of lilac [13], and the pseudomycins from a barley strain [16]. Production is not confined to Pss. For example, syringotoxin is produced by a strain of *Pseudomonas fuscovaginae* [17]. SRE and syringomycin G are produced by *Pseudomonas syringae* pv. *atrofaciens* that causes basal glume rot of cereals [18]. The structural variability among the syringomycin analogs likely co-evolved with changes in the chemistry and microbial flora of plants that host the pseudomonades. Thus, it is conceivable that further structural variations are yet to be found.

3. MECHANISM OF ACTION OF SRE

3.1. Physiological Studies

The earliest physiological studies with plant tissues and yeasts suggested that SRE interacts with biomembranes [3]. The observations pointed particularly to the plasma membrane as the cellular target. For example, SRE (1–10 µg/ml) addition to red beet slices and yeast showed rapid and pronounced Ca²⁺ and K⁺ fluxes across their cell surfaces [3]. SRE also caused pronounced changes in H⁺ fluxes and alterations in H⁺-ATPase activities [19–22]. The flux changes coincided with Ca²⁺-dependent phosphorylation and dephosphorylation of plasma membrane proteins that may result from these ion imbalances [23]. When the various physiological effects are considered together, it is reasonable to speculate that pore formation at the plasma membrane is the underlying basis for the inhibitory effects [3,24,25].

3.2. Studies Using Yeast

Studies with SRE-resistant yeast mutants provide further insight into SRE's mechanism of action. SRE-resistant gene complementation groups each corresponding to separate functional genes needed for SRE action were found and characterized [26]. One group of genes encodes sterol biosynthetic enzymes [27]. For example, *SYR1/ERG3* encodes a sterol C5,6 desaturase for the biosynthesis of ergosterol, the primary sterol in the yeast plasma membrane [27]. Another group of complementing genes functions in sphingolipid biosynthesis. *SYR2* and *FAH1* encode a sphinganine C4-hydroxylase and a very long fatty acid chain α -hydroxylase, respectively, revealing that C4-OH phytoceramide and the α -hydroxylated acyl chain moieties of sphingolipids are required for SRE action [28,29]. Also, *IPT1* and *CSG1/CSG2* encode enzymes that decorate yeast sphingolipids with phosphoinositol and mannose, respectively, showing that these sugar group moieties also promote SRE action [30]. Sphingolipids are needed for yeast cell viability [31], but these particular sphingolipid functional defects in the SRE-resistant mutants (i.e. hydroxylation and glycosylation) are not essential for growth. Apparently, their normal expression imparts structural features to sphingolipids that allow susceptibility to SRE but at the same time are dispensable for growth. Altogether, the identification of these genes reveals that sterols and sphingolipids are important for yeast's susceptibility to SRE. Both of these lipid classes occur predominantly in the plasma membrane. Therefore, recognition of their importance for SRE action is consistent with the notion that the plasma membrane is the cellular target [30,32].

Since SRE-resistant conferring sphingolipid biosynthetic defects do not prevent yeast growth, the respective resistant mutants may be propagated and the various defective sphingolipids extracted. Such defective sphingolipids can then be studied for their influences on SRE pore formation in planar lipid bilayers. The influence of sphinganine C4 hydroxylation on pore formation was studied using planar lipid bilayers containing either wild-type C4-OH sphingolipids or *syr2* mutant non C4-OH sphingolipids, each at 20 mole% with 80 mol% of dioleoylphosphatidylserine (PS): dioleoylphosphatidylethanolamine (PE): ergosterol (1:1:1). In these and farther cited papers currents induced by the one (*cis*-) side SRE (or other CLPs) addition to an electrolyte solution divided into two compartments by an artificial lipid membrane were measured. "Transmembrane positive voltage" means that the *cis*-side compartment is positive with respect to *trans*-side. With exposure to SRE, the rate of the macroscopic current increase with an applied voltage (120 mV) was ~ 40 fold lower with the mutant non C4-OH sphingolipids as compared to the case with wild-type C4-hydroxylated sphingolipids. The current responses with SRE addition to bilayers containing no sphingolipids were nearly identical to those seen with wild-type sphingolipids. In contrast to the difference in macroscopic currents, the mutant and wild-type sphingolipids showed no difference in their influences on the properties of low conductance single channels. For example, the current vs. voltage curves of the single unit currents measured between -200 and 200 mV were the same for both cases [33]. Overall, these results show that the non C4-OH sphingolipids do not affect SRE single-channel properties, but rather they impede pore-forming activity. When combined with the observation that *syr2* mutants are resistant to SRE, it is

suggested that the diminished ability to form pores is the basis for the resistance to this metabolite. Thus, pore formation is suggested to be the mechanism by which SRE inhibits the growth of yeast.

The structural features of the yeast sphingolipids that promote SRE action also contribute to the hydrogen bonding capacities of the sphingolipids. The sphingoid base C4-OH and very long fatty acid α -OH groups, and the carbonyl and hydroxyl groups of the mannosyl and phosphatidylinositol sugars are all excellent hydrogen bond donors and acceptors. Such hydrogen bonding is a strong contributor to the liquid ordered sphingolipid and sterol-rich domains in biomembranes [34] including yeast membranes [35,36]. The basis for the sphingolipid structural and sterol requirements for SRE action in yeast may lie in the degree of hydrogen bonding that occurs in these domains between the sphingolipids and SRE [37].

3.3. Studies with Erythrocytes

SRE is also capable of forming pores in the erythrocyte membrane [7,38,39]. Concentration-dependent hemolysis was induced by SRE in a fraction (24–37%) of total erythrocytes with the remainder showing SRE enhanced permeability for ^{86}Rb and monomeric hemoglobin with kinetics that indicated formation of pores [38]. As with planar lipid bilayers the erythrocyte membrane pores displayed eventual inactivation. The pore radius were estimated to range between 0.7 and 1.7 nm with increasing SRE concentration [39]—large enough to accommodate monomeric hemoglobin [38]. Cholesterol depletion or ergosterol substitution promoted the pore-forming activity [38]. This effect appears to be the same of the sterol effects in planar lipid membranes [32]. The observations support the general findings that sterols influence SRE's pore-forming capabilities.

4. CHANNELS FORMED BY SYRINGOMYCINS IN ARTIFICIAL LIPID BILAYERS

Currents induced by SRE in artificial lipid membranes were first observed by Hutchison *et al.* [24] and Feigin *et al.* [40]. Later, lipid bilayers were also used to study the channel-forming activity of this toxin and its analogs, since the work with living cells strongly indicated that such an activity formed the basis for its effects [25, 41]. From multichannel measurements with SRE-modified bilayers, a very strong dependence of the currents induced by SRE on its concentration in aqueous solution was established: the stationary currents through lipid bilayers were proportional to the sixth to seventh power of the concentration [40,42]. These findings implied that 6–7 SRE molecules participate in the conductance induced by the toxin which is similar in this respect to the polyene antibiotics that form relatively large aqueous pores stabilized by approximately the same number of molecules [43]. These experimental findings, as well as the earlier-indicated data on the SRE-induced pore formation in red blood cell membranes, led to the expectation that SRE also forms relatively large pores in lipid bilayers.

4.1. Small and Large Channels: Their Selectivity, Sizes, and Cluster Formation

Several levels of current fluctuations are observed in membranes modified by SRE. These various levels are visible in sample records (Fig. 2(A, B)) for membranes made from equimolar mixture of PS and PE (PS/PE) and bathed in different NaCl concentrations. At least two different types of channels, large and small, are present, and the dwell times of the higher-conducting channels are significantly greater than those of the lower conducting ones. Other CLPs such as syringopeptin 22A, syringostatin A, and syringotoxin B also demonstrate single channels with two levels of conductance [25].

Figure 3 illustrates the amplitude histograms of the SRE channel opening/closing measured at a fixed transmembrane potential of -200 and -50 mV with 0.1 and 1 M NaCl concentrations in the bathing solutions, respectively. For SRE channels, it was shown that value $i = 2$ resulted from the virtually simultaneous random opening and closing of two independent channels, which have equal conductance. For large channels, which correspond to values $i > 2$, such an explanation is not applicable [44,45]. So, these results indicate that the large and small channels are either two sets of channels with different structures, or they result from synchronized opening and closing of six small channels organized in a single conducting unit.

To elucidate the question whether different conducting states belong to the same type of channels, the transfer numbers for SRE-modified membranes bathed in NaCl solutions of different concentrations were measured (Table 1) [46]. These data show that the SRE channels are anion selective with a decrease in selectivity as the salt concentration in the aqueous phase increases. Anion selectivity is also observed for channels formed by the large CLP, syringopeptin 25A, in artificial and cell membranes [39,41].

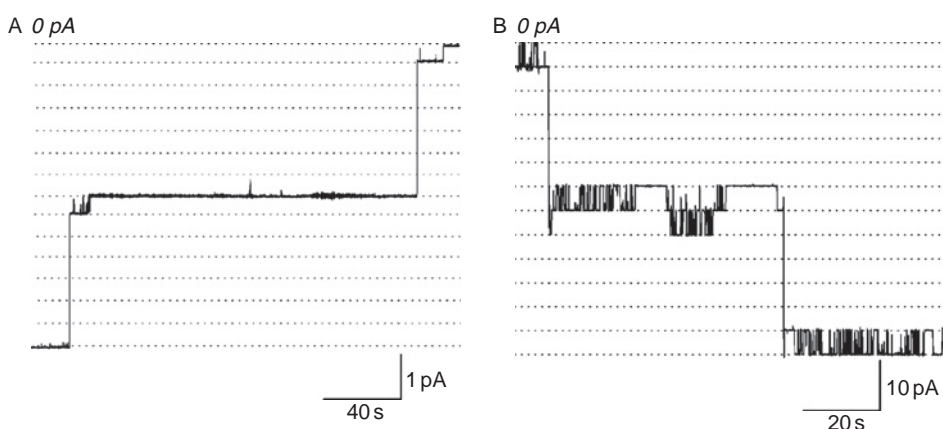


Figure 2 Records of transmembrane current fluctuations of bilayers containing a few SRE channels at different salt concentrations and $V = -100$ mV. PS/PE membranes were bathed in 0.1 M NaCl pH 6 (A); 1 M NaCl pH 6 (B).

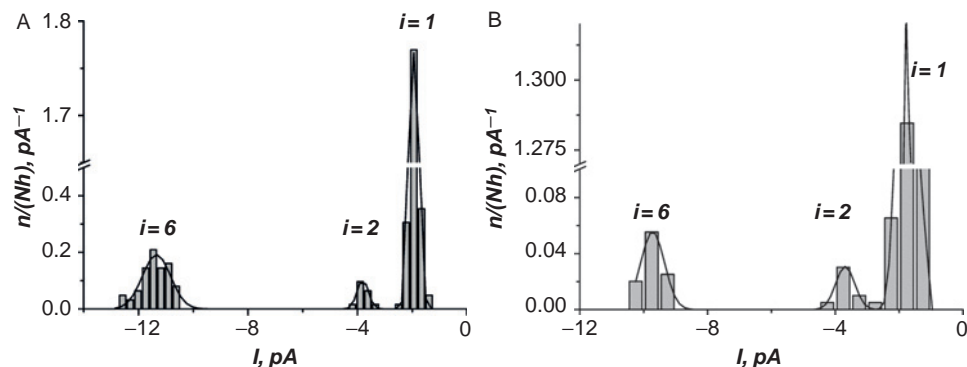


Figure 3 Amplitude histograms of SRE-induced current fluctuations measured at 0.1 M NaCl pH 6 $V = -200$ mV (A) and at 1 M NaCl pH 6 $V = -50$ mV (B). The membranes were made from PS/PE. Ratio n/Nh was set as the histogram ordinate, where n is the number of current fluctuations corresponding to a particular current level; N is the total number of fluctuations; h is the bin size. The total number of events used for the analysis was $500 \div 2000$. Curves represent the best-fits assuming a normal distribution. A multiplicity factor of a given peak (i) was defined as a ratio of the mean current value to that of the smallest current step observed.

Table 1 The Cl^- transfer number in SRE channels obtained experimentally for PS/PE bilayers

Concentration ^a (C) of NaCl, M	Cl^- transfer number (t)
0.005	0.83 ± 0.02
0.05	0.77 ± 0.01
0.5	0.70 ± 0.01

^a $C = (C_{\text{cis}} + C_{\text{trans}})/2$; $C_{\text{cis}}/C_{\text{trans}} = 2 \div 4$.

The cationic nature of the SRE molecule (Fig. 1) and of other CLPs suggests that they could impart a net positive charge to the channel, and this may provide the anion selectivity of these channels. An increase in the bathing electrolyte concentration leads to an increase in charge screening which in turn will induce a decrease in anion selectivity. This qualitatively explains the phenomenon of decreasing ion selectivity with an increase in the ionic strength of the bathing solution. Moreover, the observed changes in the selectivity of SRE channels are related to their significantly larger pore radii as compared to other peptide channels. For example, the cationic selectivity of the gramicidin A channel ($t_+ = 1$) does not depend on the concentration of RbCl in the aqueous solution (within 0.002–1 M) due to its small channel radius (about 0.2 nm) [47]. The preliminary conclusion that SRE channels have relatively large radii was confirmed by semi-quantitative estimates of anion selectivity of the channels in [46]. The relevant calculations were performed by assuming the channel radii to be the same for all the channels and basing the experimental dependence of transfer numbers on the electrolyte concentration in

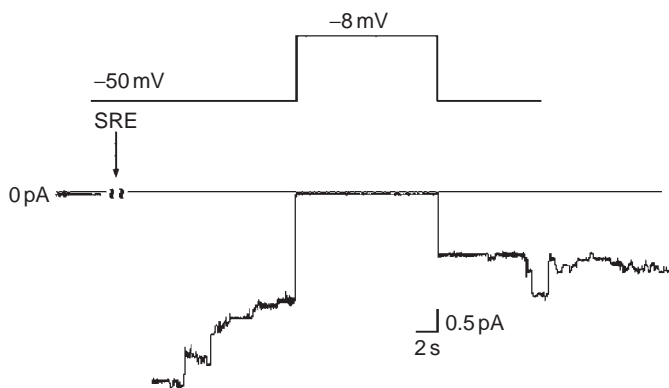


Figure 4 Representative experiment demonstrating the determination of ion selectivity of the membrane modified by SRE (5 $\mu\text{g/ml}$) in the presence of a two-fold electrolyte gradient across the bilayer (0.1 M NaCl, *cis*-side; 0.05 M NaCl, *trans*-side). Top, the potential difference applied to the membrane; bottom, a transmembrane current record at both -50 mV and -8 mV transmembrane voltages.

the bathing solution. These estimates led to an average value of a channel radius equal to approximately 1 nm.

Figure 4 shows a record of a transmembrane current in the presence of a two-fold NaCl gradient across the bilayer (0.1 *cis*-side; 0.05 M *trans*-side) at both -8 and -50 mV transmembrane potential differences. If small and large channels possess the same ionic selectivity, there must be a certain transmembrane potential that corresponds to zero current through both kinds of the channels. One can calculate that difference as a value equal to -8 mV for the conditions indicated, by using the transference numbers established previously (namely, $t_- \approx 0.77$ and $t_+ \approx 0.23$). The observed absence of any mean current or current fluctuations at -8 mV indicates that all conductance levels have the same ion selectivity. In other words, one can consider a large SRE channel be a cluster of small channels that possess the same selectivity as nonclustered channels.

Another proof of cluster organization of large SRE channels comes from a comparison between radii of small and large SRE channels. Relevant measurements were done by studying the influence of neutral polymers on the conductance of both small and large channels [44]. This method allows one to size individual pores by measuring changes in the channel conductance induced by addition of high concentrations (20% (w/w)) of neutral polymers, such as polyethylene glycols (PEGs), at either side of a membrane bilayer [48–53]. To compare the degree to which these nonelectrolytes permeated the channel pore, a ratio of the channel conductances before and after PEG addition was used. The dependence of this ratio on the PEG molecular weight is shown in Fig. 5. The PEG numbers refer to the relative molecular weights of the polymers. It shows that the influence of small PEGs, such as PEG200 and PEG300, on the channel conductance is close to that seen with the bulk solution (dashed line). This indicates that these nonelectrolytes easily penetrate the SRE channels. Larger polymers such as PEG400 to PEG1000 are also

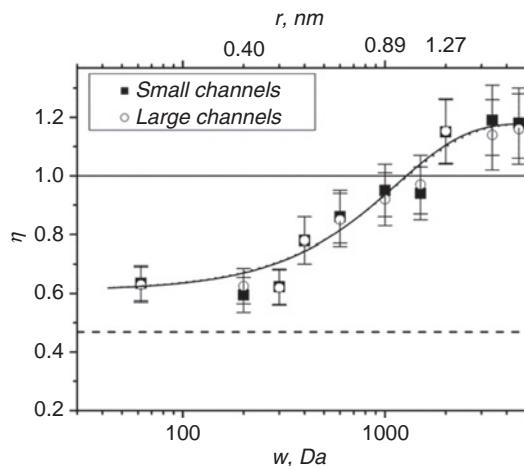


Figure 5 The dependence of a PEG-induced channel conductance change (η) on the polymer molecular weight. The membranes were made from PS/PE and bathed in 0.1 M NaCl pH 6 at $V = -150$ mV. Hydrodynamic radii of the polymers obtained from viscosity numbers or diffusion coefficients are presented on the top axis. The solid line corresponds to the unchanged channel conductance, the dashed line—to the ratio of bulk conductivities of the solutions with and without polymers.

small enough to enter the channels, but large enough to display a repulsive entropic interaction with the channel walls. As a result, the concentration of PEG inside the channel decreases and the conductance ratio grows. The reason for the rise in the channel conductance in solutions containing PEGs with the hydrodynamic radii that are either comparable to or larger than the channel radius itself is due to the fact that PEG binds water molecules and, therefore, the activity of ions in the bathing solution increases [49]. The results presented in Fig. 5 lead to two general conclusions. First, addition of solutes to the bathing solution changes conductance of both the large and small channels in the same way. Therefore both kinds of channels have a size indistinguishable one from the other. Second, it can tentatively be concluded that the radii of the large and small channels are equal approximately to 1 nm. This value is in a good agreement with the preceding estimates of the parameter [46]. As mentioned already, a pore radius of about 1 nm has also been obtained from osmotic protection studies of erythrocytes modified by SRE [24]. That study showed that the addition of PEG with radii >1 nm fully protected erythrocytes from the lytic effect of SRE. The obtained agreement in pore sizes among such diverse approaches argues for the validity of the channel radius estimations. Thus, all the earlier observations, namely multiple values of current fluctuations for SRE channels, identical anion selectivity of small and large channels, as well as the same size of these channels, indicate that the large SRE channels are clusters of the small ones.

An application of differently sized polymers applied from either the *cis*- or *trans*-side of the membrane with the impermeant PEG on the opposite side was used to specify the geometry of the SRE channel pore [54]. Under such conditions, the

relevant changes in the single-channel conductance may reflect the sizes of the channel mouths and locations of the constrictions in the pore lumen [55–58]. Figure 6 shows examples of transmembrane current fluctuations corresponding to opening/closure of small (elementary) SRE channels in PS/PE bilayers bathed in 1 M NaCl in the presence of permeant PEG200 and impermeant PEG4600 applied on different sides of the bilayer. The decrease of the channel conductance in the presence of PEG is related to its partitioning into the channel pore: PEG4600 is strongly excluded, while PEG200 permeates the pore interior, displaces ions, and decreases the channel conductance. The permeating PEG200 affects the SRE-channel conductance asymmetrically. Figure 7 shows the results of conductance

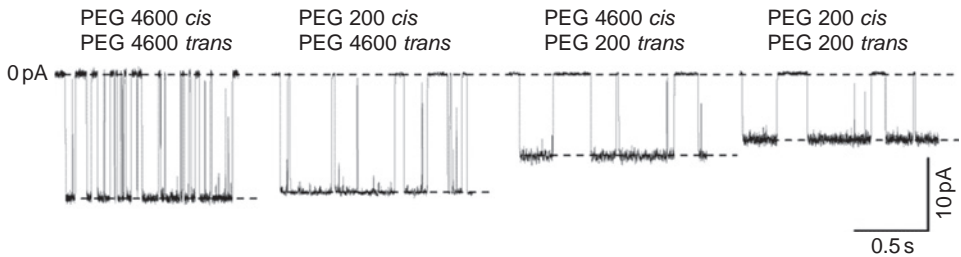


Figure 6 The effect of *cis*- and *trans*-side addition of PEG200 and PEG4600 (15% w/w) on the current through a single SRE channel in PS/PE bilayer, bathed in 1 M NaCl pH 6 at $V = -200$ mV.

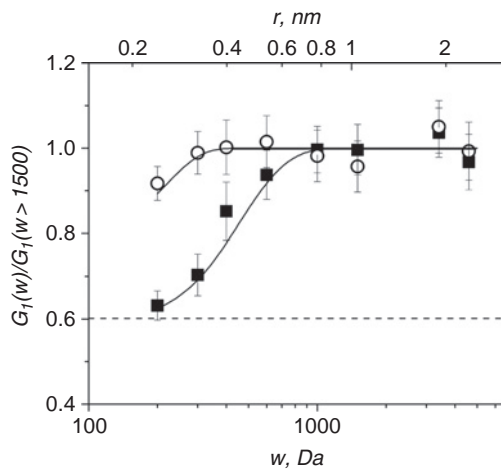


Figure 7 Relative changes in SRE-channel conductance as a function of PEG molecular weight. Experimental conditions are the same as those used in experiments of Fig. 6. Hydrodynamic radii of the polymers are denoted on the top axis. Open circles and filled squares correspond to the *cis*- and *trans*-side application of polymer of varying molecular weight, respectively (while impermeant PEG4600 was on the opposite side). The dashed line at ratio 0.6 corresponds to the ratio of bulk conductivities of the solutions with and without polymers. The solid curves present the best-fit predictions based on the scaling law (see Ref. [54]).

measurements using this system for a range of PEG sizes. To compare the degree to which these nonelectrolytes permeate the channel pores from *cis*- or *trans*-side of the bilayer, the ratios of the channel conductance in the presence of a given PEG to the mean channel conductance in the presence of impermeant PEGs are shown. If impermeant PEG4600 is added in the *cis*-compartment, the gradual decrease of the molecular weight of PEG in the *trans*-compartment from 1000 to 200 results in the monotonous reduction of the conductance ratio from 1 to 0.6, thus reaching the ratio of the solution conductivities in the presence and absence of PEG (dashed line at 0.6). With reversal of the sides of addition of the impermeable and permeable PEGs, only a slight reduction of the ratio is observed (from 1 to 0.9). A simple model based on these observations envisions the SRE channel as a water-filled pore that structurally approximates a cone. At a given channel length, its geometry can be described by only two parameters: the radii of *cis*- and *trans*-openings. Corresponding calculations were done (see [55]) and Fig. 7 shows the performed fitting of the data obtained. The result of the fitting gives the following ranges of the *cis*- and *trans*-channel radii: 0.25–0.35 nm and 0.5–0.9 nm, respectively.

The channel asymmetry may also result from an asymmetrical distribution of SRE molecules across the plane of the membrane semi-width (in thermodynamic terms, the membrane dividing surface). If so, SRE channels should yield asymmetrical current–voltage curves. Indeed, asymmetrical current responses upon application of outer potentials of different signs have been observed (Fig. 8) [40,59].

4.2. Conductance of Small and Large SRE Channels

This section of the review covers the conductance of small SRE channels, but the main conclusions to be derived are also valid for the large channels, since their conductances are multiples of the small ones [44–46].

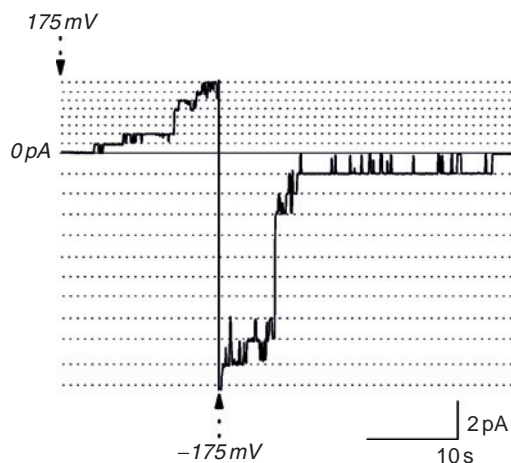


Figure 8 Current trace obtained in field-reversal experiments. SRE-modified PS/PE membrane bathed in 0.1 M NaCl pH 6.

The conductance of small SRE channels $G_1 = I_1(V)/V$, where $I_1(V)$ is the current passing through a single small channel, was measured as a function of the applied voltage, in 0.1 M NaCl pH 6 for both negatively charged (PS/PE) and neutral diphytanoylphosphatidylcholine (PC) bilayer membranes (see Fig. 9) [59]. As seen in Fig. 9, the conductance strongly depends on the membrane lipid composition. With neutral bilayers, the conductance interpolated to $V = 0$ is about three times higher than that in charged bilayers. The curves are superlinear with the applied voltage and asymmetrical in sign especially in the case of charged lipids. This asymmetry was observed for at least 6–7 h, which suggests that SRE molecules are incorporated in the channel structure asymmetrically and do not penetrate through the membrane. Malev *et al.* [59] showed that the increased conductance of SRE channels in PC membranes as compared to PS/PE membranes is a direct consequence of the absence of lipid charges and not an effect of different channel sizes in these membrane systems. Additional evidence in favor of the charge influence was obtained in experiments with varying electrolyte concentration. Figure 10 shows that the channel conductance in the limit of $V \rightarrow 0$ is a function of the electrolyte (NaCl pH 6) concentration, C_{NaCl} , for both PS/PE and PC membranes. It is seen that the channel conductance in charged membranes is proportional to the salt concentration, whereas, in neutral membranes, it is approximately proportional to the square root of C_{NaCl} . Thus, the screening of the charge of SRE species is evident only for uncharged membranes, but seems to be absent for the charged ones. These observations manifest a compensatory effect where screening of SRE positive charges and lipid negative ones works in opposite directions. With an increase in electrolyte concentration to 1 M NaCl, the channel conductances in both charged and neutral membranes converge to the same value (approximately 20 pS in the limit of $V \rightarrow 0$). This value is about an order of magnitude lower than the conductance calculated from Ohm's law if the channel radius is chosen equal to 0.3 nm. A similar large discrepancy between the measured and calculated channel conductances was also reported for other channels [55,60].

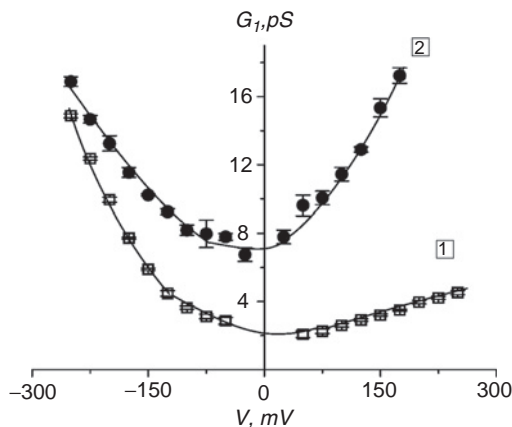


Figure 9 Voltage dependence of SRE small channel conductance in PS/PE (curve 1) and PC (curve 2) membranes bathed in 0.1 M NaCl pH 6.

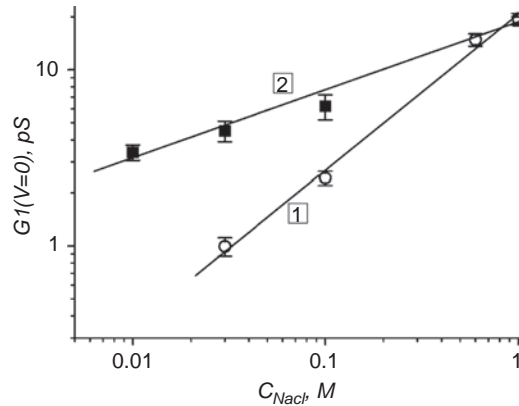


Figure 10 Concentration dependence of the small channel conductance interpolated to zero voltage ($V = 0$) in PS/PE (curve 1) and PC (curve 2) membranes.

This suggests that electrostatic interactions between ions and the channel pores significantly hinder ion movement through the SRE channels.

Additional mechanistic insights come from analysis of the super linearity of the $G_1(V)$ -curves and their asymmetry with respect to the sign of the applied voltage (see Fig. 9). As previously mentioned, the degree of asymmetry is strongly pronounced for charged membranes, and it is also dependent on the ionic concentration and pH of the bathing solution [61]. However, the conductance G_1 did not change in its values within the range of -250 and $+250$ mV, when 1 M NaCl was replaced by 1 M RbCl [61]. Since the mobility of Rb^+ -ions significantly exceeds that of Na^+ -ions, it is suggested that a possible reason for the observed super linearity of the $G_1(V)$ -curves is the absence of an influence of voltage on the expansion of the channel lumen. In the case of relatively diluted bathing solutions (0.1 M NaCl), titration of the membrane surface charge by pH (from 6 up to 2) was accompanied by decreasing asymmetry, so that it practically disappeared at pH = 3 (Fig. 11). On the other hand, $G_1(V)$ -curves remain superlinear even when the membrane surface charges (from lipid negative charges) is pH titrated or a membrane initially formed from neutral lipids is used [61]. These observations show that the total membrane surface charge resulting from lipid and SRE charges is most likely responsible for the observed asymmetry of $G_1(V)$ -curves of the SRE channels. This conclusion was directly confirmed when such polymers, as König's polyanion or polyglutamic acid were added to the *cis*-side of uncharged membranes [62]. Adsorption of the polyanions on the *cis*-membrane surface compensated the positive charges of SRE species or, moreover, recharged the membrane surface, which led to significant changes in the asymmetry of $G_1(V)$ -curves (Fig. 12).

Thus, there exists near the SRE channels some asymmetry in the local potential distribution resulted from different charges on the *trans*- and *cis*-sides of the membrane (the *trans*-side contains only lipid charges, when the *cis*-side includes also charges of SRE species). Under such asymmetric conditions, the energetic barrier for anion transport from the *cis*- to *trans*-compartment of the membrane system

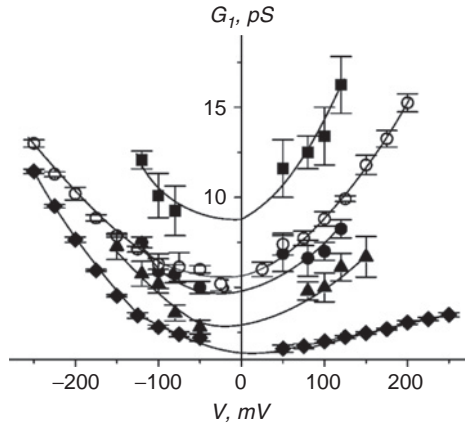


Figure 11 The conductance of small SRE channels with different bathing solution pHs and membrane lipid surface charge. Membrane lipids and pHs were: (■) PS/PE, pH 2; (●) PS/PE, pH 3; (▲) PS/PE, pH 4; (◆) PS/PE, pH 6; (○) PC, pH 6.

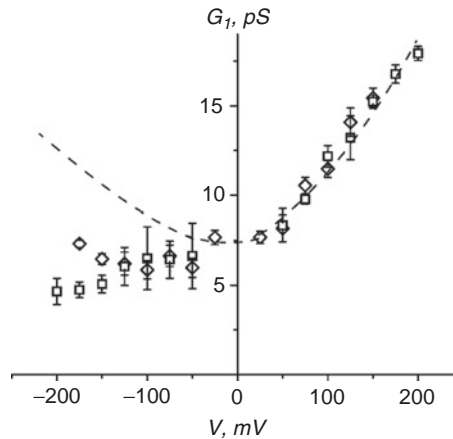


Figure 12 Conductance–voltage curves of small SRE channels in PC membranes bathed in 0.1 M NaCl pH 6 in the absence (dashed line) and in the presence Konig's polyanion (□) or polyglutamic acid (◇) in the *cis*-solution.

should differ from that for the opposite direction [62], and, as a result, the $G_1(V)$ curve of SRE channels must be asymmetrical with respect to the sign of potential V . An analogous effect was previously predicted for thin membranes with homogeneous membrane surfaces with different charges [63]. A special form of such a barrier resulted from Coulomb interactions between penetrating anions and charges of different membrane surfaces. Thus, the existence of the intermembrane local electric field can also be responsible for superlinearity of $G_1(V)$ -curves observed for diluted bathing electrolytes [61]. It may be predicted that this effect will disappear or be significantly reduced at high electrolyte concentrations (≈ 1 M) due to screening the charges of both membrane surfaces. However, the latter is not observed for the

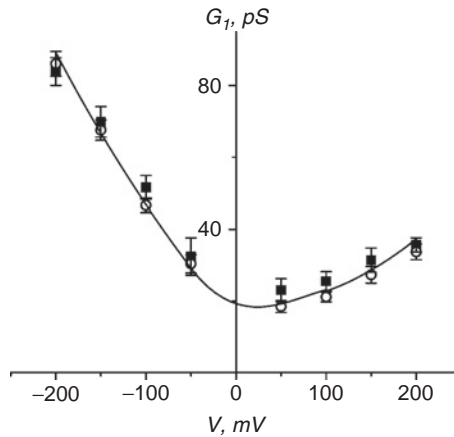


Figure 13 Voltage dependence of SRE small channel conductance in PS/PE (○) and PC (■) membranes bathed in 1 M NaCl pH 6.

charged and neutral bilayers bathed with 1 M NaCl pH 6 solutions, as it is seen from Fig. 13. Consequently, the asymmetry of the energetic barrier for anions passing through SRE channels in opposite directions results from influencing factors in addition to Coulomb interactions. In our opinion, such additional (and unknown at the moment) factors are of the same nature as those determining the significantly reduced conductance of SRE channels (see earlier text). Thus, the presence of charges of both the membrane-forming lipids and the SRE molecules plays essential roles in the ion transport properties of the SRE channels, although not completely.

As mentioned above, the conductance induced by SRE is proportional to the 6–7th power of its concentration in the *cis*-compartment of the membrane system. This means that aggregate formation of 6–7 SRE particles (precursors of the channels) should precede the opening of the channels. Such aggregate formation process may be either a limiting or a nonlimiting step in the steady-state membrane conductance relaxation induced by SRE. This uncertainty can be resolved from measurements of the membrane current relaxation under potential clamp conditions in the presence of the toxin.

4.3. Comparisons of Multi- and Single-Channel Measurements with SRE-Modified Bilayers

From voltage-clamp measurements with PS/PE lipid bilayers modified by one-side addition of SRE, it was established that transmembrane current, I , as a function of time, t , and the applied potential is described by a two-exponential dependence [42]:

$$I(V, t) = I(V, \infty) + A_1(V, 0) \exp(-t/\tau_1) + A_2(V, 0) \exp(-t/\tau_2) \quad (1)$$

Here, $I(V, \infty)$ is the steady-state current corresponding to a given transmembrane potential V . $A_1(V, 0)$ and $A_2(V, 0)$ are the current amplitudes satisfying the condition

$$I(V, \infty) + A_1(V, 0) + A_2(V, 0) = 0 \quad (2)$$

indicating the absence of transmembrane current at moment $t = 0$ in the case of initial potential $V = 0$. The typical example of such two-exponential representation of current $I(V, t)$ is given in Fig. 14. As seen in Fig. 14 (insert), the main contribution to the dependence (1) corresponds to its slow constituent $A_2(V, 0)\exp(-t/\tau_2)$, while the fast constituent is essential only at time t that is significantly lower than τ_2 . This implies that the relations between characteristic times τ_1 and τ_2 , and, at the same time, between amplitudes $A_1(V, 0)$ and $A_2(V, 0)$ are as:

$$\tau_2 \geq 3\tau_1 \text{ and } |A_2(V, 0)| \geq 3|A_1(V, 0)| \quad (3)$$

and these relations remain valid at all of the potentials studied. Here, it should be emphasized that both relaxation times τ_1 , τ_2 are independent of the concentration of SRE introduced into *cis*-compartment of the membrane system. Thus, SRE aggregation is not a limiting step of the current relaxation and the established kinetic dependence only results from the opening/closure of two kinds of SRE channels, namely “small” and “large” ones observed in single-channel measurements. Moreover, one could reasonably suppose that the precursor’s quasi-particles concentration, n_p , on the membrane surface (from the *cis*-side of the membrane system, see earlier text) remains constant during the relaxation process registered, i.e., it is in

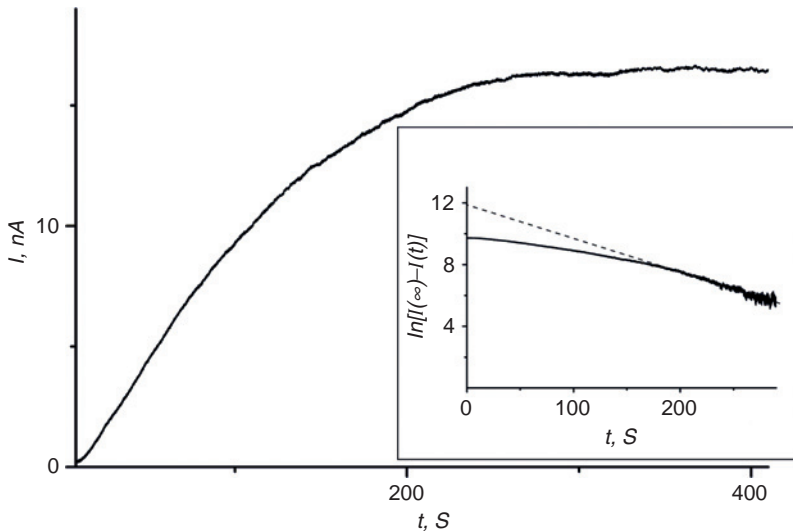
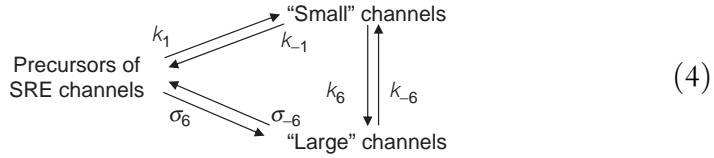


Figure 14 Multichannel kinetics of the transmembrane current induced by application of $V = 100$ mV to SRE-modified PS/PE membrane bathed in 0.1 M NaCl pH 6. Insert. Determination of the parameters τ_2 and A_2 of slow current relaxation. The dashed line is an extrapolation of the slow component at the beginning of the relaxation.

equilibrium with SRE molecules of the bathing solution. In particular, it was assumed that the opening/closure of SRE channels proceeds according to the following scheme:



This means that the master equations describing the opening/closure of SRE channels are as follows:

$$\begin{aligned}
 \frac{dn_1}{dt} &= k_1 n_p - k_{-1} n_1 - k_6 n_1 + k_{-6} n_6 \\
 \frac{dn_6}{dt} &= \sigma_6 n_p - \sigma_{-6} n_6 + k_6 n_1 - k_{-6} n_6
 \end{aligned}
 \quad (5)$$

Here, n_1 and n_6 are the numbers of open small and large channels at the unit membrane surface; $k_{\pm 1}$, $\sigma_{\pm 6}$, $k_{\pm 6}$ are the rate constants of the corresponding transitions (see Scheme (4)), which should be functions of potential V in the general case, since the opening/closure of SRE channels is a potential-dependent process similar to what takes place for ionic channels of living cells. Concrete types of such functional dependences can be obtained by comparing the observed changes in current $I(V, \infty)$ and parameters: $A_1(V, 0)$, $A_2(V, 0)$, τ_1 , and τ_2 , which accompany changes in potential V , with those followed from a theoretical solution of Eq. (5) under appropriate initial conditions. Though quantitative determinations of the dependencies were achieved, their physical nature appears more complex than what these determinations reveal. To address this problem, it is useful to reformulate the theoretical description of the opening and closure of SRE channels in terms of single-channel measurements. To be brief, the reformulation is restricted to replacing concentrations n_1 and n_6 in Eq. (5) by probabilities p_1 and p_6 that small and large channels are open (for more details see Ref. [64]). It follows that single-channel recordings of the opening/closure of SRE channels should give the same information as that from multichannel measurements provided by Scheme (4) that describes working SRE channels. If so, one must observe a potential-dependent character of mean life times of small and large channels, since in Scheme (4), these parameters are exactly the same, as characteristic times τ_1 , τ_2 registered in multichannel measurements. Indeed, as seen in Fig. 15, numbers of small and large channels increased with channel-opening potentials and decreased with channel-closing potentials with the characteristic time near time τ_2 of the slow relaxation.

In addition, multiple fluctuations of the single small channel amplitudes (and sometimes of large channels) were observed with characteristic time t_1 which was small compared to τ_2 and that did not depend on the applied potential (see Fig. 16). A strongly pronounced dependence of duration t_6 of large channel fluctuations on the potential was not observed. However, that time t_6 is independent of V cannot be affirmed since the number of the registered large channels was too small to use an averaging circuit for a current recording. So, in parallel to the existence of SRE

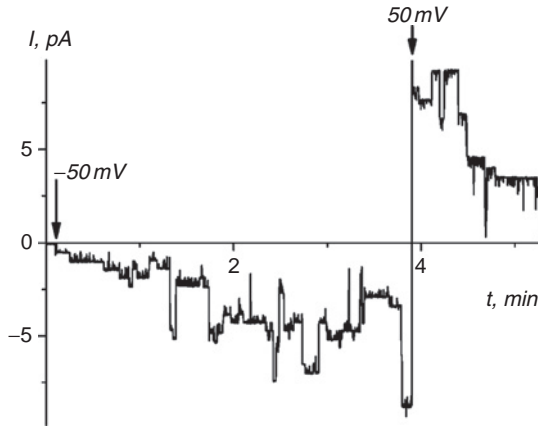


Figure 15 Single-channel kinetics of the transmembrane current induced by application of $\pm V$ to SRE-modified PC membrane bathed in 0.1 M NaCl pH 6. Applications of ± 50 mV are indicated by the arrows.

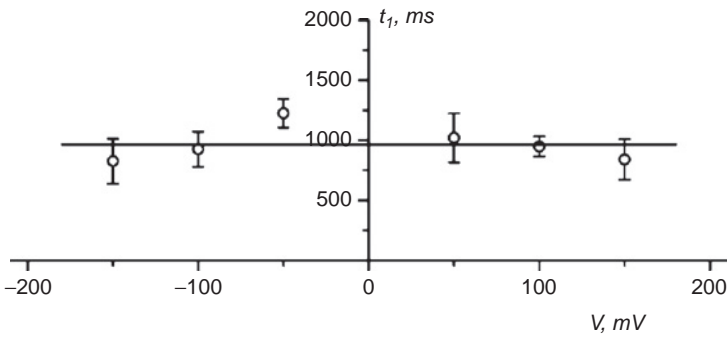
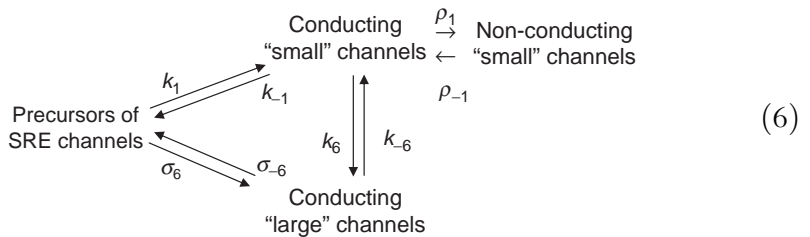


Figure 16 Voltage dependence of the mean open lifetime (t_1) of the small SRE channel. PS/PE membranes bathed in 0.1 M NaCl pH 6.

channel precursors, an additional nonconducting state for small channels is supposed. Transitions from it to the conducting state of small channels and vice versa are independent of the applied potential. Such transitions are usually treated as “burst activities” of channels [64]. As a result, Scheme 4 will have added complexity that can be illustrated as follows:



A similar nonconducting state might be proposed for large channels, since their “burst activity” is also observed. However, it cannot be excluded that the same nonconducting state is responsible for the burst activities of both small and large channels. In that case, rate constants v_1 and v_{-1} of the transitions from conducting large channels to the nonconducting state and conversely should be some functions of the applied voltage. Restricting further considerations to [Scheme \(6\)](#), it is necessary to replace the first equation of set (5) by

$$dn_1/dt = k_1 n_p - k_{-1} n_1 - k_6 n_1 + k_{-6} n_6 - \rho_1 n_1 + \rho_{-1} n_{-1} \quad (7)$$

to take into account the nonconducting state of small channels. In [Eq. \(7\)](#), n_{-1} is the number of nonconducting small channels at the unit membrane surface, and ρ_1 and ρ_{-1} are the rate constants of corresponding transitions (see [Scheme 6](#)). The introduced change in [Eq. \(7\)](#) as compared to the first equation of set (5) is not a principal character, since constants $\rho_{\pm 1}$ are much higher than $k_{\pm 1}$ and $\sigma_{\pm 6}$, as follows from the established smallness of $t_1 \approx 1/\rho_1$ compared with the characteristic time $\tau_2 \approx 3\tau_1$ of current relaxation. Therefore, during current relaxation (i.e. at time $t \geq \tau_2$), the numbers of conducting and nonconducting states are in equilibrium with each other: $n_1(V, t) = (\rho_{-1}/\rho_1)n_{-1}(V, t)$. As a result, the time dependence of $I(V, t)$ should practically coincide with what follows from the theoretical solution of set (5), i.e., equivalent to what is given by [Eq. \(1\)](#) [42].

Under the steady-state conditions ($dn_1/dt = 0$, $dn_6/dt = 0$), n_1 and n_6 should be connected with the precursor’s concentration n_p by the equations:

$$n_1(V) = [k_1(V)/k_{-1}(V)]n_p \quad \text{and} \quad n_6(V) = [\sigma_6(V)/\sigma_{-6}(V)]n_p \quad (8)$$

According to a detailed equilibrium principle, there must be the equality:

$$[k_6(V)/k_{-6}(V)] = [k_{-1}(V)\sigma_6(V)/k_1(V)\sigma_{-6}(V)] \quad (9)$$

since the equilibrium relationship $k_6(V)n_1(V) = k_{-6}(V)n_6(V)$ is valid under the same conditions. As the total transmembrane current is the sum of currents passing through small and large channels according to $I(V, t) = A[I_1(V)n_1(V, t) + 6I_1(V)n_6(V, t)]$, its stationary value $I(V, \infty)$ is given by the equation:

$$I(V, \infty) = I_1(V)[K_1(V) + 6K_6(V)]N_p \quad (10)$$

where equilibrium constant $K_1(V)$ and $K_6(V)$ are equal to $[k_1(V)/k_{-1}(V)]$ and $[\sigma_6(V)/\sigma_{-6}(V)]$, respectively; A is the membrane surface, and $N_p = n_p A$. One can, therefore, consider ratio $I(V, \infty)/I_1(V)$ be the total number of open small channels, $N_{op}(V, \infty)$, both included and not included in the channel clusters at potential V according to:

$$N_{op}(V, \infty) = I(V, \infty)/I_1(V) = [K_1(V) + 6K_6(V)]N_p \quad (11)$$

In the earlier analysis, the existence of only two kinds of SRE channels, “small” and “large” are considered. But, thorough examinations of single-channel histograms (see [Section 4.5](#)) show the existence of intermediate states of SRE channels with

conductances that are divisible by the “small” states, but smaller than clusters with the maximum number M of small channels. Thus, Eq. (11) should be generalized as

$$N_{\text{op}}(V, \infty) = I(V, \infty)/I_1(V) = \sum_{i=1}^M iK_i(V)N_{\text{p}} \quad (12)$$

as one can easily obtain by replacing Eq. (8) with more general equations: $n_i(V) = K_i(V)n_{\text{p}}$, where $i = 1, 2, \dots, M$, and $K_i(V)$ is some function of potential V .

4.4. Gating Charge of SRE Channels

Channel formation can be treated in terms of chemical work, $\Delta U_{\text{ch}}(i)$, related to conformational changes (or simply, aqueous pore formation) accompanied by transition to a quasi-particle species, and electrical work eq_iV arising from displacements of charged and/or dipolar fragments of such species during the transition so that:

$$\Delta U_i = \Delta U_{\text{ch}}(i) - eq_iV - \alpha_iV^2 \quad (13)$$

On the right side of Eq. (13), the value α_iV^2 is included to account for possible electrostriction effects, where α_i , the electrostriction coefficient; e , the electron charge; q_i is the so-called gating charge [65]. Under steady-state conditions, there must be equilibrium between precursor particles (of number N_{p}) and channel clusters of any (i th) kind (of number $An_i(V) = K_i(V)N_{\text{p}}$, see earlier text), i.e., the difference between the electrochemical potentials of these quasi-particles $\Delta\tilde{\mu}(i) = -kT\ln[K_i(V)] - [\Delta U_{\text{ch}}(i) - eq_iV - \alpha_iV^2] = 0$. The natural logarithm of the equilibrium constant $K_i(V)$ in its absolute value is only the work of formation of the i th kind of channel cluster expressed in heat units:

$$K_i(V) = \exp \{ -[\Delta U_{\text{ch}}(i) - eq_iV - \alpha_iV^2]/kT \}, (i = 1, 2, \dots, M) \quad (14)$$

This permits one to rewrite Eq. (12) as:

$$\begin{aligned} N_{\text{op}}(V, \infty) &= I(V, \infty)/I_1(V) = \sum_{i=1}^M iK_i(V)N_{\text{p}} \\ &= N_{\text{p}} \sum_{i=1}^M i \exp \{ -[\Delta U_{\text{ch}}(i) - eq_iV - \alpha_iV^2]/kT \} \end{aligned}$$

or

$$\begin{aligned} \ln[I(V, \infty)/I_1(V)] &= \ln N_{\text{p}} + \ln \left\{ \sum_{i=1}^M i \exp [-(\Delta U_{\text{ch}}(i) \right. \\ &\quad \left. - eq_iV - \alpha_iV^2)/kT] \right\} \end{aligned} \quad (15)$$

With ion channels of living cells, such equations are reduced additionally by taking into account the conservation of the total number of channels in all their states. For the case of artificial bilayer SRE channels, such considerations do not apply at time $t \gg \tau_2$, since there is a reservoir of SRE species confined to the *cis*-compartment of the membrane system. The presence of such a reservoir provides a constancy of number N_p of precursor species on *cis*-membrane surface independently of the potential value (see Section 4.3) and, thus, allows changes in the total number of channels with varying potential V .

$\sum_{i=1}^M i \exp [-(\Delta U_{\text{ch}}(i) - eq_i V - \alpha_i V^2)/kT] = \sum_{i=1}^M i n_i(V)/N_p$ included into Eq. (15), can be reduced to the form given below by introducing a mean number of synchronously working small channels in channel clusters, $m = \sum_{i=2}^M i n_i(V)/\sum_{i=2}^M n_i(V)$, and ratio $S = \sum_{i=2}^M n_i(V)/\sum_{i=1}^M n_i(V)$ that gives the relative contribution of such clusters $(\sum_{i=2}^M n_i(V))$ in total number $\sum_{i=1}^M n_i(V)$ of all the clusters including unitary ones (of number $n_1(V)$). Using these definitions, one can rewrite Eq. (15) as follows

$$\begin{aligned} \ln N_{op} &= \ln[I(V, \infty)/I_1(V)] = \ln N_p + \ln\{(n_1(V)/n_p)[1 + mS/(1 - S)]\} \\ &= \ln N_p + \ln\{\exp[-(\Delta U_{\text{ch}}(1) - eq_1 V - \alpha_1 V^2)/kT][1 + mS/(1 - S)]\} \\ &= \ln N_p + \ln[1 + mS/(1 - S)] - [\Delta U_{\text{ch}}(1) - eq_1 V - \alpha_1 V^2]/kT \end{aligned} \quad (16)$$

From the obtained equation, it is clear that at variations of the applied voltage N_{op} might be determined by the formation work of unitary clusters (with number $i = 1$), $[\Delta U_{\text{ch}}(1) - eq_1 V - \alpha_1 V^2]$, and changes in the ratio of $mS/(1 - S)$. If the later is weakly dependent on potential V , as it takes place for SRE channels [66], the slope $d(\ln N_{op})/d(eV/kT)$ of the dependence given by Eq. (16) must be equal to the sum $[q_1 + 2\alpha_1 (kT/e)V]$. This permits one to easily determine gating charge of unitary clusters q_1 . Indeed, experimental determinations $N_{op}(V) = I(V, \infty)/I_1(V)$, as a function of potential V yielded the conclusion that, in the range of ± 100 mV, function $\ln N_{op}(V)$ is approximately linearly dependent on the potential (see Fig. 17). This means that the electrostriction force responsible for the $\alpha_1 V^2$ -component of the channel formation work does not significantly affect the channel opening [59,67]. On the other hand, the obtained linear dependence of $\ln N_{op}$ on the potential indicates that possible changes in the ratio of $mS/(1 - S)$ are really insignificant probably because $S \approx 0.2$ in the case of SRE. As to the case of CCA, the corresponding value of S is about 0.6 [66], and a certain influence of that ratio is likely. Unfortunately, the relevant data that address these predictions have not been obtained.

For membranes formed from an equimolar mixture of PE and PS, gating charge of SRE channels, q_1 , is close to unity at 0.1 M NaCl concentration and pH 6. With neutral lipids (PC) in the same solution, the gating charge is negative [59]. Figure 18 illustrates changes in values of gating charge q_1 that take place for different ratios of charged (PS) to sum of charged and uncharged lipids in membranes bathed in 0.1 M NaCl pH 6 solution [67]. These results show that manipulations of lipid charge affect

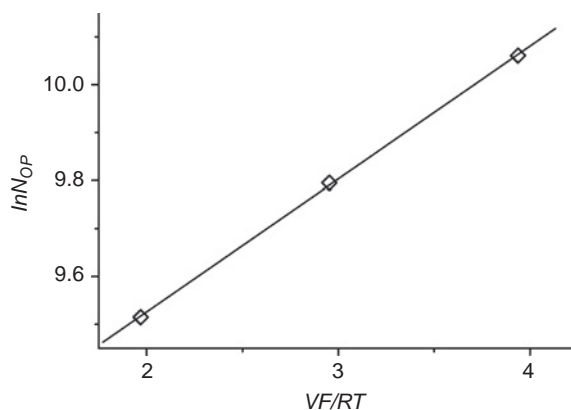


Figure 17 Logarithmic plot of the total number of open SRE channels as a function of the applied voltage. Numbers of channels were obtained from the steady-state currents in PS/PE membranes bathed in 0.3 M NaCl pH 6.

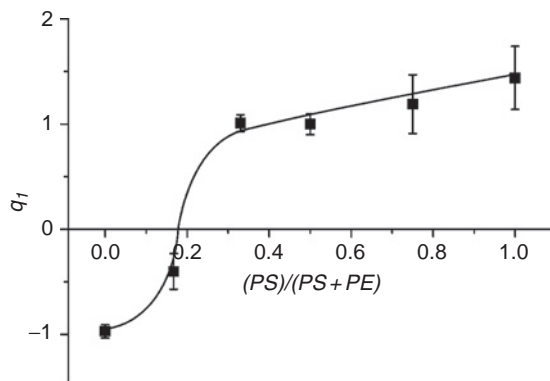


Figure 18 Dependence of the gating charge of SRE channels on the fraction of the charged lipid in the membrane-forming solution. At 0 mol% of PS, membranes were formed from PC. Membranes were bathed in 0.1 M NaCl pH 6 solution.

both the absolute value and the sign of the gating charge. Moreover, a gradual increase of sodium chloride concentration in aqueous solutions in the range of 0.1–2.5 M NaCl first decreases the gating charge and then changes its sign reaching -1.0 at 2.5 M NaCl (Fig. 19) [59]. At 0.1 M NaCl, a similar inversion of the gating charge sign is achieved by increasing the solution acidity. Changes of the bathing solution pH from 6 to 2 lead to a decrease in the q_1 -value with the transition point around pH 3 (see Fig. 20) [59]. Therefore, both lipid titration by protons and screening the membrane charge by the increased salt concentration lead to qualitatively similar effects: an initial decrease and then sign inversion of the channel gating charge. These observations reveal that channel opening (formation) involves translocation of charged lipid heads along electric field lines and implies that lipids are essential structural components of the SRE channel pore.

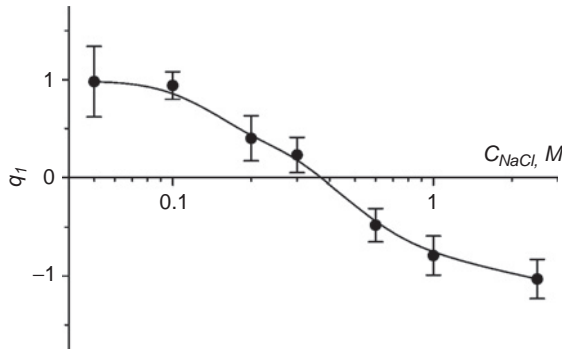


Figure 19 The gating charge of the SRE channels strongly depends on NaCl bulk concentration. Data were obtained for PS/PE bilayers at pH 6.

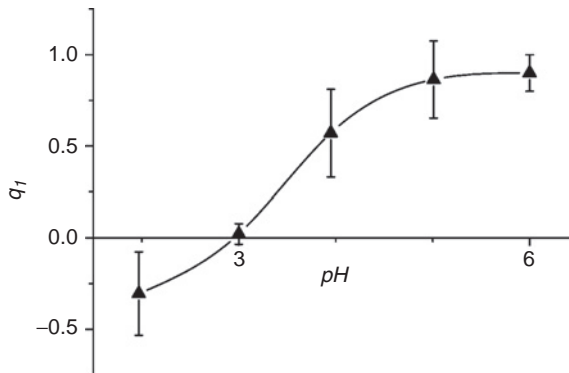


Figure 20 The gating charge of the SRE channels can be modified by bathing solution pH. Data were obtained for PS/PE bilayers in 0.1 M NaCl solutions.

A simple model of hypothetical channel formation and structure that incorporates membrane lipids is given in Fig. 21 [59]. The structure is assumed asymmetrical with the toxin lactone ring located closer to the *cis*-side (the side of SRE addition) than to the *trans*-side. This is based on the fact that the observed asymmetry (respect to the sign of potential V) of current I_1 through a single channel is due to asymmetrical location of SRE molecules (see Section 4.2). The channel asymmetry also accounts for the observation that with negatively charged bilayers (PS/PE) and dilute bathing solutions ($[NaCl] \leq 0.3$ M), the opening of the channels is favored by positive transmembrane potentials. Pore formation requires a larger amount of negatively charged lipids to move down the electric field as opposed to up the field. If the applied potential is such that the *cis*-side of the membrane is more positive, then the lipid head-groups lining the *trans*-side opening of the pore are dragged into the pore reducing the work of channel formation. The lipid groups located near the *cis*-side opening would act in the opposite direction. However, due to the channel asymmetry their total number at this side is smaller than that of *trans*-side and their translocations correspond to more small distances, so that the energy contribution of head-groups at the *trans*-side opening will dominate.

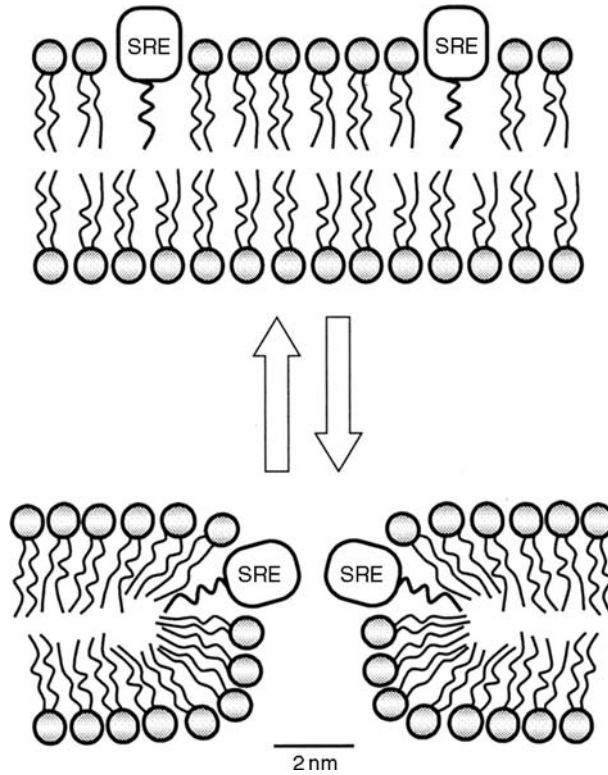


Figure 21 A simple model shows the involvement of membrane lipids in the channel functional properties.

As it was mentioned, the sign of q_1 and, hence, the sign of potentials favoring channel opening in the studied systems can be reversed by replacing charged lipids by neutral ones or by increasing either the solution acidity (to pH 2) or the salt concentration in bathing solutions. These maneuvers eliminate (or screen) the charge of the lipid head-groups, so the remaining voltage dependence of channel gating should be attributed to dipolar moments of lipid head-groups. Thus, the gating charge q_1 is a sum of effective charges of charged species (lipids, toxin, and ions entering in a channel), q_1^{ch} , and those related to translocations of lipid dipoles, q_1^{d} , i.e. $q_1 = q_1^{\text{ch}} + q_1^{\text{d}}$.

By viewing the pore (as in Fig. 21) as a cylinder and assuming that the dipoles of the *cis*- and *trans*-lipids in the pore are antiparallel, it can be estimated that the work related to the lipid dipole translocations at the transition from the precursor's state (upper part of Fig. 21) to the open state of a single channel (low part), i.e. energy $\Delta W^{\text{d}} = eq_1^{\text{d}}|V|$ may exceed $5 kT$ at potential $|V| = 100 \text{ mV}$ [59]. A more precise estimate for this energy requires more detailed information about the channel structure. However, it is seen that the energy of headgroup dipole interaction with the electric field is large enough to be measured in gating experiments. If so, then dipole-modifying agents should influence the channel gating of SRE channels.

To determine if this is the case, experiments with phloretin which compensates lipid dipole moment by aligning its own dipoles in the opposite direction [68, 69], were conducted [67,70]. It was observed that addition of phloretin to neutral lipid membranes inverts the sign of the SRE channel gating charge (see Fig. 22A). On the other hand, addition of agents like RH-421 and 6-ketocholestanol that increase the dipolar potential of lipid membranes leads to the reverse in the sign of q_1 from positive to negative (see Fig. 22B). Thus, these observations are in a good agreement with the qualitative representation of the SRE channel structure as a lipidic pore stabilized by lipopeptide.

The established negative value of the dipolar component q_1^d of the gating charge of SRE channels needs further explanation. A negative q_1^d means that from the *trans*-side of a channel pore positive poles of lipid molecules are concentrated in the nearest vicinity of SRE species, while negative poles probably contact with the same species from the channel's *cis*-side (see Fig. 23). In other words, one must assume the presence of specific dipole-lipopeptide interactions to explain the prevailing orientation of lipid dipoles within SRE channels, i.e., the phenomenon responsible for the observed dipolar component of gating charge. One can therefore expect the appearance of some specific influence of dipole-modifying agents on working the SRE channels. As shown below, such expectations are justified.

Finally, it must be emphasized that the earlier-mentioned considerations and conclusions are only valid in the case of relatively low absolute values of V , namely $|V| \leq 100$ mV. Also, an important limitation is that the used electrochemical potential equations are only valid for ideal solutions. In the general case, such equations should include the so-called activities of the quasi-particles considered instead of their concentrations. So, at high potentials, one can expect the appearance of some deviations from dependencies predicted by Eq. (16). Indeed, subsequent measurements with SRE channels in PS membranes at high salt concentration (1 M)

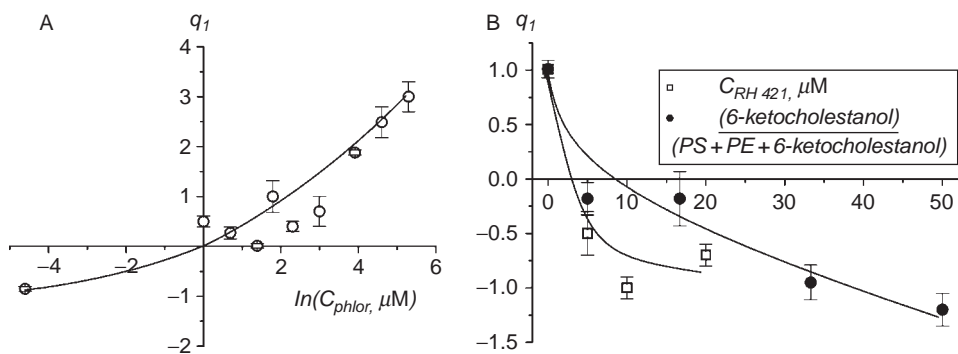


Figure 22 Gating charge of SRE channels as a function of modifying addenda concentrations of (A) phloretin in the membrane-bathing solution (membranes were prepared from PC) and of (B) RH 421 in the solution bathing PS/PE-membranes or 6-ketocholestanol in the membrane-forming solution. For the first case, abscissa shows concentration of RH 421 (μM), but gives the molar content (%) of 6-ketocholestanol, which replaced PE in PE + PS (30%) bilayers for the second case. The membrane-bathing solution was 0.1 M NaCl pH 6.

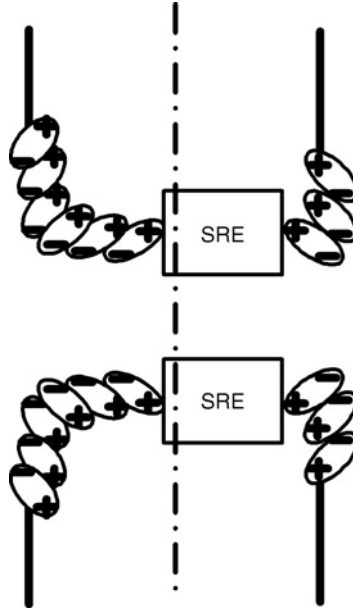


Figure 23 A model of small SRE channel. Polar heads of lipids are designed by ellipses.

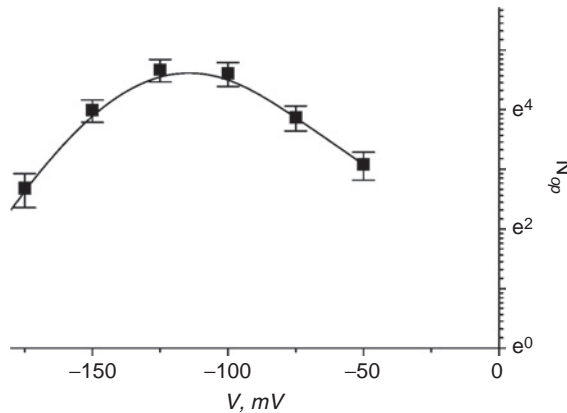


Figure 24 Dependence of the total number of open small SRE channels on the transmembrane potential. Membrane was formed from PS and bathed in 1 M NaCl pH 6.

and the range of high negative potentials V (up to -200 mV) showed that $\ln N_{op}$ is an extreme function of V (see Fig. 24) reaching its maximum at V around -120 mV. This implies that the reversion of the gating charge sign can also be attained due to the potential itself. Though this effect can be explained by an increased sorption of bathing electrolyte cations on the inner channel wall at high negative potentials and high concentrations of NaCl [67], other considerations prompted studies of voltage-dependent changes in SRE channel function.

4.5. Changes in a Mean Number of Small Channels in Channel Clusters

As shown earlier for diluted bathing electrolytes, the observed asymmetry of single-channel's $I_1(V)$ -curves most likely results from the local intra-membrane electric field that exists near the channels due to positive charges of 6–7 toxin molecules included into precursor (see Section 4.2). It is also evident that the potential-dependent opening/closure of SRE channels should be determined with changes of such a local field, which is in the first approximation proportional to $(V - V_0)/L$, where $-V_0/L$ is the local field in the absence of outer potential V , and L , the membrane thickness. This means that potential V in Eq. (16) should be replaced by difference $(V - V_0)$ to account for this circumstance. On the other hand, the earlier determinations of the gating charge in case of SRE channels assumed that the ratio of $mS/(1-S)$ is weakly dependent of potential V , i.e. the contribution of large channels (channel clusters with values of $i \geq 2$) to the channel formation work is insignificant. Hence, the observed extreme dependence of $N_{\text{op}}(V)$ might reflect changes in both mean value m and ratio S , which accompany variations of V . Thus Eq. (16) can be rewritten in the form:

$$\ln N_{\text{op}}(V) = \ln [I(V, \infty)/I_1(V)] = \ln N_p + \ln [1 + m(V - V_0)S(V - V_0)/(1 - S(V - V_0))] - [\Delta U_{\text{ch}}(1)/kT - eq_1(V - V_0)/kT] \quad (17)$$

where the established absence of an electrostriction effect is taken into account. It is clear that an essential contribution of ratio $mS/(1-S)$ to N_{op} might be expected only if $S = \sum_{i=2}^M n_i(V)/\sum_{i=1}^M n_i(V)$ is close to unity, which does not take place for the SRE case (see the preceding part and [66]). Therefore, the observed extreme character of the dependence $\ln N_{\text{op}}(V)$ should be connected with the influence of some previously unaccounted for factors such as the activities of channel quasi-particles, but not their concentrations, as discussed in a previous section.

Although reasons for the possible appearance of the $m(V - V_0)$ -dependence are still unclear, the obtained equation allows one to design experiments for its verification. First of all, it is necessary to check the introduced assumption that number m really depends on the outer potential and, moreover, is determined by the local electric field (i.e. difference $(V - V_0)$). Other verifications should include experiments with different concentrations of the bathing electrolyte solution, variations in the membrane surface charge and potential by using different lipids and dipole-modifying agents.

As expected, the mean number of small channels synchronously opening in channel clusters, m , was dependent on the voltage and bathing solution composition. To quantitatively describe this finding, we redefined quantity m in the way that requires further explanation. At different applied voltages, current transition histograms might show a number of peaks with $i > 2$, as seen in Figs. 25A, B and 26A. To trace the dependence of the mean number of synchronized small SRE channels in clusters on potential V , m was calculated as: $m = \sum_{i>2} i\rho_i / \sum_{i>2} \rho_i$, where i is, as mentioned earlier, the multiplicity factor of the peak that corresponds to synchronous opening/closure of i small channels; ρ_i is the area under the i th peak; $\rho_i / \sum_{i>2} \rho_i$

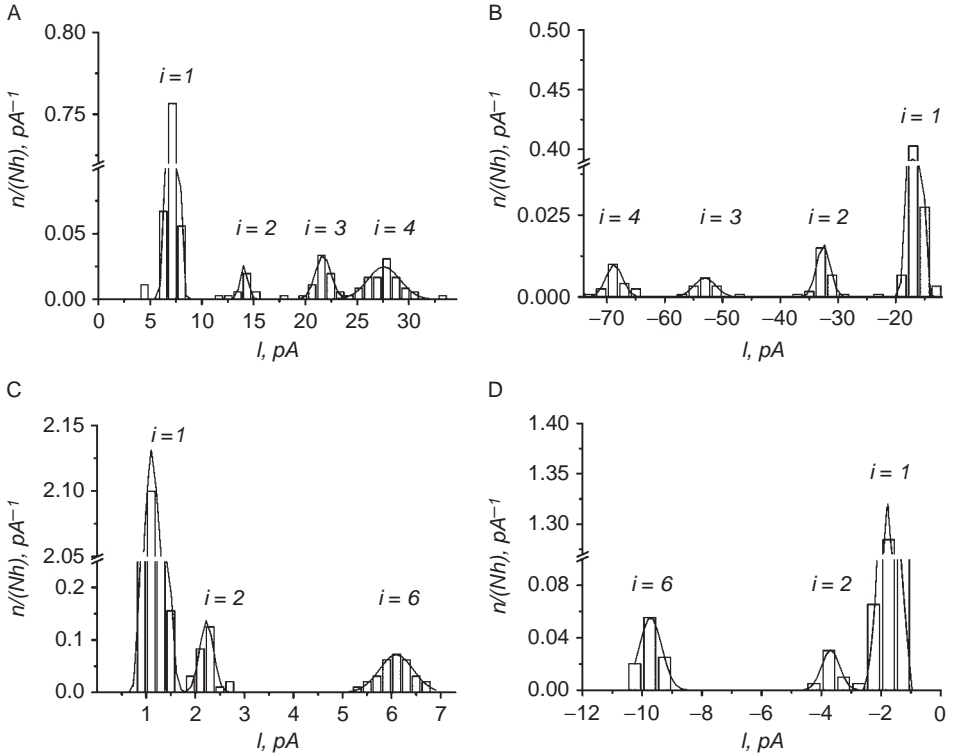


Figure 25 Current transition histograms of SRE-induced current fluctuations measured at different voltages at 1 M NaCl pH 6. (A) 200 mV; (B) -200 mV; (C) 50 mV; (D) -50 mV. The membranes were made from PC. The solid lines represent the best-fits assuming a normal distribution, i is the multiplicity factor.

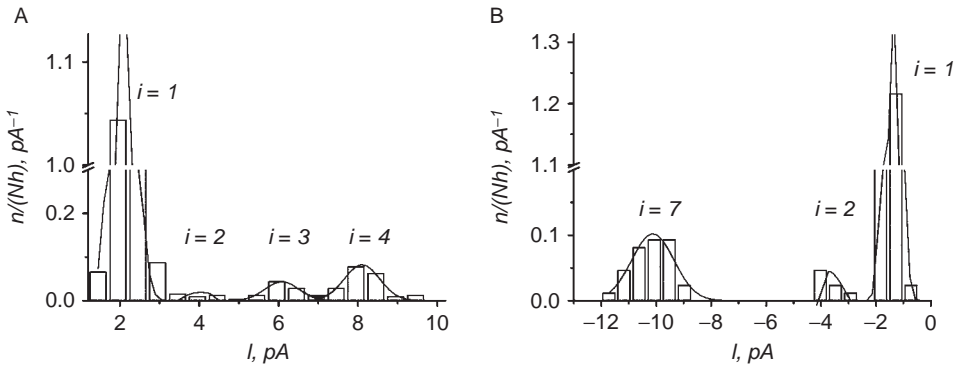


Figure 26 Amplitude histograms of SRE-induced current fluctuations at 0.1 NaCl pH 3. (A) 150 mV; (B) -150 mV. The membranes were made from PS/PE. The lines represent the best-fits assuming a normal distribution, i is the multiplicity factor.

is a normalized probability of synchronous functioning of i elementary channels, and $i\rho_i/\sum_{i>2}\rho_i$ is thus a product of the multiplicity factor and statistical contribution of the corresponding current level. In this definition, the summation applies to values $i > 2$, since it was previously established that in the case of $i = 2$, it corresponds to a random opening/closure of two small channels not included in the same cluster (see Section 4.1). This redefinition of m does not contradict the previous one, but operates with experimentally determined quantities (ρ_i) and takes into account the absence of clusters with number $i = 2$.

If, in the case of relatively low potentials ($|V| = 50$ mV), current histograms do not reveal significant changes in a cluster organization (see Fig. 25C,D), but further increases in the potential up to $|V| = 200$ mV are accompanied with such changes. As it is seen in Fig. 25A and B, a peak corresponding to synchronous opening/closure of six small channels ($i = 6$) is present at low voltages. Increasing the absolute value of the potential to 200 mV reduces the number of simultaneously gated small channels to 3–4 (see Fig. 25A,B). Similar results were obtained for charged PS/PE membranes bathed in 1 M NaCl pH 6 (data not shown). However, a ten-fold reduction in salt concentration (up to 0.1 M NaCl) changes the effect of V on the SRE channel synchronization regardless of the membrane surface charge. As shown in Fig. 26, application of a positive V results in the appearance of clusters with i equal to 3 and 4 (Fig. 26A), but at negative voltages of the same absolute value (-150 mV), factor $i = 7$ (Fig. 26B).

Thus, a distinct asymmetry in the influence of positive and negative potentials on the mean number of synchronously working small channels in their clusters was observed. This effect is most likely related to the presence of local intra-membrane fields V_0/L near the channels. Using the m -quantity, this voltage sign effect can be observed with membranes of different lipid composition at different NaCl concentrations (Fig. 27). The data of Fig. 27 shows that: (1) a sufficient increase in the absolute value of the applied voltage leads to a reduction in the mean number of synchronously working small channels in both 0.1 M and 1 M NaCl solutions, and (2) this reduction observed becomes asymmetrical with dilute solutions of NaCl.

The observation that the m -value is a strongly voltage-dependent quantity may suggest that some charged and/or dipolar residues in the channel complex control the synchronous opening/closure of small channels in clusters. However, if this were the case, the curvature of the $m(V)$ -dependence would be changed at the transition from diluted to concentrated bathing electrolytes. Since this is not observed (Fig. 27), the observed reduction of mean number m must result from some other factors. At the same time, the observed shift of the maximum m -value may be a consequence of a charge effect. This charge might be donated solely by the SRE molecules, since the system under consideration is symmetrical with respect to both lipids and electrolyte composition of bathing solutions. Indeed, when membranes were bathed by 0.1 M sodium chloride solution, a prominent asymmetry in the sign of V was observed for the $m(V)$ -dependence, and it did not suffer significant changes under transition from negatively charged to uncharged membranes (Fig. 27). Furthermore, an indistinguishable dependence of $m(V)$ was obtained with PS/PE membranes bathed in 0.1 M NaCl solution at pH 3, where the negative charges of serine residues of PS are titrated at this low pH (see Section 4.4). Therefore, the local

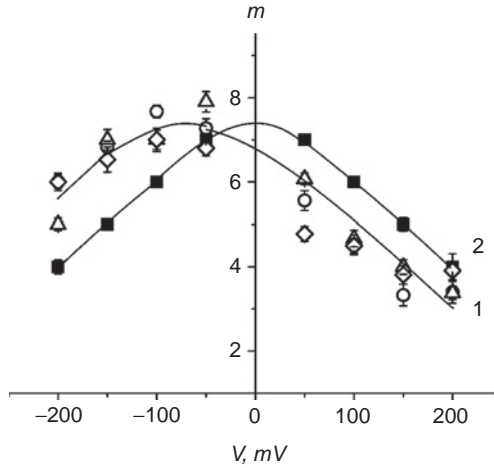


Figure 27 Voltage dependence of the mean normalized number of synchronously operating small channels in clusters. Symbols are the arithmetical means from three to five experiments. Bathing solution: 0.1 NaCl (curve 1), 1 M NaCl (curve 2). ○—membrane: PS/PE, bathing solution: 0.1 NaCl pH 6; △—membrane: PS/PE, bathing solution: 0.1 NaCl pH 3; ◇—membrane: PC, bathing solution: 0.1 NaCl pH 6; ■—membrane: PS/PE, bathing solution: 1 NaCl pH 6.

electric field caused by charged SRE species that enter into channel precursors seems responsible for the above asymmetry. If so, the asymmetry should disappear with concentrated solutions of NaCl, i.e. under conditions of screening the membrane surface charge. Such an effect does occur. In the case of 1 M NaCl solutions, the $m(V)$ -dependence becomes symmetrical for membranes composed of either charged (Fig. 27) or uncharged lipids (data not shown). Thus, the obtained data support the proposition that it is necessary to consider the local electric field in describing the formation of SRE channels.

One final set of observations related to the voltage-dependent properties of SRE channel structure must be pointed out. In field-reversal experiments with sufficiently large potential jumps, current recordings of a few large channels (see earlier text) show an instantaneous transition between channel clusters containing different numbers of synchronously working single channels (Fig. 28). This switching appears to correspond to the reciprocal transitions between clusters having different values of i (for the case of two states of channels see Scheme 6, Section 4.3). The observed kinetics for these transitions suggests that they proceed with characteristic times that are significantly lower than that of the current relaxation (τ_2 , see Section 4.3). This is the reason why the relevant changes in the concentrations of the intermediate large channels (with $i \leq m$) as function of time t do not affect the current relaxation. As a result, it instead corresponds to the two-exponential law of Eq. (1) despite the existence of different clusters.

In summary, three major conclusions about clustering of SRE channels can be drawn. First, the SRE clusters consist of at least m_{\max} small channels, where $m_{\max} \approx 7$ to 8 corresponds to the m -value extrapolated at $V = 0$. Second, the application of the membrane voltage promotes desynchronization of small channels operating in

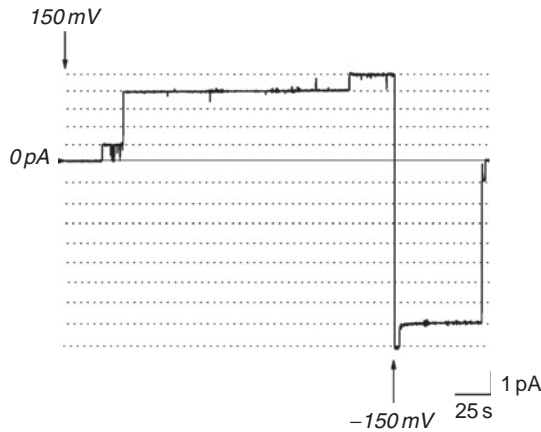


Figure 28 Current fluctuations corresponding to opening/closure of elementary SRE channels and clusters. The membranes were made from PS/PE and bathed in 0.1 M NaCl pH 6. Applications of ± 150 mV are indicated by the arrows.

the clusters. Thus, any SRE-cluster can operate as a small or large channel and the multiplicity factor of the large channels is regulated by the transmembrane potential. Third, the observed parallel shift of the $m(V)$ -curve at high ionic strength compared with that of diluted solutions suggests that charges of SRE molecules, as well as other charged and/or dipolar species, are not directly involved in cluster synchronization. This leaves us with the question: what other constituents of the channel complex or additional structural factors of its structure are responsible for the established voltage dependence of SRE cluster behavior? At the moment, answers to this question are lacking. However, it can be assumed that the observed reduction of mean number m with increasing absolute value of V results from changes in the two main radii that characterize the surface curvature in the channel pore and its environment. The necessity of such changes follows from the well-known dependence of the membrane tension, σ , on the transmembrane potential difference, V , namely $\sigma = \sigma_0 - C_m V^2/2$, where C_m is the membrane capacity and σ_0 , the membrane tension at $V = 0$ [71]. Such changes of σ vary the balance between forces acting on a channel and should be compensated by the corresponding changes of the curvature radii. The following arguments support this explanation. First, the absence of channel clusters with multiplicity factor $i = 2$ shows significant hindrances in conjugation between curvature radii of two neighboring small channels. Such hindrances are probably less expressed in cases of higher values of i , but might appear for certain values of multiplicity factor i depending on the applied voltage. Second, if changes of the membrane tension with varying potential V cause changes in the curvature radii near the channels, the registered values of $m(V)$ should be determined only by the membrane capacity C_m , i.e. the curvature of the $m(V)$ -dependence should be independent of lipid composition, dipole-modifying agents, etc., as it takes place in reality (see Section 4.6).

4.6. Influence of Dipole-Modifying Agents on Cluster Synchronization

As described in a previous section, the dipolar “heads” of the membrane-forming lipids can provide a significant impact to the voltage gating of the SRE channels [59,67,70]. This makes it possible to speculate that at small voltages lipid dipoles involved in the channel structure are specifically oriented and do not prevent synchronous opening or closure of all the small channels in a cluster, but at high voltages some hindrances occur due to polarization of lipid dipoles. However, as indicated earlier, if dipoles of lipids entering the channel structure participate in cluster synchronization, then changes of the membrane dipole potential with dipole-modifying agents or different lipids should induce some changes in the curvature of the $m(V)$ -dependence. This effect was not observed and it must be considered that the synchronization of channels included in clusters is not determined by dipolar (or charged) factors. Nevertheless, an influence on SRE channel function was observed as shown in Figs. 29 and 30.

Sample records in Fig. 29 illustrate the effect of successively increasing the membrane dipole potential on the activity of single small and large SRE channels. A rough estimation of φ_d was determined according to [67,69,72–76]. Panels A, B, and C correspond to current fluctuations in the presence of 20 μM phloretin, no dipole modifiers, and 5 μM RH 421 in the membrane-bathing solution, respectively. As a reminder, the large current fluctuations correspond to the simultaneous opening or closure of several elementary SRE channels (large SRE channels or clusters). These recordings show that the reduction of the membrane dipole potential (φ_d) to about 120 mV induced by addition of 20 μM phloretin leads to a slight increase in the number of elementary channels in clusters, but a decrease in both the elementary channel amplitude and the lifetime of small channels during their burst activity (t_1 , see Section 4.3). The increase of φ_d to ~ 300 mV by the addition of 5 μM of RH 421 (or by the inclusion of 6-ketocholestanol into the membrane-forming solution, data not shown) results in opposite effects.

Figure 30 shows the voltage dependence of the mean number of synchronously operating elementary channels in clusters (m) at 1 M pH 6 (Fig. 30A) and 0.1 M

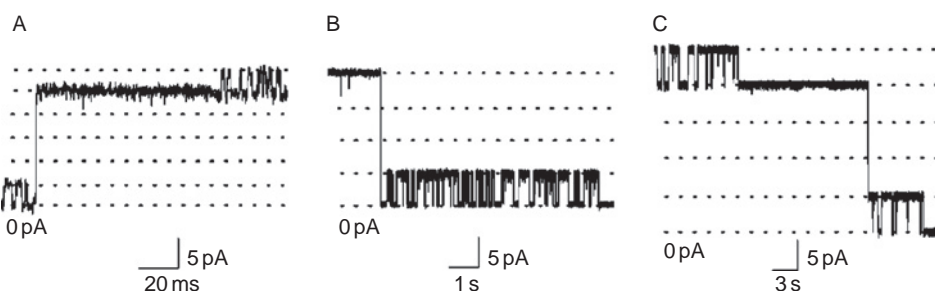


Figure 29 Current fluctuations induced by SRE in bilayers of different dipole potentials. The membranes were made from PS/PE and bathed in 1 M NaCl pH 6 $V = 160$ mV. (A) $\varphi_d = (120 \pm 20)$ mV (20 μM phloretin); (B) $\varphi_d = (230 \pm 20)$ mV (no dipole modifier); (C) $\varphi_d = (300 \pm 40)$ mV (5 μM RH 421). The intervals between the dashed lines are equal to the amplitude of the elementary SRE channel.

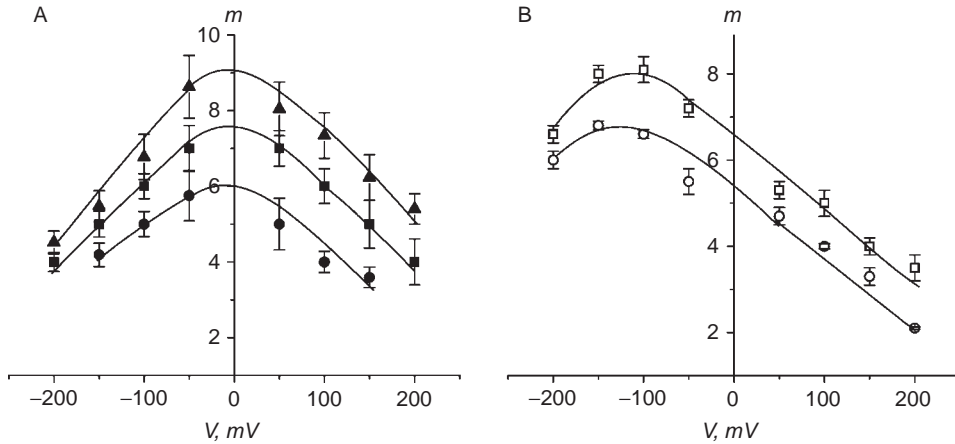


Figure 30 Voltage dependence of the mean number of synchronized elementary channels in clusters. (A) Membranes were made from PS/PE and bathed in 1 M NaCl pH 6. (\blacktriangle) $\varphi_d = (120 \pm 20)$ mV (with 20 μ M phloretin); (\blacksquare) $\varphi_d = (230 \pm 20)$ mV (no dipole modifier); (\bullet) $\varphi_d = (300 \pm 40)$ mV (with 5 μ M RH 421); (B) Membranes were made from the mixture of PS (33 mol%) and either PE or 6-ketocholestanol and bathed in 0.1 M NaCl pH 6. (\square) $\varphi_d = (230 \pm 20)$ mV (67 mol% PE, no dipole modifier); (\circ) $\varphi_d = (430 \pm 20)$ mV (67 mol% 6-ketocholestanol).

pH 6 (Fig. 30B) NaCl solutions bathing membranes of different dipole potentials. At high NaCl concentration (1 M) (Fig. 30A), the $m(V)$ -curves are symmetrical with respect to V , but their position along the ordinate is determined by the φ_d -value. The application of V of either sign or increase in φ_d induces desynchronization of elementary channels. As a result, SRE clusters with fewer (less than 9) synchronously opened channels appear. From Fig. 30B one can also see that, at low NaCl concentration (0.1 M), the maximum of the $m(V)$ -curves appears to be shifted to more negative voltages (~ -100 mV) in membranes without dipole modifier and in membranes containing 6-ketocholestanol. In other words, the asymmetry effect discussed previously occurs, and as expected it does not depend on the membrane dipole potential.

The numbers of synchronously operating elementary channels at $V \rightarrow 0$ (m_{\max}) were estimated over the entire range of φ_d values studied. Figure 31 shows the relevant dependency of m_{\max} as a function of the membrane dipole potential at 1.0 M NaCl. It is seen that a five-fold increase in φ_d results in a two-fold decrease of m_{\max} . First-order exponential fitting of these data allows us to suggest that approximately 13 elementary channels is the maximum number of synchronized units in one SRE channel cluster.

In contrast to relatively small changes in the channel conductance, the lifetime of the elementary SRE channels during their burst activity (t_1) changed dramatically as a function of φ_d . The increase of φ_d from ~ 100 to ~ 380 mV produces a 300-fold increase in t_1 (at $V = -200$ mV, 1.0 M NaCl) (see Fig. 32). The membrane dipole potential has a similar effect on the lifetime of the SRE clusters, t_6 (data not shown). At present, the mechanisms by which dipole-modifying agents regulate burst activity are not clear. Such regulation is usually related to the existence of ionic channel agonists [77]. If this applies to SRE channels, then it would mean that lipid molecules can serve as agonists.

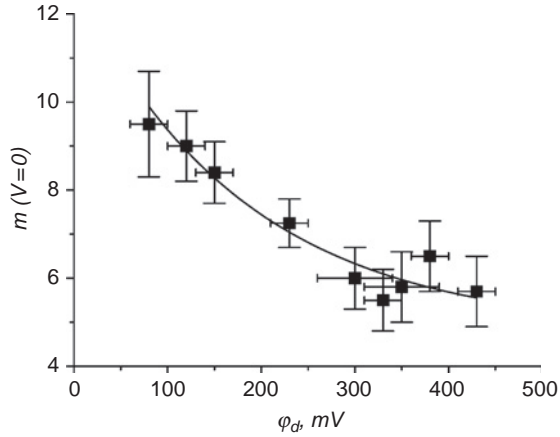


Figure 31 The mean number of synchronized elementary channels in clusters at $V \rightarrow 0$ as a function of the membrane dipole potential. The membranes were bathed in 1 M NaCl pH 6.

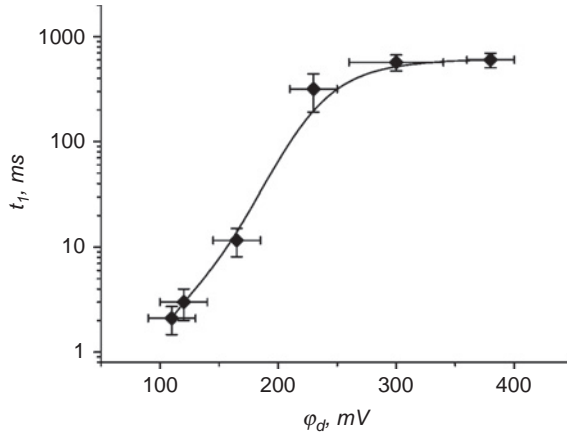


Figure 32 The mean life time of the elementary SRE channel at $V = -200$ mV as a function of the membrane dipole potential. The membranes were bathed in 1 M NaCl pH 6.

As mentioned already, the current amplitudes of the SRE elementary channel depend on φ_d (Fig. 29). The conductance of elementary SRE channels (G_1) as a function of V in 1 M and 0.1 M NaCl at different φ_d values were measured (Fig. 33). The results presented in Fig. 33 show that increasing the potential φ_d produces an increase in the elementary channel conductance at all V 's tested. The results also show that, at a given NaCl concentration, the shapes of the conductance-voltage curves are not influenced by the dipole potential. At the same time, the changes in the channel conductance values are not significant as compared to the large changes of the dipole potential. Therefore, it may be concluded that the SRE pore geometry is not influenced by φ_d .

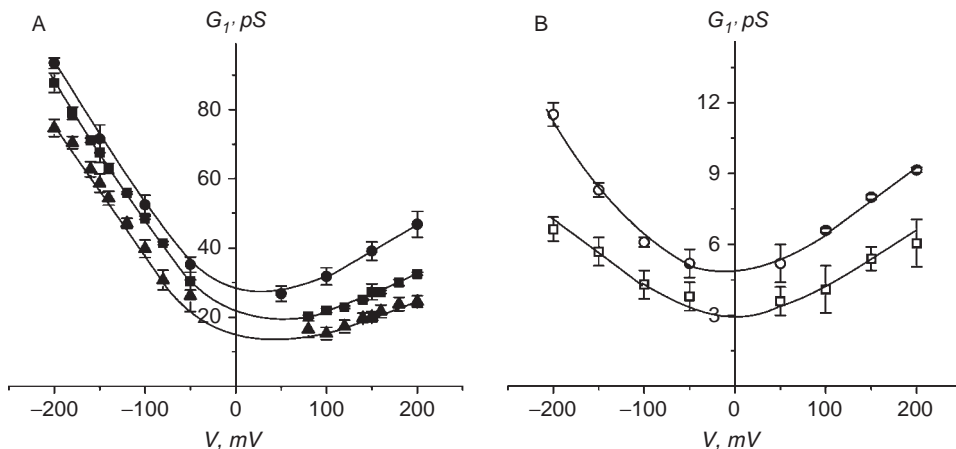


Figure 33 Conductance–voltage curves of the elementary SRE channels in the membrane of different dipole potential. (A) Membranes were made from the equimolar mixture of PS and PE or PS and 6-ketocholestanol, bathed in 1 M NaCl. (▲) $\varphi_d = (120 \pm 20)$ mV (with 20 μ M phloretin); (■) $\varphi_d = (230 \pm 20)$ mV (no dipole modifier); (●) $\varphi_d = (380 \pm 20)$ mV (50 mol% PS and 50 mol% 6-ketocholestanol); (B) Membranes were made from the mixture of PS (33 mol%) and either PE or 6-ketocholestanol. The membrane bathing solution was 0.1 M NaCl. (□) $\varphi_d = (230 \pm 20)$ mV (67 mol% PE, no dipole modifier); (○) $\varphi_d = (430 \pm 20)$ mV (67 mol% 6-ketocholestanol).

According to Andersen *et al.* [78], ion membrane conductance (G) depends on ion mobility (λ), ion concentration in the aqueous phase (C), and membrane dipole potential (φ_d) according the equation:

$$G \propto \lambda C \exp(-ze\varphi_d/kT) \quad (18)$$

where ze is the ion charge. Eq. (18) predicts a decrease in anion and an increase in cation membrane conductance with the reduction of φ_d [79–81]. For the SRE channels, which are preferentially anion-conductive [40,46], Eq. (18) qualitatively corresponds to the results given in Fig. 33. However, changes in the SRE channel conductance that can be calculated by using Eq. (18) are more pronounced than the experimental ones [82]. According to [83, 84], such a discrepancy between experimental and calculated values of channel conductance is attributed to the effect of shielding the dipole potential in the channel pore interior. Relevant estimates for SRE channels reported in [82] yield a mean value of such shielding ($\approx 93\%$), which is in accord with that observed for other channels [83].

4.7. Influence of Polymers on SRE Channel-Forming Activity

As described previously, SRE channel-forming activity is influenced by bilayer lipid composition, lipid charge, ionic strength of the bathing solution, and dipole-modifying species [25,32,33,67]. More recently, the SRE channel-forming activity has been shown to be influenced by the presence of amphiphilic polymers, such as

G- and F-actin, König's polyanion (KP), and the positively charged copolymer of lysine and tryptophan (PLT). These substances increase the channel-forming SRE activity only if they are applied to the side of a bilayer opposite of SRE addition [85–87]. An example for this is shown in Fig. 34 for the case of G-actin addition. An effect is observed only with *trans*-side addition of G-actin to bilayers exposed to SRE added on the *cis*-side. Also, *trans*-side addition of G-actin (as well as the other polymers) does not affect the amplitudes of the current fluctuations observed before and after its addition (Fig. 34). This permits one to propose that *trans*-side addition of the polymers stimulates the SRE channel-forming activity rather than forming other conducting units. This proposition was confirmed by measurements of the gating charge of SRE channels, q_1 , in the presence of actin or other polymers. Its value was the same as that in their absence (approximately equal to unity in PS/PE membranes bathed in 0.1 M NaCl), and its concrete value and sign were also dependent on the bathing electrolyte concentration (see earlier text). The time needed to achieve a steady-state current value in the systems nonequilibrated with actin was longer than required for the equilibrated systems, i.e. 100–200 min (depending on either G- or F-actin presence) for the former, and only 10 min for the latter which is also the time needed in the absence of these actins ($\approx 3\tau_2$ see earlier text). This implies that either adsorption of actins on the *trans*-side membrane surface or a slow process initiated by their adsorption is a limiting step in the observed steady-state relaxation of SRE-induced current. These observations suggest that actin directly interacts with lipid membranes without any intermediates.

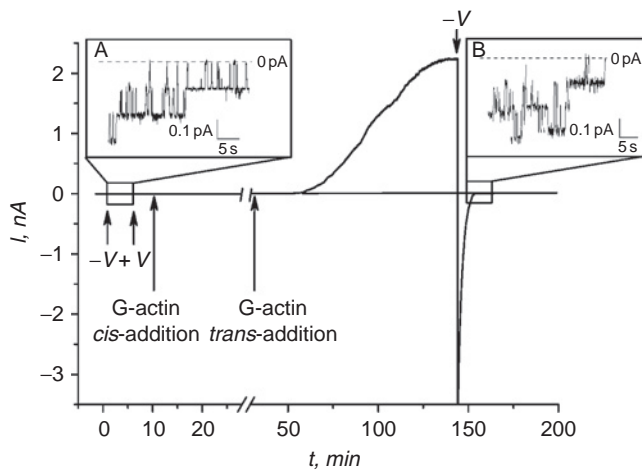


Figure 34 Typical time courses of the SRE-induced transmembrane current with addition of actin. SRE was first added to the *cis*-side of the lipid bilayer to provide the stable formation of several channels. Subsequent application of G-actin (4 $\mu\text{g}/\text{ml}$) to the *cis*-side did not produce measurable changes in membrane conductance, while *trans*-side actin addition initiated current increase at $V = 50$ mV. Reversing the voltage sign stimulated current decrease. Single-channel amplitudes, resolved at the end of the recording (inset B), did not diverge from those observed before actin addition (inset A). PS/PE membranes were bathed in 0.1 M NaCl pH 6.

It follows from the above that the kinetics of this process (the value of time τ_2) does not depend on the presence (or absence) of actin in the *trans*-compartment of the membrane system when in equilibrium with actin. Thus, changes in the mechanism of opening/closure of SRE channels do not accompany the transition from a system without actin to that which has actin. This allows the speculation that the affinity of the *cis*-membrane surface to SRE increases with the *trans*-addition of actin.

It was also established that the effects of actins, KP, and PLT on the SRE channel-forming activity do not suffer qualitative changes under replacing charged lipids by neutral ones or screening the lipid charges by high ionic strength of the bathing solution. Thus, the main contribution to the observed influence of the polymers is due to their hydrophobic interactions with bilayers. Because of their hydrophobicity, the polymers may penetrate to some degree into the inner part of *trans*-monolayer. This would change the local structure of the *cis*-monolayer within the region adjacent to the adsorbed particles and thus increase the affinity of SRE precursors to the *cis*-monolayer. Nevertheless, other substances such as vinculin, alpha-actinin, albumin, myoglobin, and lysozyme, which also adsorb on lipid membranes via hydrophobic interactions [88–93] did not affect the SRE channel-forming activity [87]. Therefore, hydrophobic interactions between adsorbing particles and the membrane are necessary, but not sufficient to increase the SRE activity. This dependence may be quantitatively characterized by analyzing changes in the total number of open elementary SRE channels, $N_{op}(V, \infty) = I(V, \infty)/I_1(V)$ (see earlier text), as a function of concentration of an introduced agent (C_a) at given potential V . For all substances that increase SRE activity (i.e., G- and F-actin, KP, PLT), the relevant curves have a sigmoid form, suggesting a cooperative character of their adsorption properties (see Fig. 35). From this analysis, it is hypothesized that adsorption of the polymers proceeds with

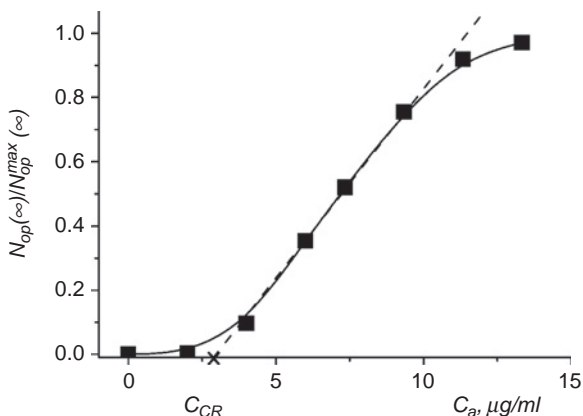


Figure 35 Dependence of $N_{op}(\infty)/N_{op}^{\max}(\infty)$ on G-actin concentration in the *trans*-compartment. PS/PE bilayers were bathed in 0.1 M NaCl pH 6 $V = 50$ mV. SRE was added in the *cis*-compartment before G-actin addition. Dashed line is given to show the determination of critical concentration, which corresponds to the domain formation, C_{CR} . $N_{op}^{\max}(\infty)$ is the maximum value of $N_{op}(\infty)$ achieved in the limit $C_a \rightarrow \infty$.

formation of some aggregates (or domains) of adsorbing particles in the *trans*-monolayer of the membrane. It is likely that the existence of such domains in *trans*-monolayer induces changes in the adjacent regions of the *cis*-monolayer, which in turn increases the affinity of precursors of SRE channels to these modified regions. Thus, it is speculated that the sufficient condition for increasing the SRE activity by adsorbing particles is their attractive interactions between one another which leads to domain (perhaps micelle) formation of the interacting molecules on the membrane.

The domain formation hypothesis is supported in the case of G-actin by the following observations. First, preliminary treatment of G-actin by trypsin, which hydrolyzes actin and, thus, hinders the ability of actin to polymerize [94], diminishes its ability to increase the SRE activity [87]. Second, the steady-state current relaxation induced by *trans*-addition of low concentrations at subcritical levels (see below) of G-actin shows a latency period τ of the actin effect (for definition of τ see Fig. 36). Such the time necessary for the beginning of essential current increases induced by actin is not a deterministic quantity, but a probabilistic one. It is characterized by a wide spectrum of accidental values, so that its mean value is commensurable with the time of attainment of the steady-state current or the steady-state total number of open elementary channels, $N_{op}(V, \infty)$. This is not surprising, since, in the case considered, the latent period is due to a slow appearance of the actin domains responsible for the increased SRE activity. Their generation is a stochastic process resulting from accidental events in the time course. Figure 36 illustrates the current responses of the membrane system with sequential additions and incremental increases in the concentration of actin. The transmembrane current as a function

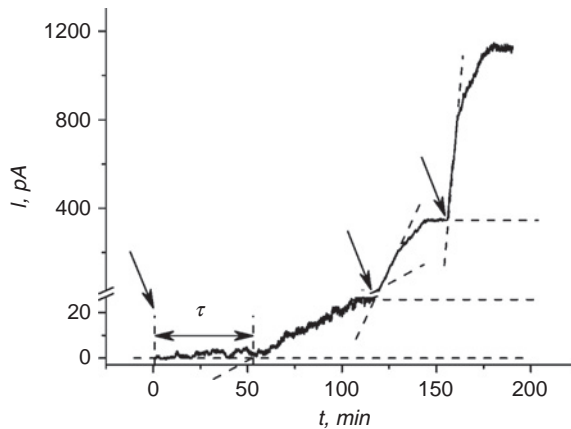


Figure 36 Time course of the transmembrane current with three successive additions of G-actin to the *trans*-compartment. The concentrations of G-actin were 2, 4 and 6 $\mu\text{g}/\text{ml}$ for the 1st, 2nd, and 3rd additions, respectively. The time period, τ , was determined as the time between actin addition (marked by arrows) and the beginning of the practically linear rise of the actin-induced current (indicated by intercepts of dashed and dotted lines). Values of τ were: 52, 1.3, and 1.7 min for the 1st, 2nd, and 3rd additions, respectively. Other experimental conditions were the same as those for Fig. 35.

of time has an essential delay (i.e. the latent time) for small subcritical concentrations ($\approx 2 \mu\text{g/ml}$), but not with further additions of actin. This suggests that domain formation begins with initial application of actin, and the subsequent current responses reflect only increases in the sizes of the domains (Fig. 36).

Using this and other simple suppositions, we performed a quantitative treatment of the kinetic changes in the $N_{op}(V, t)$ -number after each consecutive addition of G-actin beginning with the second addition (i.e., when the latent period τ is absent, see Fig. 36). The theoretical considerations used are similar to those involved in the theory of wetting processes: capillary rising [95,96], spreading of lenses and black spot growth on lipid membranes [97,98] and described in [87]. Accordingly, the time dependence of $N_{op}(t)$ at a given V should satisfy either Eq. (19) or Eq. (20) depending on whether the domain radius growth results from absorption of adsorbed G-actin particles into the domains or their inclusion into domains from the aqueous solution, respectively:

$$\sqrt{N_{op}(t)/N_{op}(\infty)} + \ln \left[1 - \sqrt{N_{op}(t)/N_{op}(\infty)} \right] - \left(\sqrt{N_{op}(0)/N_{op}(\infty)} + \ln \left[1 - \sqrt{N_{op}(0)/N_{op}(\infty)} \right] \right) = -\gamma t / \mu r^2(\infty) \quad (19)$$

$$\ln \left[1 - \sqrt{N_{op}(t)/N_{op}(\infty)} \right] - \ln \left[1 - \sqrt{N_{op}(0)/N_{op}(\infty)} \right] = -\gamma t / \mu_0 r(\infty) \quad (20)$$

Here, γ is the so-called linear tension related to the domain curvature $1/r(\infty)$ [71], where $r(\infty)$, the equilibrium value of the domain radius at fixed concentration C_a of G-actin (or other agent that increases the SRE activity); μ is a parameter similar to the surface viscosity [99]; μ_0 is a parameter, which can be called the linear viscosity; $N_{op}(0)$ and $N_{op}(\infty)$, the steady-state numbers of open elementary channels appeared on the membrane before and after *trans*-addition of G-actin, respectively. Performing the expansion of $\ln[1 - \sqrt{N_{op}(t)/N_{op}(\infty)}]$ on powers of $\sqrt{N_{op}(t)/N_{op}(\infty)} < 1$, it is easily elucidated that the functional dependences given by Eqs. (19) and (20) differ only if the ratio of $N_{op}(t)/N_{op}(\infty) \ll 1$ (which may only occur at the initial stages of increasing the $N_{op}(t)$ -number). Thus, the experimental data for G-actin and PLT formally satisfy both equations (see Fig. 37). As expected linear dependences of $Y(t)$ are observed in all the cases (here, function Y coincides to either the left part of Eq. (19) or that of Eq. (20)). The same uncertainty takes place for data obtained with KP. To discriminate the earlier-mentioned mechanisms of inclusion of the particles into their domains, the slopes of the obtained kinetic curves (curves 1 and 2 of Fig. 37A and B) as functions of concentration C_a were analyzed. The insets to the same figures show that for the case of G-actin the slopes are linear functions of $C_a^{1/2}$, while for the data obtained with PLT (and KP), they are independent of C_a . This suggests that G-actin species enter mainly into domains (after their formation) from an aqueous solution directly, while PLT (and KP) particles do so through an intermediate step of

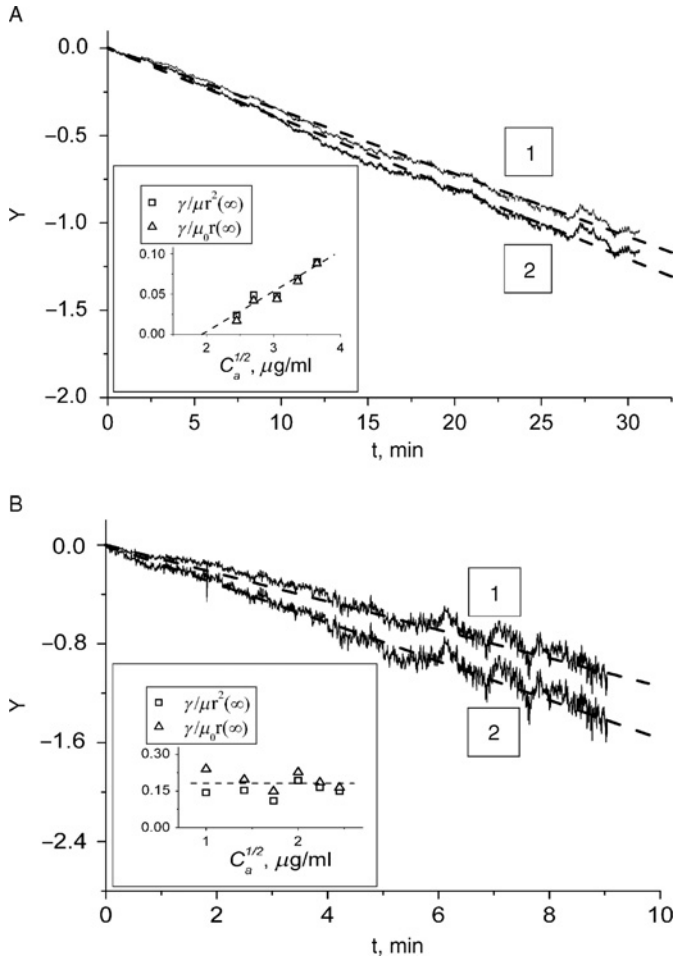


Figure 37 Treatment of experimental $N_{op}(t)$ -curves according to Eqs. (19) and (20) in the case of G-actin- (A) or PLT-addition (B) at the *trans*-side of the membrane. Y axis is either: $\sqrt{N_{op}(t)/N_{op}(\infty)} + \ln[1 - \sqrt{N_{op}(t)/N_{op}(\infty)}] - (\sqrt{N_{op}(0)/N_{op}(\infty)} + \ln[1 - \sqrt{N_{op}(0)/N_{op}(\infty)}])$ (curve 1) or $\ln[1 - \sqrt{N_{op}(t)/N_{op}(\infty)}] - \ln[1 - \sqrt{N_{op}(0)/N_{op}(\infty)}]$ (curve 2). Experimental conditions: PS/PE bilayer bathed in 0.1 M NaCl pH6 $V = 50$ mV. G-actin and PLT concentrations were 9.3 $\mu\text{g/ml}$ and 3 $\mu\text{g/ml}$, correspondingly. Inset: dependences of $\gamma/\mu^2(\infty)$ (\square) and $\gamma/\mu_0(\infty)$ (∇) on the G-actin (A) or PLT (B) concentration.

adsorption. Indeed, according to the literature [100], the concentration of monomer species should not significantly change after attainment of the critical concentration of micelle formation (domain formation in the case considered). In the alternative case of monomer inclusion from aqueous solution, the rate of inclusion must depend on concentration C_a , as observed for the case with G-actin (for details see appendix to paper [87]). Further support of this conclusion comes from extrapolation of slopes $dY(t)/(dC_a^{1/2})$ at zero values of these derivatives which

coincides with the square root of the critical concentration of the actin domain formation, C_{CR} . The latter was estimated as shown in Fig. 35, and its value lies in the interval of $3 \div 4 \mu\text{g/ml}$, i.e. the same value derived from the data of the inset of Fig. 37A. Thus, the mechanisms of events responsible for the kinetics of domain growth are slightly different for the various polymers examined, although their effects on SRE activities are qualitatively the same. Explanations for the absence of polymer influence on SRE activity when added on the same side as SRE are unclear. However, by analogy with the mechanisms invoked for opposite side addition, it may be speculated that repulsive interactions and steric hindrances between SRE species and adsorbed particles located in domains may be involved.

In conclusion, actins and other polymers strongly increase the probability of the SRE channel formation in lipid bilayers. This leads to the consideration that actin filaments of the living cell cytoskeleton can play a stabilizing role in the function of ion channels in cells. Such a role receives support from the findings of Negulyaev *et al.* [101, 102] on actin regulation of nonvoltage-gated sodium channels in leukemia K562 cells.

5. SUMMARY AND CONCLUSIONS

The biological activities of SRE and other CLPs produced by the plant bacterium *Pseudomonas. syringae* pv. *syringae* are explained by their ability to form ion channels. In model cellular systems (e.g., yeast and erythrocytes), this ability is influenced by the lipids of the target membranes and, in particular, by the sterol and sphingolipid compositions. The most informative studies of the mechanisms of SRE ion channel formation and structure have been with artificial lipid bilayers modified with one side addition of CLPs. CLPs form well-defined ion channels in such bilayers. At least two conducting states of these channels (small and large ones) are observed. Large channels (or channel clusters) result from cooperative functioning of several small ones. Both kinds of channels are predominately anion selective and possess a pronounced voltage gating similar to ionic channels of living cells. Small SRE channels are asymmetric lipid pores stabilized by toxin particles, and they have a cone shape of the radii 0.3 and 0.9 nm. The current–voltage curves of single SRE channels are nonlinear and, as a rule, asymmetric (with respect to the sign of applied voltage). Single channel measurements of channel opening/closure show the existence of more than one close state of the channels, in other words, the so-called burst activity of the SRE channels takes place. Beside the applied voltage, the membrane dipole potential is an important factor that affects the properties of SRE channels. In particular, both the values and the sign of the so-called gating charge of these channels depend on the membrane surface charge as well as the dipole moments of membrane-forming lipids. The channel-forming activity of SRE in lipid bilayers can be increased by *trans*-addition of amphiphilic agents such as G- and F-actin, Konig's polyanions, and polylysine tryptophan.

Thus, the channels formed by SRE and other CLPs reveal features that in many respects are similar to those of ionic channels of living cells. In spite of the considerable progress in studying the ion channels induced by CLPs in artificial

lipid membranes, important questions related mainly to the structures of these channels remain open for future investigation.

ACKNOWLEDGMENTS

This study was supported in part by the Russian Foundation for Basic Research (project no. 06-04-48860), the program of RAS (Molecular and Cell Biology), the National Science Foundation (USA), Eli Lilly and Co., and the Utah Agricultural Experiment Station.

REFERENCES

- [1] T. Leisinger, R. Margraff, Secondary metabolites of the fluorescent pseudomonads, *Microbiol. Rev.* 43 (1979) 422–442.
- [2] C.L. Bender, F. Alarcon-Chaidez, D.C. Gross, *Pseudomonas syringae* phytotoxins: Mode of action, regulation, and biosynthesis by peptide and polyketide synthetases, *Microbiol. Mol. Biol. Rev.* 63 (1999) 266–292.
- [3] J.Y. Takemoto, Bacterial phytotoxin syringomycin and its interaction with host membranes, *In Molecular Signals in Plant-Microbe Communications*, (D.P.S. Verma, Ed.), pp. 247–260. CRC Press, Boca Raton.
- [4] G. Dulla, M. Marco, B. Quinones, S. Lindow, A closer look at *Pseudomonas syringae* as a leaf colonist, *ASM News* 71 (2005) 469–475.
- [5] J.E. DeVay, F.L. Lukezic, S.L. Sinden, H. English, D.L. Coplin, A biocide produced by pathogenic isolates of *Pseudomonas syringae* and its possible role in the bacterial canker disease of peach trees, *Phytopathology* 58 (1968) 95–101.
- [6] N.S. Iacobellis, P. Lavermicocca, I. Grgurina, M. Simmaco, A. Ballio, Phytotoxic properties of *Pseudomonas syringae* pv. *syringae* toxins, *Physiol. Mol. Plant Pathol.* 40 (1992) 107–116.
- [7] K.N. Sorensen, K.H. Kim, J.Y. Takemoto, *In vitro* antifungal and fungicidal activities and erythrocyte toxicities of cyclic lipodepsinonapeptides produced by *Pseudomonas syringae* pv. *syringae*, *Antimicrob. Agents Chemother.* 40 (1996) 2710–2713.
- [8] M.F. Bensaci, J.Y. Takemoto, Syringopeptin SP25A-mediated killing of gram-positive bacteria and role of teichoic acid D-alanylation, *FEMS Microbiol. Lett.* 268 (2007) 106–111.
- [9] I. Grgurina, M. Bensaci, G. Pocsfalvi, L. Mannina, O. Cruciani, A. Fiore, V. Fogliano, K. N. Sorensen, J.Y. Takemoto, Novel Cyclic Lipodepsipeptide from *Pseudomonas syringae* pv. *lachrymans* strain 508 and syringopeptin antimicrobial activities, *Antimicrob. Agents Chemother.* 49 (2005) 5037–5045.
- [10] B.K. Scholz-Schroeder, M.L. Hutchison, I. Grgurina, D.C. Gross, The contribution of syringopeptin and syringomycin to virulence of *Pseudomonas syringae* pv. *syringae* strain B301D on the basis of sypA and syrB1 biosynthesis mutant analysis, *Mol. Plant Microbe. Interact.* 14 (2001) 336–348.
- [11] A.J. De Lucca, T.J. Jacks, J. Takemoto, B. Vinyard, J. Peter, E. Navarro, T.J. Walsh, Fungal lethality, binding, and cytotoxicity of syringomycin-E, *Antimicrob. Agents Chemother.* 43 (1999) 371–373.
- [12] E. Buber, A. Stindl, N.L. Acan, T. Kocagoz, R. Zocher, Antimycobacterial activity of lipodepsipeptides produced by *Pseudomonas syringae* pv. *syringae* B359, *Nat. Prod. Lett.* 16 (2002) 419–423.
- [13] N. Fukuchi, A. Isogai, J. Nakayama, S. Takayama, S. Yamashita, K. Suyama, J.Y. Takemoto, A. Suzuki, Structures and stereochemistry of three phytotoxins, syringomycin, syringotoxin and syringostatin, produced by *Pseudomonas syringae* pv. *syringae*, *J. Chem. Soc. Perkin Trans. 1* (1992) 1149–1157.
- [14] A. Segre, R.C. Bachmann, A. Ballio, F. Bossa, I. Grgurina, N.S. Iacobellis, G. Marino, P. Pucci, M. Simmaco, J.Y. Takemoto, The structure of syringomycins A1, E and G, *FEBS Lett.* 255 (1989) 27–31.

- [15] A. Ballio, F. Bossa, A. Collina, M. Gallo, N.S. Iacobellis, M. Paci, P. Pucci, A. Scaloni, A. Segre, M. Simmaco, Structure of syringotoxin, a bioactive metabolite of *Pseudomonas syringae* pv. *syringae*, FEBS Lett. 269 (1990) 377–380.
- [16] A. Ballio, F. Bossa, D. Di Giorgio, P. Ferranti, M. Paci, A. Scaloni, A. Segre, G. Strobel, Novel bioactive lipodepsipeptides from *Pseudomonas syringae*: The pseudomycins, FEBS Lett. 355 (1994) 96–100.
- [17] M.C. Flamand, S. Pelser, E. Ewbank, H. Maraite, Production of syringotoxin and other bioactive peptides by *Pseudomonas fuscovaginae*, Physiol. Mol. Plant Pathol. 48 (1996) 217–231.
- [18] V. Vassilev, P. Lavermicocca, C. Di Giorgio, N. Iacobellis, Production of syringomycins and syringopeptins by *Pseudomonas syringae* pv. *atrofaciens*, Plant Pathol. 45 (1996) 316–322.
- [19] H. Batoko, A. de Kerchove d'Exaerde, J.M. Kinet, J. Bouharmont, R.A. Gage, H. Maraite, M. Boutry, Modulation of plant plasma membrane H^+ -ATPase by phytotoxic lipodepsipeptides produced by the plant pathogen *Pseudomonas fuscovaginae*, Biochim. Biophys. Acta 1372 (1998) 216–226.
- [20] A.P. Bidwai, L. Zhang, R.C. Bachmann, J.Y. Takemoto, Mechanism of action of *Pseudomonas syringae* phytotoxin, syringomycin. Stimulation of red beet plasma membrane ATPase activity, Plant Physiol. 83 (1987) 39–43.
- [21] D. Di Giorgio, L. Camoni, K.A. Mott, J.Y. Takemoto, A. Ballio, Syringopeptins, *Pseudomonas syringae* pv. *syringae* phytotoxins, resemble syringomycin in closing stomata, Plant Pathol. 45 (1996) 564–571.
- [22] H.H. Reidl, J.Y. Takemoto, Mechanism of action of bacterial phytotoxin, syringomycin. Simultaneous measurement of early responses in yeast and maize, Biochim. Biophys. Acta. 898 (1987) 59–69.
- [23] A.P. Bidwai, J.Y. Takemoto, Bacterial phytotoxin, syringomycin, induces a protein kinase-mediated phosphorylation of red beet plasma membrane polypeptides, Proc. Natl. Acad. Sci. USA 84 (1987) 6755–6759.
- [24] M.L. Hutchison, M.A. Tester, D.C. Gross, Role of biosurfactant and ion channel-forming activities of syringomycin in transmembrane ion flux: A model for the mechanism of action in the plant-pathogen interaction, Mol. Plant-Microbe Interact. 8 (1995) 610–620.
- [25] P.A. Gurnev, Y.A. Kaulin, A.V. Tikhomirova, R. Wangsra, D. Takemoto, V.V. Malev, L. V. Schagina, Activity of toxins produced by *Pseudomonas syringae* pv. *syringae* in model and cell membranes, Tsitologiya. 44 (2002) 296–304 (in Russian.).
- [26] J.Y. Takemoto, Y. Yu, S.D. Stock, T. Miyakawa, Yeast genes involved in growth inhibition by *Pseudomonas syringae* pv. *syringae* syringomycin family lipodepsipeptides, FEMS Microbiol. Lett. 114 (1993) 339–342.
- [27] N. Taguchi, Y. Takano, C. Julmanop, Y. Wang, S. Stock, J. Takemoto, T. Miyakawa, Identification and analyses of the *Saccharomyces cerevisiae* SYR1 reveals that ergosterol is involved in the action of syringomycin, Microbiology 140 (1994) 353–359.
- [28] M.M. Grilley, S.D. Stock, R.C. Dickson, R.L. Lester, J.Y. Takemoto, Syringomycin action gene SYR2 is essential for sphingolipid 4-hydroxylation in *Saccharomyces cerevisiae*, J. Biol. Chem. 273 (1998) 11062–11068.
- [29] H. Hama, D.A. Young, J.A. Radding, D. Ma, J. Tang, S.D. Stock, J.Y. Takemoto, Requirement of sphingolipid alpha-hydroxylation for fungicidal action of syringomycin E, FEBS Lett. 478 (2000) 26–28.
- [30] S.D. Stock, H. Hama, J.A. Radding, D.A. Young, J.Y. Takemoto, Syringomycin E inhibition of *Saccharomyces cerevisiae*: Requirement for biosynthesis of sphingolipids with very-long-chain fatty acids and mannose- and phosphoinositol-containing head groups, Antimicrob. Agents Chemother. 44 (2000) 1174–1180.
- [31] R.C. Dickson, R.L. Lester, Yeast sphingolipids, Biochim. Biophys. Acta 1426 (1999) 347–357.
- [32] A.M. Feigin, L.V. Schagina, J.Y. Takemoto, J.H. Teeter, J.G. Brand, The effect of sterols on the sensitivity of membranes to the channel-forming antifungal antibiotic, syringomycin E, Biochim. Biophys. Acta 1324 (1997) 102–110.
- [33] Y.A. Kaulin, J.Y. Takemoto, L.V. Schagina, O.S. Ostroumova, R. Wangsra, J.H. Teeter, J. G. Brand, Sphingolipids influence the sensitivity of lipid bilayers to fungicide, syringomycin E, J. Bioenerg. Biomembr. 37 (2005) 339–348.

- [34] D.A. Brown, E. London, Structure and origin of ordered lipid domains in biological membranes, *J. Membr. Biol.* 164 (1998) 103–114.
- [35] M. Bagnat, S. Keranen, A. Shevchenko, A. Shevchenko, K. Simons, Lipid rafts function in biosynthetic delivery of proteins to the cell surface in yeast, *Proc. Natl. Acad. Sci. USA.* 97 (2000) 3254–3259.
- [36] E. Kubler, H. Dohlmann, M. Lisanti, Identification of Triton X-100 insoluble membrane domains in the yeast *Saccharomyces cerevisiae*. Lipid requirements for targeting of heterotrimeric G-proteins subunits, *J. Biol. Chem.* 271 (1996) 32975–32980.
- [37] J. Idkowiak-Baldys, M.M. Grilley, J.Y. Takemoto, Sphingolipid C4 hydroxylation influences properties of yeast detergent-insoluble glycolipid-enriched membranes, *FEBS Lett.* 569 (2004) 272–276.
- [38] K. Blasko, L.V. Schagina, G. Agner, Y.A. Kaulin, J.Y. Takemoto, Membrane sterol composition modulates the pore forming activity of syringomycin E in human red blood cells, *Biochim. Biophys. Acta* 1373 (1998) 163–169.
- [39] M. Dalla Serra, G. Faggioli, P. Nordera, I. Bernhart, C. Della Volpe, D. Di Giorgio, A. Ballio, G. Menestrina, The interaction of lipopeptide toxins from *Pseudomonas syringae* pv. *syringae* with biological and model membranes: A comparison of syringotoxin, syringomycin, and two syringopeptins, *Mol. Plant-Microbe Interact.* 12 (1999) 391–400.
- [40] A.M. Feigin, J.Y. Takemoto, R. Wangspa, J.H. Teeter, J.G. Brand, Properties of voltage-gated ion channels formed by syringomycin E in planar lipid bilayers, *J. Membrane Biol.* 149 (1996) 41–47.
- [41] A. Carpaneto, M. Dalla Serra, G. Menestrina, V. Fogliano, F. Gambale, The phytotoxic lipopeptide syringopeptin 25A from *Pseudomonas syringae* pv. *syringae* forms ion channels in sugar beet vacuoles, *J. Membr. Biol.* 188 (2002) 237–248.
- [42] V.V. Malev, Y.A. Kaulin, S.M. Bezrukov, P.A. Gurnev, J.Y. Takemoto, L.V. Schagina, Kinetics of opening and closure of syringomycin E channels formed in lipid bilayers, *Membr. Cell Biol.* 14 (2001) 813–829.
- [43] Kh.M. Kasumov, E.A. Liberman, Ionic permeability of bimolecular membranes in the presence of polyene antibiotics. II. Levorin, trichomycin, candicidin, *Biofizika.* 18 (1973) 264–271 (in Russian).
- [44] Y.A. Kaulin, L.V. Schagina, S.M. Bezrukov, V.V. Malev, A.M. Feigin, J.Y. Takemoto, J.H. Teeter, J.G. Brand, Cluster organization of ion channels formed by the antibiotic syringomycin E in bilayer lipid membranes, *Biophys. J.* 74 (1998) 2918–2925.
- [45] O.S. Ostroumova, V.V. Malev, Y.A. Kaulin, P.A. Gurnev, J.Y. Takemoto, L.V. Schagina, Voltage-dependent synchronization of gating of syringomycin E ion channels, *FEBS Lett.* 579 (2005) 5675–5679.
- [46] L.V. Schagina, Y.A. Kaulin, A.M. Feigin, J.Y. Takemoto, J.G. Brand, V.V. Malev, Properties of ionic channels formed by the antibiotic syringomycin E in lipid bilayers: Dependence on the electrolyte concentration in the bathing solution, *Membr. Cell Biol.* 12 (1998) 537–555.
- [47] L.V. Schagina, A.E. Grinfeldt, A.A. Lev, Concentration dependence of bidirectional flux ratio as a characteristic of transmembrane ion transporting mechanism, *J. Membr. Biol.* 73 (1983) 203–216.
- [48] O.V. Krasilnikov, R.Z. Sabirov, V.I. Ternovsky, P.G. Merzliak, J.N. Muratkhodjaev, A simple method for the determination of the pore radius of ion channels in planar lipid bilayer membranes, *FEMS Microbiol. Immunol.* 5 (1992) 93–100.
- [49] S.M. Bezrukov, I. Vodyanoy, Probing alamethicin channels with water-soluble polymers. Effect on conductance of channel states, *Biophys. J.* 64 (1993) 16–25.
- [50] Y.E. Korchev, C.L. Bashford, G.M. Alder, J.J. Kasianowicz, C.A. Pasternak, Low conductance states of a single ion channel are not “closed” *J. Membr. Biol.* 147 (1995) 233–239.
- [51] V.A. Parsegian, S.M. Bezrukov, I. Vodyanoy, Watching small molecules move: Interrogating ionic channels using neutral solutes, *Biosci. Rep.* 15 (1995) 503–514.
- [52] S.M. Bezrukov, R. Vodyanoy, R.A. Brutian, J.J. Kasianowicz, Dynamics and free energy of polymers partitioning into a nanoscale pore, *Macromolecules.* 29 (1996) 8517–8522.
- [53] S.A. Desai, R.L. Rosenberg, Pore size of the malaria parasite’s nutrient channel, *Proc. Natl. Acad. Sci. USA.* 94 (1997) 2045–2049.
- [54] O.S. Ostroumova, P.A. Gurnev, L.V. Schagina, S.M. Bezrukov, Asymmetry of syringomycin E channel studied by polymer partitioning, *FEBS Lett.* 581 (2007) 804–808.

- [55] O.V. Krasilnikov, J.B. Da Cruz, L.N. Yuldasheva, W.A. Varanda, R.A. Nogueira, A novel approach to study the geometry of the water lumen of ion channels: Colicin Ia channels in planar lipid bilayers, *J. Membr. Biol.* 161 (1998) 83–92.
- [56] P.G. Merzlyak, L.N. Yuldasheva, C.G. Rodrigues, C.M. Carneiro, O.V. Krasilnikov, S.M. Bezrukov, Polymeric nonelectrolytes to probe pore geometry: Application to the alpha-toxin transmembrane channel, *Biophys. J.* 77 (1999) 3023–3033.
- [57] L.N. Yuldasheva, P.G. Merzlyak, A.O. Zitzer, C.G. Rodrigues, S. Bhakdi, O.V. Krasilnikov, Lumen geometry of ion channels formed by *Vibrio cholerae* EL Tor cytolysin elucidated by nonelectrolyte exclusion, *Biochim. Biophys. Acta.* 1512 (2001) 53–63.
- [58] C.M. Carneiro, P.G. Merzlyak, L.N. Yuldasheva, L.G. Silva, F.P. Thinnes, O.V. Krasilnikov, Probing the volume changes during voltage gating of Porin 31BM channel with nonelectrolyte polymers, *Biochim. Biophys. Acta.* 1612 (2003) 144–153.
- [59] V.V. Malev, L.V. Schagina, P.A. Gurnev, J.Y. Takemoto, E.M. Nestorovich, S.M. Bezrukov, Syringomycin E channel: A lipidic pore stabilized by lipopeptide? *Biophys. J.* 82 (2002) 1985–1994.
- [60] A. Finkelstein, The ubiquitous presence of channels with wide lumens and their gating by voltage, *Ann. N Y Acad. Sci.* 456 (1985) 26–32.
- [61] V.V. Malev, Y.A. Kaulin, P.A. Gurnev, S.M. Bezrukov, J.Y. Takemoto, L.V. Schagina, Spatial charge distribution effects in the conductance of syringomycin E ion channels formed in lipid bilayers, *Biol. Membrany* 18 (2001) 145–153 (in Russian).
- [62] P.A. Gurnev, A.N. Bessonov, J.Y. Takemoto, L.V. Shchagina, V.V. Malev, Conductance of ion channels induced by syringomycin E in lipid bilayers with asymmetrically distributed surface charge, *Biol. Membrany* 21 (2004) 325–332 (in Russian).
- [63] P. Läuger, B. Neumke, Theoretical analysis of ion conductance in lipid bilayer membrane, in: G. Eisenmann (Ed.), *Membrane Lipids, Bilayer and Antibiotics*, Vol. 2, Marcel Dekker Inc., New York, 1973, pp. 1–59.
- [64] D. Colquhoun, A.G. Hawkes, The principles of the stochastic interpretation of ion-channel mechanisms, in: B. Sakman and E. Neher (Eds.), *Single-channel recording*, Plenum Press, N.Y. and London, 1995, pp. 397–482.
- [65] B. Hille, *Ion Channels of Excitable Membranes* (3rd Ed.) Sinauer Associates, Inc., Sunderland, MA, 2001.
- [66] O.S. Ostroumova, P.A. Gurnev, J.Y. Takemoto, L.V. Shchagina, V.V. Malev, Kinetic parameters of single ion channels and stationary conductivities of phytotoxin modified lipid bilayers, *Tsitologiya.* 47 (2005) 338–343 (in Russian).
- [67] L.V. Schagina, P.A. Gurnev, J.Y. Takemoto, V.V. Malev, Effective gating charge of ion channels induced by toxin syringomycin E in lipid bilayers, *Bioelectrochemistry.* 60 (2003) 21–27.
- [68] E. Melnik, R. Latorre, J.E. Hall, D.C. Tosteson, Phloretin-induced changes in ion transport across lipid bilayer membranes, *J. Gen. Physiol.* 69 (1977) 243–257.
- [69] R. Cseh, R. Benz, The adsorption of phloretin to lipid monolayers and bilayers cannot be explained by langmuir adsorption isotherms alone, *Biophys. J.* 74 (1998) 1399–1408.
- [70] P.A. Gurnev, Y.A. Kaulin, J.Y. Takemoto, L.V. Schagina, V.V. Malev, Effects of charges and dipole moments of membrane lipids on gating properties of ion channel induced by syringomycin E, *Biol. Membr.* 19 (2002) 244–250 (in Russian).
- [71] A.I. Rusanov, *Phasengleichgewichte und Grenzflächenerscheinungen* Academic Verlag, Berlin, 1978.
- [72] R.F. Flewelling, W.L. Hubbell, The membrane dipole potential in a total membrane potential model. Applications to hydrophobic ion interactions with membranes, *Biophys. J.* 49 (1986) 541–552.
- [73] A.D. Pickar, R. Benz, Transport of charged lipophilic probe ions in lipid bilayer membranes having various structures, *J. Membr. Biol.* 44 (1978) 353–376.
- [74] R. Cseh, M. Hetzer, K. Wolf, J. Kraus, G. Bringmann, R. Benz, Interaction of phloretin with membranes: On the mode of action of phloretin at the water-lipid interface, *Eur. Biophys. J.* 29 (2000) 172–183.

- [75] U. Peterson, D.A. Mannock, R.N. Lewis, P. Pohl, R.N. McElhaney, E.E. Pohl, Origin of membrane dipole potential: Contribution of the phospholipid fatty acid chains, *Chem. Phys. Lipids*. 117 (2002) 19–27.
- [76] J.C. Franklin, D.S. Cafiso, Internal electrostatic potentials in bilayers: Measuring and controlling dipole potentials in lipid vesicles, *Biophys. J.* 65 (1993) 289–299.
- [77] D. Colquhoun, B. Sakmann, From muscle endplate to brain synapses: A short history of synapses and agonist-activated ion channels, *Neuron*. 20 (1998) 381–387.
- [78] O.S. Andersen, A. Finkelstein, I. Katz, A. Cass, Effect of phloretin on the permeability of thin lipid membranes, *J. Gen. Physiol.* 67 (1976) 749–771.
- [79] T.I. Rokitskaya, Y.N. Antonenko, E.A. Kotova, Effect of the dipole potential of a bilayer lipid membrane on gramicidin channel dissociation kinetics, *Biophys. J.* 73 (1997) 850–854.
- [80] T.I. Rokitskaya, Y.N. Antonenko, E.A. Kotova, Membrane dipole potential modulates proton conductance through gramicidin channel: Movement of negative ionic defects inside the channel, *Biophys. J.* 82 (2002) 865–873.
- [81] D.D. Busath, C.D. Thulin, R.W. Hendershot, L.R. Phillips, P. Maughan, C.D. Cole, N. C. Bingham, S. Morrison, L.C. Baird, R.J. Hendershot, M. Cotten, T.A. Cross, Noncontact dipole effects on channel permeation. I. Experiments with (5F-indole)Trp13 gramicidin A channels, *Biophys. J.* 75 (1998) 2830–2844.
- [82] O.S. Ostroumova, Y.A. Kaulin, P.A. Gunnev, L.V. Schagina, Effect of agents modifying the membrane dipole potential on properties of syringomycin E channels, *Langmuir* 23 (2007) 6889–6892.
- [83] P.C. Jordan, Electrostatic modeling of ion pores. II. Effects attributable to the membrane dipole potential, *Biophys. J.* 41 (1983) 189–195.
- [84] D.Y. Malkov, V.S. Sokolov, Fluorescent styryl dyes of the RH series affect a potential drop on the membrane/solution boundary, *Biochim. Biophys. Acta*. 1278 (1996) 197–204.
- [85] A.N. Bessonov, P.A. Gunnev, I.M. Kuznetsova, J.Y. Takemoto, K.K. Turoverov, V.V. Malev, L. V. Schagina, Interaction between filamentous actin and lipid bilayer causes the increase of syringomycin E channel-forming activity, *Tsitologiiia*. 46 (2004) 628–633 (in Russian).
- [86] P.A. Gunnev, A.N. Bessonov, I.M. Kuznetsova, V.V. Malev, V.P. Pershina, G.P. Pinaev, K. K. Turoverov, J.Y. Takemoto, A.V. Tikhomirova, L.V. Schagina, Effects of actin and some polyions on channel-forming activity of syringomycin E in bilayer lipid membranes, *Biol. Membrany*. 20 (2003) 421–428 (in Russian).
- [87] A.N. Bessonov, L.V. Schagina, J.Y. Takemoto, P.A. Gunnev, I.M. Kuznetsova, K.K. Turoverov, V.V. Malev, Actin and amphiphilic polymers influence on channel formation by syringomycin E in lipid bilayers, *Eur. Biophys. J.* 35 (2006) 382–392.
- [88] V. Niggli, D.P. Dimitrov, J. Brunner, M.M. Burger, Interaction of the cytoskeletal component vinculin with bilayer structures analyzed with a photoactivatable phospholipids, *J. Biol. Chem.* 261 (1986) 6912–6918.
- [89] X. Han, G. Li, K. Lin, Interactions between smooth muscle alpha-actinin and lipid bilayers, *Biochemistry*. 36 (1997) 10364–10371.
- [90] W.H. Goldmann, J.M. Teodoridis, C.P. Sharma, J.L. Alonso, G. Isenberg, Fragments from alpha-actinin insert into reconstituted lipid bilayers, *Biochem. Biophys. Res. Commun.* 264 (1999) 225–229.
- [91] V. Niggli, Structural properties of lipid-binding sites in cytoskeletal proteins, *Trends Biochem. Sci.* 26 (2001) 604–611.
- [92] T. Tsunoda, T. Imura, M. Kadota, T. Yamazaki, H. Yamauchi, K.O. Kwon, S. Yokoyama, H. Sakai, M. Abe, Effects of lysozyme and bovine serum albumin on membrane characteristics of dipalmitoylphosphatidylglycerol liposomes, *Colloids Surf. B Biointerfaces* 20 (2001) 155–163.
- [93] J. Buijs, M. Ramstrom, M. Danfelter, H. Larsericsdotter, P. Hakansson, S. Oscarsson, Localized changes in the structural stability of myoglobin upon adsorption onto silica particles, as studied with hydrogen/deuterium exchange mass spectrometry, *J. Colloid Interface Sci.* 263 (2003) 441–448.
- [94] G.R. Jacobson, J.P. Rosenbusch, ATP binding to a protease-resistant core of actin, *Proc. Natl. Acad. Sci. USA*. 73 (1976) 2742–2746.

- [95] B.V. Deryaguin, Determination of porous body specific surface due to the rate of capillary impregnation, *Kolloidny Zhurnal*. 8 (1946) 27–30 (in Russian).
- [96] V.V. Malev, E.V. Gribanova, Wetting resistance in kinetics of capillary rise of liquids, *Dokl. Akad. Nauk SSSR*. 272 (1983) 413–416 (in Russian).
- [97] V.V. Malev, A.I. Matveeva, Kinetics of lenses spreading on free liquid films, *Dokl. Akad. Nauk SSSR*. 261 (1981) 685–689 (in Russian).
- [98] V.V. Malev, A.I. Matveeva, Kinetics of bilayer lipid membrane formation, *Biofizika*. 28 (1983) 50–55 (in Russian).
- [99] V.V. Krotov, V.V. Malev, Rheology of free liquid films with surfactants, *Kolloidnyi Zhurnal*. 41 (1979) 49–53 (in Russian).
- [100] K. Shinoda, T. Nakagawa, B.I. Tamamushi, T. Isemura, *Colloidal Surfactants: Some Physico-chemical Properties* Academic Press, New York, 1963.
- [101] Y.A. Negulyaev, E.A. Vedernikova, A.V. Maximov, Disruption of actin filaments increases the activity of sodium-conducting channels in human myeloid leukemia cells, *Mol. Biol. Cell* 7 (1996) 1857–1864.
- [102] Y.A. Negulyaev, S.Y. Khaitlina, H. Hinssen, E.V. Shumilina, E.A. Vedernikova, Sodium channel activity in leukemia cells is directly controlled by actin polymerization, *J. Biol. Chem.* 275 (2000) 40933–40937.

MEMBRANE ELECTROSTATICS—A STATISTICAL MECHANICAL APPROACH TO THE FUNCTIONAL DENSITY THEORY OF ELECTRIC DOUBLE LAYER

Klemen Bohinc,^{1,2} Tomaž Slivnik,¹ Aleš Igljč,¹ and Veronika Kralj-Igljč^{3,*}

Contents

1. Introduction	108
2. Electrostatic Free Energy	111
2.1. Electrostatic Energy	111
2.2. Entropy	112
2.3. Functional Density Theory of Electric Double Layer	119
3. Linearized Poisson–Boltzmann Theory	130
3.1. Planar Geometry	131
3.2. Cylindrical Geometry	132
3.3. Spherical Geometry, Convex Case	134
4. Thickness of Electric Double Layer	135
5. Effect of Intra-Ionic Correlations on the Interaction between Two Electric Double Layers	138
5.1. A System of Two Interacting Double Layers Composed of Point-like Ions	138
5.2. Rod-like Quadrupolar (Divalent) Nanoparticles	140
5.3. Dipolar Rod-like Nanoparticles in Electrolyte Solution	145
6. Concluding Remarks	150
References	152

Abstract

We describe physical properties of the electric double layer composed of a charged surface in contact with a solution of counter-ions and coions representing nanoparticles. The electrostatic free energy of the electric double layer is derived using a statistical mechanical approach. The consistently related expressions for the equilibrium ion and solvent distribution functions and the differential equation for the electric potential are derived by minimization of the electrostatic free energy of the system. The finite size of nanoparticles constituting the solution is taken into account by means of the excluded

* Corresponding author. Tel.: +386 1 5437620; Fax: +386 1 4768 850;
E-mail address: veronika.kralj-iglic@fe.uni-lj.si.

¹ Laboratory of Physics, Faculty of Electrical Engineering, University of Ljubljana, Ljubljana, Slovenia

² Faculty of Health Studies, University of Ljubljana, Ljubljana, Slovenia

³ Laboratory of Clinical Biophysics, Faculty of Medicine, University of Ljubljana, Ljubljana, Slovenia

volume within the lattice model. Different geometries of the electric double layer are considered. We found that an increased size of charged nanoparticles (ions) reduces the number of counter-ions near the charged surface, leading to an enhancement of the electrostatic surface potential. The linearized Poisson–Boltzmann theory and the influence of the finite size of ions (nanoparticles) on the thickness of the electric double layer are described.

Also the intra-ionic correlations within charged nanoparticles, which have spatially distributed (quadrupolar or dipolar) electric charge, are considered. The interaction between two charged surfaces in the solution composed of charged quadrupolar (divalent) or dipolar rod-like nanoparticles is calculated. It is shown that for large enough dimensions of charged quadrupolar (divalent) nanoparticles and for large enough surface charge densities of the charged surfaces, two equally charged surfaces experience attractive force owing to spatially distributed charge within the nanoparticles. Also, it is shown that in the vicinity of the charged surface (wall), large rod-like quadrupolar or dipolar nanoparticles orient in the electric field within the electric double layer. Close to the charged surfaces the orientation of the rod-like quadrupolar or the dipolar nanoparticles is hindered because of steric restrictions (hard wall).

1. INTRODUCTION

Biopolymers (DNA, polyelectrolytes, polystyrene sulfonate), biological membranes, cellular components, and globular proteins are electrically charged. Electrostatic interactions in biological systems are therefore of great importance for understanding of interactions between charged molecules and membrane surfaces.

Examples of electrically charged systems from biology include also self-assembling dispersions such as spherical inverse micelles, phospholipid vesicles, and microemulsions [1,2]. Such objects are formed by aggregation of amphiphilic molecules in a way that the hydrophilic parts of the molecules are in contact with electrolyte solution, while the hydrophobic parts avoid such contact. Micelles are small aggregates of amphiphilic molecules in aqueous solutions. Microemulsions are formed in mixtures of amphiphiles, water and oil, where domains of water (in oil) or oil (in water) are separated by surfactant monolayers. Multilamellar vesicles can then be formed by several surfactant bilayers separating an internal compartment from the continuous phase of the solution.

In biological medium (ionic solution) free ions are always present. The charges of ions and molecules are multiples of elementary charge. Multivalent ions are commonly treated as point charges. However, real ions (and particularly organic *nanoparticles*) often possess an internal structure with the individual charges being located at distinct, well-separated positions [3–5]. Among others [6], a characteristic example is the rod-like backbone structure of various DNA condensing agents such as the three- and tetra-valent ions spermine and spermidine, different proteins [7], protamine sulfate, or poly-lysine.

As already mentioned, some of the constituents of the biological membranes are ionized and therefore the biological membranes are electrically charged. The membrane charge, its spatial distribution, and the spatial distribution of ions in the

solution in the close proximity of the inner and outer membrane surfaces determine the profile of electric potential across the membrane [8,9]. The electrically charged molecular groups on both membrane surfaces protrude into the solution phase and therefore the inner and outer membrane surface potentials are smaller in comparison with the situation where the charge would be distributed in the planes of both membrane surfaces [9,10]. Nevertheless, for the sake of simplicity the electric charge distribution of membrane surfaces is usually described by effective surface charge characterized by the surface charge density σ .

Recently, much attention is devoted to inorganic and organic hollow bilayer membrane cylindrical structures in the nanometer range. Among other systems, nanotubes have been found in different phospholipid systems [11,12]. In cellular systems a direct transport between different cells or cellular organelles has been observed through hollow nanotubes or by carrier vesicles guided by nanotubes [13–15]. In membrane nanotubes, the walls of organic nanotubes are usually charged and are in contact with electrolyte solution [16]. Ion channels or pores in biological membranes and blood capillaries are also examples of cylindrical nanotubes.

The *electric double layer* is composed of a charged surface and the electrolyte solution is in contact with the charged surface.

The distribution of the ions in the electrolyte solution close to the charged surface is given by the competition between the electrostatic interactions and the entropy of the ions in the solution. Owing to the electrostatic forces between the charged surface and the ions in the solution, the counter-ions (the ions with the charge of the opposite sign than the charged surface) are accumulated close to the surface and the coions (the ions with the charge of the same sign than the surface) are depleted from the surface. A diffuse electric double layer influences the overall electrostatic interaction of the charged surface with its environment as well as the internal properties of the membrane carrying the surface charge. With respect to the geometry we distinguish planar [8], cylindrical [17–19], spherical [20], and other electric double layers.

The electric double layer has been a subject of extensive study since the pioneering work of Gouy [21] and Chapman [22]. The ions within the so-called Poisson–Boltzmann theory [1,2,8] were treated as dimensionless, while the electrolyte solution was accounted for by a uniform dielectric constant. The charged surfaces were considered as uniformly charged (see also [8–10]).

The improvement of the Gouy–Chapman theory can be obtained by including the direct ion–ion interactions. The fluctuation potential [23] due to the self-atmosphere of ion and the ion–ion exclusion volume term were taken into account in the modified Poisson–Boltzmann equation [24–26]. The integral equation methods, such as the hypernetted chain (HNC) approximation, have also been carried out [27–31]. Many different attempts have been made to incorporate steric effects into the PB equation. Freise [32] introduced the excluded volume effect by a pressure-dependent potential, while Wicke and Eigen [33] used a thermodynamic approach, multiplying the numerical density of ions by a factor containing the number of the vacant sites. More recently, the finite size of particles has been incorporated into the PB theory in a transparent way, based on a lattice statistics model [34–37], by using functional density approaches [38–40] and by a model including the surface charge

correlations, where the ions and solvent molecules were treated as hard spheres [41]. Monte Carlo simulations incorporate the direct interactions between ions and interactions between the ions and charged surfaces [24–26,42,43]. With the Monte Carlo technique it is possible to obtain numerically exact data and compare these data with the approximate theories. The advanced approaches [43] and the hypernetted chain integral equations [44,27] lead to a better agreement with Monte Carlo (MC) simulations for divalent counter-ions.

The Poisson–Boltzmann (PB) theory is a widely used mean-field level method to calculate interactions between charged surfaces in aqueous solution of counter-ions and coions. For monovalent salt, its predictions are generally found to agree well with experimental results and computer simulations. However, the presence of *multivalent* ions can affect the nature of the interactions between charged surfaces in a way that qualitatively differs from the PB prediction. A remarkable example is the possibility of *attraction* between two identical, like-charged surfaces that the mean-field Poisson–Boltzmann approach is unable to predict. This attraction receives much interest [45] because it is observed in several biologically relevant processes such as condensation of DNA [46], network formation in actin solutions [47], virus aggregation [48], and interactions between like-charged lipid membranes that occur during adhesion [7] and fusion. Various theoretical approaches ascribe this attraction to the presence of the direct ion–ion correlations [49,50]. An intuitive understanding of these correlations can be based on the formation of a periodic counter-ion arrangement in the vicinity of each macroion, similar to a Wigner crystal. The two inter-locked counter-ion-decorated charged surfaces then experience a short-range attraction. However, Linse [51] has shown that correlation attraction occurs even if no Wigner crystal arrangement is present.

The Monte Carlo (MC) simulations of Guldbrand *et al.* [52] first confirmed the existence of attraction between equally charged surfaces immersed into the solution composed of quadrupolar (divalent) ions in the limit of high surface charge density, which were originally predicted by Oosawa [18]. The anisotropic hypernetted chain approximation within the primitive electrolyte model for divalent ions was used [53,54], where the ions are described as charged hard spheres immersed in a dielectric continuum. Attractive interaction between identical, like-charged surfaces in aqueous solution composed of short divalent rod-like ions was predicted [3].

Here we present a statistical mechanical approach to the functional density theory of the electric double layer. First, in the mean field approximation the consistently related free energy, ion distribution function, and differential equation for the electrostatic potential were obtained. We upgrade the description of the Poisson–Boltzmann theory by considering the effect of the size of ions (i.e., charged nanoparticles). The influence of the ion size on the properties of the electric double layer is discussed. The effective thickness of electric double layer in different geometries is derived. Further, we formulate a description of a solution composed of large charged nanoparticles with spatially distributed charge. We discuss the interaction between two charged surfaces immersed in the solution of charged nanoparticles (quadrupolar or dipolar) with spatially distributed internal charge [5] (see also Fig. 1).

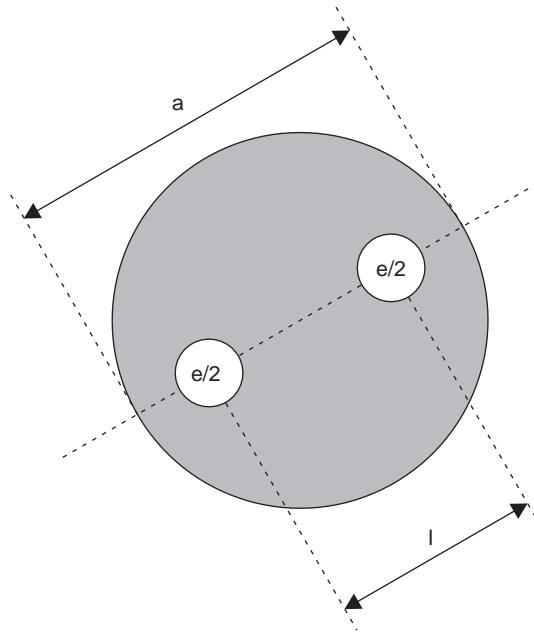


Figure 1 Schematic figure of a large spheroidal multivalent ion with net electric charge e and average diameter a . In the model the space charge distribution of the multivalent ion is described by two effective poly-ions of charge $e/2$ located at different well-separated positions (i.e., at the distance $l \leq a$). The main axis of the ion coincides with the line connecting the two poly-ions.

2. ELECTROSTATIC FREE ENERGY

2.1. Electrostatic Energy

The distribution of ions in the electric double layer reflects a balance between electrostatic interactions and entropy. First we consider the electrostatic interactions. The Poisson equation expresses the general relation between the charge distribution and the electrostatic potential. It follows from the Gauss law $\nabla \cdot \mathbf{E} = \rho / \varepsilon \varepsilon_0$ in which we insert the definition of the electrostatic potential $\mathbf{E} = -\nabla \Phi$ [55] so that

$$\nabla^2 \Phi = -\frac{\rho}{\varepsilon \varepsilon_0} \quad (1)$$

where ∇^2 is the Laplace operator, ∇ is the nabla operator, \mathbf{E} is the electric field strength, ε is the dielectric constant, and ε_0 is the permittivity of the free space. From a given space charge distribution $\rho(x, y, z)$, the electrostatic potential $\Phi(x, y, z)$ can be calculated provided the conditions to be satisfied at geometrical boundaries.

The electrostatic energy of the system can be expressed as an integral of the square of the electric field strength over the system [55]:

$$F_{\text{el}} = \frac{1}{2} \int \varepsilon \varepsilon_0 E^2 dV. \quad (2)$$

If the system possesses the radial symmetry then the electrostatic energy can be written as

$$F_{\text{el}} = \frac{1}{2} \int \varepsilon \varepsilon_0 \left(\frac{d\Phi}{dr} \right)^2 J(r) dr, \quad (3)$$

where r is the radial coordinate in cylindrical and spherical geometry, while in the planar geometry r denotes the distance from the charged plane in the direction perpendicular to the plane. $J(r)$ is defined as

$$\begin{aligned} J(r) &= A && \text{in planar geometry,} \\ J(r) &= 2\pi r l && \text{in cylindrical geometry,} \\ J(r) &= 4\pi r^2 && \text{in spherical geometry} \end{aligned} \quad (4)$$

where in the planar geometry A denotes the area of the charged surface, while l is the elongation of the cylinder.

2.2. Entropy

2.2.1. Solution of counter-ions

We consider the entropy of the system composed of only a finite size counter-ions (nanoparticles). The lattice model is used (Fig. 2).

The system is divided into cells of equal volume ΔV . In a particular cell chosen, there are N counter-ions. The excluded volume effect is taken into account in the description by considering that the counter-ions are distributed over M lattice sites. The number of spatial arrangements of N non-interacting counter-ions in a small cell with M lattice sites is

$$W = \frac{M(M-1)(M-2)\dots(M-(N-1))}{N!} \quad (5)$$

and can be rewritten into

$$W = \frac{M!}{N!(M-N)!}. \quad (6)$$

The configurational entropy of the cell S_{cell} can be computed by using the Boltzmann equation [56]

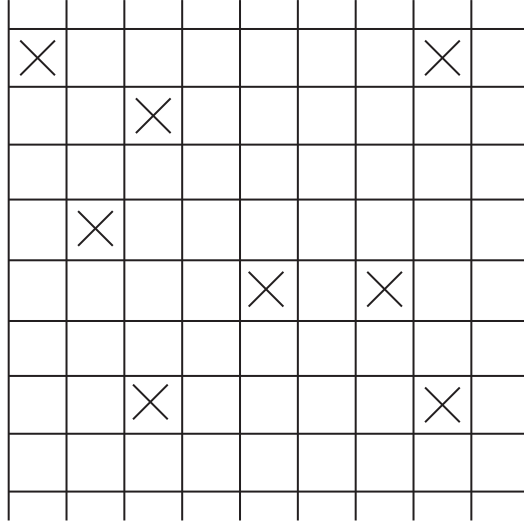


Figure 2 Schematic presentation of the lattice model, only counter-ions are included.

$$S_{\text{cell}} = k \ln W \quad (7)$$

where k is the Boltzmann constant. Using the Stirling's approximation for large N : $\ln N! \simeq N \ln N - N$ we get for $\ln W$:

$$\begin{aligned} \ln W &= M \ln M - M - N \ln N + N - (M - N) \\ &\quad \ln (M - N) + (M - N). \end{aligned} \quad (8)$$

The redistribution of the terms in Eq. (8) gives

$$\begin{aligned} \ln W &= M \ln M - N \ln N - (M - N) \ln \left(M \left(1 - \frac{N}{M} \right) \right) \\ &= M \ln M - N \ln N - (M - N) \ln M - (M - N) \ln \left(1 - \frac{N}{M} \right) \\ &= -N \ln N + N \ln M - (M - N) \ln \left(1 - \frac{N}{M} \right). \end{aligned} \quad (9)$$

After the summation of the first and the second term in Eq. (9) we get

$$\ln W = -N \ln \left(\frac{N}{M} \right) - (M - N) \ln \left(1 - \frac{N}{M} \right). \quad (10)$$

By inserting Eq. (10) into Eq. (7) we get the expression for the entropy of a single cell

$$S_{\text{cell}} = -k \left(N \ln \frac{N}{M} + (M - N) \ln \left(1 - \frac{N}{M} \right) \right). \quad (11)$$

In the following we introduce the volume of a single counter-ion (nanoparticle) v_0 . The volume of the cell with M lattice sites is then given by $\Delta V = M v_0$. The entropy of the whole system can be thus obtained by the integration of entropy over all cells of the system:

$$S = \int S_{\text{cell}} \frac{dV}{\Delta V}, \quad (12)$$

where S_{cell} is given by Eq. (11). We insert Eq. (11) into Eq. (12) and get

$$S = -k \int \left[n \ln (n v_0) + \frac{1}{v_0} (1 - n v_0) \ln (1 - n v_0) \right] dV, \quad (13)$$

where the number density of counter-ions is defined by $n = N/\Delta V$ and $v_0 = \Delta V/M$. Equation (13) takes into account the finite size of counter-ions and coions (nanoparticles). If we assume a very dilute system ($n v_0 \ll 1$ everywhere in the solution) the second term in Eq. (13) can be approximated by $\ln(1 - n v_0) \approx -n v_0$, where we have neglected quadratic and higher order terms. In the limit of very dilute system the entropy (Eq. 13) becomes

$$S = -k \int [n \ln (n v_0) - n] dV. \quad (14)$$

The entropic contribution to the free energy $F_{\text{ent}} = -TS$ can be therefore expressed as [2]

$$F_{\text{ent}} = kT \int [n \ln (n v_0) - n] dV, \quad (15)$$

where T is the absolute temperature.

2.2.2. Solution of counter-ions and coions

We consider now the entropy of the solution composed of counter-ions and coions. The finite sizes of ions (nanoparticles) are again considered within the lattice model (Fig. 3).

The system is divided into cells of equal volume ΔV . In the particular cell chosen, there are N_+ counter-ions and N_- coions. The number of spatial arrangements of non-interacting counter-ions and coions in small cell with M lattice sites is (see Fig. 3):

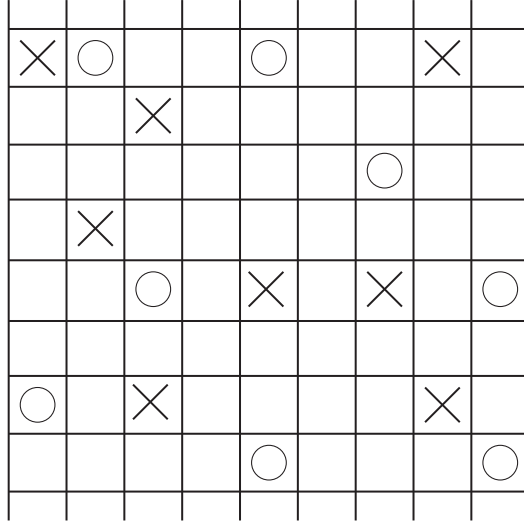


Figure 3 Schematic presentation of the lattice model, counter-ions (×) and coions (○) are included.

$$W = \frac{M(M-1)(M-2)\dots(M-(N-1))}{N_+!N_-!} \quad (16)$$

and can be rewritten into

$$W = \frac{M!}{N_+!N_-!(M-N)!}, \quad (17)$$

where

$$N = N_+ + N_- \quad (18)$$

The translational entropy of the mixed system of the single cell S_{cell} is then [56]

$$S_{\text{cell}} = k \ln W \quad (19)$$

Using the Stirling's approximation for large N_i : $\ln N_i! \simeq N_i \ln N_i - N_i$, $i = \{+, -\}$, the expression for $\ln W$ transforms into:

$$\begin{aligned} \ln W = & M \ln M - M - N_+ \ln N_+ + N_+ - N_- \ln N_- + N_- \\ & - (M - N) \ln (M - N) + (M - N). \end{aligned} \quad (20)$$

The redistribution of the terms in Eq. (20) gives

$$\ln W = -N_+ \ln \left(\frac{N_+}{M} \right) - N_- \ln \left(\frac{N_-}{M} \right) - (M - N) \ln \left(1 - \frac{N}{M} \right). \quad (21)$$

To simplify calculations we assume in the following that counter-ions and coions have the same volume v_0 . The volume of the cell with M sites is then given by $\Delta V = M v_0$. The number density of counter-ions is defined as

$$n_+ = N_+/\Delta V, \quad (22)$$

while the number density of coions is

$$n_- = N_-/\Delta V. \quad (23)$$

The configurational entropy of the whole system is obtained by the integration over all cells of the system:

$$S = \int S_{\text{cell}} \frac{dV}{\Delta V} \quad (24)$$

where S_{cell} is given by Eq. (19). We insert Eq. (21) into Eq. (19) to get

$$S = -k \int [n_+ \ln (n_+ v_0) + n_- \ln (n_- v_0) + \frac{1}{v_0} (1 - n_+ v_0 - n_- v_0) \ln (1 - n_+ v_0 - n_- v_0)] dV \quad (25)$$

Equation (25) takes into account the finite size of counter-ions (nanoparticles). If we assume that $(n_+ + n_-) v_0 \ll 1$ everywhere in the solution then the second term in Eq. (25) can be approximated by

$$\ln (1 - n_+ v_0 - n_- v_0) \approx -(n_+ + n_-) v_0 \quad (26)$$

where we neglected the quadratic and higher order terms. The entropy (Eq. (25)) thus becomes

$$S = -k \int [n_+ \ln (n_+ v_0) - n_+ + n_- \ln (n_- v_0) - n_-] dV \quad (27)$$

The entropic part of the free energy $\tilde{F}_{\text{ent}} = -TS$ is therefore

$$\tilde{F}_{\text{ent}} = kT \int \sum_{i=+,-} [n_i \ln (n_i v_0) - n_i] dV \quad (28)$$

where the sum runs over counter-ions and coions. From the expression for the configurational free energy (Eq. (28)) we need to subtract the reference free energy, i.e., the translational free energy of the system with vanishing electrostatic potential. We assume that the bulk (where the electrostatic potential is zero) number densities of counter-ions (n_{+0}) and coions (n_{-0}) are equal

$$n_0 = n_{+0} = n_{-0} \quad (29)$$

The difference between the entropic part of the free energy $F_{\text{ent}} \sim$ and the reference entropic part of the free energy F_{ref} is then:

$$\begin{aligned} \tilde{F}_{\text{ent}} - F_{\text{ref}} &= kT \sum_{i=+,-} \int [n_i \ln (n_i v_0) - n_i] dV \\ &\quad - 2kT \int [n_0 \ln (n_0 v_0) - n_0] dV. \end{aligned} \quad (30)$$

By taking into account the relation

$$\int dV [2n_0 - \sum_{i=+,-} n_i] = 0 \quad (31)$$

we Eq. (30) into:

$$\begin{aligned} \tilde{F}_{\text{ent}} - F_{\text{ref}} &= kT \sum_{i=+,-} \int [n_i \ln (n_i v_0) - n_i] dV \\ &\quad - 2kT \int [n_0 \ln (n_0 v_0) - n_0] dV \\ &\quad - kT \sum_{i=+,-} \int n_i \ln (n_0 v_0) dV + kT \int 2n_0 \ln (n_0 v_0) dV. \end{aligned} \quad (32)$$

Note that the validity of the Eq. (31) implies that the sum of the last two terms in Eq. (32) is zero, where it is taken into account that $\ln(n_0 v_0) = \text{const}$. After some calculation we get from Eq. (32) the entropic part of the free energy for the solution composed of counter-ions and coions $F_{\text{ent}} = \tilde{F}_{\text{ent}} - F_{\text{ref}}$ in the form (see also [34])

$$F_{\text{ent}} = kT \sum_{i=+,-} \int \left[n_i \ln \left(\frac{n_i}{n_0} \right) - (n_i - n_0) \right] dV. \quad (33)$$

In the derivation of Eq. (33) we assumed that $(n_+ + n_-) v_0 \ll 1$ everywhere in the solution. In the following the assumption $(n_+ + n_-) v_0 \ll 1$ will be abandoned and the entropic part of the free energy $\tilde{F}_{\text{ent}} = -TS$ will be calculated directly from the Eq. (25) without any additional simplifications:

$$\begin{aligned} \tilde{F}_{\text{ent}} &= kT \int \left[\sum_{i=+,-} n_i \ln (n_i v_0) + \frac{1}{v_0} \left(1 - \sum_{i=+,-} n_i v_0 \right) \ln \left(1 - \sum_{i=+,-} n_i v_0 \right) \right] \\ &\quad dV. \end{aligned} \quad (34)$$

Similarly as in Eq. (30) we need to subtract the reference free energy. The difference between the entropic part of the free energy \tilde{F}_{ent} and the reference entropic part of the free energy F_{ref} is thus

$$\begin{aligned} \tilde{F}_{\text{ent}} - F_{\text{ref}} = kT \int dV & \left[\sum_{i=+,-} n_i \ln(n_i v_0) - 2n_0 \ln(n_0 v_0) \right] + \\ & + kT \int dV \frac{1}{v_0} \left(1 - \sum_{i=+,-} n_i v_0 \right) \ln \left(1 - \sum_{i=+,-} n_i v_0 \right) - \\ & - kT \int dV \frac{1}{v_0} (1 - 2n_0 v_0) \ln(1 - 2n_0 v_0). \end{aligned} \quad (35)$$

By taking into account the relation (31) we transformed Eq. (35) into:

$$\begin{aligned} \tilde{F}_{\text{ent}} - F_{\text{ref}} = kT \int dV & \left\{ \sum_{i=+,-} n_i \ln(n_i v_0) - 2n_0 \ln(n_0 v_0) \right. \\ & - \sum_{i=+,-} n_i \ln(n_0 v_0) + 2n_0 \ln(n_0 v_0) \\ & + \frac{1}{v_0} \left(1 - \sum_{i=+,-} n_i v_0 \right) \ln \left(1 - \sum_{i=+,-} n_i v_0 \right) \\ & - \frac{1}{v_0} (1 - 2n_0 v_0) \ln(1 - 2n_0 v_0) - \\ & - \frac{1}{v_0} \left(1 - \sum_{i=+,-} n_i v_0 \right) \ln(1 - 2n_0 v_0) \\ & \left. + \frac{1}{v_0} (1 - 2n_0 v_0) \ln(1 - 2n_0 v_0) \right\}. \end{aligned} \quad (36)$$

By taking into account Eq. (36), $\ln(n_0 v_0) = \text{const}$, and $\ln(1 - 2n_0 v_0) = \text{const}$, we get the entropic part of the free energy

$$\begin{aligned} F_{\text{ent}} = \tilde{F}_{\text{ent}} - F_{\text{ref}} = +kT \int dV & \sum_{i=+,-} n_i \ln \left(\frac{n_i}{n_0} \right) \\ & + kT \int dV \left(\frac{1}{v_0} - \sum_{i=+,-} n_i \right) \ln \left(\frac{\frac{1}{v_0} - \sum_{i=+,-} n_i}{\frac{1}{v_0} - 2n_0} \right). \end{aligned} \quad (37)$$

In our model the volume of a single nanoparticle (v_0) is equal to the volume of one lattice site

$$n_s = \frac{1}{v_0} = \frac{1}{a^3} \quad (38)$$

where we define a as a lattice constant. All lattice sites are occupied by either solvent molecules or nanoparticles (ions), therefore

$$n_s = n_w + \sum_{j=+,-} n_j \quad (39)$$

where n_w is the number density of lattice sites occupied by solvent (water) molecules. Different values of the lattice constant a describe different sizes of the ions (nanoparticles). In the following the number densities of counter-ions and coions are referred to as the respective concentrations. By taking Eq. (38) into account we may rewrite Eq. (37) in the following form:

$$F_{\text{ent}} = kT \int dV \sum_{i=+,-} n_i \ln \left(\frac{n_i}{n_0} \right) + kT \int dV (n_s - \sum_{i=+,-} n_i) \ln \left(\frac{n_s - \sum_{i=+,-} n_i}{n_s - 2n_0} \right). \quad (40)$$

2.3. Functional Density Theory of Electric Double Layer

In the described model of electric double layer the charged surface is assumed to carry an uniformly distributed charge with the surface charge density σ . The solution is composed of solvent molecules and nanoparticles. The nanoparticles are in general counter-ions and/or coions. We restrict our consideration to the planar, cylindrical, and spherical electric double layers. The geometry of cylindrical surface is described by the radius of curvature r_0 and length l , the spherical surface is described by the radius of curvature r_0 (Figs. 4 and 5).

In the non-planar geometry the electric field must vanish far from the charged surface in the convex case and at the cylinder axis or at the centre of the sphere in the concave case.

The electrostatic interactions are described within the mean field approximation while the finite size of the nanoparticles in the solution is considered by means of excluded volume effect. The latter is taken into account within a statistical mechanical description as described in the previous section, where each particle in the solution occupies one and only one site of a finite volume [34,35].

2.3.1. Solution of counter-ions only

2.3.1.1. Single double layer We consider a system composed of a charged surface and a solution of counter-ions only. The solvent (water) molecules are accounted for by a uniform dielectric constant $\epsilon \sim 78.5$ and by the excluded volume principle.

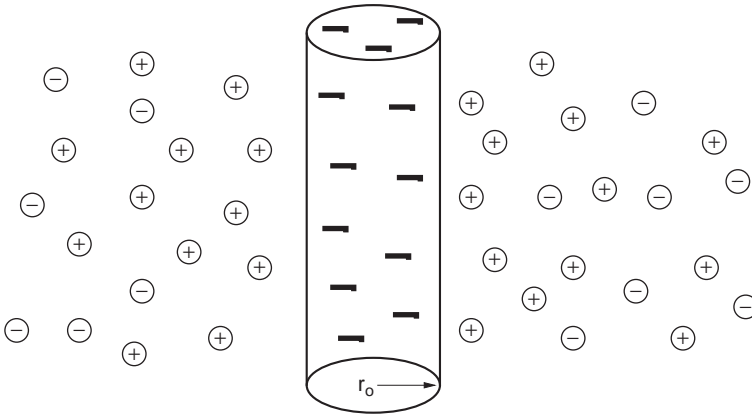


Figure 4 Schematic presentation of a cylindrical electric double layer outside the tube with radius r_o and surface charge density σ_o . The counter-ions are accumulated near the charged surface while the coions are depleted from the vicinity of the charged surface [57].

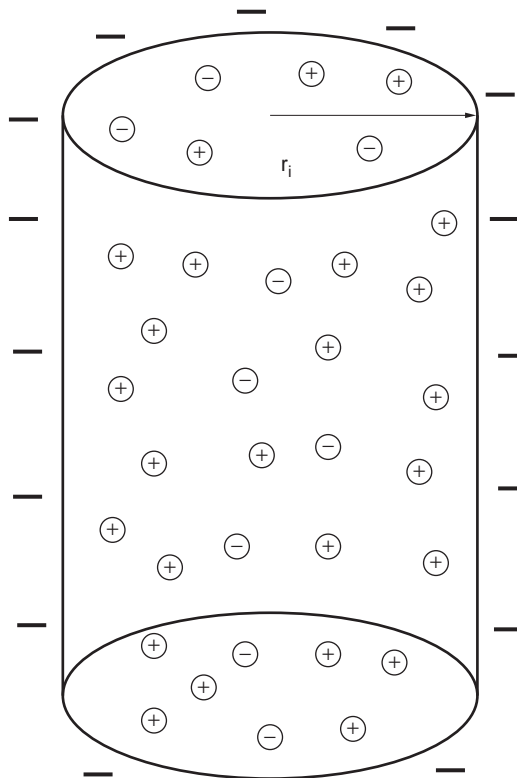


Figure 5 Schematic presentation of a cylindrical electric double layer inside the tube with radius r_i and surface charge density σ_i . The counter-ions are accumulated near the charged surface while the coions are depleted from the vicinity of the charged surface.

The electrostatic free energy of the system can be written as a sum of electrostatic energy (Eq. (3)) and the entropic contribution to the free energy (Eq. (13)):

$$F = \frac{1}{2} \varepsilon \varepsilon_0 \int_{r_0}^R E^2(r) J(r) dr + kT \int_{r_0}^R J(r) \left[n(r) \ln (n(r)v_0) + \frac{1}{v_0} (1 - n(r)v_0) \ln (1 - n(r)v_0) \right] dr. \quad (41)$$

where $E(r)$ is the electric field strength, $n(r)$ is the counter-ion concentration, and $J(r)$ is defined by Eq. (4). In cylindrical and spherical geometry, r_0 denotes the radius of the charged cylindrical or spherical surface, while in the planar geometry $r_0 = 0$. In the planar geometry and in the convex cylindrical and spherical geometry $R \rightarrow \infty$, while in concave cylindrical and spherical geometry $R = 0$. In the cylindrical and spherical geometries the electrostatic field depends on the radial coordinate r . In the planar geometry r denotes the distance from the charged plane in the direction perpendicular to the plane.

The free energy of the whole system, subject to the local thermodynamic equilibrium, is

$$F = \int_{r_0}^R f(E(r), n(r)) J(r) dr, \quad (42)$$

where the density of the free energy is given by

$$f(E(r), n(r)) = \frac{1}{2} \varepsilon \varepsilon_0 E^2(r) + kT \left[n(r) \ln (n(r)v_0) + \frac{1}{v_0} (1 - n(r)v_0) \ln (1 - n(r)v_0) \right]. \quad (43)$$

The counter-ion concentration $n(r)$ and the electric field strength are not known in advance. Thus, in the following, explicit expressions for $n(r)$ and $E(r)$ are obtained using the condition of the free energy to be at its minimum at thermodynamic equilibrium of the whole system. The condition for the global equilibrium

$$\delta F = 0 \quad (44)$$

is subject to [34] the followings:

- the global constraint requiring the electro-neutrality of the whole system

$$\int_{r_0}^R n(r) J(r) dr - \frac{\sigma A}{Ze_0} = 0, \quad (45)$$

- the local constraint requiring the validity of the differential form of the Gauss's law $\varepsilon\varepsilon_0 \nabla \cdot \mathbf{E} = \rho(r)$, where $\rho(r) = e_0\nu Zn(r)$ is the volume charge density and

$$\varepsilon\varepsilon_0 \frac{1}{r^\alpha} \frac{\partial(r^\alpha E(r))}{\partial r} - e_0 Zn(r) = 0, \quad (46)$$

where in the planar geometry $\alpha = 0$, in the spherical geometry $\alpha = 2$ while in the cylindrical geometry $\alpha = 1$ and Z is the valency of counter-ions.

The method of undetermined multipliers [34,57,58] is used to determine the extreme of the free energy (42) taking into account the constraints (45) and (46). The variational problem can be expressed by the Euler–Lagrange equations

$$\frac{\partial L^*}{\partial E} - \frac{d}{dr} \left(\frac{\partial L^*}{\partial \left(\frac{\partial E}{\partial r} \right)} \right) = 0 \quad (47)$$

$$\frac{\partial L^*}{\partial n} = 0 \quad (48)$$

where

$$\begin{aligned} L^* & \left(E(r), n(r), \frac{\partial E(r)}{\partial r}, \eta(r) \right) \\ & = J(r) * \left[f(E(r), n(r)) + \mu n(r) - \eta(r) \left(\varepsilon\varepsilon_0 \frac{1}{r^\alpha} \frac{\partial(r^\alpha E(r))}{\partial r} - e_0 Zn(r) \right) \right] \end{aligned}$$

μ is the global Lagrange multiplier, while $\eta(r)$ is the local Lagrange multiplier. The local Lagrange multiplier $\eta(r)$ can be expressed from the Euler–Lagrange Eq. (47):

$$\eta(r) = \Phi(r) \quad (49)$$

where we took into account that $\mathbf{E} = -\nabla\Phi$, while it follows from the Euler–Lagrange Eq. (48) that

$$kT [\ln(n\nu_0) - \ln(1 - n\nu_0)] + \mu + e_0 Z \eta(r) = 0. \quad (50)$$

From Eqs. (49) and (50) the counter-ion distribution function is obtained:

$$n(r) = \frac{1}{\nu_0} \times \frac{1}{1 + e^{(\mu + e_0 Z \Phi(r))/kT}}, \quad (51)$$

where the Lagrange multiplier μ can be determined from the condition of electro-neutrality (Eq. (45)). The Gauss law (Eq. (46)) and the particle distribution functions (Eq. (51)) give the differential equation for the electrostatic potential $\Phi(r)$:

$$\frac{d^2\Phi(r)}{dr^2} + \frac{\alpha}{r} \frac{d\Phi(r)}{dr} = - \frac{e_0 Z}{\varepsilon\varepsilon_0 \nu_0} \frac{1}{1 + e^{(\mu + e_0 Z \Phi(r))/kT}} \quad (52)$$

In the following the Lagrange multiplier μ is expressed from Eq. (51) as a function of concentration of counter-ions (nanoparticles) for $\Phi = 0$:

$$e^{\mu/kT} = \frac{1}{(n_0/n_s)} - 1, \quad (53)$$

where the number density of the lattice sites is $n_s = 1/v_0$ (see Eq. (38)). In the limit of very dilute system ($n_0/n_s \ll 1$) Eq. (53) becomes

$$e^{\mu/kT} \simeq \frac{1}{(n_0/n_s)}. \quad (54)$$

Taking into account the approximative expression (54) we can transform Eq. (51) to the form of the Boltzmann distribution function:

$$n(r) = \frac{n_s}{1 + (n_s/n_0)e^{e_0 Z \Phi(r)/kT}} \simeq n_0 e^{-e_0 Z \Phi(r)/kT} \quad (55)$$

In accordance, also the Eq. (52) transforms into the so-called Poisson–Boltzmann equation:

$$\frac{d^2 \Phi(r)}{dr^2} + \frac{\alpha}{r} \times \frac{d\Phi(r)}{dr} = -\frac{e_0 Z}{\epsilon \epsilon_0} n_0 e^{-Z e_0 \Phi(r)/kT}. \quad (56)$$

The condition of electro-neutrality of the whole system (Eq. (45)) is equivalent to two boundary conditions. The first boundary condition states that the electric field is zero far from the charged surface:

$$\left. \frac{d\Phi(r)}{dr} \right|_{r=R} = 0, \quad (57)$$

where $R \rightarrow \infty$, while the second boundary condition (at the interface) is:

$$\left. \frac{d\Phi(r)}{dr} \right|_{r=r_0} = -\frac{\sigma}{\epsilon \epsilon_0}. \quad (58)$$

In the planar geometry r denotes the distance from the charged plane in direction perpendicular to the plane, therefore in Eq. (58) $r_0 = 0$ for planar geometry.

2.3.1.2. Two interacting double layers In the following we shall consider a system composed of two flat and equally uniformly charged surfaces immersed in an aqueous solution composed of counter-ions only (Fig. 6). The surface charge density of each surface is σ . The first charged surface is located at $x = 0$ ($r_0 = 0$), while the second charged surface is located at $x = D$ ($R = D$), where $x \equiv r$ is the coordinate

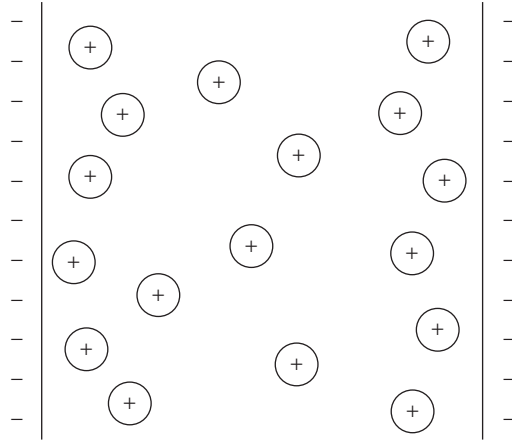


Figure 6 Two flat and equally charged surfaces immersed in aqueous solution composed of counter-ions only.

perpendicular to the charged surfaces. The distance between the charged surfaces is D . Assuming the symmetry of the system with respect to the plane $x = D/2$, the boundary conditions (76) and (58) should be replaced by

$$\left. \frac{d\Phi(x)}{dx} \right|_{x=0} = -\frac{\sigma}{\epsilon\epsilon_0}, \tag{59}$$

$$\left. \frac{d\Phi(x)}{dx} \right|_{x=\frac{D}{2}} = 0. \tag{60}$$

The electrostatic potential $\Phi(x)$ is calculated by numerically solving the Eq. (56), taking into account the boundary conditions (59) and (60). Then the concentration of counter-ions $n(x)$ is determined by using Eq. (55). Finally, the electrostatic free energy of the system is calculated in the limit of very dilute solution (see also Eq. (15));

$$F/A = \frac{1}{2} \epsilon\epsilon_0 \int_0^D \left(\frac{d\Phi}{dx} \right)^2 dx + kT \int_0^D [n(x) \ln (n(x)v_0) - n(x)] dx. \tag{61}$$

Figure 7 shows the electrostatic free energy F (full line) as a function of the distance between the equally charged planar surfaces D . We see that the free energy F decreases with increasing distance between the surfaces D , which corresponds to the repulsive force between equally charged surfaces. This is the consequence of decreasing entropic contribution to the free energy, which prevails over the increase of the electrostatic part of the free energy with increasing D .

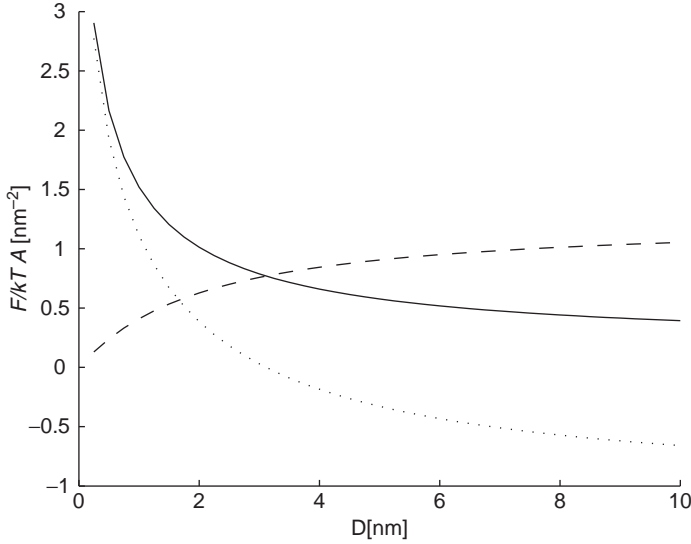


Figure 7 Free energy (full line), electrostatic energy (dashed line) and configurational entropy (dotted line) of a system with counter-ions only as a function of the distance between the equally charged surfaces D . Model parameters are $|\sigma| = 0.1 \text{ As/m}^2$ and $v_0 = 5 \text{ nm}^3$.

2.3.2. Solution of counter-ions and coions

Electrostatic free energy of the system composed of counter-ions and coions is derived from Eq. (3) and (4) [34,57,56]:

$$\begin{aligned}
 F = & \frac{1}{2} \varepsilon \varepsilon_0 \int_{r_0}^R E^2(r) J(r) dr \\
 & + kT \sum_{j=+,-} \int_{r_0}^R J(r) n_j(r) \ln \left(\frac{n_j(r)}{n_0} \right) dr \\
 & + kT \int_{r_0}^R J(r) \left(n_s - \sum_{j=+,-} n_j(r) \right) \ln \left(\frac{n_s - \sum_{j=+,-} n_j(r)}{n_s - 2n_0} \right) dr,
 \end{aligned} \tag{62}$$

where n_+ is concentration of counter-ions, n_- is concentration of coions, n_0 is the bulk concentration of counter-ions and of coions, n_s is defined by Eqs. (38) and (39) and $J(r)$ is given by Eq. (4).

The free energy of the whole system, subject to the local thermodynamic equilibrium, is

$$F = \int_{r_0}^R f(E(r), n_+(r), n_-(r)) J(r) dr, \tag{63}$$

where the density of the free energy is given by

$$\begin{aligned}
 f(E(r), n_+(r), n_-(r)) = & \frac{1}{2} \varepsilon \varepsilon_0 E^2(r) \\
 & + kT \sum_{j=+,-} n_j(r) \ln \left(\frac{n_j(r)}{n_0} \right) \\
 & + kT \left(n_s - \sum_{j=+,-} n_j(r) \right) \ln \left(\frac{n_s - \sum_{j=+,-} n_j(r)}{n_s - 2n_0} \right) dr
 \end{aligned} \tag{64}$$

The particle distribution functions $n_+(r)$ and $n_-(r)$ and the electric field strength $E(r)$ are obtained by using the condition of the free energy to be at its minimum at thermodynamic equilibrium of the whole system. The condition for the global equilibrium

$$\delta F = 0 \tag{65}$$

is subject to the following [34]:

- The global constraint requiring that the total number of particles of each species per volume of the whole system, Λ_j , is constant

$$\int_{r_0}^R (n_j(r) - \Lambda_j) J(r) dr = 0, \quad j = +, -. \tag{66}$$

- The local constraint requiring the validity of the differential form of Gauss law $\varepsilon \varepsilon_0 \nabla \cdot \mathbf{E} = \rho(r)$, where $\rho(r) = e_0 \sum_{j=+,-} Z_j n_j(r)$ is the volume charge density:

$$\varepsilon \varepsilon_0 \frac{1}{r^\alpha} \frac{\partial(r^\alpha E(r))}{\partial r} - e_0 \sum_{j=+,-} Z_j n_j(r) = 0, \tag{67}$$

where in the planar geometry $\alpha = 0$, in the spherical geometry $\alpha = 2$, and in the cylindrical geometry $\alpha = 1$, while Z_j is the valency of the counter-ions ($j = +$) and coions ($j = -$).

The method of undetermined multipliers [34,58,57] is used to find the extreme of the free energy (63) taking into account the constraints (66) and (67). The described variational problem can be expressed by the Euler–Lagrange equations:

$$\frac{\partial L^*}{\partial E} - \frac{d}{dr} \left(\frac{\partial L^*}{\partial \left(\frac{\partial E}{\partial r} \right)} \right) = 0, \tag{68}$$

$$\frac{\partial L^*}{\partial n_j} = 0, j = +, - \tag{69}$$

where

$$\begin{aligned}
 L^* & \left(E(r), n_+(r), n_-(r), \frac{\partial E(r)}{\partial r}, \eta(r) \right) \\
 & = J(r) \left[f \left(E(r), n_+(r), n_-(r) \right) + \sum_{j=+,-} \lambda_j \left(n_j(r) - A_j \right) \right. \\
 & \quad \left. - \eta(r) \left(\varepsilon \varepsilon_0 \frac{1}{r^\alpha} \frac{\partial \left(r^\alpha E(r) \right)}{\partial r} - e_0 \sum_{j=+,-} Z_j n_j(r) \right) \right], \quad (70)
 \end{aligned}$$

λ_j , $j = +, -$, are the global Lagrange multipliers while $\eta(r)$ is the local Lagrange multiplier. Eqs. (68), (69) and (70) give

$$\eta(r) = \Phi(r) \quad (71)$$

$$kT \ln \frac{n_j n_{w0}}{n_0 (n_s - \sum_i n_i)} + \lambda_j + e_0 Z_j \Phi(r) = 0. \quad (72)$$

From Eqs. (71), (72), and (39) the particle distribution functions are obtained [34,35]:

$$n_j(r) = \frac{n_s (n_0 / n_{w0}) \exp \left(- Z_j e_0 \Phi(r) / kT \right)}{1 + (2n_0 / n_{w0}) \cosh \left(Z_j e_0 \Phi(r) / kT \right)}, \quad (73)$$

where n_{w0} is the bulk concentration of *lattice sites occupied by water molecules* (see Eq. (39)):

$$n_{w0} = n_s - 2n_0. \quad (74)$$

It can be seen from Eq. (73) that close to the charged plane there may be a considerable excluded volume effect on the density profile of the counter-ions and on the solvent molecules. The concentration of the counter-ions is there comparable to the concentration of the solvent lattice sites so that the concentration of the solvent lattice sites deviates significantly from its value far from the charged surface [34]. Equation (73) also predicts a Fermi-Dirac-like distribution for counter-ions if the lattice constant a is large enough (see also Fig. 8). For higher values of surface charge density ($|\sigma|$) the counter-ion density saturates close to the charged surface to its close packing value, while the usual Poisson-Boltzmann theory predicts unreasonable high values beyond the close-packing value (see also [34,35,57]).

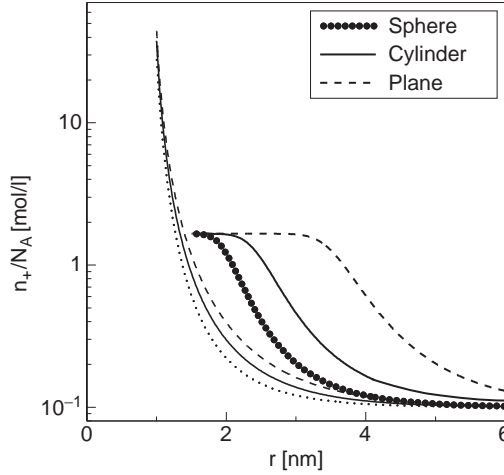


Figure 8 The concentration of counter-ions as a function of the distance from the charged surface. The results for the planar, cylindrical and spherical geometries are presented. The bold curves present results for the lattice constant of $a = 1$ nm, while the normal lines present the dimensionless ions. The model parameters are $\varepsilon = 78.5$, $T = 310$ K, $n_0/N_A = 0.1$ mol/l, $r_0 = 1$ nm and $|\sigma| = 0.4$ As/m²[59], where N_A is Avogadro number.

The Gauss's law (Eq. (67)) and the particle distribution functions (Eq. (73)) give the differential equation for the electrostatic potential $\Phi(r)$:

$$\frac{d^2\Phi(r)}{dr^2} + \frac{\alpha}{r} \frac{d\Phi(r)}{dr} = \frac{2e_0 n_s n_0 Z}{\varepsilon \varepsilon_0 n_{w0}} \times \frac{\sinh\left(\frac{Ze_0\Phi(r)}{kT}\right)}{1 + (2n_0/n_{w0})\cosh\left(\frac{Ze_0\Phi(r)}{kT}\right)}, \quad (75)$$

where we take that $Z = |Z_+| = |Z_-|$.

The first boundary condition states that the electric field is zero far away from the charged surface:

$$\left. \frac{d\Phi(r)}{dr} \right|_{r=R} = 0, \quad (76)$$

where $R \rightarrow \infty$. The second boundary condition at the charged surface demands the electro-neutrality of the whole system:

$$\left. \frac{d\Phi(r)}{dr} \right|_{r=r_0} = -\frac{\sigma}{\varepsilon \varepsilon_0}. \quad (77)$$

In the limit of very dilute solution everywhere in the system: $\sum_{j=+,-} n_j(r) \ll n_w(r)$, and by taking into account the approximation $n_{w0} \simeq n_s$, where $n_w(r)$ is the concentration of lattice sites occupied by water (solvent) molecules, the second term in the denominator of Eq. (75) can be neglected. Equation (75) then becomes:

$$\frac{d^2\Psi(r)}{dr^2} + \frac{\alpha}{r} \frac{d\Psi(r)}{dr} = \frac{\kappa^2}{Z} \sinh\left(Z\Psi(r)\right), \quad (78)$$

which is the well known PB equation (valid in the limit of dimensionless ions: $a \rightarrow 0$). We introduced the reduced electrostatic potential

$$\Psi = e_0\Phi/kT \quad (79)$$

and the Debye length

$$l_D = \kappa^{-1} = \sqrt{\frac{\varepsilon\varepsilon_0kT}{2n_0Z^2e_0^2}}. \quad (80)$$

Neglecting the second term in denominator of Eq. (73) the particle distribution function (73) transforms into to the well known Boltzmann distribution function

$$n_j(r) = n_0 \exp\left(-Z_j\Psi(r)\right) \quad (81)$$

For illustration, Fig. 8 shows the concentration n_+ as a function of the distance r from the charged surface. The results are given for three different geometries: planar, cylindrical and spherical. The results of the Poisson–Boltzmann theory and the results of the functional density theory modified by the excluded volume effect with the lattice constant $a = 1$ nm are presented. In the planar geometry the excess of counter-ion concentration (calculated relative to its value far from the charged surface) protrudes deeper in the solution than in the cylindrical case, while in the cylindrical geometry the excess of the concentration distribution protrudes deeper into the solution than in the spherical geometry. The effect is more pronounced for larger ions. In all three geometries the saturation of the counter-ions near the charged surface (i.e. the Fermi-Dirac-like shape of distributions) for ions of finite size is obtained. The saturation value of the concentration of counter-ions is the same for all three geometries.

Figure 9 shows the electric potential dependence on the distance from the charged surface. The results for three different geometries are shown. The electric potential for the cylindrical geometry is smaller than the electric potential for the planar geometry whereas the electric potential for the cylindrical geometry is greater than the electric potential for the spherical geometry. Far from the charged surface the electric potential is insensitive to the geometry and to the lattice constant. The electric potential is higher for ions of finite size than for dimensionless ions.

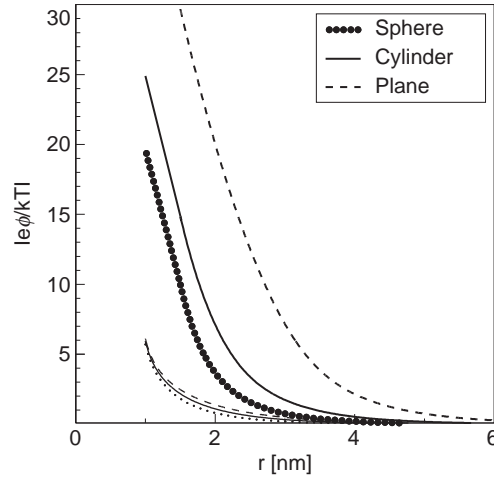


Figure 9 The electric potential as a function of the distance from the charged surface. The results for the planar, cylindrical and spherical geometries are presented. The bold curves present results for the lattice constant $a = 1$ nm, while the normal lines present the dimensionless ions. The model parameters are $\varepsilon = 78.5$, $T = 310$ K, $n_0/N_A = 0.1$ mol/l, $r_0 = 1$ nm, and $|\sigma| = 0.4$ As/m²[59].

The ratio between the concentration of the counter-ions near the charged planar, cylindrical and spherical surfaces and the bulk counter-ion concentration in dependence on the surface charge density σ is presented in Fig. 10. This ratio is higher for dimensionless ions than for the ions of finite size. The discrepancy between the results for dimensionless ions and for the ions of finite size grows with increasing $|\sigma|$. The deviation can be attributed to steric effect of counter-ions and solvent molecules in a small region in the vicinity of the charged surface. The counter-ion concentration profile shows a rapid decrease for small lattice constant and a plateau region near the charged plane for large lattice constant. For large counter-ions we can therefore distinguish between two regions within the electric double layer: the saturated layer dominated by the steric repulsion and the diffuse layer extending into the solution.

3. LINEARIZED POISSON–BOLTZMANN THEORY

We consider a linear regime of Poisson–Boltzmann (PB) equation for monovalent ions ($Z = 1$), i.e., we assume that the electrostatic potential energy of an ion is much smaller than its thermal energy ($\Psi \ll 1$). We linearize $\sinh(Z\Psi(r))$ in Eq. (78) and get:

$$\frac{d^2\Psi(r)}{dr^2} + \frac{\alpha}{r} \frac{d\Psi(r)}{dr} = \kappa^2\Psi(r) \quad (82)$$

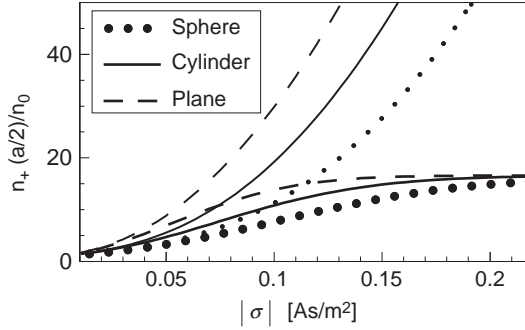


Figure 10 The ratio between the concentration of monovalent counterions near the charged planar, cylindrical, and spherical surfaces and the bulk counter-ion concentration in dependence on $|\sigma|$ [60]. The bold curves represent calculation for lattice constant 0.8 nm. The result of the Poisson–Boltzmann theory is given by the light curves. The model parameters are $\varepsilon = 78.5$, $T = 310$ K and $r_0 = 1$ nm.

3.1. Planar Geometry

In planar geometry ($\alpha = 0$), the Eq. (82) reduces to

$$\frac{d^2\Psi(r)}{dr^2} = \kappa^2\Psi(r). \quad (83)$$

By taking into account the boundary conditions (76) and (77) the solution of Eq. (83) for $r_0 = 0$ is

$$\Psi(r) = \Psi_0 e^{-\kappa r}, \quad (84)$$

where

$$\Psi_0 = 4\pi\sigma l_B l_D / \varepsilon_0 \quad (85)$$

is the electrostatic potential near the charge surface and

$$l_B = \frac{e_0^2}{4\pi\varepsilon\varepsilon_0 kT}. \quad (86)$$

is the Bjerrum length. Note that the electrostatic potential is proportional to the surface charge density. The electrostatic potential exponentially decreases with increasing distance from the charged surface. The thickness of the electric double layer is given by the Debye length $l_D = 1/\kappa$ (see Eq. (80)).

3.2. Cylindrical Geometry

We consider a charged tube in contact with a solution of a symmetric monovalent solution of counter-ions and coions. The electric double layer inside the tube (concave case, Fig. 5) and outside the tube (convex case, Fig. 4) is considered.

In cylindrical geometry, $\alpha = 1$. Multiplying Eq. (82) by r^2 we get

$$r^2 \frac{d^2\Psi(r)}{dr^2} + r \frac{d\Psi(r)}{dr} - \kappa^2 r^2 \Psi(r) = 0. \quad (87)$$

The solution of differential Eq. (87) is [55]:

$$\Psi(r) = B_1 I_0(\kappa r) + B_2 K_0(\kappa r), \quad (88)$$

where I_0 is the modified Bessel function of first kind and 0-th order, while K_0 is the modified Bessel function of second kind and 0-th order. The constants B_1 and B_2 are determined from the boundary conditions.

In the case of the **concave** cylindrical electric double layer, the inner surface of the charged tube is in contact with the inner electrolyte solution. The boundary condition for the reduced potential $\Psi(r)$ inside the tube at the geometrical axis of the tube is

$$\left. \frac{d\Psi(r)}{dr} \right|_{r=0} = 0, \quad (89)$$

while the boundary condition at the inner charged surface of the tube is:

$$\left. \frac{d\Psi(r)}{dr} \right|_{r=R_i} = \frac{\sigma_i e_0}{\epsilon \epsilon_0 k T}, \quad (90)$$

where σ_i is the surface charge density of the inner surface of the tube, and R_i is the radius of the curvature of the inner charged surface of the tube (concave case). The boundary condition (90) reflects the electro-neutrality of the inner surface of the charged tube and the solution inside the tube

$$\int \rho_i dV + \oint \sigma_i dA = 0, \quad (91)$$

where ρ_i is the volume charge density of the inner solution. The first integral in Eq. (91) represents the total charge of the solution inside the tube, while the second integral represents the charge of the inner surface of the tube. Taking into account the Poisson Eq. (1)

$$\nabla^2 \Psi = \frac{-4\pi l_B \rho_i}{e_0} \quad (92)$$

and the Gauss theorem, Eq. (91) transforms into the boundary condition (90). The first boundary condition (Eq. (89)) gives $B_2 = 0$, while from the second boundary condition (Eq. 90) the constant B_1 is determined. Inserting the constants B_1 and B_2 into Eq. (88) we obtain the electrostatic potential inside the tube:

$$\Psi(r) = \frac{\sigma_i e_0}{kT \varepsilon \varepsilon_0 \kappa_i} \frac{I_0(\kappa_i r)}{I_1(\kappa_i R_i)}, \quad (93)$$

where I_1 is the modified Bessel function of the 1-st kind and $1/\kappa_i$ is Debye length inside the tube:

$$1/\kappa_i = \sqrt{\frac{\varepsilon \varepsilon_0 kT}{2e_0^2 n_0^i}}. \quad (94)$$

The concentration of counter-ions inside the tube is given by the Boltzmann distribution

$$n_+^i = n_0^i e^{-\Psi(r)}, \quad (95)$$

where n_0^i is the bulk concentration of counter-ions and coions (the bulk solution often provides a suitable reference for the potential, see also [61]). In the linearized Poisson–Boltzmann theory the exponent in Eq. (95) can be expanded up to first order:

$$n_+^i = n_0^i (1 - \Psi(r)). \quad (96)$$

Inserting Eq. (93) into Eq. (96) we obtain

$$n_+^i = n_0^i \left(1 - \sigma_i \frac{4\pi l_B}{e_0 \kappa_i} \frac{I_0(\kappa_i r)}{I_1(\kappa_i R_i)} \right), \quad (97)$$

where l_B is the Bjerrum length (see Eq. (86) for definition).

In the case of **convex** cylindrical electric double layer the outer surface of the charged tube is in contact with the outer solution of counter-ion and coions. The boundary condition for the reduced potential $\Psi(r)$ outside the tube is

$$\left. \frac{d\Psi(r)}{dr} \right|_{r=R} = 0, \quad (98)$$

where $R \rightarrow \infty$. The boundary condition at the outer charged surface of the tube is

$$\left. \frac{d\Psi(r)}{dr} \right|_{r=R_0} = -\frac{\sigma_o e_0}{\varepsilon \varepsilon_0 kT} \quad (99)$$

where σ_o is the surface charge density of the outer surface of the tube and R_o is the radius of curvature of the outer charged surface of the tube (convex case). Taking into account the boundary conditions (98) and (99) the solution of Eq. (87) for the electrostatic potential $\Psi(r)$ is [61]

$$\Psi(r) = \frac{\sigma_o \epsilon_0}{kT \epsilon \epsilon_0 \kappa_o} \frac{K_0(\kappa_o r)}{K_1(\kappa_o R_o)}. \quad (100)$$

The corresponding approximative expression (in linearized PB theory) for the concentration of counter-ions outside the charged tube is

$$n_+^o = n_0^o \left(1 - \sigma_o \frac{4\pi l_B}{e_0 \kappa_o} \frac{K_0(\kappa_o r)}{K_1(\kappa_o R_o)} \right), \quad (101)$$

where K_1 is the modified Bessel function of the second kind and first order, $1/\kappa_o$ is Debye length outside the tube:

$$1/\kappa_o = \sqrt{\frac{\epsilon \epsilon_0 kT}{2e_0^2 n_0^o}} \quad (102)$$

and n_0^o is the concentration of counter-ions and coions far from the charged surface ($R \rightarrow \infty$), where the effect of the charged surface is negligible.

Similarly as in the concave case, the boundary condition (99) in the convex case reflects the electroneutrality of the outer surface of the charged tube and the solution of counter-ions and coions outside the tube:

$$\int \rho_o dV + \oint \sigma_o dA = 0, \quad (103)$$

where ρ_o is the volume charge density of the outer solution. The first integral in Eq. (103) represents the charge of the solution outside the tube, while the second integral represents the charge of the outer surface of the tube. Here we took into account the electro-neutrality of the outer surface of the charged tube and the solution outside the tube.

3.3. Spherical Geometry, Convex Case

In spherical geometry ($\alpha = 2$) and Eq. (82) reduces to

$$\frac{d^2\Psi(r)}{dr^2} + \frac{2}{r} \frac{d\Psi(r)}{dr} = \kappa^2\Psi(r). \quad (104)$$

The ansatz for the solution of this differential equation is

$$\Psi(r) = B_1 \frac{e^{-\kappa r}}{r} + B_2 \frac{e^{\kappa r}}{r} \quad (105)$$

In the case of charged spherical surface being on the outer side in contact with a solution of counter-ions and coions (convex case) the coefficients B_1 and B_2 are determined from the boundary conditions (see Eqs. (76) and (77)):

$$\left. \frac{d\Psi(r)}{dr} \right|_{r=R} = 0, \quad (106)$$

$$\left. \frac{d\Psi(r)}{dr} \right|_{r=r_0} = -\frac{\sigma e_0}{\epsilon \epsilon_0 k T}. \quad (107)$$

The boundary condition (106) demands that the electric field far from the charged spherical surface ($R \rightarrow \infty$) is zero and determines $B_2 = 0$. The boundary condition (107) at the charged surface yields

$$B_1 = \frac{r_0^2 e^{\kappa r_0}}{1 + \kappa r_0} \cdot \frac{\sigma l_B 4\pi}{e_0} \quad (108)$$

The final solution of Eq. (104) is thus given by

$$\Psi(r) = \Psi_0 \frac{r_0}{r} e^{\kappa(r_0-r)} \quad (109)$$

where

$$\Psi_0 = \frac{r_0}{1 + \kappa r_0} \times \frac{\sigma l_B 4\pi}{e_0} \quad (110)$$

4. THICKNESS OF ELECTRIC DOUBLE LAYER

In this section the thickness of a single electric double layer is considered. The screening of the electrostatic field by the counter-ions that accumulate near the charged plane can be represented by the effective thickness of the electric double layer. The thickness of electric double layer measures the range of the electrostatic influence of the charged surface in the surroundings. In the planar geometry we introduce the distance x_ϑ where the concentration of the counter-ions (calculated relative to its value far from the charged surface) drops to a fraction $(1 - \vartheta)$ of the value of n_+ ($a/2$) [59]

$$n_+(x_\vartheta) - n_0 = (1 - \vartheta)(n_+(a/2) - n_0), \quad (111)$$

where $\frac{a}{2}$ is the distance of the closest approach.

We introduce another measure of the thickness of the electric double layer, namely the distance d_ϑ , defining the region that contains a certain fraction ϑ of the excess of the counter-ions [59]

$$\int_{a/2}^{d_\vartheta} (n_+(x) - n_0) dx = \vartheta \int_{a/2}^d (n_+(x) - n_0) dx \quad (112)$$

For vanishing ion size (in the limit of the validity of the Poisson–Boltzmann theory) x_ϑ is expressed analytically:

$$x_\vartheta = \frac{1}{\kappa} \ln \left(\frac{\left(\sqrt{(1+(1-\vartheta)\left(\exp\left(\frac{-Z_+e_0\Phi(0)}{kT}\right) - 1\right) + 1)} \right) \left(1 - \exp\left(\frac{Z_+e_0\Phi(0)}{2kT}\right)\right)}{\left(\sqrt{(1+(1-\vartheta)\left(\exp\left(\frac{-Z_+e_0\Phi(0)}{kT}\right) - 1\right) - 1)} \right) \left(1 + \exp\left(\frac{Z_+e_0\Phi(0)}{2kT}\right)\right)} \right), \quad (113)$$

where

$$\Phi(0) = -\frac{2kT}{Z_+e_0} \ln \left(\sqrt{1 + (\sigma/c)^2} + |\sigma|/c \right) \quad (114)$$

and

$$c = \sqrt{8kT\varepsilon\varepsilon_0n_0}. \quad (115)$$

Subject to the same limit, and taking that $R \rightarrow \infty$, the parameter d_ϑ may be expressed as

$$d_\vartheta = \frac{1}{\kappa} \ln \left(\frac{1 + \frac{1+\vartheta}{1-\vartheta} \exp\left(\frac{Z_+e_0\Phi(0)}{2kT}\right)}{\left(1 + \exp\left(\frac{Z_+e_0\Phi(0)}{2kT}\right)\right)} \right). \quad (116)$$

If, in addition, $|e_0\Phi(x)/kT| \ll 1$ for all x , i.e., the linearized Poisson–Boltzmann theory is applied, both measures further simplify into the expression

$$x_\vartheta = d_\vartheta = \frac{1}{\kappa} \ln \frac{1}{1-\vartheta}, \quad (117)$$

where $1/\kappa$ is the Debye screening length (see Eq. (80)), which describes the effective thickness of the electric double layer in the linearized Poisson–Boltzmann theory.

Figure 11 shows the parameters x_ϑ (representing the effective thickness of the electric double layer) in dependence of the lattice size a that represents the ion size for three choices of ϑ : 0.9, 0.8, and 0.5. The points marked by the dots show the results of the Poisson–Boltzmann theory. The values of the parameters x_ϑ are larger for higher ϑ , however, qualitative dependence is equal for all three choices. For small values of ϑ both parameters diminish while as ϑ approaches 1, both parameters increase beyond every bound. We see that the effective thickness of the electric

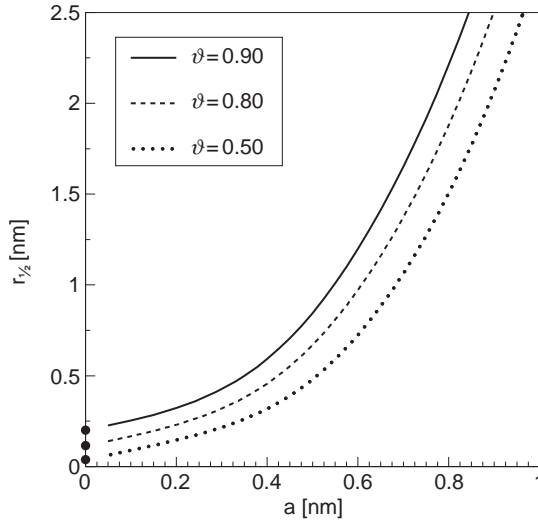


Figure 11 Thickness $r_{1/2}$ of the planar electric double layer as a function of the lattice constant a [59]. The point denotes the corresponding results of the nonlinearized PB theory. The model parameters are $\varepsilon = 78.5$, $T = 310$ K, $n_0/N_A = 0.1$ mol/l and $|\sigma| = 0.4$ As/m².

double layer increases with increasing size of the counter-ions, reaching the values of several nanometers for lattice constants of about 1 nanometer. The limit of small lattice constant a corresponds well with the Poisson–Boltzmann theory.

The parameter ϑ should not be too low as for small ϑ only a small part of the excess of the counter-ions is involved in the region $x < x_\vartheta$. On the other hand, for ϑ very close to 1 the thickness of electric double layer is almost independent of all the parameters as the region must contain almost all the excess counter-ions. It is sensible to choose ϑ somewhere between 0.4 and 0.8 where the effect of different other parameters is clearly exhibited.

The thickness of the electric double layer in cylindrical geometry (see. Fig. 12 is described by the characteristic length $r_{1/2}$, i.e., the distance from the charged surface where the excess of the counter-ions drops to a half of its value near the distance of closest approach to the charged cylindrical surface. Within the presented theory where the excluded volume effect is taken into account, the thickness of the diffuse layer $r_{1/2}$ is always larger than within the PB theory. When finite size of ions is considered, the shielding of the electric field of the charged surface is less effective than in the PB theory where there is no limit regarding to the concentration of counter-ions. For small parameters $\xi = \sigma r_0 e_0 / 2 \varepsilon \varepsilon_0 k T$ the effective thickness of the electric double layer is decreasing with increasing ξ as the surface bearing higher charge attracts in its vicinity larger number of counter-ions. Consequently the screening is more effective. If we further increases the parameter ξ , the influence of the excluded volume effect increases with increasing ξ . The effective thickness $r_{1/2}$ after reaching its minimum, begins to increase with increasing ξ . This is the result of the fact that the excluded volume imposes an upper limit on the

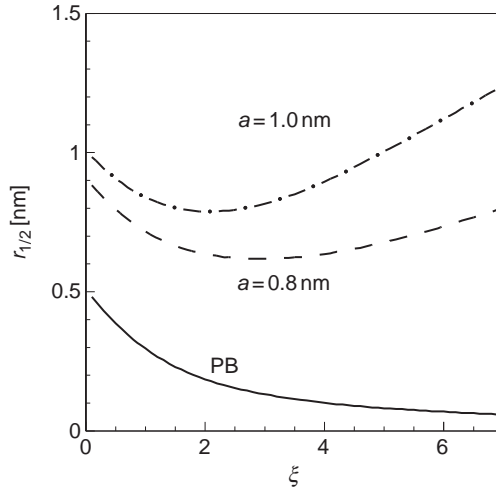


Figure 12 Thickness r_{ϑ} of the cylindrical electric double layer as a function of the linear charge parameter ζ for two different lattice constants a [59]. The results of PB theory is also shown. The model parameters are $\varepsilon = 78.5$, $T = 310$ K, $n_0/N_A = 0.1$ mol/l and $r_0 = 1$ nm.

concentration of counter-ions. There is no upper limit of the concentration of ions in the PB theory and the effective thickness in the PB theory decreases monotonously with ζ . No minimum is reached.

5. EFFECT OF INTRA-IONIC CORRELATIONS ON THE INTERACTION BETWEEN TWO ELECTRIC DOUBLE LAYERS

First we consider an aqueous electrolyte solution sandwiched between two large, planar equally charged surfaces. Each surface is carrying a uniform average negative surface charge density $\sigma = -e_0/a$ where e_0 is the elementary charge and a is the average cross-sectional area per charge on the surface. The distance between the two surfaces is D . The electrostatic field varies only in the normal direction between charged surfaces (x -direction). We assume that there is no electric field behind the charged plates. The solution is composed of rod-like quadrupolar (divalent) ions with charge spatially distributed within the ion (see also Fig. 13).

5.1. A System of Two Interacting Double Layers Composed of Point-like Ions

We consider a system of two parallel like-charged planar surfaces immersed in the solution of point-like counter-ions and coions. Electrostatic free energy of the system is composed of the electrostatic energy and the entropic contribution to the free energy (see Eqs. (3) and (33)) [34,62]:

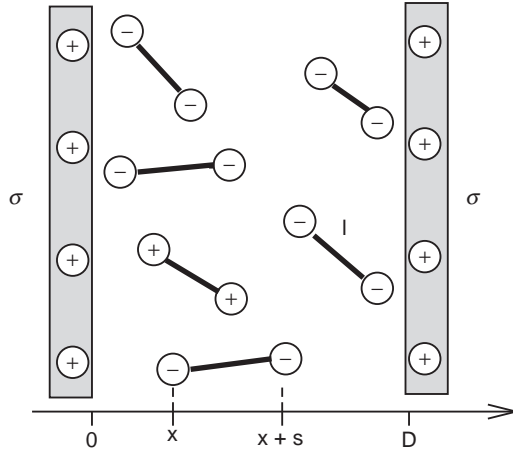


Figure 13 Schematic illustration of two like-charged planar surfaces, located at $x = 0$ and $x = D$ with σ denoting the corresponding surface charge density. The surfaces are immersed in an electrolyte solution that contains negatively and positively charged rod-like divalent counter-ions and coions. The separation between the individual charges of each rod-like ion is denoted by l . The coordinates x and $x + s$ specify the instantaneous positions of the two charges in a given rod-like ion along the horizontal axis [5].

$$\frac{F}{AkT} = \frac{1}{8\pi l_B} \int_0^D \Psi'^2 dx + \int_0^D \left[n_+ \ln \frac{n_+}{n_0} + n_- \ln \frac{n_-}{n_0} - (n_+ + n_- - 2n_0) \right] dx, \quad (118)$$

where Ψ is the reduced electrostatic potential (see Eq. (79)), $n_+(x)$ is the concentration of counter-ions, $n_-(x)$ is the concentration of coions, and n_0 is the bulk concentration of counter-ions and coions. The first variation of the electrostatic free energy (Eq. 118) takes the form:

$$\frac{\delta F}{AkT} = \int_0^D dx \left\{ \delta n_+ \left[Z\Psi + \ln \frac{n_+}{n_0} \right] + \delta n_- \left[-Z\Psi + \ln \frac{n_-}{n_0} \right] \right\}, \quad (119)$$

where Z is the valency of counter-ions and coions. The variation δF depends only on the variations of n_+ and δn_- . Here the variation of the Ψ'^2 in F was performed by taking into account the relation $\Psi' \delta \Psi' = (\Psi \delta \Psi) - \Psi \delta \Psi''$ and

$$\delta'' \Psi = -4\pi l_B \frac{\delta \rho}{e_0}, \quad (120)$$

where the volume charge density is given by $\rho = Ze_0 (n_+ - n_-)$. In the thermodynamic equilibrium the electrostatic free energy has to be minimal with respect to n_+ and n_- . Therefore we have to fulfill the condition:

$$\delta F = 0. \quad (121)$$

The result of the variational procedure gives the concentration profiles:

$$n_+ = n_0 e^{-Z\Psi}, \quad (122)$$

$$n_- = n_0 e^{Z\Psi}. \quad (123)$$

Inserting Eqs. (122) and (123) into the Poisson equation gives the following differential equation:

$$\psi'' = \frac{2Ze_0^2 n_0}{\epsilon\epsilon_0 kT} \sinh(Z\Psi). \quad (124)$$

The boundary conditions are given at the charged surfaces:

$$\frac{d\Psi}{dx}(x=0) = -\frac{4\pi l_B \sigma}{e_0}, \quad (125)$$

and

$$\frac{d\Psi}{dx}(x=D) = \frac{4\pi l_B \sigma}{e_0}, \quad (126)$$

which are equivalent to the overall electroneutrality of the system.

The equilibrium free energy of the system is obtained by inserting the concentration profiles (122) and (123) into the Eq. (118)

$$\frac{F}{AkT} = \frac{1}{8\pi l_B} \int_0^D \left[\psi'^2 + \frac{2\Psi}{Z} \sinh(Z\Psi) - \frac{2}{Z^2} \cosh(Z\Psi) + \frac{2}{Z^2} \right] dx. \quad (127)$$

The electrostatic free energy depends on the distance between the charged surfaces, the surface charge density and the valency Z . The PB theory for divalent point-like ions always gives a repulsive interaction between equally charged surfaces.

5.2. Rod-like Quadrupolar (Divalent) Nanoparticles

We consider a system of two parallel charged surfaces immersed in the solution of multivalent rod-like counter-ions and coions (Fig. 13). In our model the rod-like ions are composed of two individual charges of valency Z separated by a fixed distance l . The rod-like counter-ions are characterized by positional and orientational degrees of freedom. We describe them by referring to one of the two charges of each particle as a reference charge, denoting the local concentration of all the reference charges by $n_i(x)$. The location of the second charge of a given counter-ion will be specified by the conditional probability distribution $p_i(s|x)$, denoting the

probability to find the second charge at position $x + s$ if the first is at x . At any given position x , we require the normalization condition $\frac{1}{2l} \int_{-l}^l ds p_i(s|x) = 1$ to be fulfilled. Note also that $p_i(s|x) = 0$ for $|s| > l$.

The free energy of the system, measured per unit area of the surface and divided by unit of energy kT , consists of three terms: electrostatic energy (Eq. (3)), configurational entropy (Eq. (33)) and orientational entropy of the multivalent rod-like particles [5]

$$\begin{aligned} \frac{F}{AkT} = & \frac{1}{8\pi l_B} \int_0^D dx \Psi'(x)^2 \\ & + \sum_{i=\{+,-\}} \int_0^D dx \left[n_i(x) \ln \left[\frac{n_i(x)}{n_0} \right] - (n_i(x) - n_0) \right] \\ & + \sum_{i=\{+,-\}} \int_0^D dx n_i(x) \frac{1}{2l} \int_{-l}^l ds p_i(s|x) [\ln p_i(s|x) + U(x,s)], \end{aligned} \quad (128)$$

where Ψ is the reduced electrostatic potential (see Eq. (79)), l_B is the Bjerrum length (see Eq. (86) for definition), and n_0 is bulk value of ion concentration. We introduce a function:

$$U(x,s) = \begin{cases} 0, & x > 0 \text{ and } x+s > 0 \text{ and } x > D \text{ and } D-x-s > 0 \\ \infty, & \text{elsewhere} \end{cases}$$

which takes into account that integration over ds for the rod-like counter-ions near the boundaries can not be held over the whole integration range from $-l$ to l if the distance between the reference charge and the charged surface is less than l . In thermal equilibrium, the free energy $F = F[n_i(x), p_i(s|x)]$ is minimal with respect to $n_i(x)$ and $p_i(s|x)$. The results of variation ($\delta F = 0$) gives the normalized conditional probability density

$$p_i(s|x) = \frac{e^{-U(x,s) - Zi\Psi(x+s)}}{(1/2l) \int_{-l}^l d\bar{s} e^{-U(x,\bar{s}) - Zi\Psi(x+\bar{s})}} \quad (129)$$

and the local concentration of reference charges $n_i(x)$ of multivalent rod-like ions

$$n_i(x) = n_0 e^{-Zi\Psi(x)} \frac{1}{2l} \int_{-l}^l ds e^{-U(x,s) - Zi\Psi(x+s)} \quad (130)$$

The volume charge density

$$\frac{\rho(x)}{e_0} = \sum_{i=\{+,-\}} \left[Zn_i(x) + Z \frac{1}{2l} \int_{-l}^l ds n_i(x-s) p_i(s|x-s) \right]. \quad (131)$$

includes contributions from a reference charge located at x and from a second, orientationally mobile charge located at $x - s$. If we insert the concentration $n_i(x, s)$ (Eq. (130)) and the conditional probability density (Eq. (129)) into the volume charge density Eq. (131) and use the Poisson equation $\Psi''(x) = -4\pi l_B \rho(x)/\epsilon_0$, we obtain the nonlinear integro-differential equation

$$2\Psi''(x) = \kappa^2 \frac{1}{2l} \int_{-\min(l,x)}^{\min(l,D-x)} ds \sinh[\Psi(x) + \Psi(x+s)], \quad (132)$$

where $\kappa^2 = 4 \times 8\pi l_B n_0$. Integration limits are defined by the minimum or the maximum of the both values given in brackets. Equation (132) is valid in the region $0 \leq x \leq D$. The boundary conditions at the charged surfaces are:

$$\begin{aligned} \Psi'(x=0) &= -\frac{4\pi l_B \sigma}{\epsilon_0}, \\ \Psi'(x=D) &= -\frac{4\pi l_B \sigma}{\epsilon_0}. \end{aligned} \quad (133)$$

Fig. 14A shows the reduced electrostatic potential $\Psi(\bar{x})/p$ as a function of the distance \bar{x} from the macroion. The length are scaled by the Debye length $l_D = 1/\kappa$. The dimensionless charge parameter is given by $p = 2\pi l_B l_D/a$. The different curves correspond to different rod length \bar{l} . Plotting $\Psi(\bar{x})/p$ is convenient because $\Psi(\bar{x}) \sim p$ in the linear regime. Clearly, for $\bar{l} = 0$ the potential agrees with the Poisson–Boltzmann theory for monovalent ions. Note that the potential increases more rapidly with decreasing x for non-vanishing \bar{l} than for $\bar{l} = 0$. Upon increasing \bar{l} beyond $\bar{l} > \bar{l}_c \approx 2$ the potential develops non-monotonic behavior. This behavior directly implies “overcharged” regions where the charges from the rod-like ions over-compensate the macroion charge density at a certain distance away from the macroion. This conclusion follows from the scaled integrated charge (charge per unit area) at distance \bar{x} ,

$$Q(\bar{x}) = -\frac{l_D}{\sigma} \int_0^{\bar{x}} \rho(\bar{x}) d\bar{x}, \quad (134)$$

which generally adopts the values $Q(0) = 0$ and $Q(\bar{D}/2) = 1$. In addition, $Q(\bar{x}) > 1$ signifies “overcharging.” Rewriting $Q(\bar{x}) = 1 + \Psi'(\bar{x})/(2p)$ we see that regions with $\Psi'(\bar{x}) > 0$ imply $Q(\bar{x}) > 1$. The inset of Fig. 14A displays $Q(\bar{x})$ corroborating “overcharging” for $\bar{l} \gtrsim 2$. For $\bar{l} \gtrsim 2$ there is no critical charge parameter p at which the overcharging first appears.

Even though the potential $\Psi(\bar{x})$ in Fig. 14A is smooth, the corresponding ionic densities $n_{\pm}(\bar{x})$ are not. This can be seen for any $\bar{l} > 0$ directly in the limit of $p = 0$ where electrostatic interactions are not relevant any more; $\Psi \equiv 0$ and $n_{+}(\bar{x}) = n_{-}(\bar{x})$. The steric interactions of the rod-like ions still lead to a depletion from the macroions; for $\bar{D} > 2\bar{l}$ the densities are $n_{\pm}(\bar{x})/n_0 = (1 + \bar{x}/\bar{l})/2$ for $0 \leq \bar{x} \leq \bar{l}$

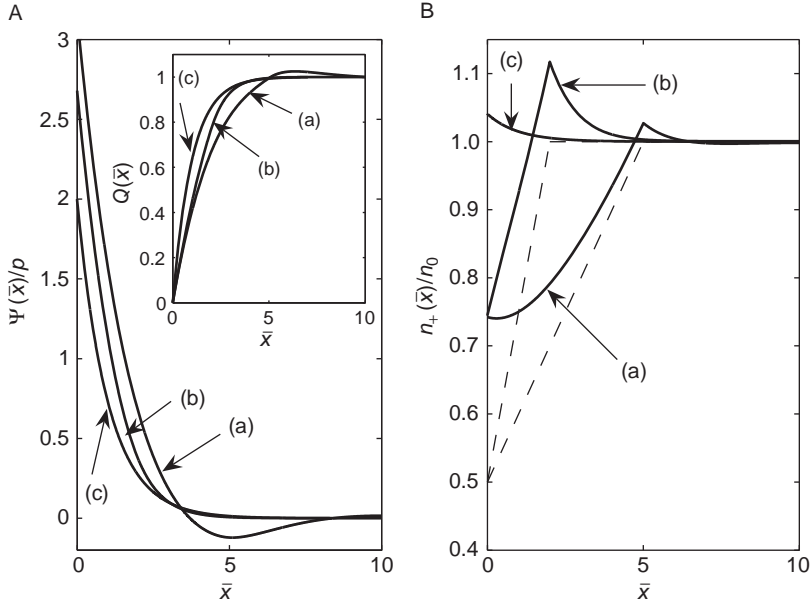


Figure 14 Results for the linearized theory, derived for large distance $\bar{D} = 20$ between the two surfaces [5]. (A) Electrostatic potential $\Psi(\bar{x})/p$ as a function of the distance \bar{x} from the charged surface. The inset shows the scaled integrated charge according to Eq. (134). (B) Local concentration of reference charges $n_+(\bar{x})/n_0$ as a function of \bar{x} , derived for $p = 0.1$. Dashed lines display corresponding calculations where electrostatics is excluded ($p = 0$). In all diagrams the different curves correspond to $\bar{T} = 5$ (a), $\bar{T} = 2$ (b), and $\bar{T} = 0$ (c).

and $n_{\pm}(\bar{x})/n_0 = 1$ for $\bar{T} \leq \bar{x} \leq \bar{D}/2$. These functions are plotted in Fig. 14B (dashed curves, for different rod-lengths \bar{T}) together with the corresponding results (solid curves) for $n_+(\bar{x})$ in the presence of electrostatic interactions for $p = 0.1$. Again, different curves (a), (b), and (c) correspond to different rod lengths \bar{T} .

From known electrostatic potential $\Psi(\bar{x})$ the electrostatic free energy can be calculated. Fig. 15 shows the electrostatic free energy as a function of the distance between two equally charged surfaces. The free energy F is calculated in linear and in the nonlinear regime. Fig. 15 shows results for a characteristic case of long ions; $\bar{T} = 5$. We see that in the limit of $p = 0$ and for $\bar{D} > \bar{T}$, we find $F \times 16\pi l_B l_D / (AkT) = \bar{T}/2$, (or, equivalently, $F/(AkT) = ln_0$), indicating that the two flat surfaces no longer interact with each other. For small distances, $\bar{D} < \bar{T}$, there is entropy loss of the mobile rods due to their interaction with both surfaces occurs. The corresponding depletion attraction continues to dominate the system for weakly charged surfaces where $p \ll 1$, leading to a minimum in $F(\bar{D})$ at small $\bar{D} < \bar{T}$. For larger surface charge density, $p \gtrsim 1$, a depletion minimum is absent. A second minimum, located roughly at $\bar{D} \approx \bar{T}$, is weak for $p \ll 1$ but dominates the system for $p \gtrsim 1$. This second minimum is distinct from the depletion minimum; it is electrostatic in origin and can be ascribed to a *bridging mechanism* (Fig. 16). In support of this notion, the bridging minimum occurs for highly charged surfaces almost exactly at $\bar{D} = \bar{T}$; see curve (a) in Fig. 15. The linearized integro-differential

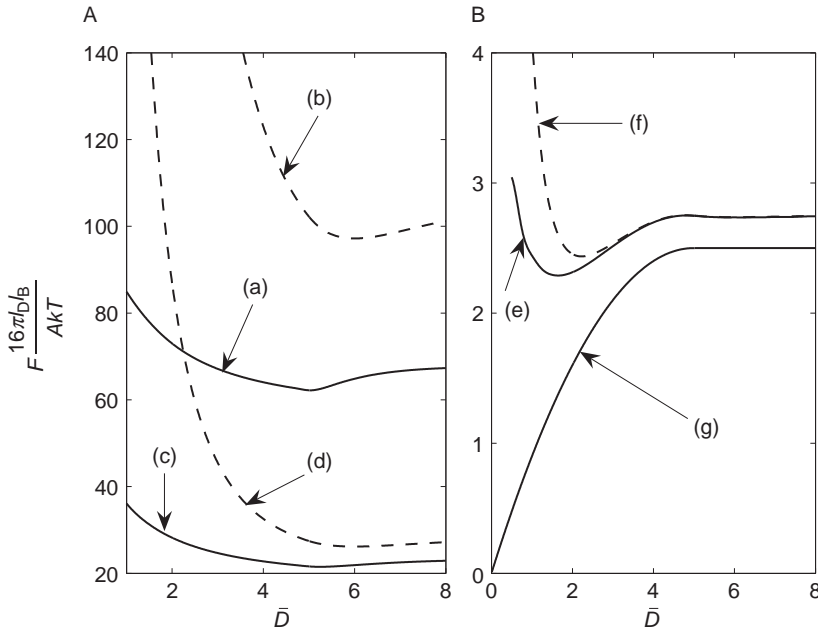


Figure 15 Scaled free energy F as a function of the distance between the two charged planar surfaces, \bar{D} , for $\bar{T} = 5$ [5]. In both diagrams, the solid curves are derived using nonlinear theory, while the dashed curves are based on linearized theory. The charge parameters correspond to $p = 2$ (a,b), $p = 1$ (c,d), and $p = 0.1$ (e,f). Finally, for curve (g) it is $p = 0$, and no electrostatic interactions are present.

equation (see the dashed curves in Fig. 15) yields qualitatively the same predictions as the full nonlinear theory (see the solid curves in Fig. 15). Yet, as for point-like mobile ions, the free energies of the former are much larger if $p \gtrsim 1$.

The theoretical studies of electric double layer of large rod-like quadrupolar (divalent) ions in contact with charged (membrane) planar surface [3,5] have motivated further theoretical studies of the physical properties of a solution of large multivalent ions in contact with a highly charged plane [7,63], such as a solution of large phosphotungstate charged nanoparticles (with diameter around 1 nm) in contact with a highly charged monolayer composed of eicosylamine [64]. The counter-ions were described as spheres with spatially distributed charge [7,63] (see also Fig. 1).

It was shown that at finite temperatures and high enough surface charge densities, the internal charge distribution within a single spherical multivalent charged nanoparticle (with the internal charges located at large enough distances l , see Fig. 1) may lead to the orientational ordering of these multivalent nanoparticles near a charged surface, where the main axis of the nanoparticles (which coincides with the line connecting the two poly-ions with charge $e/2$) is predominantly oriented perpendicularly to the charged surface [63].

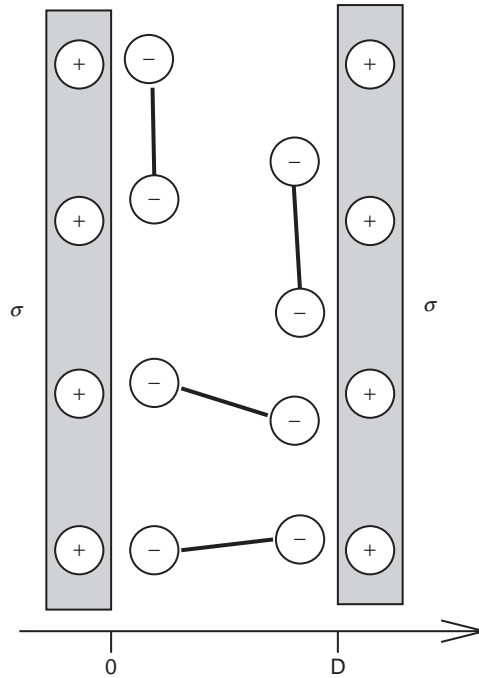


Figure 16 Schematic illustration of the bridging mechanism. For long rod-like ions, $T \gg 1$, there exists a stable equilibrium between the two charged surfaces at $D \approx T$. Here, the ions preferentially orient either parallel or normal to the macroion surfaces. Those aligning normal give rise to the bridging equilibrium [5].

Moreover, it was shown recently that the above described orientational ordering of spherical multivalent charged nanoparticles may give rise to an attractive interaction between like-charged membrane surfaces for high enough surface charge densities of the interacting surfaces and large enough separations between internal charges l [63]. In accordance, we also experimentally observed monoclonal antibody-mediated coalescence of negatively charged giant unilamellar phospholipid vesicles upon close approach of the vesicles [7].

5.3. Dipolar Rod-like Nanoparticles in Electrolyte Solution

Recently, small dipoles [65] and large dipolar rod-like nanoparticles [4] in electrolyte solution of monovalent ions between two oppositely charged planes have also been studied. In this section we describe only the second case (Fig. 17). The dipolar nanoparticles have internal structure, each dipole is composed of negative and positive elementary charges of valency Z , separated by a distance l , i.e., the dipole moment of each dipole is Ze_0l , where e_0 is the elementary charge. The dipoles are characterized by the positional and the orientational degrees of freedom while the monovalent ions are characterized only by the positional degree of freedom. We describe the dipole by referring to the positive charge as a reference charge, denoting the local concentration of all the reference charges by $n(x)$. The location of the

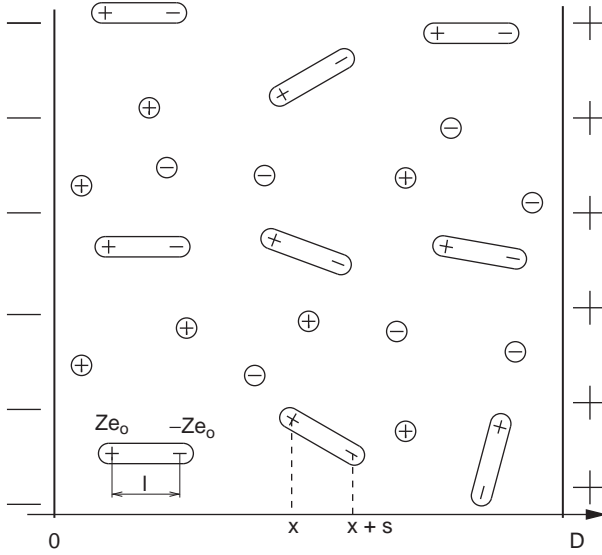


Figure 17 Schematic presentation of two oppositely charged planar surfaces, which is filled with water containing dipoles with dipole moment Ze_0l and monovalent positive and negative ions. The separation between the individual charges of each dipole is denoted by l . The valency of each charge of the dipole is Z .

negative charge of a given dipole is specified by the conditional probability density $p(s|x)$, denoting the probability to find the negative charge at position $x + s$ if the positive is at x . At any given position x , we require the normalization condition

$$\frac{1}{2l} \int_{-l}^l ds p(s|x) = 1 \text{ to be fulfilled. Note also that } p(s|x) = 0 \text{ for } |s| > l.$$

The free energy of the system per unit area of the surface A and thermal energy kT is composed of the energy stored in the electrostatic field (Eq. (3)), the configurational (Eq. (15)) and orientational entropy of the dipoles as well as the configurational entropy of the monovalent ions (Eq. (33)) [4]:

$$\begin{aligned} \frac{F}{AkT} = & \frac{1}{8\pi l_B} \int_0^D dx \psi'(x)^2 + \int_0^D dx [n(x) \ln v_0 n(x) - n(x)] \\ & + \int_0^D dx n(x) \frac{1}{2l} \int_{-l}^l ds p(s|x) [\ln p(s|x) + U(x, s)] \\ & + \int_0^D dx n(x) \lambda(x) \left[\frac{1}{2l} \int_{-l}^l ds p(s|x) - 1 \right] \\ & + \mu \int_0^D dx \left[n(x) - \frac{N}{AD} \right] \\ & + \int_0^D dx \sum_{i=\{+,-\}} \left[n_i(x) \ln \frac{n_i(x)}{n_{0s}} - (n_i(x) - n_{0s}) \right] \end{aligned} \quad (135)$$

where Ψ is the reduced electrostatic potential (see Eq. (79)), μ is global Lagrange multiplier, v_0 is the volume of the dipole, l_B is the Bjerrum length (see Eq. (86) for definition), N is the number of dipoles, n_i is the concentration of the monovalent ions of the i -th type and n_{0s} is the bulk concentration of monovalent ions. The sum in Eq. (135) runs over positive “ $i = +$ ” and negative “ $i = -$ ” monovalent ions. The Lagrange parameter $\lambda(x)$ ensures the normalization condition for the conditional probability density. The fifth term in Eq. (135) ensures the constant number of dipoles in the solution. We introduce the external reduced potential of the charged wall

$$U(x, s) = \begin{cases} 0, & x > 0 \text{ and } x + s > 0 \text{ and } x < D \text{ and } D - x - s > 0 \\ \infty, & \text{elsewhere} \end{cases}$$

which ensures that the dipoles could not penetrate into the charged wall.

In thermal equilibrium, the free energy $F = F[n(x), p(s|x), n_i(x)]$ is minimal with respect to the functions $n(x)$, $p(s|x)$ and $n_i(x)$. The variational procedure ($\delta F = 0$) gives the local concentration of monovalent ions

$$n_i(x) = n_{0s} e^{-i\Psi(x)}, \quad (136)$$

the conditional probability density

$$p(s|x) = \frac{e^{-U(x,s)+Z\Psi(x+s)}}{q(x)} \quad (137)$$

and the local concentration of reference charges of dipoles

$$n(x) = n_0 e^{-Z\Psi(x)} q(x) \quad (138)$$

where $n_0 = \frac{1}{v_0} e^{-\mu}$ is the concentration of reference charges at vanishing electrostatic ($\Psi = 0$) and external ($U = 0$) potentials, and

$$q(x) = \frac{1}{2l} \int_{-l}^l ds e^{-U(x,s)+Z\Psi(x,s)} \quad (139)$$

is the orientational partition function of a single dipole with the position of its reference charge at x . In Eq. (138) the term $e^{-Z\Psi(x)}$ corresponds to the Boltzmann distribution of the reference charges of dipoles.

The local charge density includes contributions from positive reference charges that are located at x and from the orientational mobile negative charges, located at $x - s$ with the corresponding probability density $p(s|x - s)$ as well as from the positive and negative charges of monovalent ions. Inserting the local charge density

$$\frac{\rho(x)}{e_0} = Z n(x) - Z \frac{1}{2l} \int_{-l}^l ds n(x - s) p(s|x - s) + \sum_{i=\{+,-\}} i n_i(x) \quad (140)$$

into the Poisson equation $\Psi''(x) = -4\pi l_B(\rho(x)/e_0)$ we obtain the integro-differential equation for the reduced electrostatic potential

$$\Psi''(x) = 8\pi l_B Z n_0 \frac{1}{2l} \int_{\max[-l, -x]}^{\min[l, D-x]} ds \sinh[Z\Psi(x) - Z\Psi(x+s)] + 8\pi l_B n_{0s} \sinh[\Psi(x)] \quad (141)$$

The boundary conditions are given at the charged plates:

$$\Psi'(x=0) = -\sigma \frac{4\pi l_B}{e_0} \quad (142)$$

$$\Psi'(x=D) = -\sigma \frac{4\pi l_B}{e_0} \quad (143)$$

These boundary conditions demand a neutral overall charge for the system.

In the case of the solution composed of only monovalent ions ($n_0 = 0$, the dipoles are not present) the integro-differential Eq. (141) reduces to the well known PB equation for the monovalent salt of ions $\Psi''(x) = 8\pi l_B n_{0s} \sinh[\Psi(x)]$.

If the electrostatic potential is small compared to the thermal energy ($\Psi \ll 1$), we can linearize the term $\sinh[Z\Psi(x) - Z\Psi(x+s)]$ in Eq. (141) to $Z\Psi(x) - Z\Psi(x+s)$ and the term $\sinh[\Psi(x)]$ to $\Psi(x)$. The linearized integro-differential equation is

$$\Psi''(x) = 8\pi l_B Z n_0 \frac{1}{2l} \int_{\max[-l, -x]}^{\min[l, D-x]} ds [Z\Psi(x) - Z\Psi(x+s)] + 8\pi l_B n_{0s} \Psi(x) \quad (144)$$

with the same boundary conditions (142) and (143).

Figure 18A shows the reduced electrostatic potential Ψ and the electric field strength E (in the inset) as a function of the distance from the left charged surface (x) for three different lengths of dipoles. The electrostatic potential Ψ monotonously increases with increasing distance from the left charged surface. The electric field strength E is symmetric with respect to the midplane of the system. In the limit of very small dipoles the electrostatic potential reduces to the electrostatic potential of the condenser filled with water and the electric field strength becomes constant $E_0 = -7.1 \cdot 10^6$ V/m. The difference between the field strength and the constant value E_0 increases with increasing length of dipoles.

Figure 18B shows the concentration of reference charges n while Figure 18C shows the charge density ρ as a function of the distance from the left charged plate (x) for three different lengths of dipoles. The concentration of reference charges n first increases, reaches maximum value and then decreases with increasing x . In the

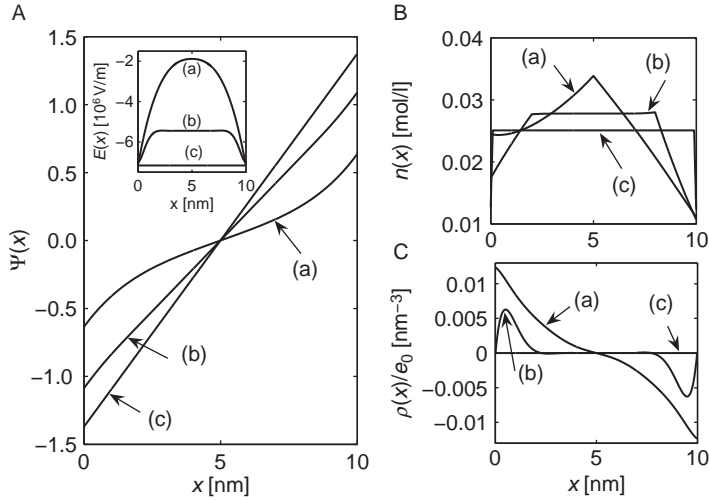


Figure 18 Linearized theory. Salt of monovalent ions is not present [4]. (A) Reduced electrostatic potential $\Psi(x)$ and electric field strength $E(x)$ (in inset), (B) local concentration of reference charges $n(x)$ and (C) charge density $\rho(x)$ as a function of the distance from the left charged plate x . The length of dipoles $l = 5$ nm (a), $l = 2$ nm (b) and $l = 0.1$ nm (c) are shown. The volume of dipole is $v_0 = la_0$. Model parameters are $D = 10$ nm, $a_0 = 1$ nm², $\sigma = 0.005$ As/m², $Z = 1$, $\epsilon = 78$, $T = 300$ K and $N = 25$ for $A = 100$ nm².

limit $l = 0$ the concentration n reaches a constant value. The local concentration of reference charges $n(x)$ is not smooth (Fig. 18B). The first derivative of $n(x)$ is discontinuous at $x = l$ and $x = D - l$. In the regions $0 < x < l$ and $D - l < x < D$ the orientational restriction of dipoles is present. In the region $l < x < D - l$ the orientational restriction of dipoles is not present. For longer dipoles l the absolute value of the charge density ρ decreases with increasing distance from the left charged surface. For smaller l the absolute value of the charge density ρ first increases, reaches a maximum and then decreases with increasing distance to attain the zero value in the centre of the system. In the limit of very small dipoles the charge density vanishes.

Figure 19 shows the conditional probability density $p(s|x)$ as a function of the projection s of dipoles to the x direction. Two different surface charge densities are given for the dipoles of length $l = 2$ nm. We use nonlinearized modified PB theory. The calculation is made for reference charges located at coordinates $x = 0$, $x = 1$ nm, $x = 5$ nm, and $x = 10$ nm. In the interval $0 < x < 2$ nm the conditional probability densities are defined only in the interval $-x < s < l$, while in the interval 8 nm $< x < 10$ nm the conditional probability densities are defined in the interval $-l < s < D - x$. The conditional probability density increases with increasing s . For $x = 0$, $x = 1$ nm and $x = 5$ nm the conditional probability density reaches its maximum at $s = +l$, while for $x = 10$ nm the conditional probability density reaches its maximum at $s = D - x$.

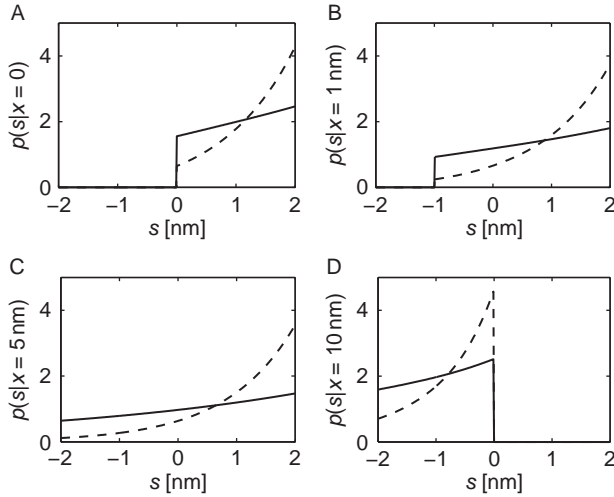


Figure 19 Conditional probability density as a function of the projection of the dipoles with respect to the axis x for four different coordinate of the reference charge (A) $x = 0$, (B) $x = 1$ nm, (C) $x = 5$ nm and (D) $x = 10$ nm [4]. The surface charge densities are $\sigma = 0.005$ As/m² (full lines) and $\sigma = 0.02$ As/m² (dashed lines). The volume of dipole is $v_0 = l a_0$. The nonlinear PB theory is used. The model parameters are $l = 2$ nm, $D = 10$ nm, $a_0 = 1$ nm² and $Z = 1$ and $N = 25$ for $A = 100$ nm².

6. CONCLUDING REMARKS

In this work we present the review on the functional density theory of the electric double layer developed on the basis of statistical mechanical description. The procedure is derived, which starts with the energies of individual particles, obtaining expressions for particle distribution functions and differential equation for the electrostatic potential in different geometries and considering different properties of charged nanoparticles composing the solution. The finite size of charged nanoparticles is considered by the excluded volume effect. We have derived a density functional theory for rod-like ions of arbitrary length. The specific application to the case of two interacting, like-charged, planar charged surfaces reveals the possibility of attractive interactions, introduced solely by correlations within the rod-like ions.

The introduction of the excluded volume effect in the PB theory within the lattice model approach [34] allows for an improved description of the electrostatics of charged membranes, charged cylindrical tubes and spheres filled with electrolyte solution. The model distinguishes between occupied and free lattice sites. Free lattice sites are assumed to be occupied by water with a relative permittivity of 78.5. Consequently, the ions are assumed to be suspended in a continuous dielectric medium.

In PB theory, ions are considered to be dimensionless. Thus, the counter-ion concentration near a charged surface can increase boundlessly. As a result, the results

of the PB theory show a continuous increase in counter-ion concentration near the surface, with increasing $|\sigma|$ (Fig. 8). In contrast to the PB theory, in *excluded volume functional density* (EVFD) theory the ions are assumed to have finite size. This assumption has a considerable effect on counter-ion concentration and the electrostatic potential profiles. The EVFD theory predicts a plateau of counter-ion concentration close to the charged surface [34,35,59,57], a finding supported by recent experimental findings on planar electric double layers [64]. The deviation from the predictions of the PB theory could be attributed to the steric effect (Fig. 8) where the number density of ions cannot exceed the density of the lattice sites.

With decreasing radius, the number of lattice sites declines faster in the spherical than in the cylindrical geometry. Therefore the concentration of counter-ions at the axis of a cylinder reaches a plateau at lower $|\sigma|$ than in the center of a sphere. In cylindrical geometry, counter-ion condensation is observed at lower $|\sigma|$ than in the spherical geometry.

The measure was introduced that describes an effective thickness of the electric double layer, a distance where the density of the number of counter-ions drops to a chosen fraction of its maximal value. It was shown that the effective thickness of the electric double layer increases with increasing counter-ion size.

The functional density theory for rod-like ions of arbitrary length, l , used in the case of two interacting, like-charged, planar surfaces, reveals the possibility of attractive interactions. In our present approach, the critical rod length for the attraction (l_c) is roughly given by twice the Debye length l_D that characterizes the electrostatic screening length (i.e., $l_c \approx 2l_D$). In the limit of large rod length ($l \gg l_D$) an equilibrium distance $D \approx l$ between the charged surfaces results from a bridging interaction. We expect that our present results contribute to better understanding of protein-induced agglutination of like-charged membrane surfaces [7,63] and the nature of condensation of DNA [66,67] and other macroions by the rod-like structured common condensing agents such as polyamines and certain linear peptides.

We also considered a system of two oppositely charged surfaces in a solution composed of dipoles and monovalent ions. The density functional theory for dipoles of arbitrary length was introduced. The spatial distribution of electric charge within the dipoles, the orientations of dipoles and their restrictions near the charged surface were taken into account. The numerical solution showed that the dipoles are predominantly oriented parallel to the electric field, i.e., perpendicular to the charged surfaces. The interaction between oppositely charged surfaces mediated by dipoles was discussed. The presence of the dipoles in the electrolyte solution affects the interaction between two oppositely charged surfaces. The force between the oppositely charged surfaces is especially pronounced at the distance between charged surface being equal to the length of the dipoles, which is related to the bridging mechanism [68].

In summary, we studied the electric double layer in different geometries and compositions. In our theory the finite size of ions and charge distribution within the large quadrupolar (divalent) or dipolar ions was taken into account. The described physical properties of the electric double layer may in the future attract increasing attention owing to their benefit in technology, biology and medicine.

REFERENCES

- [1] J.N. Israelachvili, *Intermolecular and Surface Force* Academic Press, London/San Diego, 1992.
- [2] A. Safran, *Statistical Thermodynamics of Surfaces, Interfaces, and Membranes* Addison-Wesley, Colorado, 1994.
- [3] K. Bohinc, A. Iglič, S. May, Interaction between macroions mediated by divalent rod-like ions, *Europhys. Lett.* 68 (2004) 494–500.
- [4] S. Maset, K. Bohinc, Orientations of dipoles restricted by two oppositely charged walls, *J. Phys. A: Math. theor.* 40 (2007) 11815–11826.
- [5] S. Sylvio May, A. Iglič, J. Reščič, S. Maset, K. Bohinc, Bridging like-charged macroions through long divalent rod-like ions, *J. Phys. Chem. B* 112 (2008) 1685–1692.
- [6] O. Alvarez, M. Brodwick, R. Latorre, A. Mclaughlin, S. Mclaughlin, G. Szabo, Large divalent cations and electrostatic potentials adjacent to membranes, *Biophys J.* 44 (1983) 333–342.
- [7] J. Urbanija, N. Tomšič, M. Lokar, A. Ambrožič, S. Čučnik, B. Rozman, M. Kandušar, A. Iglič, V. Kralj-Iglič, Coalescence of phospholipid membranes as a possible origin of anticoagulant effect of serum proteins, *Chem. Phys. Lipids* 150 (2007) 49–57.
- [8] S. McLaughlin, The Electrostatic properties of membranes, *Ann. Rev. Biophys. Chem.* 18 (1989) 113–136.
- [9] R. Heinrich, M. Gaestel, R. Glaser, The electric potential profile across the erythrocyte membrane, *J. Theor. Biol.* 96 (1982) 211–231.
- [10] A. Iglič, M. Brumen, S. Svetina, Determination of the inner surface potential of the erythrocyte membrane, *Bioelectrochemistry* 43 (1997) 97–103.
- [11] A. Karlsson, R. Karlsson, M. Karlsson, A.S. Cans, A. Strömberg, F. Ryttsen, O. Orwar, Networks of nanotubes and containers, *Nature* 409 (2001) 150–152.
- [12] V. Kralj-Iglič, A. Iglič, G. Gomišček, V. Arrigler, H. Hägerstrand, Microtubes and nanotubules of phospholipid bilayer vesicles, *J. Phys. A: Math. Gen.* 35 (2002) 1533–1549.
- [13] A. Iglič, H. Hägerstrand, V. Arrigler, V. Kralj-Iglič, Possible role of phospholipid nanotubules in directed transport of membrane vesicles, *Phys. Lett.* 310 (2003) 493–497.
- [14] A. Rustom, R. Saffrich, I. Markovič, P. Walther, H.H. Gerdes, Nanotubular highways for intercellular organelle transport, *Science* 303 (2004) 1007–1010.
- [15] A. Iglič, M. Lokar, B. Babnik, T. Slivnik, P. Veranič, H. Hägerstrand, V. Kralj-Iglič, Possible role of flexible red blood cell membrane nanodomains in the growth and stability of membrane nanotubes, *Blood Cells Mol. Dis.* 39 (2007) 14–23.
- [16] K. Bohinc, T. Slivnik, A. Iglič, M. Brumen, V. Kralj-Iglič, Transmembrane distribution of membrane constituents in organic nanotubes driven by electric charge and intrinsic anisotropy of molecules, *J. Phys. Chem. C* 111 (2007) 9709–9718.
- [17] N. Imai, T. Ohinshi, Analytical solution of Poisson–Boltzmann equation for two-dimensional many-center problem, *J. Chem. Phys.* 30 (1959) 1115–1116.
- [18] F. Oosawa, *Polyelectrolytes* Marcel Dekker, New York, 1970.
- [19] G.S. Manning, Limiting Laws and Counterion Condensation in Polyelectrolyte Solutions I Colligative Properties, *J. Chem. Phys.* 51 (1969) 924–933.
- [20] K.S. Schmitz, *Macroions in Solution and Colloidal Suspension*, VCH Publishers, New York, 1993.
- [21] M.G. Gouy, Sur la constitution de la charge électrique à la surface d'un électrolyte, *J. Phys. Radium (Paris)* 9 (1910) 457–468.
- [22] D.L. Chapman, A Contribution to the Theory of Electrocapillarity, *Philos. Mag.* 6 (1913) 475–481.
- [23] S.L. Carnie, D.Y.C. Chan, J. Stankovich, Computation of forces between spherical colloidal particles–nonlinear Poisson–Boltzmann theory, *J. Coll. Interface Sci.* 165 (1994) 116–128.
- [24] D. Bratko, V. Vlady, Distribution of counterions in the double layer around a cylindrical polyion, *J. Phys. Chem.* 90 (1982) 434–438.
- [25] T. Das, D. Bratko, L.B. Bhuiyan, C.W. Outhwaite, Modified Poisson–Boltzmann Theory Applied to Linear Polyelectrolyte Solutions, *J. Phys. Chem.* 99 (1995) 410–418.

- [26] T. Das, D. Bratko, L.B. Bhuiyan, C.W. Outhwaite, Polyelectrolyte solutions containing mixed valency ions in the cell model: A simulation and modified Poisson–Boltzmann theory, *J. Phys. Chem.* 107 (1997) 9197–9207.
- [27] E. Gonzalez-Tovar, M. Lozada-Cassou, D. Henderson, Hypernetted chain approximation for the distribution of ions around a cylindrical electrode. II. Numerical solution for a model cylindrical polyelectrolyte, *J. Chem. Phys.* 83 (1985) 361–372.
- [28] G.M. Torrie, J.P. Valleau, Electrical double-layers 4 Limitations of the Gouy–Chapman theory, *J. Phys. Chem.* 86 (1982) 3251–3257.
- [29] M. Lozada-Cassou, D. Henderson, Application of the hypernetted chain approximation to the electrical double layer Comparison with Monte Carlo results for 2:1 and 1:2 salts, *J. Phys. Chem.* 87 (1983) 2821–2824.
- [30] R. Bacquet, P.J. Rossky, Corrections to the HNC equation for associating electrolytes, *J. Chem. Phys.* 79 (1983) 1419–1426.
- [31] R. Bacquet, P.J. Rossky, Ionic Atmosphere of Rodlike Polyelectrolytes. A Hypernetted Chain Study, *J. Phys. Chem.* 88 (1984) 2660–2669.
- [32] V. Freise, Zur Theorie der Diffusendoppelschicht, *Z. Elektrochem.* 56 (1952) 822–827.
- [33] M. Eigen, E. Wicke, The Thermodynamics of Electrolytes at Higher Concentrations, *J. Phys. Chem.* 58 (1954) 702–714.
- [34] V. Kralj-Iglič, A Simple Statistical Mechanical Approach to the Free Energy of the Electric Double Layer Including the Excluded Volume Effect, *J. Phys II France* 6 (1996) 477–491.
- [35] I. Borukhov, D. Andelman, H. Orland, Steric Effects in Electrolytes: A Modified Poisson Boltzmann Equation, *Phys. Rev. Lett.* 79 (1997) 435–438.
- [36] M. Manciu, E. Ruckenstein, Lattice Site Exclusion Effect on the Double Layer Interaction, *Langmuir* 18 (2002) 5178–5185.
- [37] I. Borukhov, Charge renormalization of cylinders and spheres: Ion size effect, *J. Pol. Sci. B: Pol. Phys* 42 (2004) 3598.
- [38] E. Trizac, J.L. Raimbault, Long-range electrostatic interactions between like-charged colloids: Steric and confinement effects, *Phys. Rev. E* 60 (1999) 6530–6533.
- [39] G. Barbero, L.R. Evangelista, D. Olivero, Asymmetric ionic adsorption and cell polarization in liquid crystals, *J. Appl. Phys.* 87 (2000) 2646–2648.
- [40] L. Lue, N. Zoeller, D. Blankschtein, Incorporation of Nonelectrostatic Interactions in the Poisson–Boltzmann Equation, *Langmuir* 15 (1999) 3726–3730.
- [41] S. Lamperski, C.W. Outhwaite, Exclusion volume term in the inhomogeneous Poisson–Boltzmann theory for high surface charge, *Langmuir* 18 (2002) 3423–3424.
- [42] P. Mills, C.F. Anderson, M.T. Record, Monte Carlo studies of counterion–DNA interactions. Comparison of the radial distribution of counterions with predictions of other polyelectrolytes theories, *J. Phys. Chem.* 89 (1985) 3984–3994.
- [43] L.B. Bhuiyan, C.W. Outhwaite, D. Bratko, Structure and thermodynamics of micellar solutions in the modified Poisson–Boltzmann theory, *Chem. Phys. Lett.* 193 (1992) 203–210.
- [44] D. Bratko, Hypernetted chain approximation for ion distribution in reverse micelles, *Chem. Phys. Lett.* 169 (1990) 555–560.
- [45] W.M. Gelbart, R. Bruinsma, P.A. Pincus, V.A. Parsegian, DNA-Inspired Electrostatics. Not just the repository of our genetic information, DNA is also a fascinating, shape-shifting molecule whose behavior in solution counters our intuition and challenges our physical understanding, *Phys. Today* 53 (2000) 38–44.
- [46] V.A. Bloomfield, DNA condensation, *Curr. Opin. Struct. Biol.* 6 (1996) 334–341.
- [47] T.E. Angelini, H. Liang, W. Wriggers, G.C.L. Wong, Like-charge attraction between polyelectrolytes induced by counterion charge density waves, *Proc. Natl. Acad. Sci. USA* 100(15), (2003) 8634–8637.
- [48] J.C. Butler, T. Angelini, J.X. Tang, G.C.L. Wong, Ion multivalence and like-charge polyelectrolyte attraction, *Phys. Rev. Lett.* 91(2), (2003) 028301/1–4.
- [49] A.Y. Grosberg, T.T. Nguyen, B.I. Shklovskii, The physics of charge inversion in chemical and biological systems, *Mod. Rev. Phys.* 74 (2002) 329–345.
- [50] R.R. Netz, Electrostatics of counter-ions at and between planar charged walls: From Poisson–Boltzmann to the strong-coupling theory, *Eur Phys. J. E* 5 (2001) 557–574.

- [51] P. Linse, Mean force between like-charged macroions at high electrostatic coupling, *J. Phys.: Condens. Matter* 14 (2002) 13449–13467.
- [52] L. Gulbrand, B. Jönsson, H. Wennerström, P. Linse, Electrical double layer forces. A Monte-Carlo study, *J. Chem. Phys.* 80(5), (1984) 2221–2228.
- [53] R. Kjellander, S. Marčelja, Surface interactions in simple electrolytes, *J. Phys. France* 49(6) (1988) 1009–1015.
- [54] R. Kjellander, Ion–ion correlations and effective charges in electrolyte and macroion systems, *Ber. Bunsenges. Phys. Chem.* 100(6), (1996) 894–904.
- [55] J.D. Jackson, *Classical Electrodynamics* Wiley, New York, 1999.
- [56] T.L. Hill, *An Introduction to Statistical Thermodynamics*, Adison-Wesley, Reading, MA/Toronto, Canada, 1962.
- [57] K. Bohinc, J. Gimsa, V. Kralj-Iglič, T. Slivnik, A. Iglič, Excluded volume driven counterion condensation inside nanotubes in a concave electrical double layer model, *Bioelectrochemistry* 67 (2005) 91–99.
- [58] L.E. Elsgolc, *Calculus of Variations*, Pergamon Press, Oxford, UK, 1961.
- [59] K. Bohinc, V. Kralj-Iglič, A. Iglič, Thickness of electrical double layer Effect of ion size, *Electrochim. Acta* 46 (2001) 3033–3040.
- [60] K. Bohinc, A. Iglič, T. Slivnik, V. Kralj-Iglič, Planar, cylindrical and spherical electrical double layers in biological systems. The effect of counterions, *Cell. Mol. Biol. Lett.* 7 (2002) 839–843.
- [61] D.F. Evans, H. Wennerström, *The colloidal domain, where physics, chemistry, and biology meet* (2nd ed.), VCH, New York, 1994.
- [62] D. Andelman, *Handbook of Biological Physics*, Vol. 1. Elsevier, Amsterdam, 1995.
- [63] J. Urbanija, V. Kralj-Iglic, A. Bellen, S. Maset, P.B.S. Kumar, A. Iglic, K. Bohinc, Attraction between negatively charged surfaces mediated by extended charges, submitted for publication.
- [64] N. Cuvillier, F. Rondelez, Breakdown of the Poisson–Boltzmann description for electrical double layers involving large multivalent ions, *Thin Solid Films* 327–329 (1998) 19–23.
- [65] A. Abrashkin, D. Andelman, H. Orland, Dipolar Poisson–Boltzmann Equation: Ions and Dipoles Close to Charge Interfaces, *Phys. Rev. Lett.* 99(2007) 077801/1–4.
- [66] V.A. Bloomfield, DNA condensation by multivalent cations, *Biopolymers* 44 (1997) 269–282.
- [67] V.B. Teif, Ligand-induced DNA condensation: Choosing the model, *Biophys. J.* 89 (2005) 2574–2587.
- [68] E.E. Meyer, Q. Lin, T. Hassenkam, E. Oroudjev, J.N. Israelachvili, Origin of the long-range attraction between surfactant-coated surfaces, *Proc. Natl. Acad. Sci. USA* 102 (2005) 6839–6842.

ENERGETICS OF MEMBRANE PERMEABILITY

Alexander G. Volkov^{1,*} and Talitha Hampton²

Contents

1. Introduction: BLM Permeability	156
2. Partition	161
2.1. Electrostatic Contribution to the Solvation Energy	162
2.2. The Born Model	165
2.3. The Nonlocal Electrostatics Method	170
2.4. Hydrophobic Effect	174
2.5. The Total Partition Energy	177
2.6. Image Forces	179
2.7. Dipolar Potential	180
2.8. Dipole Partition	183
3. Transient Pore Mechanisms of Passive Transport Across BLM	187
4. Partitioning or Transient Pores: A Critical Test	190
5. Conclusions	194
References	196

Abstract

The Gibbs free energy of dipole or ion permeation of lipid bilayers is calculated as the sum of all electrostatic, solvophobic and specific interactions. Partitioning models are consistent with dipole permeation and some features of ionic permeation, particularly, if the solvophobic energy is taken into account. Ionic and dipole permeability are extremely sensitive to the ionic/dipolar radius. Despite this sensitivity, calculations of the permeability can be carried out for typical monovalent cations, and provide reasonable estimates, but only for hydrated species. An alternative mechanism proposed for ionic permeation involves the occurrence of transient pore-like defects in lipid bilayers which permit ions to bypass the Born energy barrier. The two alternative hypotheses, partitioning vs. transient pores, can be tested by measuring the ionic and dipolar permeation through bilayers of varying thickness. Experimental observations for ions permeability are consistent with the transient pore mechanism for shorter chain lipids, but tend towards the theoretical line for partitioning models for longer chain lipids. Results for small neutral solutes are best explained by the solubility-diffusion mechanism. The proposed method of calculation of the Gibbs free energy of ion or dipole membrane transfer can be effectively used not only in describing the biophysical properties of bilayers, but also in extraction

* Corresponding author: Tel./Fax: +256 726 7113;

E-mail address: agvolkov@yahoo.com.

¹ Department of Chemistry and Biochemistry, Oakwood University, Huntsville, AL 35896, USA

² Department of Chemical Engineering, University of Alabama in Huntsville, AL 35899, USA

processes, pharmaceutical applications and liquid membrane separations. In this method it has been found that the free energy of the solvophobic effect is opposite in sign to the electrostatic effect. As a result, the sum of the electrostatic and solvophobic components of the Gibbs free energy decreases with ionic size. The specific energy of ion/dipolar layer interaction depends on the dipolar membrane surface potential. These calculations yielded the permeability of different ions and molecules through bilayer membranes in good agreement with experimental data.

1. INTRODUCTION: BLM PERMEABILITY

The cell membrane consists primarily of two monolayers of phospholipids spontaneously arranged so that hydrophobic “tail” regions are shielded from the surrounding polar fluid, causing the more hydrophilic “head” regions to associate with the cytosolic and extracellular faces of the resulting bilayers [1,2]. This results in the formation of continuous lipid bilayers that is approximately 6–7 nm thick [3–5]. The cell membrane acts as a barrier that separates the cell contents from the external medium. The barrier is selectively permeable and regulates the transport of ions and other materials into and out of the cell. Lipid bilayers have sufficiently low permeability so that transport systems in the membrane can maintain suitable gradients of ions or polar solutes against a substantial leak [2–5].

The mechanism by which ions permeate the BLM and their regulation is a key problem in membrane biophysics. Planar lipid bilayers, also called black-lipid membranes, and liposomes are two most frequently used systems to study bilayer permeation kinetics [6–12]. The permeation of ions across the BLM depends on ion gradients. The presence of ion gradients is vital for the functioning of most living cells. Ion gradients are required as an energy source, for signal transmission, and as a tool to orient proteins [1]. Ion transport across cell membranes is essential for several cellular functions. In cells, this process is aided by ion channels, carriers, and pumps, which lower the free energy barrier associated with the transfer of ions from the polar aqueous environment to the nonpolar interior of the membrane. However, ions can permeate lipid membranes even in the absence of special molecules to assist the transport [1,2,6–10].

The transport across membranes can be passive or active. Active transport is an energy-requiring process that moves ions across the membrane. Passive transport, unlike active transport, does not involve the input of the Gibbs energy and is dependent on the permeability of the cell membrane. Passive transport operates on the existing electrochemical potential gradients of the permeant, and its work leads to the disappearance of this gradient. Subsequently, understanding the mechanism of passive ion and dipole transport at a molecular level could offer valuable insight into the induced charge transport.

The balance between maintenance and dissipation of concentration gradients across bilayer membranes is crucial for the function of biological systems. Processes such as oxidative and photosynthetic phosphorylation require membranes that provide effective barriers to passive diffusion of protons. In other cases, the rapid

exchange of molecules such as water across a cell membrane is essential, which demands water channel proteins to increase the intrinsic water permeability of the membrane. Permeability coefficients of many ions and small neutral molecules have been determined experimentally and vary over a remarkably broad range. Despite the availability of these data, the mechanism of passive permeation is still not completely understood. Two alternative mechanisms are commonly used to explain ion permeation of biological membranes in the absence of channel or transport proteins. One is referred to as the solubility–diffusion mechanism, in which it is proposed that ions may diffuse across the hydrophobic interior of the membrane. The other is the pore mechanism, in which the ion transport is assumed to be supported by water pores in the membrane [1]. Ions may be expected to permeate more easily via such pores, because the water molecules of the pore can reduce the repulsive hydrophobic interaction of the membrane to the penetrated ion.

Generally, the most commonly used models for describing the passive transport of ions across lipid bilayers in biological membranes is the solubility–diffusion model, which relates a given solute's permeability coefficient to its ability to partition into and diffuse across the phospholipid membrane [1,7–10,13–21]. This model treats the membrane as a thin static slab of hydrophobic matter embedded in an aqueous environment. To cross the membrane, the permeating particle must dissolve in the hydrophobic region, diffuse across, and leave by redissolving into the second aqueous phase. If the membrane thickness and the diffusion and partition coefficients of the permeating species are known, the permeability coefficient can be calculated [7,10,18].

When considering the solubility–diffusion model for ion permeation, many diverse and complex properties of real bilayers and membranes must also be considered. It has been a general assumption that Low permeability reflects the electrostatic energy for partitioning an ion or dipole in the low dielectric hydrocarbon interior, an energy term so large that it represents a nearly insurmountable barrier [22]. Although this has been a satisfying general explanation, when the expectations of electrostatic energy calculations are compared with experimental measurements of ionic flux, it becomes clear that other factors must be considered as well [1,7,10,18]. For instance, the passive transfer of an ion across a lipid bilayer, although measurable, is in fact a rare event, and it is possible that transient defects can account for much, if not all, of the measured diffusion.

The barrier of the BLM is selectively permeable and can regulate what enters and exits the cell. The partition coefficients of ions and neutral molecules are usually determined by experiments and estimated theoretically [23–27]. The most traditional view in the literature is that partition coefficients for ions can be derived from Born energy—the energy required to transfer a charged particle from the high dielectric aqueous phase to the low dielectric membrane interior [16,17,22,28,29]. Parsegian [22] described the barrier properties of lipid bilayers in terms of Born energy required to bring an ion from a high dielectric aqueous phase to the low dielectric medium of the hydrocarbon chains composing the membrane interior. This energy, in the range of 100–300 kJmol⁻¹ for inorganic monovalent cations, is an immense energy barrier, and has been generally accepted as a reasonable explanation for the relative impermeability of bilayer membranes to ion flux.

The approach developed by Parsegian [22] was further developed by Dilger *et al.* [28], who tested the prediction that increasing the dielectric constant of the bilayer phase would lead to significant increases in ionic permeability of a planar lipid bilayer membrane. The membrane dielectric constant was increased by replacing the normal decane solvent with chlorodecane, and it was found that permeability to anions was in fact increased by three orders of magnitude [28]. This result, while qualitatively consistent with expectations of the Born theory, did not represent a critical quantitative test of the hypothesis that Born energy represents the primary barrier to ion diffusion across bilayers. Many cases citing the discrepancies between predicted and measured permeabilities have raised questions about this approach. For example, the observed permeability of sodium ions exceeds the calculated value by three orders of magnitude [30]. Proton permeation rates were found to be even larger, five to six orders of magnitude above the values estimated from comparisons with other monovalent cations [11,12,31,32].

An alternative mechanism to the solubility–diffusion description was proposed, which suggests that permeation across a bilayer membrane occurs through hydrated transient defects produced by thermal fluctuations [33–44]. By passing through pores, the permeating particle can avoid the Born energy barrier associated with the solubility–diffusion model. Furthermore, protons can be translocated by a Grotthus-type mechanism along water “wires” spanning the membrane in such defects. Because this process is intrinsically much faster than diffusion, the transient pore model can also explain the high permeability observed for protons. Mechanisms of ions, water and small neutral molecules permeation across membranes will be discussed in this chapter.

Other studies also investigated the quantitative discrepancies of the Born theory with respect to experimental results. Among the first was Bell [45] who noted that measured partitioning of ions between polar and nonpolar media was only in qualitative agreement with expectations from Born calculations. Hauser *et al.* [30] calculated the rate predicted by Born theory at which sodium ions were expected to escape from liposomes. The calculated rates were then compared with measured efflux rates and found to be too slow by three orders of magnitude. To explain this discrepancy, it was suggested that substantial transbilayer defects were contributing to loss of sodium ions from the vesicles.

Macdonald [46] noted that Born energy calculations for ionic permeation predicted an extreme sensitivity to the diameter of the permeating ion. Permeability would be expected to vary over ranges in excess of 10^{10} when smaller and larger monovalent ions were compared. However, experimental measurements of sodium and potassium flux showed relatively little difference [47]. Macdonald [46] attempted to explain this by suggesting that the free energy of transfer of ions from an aqueous phase to the hydrocarbon interior of a bilayer has a uniform energy minimum for all ions that is related to their hydration state. Therefore it would be expected that the hydrated ions would not behave according to Born energies calculated for the bare ionic radii. This expectation was confirmed by Georgallas *et al.* [48], who reported only small variations in the permeability of multilamellar liposomes to monovalent cations (Li^+ , Na^+ , K^+ , and Cs^+). The permeability varied

inversely with the hydrated ionic radius, suggesting that it was the hydrated species that was permeating, rather than bare ions.

Flewelling and Hubbell [49,50] noted another discrepancy that permeability of bilayers to hydrophobic anion tetraphenylborate was considerably greater than to a cation tetraphenylphosphonium with virtually identical size and hydrophobicity even though Born theory would not predict any difference between monovalent anions and cations. These authors found that energetics of membrane permeability includes not only Born energy, but also dipole energy, hydrophobic energy, and image energy terms related to ions approaching and permeating an actual lipid bilayer. A major differentiating factor, which favors anion permeation, appears to be the dipole potential. The expanded equation does account for the difference between anions and cations, but does not predict actual rates at which various ions permeate the bilayer.

The most dramatic inconsistency with the Born [51] theory is probably seen with the investigation of proton permeability across bilayer membranes. Remarkably high proton permeability was first reported by Nichols and Deamer [31,32] and confirmed by other laboratories [14,52–54]. There is no reason to expect proton permeation to differ from that of other cations, yet calculated fluxes of protons down a concentration gradient of 10^{-6} to 10^{-7} M (pH 6–7) are in the same range as the flux of potassium ions down a gradient of 10^{-1} to 10^{-2} M. That is, proton and potassium fluxes down tenfold gradients are similar even though the potassium concentration at 0.1 M is 10^5 times that of protons at pH 6.

A second unusual feature of proton translocation across membranes is that measured fluxes depend on the pH gradient or membrane potential driving the flux, as expected, but the absolute value of the flux is essentially independent of the pH at which the measurements are made. This was first noted in liposomes by Nichols and Deamer [31] then confirmed by Gutknecht [52] for planar lipid bilayers over a pH range from near 2 to near 11. That is, at a given voltage driving proton currents, virtually the same proton conductance was measured at low, neutral and high pH ranges.

Several attempts have been made to account for these discrepancies. Solvophobic and image energies have been added to the Born energy term, yielding a smaller net energy of transfer and thus increasing the predicted permeability. It has also been suggested to use the hydrated radii instead of the bare ionic radii which leads to lower translocation energies and therefore higher permeation rates [18].

It follows from these observations that protons can have a permeation mechanism quite different than that of other monovalent cations. This might at first seem to be a laboratory curiosity, but in fact proton permeation mechanisms are fundamental to our understanding of bioenergetics [55]. For instance, electrochemical proton gradients are the energy source for ATP synthesis by ATP synthase at coupling membranes. The F_o subunit has a channel-like structure that allows protons to be conducted to an active site at which proton translocation is coupled to the release of ATP from the F_1 subunit (Fig. 1).

The discrepancies described above suggest that considerations of ion permeation mechanisms must be expanded to include other conductive processes. In this chapter, we will discuss two mechanisms of passive transmembrane transport that

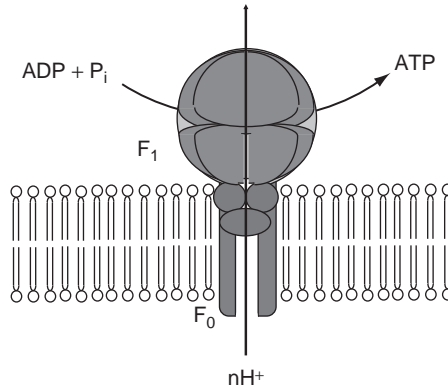


Figure 1 The ATP synthesis by ATPsynthase using transmembrane proton gradient.

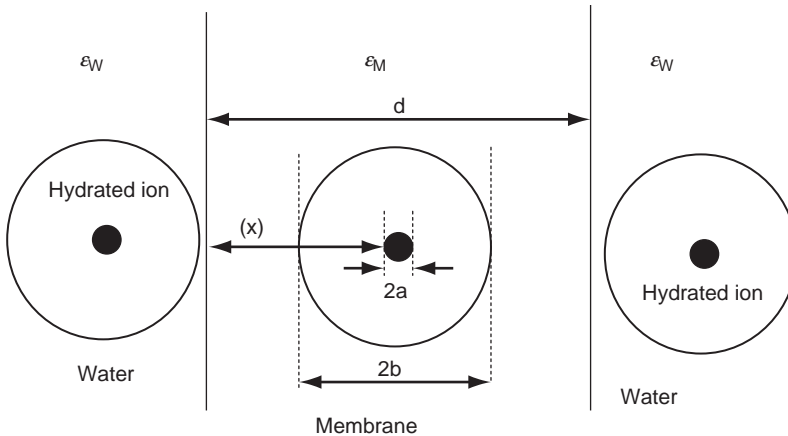


Figure 2 The partition model for ion permeation of a lipid bilayer. ϵ_w , ϵ_m and ϵ_s are the dielectric constants of the aqueous phase, membrane phase and the ion solvation shell; a is the bare ionic radius, b is the radius of hydrated ion, x the distance the ion penetrates into the bilayer, q is the ionic electrical charge, and d is the thickness of hydrophobic part of bilayer.

essentially represent alternative hypotheses [18]. The first possibility is that ion or dipole permeation can be understood in terms of energy related to partitioning of ions or dipoles into the nonpolar phase of the lipid bilayer (Fig. 2). The second possibility is that high dielectric defects in the form of transient pores occur in the BLM and allow permeating ions or dipoles to bypass the partitioning energy barriers. The two hypotheses were tested by experimental measurements of proton, potassium, water and small organic molecules fluxes [1, 7–10, 18] across lipid bilayers of varying thickness.

Mechanisms of ions, water and small neutral molecules permeation across membranes will be discussed in this chapter.

2. PARTITION

In recent years there has been a great surge of interest in the experimental determination and theoretical calculation of the standard Gibbs energy of ion transfer for individual ions moving between two solvents (Gibbs energy of partitioning or resolution). The Gibbs energy of ion resolution is a key concept intimately related to the electrochemistry of the interface between two immiscible liquids, ion transport across biological and artificial membranes, the mechanisms of interfacial and surface catalysis, the kinetics of ion transfer across an liquid interfaces, the coupling of heterogeneous reactions in bioenergetics, extraction, drug delivery in pharmaceutical chemistry, and the design and manufacture of ion-selective electrodes and sensors [1, 56–64].

By solvation we mean the sum of all structural and energy changes occurring in a system when ions pass from the gaseous phase into solution. It has become customary to divide the interaction between ion and solvent and the corresponding energy, into several components. To understand the energies involved in transferring an ion or dipole between two solvent phases, one must take the following effects into account:

- (i) Electrostatic polarization of the medium
- (ii) Production in a medium of a cavity to accommodate the ion also known as the solvophobic or hydrophobic
- (iii) Changes in the structure of the solvent that involve the breakdown of the initial structure and the production of a new structure in the immediate vicinity of the ion
- (iv) Specific interactions of ions with solvent molecules, such as hydrogen bond formation, donor–acceptor, and ion–dipole interactions
- (v) Annihilation of defects: a small ion may be captured in a “statistical micro-cavity” within the local solvent structure so far releasing energy of this defect
- (vi) The correction term for different standard states

This sub-division is purely conditional since many of these different effects may overlap: for example, electric polarization of the medium may significantly influence its structure. Assigning such a division does permit analysis of the individual components. However, sometimes, components can be grouped into “blocks.” For example, one may speak about the solvophobic effect which combines the formation of a cavity and structural changes of the solvent in the vicinity of the new particle. This is quite justifiable because the solvophobic effect, together with the electrostatic effect, provides the major contribution to the solvation energy. On the other hand, sometimes it becomes necessary to consider each individual component of a given effect.

For example, the total solvation (or resolution) energy can be divided into electrostatic $\Delta G(\text{el})$ and nonelectrostatic parts $\Delta G(\text{svph})$:

$$\Delta_{\beta}^{\alpha} G_{\text{i}}^0 = \Delta_{\beta}^{\alpha} G_{\text{i}}^0(\text{el}) + \Delta_{\beta}^{\alpha} G_{\text{i}}^0(\text{svph}) \quad (1)$$

To find the Gibbs standard free solvation energy, one needs to compare the Gibbs energies for a given ion in each media. If one of the phases (β) is a vacuum (vac), the difference:

$$\Delta_{\text{vac}}^{\alpha} G_i^0 = G_i^{0,\alpha} + G_i^{0,\text{vac}} \quad (2)$$

is called the solvation energy of the ion i in the α phase. The resolution energy can be represented as the difference of two solvation energies:

$$\Delta_{\beta}^{\alpha} G_i^0 = -\frac{\Delta_{\beta}^{\alpha} \phi_i^0}{z_i F} = \Delta_{\text{vac}}^{\alpha} G_i^0 - \Delta_{\text{vac}}^{\beta} G_i^0 \quad (3)$$

where $\Delta_{\beta}^{\alpha} \phi_i^0$ is the standard potential for transfer of ion i from α to β phase.

Table 1 lists the standard free energies of ion transfer from water into different organic solvents obtained by cyclic voltammetry, chronopotentiometry, polarography and spin-lattice relaxation of quadruple nuclei of ions, using solubility and extraction data. As can be seen from Table 1, the standard free energy of ion transfer from one solvent to another strongly depends on the nature of both ion and solvent.

The resolution (hydration) energy decreases significantly with increasing ion size and static and optical permittivities. The standard free energies of ion resolution when determined by different methods do not coincide exactly. The ion resolution energy can be calculated or measured by two methods. For example, the ion solvation energy can be determined in each of the two solvents, α or β , which then yield, by virtue of Eq. (3), the standard free energy of the transfer of ion i from solvent β to solvent α .

If two immiscible liquids α and β are mutually saturated, a certain amount of one solvent will be dissolved in the other solvent and *vice versa*. The corresponding energy of resolution between two mutually balanced solvents is called the Gibbs partition energy. For most ions and solvents the standard Gibbs energies of transfer and partition coincide within experimental error. However, for some solvents and ions these quantities may differ significantly.

When considering the standard Gibbs resolution energy attention should be paid to whether one deals with ion transfer between pure or mutually saturated solvents.

2.1. Electrostatic Contribution to the Solvation Energy

Two sets of models exist to calculate the electrostatic portion of the solvation energy [64–67]. In the first set the medium is considered as a structureless continuum, while in the second set it is represented by a set of individual particles having either realistic or simplified properties. In early works the solvent structure was taken into account by directly calculating the energies of particular configurations of solvent molecules in the vicinity of the ion. The configuration and the number of molecules in it were chosen with a certain degree of arbitrariness, proceeding from some physical considerations, which ensured an excellent fit between experimental and theoretical data. Such models completely ignored the statistical properties of the solution which are very important for obtaining a correct description of solvation. The modern

Table 1 The standard Gibbs free energies (kJ mol^{-1}) of ions transfer from water into selected nonaqueous solvents at 298 K

Ion	PC	FA	DMF	MeCN	PhNO ₂	IBMK	ACPH	DCIMe	1,1-DCIE	1,2-DCIE
H ⁺	50	-10	-18	44	33					56
Li ⁺	24	-10	-10	25	38	20				56
Na ⁺	15	-8	-10	15	36					52
K ⁺	5	-4	-10	8	24				30	46
Rb ⁺	-1	-5	-10	6	20				29	37
Cs ⁺	-7	-6	-11	6	16					24
Sr ²⁺					67					
Ag ⁺	19	-15	-21	-31	30					5
Tl ⁺	11	-1	-12	8	17					26
NH ₄ ⁺					27					
Me ₄ N ⁺	-11	3	-5	3	4	9		18		16
Et ₄ N ⁺	-13		-8	-7	-6			4	18	5
Pr ₄ N ⁺	-22	-10	-17	-13	-16			-9	11	-9
Bu ₄ N ⁺	-31		-29	-32	-25	-19	-15	-22	-2	-18
Ph ₄ As ⁺	-36	-24	-39	-33	-36		-16		-27	-33
Mg ²⁺					69				29	
Ca ²⁺					68					
Ba ²⁺	46		-21	57	62					
Cu ²⁺	73	-4	-18	68	115					
Zn ²⁺	81		-30	69	140					

(continued)

Table 1 (continued)

Ion	PC	FA	DMF	MeCN	PhNO ₂	IBMK	ACPH	DCIMe	1,1-DCIE	1,2-DCIE
Cd ²⁺	70	-28	-34	42	93					
Hg ²⁺	80		-44	28	44					
Pb ²⁺	47	-12	-34	64	71					
F ⁻	56	25	85	71	70					65
Cl ⁻	40	14	48	42	31	50		46	58	54
Br ⁻	30	11	36	31	29			39	43	38
I ⁻	14	7	20	17	19		12	26	31	25
CN ⁻	36	13	40	35	38					41
N ₃ ⁻	27	11	36	37						
SCN ⁻	7	7	18	14	16		11			26
NO ₃ ⁻				21	24		20			34
ClO ₄ ⁻	- 3	- 12	4	2	8		2	21	22	17
IO ₄ ⁻					7		2			15
BF ₄ ⁻					11					18
DCC ⁻					- 50					
2,4-DNP -					7					
Pi ⁻		- 7		- 3	- 5	12		- 7		- 3
BPh ₄ ⁻	- 36	- 24	- 39	- 33	- 36		- 16		- 27	- 33
SO ₄ ²⁻			78	88	141					

PhNO₂, nitrobenzene; DCIE, dichloroethane; PC, propylene carbonate; FA, formamide; DMF, *N,N*-dimethylformamide; MeCN, acetonitrile; ACPH, acetophenone; IBMK, isobutylmethylketone; DCIMe, dichloromethane; Pi, picrate; Ph, phenyl; DNP, dinitrophenol; DCC, 3,3'-bis(undecahydro-1,2-dicarbo-3-cobalta-closedodecador); Alk₄N⁺, tetraalkylammonium.

approach lies in developing a statistical theory of ion–dipole plasma which describes both the energy and the statistical aspects of the phenomenon [1, 64–67].

It is also necessary to take into account the differences between larger and smaller ions in the short range interaction of the ion with each solvent. With large ions, such a contribution is concerned primarily with the work spent on creating a cavity in the medium in which the ion will be placed. Entropy effects related to the disordering induced by the structure-breaking ion also fall in this category. The opposite effect may occur in the case of smaller ions, a process we will refer to as defect annihilation. For instance, an ion may be captured in a statistically probable micro-cavity in the local structure of solvent, thereby releasing the energy of this defect. Other examples are the energy release due to ion–solvent hydrogen bonding via individual protons, and the entropy effect of structure-making ions. Contributions of this kind are very sensitive to the nature of both the ion and the solvent.

There is also an intermediate approach, in which, while remaining within the framework of continuum theories, attempts are made to take account of the influence of the discrete nature of the solvent on the effective parameters of the model. For this purpose, account is taken of nonlinear dielectric effects, and the mutual correlation of the polarization vectors of the solvent molecules, situated at short distances from one another, is analyzed using the theory of nonlocal electrostatics. Each of these approaches, reflecting the role of different effects, has its own advantages.

In general, for small ions of low chemical activity, the electrostatic contribution dominates. With increasing an ionic radius, the electrostatic contribution decreases, becoming comparable to the rising solvophobic contribution. We can now discuss electrostatic considerations in more detail.

2.2. The Born Model

Electrostatic interactions play a central role in a variety of biophysical processes in plants. The electrostatic contribution to the Gibbs energy of ion resolution has often been estimated with the aid of Born's continuum model [51] in which the ion is described as a sphere of a radius a with charge q distributed uniformly over its surface, while the solvent is considered a structureless medium with a macroscopic dielectric constant ϵ . The Born model (Fig. 3) is assuming that it is only the charge on the ion that is responsible for ion–solvent interactions. The interactions between the solvent and the ion are considered to be electrostatic in origin. Born model considered ion as equivalent to a charged sphere and structured solvent as a structureless continuum with dielectric constant ϵ . In this model free energy of ion transfer between two phases is considered as a sum of work of discharging an equivalent sphere in one phase and work of charging an equivalent sphere in other solvent. The work of charging of an uncharged sphere of a radius a is

$$A = \int_0^q \varphi dq = \int_0^q \frac{q}{4\pi\epsilon_0\epsilon a} dq = \frac{q^2}{8\pi\epsilon_0\epsilon a} \quad (4)$$

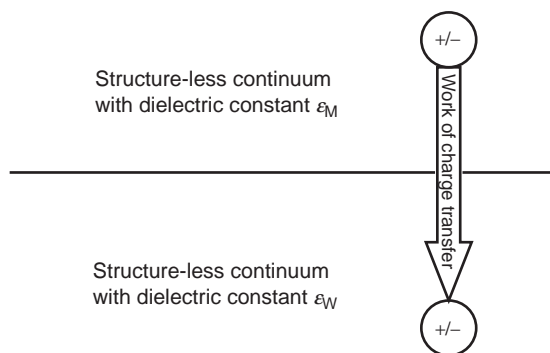


Figure 3 The Born model for electrostatic contribution to ion-solvent interactions considers ion as a charged sphere and the solvent as a structureless continuum.

and work of discharging can be written as

$$A = \int_q^0 \varphi dq = \int_q^0 \frac{q}{4\pi\epsilon_0\epsilon a} dq = \frac{q^2}{8\pi\epsilon_0\epsilon a} \quad (5)$$

The relationship between an ionic radius a and the electrostatic (Born) component of the Gibbs energy of ion transfer from medium w into the medium m is calculated from the expression

$$\Delta_m^w G(\text{Born}) = -\frac{q^2}{8\pi\epsilon_0 a} \left(\frac{1}{\epsilon_w} - \frac{1}{\epsilon_m} \right) \quad (6)$$

For hydrated ion transfer from medium w into the medium m (Fig. 2) Gibbs energy is equal to:

$$\begin{aligned} \Delta_m^w G(\text{Born}) &= -\frac{q^2}{8\pi\epsilon_0} \left[\left(1 - \frac{1}{\epsilon_s} \right) \left(\frac{1}{a} - \frac{1}{b} \right) + \left(1 - \frac{1}{\epsilon_m} \right) \frac{1}{b} \right. \\ &\quad \left. - \left(1 - \frac{1}{\epsilon_s} \right) \left(\frac{1}{a} - \frac{1}{b} \right) - \left(1 - \frac{1}{\epsilon_w} \right) \frac{1}{b} \right] \\ &= -\frac{q^2}{8\pi\epsilon_0 b} \left(\frac{1}{\epsilon_w} - \frac{1}{\epsilon_m} \right) \end{aligned} \quad (6a)$$

where ϵ_w , ϵ_m , and ϵ_s are dielectric permittivities of phases w , m and a hydrated shell; a is bare ion radius; b is hydrated ion radius. The dependence of Born component of free energy of ion transfer between two immiscible liquid phases such as water-hexadecane on ionic radius a is shown on Fig. 4, curve 1. From Eq. (6) it follows that Born component of free energy of ion transfer between two immiscible liquid phases strongly depends on dielectric permittivities of both phases (Fig. 5).

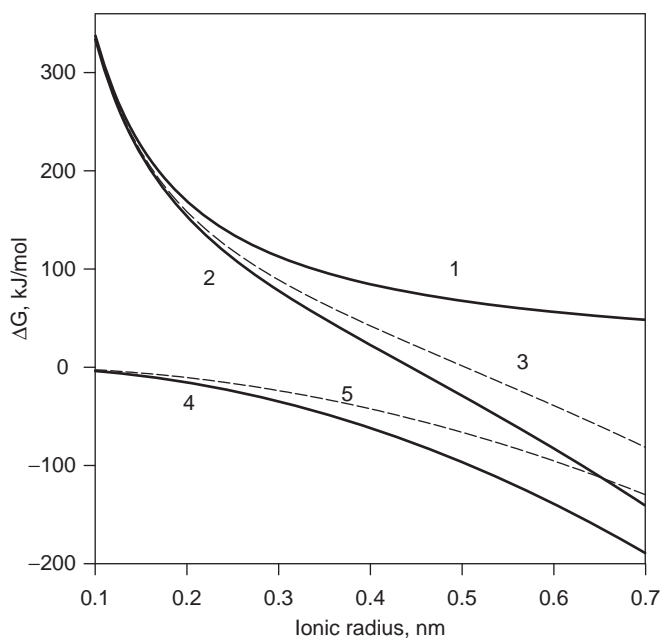


Figure 4 Gibbs energy of ion transfer from water to a liquid hydrocarbon calculated according to the Born Eq. (1), Born equation and solvophobic effect together (2, 3) and solvophobic effect according to the Eq. (3); $T = 25\text{ }^{\circ}\text{C}$, $\epsilon_w = 78.5$, $\epsilon_m = \epsilon_s = 2$, $\gamma_{wm} = 51\text{ mN m}^{-1}$ (2, 4), $\gamma_{wm} = 35\text{ mN m}^{-1}$ (3, 5).

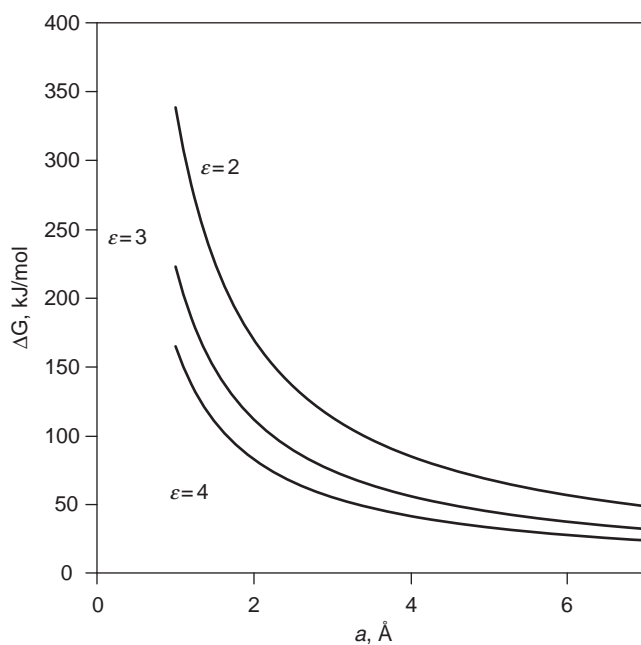


Figure 5 Electrostatic contribution to the Gibbs energy of ion transport from water to a low dielectric slab according to the Born equation.

An obvious inherent error of this estimate is that it neglects structural characteristics of the media being considered. The predictions of Eq. (6) are also in poor agreement with experimental results [23,24,27,64,66]. Specifically, according to Eqs. (6) and (6a) for $\epsilon_w > \epsilon_m$, the lowest energy state of the ion is in medium (w) regardless of its radius. This is inconsistent with experimental measurements of ion distribution between two immiscible electrolyte solutions, or in water/liquid membranes. The results indicate that small ions prefer the polar solvent, while large organic ions prefer the hydrophobic phase. Figure 6 shows that even for relatively straightforward estimates of the hydration energy of monovalent ions in water, Born theory predicts values approximately twice that of experimental results.

The main weakness of the Born continuum model is that all of the information about the dielectric properties of a pure solvent is contained in the dielectric constant ϵ , which treats the solvent as a structureless screening background. However, Born formulated his model in 1920 on the basis of Lorentz macroscopic electrostatics, assuming that they could be extrapolated to localized induction and electric field effects of the ion. In calculations of fields produced by microscopic sources such as ions, it is necessary to take into account the microscopic structure of the medium. One way to do this is to apply nonlocal electrostatics, which is now widely used both in solid-state theory and in the theory of liquid solution.

The solvation energies calculated by the Born formula differ noticeably from experimental values. Since, in most of the cases, the resolution energy is the difference between two comparatively large solvation energies, even a relatively small error in each energy may give rise to considerable error in the resolution energy, even an incorrect sign. For example, Eq. (6) implies that if $\epsilon_w > \epsilon_m$ there is a higher probability for the ion to reside in solvent w , irrespective of ion size.

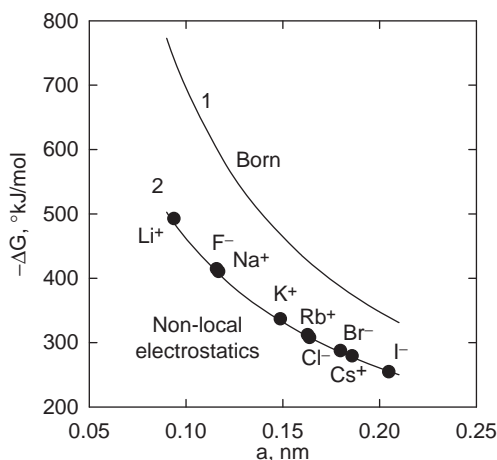


Figure 6 Gibbs energy of ionic hydration as a function of an ionic radius. Curve 1 was calculated from Born theory. Curve 2 was calculated from nonlocal electrostatic theory. The points are experimental data with hydrated ionic radii taken from Gourary and Adrian [68]; $\lambda = 0.1$ nm, $\Lambda = 0.7$ nm.

In practice this is not always the case. It is known that small ions of radius $a < 0.2$ nm reside mainly in a polar solvent of high permittivity, while large organic ions reside preferably in the hydrophobic phase. Data on the partition coefficients, extraction, solubility, and current–voltage characteristics show that the standard free energy of ion transfer from water into a less polar solvent is positive for small radius ions and negative for large radius ions, while Eq. (6) implies that the sign of this energy does not depend on the ion radius.

The Born relation overestimates the solvation energy and provides values which are too negative (Fig. 6). However, when particular energy values are compared with experimental data, a certain radius must be assigned to each ion. This procedure is arbitrary to a certain extent because an ion is not a hard sphere of a definite radius. The ion radius is solely an effective parameter which enables a convenient description of different properties of an ionic system [69,70]. It is frequently the case that different properties of a system are best described in terms of different ion radii. Although there are reasonable physical restrictions on the range within which an ion radius may change, it is meaningless to select one radius as better than another.

The difficulty encountered in selection of an ion radius is confirmed by the existence of at least 4 ion radius scales which have been calculated using different assumptions: namely the Pauling scale [71]; the Goldschmidt scale [72]; the Waddington scale [73]; the Gourary–Adrian scale [68]. There is minimal variation between the first three scales; however, the fourth scale is very different. Blandamer and Simons [69] have attempted to choose the most relevant scales of ion radii by comparing the Gibbs energy with the ion hydration entropy. They demonstrated that if any of these quantities is plotted as a function of $1/a$, all the points corresponding to alkali cations and anions of halide compounds fit the same smooth curve, provided the Gourary–Adrian scale is used. Other sets of ionic radii lead to two different curves: one for cations and the other for anions. It is difficult to say whether much attention should be paid to this fact since it does not have a theoretical explanation. For the Gourary–Adrian scale (Table 2) experimental data points ideally fit an ideal straight line, thereby confirming the conclusion of Blandamer and Simons [69]. We believe this fact undoubtedly deserves attention. For the other three scales, the fit is not very good, although deviation from a straight line is noticeable only for the smallest ions: Li^+ , Na^+ , K^+ but not for Cl^- , Br^- and I^- deviation is small [23,24].

The electrostatic part of the hydration energy, as calculated by the Born relation, is shown by curve 1 on Fig. 6. It can be seen that the calculated values are indeed lower (by approximately 50%) than experimental $\Delta_{\text{vac}}^{\text{w}} G^0$ values. Thus, the Born theory requires improvement. Eq. (6) includes only two experimental parameters: the ion radius and dielectric permittivity ϵ . By appropriately changing one of these parameters, one can, in principle, achieve satisfactory agreement with experimental results. However, this formal “fitting” of the ion radius leads to unreasonable values which fall onto none of the four acceptable scales. Therefore, although such a fitting provides an empirical relation which is in good agreement with experiment, it still cannot constitute a physical explanation of the solvation phenomenon.

Table 2 Bare and hydrated radii of ions

Ion	Bare ion radius (nm)	Hydrated radius (nm)
H ₃ O ⁺	0.115	0.28
H ₉ O ₄ ⁺	0.395	0.395
Li ⁺	0.094	0.382
Na ⁺	0.117	0.358
Ag ⁺	0.126	0.341
Tl ⁺	0.144	0.330
NH ₄ ⁺	0.148	0.331
K ⁺	0.149	0.331
Rb ⁺	0.163	0.329
Cs ⁺	0.186	0.329
Be ²⁺	0.031	0.459
Mg ²⁺	0.072	0.428
Zn ²⁺	0.074	0.430
Cd ²⁺	0.097	0.426
Ca ²⁺	0.100	0.412
Pb ²⁺	0.132	0.401
Al ³⁺	0.053	0.480
OH ⁻	0.133	0.300
F ⁻	0.116	0.352
Cl ⁻	0.164	0.332
Br ⁻	0.180	0.330
I ⁻	0.205	0.331
NO ₃ ⁻	0.179	0.340
Me ₄ N ⁺	0.285	0.347
Et ₄ N ⁺	0.348	0.400
Pr ₄ N ⁺	0.398	0.452
Bu ₄ N ⁺	0.437	0.494

2.3. The Nonlocal Electrostatics Method

Another rapidly developing semi-macroscopic approach is to calculate the electrostatic part of the solvation energy using the nonlocal electrostatics method [64–67]. Nonlocal electrostatics takes into account that fluctuations of solvent polarization are correlated in space, since liquid has a structure caused by quantum interaction between its molecules. This means that the average polarization at each point depends on the electric displacement at all other points of the space correlated with a given point [74]. Kornyshev and Volkov [66] used a generalization of the Born model to describe the electrostatic contribution to the free energy of resolvation. In this approach, nonlocal electrostatics were used to describe the dielectric response of a solvent in terms of the static dielectric function $\epsilon(\mathbf{k})$. This function contains information about special features of screening at short distances associated with liquid structure.

In nonlocal electrostatics the electric displacement D and electric field E are related by the tensor $\varepsilon_{mn}(\mathbf{r})$:

$$D^m(\mathbf{r}) = \sum_n \int d\mathbf{r}' \varepsilon_0 \varepsilon_{mn}(\mathbf{r} - \mathbf{r}') E^n(\mathbf{r}'), \quad (m, n = x, y, z) \quad (7)$$

It should be noted that although this relation is spatially complicated, it is linear. Further calculations are carried out in terms of the Fourier transform of the tensor $\varepsilon_{mn}(\mathbf{r})$ which is called the static dielectric function $\varepsilon(\mathbf{k})$:

$$\varepsilon(\mathbf{k}) = \sum_{m,n} \frac{k_m k_n}{k^2} \int d(\mathbf{r} - \mathbf{r}') e^{-ik(\mathbf{r}-\mathbf{r}')} \varepsilon_{mn}(\mathbf{r}-\mathbf{r}') \quad (8)$$

Approximations for $\varepsilon_{(\alpha)}(\mathbf{k})$ and $\varepsilon_{(\beta)}(\mathbf{k})$ must be used to obtain an analytical function for $\Delta_{\beta}^{\alpha} G(\text{el})$. To this end, we can apply the results of an analysis by Dogonadze and Kornyshev (1974) according to which the expression

$$\frac{1}{\varepsilon(k)} = \frac{1}{\varepsilon_{\text{opt}}} - \left(\frac{1}{\varepsilon_{\text{opt}}} - \frac{1}{\varepsilon_*} \right) \frac{1}{1 + k^2 \lambda^2} + \left(\frac{1}{\varepsilon_*} - \frac{1}{\varepsilon} \right) \frac{1}{1 + k^2 \Lambda^2} \quad (9)$$

can serve as a reasonable approximation for $\varepsilon(\mathbf{k})$ of polar liquids. It corresponds to provisional splitting of the medium polarization fluctuations $\vec{P}(\vec{r})$ into three modes $\vec{P} = \vec{P}_e + \vec{P}_i + \vec{P}_D$ associated with the excitation of electronic (e), vibrational (i), and orientational (Debye, D) degrees of freedom. Since these are markedly separated in frequency, we can write

$$\begin{aligned} \langle \vec{P}(r) \vec{P}(0) \rangle &\approx \langle \vec{P}_e(r) \vec{P}_e(0) \rangle + \langle \vec{P}_i(r) \vec{P}_i(0) \rangle + \\ &\langle \vec{P}_D(r) \vec{P}_D(0) \rangle. \end{aligned} \quad (10)$$

Equation (9) corresponds to an exponential attenuation of these correlations in space with correlation radii Λ and λ for the Debye and vibrational polarization, respectively, and with a negligibly small correlation radius for the electronic polarization. Quantities ε_{opt} and ε^* are the values of the liquid's dielectric permittivities at frequencies corresponding to the transparent bands separating the electronic and vibrational and orientational (ε^*) regions of the spectrum, respectively. Although the values of λ and Λ are rather uncertain, they cannot be regarded as purely adjustable parameters of the theory. By its physical meaning, λ is of the order of the radius of a water molecule. Λ is comparable with the characteristic length of the hydrogen bonding chain which, according to diffraction data [75], is of the order of 0.7 nm. The potential produced in a medium by a charged sphere of radius a at a distance r from its center is given by:

$$\varphi(\mathbf{r}) = \frac{ze_0}{2\pi^2 \varepsilon_0} \int_0^\infty \frac{dk}{\varepsilon(k)} \frac{\sin kr}{kr} \frac{\sin ka}{ka} \quad (11)$$

hence we can easily find the electrostatic contribution to the solvation energy:

$$\Delta_{\text{vac}}^{\alpha} G^0(\text{el}) = \frac{ze_0}{4\pi^2\epsilon_0} \int_0^{\infty} dk \frac{\sin ka}{k^2 a^2} \left[1 - \frac{1}{\epsilon(k)} \right] \quad (12)$$

Polarization of the medium can be divided into three main groups: optical, vibrational and orientational. To evaluate Eq. (12), one has to specify the function $\epsilon(\mathbf{k})$. This can be done, for example, by subdividing fluctuations of the medium polarization into three modes relating to different degrees of freedom: namely, electronic or optical (1); vibrational or infra-red (2); orientational or Debye (3). If the radius of the correlation of the i th mode of a fluctuation is λ_i , then

$$1 - \frac{1}{\epsilon(k)} = 1 - \frac{1}{\epsilon_{\text{opt}}} + \left(\frac{1}{\epsilon_{\text{opt}}} - \frac{1}{\epsilon_2} \right) \frac{1}{1 + k^2 \lambda_2^2} + \left(\frac{1}{\epsilon_2} - \frac{1}{\epsilon_3} \right) \frac{1}{1 + k^2 \lambda_3^2} \quad (13)$$

In this expression the correlation length of the electronic mode is set equal to zero. The exact values of the correlation lengths λ_2 and λ_3 cannot be determined *a priori* but they can be approximated from physical considerations. In the infra-red region, the length λ_3 depends on liquid type. In the case of nonassociated liquids the correlation length for orientational vibration is approximately equal to the intermolecular distance; while for associated liquids (water for example) λ_3 is equal to the characteristic length of the hydrogen bond chain, i.e. 0.5–0.7 nm [64,66].

Integration of Eq. (12) with $(1-1/\epsilon(k))$ expressed by Eq. (13) yields:

$$\Delta_{\text{water}}^{\text{vacuum}} G(\text{el}) = \frac{q^2}{8\pi\epsilon_0 a} \left\{ 1 - \frac{1}{\epsilon_{\text{opt}}} + \left(\frac{1}{\epsilon_{\text{opt}}} - \frac{1}{\epsilon_2} \right) \varphi\left(\frac{2a}{\lambda_2}\right) + \left(\frac{1}{\epsilon_2} - \frac{1}{\epsilon_3} \right) \varphi\left(\frac{2a}{\lambda_3}\right) \right\} \quad (14)$$

where:

$$\psi(x) = 1 - (1 - e^{-x}) \frac{1}{x} \quad (15)$$

The result obtained in calculations of the electrostatic component of the Gibbs energy of ion hydration with relation (9) are plotted in Fig. 6 together with data for the measured free energy of hydration of individual ions. The fit is remarkably good for both cations and anions. A minor deviation is seen for the very small Li^+ ion, which could be due to entropy effects in structure formation or to defect annihilation effects described earlier. That is, the ion could be trapped in a statistically probable microcavity in the water structure, and this would liberate the energy of the defect microcavity. The obvious differences between theory and experiment found in the case of large ions provide evidence for the importance of hydrophobic effects in creating a cavity in the medium able to accommodate the ion.

Figure 7 shows the dependence of the Gibbs energy of hydration for an ion with radius equal to 0.149 nm (for example, K^+) on correlation lengths λ and Λ . The largest value for the hydration energy is obtained in the Born limit $\lambda = 0$, that is, in a

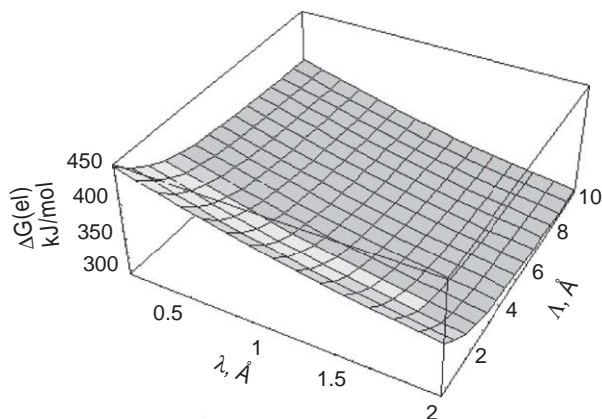


Figure 7 Electrostatic contribution to the Gibbs energy of K^+ hydration ($\Delta G(\text{el})$) as a function of correlation radii λ and Λ .

structureless solvent. The finiteness of λ and Λ reduces the contribution of any one of the three modes P_i , P_e or P_D . In Eq. (9), the correlation length of the electronic mode P_e is set equal to zero. The exact values of the correlation lengths λ and Λ cannot be determined *a priori*, but they can be estimated from infra-red spectral characteristics. In the infra-red region, the length Λ depends on the properties of the liquid. In the case of nonassociated liquids the correlation length for orientational vibration is approximately equal to the intermolecular distance, while for associated liquids Λ is equal within an order of magnitude to the characteristic length of the hydrogen bond chain.

The nonelectrostatic portion of the total Gibbs energy is usually assumed to arise from the energy of solvation of a hypothetical ion that lacks electrical charge, but with all other characteristics unchanged. This can be estimated by comparison with a proper neutral analogue, such as a noble gas, and it is assumed that for particles of the same shape and size the energies needed to form a cavity and modify the solvent structure are equal, irrespective of the particle charge. This approach has an important advantage. If the ion and analogue neutral particle are assumed to be in identical standard states in the gaseous phase and solution, then a comparison of the theoretical results with experimental data no longer requires a correction for the loss of translational entropy of ions in the solution.

The electrostatic contribution to the hydration energy calculated by these relations is shown in Fig. 6, together with experimental data for small monovalent ions. The permittivities used in those calculations were taken from Table 3. The correlation lengths were chosen to provide the best fit between theoretical and experimental data: $\lambda_2 = 0.1$ nm and $\lambda_3 = 0.7$ nm. As can be seen from Fig. 6, the agreement between theory and experiment obtained by Kornyshev and Volkov [64, 66] is more than satisfactory. The nonlocal electrostatics method refers to the continuum models, but the effective parameters needed for calculation are chosen by analyzing the solvent structure. This method gives rather accurate values for the

Table 3 Dielectric permittivities ϵ_i in the three mode polarization model ($T = 293$ K)

Solvent	ϵ_1	ϵ_2	ϵ_3
Water	1.8	4.9	78.8
Nitrobenzene	2.4	3.7	35.0
1,2-Dichloroethane	2.0		10.4
Acetophenone	2.45		17.4
Dichloromethane	2.04		9.1
Methylbutylketone	1.9		14.9

solvation energy for small ions and also permits calculation, by virtue of Eq. (14), of the resolution energy. For large ions there remains considerable discrepancy between theory and experiment, which makes it necessary to take into account other effects. In our case, these effects are the work done in the formation of a cavity in the solvent and the solvophobic effect. The largest value for the solvation energy is obtained in the Born limit $\lambda_2 = \lambda_3 = 0$, i.e. in a structureless solvent.

The major disadvantage of the continuum and semi-continuum approaches to the solvation problem lies in the solvent model itself. An allowance for dielectric saturation or dipole correlation is an attempt to partially describe the discrete properties of the solvent within the framework of the continuum model. Other analogous approaches attempt to take into account the unknown effect of the solvent molecular structure on the thermodynamic properties of a system. However, the problem can only be solved correctly using a statistical model of the solvent and taking into account its discrete structure.

2.4. Hydrophobic Effect

The calculation of the hydrophobic interaction is a focus of intense interest in the context of membrane biophysics [1, 64, 66, 76–78]. Contemporary approaches to such problems are based on phenomenological, semi-phenomenological and microscopic statistical-mechanics models. All of these use several poorly defined parameters to characterize solute interaction with the solvent. To avoid uncertainty, the hydrophobic contribution to the Gibbs energy of ion or dipole resolution can be calculated using the solvophobic equation [64, 66]. The surface energy, when expressed in terms of surface tension at the ion-solvent interface $\gamma_{o,m}$, is equal to $4\pi a^2 \gamma_{o,m}$, and the difference in the surface energies in the media w and m is $4\pi a^2(\gamma_{m,w} - \gamma_{m,m})$ [64, 66]. According to Antonov's rule [79],

$$\gamma_{o,w} - \gamma_{o,m} = \gamma_{w,m} \text{sign}(\gamma_w - \gamma_m) \quad (16)$$

where $\text{sign } \gamma = +1$ if $\gamma > 0$, and $\text{sign } \gamma = -1$ if $\gamma < 0$, and $\gamma_{w,m}$ is the interfacial tension at the planar boundary between the media w and m . The surface tensions at the boundaries between air and the solvents w and m respectively at the same

pressure and temperature are γ_w and γ_m . Here, the solvophobic equation for the solvophobic contribution to the energy of resolution has the form [64, 66]:

$$\Delta_{\beta}^{\alpha} G^0(\text{solv}) = -4\pi a^2 \gamma_{wm} \text{sgn}(\gamma_w - \gamma_m) \quad (17)$$

Relation (17) infers that the molecules of the two solvents w and m do not mix or react chemically with each other. The hydrophobic contribution to the Gibbs energy of ion or molecule (dipole, multipole) transfer from water to hydrocarbon is negative and the absolute value is obviously greater for particles with larger radii, a .

The effect of curvature on the surface tension at a molecularly sized sphere was calculated by Tolman [80]. The surface tension at radius a can be written as

$$\gamma_a = \gamma / (1 + \frac{2\delta}{a}) \quad (18)$$

where δ is a parameter, which according to Tolman [80] is the distance from the surface of tension to the dividing surface for which the surface excess of fluid vanishes. Parameter δ can vary between 0 and a few angstroms [80]. Dependence of the change in surface tension with radius is shown on Fig. 8.

From the theoretical point of view, the limits of applicability of the hydrophobic formula are not quite clear. Nonetheless, it works surprisingly well for calculation of the partition coefficients of a system of two immiscible liquids [1,23–27,64,66,81]. Some deviation from the solvophobic formula is observed if the interfacial tension of two pure immiscible solvents is less than 10 mN m^{-1} and if the size of the dissolved particle is less than 0.2 nm . An important advantage of the solvophobic formula is that it does not involve fitting parameters because $\gamma\alpha\beta$ is determined in experimentally.

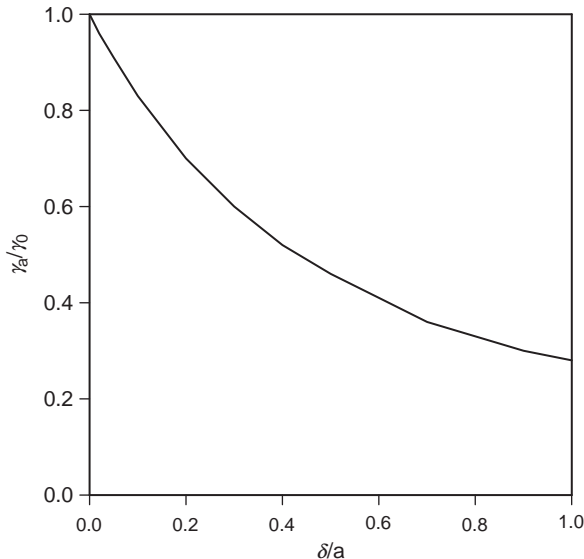


Figure 8 Dependence of surface tension on radius of curvature.

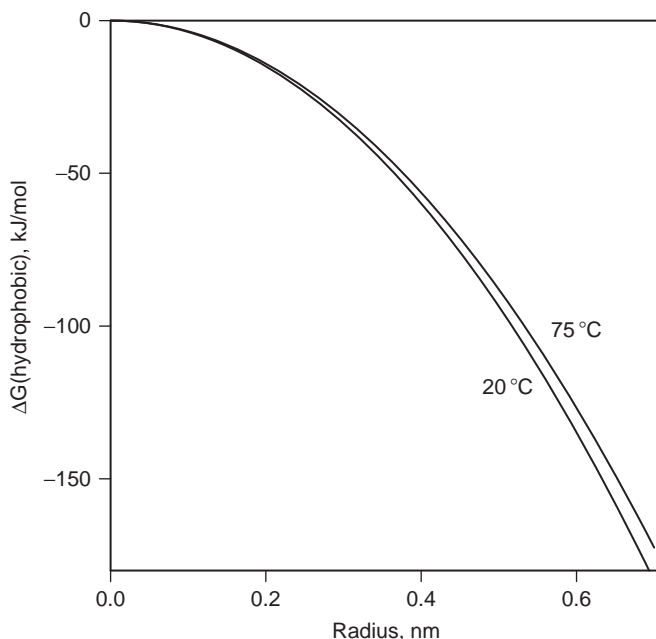


Figure 9 The hydrophobic contribution to the energy of resolution of particles of radius a from water into n -decane.

Using the solvophobic equation in the form of Eq. (17), we can calculate the hydrophobic (solvophobic, neutral) energy of ion or dipole transfer from water to a liquid hydrocarbon. The results are presented graphically in Fig. 9. The hydrophobic contribution to the Gibbs energy of ion or molecule (dipole, multipole) transfer from water to hydrocarbon is negative and the absolute value is obviously greater for particles with larger radii, a . An important advantage of the solvophobic equation is that it does not contain fitting parameters, since $\gamma\alpha\beta$ is measured experimentally. It has been surprisingly useful for calculations of partition coefficients in systems consisting of two immiscible liquids [81]. Figure 9 shows that hydrophobic effect slightly depends on temperature.

Hydrophobic effects are a function of the interfacial tension at the oil/water interface (Eq. (17) and Table 4). Although the interfacial tension at the liquid hydrocarbon/water interface is about 50–52 mN m⁻¹ for saturated alkanes (Table 4), it is much lower in unsaturated hydrocarbons, which in turn should be reflected in the related hydrophobic effect. It is clear that the presence of double bonds should decrease the hydrophobic effect. On the other hand, experimental measurements show that double bonds generally increase permeability of a bilayer to ions and polar molecules. This is presumably due to the fact that although alkanes have a dielectric moment equal to zero, the double bond in alkenes induces a dielectric moment of about half a Debye unit that can cause specific ion–dipole and dipole–dipole interactions among solvent molecules. This in turn produces a higher

Table 4 Interfacial $\gamma_{o/w}$ and surface γ tension for oil/water and liquid/air interfaces at 20 °C

Compound	Formula	$\gamma_{o/w}$, mN m ⁻¹	γ , mN m ⁻¹
Trimethylethylene	C ₅ H ₁₀	36.69	17.26
Isopentane	C ₅ H ₁₂	49.64	13.72
Benzene	C ₆ H ₆	35.00	28.86
<i>n</i> -Hexane	C ₆ H ₁₄	51.10	18.43
Toluene	C ₇ H ₈	36.1	
Styrene	C ₈ H ₈	35.48	32.14
<i>o</i> -Xylene	C ₈ H ₁₀	36.06	29.89
<i>p</i> -Xylene	C ₈ H ₁₀	37.77	28.33
<i>n</i> -Octane	C ₈ H ₁₈	50.81	21.77
<i>p</i> -Cymene	C ₁₀ H ₁₄	34.61	28.09
<i>n</i> -tetradecane	C ₁₄ H ₃₀	52	27
<i>n</i> -hexadecane	C ₁₆ H ₃₄	52	28
Octadecane	C ₁₈ H ₃₈	52	28
Octadecene	C ₁₈ H ₃₆	19	
Octadecadiene	C ₁₈ H ₃₄	15	
Water	H ₂ O		72.8

dielectric permittivity and increased partition coefficient, with the end result being that unsaturated lipid bilayers are more permeable than saturated lipid bilayers.

A significant point is that the free energy of the solvophobic effect is opposite in a sign to the electrostatic effect (Fig. 9). As a result, the sum of electrostatic and hydrophobic components of Gibbs energy decreases with ionic size, so that $\Delta G(\text{tr}) > 0$ only for small ions. For ions with radii larger than 0.45 nm, $\Delta G(\text{tr}) < 0$. This prediction is consistent with experimental data [23–27, 64, 66].

2.5. The Total Partition Energy

In the preceding sections we considered different effects which contribute to the energy of ion resolution. However, for most solvents which are of practical interest the greatest contribution is due to the electrostatic and solvophobic effects. Therefore, the resolution energy can be represented as a sum of all contributions:

$$\Delta G(\text{tr}) = \Delta G(\text{el}) + \Delta G(\text{solv}) + \Delta G(\text{si}) \quad (19)$$

where $\Delta G(\text{el})$ is electrostatic contribution, $\Delta G(\text{solv})$ is the hydrophobic effect and $\Delta G(\text{si})$ is caused by specific interactions of the transferred particle (ion, dipole) with solvent molecules, such as hydrogen bond formation, donor–acceptor and ion–dipole interactions.

Figure 10 shows that the solvophobic effect can make the resolution energy change sign as the ion radius varies. The calculation results are in excellent agreement with experimental data. The discrepancy observed for small radius anions may be attributed to the formation of hydrogen bonds between anion and solvent or to

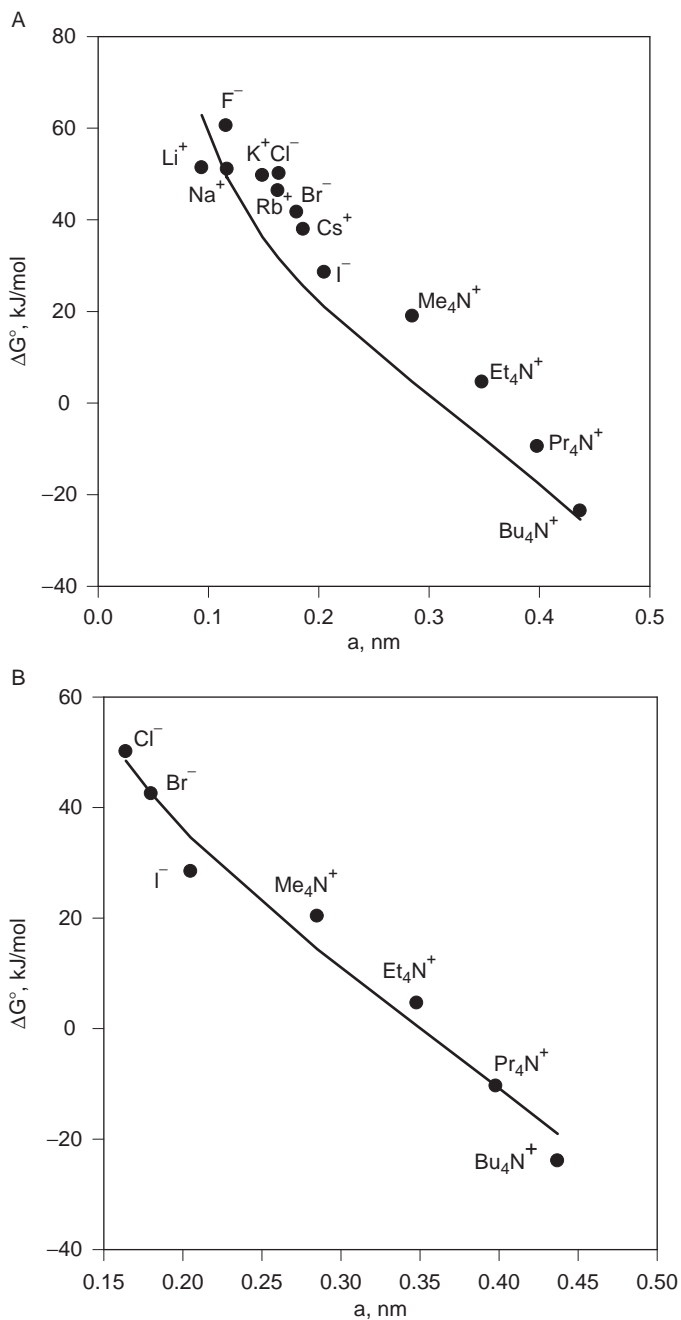


Figure 10 The resolution energy versus the ion radius in the water-1,2-dichloroethane (A) and water-dichloroethane systems. Solid line is calculated using Eqs. (1, 6, 17).

defect annihilation. The energy corresponding to this discrepancy is on the same order of magnitude as the energy gain obtained in the formation of a weak hydrogen bond between anion and solvent. It should, however, be noted that for small anions resolution energies reported by different authors differ considerably.

The transfer of small inorganic ions with radii less than 0.3 nm through the interface between two immiscible liquids is impeded, because it requires considerable energy for the resolution and penetration of small charged particles into nonpolar or low polar solvents. It is possible to facilitate the ion transfer from water to a nonpolar solvent using complexing agents or chelators, which have relatively large sizes and can screen the charge of ion. Chelators are well soluble in organic solvent due to a large hydrophobic effect and small electrostatic contribution and thereby facilitate the ion transfer between two contacting liquid phases.

2.6. Image Forces

The image forces acting on charged particles near interfaces are defined as the forces of interaction between these particles and the “image” of free and bound charges induced by them in the region next to the interface, minus the analogous quantity in one bulk phase. As a rule, positive or negative adsorption of ions arises at the oil/water interphase due to the effect of image forces. This effect is caused by different dielectric bulk properties of contact phases and by the inhomogeneous transition region where the ions and their solvation shells have a different size. As a result, different planes of closest approaches arise where ions and dipolar molecules can interact specifically with the interfacial region.

The electrostatic Gibbs energy for an ion in the vicinity of a boundary between two liquids with dielectric constants ϵ_1 and ϵ_2 (Fig. 2) is determined by the Born ion solvation energy and by the interaction with its image charge. In research dealing with the energy of image forces and with the interactions of charges at the oil/water interface, approximate models of the interface are often employed which are based on the traditional description of the interface between two local dielectrics.

In the water/hydrocarbon system the force of attraction (or repulsion) of charge in the oil phase with its image in the aqueous phase is given by

$$f(x) = -\frac{\epsilon_w - \epsilon_m}{\epsilon_w + \epsilon_m} \frac{q^2}{16\pi\epsilon_0\epsilon_m x^2} \quad (20)$$

where x is the distance from the interface [82]. If $\epsilon_w > \epsilon_m$, the charge in the nonpolar phase is attracted to its image, but if $\epsilon_w < \epsilon_m$, there is repulsion between the charge in a hydrocarbon phase and its image. From Eq. (20) it follows that charge in the hydrocarbon phase is attracted to the water/hydrocarbon interface. In the case of a thin membrane placed in a medium with high dielectric permittivity, the sum from an infinite number of images must be calculated. The combined Born and image energy of an ion in a thin membrane can be estimated [83] as follows:

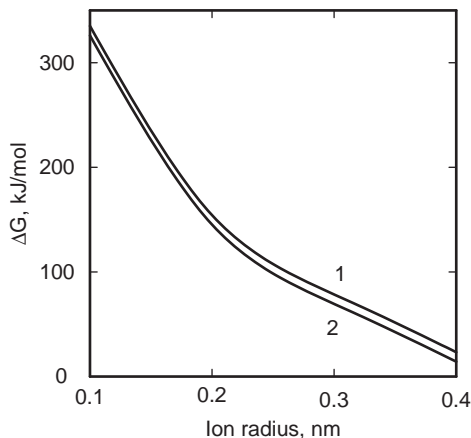


Figure 11 Dependencies of the Gibbs energy of ion transfer on ion size calculated according to the Born equation and solvophobic effect together (1). Curve (2) is the same as 1 but corrected for image forces ($d = 6$ nm, $T = 25^\circ\text{C}$).

$$\Delta G(\text{el}) = \Delta G(\text{Born})$$

$$- \frac{q^2}{16\pi\epsilon_0\epsilon_w} \left\{ \frac{1}{x} + \frac{1}{d} \sum_{n=1}^{\infty} \left[\frac{\theta^{2n}}{n + x/d} + \frac{\theta^{2n-2}}{n - x/d} - \frac{\theta^{2n}}{n + a/d} - \frac{\theta^{2n-2}}{n - a/d} \right] \right\} \quad (21)$$

where

$$\theta = - \frac{\epsilon_m - \epsilon_w}{\epsilon_m + \epsilon_w}. \quad (22)$$

The effect of image forces is small compared with Born electrostatic effects [10] and depends on the ion size (Fig. 11) and membrane thickness (Fig. 12).

We can calculate the Gibbs energy of ion or dipole transfer $\Delta G(\text{tr})$ from an aqueous phase to a hydrocarbon phase according to the equation (19).

For small ions, the electrostatic contribution is predominant in $\Delta G(\text{tr})$, so that the discrepancies of the solvophobic relation, which becomes evident with small ions, are negligible. At large ionic radii the solvophobic term predominates, so that calculations according to the solvophobic equations are consistent with experimental results [81].

2.7. Dipolar Potential

Bilayers differ from water/liquid hydrocarbon membranes by the presence of a two-dimensional layer of adsorbed water dipoles and lipid heads [24]. Even if lipids are neutral there is a positive dipolar potential within the membrane surface layer, which should be taken into account when describing specific interaction of ions with the

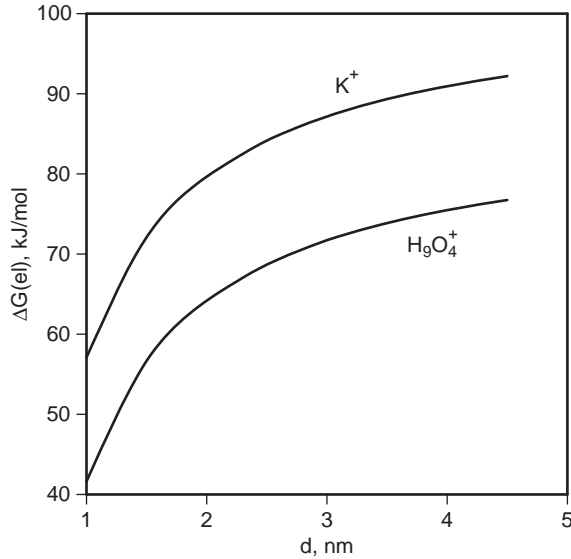


Figure 12 Dependencies of the electrostatic Gibbs energy of ion transfer on membrane thickness calculated according to the Born equation corrected for image forces ($T = 25^\circ\text{C}$).

membrane surface [1, 7, 18, 59, 84]. For instance, the dipole-dipole specific interactions create different concentrations of cations and anions at water/membrane interfaces. Rusanov *et al.* [85] and Rusanov and Kuni [86] calculated this energy as $4\pi q\Delta P_S$, where P_S is a characteristic of the surface excess polarization, which is defined as

$$P_S = \int_a^\infty [P - P(\infty)] dr \quad (23)$$

P is the local polarization vector, and the sign Δ denotes a change in the quantity upon the passage of the sphere from one medium to another.

We can estimate the specific energy of ion/dipolar layer interaction as a function of a dipole potential

$$\Delta G(\text{si}) = -zeF\phi_s \quad (24)$$

where ze is the charge of ions, F is the Faraday potential, and ϕ_s is dipolar membrane surface potential. Usually ϕ_s is estimated for bilayers to be between -100 and -200 mV [50, 84, 87]. At nitrobenzene/water and 1,2-dichloroethane/water interfaces dipolar potential, measured directly at the point of zero free charge, is about -20 to -50 mV [84] in the absence of phospholipids and -100 to -200 mV in the presence of phospholipid monolayer [88–91]. The direct method of dipolar potential determination at bilayers is to measure the dependence of membrane permeabilities of two opposite charged hydrophobic ions having the same ionic radius. Such ions can be, for example, tetraphenylphosphonium (TPhP⁺) and tetraphenylborate (TPhB⁻). They have the same electrostatic and hydrophobic effects, but opposite

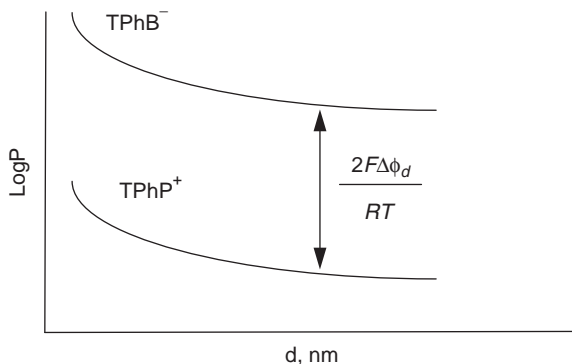


Figure 13 The method of a membrane dipolar potential determination from the measurement of the difference in membrane permeabilities of a hydrophobic cation tetraphenylphosphate (TPhP^+) and hydrophobic anion tetraphenylborate (TPhB^-) of the same radius.

effects as to a dipole potential sign. Figure 13 shows the dependence of membrane permeability coefficient of cations and anions on the membrane thickness.

It is possible to calculate the ion permeability of membranes for the partition model of ion transfer. The partition coefficient of an ion (K_i) is equal [24] to:

$$K_i = \exp(-\Delta G_i^0(\text{tr})/RT) \quad (25)$$

A permeability coefficient (P_i) is the number of ions or molecules of crossing in unit time a unit area of the membrane, when a unit concentration difference is applied across the membrane. The permeability coefficient is a directly measurable quantity and it is related to the partition coefficient by the expression

$$P_i = D_i K_i / d \quad (26)$$

where D_i is ion diffusion coefficient and d is the membrane thickness. Substituting K_i from Eq. (25) into Eq. (26) allows P_i to be calculated directly, and the results are plotted in Fig. 14. From this it is clear that the partition coefficient and calculated permeability coefficient have extreme parameter sensitivity with respect to an ionic radius, varying over 65 orders of magnitude as the radius increases from 0.1 to 0.5 nm. Substituting radii of bare (nonhydrated) ions (Table 2) such as sodium and potassium in this calculation gives values much too small for bilayer permeability when compared with experimental data, and the radius of a bare proton leads to absurd values. On the other hand, substituting hydrated radii taken from Table 2 gives permeability values surprisingly close to those measured experimentally.

The transport rate of ions across bilayer membranes can be calculated from the decay times of concentration gradients, or from conductance measurements. If the driving force is concentration gradient Δc , the permeability coefficient P can be calculated as

$$P = \frac{J}{\Delta c} \quad (27)$$

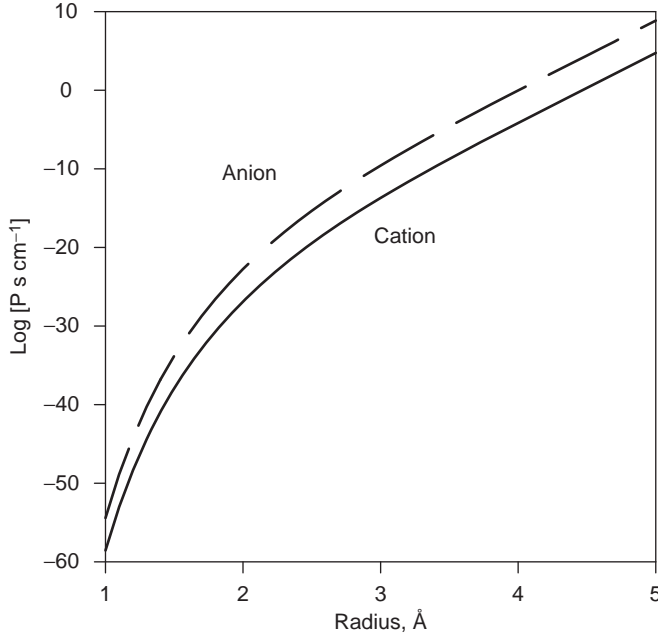


Figure 14 Dependence of the ionic permeability of the bilayer ($d = 3$ nm) on the radius of a permeating ion at 25 °C ($\epsilon_w = 78.5$, $\epsilon_m = \epsilon_s = 2$, $\gamma_{wm} = 51$ mN m⁻¹ (1, 2); $\gamma_{wm} = 35$ mN m⁻¹ (3, 4), $\Delta G(\text{si}) = 12z$ kJ mol⁻¹, $z = +1$ for cations and -1 for anions).

where J is the molar ion flux per unit of interfacial area. If the driving force is a transmembrane potential $\Delta\phi$, the conductance G can be calculated as

$$G = \frac{zFJ}{\Delta\phi} \quad \text{or} \quad G = \frac{cz^2F^2}{RT} P \quad (28)$$

2.8. Dipole Partition

It is important to analyze the energetic profile of dipole molecules at the interface between two immiscible liquids. Let us consider that molecule has dipolar moment μ_1 and it is located in the phase w with the dielectric permittivity ϵ_w . Its image μ_2 is located in the phase m with the dielectric permittivity ϵ_m . The dipole μ_1 has angle Θ with an axis x . The interface is located at $x = 0$. The force of an interaction of a dipole with its image [1] is:

$$f(x) = -\frac{3(\epsilon_w - \epsilon_m)\vec{\mu}_1^2}{4\pi\epsilon_0(\epsilon_w + \epsilon_m)\epsilon_m(2x)^4} (1 + \cos^2\Theta) \quad (29)$$

If $\epsilon_w < \epsilon_m$ the force $f(x)$ is negative and there an attraction of a dipole to the interface. $f(x)$ is positive if $\epsilon_w > \epsilon_m$ and there exists a repulsion of the dipole from the interface.

Energy of the dipole interaction with its image [92, 93] can be calculated as

$$E(x, \Theta) = \int_0^\infty f(x) dx \quad (30)$$

and substituting (29) in (30) gives the equation:

$$E(x, \Theta) = -\frac{(\varepsilon_w - \varepsilon_m)\mu_1^2}{8\pi\varepsilon_0(\varepsilon_w + \varepsilon_m)\varepsilon_m(2x)^3}(1 + \cos^2\Theta). \quad (31)$$

There are two equilibrium conditions $\Theta = 0$ and $\Theta = \pi/2$ and stable state will be when a dipole is perpendicular to the interface. It is possible to determine the thickness of a layer in which dipoles are oriented perpendicular to the interface supposing that $E(x, 0) - E(x, \pi/2)$ is equal to kT :

$$x \approx \sqrt[3]{\frac{(\varepsilon_w - \varepsilon_m)\mu_1^2}{64\pi\varepsilon_0(\varepsilon_w + \varepsilon_m)\varepsilon_mkT}} \quad (32)$$

For the water/octane interface, $x = 0.14$ nm and this result means that only one monolayer of water is oriented at the interface by image forces.

When a molecule with a permanent dipole moment μ is surrounded by other particles, the inhomogeneous field of the permanent dipole polarizes its environment. In the surrounding particles moments proportional to the polarizability are induced, and if these particles have a permanent dipole moment their orientation is influenced. An exact calculation of the consequences of these two effects may be made using nonlocal electrostatics.

Bell [45] considered an ideal dipole in the center of a spherical cavity and calculated the Gibbs energy of a dipole molecule transferred from vacuum to a medium of dielectric constant ε :

$$\Delta_{\text{vac}}^i G = -\frac{\mu^2}{12\pi\varepsilon_0 a^3} \left(\frac{\varepsilon - 1}{2\varepsilon + 1} \right). \quad (33)$$

Bell's model consists of a spherical cavity with radius a in a continuous dielectric of dielectric constant ε . Situated in the centre of the cavity is a nonpolarizable point dipole with moment μ . In this simplified picture of the interaction between a permanent dipole and its surroundings, the value has chosen for a influences the result. Bell took a about equal to the radius of the molecule.

The electrostatic ("Born") Gibbs energy of an ideal dipole transfer from the phase w to the solvent m can be calculated using the thermodynamic cycle:

$$\Delta G_{\text{dip}} = -\frac{v_1^2}{12\pi\varepsilon_0 a^3} \left(\frac{\varepsilon_m - 1}{2\varepsilon_m + 1} - \frac{\varepsilon_w - 1}{2\varepsilon_w + 1} \right) = \frac{\mu_1^2}{4\pi\varepsilon_0 a^3} \left(\frac{\varepsilon_w - \varepsilon_m}{(2\varepsilon_w + 1)(2\varepsilon_m + 1)} \right) \quad (34)$$

where μ_1 is the dipole moment and a is the effective dipole size. Generally speaking, the dipole moment μ_1 can vary from solvent to solvent. For simplicity, we will discuss the case when the dipolar moment of a solute is the same in phases w and m .

The Gibbs energy of image forces for dipole in membrane [92, 93] is

$$\Delta G_{I(\text{dip})} = -\frac{\mu_1^2}{6\pi\epsilon_0\epsilon_m d^3} \sum_{i=1}^{\infty} \left(\frac{\Theta^{2i-1}}{(2i-1-\alpha)^3} + \frac{\Theta^{2i-1}}{(2i-1+\alpha)^3} \right) \quad (35)$$

where

$$\Theta = (\epsilon_w - \epsilon_m)/(\epsilon_w + \epsilon_m) \text{ and } a = 2x/d \quad (36)$$

In Eq. (36), x is the distance between dipole and the middle of a membrane.

The total electrostatic Gibbs energy of the dipole profile can be evaluated from Eqs. (5.34) and (5.35):

$$\begin{aligned} \Delta G_{\text{dip}} &= \frac{\mu_1^2}{4\pi\epsilon_0 d^3} \left(\frac{\epsilon_w - \epsilon_m}{(2\epsilon_w + 1)(2\epsilon_m + 1)} \right) \\ &- \frac{\mu_1^2}{6\pi\epsilon_0\epsilon_m d^3} \sum_{i=1}^{\infty} \left(\frac{\Theta^{2i-1}}{(2i-1-\alpha)^3} + \frac{\Theta^{2i-1}}{(2i-1+\alpha)^3} \right) \end{aligned} \quad (37)$$

Figure 15 shows the dependence of the electrostatic image energy of the water dipole on the thickness of a liquid membrane. The image energy strongly depends on the membrane thickness and decreases with increasing thickness.

The water concentration in a hydrophobic region of a membrane can be calculated from the estimated Gibbs energy of water molecule transfer from water to the liquid hydrocarbon as

$$c_m = c_w \exp(-\Delta G(\text{tr})/RT) \quad (38)$$

Figure 16 shows the dependence of water concentration on liquid membrane thickness.

Using Eqs. (17) and (37), it is possible to calculate the permeability of molecules across a membrane (Fig. 17). $\Delta G(\text{si})$ is approximated by 19 kJ mol⁻¹ for the breakage of a hydrogen bond between water molecules.

Figure 17 illustrates how the water permeability coefficient is affected by the thickness of the bilayer. Although permeability becomes noticeably smaller with increasing bilayer thickness, the magnitude of this decrease is much smaller than that observed for protons. The permeability coefficient for the longest lipid (2.4×10^{-2} cm/s) is only about five times lower than for the shortest (5.0×10^{-3} cm/s). Furthermore, the slope of the curve is roughly constant which is in sharp contrast to the biphasic behavior observed for potassium ions.

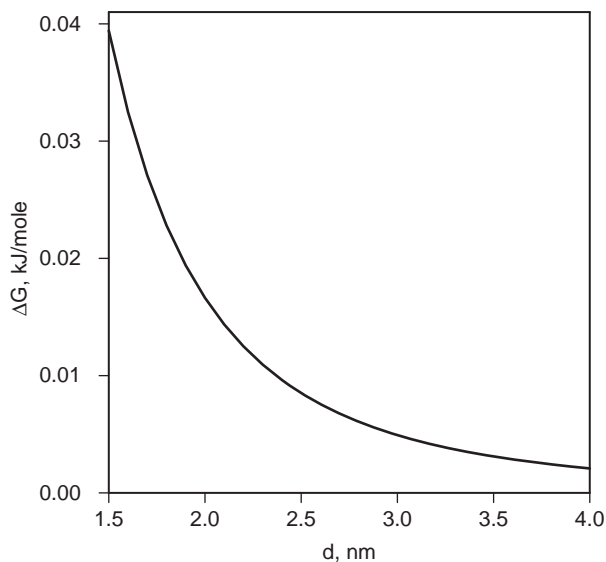


Figure 15 Dependence of the image energy for the water dipole on liquid membrane thickness. Parameters: $p = 1.85$ D, $l = 0.138$ nm, $\epsilon_w = 78$, $\epsilon_m = 2$.

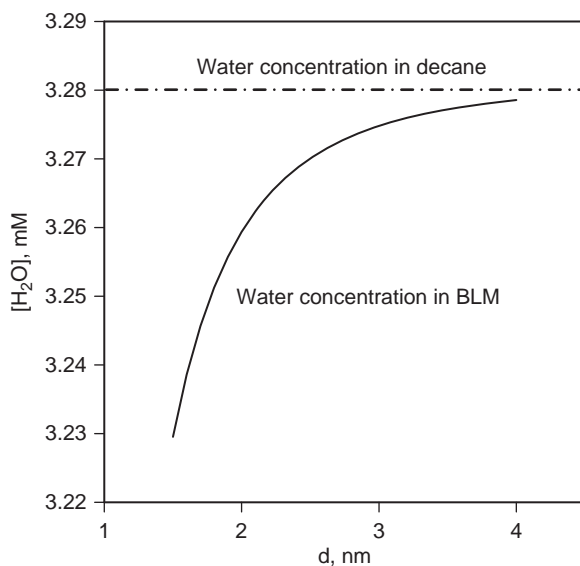


Figure 16 Dependence of the water concentration in a membrane on the thickness of membrane.

Glycerol and urea display quite similar permeabilities (see Fig. 17), with glycerol being slightly more permeable than urea. The values were in the range of 1.1×10^{-6} – 6.2×10^{-6} cm/s and 3.4×10^{-6} – 6.0×10^{-7} cm/s, for glycerol and urea,

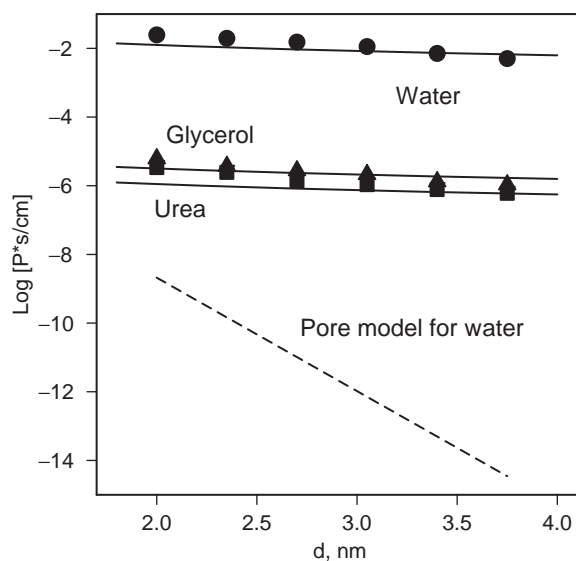


Figure 17 Dependence of water, urea, and glycerol permeability on membrane thickness d . Points are experimental data, solid lines are calculated according to the solubility–diffusion model. Parameters: $r_{\text{water}} = 0.12$ nm, $r_{\text{urea}} = 0.28$ nm, $r_{\text{glycerol}} = 0.29$ nm, $\gamma\alpha/\beta = 51$ mN m^{-1} , $p_{\text{water}} = 1.85$ D, $a_{\text{water}} = 1.38$ Å, $\Delta G(\text{si})(\text{water}) = 33$ kJ mol^{-1} , $\Delta G(\text{si})(\text{urea/glycerol}) = 3 \times 25$ kJ mol^{-1} , $D_{\text{water}} = 4.59 \times 10^{-5}$ $\text{cm}^2 \text{s}^{-1}$, $D_{\text{urea}} = 1.38 \times 10^{-5}$ $\text{cm}^2 \text{s}^{-1}$, $D_{\text{glycerol}} = 1.06 \times 10^{-5}$ $\text{cm}^2 \text{s}^{-1}$ (after Volkov *et al.* [7]).

respectively. This indicates that the membrane represents a significantly higher diffusion barrier to these molecules than to water or protons. The slope of permeability coefficient plotted against bilayer thickness resembles that of water (Fig. 17), with permeability values for the longest and shortest lipid differing by roughly fivefold.

Despite the interesting results arising from considerations of both electrostatic and solvophobic contributions to ionic permeation, we must be careful in applying them uncritically to ionic permeation events in bilayers. The main difficulty is that lipid bilayers are not ideal slabs of a hydrocarbon with uniform dielectric properties, but instead are highly dynamic, with considerable fluctuation around the means of thickness and intermolecular distance within the bilayer [19,94]. In the section to follow, we will examine an alternative mechanism for permeation of ions across lipid bilayers, and then compare experimental results with theoretical predictions from both models.

3. TRANSIENT PORE MECHANISMS OF PASSIVE TRANSPORT ACROSS BLM

Although the partition model can describe the barrier property of lipid bilayers under specified conditions, certain assumptions regarding the hydrated radius of the permeating species are required. We will now consider an alternative hypothesis, in

which fluctuations in bilayer structure produce rare transient defects that allow solutes to bypass the electrostatic and solvophobic energy barriers.

For the barrier function to operate, the lipid bilayer forming the basis of the membrane must be continuous and devoid of structural defects. If the bilayer is rearranged so that the defects of the through type appear, the membrane properties change. If pores that are small relative to the cell radius appear, an elevated background conductance of the membrane can arise for ions from both extra- and intracellular solutions. If the pore size is comparable with that of the intracellular protein molecules, cell lysis takes place, i.e., all the cell contents are released into the external medium.

Two types of pore structures in the lipid bilayer are possible. They can be roughly classified as hydrophobic and hydrophilic defects. During formation of a transient hydrophobic defect, lipid molecules are moved apart by thermal fluctuations so that the membrane hydrophobic core makes contact with and is penetrated by the aqueous bulk phase. Hydrophilic defects are formed if the lipid molecules are tilted into the transient defect so that it is lined with lipid polar head groups. In both the hydrophobic and hydrophilic defects pore formation results from dynamic properties of the lipid bilayers and the equilibrium pore distribution is relatively constant over time. However, formation of hydrophilic pores is more likely. Hydrophilic pores can arise due to bilayer thermal fluctuation or as a result of external stimuli, such as membrane extension by osmotic pressure, reactions with chemical compounds, and electrical field effects. Pore formation results in dynamic changes of the membrane properties, but thermal fluctuations in the bilayer lead to an equilibrium pore distribution in the membrane.

Markin and Kozlov [35] analyzed the distribution of hydrophilic pore radii in a membrane at thermodynamic equilibrium from the point of view of the elasticity or flexure of the lipid bilayer and its spontaneous curvature. The pore size distribution was calculated for three model membranes: uniform membranes with a constant spontaneous curvature, membranes with clusters of high spontaneous curvature, and membranes composed of two types of lipids, one with a high spontaneous curvature. Their calculations showed that the presence of asymmetric lipid molecules with positive spontaneous curvature should increase the number of pores in the membrane. The pore-related membrane permeability to uncharged molecules was estimated on the basis of this theory. The calculated values for water permeability were distinctly lower than the experimentally estimated values, suggesting that the mechanism of water transport across the membrane is mainly due to the direct passage of water molecules across the membrane hydrophobic layer.

Although small, neutral substances like water generally move across bilayers by diffusion of individual molecules, there is still the possibility that water is occasionally involved in the formation of transient hydrated defects. A pertinent model was recently presented by Benjamin [63] who used molecular dynamics and computer simulations to investigate the interface between water and a nonpolar phase. An intriguing property of the interface is that it is surprisingly rough, with “fingers” of several water molecules occasionally entering the nonpolar phase. Benjamin showed that ion permeation of the interface is linked to the presence of such water fingers. Wilson and Pohorille [20, 21] performed molecular dynamics simulations of the transport of Na^+ and Cl^- across a lipid bilayer located between two water lamellae.

The ion located in water has no influence on the structure of the membrane. Permeation of hydrated ions into membrane is accompanied by the formation of deep, asymmetric thinning defects in the bilayer. As the hydrated ion crosses the midplane of the membrane, the deformation switches sides. The initial defect slowly relaxes, and a defect forms in the outgoing side of the membrane [20, 21].

Thermal fluctuations in bilayers produce transient pores lined with lipid head groups [33, 34]. The formation of pores considerably lowers the free Gibbs energy barrier to transfer of the ions across the membrane and increases the permeabilities of bilayers to ions (Fig. 18). Ion flux was calculated from the collision frequency of the ions with the bilayer surface, and the total area of pores in the bilayer that are large and deep enough to allow an ion to cross the bilayer. The total number of pores, f_p can be expressed as the following integral:

$$f_p = \int_{s_1}^{\infty} sn(s)ds \quad (39)$$

where $n(s)ds$ is the number of pores per membrane area between pore area s and $s + ds$. The pore area distribution can be written as

$$n(s) = n_0 \exp(-k_1 s/RT) \exp(-k_2 d/RT) \quad (40)$$

where n_0 is the maximum number of discrete pores in the bilayer (taken to be half the number of lipid molecules in the bilayer), and the exponential terms are related to the probabilities of forming a pore of area s and depth d , respectively (Fig. 18). If an ion of a given radius can permeate the bilayer, s is taken to be the area of that ion, and d is the bilayer thickness. Given these assumptions the ionic permeability P_i [33, 34] is

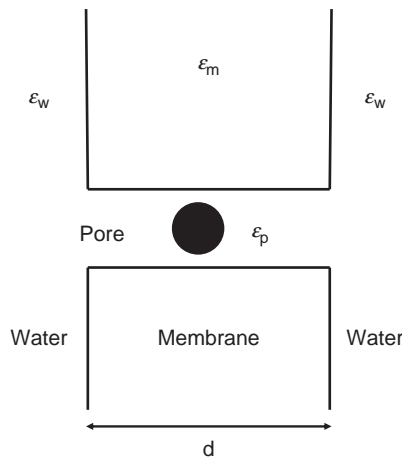


Figure 18 The pore model for ion permeation.

$$P_i = \frac{D_i \sigma n_0 RT}{R_{\text{avg}} A_{\text{mem}} k_1} \left[s_i + \frac{RT}{k_1} \right] \exp[-k_1 s_i / RT] \exp[-k_2 d / RT] \quad (41)$$

Here D_i is the ion diffusion coefficient, $\exp(-k_1 s / RT)$ is the probability of forming a pore of area s , $\exp(-k_2 d / RT)$ is the probability of forming a pore of depth d , σ is the concentration enhancement at the membrane surface due to the electrical double layer effects, R_{avg} is the vesicle radius, A_{mem} is the membrane area per mL of solution, R is the gas constant, and T the absolute temperature. Pores can be induced in membranes by applying mechanical stress or an electric field.

4. PARTITIONING OR TRANSIENT PORES: A CRITICAL TEST

The two models described earlier were tested [7–10,18]. An important variable under experimental control is bilayer thickness, which can be changed by choosing lipids with longer or shorter hydrocarbon chains. Proton and potassium fluxes across liposomes composed of phospholipids with fatty acid chain lengths varying from 14 to 24 carbons were measured [8]. Results expressed as proton and potassium permeability coefficients are shown in Fig. 19, and compared with the theoretical lines calculated from Eq. (40) (transient pore mechanism) and Eq. (23) (partitioning model). Permeability decreased logarithmically as bilayer thickness increased in the shorter chain lipids, following the slope of the line predicted by the transient pore mechanism. However, permeability tended to level off in the thicker bilayers (C_{16} and C_{18} lipids) approaching the lines predicted by the partitioning model [8]. The results suggest that the mechanism of ionic permeation may depend on bilayer thickness: thinner bilayers have many transient defects that allow rapid permeation of small ionic species, while in thicker bilayers defects become so rare that partitioning mechanisms dominate ionic flux [10,18].

Earlier work has shown that the permeability of lipid bilayers to protons is five to six orders of magnitude greater than to other monovalent cations [11,12,31,32]. This result is consistent with the partitioning model only if every proton carries at least four waters of hydration into the bilayer phase. The alternative proposed here is that transient hydrated defects occur in the bilayer. Figure 20 summarizes the Grotthuss mechanism [95]: an excess proton is incorporated at one end of a single file of water molecules, and a series of proton transfers takes place between adjacent water molecules until a proton is released at the other end. If water in the defects has significant hydrogen bonding, as it does in the bulk phase, hydrogen bond exchange could account for the vastly greater proton permeation rates without any assumptions regarding water of hydration. That is, protons could cross the membrane by “hopping” along hydrogen bonded chains of water in the defect (Figs. 20 and 21). This concept was proposed by Nagle and Morowitz [39, 40] who coined the term “proton wire” for hydrogen bonded networks of amino acid side chains. Nagle and Tristram-Nagle extended this concept to more general proton transport mechanisms, including water, and developed the concept of “transient hydrogen bonded

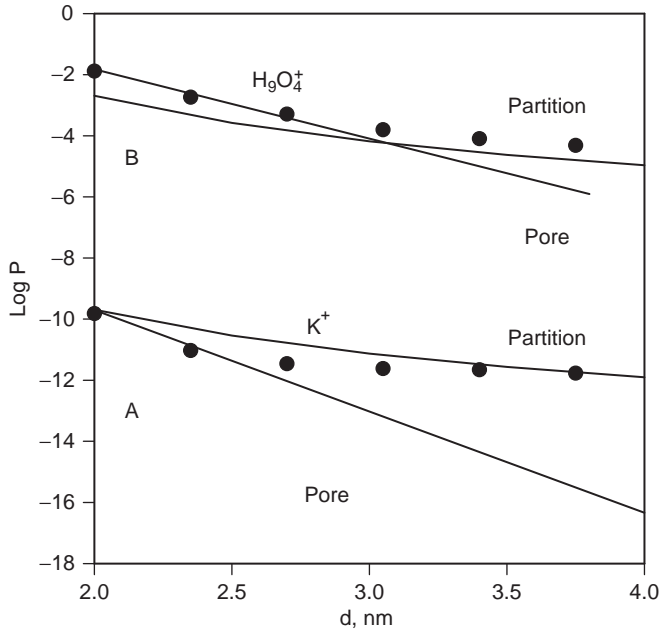


Figure 19 (A) Dependence of K^+ permeability on d calculated from Eqs. (26) and (41). Points (\bullet)—Experimental data. Parameters: $D_i = 2 \cdot 10^{-5} \text{ cm}^2 \text{ s}^{-1}$, $s = 10$, $R_{\text{avg}} = 1.05 \cdot 10^{-6} \text{ cm}$, $A_{\text{mem}} = 26,000 \text{ cm}^{-1}$, $T = 300 \text{ K}$, $a = 0.149 \text{ nm}$, $k_1 = 2.2 \cdot 10^{15} \text{ kJ}/(\text{mol}^{-1} \text{ cm}^{-2})$, $k_2 = 1.9 \cdot 10^8 \text{ kJ}/(\text{mol}^{-1} \text{ cm}^{-1})$, $n_0 = 1.04 \cdot 10^{33} \text{ cm}^5$, $\chi d = -130 \text{ mV}$. (B) Dependence of the H^+ permeability on d calculated from Eqs. (26) and (41). Points (\bullet)—Experimental data. Parameters: $D_i = 1.4 \cdot 10^{-4} \text{ cm}^2 \text{ s}^{-1}$, $s = 10$, $R_{\text{avg}} = 1.05 \cdot 10^{-6} \text{ cm}$, $A_{\text{mem}} = 26,000 \text{ cm}^{-1}$, $T = 300 \text{ K}$, $a = 0.13 \text{ nm}$, $k_1 = 2.2 \cdot 10^{15} \text{ kJ}/(\text{mol}^{-1} \text{ cm}^{-2})$, $k_2 = 1.2 \cdot 10^8 \text{ kJ}/(\text{mol}^{-1} \text{ cm}^{-1})$, $n_0 = 1.04 \cdot 10^{33} \text{ cm}^5$, $\phi d = -130 \text{ mV}$. Ionic radiuses are taken from the Table 2. (After Paula *et al.* [8]).

chains'' (tHBC) to describe proton transport in clusters of water molecules associated through hydrogen bonds [40].

Thermal fluctuations in shorter chain phospholipids produce large numbers of transient defects that cause such bilayers to be relatively permeable to ions, including protons. Because the slopes of the curves for proton and potassium fluxes are similar, with a reasonable fit to the theoretical expectation of the pore model, both protons and potassium ions presumably have access to the same transient defects. If protons are able to cross the bilayer by hydrogen-bond exchange along water chains in the transient defects, the relatively high permeability of protons can be understood. These results are consistent with the transient pore model described earlier.

As chain length increases, the transient fluctuations become rare and it becomes possible that partitioning is the dominant factor limiting permeation of ions such as potassium, and perhaps protons if they cross as $H_9O_4^+$. Both models, partition and transient aqueous pores, contribute to the membrane permeability. Zahn and Brickman [14] studied proton transport across BLM according to diffusive permeation and transport via aqueous pores using a mixed quantum-classical molecular dynamics simulation technique. Authors found that proton diffusion through BLM requires

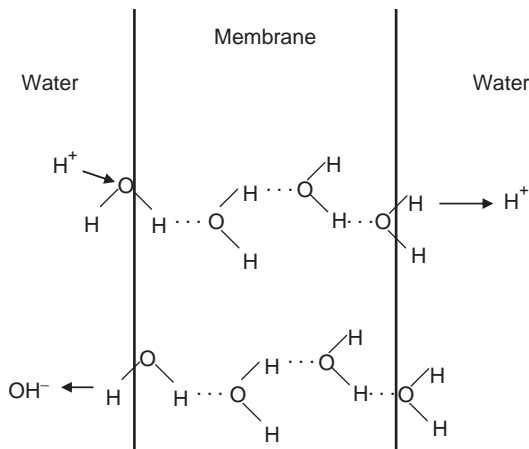
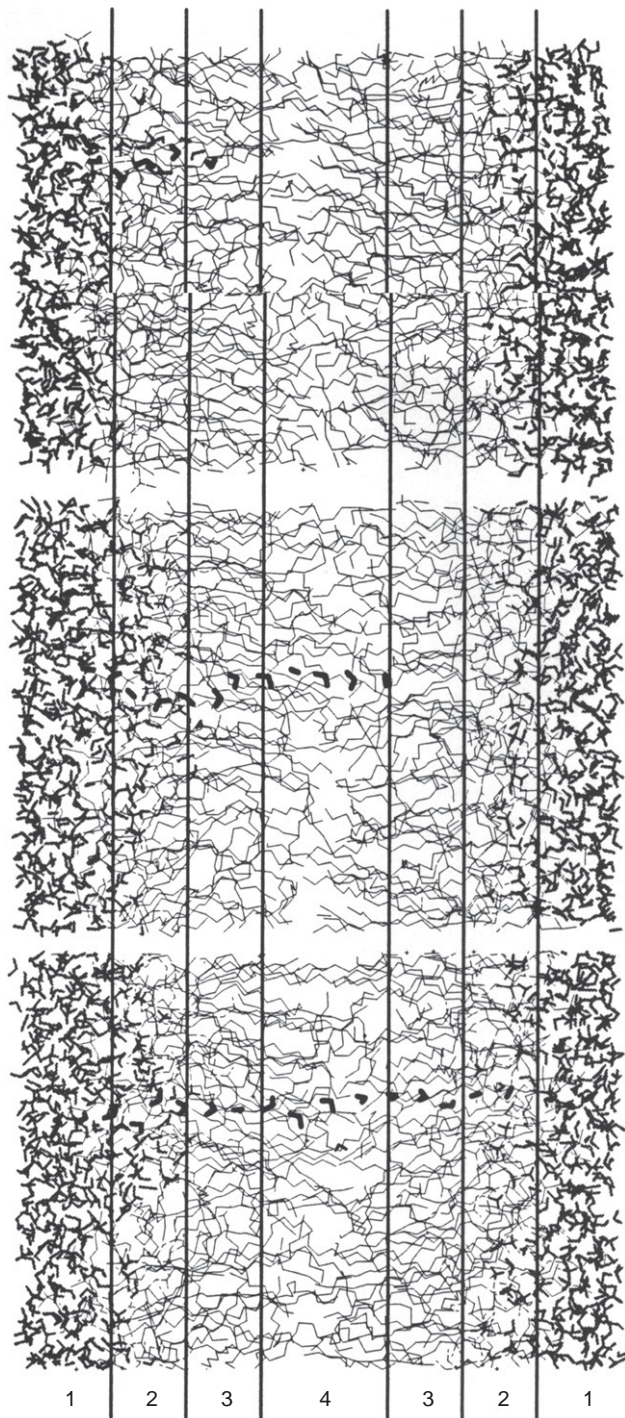


Figure 20 Grotthuss mechanism [95] of proton transfer through an aqueous chain.

the permeation of an H^+ (H_2O) $_n$ complex with $n \geq 4$. A similar observation was made for proton transport via an artificially formed water pore.

Marrink *et al.* [36–38] studied proton transport across transient single-file water pores in lipid membrane by molecular dynamics simulations and found that the nature of the pore is very transient, with a mean lifetime of a few picoseconds. Figure 21 shows the transient pore formation process. The total excess free energy for the full water pore is $108 \pm 10 \text{ kJ mol}^{-1}$ and this value indicates that such a complete water pore spanning the membrane is a rare phenomenon. Per pore molecule the average free energy is 6.4 kJ mol^{-1} [38]. The rapid translocation of protons along a chain of hydrogen-bonded water molecules, or proton wire, is thought to be an important mechanism for proton permeation through transmembrane channels or thin lipid membranes. Proton transfer in the wire is a semicollective process that results from the subtle interplay of rapid hydrogen-bond length fluctuations along the water chain.

Two mechanisms have been proposed to account for solute permeation of lipid bilayers. Partitioning into the hydrophobic phase of the bilayer, followed by diffusion is accepted by many for the permeation of water and other small neutral solutes, but transient pores have also been proposed to account for both water and ionic solute permeation. These two mechanisms make distinctively different predictions about the permeability coefficient as a function of bilayer thickness. Whereas the solubility–diffusion mechanism predicts only a modest variation related to bilayer thickness, the pore model predicts an exponential relationship. To test these models, Paula *et al.* [9] measured the permeability of phospholipid bilayers to water, urea, and glycerol. Bilayers were prepared as liposomes, and thickness was varied systematically by using unsaturated lipids with chain lengths ranging from 14 to 24 carbon atoms. The permeability coefficient of water and neutral polar solutes displayed a modest dependence on bilayer thickness, with an approximately linear fivefold decrease as the carbon number varied from 14 to 24 atoms. In contrast, the



permeability to protons and potassium ions decreased sharply by two orders of magnitude between 14 and 18 carbon atoms, and leveled off when the chain length was further extended up to 24 carbon atoms. The results for water and the neutral permeating solutes are best explained by the solubility–diffusion mechanism. The results for protons and potassium ions in shorter chain lipids are consistent with the transient pore model, but better fit the theoretical line predicted by the solubility–diffusion model at longer chain lengths.

5. CONCLUSIONS

Lipid bilayers have important structural and functional roles in the human physiology [96]. Ionic permeability is extremely sensitive to ionic radius. The Gibbs energy of partitioning has two primary contributing factors, which were described in terms of electrostatic and solvophobic effects. The electrostatic term dominates permeation of smaller ions, but the solvophobic effect becomes significant for larger ions to the extent that the Gibbs energy can be negative for ions larger than 0.45 nm diameter. A significant point is that the free energy of the solvophobic effect is opposite in sign to the electrostatic effect.

The effect of image forces is small compared with solvophobic and Born electrostatic effects. Additionally, they depend on the ion size and membrane thickness. Even if the lipids are neutral, there is a dipolar potential within the membrane surface layer, which should be taken into account when describing the specific interaction of ions with the membrane interface. For instance, the ion–dipole and dipole–dipole specific interactions create different concentrations of cations and anions at water/membrane interfaces.

Surface potentials represent a potential difference between the membrane interface and the bulk aqueous phase. These potentials are responsible for ion binding at the membrane/water interface and significant difference between cation and anion membrane permeabilities.

In order to partition into hydrophobic region of the bilayer, penetrating molecules must be hydrophobic enough to overcome the energy losses that occur in breaking the hydrogen bonds with water or the lipid head groups. This process has a considerable energy barrier for water and other molecules, which exhibit strong hydrogen bonding tendencies.

Partitioning models are consistent with some features of ionic permeation, particularly if solvophobic energy is taken into account. A partition model can account for the observation that proton permeability of bilayers to protons is 5–6

Figure 21 Snapshot of the water pore during the process of formation [38]. The pore molecules are drawn with bold black lines; the other water molecules, in lighter lines. The four different membrane regions (small headgroup density, large headgroup density, large tail density, and small tail density, shown in sections 1, 2, 3, and 4, respectively) are also indicated. Reproduced by permission of Biophysical Society.

orders of magnitude greater than to other monovalent cations, but only because of the extreme parameter sensitivity of the equations relating partitioning energy to permeability coefficients. An alternative hypothesis is that fluctuations in bilayer structure produce transient hydrated defects which permit ionic solutes to bypass the electrostatic energy barrier. In such defects, if water is hydrogen bonded, permeability to protons should be relatively high, since protons can move rapidly along water chains by hydrogen bond exchange mechanisms. This conductive mechanism is not available to other cations.

The two alternative hypotheses, partitioning versus transient pores, can be tested by measuring ionic permeation through bilayers of varying thickness (Table 5). If the partition model is correct, a substantial barrier to ionic flux should occur as soon as a stable bilayer is produced even with relatively short-chain lipids, and permeability will not vary significantly with bilayer thicknesses typical of biological lipids and the transient pore model predicts that ionic permeability will decrease as a logarithmic function of bilayer thickness. Experimental observations for both potassium and proton permeability are consistent with the transient pore mechanism for shorter chain lipids, but trend toward the theoretical line for partitioning models for longer chain lipids. Both mechanisms may play a role for typical hydrated monovalent ions, depending on lipid chain length.

Finally, the mechanism of water transport across membranes is mainly due to the direct passage of water molecules across the membrane hydrophobic layer by the solubility–diffusion mechanism.

Table 5 Comparison of the partition–diffusion and the pore mechanisms

Parameter	Partition–diffusion mechanism [1, 7–10, 18]	Pore mechanism [33, 34]
Temperature	Dependence P on $1/T$ gives value of the slope close to experimental data	Dependence P on $1/T$ gives too large value of the slope
Sign of ion charge for ions of the same size	$P_{\text{anion}} > P_{\text{cation}}$	$P_{\text{cation}} \geq P_{\text{anion}}$
Bilayer thickness	P varies moderately with the bilayer thickness	P varies strongly with the bilayer thickness
Ion radius	P increases with increasing hydrated ion radius	P decreases with increasing bare ion radius
Hydrogen bonding	P of water and molecules, which exhibit strong hydrogen bonding, decreases	Permeability of protons increases due to the Grotthuss or the protonhopping mechanism

REFERENCES

- [1] A.G. Volkov, D.W. Deamer, D.I. Tanelian, V.S. Markin, *Liquid Interfaces in Chemistry and Biology* Wiley, New York, 1997.
- [2] H. Ti Tien, *Bilayer Lipid Membranes (BLM) Theory and Practice*, Dekker, New York, 1974.
- [3] P. Mueller, D.O. Rudin, H. Ti Tien, W.C. Wescott, Reconstitution of cell membrane structure *in vitro* and its transformation into an excitable system, *Nature* 194 (1962) 979–980.
- [4] H. Ti Tien, *Membrane Biophysics as Viewed from Experimental Bilayer Lipid Membranes*, Elsevier, Amsterdam, 2000.
- [5] A. Ottova-Leitmannova, H. Ti Tien, Bilayer lipid membranes: An experimental system for biomolecular electronic devices development, *Prog. Surf. Sci.* 41 (1992) 337–445.
- [6] A.G. Volkov, B.T. Lozhkin, L.I. Boguslavsky, Proton and electron transfer across bilayer membranes and the decane/water interface in the presence of chlorophyll, *Dokl. Akad. Nauk SSSR* 220 (1975) 1207–1210.
- [7] A.G. Volkov, S. Paula, D.W. Deamer, Two mechanisms of permeation of small neutral molecules and hydrated ions across phospholipid bilayers, *Bioelectrochem. Bioenerg.* 42 (1997) 153–160.
- [8] S. Paula, A.G. Volkov, A.N. Van Hoek, T.H. Haines, D.W. Deamer, Permeation of protons, potassium ions, and small polar molecules through phospholipid bilayers as a function of membrane thickness, *Biophys. J.* 70 (1996) 339–348.
- [9] S. Paula, A.G. Volkov, D.W. Deamer, Permeation of halide anions through phospholipid bilayers occurs by the solubility–diffusion mechanism, *Biophys. J.* 74 (1998) 319–327.
- [10] D.W. Deamer, A.G. Volkov, Proton permeation of lipid bilayers, in: E.A. Disalvo and S.A. Simon, (Eds.), *Permeability and Stability of Lipid Bilayers*, CRC Press, Boca Raton, pp. 161–177.
- [11] D.W. Deamer, J.W. Nichols, Proton-hydroxide permeability of liposomes, *Proc. Natl. Acad. Sci. USA* 80 (1983) 165–168.
- [12] D.W. Deamer, J.W. Nichols, Proton flux mechanisms in model and biological membranes, *J. Membr. Biol.* 107 (1989) 91–103.
- [13] A. Finkelstein, *Water Movement through Lipid Bilayers, Pores, and Plasma Membranes: Theory and Reality*, Wiley Interscience, New York, 1987.
- [14] D. Zahn, J. Brickmann, Quantum-classical simulation of proton transport via a phospholipid bilayer, *Phys. Chem. Chem. Phys.* 3 (2001) 848–852.
- [15] O.S. Ksenzhek, A.G. Volkov, *Plant Energetics*, Academic Press, San Diego, 1998.
- [16] S.M. Saparov, Y.N. Antonenko, P. Pohl, A new model of weak acid permeation through membranes revisited: Does Overton still rule? *Biophys. J.* (2006) L86–L88.
- [17] A.V. Thomae, H. Wunderli-Allenspach, S.D. Kramer, Permeation of aromatic carboxylic acids across lipid bilayers: The pH-partition hypothesis revisited, *Biophys. J.* 89 (2005) 1802–1811.
- [18] A.G. Volkov, D.W. Deamer, Mechanisms of the passive ion permeation of lipid bilayers: Partition or transient aqueous pores, in: M.J. Allen, S.F. Cleary, and A.E. Sowers, (Eds.) *Charge and Field Effects in Biosystems-4*, World Scientific, Singapore, pp. 145–155.
- [19] M.C. Wiener, G.I. King, S. White, Structure of a fluid dioleoylphosphatidylcholine bilayer determined by joint refinement of X-ray neutron diffraction data. I. Scaling of neutron data and the distribution of double bonds and water, *Biophys. J.* 60 (1991) 568–576.
- [20] M.A. Wilson, A. Pohorille, Mechanism of unassisted ion transport across membrane bilayers, *J. Am. Chem. Soc.* 118 (1996) 6580–6587.
- [21] A. Pohorille, M.A. Wilson, Excess chemical potential of small solutes across water-membrane and water-hexane interfaces, *J. Chem. Phys.* 104 (1996) 3760–3773.
- [22] A. Parsegian, Energy of ion crossing a low dielectric membrane: Solutions to four relevant electrostatic problems, *Nature* 221 (1969) 844–846.
- [23] V.S. Markin, A.G. Volkov, The standard Gibbs energy of ion resolution and non-linear dielectric effects, *J. Electroanal. Chem.* 235 (1987) 23–40.
- [24] V.S. Markin, A.G. Volkov, The Gibbs energy of ion transfer between two immiscible liquids, *Electrochim. Acta.* 34 (1989) 93–107.

- [25] V.S. Markin, A.G. Volkov, Interfacial potentials at the interface between two immiscible electrolyte solutions—Some problems in definitions and interpretation, *J. Colloid Interface Sci.* 131 (1989) 382–392.
- [26] V.S. Markin, A.G. Volkov, Potentials at the interface between two immiscible electrolyte solution, *Adv. Colloid Interface Sci.* 31 (1990) 111–152.
- [27] V.S. Markin, A.G. Volkov, The standard Gibbs free energy of ion transfer, *Sov. Electrochemistry* 23 (1987) 1105–1112.
- [28] J.P. Dilger, S.G. McLaughlin, T.J. McIntosh, S.A. Simon, Dielectric constant of phospholipid-bilayers and the permeability of membranes to ions, *Science* 206 (1979) 1196–1198.
- [29] R.B. Gennis, *Biomembranes: Molecular Structure and Function*, Springer Verlag, New York, 1989, pp. 241–247.
- [30] H. Hauser, D. Oldani, M.C. Phillips, Mechanism of ion escape from phosphatidylcholine and phosphatidylserine single bilayer vesicles, *Biochemistry*, 12 (1973) 4507–4517.
- [31] J.W. Nichols, D.W. Deamer, Net proton-hydroxyl permeability of large unimolecular liposomes measured by an acid–base titration technique, *Proc. Natl. Acad. Sci. USA* 77 (1980) 2038–2042.
- [32] J.W. Nichols, D.W. Deamer, Proton and hydroxide permeability coefficient measured for unilamellar liposomes, in: P.L. Dutton, J.S. Leigh, A. Scarpa, (Eds.) *Frontiers of Biological Energetics*, Vol. 2, Academic Press, New York, 1978, pp. 1273–1283.
- [33] R.T. Hamilton, E.W. Kaler, Facilitated ion transport through thin bilayers, *J. Memb. Sci.* 54 (1990) 259–269.
- [34] R.T. Hamilton, E.W. Kaler, Alkali metal ion transport through thin bilayers, *J. Phys. Chem.* 94 (1990) 2560–2566.
- [35] V.S. Markin, M.M. Kozlov, Pores statistics in bilayer lipid membranes, *Biol. Membr.* 2 (1985) 205–223.
- [36] S.J. Marrink, H.J.C. Berendsen, Permeation process of small molecules across lipid membranes studied by molecular dynamics simulations, *J. Phys. Chem.* 100 (1996) 16729–16738.
- [37] S.J. Marrink, H.J.C. Berendsen, Simulation of water transport through a lipid membrane, *J. Phys. Chem.* 98 (1994) 4155–4168.
- [38] S.J. Marrink, F. Jahnig, H.J.C. Berendsen, Proton transport across transient single-file water pores in a lipid membrane studied by molecular dynamics simulations, *Biophys. J.* 71 (1996) 632–647.
- [39] J.F. Nagle, H.J. Morowitz, Molecular mechanisms for proton transport in membrane, *Proc. Natl. Acad. Sci. USA* 75 (1978) 298–302.
- [40] J.F. Nagle, S. Tristram-Nagle, Hydrogen bonded chain mechanisms for proton conduction and proton pumping, *J. Memb. Biol.* 74 (1983) 1–14.
- [41] J.F. Nagle, H.L. Scott, Lateral compressibility of lipid mono- and bilayers. Theory of membrane permeability, *Biochim. Biophys. Acta.* 513 (1978) 236–243.
- [42] D.P. Tieleman, H. Leontiadou, A.E. Mark, S.J. Marrink, Stimulation of pore formation in lipid bilayers by mechanical stress and electric fields, *J. Am. Chem. Soc.* 125 (2003) 6382–6383.
- [43] H. Leontiadou, A.E. Mark, S.J. Marrink, Molecular dynamics simulation of hydrophobic pores in lipid bilayers, *Biophys. J.* 86 (2004) 2156–2164.
- [44] D. Bemporad, C. Luttmann, J.W. Essex, Computer simulation of small molecule permeation across a lipid bilayer: Dependence on bilayer properties and solute volume, size, and cross-sectional area, *Biophys. J.* 87 (2004) 1–13.
- [45] R.P. Bell, The electrical energy of dipole molecules in solution and solubilities of ammonia, hydrogen chloride, and hydrogen sulfite in various solvents, *J. Chem. Soc.* 32 (1931) 1371–1382.
- [46] R.C. Macdonald, Energetics of permeation of thin lipid membranes by ions, *Biochim. Biophys. Acta.* 448 (1976) 193–198.
- [47] A.D. Bangham, M.M. Standish, J.C. Watkins, Diffusion of monovalent ions across the lamellas of swollen phospholipids, *J. Mol. Biol.* 13 (1965) 238–252.
- [48] A. Georgallas, J.D. MacArthur, X.P. Ma, C.V. Nguyen, G.R. Palmer, The diffusion of small ions through phospholipid bilayers, *J. Chem. Phys.* 86 (1987) 7218–7226.
- [49] R.F. Flewelling, W.L. Hubbell, Hydrophobic ion interactions with membranes: Thermodynamic analysis of tetraphenylphosphonium binding to vesicles, *Biophys. J.* 49 (1986) 531–540.
- [50] R.F. Flewelling, W.L. Hubbell, The membrane dipole potential in a total membrane potential model, *Biophys. J.* 49 (1986) 541–552.

- [51] M. Born, Volumen und Hydrationswärme der Ionen, *Z. Phys.* 1 (1920) 45–48.
- [52] J. Gutknecht, Proton/hydroxide conductance through lipid bilayer membranes, *J. Memb. Biol.* 82 (1984) 105–112.
- [53] J. Gutknecht, J.S. Graves, D.C. Tosteson, Electrically silent anion transport through lipid bilayer membranes containing a long-chain secondary amine, *J. Gen. Physiol.* 71 (1978) 269–284.
- [54] W.R. Perkins, D. Cafiso, An electrical and structural characterization of H^+/OH^- currents in phospholipid vesicles, *Biochemistry* 25 (1986) 2270–2276.
- [55] L.S. Yaguzhinsky, L.I. Boguslavsky, A.G. Volkov, A.B. Rakhmaninova, Synthesis of ATP coupled with action of membrane proton pumps at the octane–water interface, *Nature* 259 (1976) 494–496.
- [56] A.G. Volkov (Ed.) *Interfacial Catalysis*, Dekker, New York, 2003.
- [57] A.G. Volkov (Ed.) *Plant Electrophysiology*, Springer, New York, 2006.
- [58] A.G. Volkov (Ed.) *Liquid Interfaces in Chemical, Biological, and Pharmaceutical Applications*, Surfactant Science Series, Vol. 95, Dekker, New York, 2001.
- [59] A.G. Volkov, D.W. Deamer, *Liquid–Liquid Interfaces: Theory and Methods*, CRC Press, Boca Raton, 1996.
- [60] A.G. Volkov, D.W. Deamer, D.I. Tanelian, V.S. Markin, Electrical double layers at the oil/water interface, *Prog. Surf. Sci.* 53 (1996) 1–136.
- [61] A.G. Volkov, V.S. Markin, Electrochemical double layers: Liquid–liquid interfaces, in: A.J. Bard and M. Stratmann, (Eds.), *Encyclopedia of Electrochemistry*, Vol. 1: Thermodynamics of Electrified Interfaces, Wiley-VCH, Weinheim, 2002, Vol. 1.
- [62] A.G. Volkov, C.L. Brown, Nanodevices in nature, in: C.S.S.R. Kumar, (Ed.), *Nanodevices for Life Sciences*, Wiley-VCH, Weinheim, 2006, pp. 440–463.
- [63] I. Benjamin, Mechanism and dynamics of ion transfer across a liquid–liquid interface, *Science* 261 (1993) 1558–1560.
- [64] A.G. Volkov, A.A. Kornyshev, Dependence of the free Gibbs energy of resolution during ion transfer from one solvent to another on the ion size, *Sov. Electrochemistry* 21 (1985) 814–817.
- [65] A.A. Kornyshev, Nonlocal screening of ions in a structured polar liquid. New aspects of solvent description in electrolyte theory, *Electrochim. Acta.* 26 (1981) 1–20.
- [66] A.A. Kornyshev, A.G. Volkov, On the evaluation of standard Gibbs energies of ion transfer between two solvents, *J. Electroanal. Chem.* 180 (1984) 363–381.
- [67] R.R. Dogonadze, A.A. Kornyshev, Polar–solvent structure in theory of ion solvation, *J. Chem. Soc. Faraday Trans. 2*(70), (1974) 1121–1132.
- [68] B.S. Gourary, F.S. Adrian, Wave functions for electron-excess color centers in alkali halide crystals, *Solid State Phys.* 10 (1960) 127–247.
- [69] M.J. Blandamer, M.C.R. Symons, Significance of new values for ionic radii to solvation phenomena in aqueous solution, *J. Phys. Chem.* 67 (1963) 1304–1306.
- [70] W.L. Masterdon, D. Bolocofsky, T.P. Lee, Ionic radii from scaled particle theory of the salt effect, *J. Phys. Chem.* 75 (1971) 2809–2815.
- [71] L. Pauling, The sizes of ions and the structure of ionic crystals, *J. Am. Chem. Soc.* 49 (1927) 765–790.
- [72] V.M. Goldschmidt, *Geochem. Vert. Ges. der Elemente*, Oslo, 1926.
- [73] T.C. Waddington, Ionic radii and the method of the undetermined parameter, *Trans. Faraday Soc.* 62 (1966) 1482–1492.
- [74] M.A. Vorotyntsev, A.A. Kornyshev, *Electrostatics of a Medium with the Spatial Dispersion*, Nauka, Moscow, 1993.
- [75] G. Palinkas, E. Kalman, P. Kovacs, Liquid water. II. Experimental atom pair—correlation functions of liquid D_2O , *Mol. Phys.* 34 (1977) 525–537.
- [76] B. Siskind, J. Kasarnowsky, Studying of gases solubilities. II. The solubility of argon, *Zh. Fiz. Khim.* 4 (1933) 683–690.
- [77] C. Tanford, *The Hydrophobic Effect: Formation of Micelles and Biological Membranes*, Wiley, New York, 1980.
- [78] H.H. Uhlig, The solubilities of gases and surface tension, *J. Phys. Chem.* 41 (1937) 1215–1225.
- [79] G. Antonow, Sur la tension superficielle a la limite de deux couches, *J. Chim. Phys.* 5 (1907) 372–385.

- [80] R. Tolman, The effect of droplet size on surface tension, *J. Chem. Phys.* 17 (1949) 333–337.
- [81] A.A. Abramson, *Surface Active Compounds. Properties and Applications* Khimiya, Leningrad, 1981.
- [82] L.D. Landau, E.M. Lifshitz, *Electrodynamics of Continuous Media*, (2nd ed.), Pergamon, New York, 1984.
- [83] B. Neumke, P. Lauger, Nonlinear electrical effects in lipid bilayer membranes. II. Integration of the generalized Nernst–Planck equations, *Biophys. J.* 9 (1969) 1160–1170.
- [84] A.G. Volkov, Potentials of thermodynamic and free zero charge at the interface between two immiscible electrolytes, *Langmuir* 12 (1996) 3315–3319.
- [85] A.I. Rusanov, F.M. Kuni, Theory of nucleation on charged nuclei. 1. General thermodynamic relationships, *Kolloidnyi Zh.* 44 (1982) 934–941.
- [86] A.I. Rusanov, S.S. Dukhin, A.E. Yaroshchuk, Problem of the surface layer in liquid mixtures and the electric double layer, *Kolloidnyi Zh.* 46 (1984) 490–494.
- [87] K. Gawrish, D. Ruston, J. Zimmerberg, V.A. Parsegian, R.P. Rand, N. Fuller, Membrane dipole potentials, hydration forces, and the ordering of water at membrane surfaces, *Biophys. J.* 61 (1992) 1213–1223.
- [88] T. Kakiuchi, Phospholipid monolayers and phospholipases, in: A.G. Volkov and D.W. Deamer, (Eds.), *Liquid-Liquid Interfaces. Theory and Methods*, CRC-Press, Boca Raton, 1996, pp. 317–331.
- [89] A. Mälkiä, L. Murtomäki, A. Urtti, K. Kontturi, Drug permeation in biomembranes *in vitro* and *in silico* prediction and influence of physicochemical properties, *Eur. J. Pharm. Sci.* 23 (2004) 13–47.
- [90] M. Ikonen, L. Murtomaki, K. Kontturi, An electrochemical method for the determination of liposome–water partition coefficients of drugs, *J. Electroanal. Chem.* 602 (2007) 189–194.
- [91] L. Murtomaki, J.A. Manzanares, S. Mafe, K. Kontturi, Phospholipids at liquid-liquid interfaces and their effect on charge transfer, in: A.G. Volkov, (Ed.), *Liquid Interfaces in Chemical, Biological, and Pharmaceutical Applications*, Surfactant Science Series, Vol. 95, Dekker, New York, 2001, pp. 533–551.
- [92] V.B. Arakelyan, S.B. Arakelyan, Energetic profile of a dipole molecule in the thin membrane, *Biolog. Zh. Armenii* 36 (1983) 775–779.
- [93] V.B. Arakelyan, S.B. Arakelyan, T.s.M. Avakyan, V.M. Aslanyan, Electrostatic effects on transport of water across bilayer lipid membranes, *Biofizika* 30 (1985) 170–171.
- [94] E. Evans, Composite membranes and structured interfaces: From simple to complex design in biology, in: B.P. Gaber and K.R.K. Easwaran (Eds.), *Biomembrane Structure and Function: The State of the Art*, Adenine Press, New York, pp. 81–101.
- [95] C.J.T. de Grotthuss, Sur la décomposition de l'eau et des corps qu'elle tient en dissolution à l'aide de l'électricité galvanique, *Ann. Chim.* 58 (1806) 54–73.
- [96] T.M. Suhonen, P. Suhonen, A. Urtti, Lipid bilayers in cells: Implications in drug and gene delivery, in: A.G. Volkov, (Ed.), *Liquid Interfaces in Chemical, Biological, and Pharmaceutical Applications*, Surfactant Science Series, Vol. 95, Dekker, New York, 2001, pp. 807–838.

FUNCTIONALIZATION OF CARBON NANOTUBES AND NANOPARTICLES WITH LIPID

Jian-Shan Ye^{1,*} and Angela Leitmannova Liu^{2,3}

Contents

1. Introduction of Self-Assembled Lipid Membranes	202
2. Functionalization of Nanomaterials with Self-Assembled Lipid Membranes	203
3. Self-Assembly of Lipid Membranes at Carbon Nanotubes	203
3.1. Introduction of Carbon Nanotubes	203
3.2. Functionalization of Carbon Nanotubes	204
3.3. Supported Lipid Bilayer/Carbon Nanotube Hybrids	208
3.4. Application of Lipid–Carbon Nanotubes Nanomaterials	209
3.5. Conclusion and Perspectives	213
4. Self-Assembly of Lipid Membranes at Nanoparticles	213
4.1. Introduction of Nanoparticles	213
4.2. Lipid-Functionalized Nanoparticle Hybrids	213
4.3. Application of Lipid–Nanoparticle Hybrids	214
4.4. Conclusion and Perspectives	218
References	218

Abstract

Lipid researches ranging from biophysics, bioreactors, to medicine, have been a growing area. The liquid-crystalline phospholipid bilayer, which has similar dimension as nanomaterials, is the fundamental structural element of all cell membranes. The emergence of the novel nanomaterials is anticipated to lead to advancements in understanding biological processes at the molecular level in addition to progress in the development of innovative therapies, nanodevices, and nanosensors. This chapter focuses on the functionalization of nanomaterials, particularly carbon nanotubes (CNTs) and nanoparticles, with lipid in the past few years.

* Corresponding author: Tel: 86 20 8711 3241; Fax: 86 20 8711 2907;
E-mail address: jsye@scut.edu.cn.

¹ School of Chemistry and Chemical Engineering, South China University of Technology, Wushan, Guangzhou 510640, P. R. China

² Membrane Biophysics Laboratory, Department of Physiology, 2201 Biomedical and Physical Sciences Building, Michigan State University, East Lansing, MI 48824, USA

³ Center for Interface Sciences, Department of Microelectronics, Faculty of Electrical Engineering & Information Technology, Slovak University of Technology, Bratislava, Slovak Republic

CNTs possess high electrical conductivity, high chemical stability, and extremely high mechanical strength and modulus. Functionalization of CNTs is one of the most active fields in nanotube research, which provides an effective tool to broaden the application spectrum. The self-assembly of lipid molecules on CNTs to create stable and supramolecular assemblies pave the ways for the development of novel nonosensors/biosensors and nanodevices. The creation of hybrid nanomaterials that combine the novel properties of lipid with the unique electronic, optical and catalytic functions of nanoparticles has been achieved by the functionalization of nanoparticles with lipids. Substantial research efforts were recently directed to syntheses the lipid–nanoparticle hybrid systems. Furthermore, the lipid–nanoparticle nanomaterials, which have novel bioelectronic properties, have been applied in molecular recognition and controlled release for drug delivery as well as the design of sensors and biosensors. The functionalization of the nanotubes and nanoparticles with lipid generates a novel, interesting class of materials, which combines the properties of the nanomaterials and the lipid functional moiety, thus offering new opportunities in membrane biochemistry, biophysics, and cell biology as well as in biosensor design and molecular nanodevice development.

1. INTRODUCTION OF SELF-ASSEMBLED LIPID MEMBRANES

The liquid-crystalline phospholipid bilayer is the fundamental structural element of all cell membranes [1]. It not only provides a protective container for cells and subcellular compartments, but also hosts much of the machinery for cellular communication and transport across the cell membrane. With the development of bilayer lipid membranes (BLMs), it is possible to directly investigate electrical properties and transport phenomena across a 5 nm ultrathin lamina separating two phases by using the supported BLMs (s-BLMs) as a biological model [2,3].

Formation of BLMs is based on the self-assembly in nature and the self-assembly can be used as a strategy to create complex, functional structures. Several methods for forming BLMs and/or nanoliposomes have been discovered. For examples, s-BLMs, which possess the properties resembling those of biomembranes, can be formed on solids such as metallic wires [4–6], Pt electrode [7], and gel substrates [8] as well as on microchips [9]. These self-assembled s-BLMs have opened research opportunities for studying hitherto unapproachable phenomena at interfaces and bifaces. Some recent findings demonstrate potentials for investigating processes at solid–liquid interfaces. As a result of these studies, biomembranes have now been recognized as the basic structure of Nature’s sensors and molecular devices. For example, the plasma membrane of cells provides sites for a host of ligand–receptor contact interactions such as the antigen–antibody binding. To impart relevant functions in BLMs, a variety of compounds such as ionophores, enzymes, receptors, pigments, and so on have been embedded. Some of these incorporated compounds cause the BLMs to exhibit nonlinear phenomena and photoelectric effects. A modified or reconstituted BLM is viewed as a dynamic system that changes both in time and in response to environmental stimuli. The self-assembled lipid bilayer, the crucial component of most, if not

all biomembranes, is in a liquid crystalline and dynamic state. The self-assembly of lipid membranes at the interfaces may provide a simple yet useful method for the functionalization of nanomaterials. The planar BLM together with spherical lipid bilayers (liposomes), upon suitable modification, have been successfully used in the development of biosensors and transducers [10–14], biomolecular electronics, solar cells, and antioxidant carriers in foods [15].

2. FUNCTIONALIZATION OF NANOMATERIALS WITH SELF-ASSEMBLED LIPID MEMBRANES

Biomolecules such as enzymes, antibodies, or DNA have been successfully used to interact with nanomaterials for the synthesis of biomolecule–nanomaterials hybrid systems where the unique electronic, photonic, and catalytic properties of NPs are combined with the specific recognition and biocatalytic properties of biomolecules [16]. Lipids are special biomolecules with similar dimensions as CNTs or nanoparticles and suitable for the construction of lipid–nanomaterials hybrid system [17,18]. Recently, the functionalization of nonmaterial, particularly the CNTs or nanoparticles, with lipid membranes has attracted considerable interests owing to its wide potential applications in nanotechnology. The understanding of the formation of lipid-based nanocomposites and their electrical properties is the basis for the development of sensors and biosensors. Many factors, such as preparation, composition, and environmental conditions, can influence the properties of lipid-functionalized nanocomposites. The unique functions of lipid-functionalized nanohybrid systems were extensively used as electrochemical or optical labels in biorecognition processes for developing novel sensors and biosensors. For example, poly(lipid)-coated, highly luminescent silica nanoparticles can be used as fluorescent probes for labeling cultured cells [18]. The core of the probe is a sol-gel-derived silica nanoparticle (65–100 nm diameter) in which up to several thousand dye molecules are encapsulated. The poly(lipid) functionalized luminescent silica nanoparticles have special functions such as reduction of nonspecific interactions and creation of a probe that can be used to target both dissolved protein receptors as well as receptors on the membranes of cultured cells.

3. SELF-ASSEMBLY OF LIPID MEMBRANES AT CARBON NANOTUBES

3.1. Introduction of Carbon Nanotubes

The observation of fullerene-like carbon materials with high-resolution transmission electron microscopy (HRTEM) in 1991 by Iijima [19] marks the beginning of the CNT era. CNTs, consisting of only sp^2 hybridized carbon atoms, are cylindrical nanostructures with diameters ranging from one to several nanometers and a length

of tens of micrometers. They are made of graphene sheets wrapped into a hollow cylinder and capped by fullerene-like structures. There are two typical types of CNTs—singlewalled carbon nanotubes (SWCNTs) and multiwalled carbon nanotubes (MWCNTs). An ideal SWCNT can be viewed as an “extended” fullerene, and consists of a single-layer graphite wrapped into one seamless hollow cylinder. SWCNTs normally have a narrow diameter distribution (with diameter of the order of 1 nm) but tend to assemble in nanotube bundles during the growth process.

CNTs possess many special properties, such as open mesoporous structure, high electrical conductivity, and chemical stability as well as extremely high mechanical strength and modulus. These properties, which not only help in the transportation of ions but also facilitate the charging of the double layer, will exhibit advantageous attributes in the developments of molecular devices [20] and in the preparation of blue luminescent nanocrystals [21]. Both SWCNTs and MWCNTs have been recognized as a potential electrode material for electrochemical capacitors [11,22–26]. Furthermore, SWCNTs and MWCNTs have attracted much attention in electrocatalysis [27–33], chemical sensors/biosensors [11,17,21,29,34–48], and nanotoxicological studies [49].

3.2. Functionalization of Carbon Nanotubes

CNTs are insoluble in most common solvents, which limits their application. To solve this problem, considerable effort has been made by functionalization of CNTs, which might pave the way to many useful applications. For examples, several routes [50] have been introduced to improve the solubility of CNTs in water or in organic solvents by noncovalent interaction. A very general and versatile method for functionalizing different types of CNTs is described, using 1,3-dipolar cycloadditions [51] to yield remarkably soluble bundles of nanotubes. Furthermore, the covalent and noncovalent approaches have been examined to functionalize and solubilize nanotubes [52], with particular emphasis on the change of properties that accompany the chemical modification. The solubilization and functionalization of the nanotubes [50] generates a novel, interesting class of materials, which combines the properties of the nanotubes and the organic moiety, thus offering new opportunities in nanocomposites.

3.2.1. Oxidation and subsequent treatment

Gas-phase photo-oxidation can introduce oxygenated functional groups on the surfaces of CNTs without the generation of liquid waste. Krysak *et al.* [53] investigated downstream from an Ar microwave plasma vacuum UV photo-oxidation of MWCNT paper. X-ray Photoelectron Spectroscopy (XPS) was used to detect the carbon- and oxygen-containing functional groups in the top 2–5 nm of the sample's surface. In a similar approach, Parekh and coworkers [54] reported surface photo-oxidation of MWCNTs at room temperature with UV (253.7 and 184.9 nm) and vacuum UV (VUV) (106.7 and 104.8 nm) radiation. XPS showed rapid UV photo-oxidation during the first hour of treatment and then an increase directly proportional to the time of treatment up to 4 h. VUV photo-oxidation resulted in an oxygen concentration up to 9.5 at% with exposure time for the initial 2 h of treatment. Beyond 2 h, the oxygen concentration decreased with exposure to

VUV photo-oxidation. Curve fitting of the XPS C-1s spectra revealed mainly C—O—C, as ether or epoxy functional groups, with the presence of C=O, O—C=O and O=C—O—C=O or carbonate moieties. SEM micrographs showed no apparent effect on the structure or appearance of the MWCNTs as expected from surface modification. Gas-phase UV and VUV photo-oxidation effectively functionalize MWCNTs for potential adhesion improvement without resulting in liquid waste as from the traditional bulk processing method involving acidic oxidation.

For bulk processing of CNTs, liquid-phase functionalization through chemical oxidation with acids (e.g., nitric and sulfuric), peroxides and/or potassium permanganate has been achieved. Various oxidants, such as oxygen-containing acids, including HNO₃, H₂SO₄+HNO₃, HClO₄, H₂SO₄+KMnO₄ or other oxidants such as OsO₄ and H₂O₂, have been shown to react with CNTs. In addition to cleaning of raw nanotube material by removal of amorphous and graphitic carbon and opening of closed-ends of CNTs, the oxidation procedure often generate various functional groups, such as —COOH, —OH, —C=O at the opened ends. For comparison, Nagasawa and coworkers [55] used two common methods of oxidation—gas-phase oxidation by heat treatment in oxygen gas and liquid-phase oxidation using nitric acid—to treat SWCNT. The heat treatment in oxygen showed that thinner SWCNTs burn more quickly. The nitric acid treatment showed that SWCNTs are relatively inert to oxidation using acids. When the nitric acid treated samples were further oxidized by heat treatment in oxygen, selective oxidation of thinner SWCNTs occurred.

The oxidized CNTs can be further chemical decoration, such as reacting with molecular fluorine or rhodamine B [56]. However, the conventional liquid-phase oxidation of MWCNTs using concentrated acids generates contaminating debris that should be removed using aqueous base before further reaction [57]. Long alky chain or polymers can also be attached onto oxidized CNTs through an amidation reaction, or etherification reaction. In a amidation reaction, the carboxylic acid functionalized CNTs were firstly converted into alky chloride by treatment with SOCl₂; aryl amine then react with the alky chloride to form an amide group between the CNT and the aryl group. Using this approach, Narayanan and Jeykumari [58] reported the successful covalent-linked of the redox mediator toluidine blue (TB) to the carboxyl group of the MWCNTs by coupling reactions, in which *N*-hydroxysuccinimide was used to assist 1-ethyl-3-(3-dimethylaminopropyl) carbodiimide hydrochloride catalyzed amidation reaction. The results from cyclic voltammetry (CV) and amperometry suggested that the redox mediator is linked to the surface of the MWCNTs. Furthermore, the TB functionalized nanotubes showed an obvious promotion for the direct electron transfer between the redox mediator and the electrode. A couple of well-defined redox peak of TB was observed in a phosphate buffer solution (pH 7.0). The redox mediator immobilized to MWCNTs exhibits remarkable electrocatalytic activity for the reduction of H₂O₂.

3.2.2. Covalent functionalization of CNTs

Covalent functionalization is one of the most effective ways to improve their solubility and dispersion of CNTs. Currently, two kinds of reactions are often employed, including derivation of carboxy groups and direct addition. The

treatment of SWCNTs with dichlorocarbene, 1,1-dichlorocarbene, can attack C=C bonds connecting two adjacent six-member carbon rings to produce 1,1-dichlorocyclopropane. The transient species for this type of functionalization were generated by classical methods for carbene generation such as chloroform—sodium hydroxide interaction [59] or phenyl(bromodichloromethyl)mercury [60,61]. Later, Hirsch *et al.* reported functionalization of SWCNTs with the nucleophilic carbene, generated by deprotonation of the stable imidizolinium cation [51,62].

Proto *et al.* have developed a strategy for functionalizing CNTs utilizing the 1,3-dipolar addition [63]. The main advantage of this reaction is the easy attachment of pyrrolidine rings substituted by with chemical functions to the side walls of the CNT, which can lead to the construction of novel materials with diverse applications. The modified CNTs showed a high solubility in chloroform. Recently, Wei *et al.* [64] reported a method for covalent sidewall functionalization of SWCNTs via one-electron reduction of benzophenone by potassium. The reaction of a potassium atom with a benzophenone molecule results in transferring one electron from the potassium to the benzophenone, forming a radical anion, which adds readily to nanotubes. Raman and UV–vis spectroscopy confirm unambiguously that covalent functionalization has taken place. More recently, a rapid and controllable covalent functionalization of SWCNTs at room temperature was achieved by Simard's group [65]. The efficient procedure uses free radicals generated by a redox reaction between reduced SWCNT and diacyl peroxide derivatives to covalently attach to the SWCNT wall.

3.2.3. Non-covalent modification of CNTs

Noncovalent chemistry involves self-assembly of molecules or macromolecules to thermodynamically stable structures, which are hold together by weak, noncovalent interactions. Noncovalent interactions include hydrogen bond, electrostatic forces and van der Waal's forces. Noncovalent chemistry offers a great advantage in retaining sp^2 nanotube structured and hence not changing its properties. Dai *et al.* [25,66,67] reported the noncovalent functionalization of CNTs involving a bifunctional molecule, 1-pyrenebutanoic acid, succinimidyl ester irreversibly adsorbed onto the surfaces of SWCNTs in an organic solvent dimethylformamide or methanol by strong interaction between the highly aromatic pyrenyl group and the basal plane of graphite via π -stacking. The anchoring molecules are so stable in aqueous solution that they can be used to attach biomolecules or proteins onto the sidewall of SWCNTs because this approach leads to functionalization of SWCNTs with succinimidyl ester groups that are highly reactive to nucleophilic substitution by primary and secondary amines that exist in abundance on the surface of most proteins. In addition, SWCNTs are used as a platform for investigating surface-protein and protein-protein binding and developing highly specific electronic biomolecule detectors [66]. Nonspecific binding on nanotubes, a phenomenon found with a wide range of proteins, is overcome by immobilization of polyethylene oxide chains. The approach enables highly specific electronic sensors for detecting clinically important biomolecules such as antibodies associated with human autoimmune diseases. Davis and coworkers [68] demonstrated successful examples of

noncovalent immobilization of SWCNTs with biomolecules, such as cytochrome *c* molecules and ferritin.

In a different approach for the noncovalent functionalization of CNTs, bundles of SWCNTs helically wrapped with a conjugated polymer (such as poly-(*m*-phenylenevinylene)) by π - π stacking interactions were synthesized [69] by Star and coworkers. More recently, they [69] designed and synthesized a family of polymer to solubilize SWCNT bundles in organic solvents by wrapping themselves around the nanotube bundles. Wrapping of the functionalized polymers around SWCNTs results in the grafting of pseudorotaxanes along the walls of the nanotubes in a periodic fashion. The results hold out the prospect of being able to construct arrays of molecular switches and actuators.

3.2.4. Biological functionalization of CNTs

Biological functionalization of CNTs has come to be of significant interest in recent years due to the possibility of developing sensitive and ultra-fast detection systems in biomedical sciences and biotechnological application. Functionalization of CNT surfaces using proteins and antibodies could enable specific interactions and selective binding to target biomolecules with a very low sample size, often approaching single protein. For example, CNTs can be nondestructively oxidized along their sidewalls or ends and subsequently covalently functionalized with colloidal particles or polyamine dendrimers via carboxylate chemistry. Proteins adsorb individually, strongly and noncovalently along nanotube lengths. Several metalloproteins and enzymes have been bound on both the sidewalls and termini of SWCNTs. Importantly, in terms of possible device applications, protein attachment appears to occur with retention of native biological structure [70]. It was demonstrated functionalization of CNTs with proteins like streptavidin and biotin with the help of a polymer coating with poly-ethylene glycol (PEG), and covalent interactions with its amine-terminated variant [71]. Proteins are rich in structure and function which have specific and tailorable interactions with their environment. Furthermore, proteins present numerous reactive groups such as hydroxyls, amines, thiols, carboxylic acids, and others, which provide sites for further surface modification of the SWCNTs. Kane and coworkers [72] reported a simple and scalable method for solubilizing SWCNTs in water using commercially available proteins. A number of proteins differing in size and structure were used to solubilize purified SWCNTs to the individual level in water. It was found that various natural proteins are able to efficiently disperse SWCNTs in water not only extends the repertoire of biomolecules available for solubilizing SWCNTs, but also is an interesting example of the unique interactions that natural biomolecules have with nanomaterials. Biological functionalized CNTs can act as new kinds of materials for the delivery of drugs, DNA, protein, RNA, and other biological molecules. Immobilizing these biological molecules onto CNTs via stimuli-sensitive covalent bonds and employing controlled cleaving of these covalent bonds to release biological molecules from CNTs in the presence of stimuli have been recently explored [73]. CNTs with simple chemically decoration can easily conjugate with biological molecules such as protein. Furthermore, biological molecules functionalized at the surface of CNTs can be released in response to biological or chemical stimuli. On the basis of the results of

AFM and HRTEM, this is very important to realize the application of CNTs to nanomedicine, biotechnology, or drug delivery.

3.3. Supported Lipid Bilayer/Carbon Nanotube Hybrids

Surfactant adsorption at interfaces has been widely studied because of its importance in detergents, lubrication, and colloid stabilization. The solubility of CNTs can be greatly enhanced by mixing and shaking the surfactants with nanotubes to form stable suspensions [74]. For example, the sodium dodecyl sulfate (SDS) molecules can be oriented perpendicularly to the surface of the nanotube, forming a monolayer [75]. SDS as a useful dispersing agent for pristine and purified MWCNTs to prepare MWCNTs-modified electrodes is achieved. Voltammetric responses at MWCNTs-SDS modified glassy carbon electrodes towards detecting H_2O_2 are observed to compare the electrochemical action of MWCNTs in different circumstances. The best electrochemical action of pristine MWCNTs toward H_2O_2 is at about 0.4 wt% MWCNTs dispersed in 2 wt% SDS aqueous solution modified electrode. Furthermore, surface adsorption of an anionic surfactant, and activation by metal cations, were used to investigate their effects on the decoration of MWCNTs with ruthenium nanoparticles prepared by the reduction of ruthenium chloride in ethylene glycol [76]. Surface adsorption of SDS enabled the decoration of MWCNTs with a monolayer of uniform ruthenium nanoparticles on the surface. The superior amount of decoration is interpreted in terms of the bridging role of SDS surfactant in increasing the number of active sites for the adsorption and nucleation of ruthenium nanoparticles.

The self-assembly of lipid molecules on CNTs to create stable assemblies were achieved by Richard *et al.* [77]. TEM results indicated the formation of supramolecular assemblies of lipid molecules on the surface of the nanotubes. To explore the possibility of functionalizing the surface of CNTs in a noncovalent but permanent way with different reagents, the self-assembly of a series of molecules made of a double lipidic chain was further tested. In contrast to the single-chain lipids, no organization was detected by TEM when an aqueous solution (1 mg/ml) of the second series of molecules was directly sonicated with 1 mg of MWCNTs. This result indicates that the formation of micelles appears to be a key step for the formation of supramolecular assemblies on the CNT surface. This process constitutes a simple and versatile protocol for the noncovalent functionalization of nanotubes.

The interplay between nanocomposites and biomolecules forms an emerging research field of broad importance in biosensor development. The integration of 1D nanomaterials, such as nanowires, into electrical devices offers substantial advantages for the detection of biological species. Among these nanometer-scale materials, SWCNTs offer the advantages of possible biocompatibility, size compatibility, and sensitivity towards minute electrical perturbations, with unique opportunities for chemical and biological sensing [78].

BLMs on solid surface have opened broad possibilities for their application in novel biosensors. Several biosensing devices have been developed based on electrical elements (resistance, capacitance, diode) of electrical, electromechanical

(electrostriction) and electrochemical (redox reactions) properties of s-BLMs [9, 79]. Recently, Zhou *et al.* [21] reported the formation of supported lipid bilayers (SLBs) over SWCNT transistors to study the physical properties of the nanotube/supported lipid bilayer structure using fluorescence techniques. It was found that lipid molecules can diffuse freely across the SWCNT, a membrane-bound protein (tetanus toxin) sees the nanotube as a barrier. Moreover, the size of the barrier depends on the diameter of the nanotube with larger nanotube presenting bigger obstacles to diffusion. The detection of protein binding (streptavidin) to the supported lipid bilayer using the nanotube transistor as a charge sensor was demonstrated. This lipid-SWCNTs system can be used as a platform to examine the interactions of single molecules and has many potential applications for the study of molecular recognition and other biological processes occurring at cell membranes.

One major drawback associated with SWCNTs in the liquid phase is their hydrophobicity-induced aggregation, which prevents utilization of the unique physical and chemical properties of single SWCNTs. Recently it has been found that lysophospholipids [77], or single-tailed phospholipids [80], can readily form supramolecular complexes with SWCNTs and the resultant SWCNT solubility is superior to that provided by nucleic acids, proteins, and surfactants such as SDS. Using transmission electron microscopy (TEM), Qiao *et al.* [81] found that lysophospholipids can form striations on SWCNTs in a vacuum. The morphology of the striations seemingly favors the hemimicellar model. The binding of lipid amphiphiles to SWCNTs facilitates the bottom-up design of novel nanostructures for supramolecular chemistry and nanotechnology and fuels new field studies of nanotoxicity and nanomedicine.

3.4. Application of Lipid–Carbon Nanotubes Nanomaterials

3.4.1. Lipid–carbon nanotubes nanocomposites for the development of sensors and biomolecular electronics

BLMs are potentially useful for technological applications in the area of biosensors, enzyme electrodes, and molecular electronics as well as biochips. The biomimetic approach copying the supramolecular building principle of cell envelopes composed of a plasma membrane and a closely associated lattice has resulted in novel lipid nanocomposites. The developments in lipid-based functional nanocomposites will greatly aid in research areas of membrane biochemistry, biophysics and cell biology as well as in biosensor design and molecular device development.

SWCNTs, being hydrophobic by nature, aggregate in water to form large bundles, which limit their application. However, isolated SWCNTs possess unique physical and chemical properties that are desirable for sensing and biological applications. Recently, Wu and colleges [80] characterized the efficacies of solubilizing SWCNTs through various types of phospholipids and other amphiphilic surfactants. It was found that lysophospholipids, or single-chained phospholipids offer unprecedented solubility for SWCNTs, while double-chained phospholipids are ineffective in rendering SWCNTs soluble. Furthermore, the wrapping is only observed when SWCNTs are in the lipid phase and not the vacuum phase, suggesting that the environment has a pertinent role in the binding process.

CNT transistors combine molecular-scale dimensions with excellent electronic properties, offering unique opportunities for chemical and biological sensing. Recently, Zhou and his colleagues [21] reported the formation of SLBs over SWCNTs transistors. Fluorescence techniques were used to study the physical properties of the nanotube/supported lipid bilayer structure. It was found that lipid molecules can diffuse freely across the nanotube, where a membrane-bound protein (tetanus toxin) sees the nanotube as a barrier. Moreover, the size of the barrier depends on the diameter of the nanotube—with larger nanotubes presenting bigger obstacles to diffusion. The detection of protein binding (streptavidin) to the supported lipid bilayer using the nanotube transistor as a charge sensor was achieved. The lipid–CNTs system can be used as a platform to examine the interactions of single molecules with CNTs and has many potential applications for the study of molecular recognition and other biological processes occurring at cell membranes.

Lipid bilayers–functionalized MWCNTs has been successfully constructed [82] recently. Ye *et al.* [11] reported the self-assembly of BLM on a uniquely fabricated hydrophilic surface, containing N atoms from the carbon source of ethylene amine, of MWCNTs to form the BLM/MWCNTs nanocomposites. The thickness of the BLM, which was calculated from the electrochemical data obtained at BLM/MWCNTs electrode, turned out to be 4.38 nm, suggesting that the lipid self-assembled at the nanotubes surface was consistent with a bilayer structure. C_{60} -incorporated BLM could also be self-assembled at the nanotubes surface (C_{60} -BLM/MWCNTs). The result showed that the novel self-assembled BLM/MWCNTs nanocomposites provided a simple yet useful model to study the C_{60} -mediated photoelectric properties of the BLM/MWCNTs (Figure 1) which may be applicable to develop new biosensors and molecular devices. It is noted that various approaches to functionalize CNTs for the development of novel electrochemical sensors have been achieved [83]. The lipid-functionalized CNTs nanomaterial is promising for the development of sensors and biosensors and for the fabrication of photo switched–functional devices.

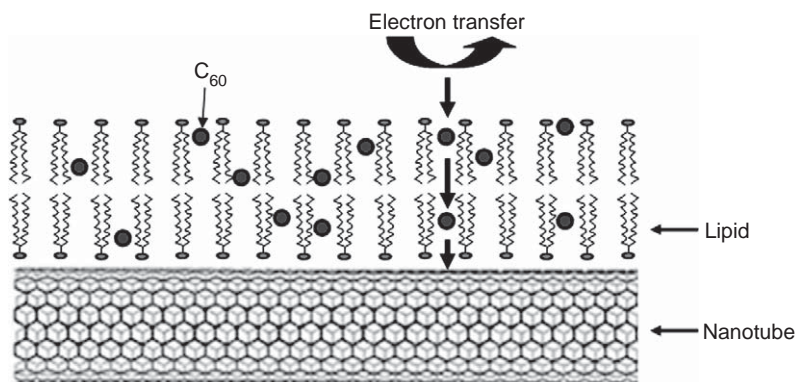


Figure 1 Insert C_{60} -BLMs and photo response of CNTs.

3.4.2. Photosensitive liposomes and lipid-based nanocomposite solar cell

Photo triggered release has been one of promising strategies to improve therapeutic index of drugs encapsulated within liposomes. Most of the photo triggered drug release from liposomes has been based on the photoinduced rearrangements of liposome bilayer, such as isomeration, fragmentation, or polymerization [84].

Supported BLMs with excellent stability, possessing the structural and dynamic properties of conventional planar lipid bilayers, are excellent models for investigating light-induced electron transfer across the lipid bilayer. For practical applications, the s-BLMs are ideal systems for incorporating a host of compounds, including fullerenes, semiconducting nanoparticles, receptor proteins and polymeric materials. In 1997, Tien *et al.* [5] reported the light-induced voltage and current generated by doping a self-assembled and s-BLM with buckminsterfullerene C_{60} . The C_{60} -containing s-BLM, considered basically as a “molecular device,” is a light-sensitive diode capable of photoinduced charge separation which undergoes redox reactions across the substrate-hydrophobic lipid bilayer-aqueous solution junctions. Using these s-BLMs, it is possible to investigate redox reactions and light-induced electron transfer across the lipid bilayer. Using the CV technique, the results show that C_{60} embedded in the BLM acts as an excellent electron carrier/mediator and should be useful for electrochemical sensor and molecular electronics device development.

Chlorophyll molecules [85–87] have been widely used in dye sensitization cells as biometric or bionic models for photocurrent generating and solar energy converting. Dye sensitization cells normally use electrolytic (wet, polymeric, solid) and solid state electronic conduction to generate the electrical circuit which supplies the photo-generated power. The photosynthetic membrane, however, is composed mostly of glycerol lipids in the form of a bilayer into which the protein complexes are embedded, which make up the photosynthetic apparatus. Photosynthetic electron transport consists of a series of electron transfer steps, from one electron carrier to another over relatively short distances [88]. Most electron carriers are metal ion complexes bound with proteins but a few carriers also consist of aromatic groups. There are also electron carriers, which simultaneously act as proton shuttles.

It is known that in BLMs, the electronic charge can only be transmitted in very small currents of the order of nano- to picoamperes. However, with the dispersions of electronically and ionically conducting particles in lipid environment as shown in Fig. 2, the photocurrent density can be increased and a high photovoltage can be reached. Recently, a lipid-based dye sensitization solar cell without liquid or solid electrolyte has been demonstrated by Maruthamuthu and colleges [89] as a biomimetic model for macromolecular-biological photosynthetic reaction center in bi-lipid environment. The photosynthetic model consists of a nanostructured- TiO_2 layer with ruthenium dye exposed to Triton-X ($C_{16}H_{26}O_2$)_n, with a particle mixture of surface treated powder of carbon, of ion conducting materials and dissolved iodine. Realistically high photovoltages of 0.45 V, photocurrents of 1.5 mA/cm² and an energy conversion efficiency of 0.22% have been observed under simulated solar light in nonoptimized cells. This interesting result shows that

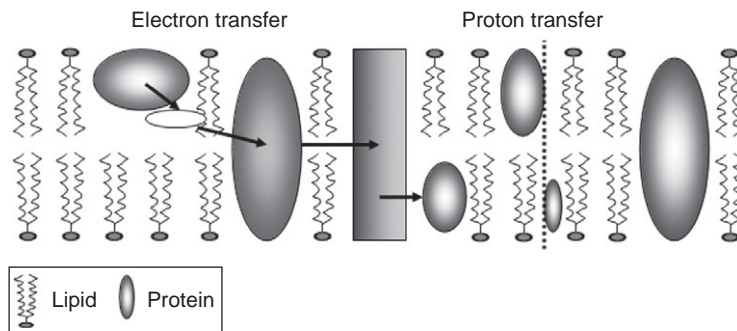


Figure 2 Fluidmosaic model for electron transfer/proton transfer protein chains suspended in lipid environment.

conducting particles in nm- μ m dimension dispersed in lipid environment can effectively transfer electronic charges and the reverse reaction of electrons from the sensitizing dye and from TiO_2 is efficiently suppressed.

3.4.3. Lipid-carbon nanotubes nanocomposites for nanotoxicological studies

As the leading nanodevice candidate, SWCNTs have potential therapeutic applications in gene therapy and novel drug delivery. Recently, Qu and colleagues [90] found that SWCNTs can inhibit DNA duplex association and selectively induce human telomeric i-motif DNA formation by binding to the 5'-end major groove under physiological conditions or even at pH 8.0. The study of the SWCNT binding to telomeric DNA suggest that SWCNTs might have the intriguing potential to modulate human telomeric DNA structures *in vivo*, like biologically relevant B-A and B-Z DNA transitions, which is of great interest for drug design and cancer therapy. More recently, Spurlin *et al.* [91] found that water-soluble fullerenes accumulate on the surface of zwitterionic and cationic supported bilayers to different extents. They propose on the basis of bilayer thicknesses, phase-transition temperatures, and fullerene movement that the water-soluble fullerenes do not penetrate into the hydrocarbon tails of supported bilayers. These findings are important to toxicity issues concerning fullerene materials and the development of decorated lipid bilayers for future drug delivery.

The field of CNT-amphiphile self assembly has been reviewed to address the ongoing debate regarding their binding. Based on the single-molecule fluorescence microscopy and TEM studies, Ke [49] found that the binding of lysophospholipids onto CNTs is dependent on the charge and geometry of the lipids and the pH of the solvent, and independent of solvent temperature. From molecular dynamics simulations, the binding of lysophospholipids onto CNTs does not fully obey any of the models proposed in the literature. Furthermore, the use of CNT-lipid assembly for enabling nanotoxicological studies is demonstrated by the uptake of the assembly in the living organism *Daphnia magna*.

3.5. Conclusion and Perspectives

The insolubility of CNTs in most common solvents limits the application. Functionalization of CNTs with lipid provides an effective tool to broaden the application spectrum. The creation of stable and supramolecular lipid–CNTs hybrid nanomaterials that combine the novel properties of lipid with the unique electronic, optical and catalytic functions of CNTs has been achieved. The field is still rapidly evolving, and it is likely that significant new results will be reported while this chapter is in press. The development and application of a series of novel lipid–CNTs nanocomposites led to enormous advances in nanotechnology and will greatly aid in research areas of membrane biochemistry, biophysics and cell biology as well as in biosensor design and molecular device development.

4. SELF-ASSEMBLY OF LIPID MEMBRANES AT NANOPARTICLES

4.1. Introduction of Nanoparticles

Nanoparticles are often defined as particles of less than 100 nm diameter. Nanoparticles are of interest because of the novel properties that they exhibit compared with larger particles of the same materials. The relatively larger surface area, more chemical reactivity, and special size-dependent properties make nanoparticles attractive for many potential applications. For example, nanoparticles are successfully used as novel materials for drug delivery, fuel cell development and sensor/biosensors designs. The nano-sized Pt and Pt alloy particles are widely used as electrocatalysts for fuel cells. Furthermore, Pt oxygen-reduction fuel-cell electrocatalysts can be stabilized against dissolution under potential cycling regimes (a continuing problem in vehicle applications) by modifying Pt nanoparticles with gold (Au) clusters [34].

Nanoparticles are viewed by many as fundamental building blocks of nanotechnology. They are the starting point for many “bottom-up” approaches for preparing nanomaterials and nanodevices. As such, their synthesis is an important component of rapidly growing research efforts in nanotechnology. Nanoparticles of a wide range of materials can be prepared by a variety of methods such as liquid-phase or gas-phase synthesis [92]. The recent progress on the methods to functionalize nanoparticles with lipid will lead to enormous advances in lipid-based nanotechnology and broaden the application area of nanoparticles.

4.2. Lipid-Functionalized Nanoparticle Hybrids

A lipid bilayer is a basic component of a cell membrane to host many transmembrane proteins [69]. In this structure, SLBs are used to immobilize such proteins on solid surfaces. SLBs are good electrical insulators with biocompatible characteristics to be used as a fluidic membrane supported on a solid surface and for applications such as biosensors. This makes the SLB a novel material with regard to realizing nanodevices

that utilize biomolecule functions together with nanocomposites. Recently, the self-spreading of SLBs on uneven surfaces with 100 nm level nanostructures was examined by Furukawa and coworkers [93] on surfaces with hydrophilic/hydrophobic patterns. It was found that the self-spreading occurred successfully on a flat surface and uneven surfaces with 100 nm up-and-down nanostructures to form a very large homogeneous single-layer SLB with an area on the order of millimeters squared.

Liposomes are artificially constructed spherical lipid vesicles with a small size, whose controllable diameter from tens to thousands of nanometers that can be used to encapsulate and store various cargoes, such as proteins, DNA, and drug molecules [94,95]. One of the limitations in liposome applications is that, when liposomes encounter planar solid substrates, they fuse to form a planar supported bilayer if the solid is hydrophilic or a planar monolayer if the surface is hydrophobic. To overcome this problem, several effective methods have been proposed recently [96–99]. However, it is still desirable to develop an immobilization scheme that is simpler chemically and applies generally to immobilize liposomes onto solid surfaces that can equally well be hydrophilic or hydrophobic. More recently, Granick group [100] recently showed that stabilization with adsorbed nanoparticles meets this need. The pioneering work is achieved by mixing phospholipids liposomes with charged nanoparticles and using low-power sonication to mix them at low volume fraction produces particle-stabilized liposomes that repel one another and do not fuse. Phospholipid liposomes (100~200 nm diameter) are deposited onto solid substrates after stabilizing them against fusion with the solid. Furthermore, the immobilized vesicles remain stable over a period of days and can diffuse freely over surfaces with the same charge but adsorb tightly onto surfaces with opposite charge. The facile method to create large-scale surface-supported arrays of intact liposomes at solid surfaces that can be hydrophobic or hydrophilic may find diverse applications in the emerging field of nanobiotechnology.

Recently, Zhang and colleges [101] described the synthesis of lipid bilayer protected gold nanoparticles (AuNPs) by in situ reduction of HAuCl₄ with NaBH₄ in an aqueous medium. The lipid protected AuNPs were stable and hydrophilic. Fourier transform infrared spectroscopy (FTIR) and differential thermal analysis data revealed that lipid existed in a bilayer structure formed on the particle surface, resulting in a positively charged particle surface. The FTIR spectra also indicated that the bilayer coated on the surface of AuNPs was probably in the ordered gel phase with some end-gauche defects. On the basis of electrostatic interactions between such AuNPs and anionic polyelectrolyte poly(sodium 4-styrenesulfonate) (PSS), (PSS/AuNP)(n) multilayers were successfully fabricated on a cationic polyelectrolyte poly(ethylenimine) coated indium tin oxide substrate via the layer-by-layer self-assembly technique.

4.3. Application of Lipid–Nanoparticle Hybrids

BLMs and/or liposomes, which exhibit nanometric sizes, are comparable to those of nanomaterials such as nanoparticles, nanowires, or CNTs. Thus, by the functionalization of nanoparticles with lipids, it is possible to create hybrid nanomaterials that combine the novel properties of lipid with the unique electronic, optical and

catalytic functions of nanoparticles. Indeed, substantial research efforts were recently directed to use lipid–nanoparticle hybrid systems to tailor novel bioelectronic systems [102,103] that may be applied in molecular recognition and controlled release for drug delivery [104,105], the design of sensors and biosensors [100], the fabrication of electronic nanocircuitry, and even the development of nanodevices [106]. The achievement in the field of nanobiotechnology, particularly the application of metal and/or semiconductor nanoparticles, may be harnessed to resolve fundamental aspects in bioelectrochemistry.

4.3.1. Biolabeling and cellular imaging

The emergence of the novel nanoparticles is anticipated to lead to advancements in understanding biological processes at the molecular level in addition to progress in the development of diagnostic tools and innovative therapies. Recently, fluorescent dye-doped silica nanoparticles, quantum dots (QDs) and gold nanoparticles have been used [107] as imaging agents to overcome many of the limitations of conventional contrast agents (organic dyes) such as poor photostability, low quantum yield, insufficient *in vitro* and *in vivo* stability, etc. More recently, the fabrication, characterization, and implementation of poly(lipid)-coated, highly luminescent silica nanoparticles as fluorescent probes for labeling of cultured cells are described by Senarath-Yapa *et al.* [18]. The core of the probe is a sol-gel-derived silica nanoparticle, 65–100 nm in diameter, in which up to several thousand dye molecules are encapsulated. The core is coated with a membrane composed of bis-sorbylphosphatidylcholine, a synthetic polymerizable lipid that is chemically cross-linked to enhance the environmental and chemical stability of the membrane relative to a fluid lipid membrane. It was found that the poly(lipid) coating can reduce nonspecific interactions, based on the inherently biocompatible properties of the phosphorylcholine headgroup, and permit functionalization of the particle, by doping the coating with lipids bearing chemically reactive or bioactive headgroups. Nonspecific adsorption of dissolved proteins to bare silica nanoparticles and of bare nanoparticles to cultured cells is significantly reduced by application of the poly(lipid) coating. Furthermore, functionalization of poly(lipid)-coated nanoparticles with a biotin-conjugated lipid creates a probe that can be used to target both dissolved protein receptors as well as receptors on the membranes of cultured cells. Measurements performed on single nanoparticles bound to planar SLBs verify that the emission intensity of these probes is significantly greater than that of single protein molecules labeled with several fluorophores [18].

QDs, with zero-dimensional electronic properties, have stimulated great interest due to their important roles in fundamental physical/chemical research and for developing novel devices. In recent years, it has been one of frontier topics of bionanotechnology to study the application of QDs in biological systems. The coating of hydrophobic QDs with phospholipids is a generic method for making QDs water-soluble and biocompatible [108,109], which is useful for investigating biochemical reactions *in vitro* and microinjection into live cells. Vogel and colleges [110] investigated QDs, which are inorganic, strongly fluorescent nanoparticles of exceptional photostability, for the *in vivo* imaging of cellular processes. It was found that hydrophobic QDs can be readily incorporated into the bilayers membrane of

lipid vesicles. Such lipid/QD hybrid vesicles are capable of fusing with live cells, thereby staining a cell's plasma membrane selectively with fluorescent QDs and transferring the vesicle's cargo into the cell. The functionalization of QDs with lipid may have wide ranging potential for cellular imaging and manipulation.

4.3.2. Lipid-based nanoparticles for nucleic acid delivery

Nonviral gene therapy or other nucleic acid therapies have been proposed to treat the some serious diseases which require systemic administration for the gene to enter the target cells affected by genetic diseases, viral infections or cancer. In this connection, the production of effective gene delivery vectors is the critical steps for gene-based drugs in clinical trials. However, the success of gene-based drugs is limited by effective gene delivery vectors. Luckily, liposomes have been demonstrated to be used as vectors of efficient gene delivery. For examples, cationic liposomes have been used as an efficient synthetic gene delivery reagents *in vitro* [111,112]. In addition, cationic liposomes can condense DNA into a cationic particle when the two components are mixed together. The cationic DNA-liposome complex was used as an improved expression vector and lipid, *N*-(3-aminopropyl)-*N,N*-dimethyl-2,3-bis(dodecyloxy)-1-propa nimuminium bromide/dioleoyl phosphatidylethanolamine (GAP-DL-RIE/DOPE) to optimize catheter-mediated gene transfer in porcine arteries [112]. When used in optimal ratios, GAP-DL-RIE/DOPE liposomes provided a 15-fold higher level of gene expression in arteries compared to DNA alone or DMRIE/DOPE. Significant improvements in the efficacy of arterial gene expression can be achieved by optimization of transfection conditions with DNA-liposome complexes *in vivo* that may prove useful for arterial gene delivery in cardiovascular diseases and cancer.

The delivery of naked nucleic acids locally into specific organs such as muscle or liver has been successfully achieved by physical methods, such as electroporation [10,113] or hydrodynamic injection [114,115]. However, these methods are not applicable for systemic gene delivery or are unrealistic for a commercial gene therapy. Lipid-based particles have been extensively studied as systemic gene delivery carriers. Recently, Hayes and coworkers [116,117] found that DNA-lipid assembly is optimal if started from a liquid monophase where both DNA and lipids separately form molecular or micellar solutions prior to mixing, without preexisting condensed lipid phases. This technology allows DNA-lipid assembly under conditions close to equilibrium. For comparison with well-known technologies, different DNA-lipid particles were prepared by interaction of plasmid DNA and stable or ethanol-destabilized lipid vesicles by combining the components in water or 30% (v/v) aqueous ethanol, respectively. Among the three studied DNA-lipid assembly methods, only genospheres combined the properties of small I size (less than or around 100 nm), high incorporation of both lipid and DNA, high degree of DNA protection (dye accessibility 5–12%), a narrow distribution of particle density and when immuno-targeted, the highest transfection efficiency in HER2-overexpressing cells *in vitro*. The assembly methodology to prepare DNA-lipid particles offers advantages for the development of effective, scalable and targetable nonviral gene delivery vectors. More recently, Szoka and Li [118] summarized the recent achievement in formulation/assembly of lipid-based nanoparticles with diameter under 100 nm for delivering nucleic acid *in vivo*. The results show that the diameter of

the nanoparticle is an important attribute to enable nanoparticle to overcome the various *in vivo* barriers for systemic gene delivery such as the blood components, reticuloendothelial system uptake, tumor access, extracellular matrix components, and intracellular barriers. The particle assembly step is a critical one to make lipid-based nanoparticle suitable for *in vivo* gene delivery. The ordered assembly strategy enables one to optimize the particle physico-chemical attributes to devise a biocompatible particle with increased gene transfer efficacy *in vivo*.

4.3.3. Solid lipid nanoparticles (SLNs) for drug delivery

Nitrendipine is an antihypertensive drug with poor oral bioavailability ranging from 10% to 20% due to the first pass metabolism. For improving the oral bioavailability of nitrendipine, nitrendipine loaded SLNs have been developed using triglyceride (tripalmitin), monoglyceride (glyceryl monostearate) and wax (cetyl palmitate) [119]. The dispersions of solid lipid nanoparticles was achieved by hot homogenization of melted lipids and aqueous phase, followed by ultrasonication at temperature above the melting point of lipid. *In vitro* release studies were performed in phosphate buffer of pH 6.8 using Franz diffusion cell. Pharmacokinetics of nitrendipine loaded SLNs after intraduodenal administration to conscious male Wistar rats showed that the bioavailability of nitrendipine was increased three- to four-fold after intraduodenal administration compared to that of nitrendipine suspension. The results indicates that solid lipid nanoparticles can be used as carriers for improving the bioavailability of lipophilic drugs such as nitrendipine by minimizing first pass metabolism.

The preparation of SLNs was achieved by ultrasonication. The model traditional Chinese medicine, tetrandrine, was incorporated into SLN. The tetrandrine-loaded SLN were spherical with particle size to be 157.3 ± 8.2 nm [120]. The entrapment efficiency was determined with the sephadex gel chromatogram and high-performance liquid chromatogram and up to 90.59% of tetrandrine was incorporated. Stability evaluation showed relatively long-term stability with only slight particle growth ($P > 0.05$) after storage at room temperature for 4 weeks. Therefore, ultrasonication is demonstrated to be a simple, available and effective method to prepare high quality SLN loaded traditional Chinese medicine. To characterize the thermodynamics and solid state properties of components and interactions in a formulation for polymer-lipid hybrid nanoparticles [121], verapamil HCl (VRP) was chosen as a model drug and dextran sulfate sodium as a counter-ionic polymer for screening lead lipid carriers and rational design of lipid hybrid nanoparticles. Drug loading efficiency and capacity of a lipid matrix depend on the binding and the interactions of the complex with the lipid. A combined analysis of solubility parameters and partition coefficients is useful for screening lipid candidates for the preparation of polymer-lipid nanoparticles.

The isotretinoin-loaded SLN formulation was constructed with skin targeting for topical delivery of isotretinoin [122]. Tween 80 and soybean lecithin were used as the surfactants to stabilize SLN. The hot homogenization method was performed to prepare the drug-loaded SLN. The various formulations were characterized by photon correlation spectroscopy and all the SLN formulations had low average size between 30 and 50 nm. All the formulations had high entrapment efficiency ranging from 80% to 100%. The penetration of isotretinoin from the isotretinoin-SLN formulations

through skins and into skins were evaluated *in vitro* using Franz diffusion cells fitted with rat skins. The *in vitro* permeation data showed that all the isotretinoin-SLN formulations can avoid the systemic uptake of isotretinoin in skins. In a similar approach, lectin-modified SLNs containing insulin was used as colloidal carriers for oral administration of peptide and protein drugs [105]. These results indicate that the drug-SLN formulation with targeting drug may be a promising carrier for drug delivery.

Recently, Derakhshandeh *et al.* [123] developed a polymeric drug delivery system for a new and potent antitumor drug, 9-nitrocamptothecin (9-NC), intended for both intravenous administration and improving the therapeutic index of the drug. To achieve these goals, 9-NC loaded nanoparticles were prepared by nanoprecipitation method and characterized. The full factorial experimental design was used to study the influence of four different independent variables on response of nanoparticle drug loading. The results of optimized formulations showed a narrow size distribution, and a drug loading of more than 30%. The *in vitro* drug release profile showed a sustained 9-NC release up to 160 h, indicating the suitability of PLGA nanoparticles in controlled 9-NC release. Lipid nanoparticles were fabricated by Yegin and colleges [124] as an injectable carrier system for paclitaxel. The components for the lipid matrix were based on phospholipids, and sucrose fatty acid ester was used as an emulsifier. Formulation prepared with solvent injection has a slightly larger particle size (187.6 nm) than the formulation (147.7 nm) prepared with ultrasound emulsification. Differential scanning calorimetry results indicated that paclitaxel entrapped in the lipid nanoparticles existed in an amorphous state in the lipid matrix. *In vitro* drug release was rather slow; only 12.5–16.5% of the drug was released from the formulations within 14 days. Lipid nanoparticles demonstrated their potential as a promising pharmaceutical formulation of paclitaxel, and the lipid-functionalized nanoparticles may be of clinical importance in stabilizing and delivering camptothecins for cancer treatment.

4.4. Conclusion and Perspectives

Self-assembly is an interesting process both for its biological relevance and because it provides a novel approach to supramolecular structures having nanometer-scale dimensions. These structures are difficult or impossible to prepare by traditional methods. As such, the functionalization of nanoparticles with self-assembled lipids has been successfully achieved. In the future, technology to functionalize nanomaterials with lipid will continue to play a pivotal role in the development of bionanotechnology. The novel lipid–nanoparticle hybrid systems to tailor novel bioelectronic systems will find application in molecular recognitions and controlled release for drug delivery as well as in the design of sensors, biosensors, and nanodevices.

REFERENCES

- [1] H.T. Tien, Z. Salamon, A. Ottova, Lipid bilayer-based sensors and biomolecular electronics, *Crit. Rev. Biomed. Eng.* 18 (1991) 323–340.
- [2] L. Du, X. Liu, W. Huang, E. Wang, A study on the interaction between ibuprofen and bilayer lipid membrane, *Electrochim. Acta.* 51 (2006) 5754–5760.

- [3] J.K. Ulrich, Bilayer lipid membrane ion permeability, *J. Electrochem. Soc.* 134 (1987) 1910–1914.
- [4] H.T. Tien, S.H. Wurster, A.L. Ottova, Electrochemistry of supported bilayer lipid membranes: Background and techniques for biosensor development, *Bioelectrochem. Bioenerg.* 42 (1997) 77–94.
- [5] H.T. Tien, L.G. Wang, X. Wang, A.L. Ottova, Electronic processes in supported bilayer lipid membranes (s-blms) containing a geodesic form of carbon (fullerene c-60), *Bioelectrochem. Bioenerg.* 42(2) (1997) 161–167.
- [6] H.T. Tien, Self-assembled lipid bilayers as a smart material for nanotechnology, *Mater. Sci. Eng. C-Biomimetic Mater. Sens. Syst.* 3 (1995) 7–12.
- [7] D. Jiang, P. Diao, R. Tong, D. Gu, B. Zhong, Ca^{2+} induced $\text{Fe}(\text{CN})_6^{3-/4-}$ electron transfer at Pt supported blm electrode, *Bioelectrochem. Bioenerg.* 44 (1998) 285–288.
- [8] A.L. Ottova, H.T. Tien, Self-assembled bilayer lipid membranes: From mimicking biomembranes to practical applications, *Bioelectrochem. Bioenerg.* 42 (1997) 141–152.
- [9] E.T. Castellana, P.S. Cremer, Solid supported lipid bilayers: From biophysical studies to sensor design, *Surf. Sci. Rep.* 61 (2006) 429–444.
- [10] M.N. Ahmad, Z. Ismail, O.S. Chew, A. Islam, A.Y.M. Shakaff, Development of multichannel artificial lipid-polymer membrane sensor for phytomedicine application, *Sensors* 6 (2006) 1333–1344.
- [11] J. Weng, J.M. Xue, J. Wang, J.S. Ye, H.F. Cui, F.S. Sheu, Q.Q. Zhang, Gold-cluster sensors formed electrochemically at boron-doped-diamond electrodes: Detection of dopamine in the presence of ascorbic acid and thiols, *Adv. Funct. Mater.* 15 (2005) 639–647.
- [12] R. Zadmand, T. Schrader, Nanomolar protein sensing with embedded receptor molecules, *J. Am. Chem. Soc.* 127 (2005) 904–915.
- [13] B. Mecheri, L. Piras, G. Caminati, Langmuir-blodgett films incorporating redox mediators for molecular recognition of nadh, *Bioelectrochemistry* 63 (2004) 13–18.
- [14] J.G. Wang, L. Wang, S.Q. Liu, X.J. Han, W.M. Huang, E.K. Wang, Interaction of k7fe3+p2w17o62h2 with supported bilayer lipid membranes on platinum electrode, *Biophys. Chem.* 106 (2003) 31–38.
- [15] M.R. Mozafari, J. Flanagan, L. Matia-Merino, A. Awati, A. Omri, Z.E. Suntres, H. Singh, Recent trends in the lipid-based nanoencapsulation of antioxidants and their role in foods, *J. Sci. Food Agric.* 86 (2006) 2038–2045.
- [16] D. Chen, G. Wang, J.H. Li, Interfacial bioelectrochemistry: Fabrication, properties and applications of functional nanostructured biointerfaces, *J. Phys. Chem. C* 111 (2007) 2351–2367.
- [17] L.D. Zhu, J.L. Zhai, Y.N. Guo, C.Y. Tian, R.L. Yang, Amperometric glucose biosensors based on integration of glucose oxidase onto prussian blue/carbon nanotubes nanocomposite electrodes, *Electroanalysis* 18 (2006) 1842–1846.
- [18] M.D. Senarath-Yapa, S. Phimphivong, J.W. Coym, M.J. Wirth, C.A. Aspinwall, S.S. Saavedra, Preparation and characterization of poly(lipid)-coated, fluorophore-doped silica nanoparticles for biolabeling and cellular imaging, *Langmuir* 23 (2007) 12624–12633.
- [19] S. Iijima, Helical microtubules of graphitic carbon, *Nature* 354 (1991) 56–58.
- [20] Y.H. Yan, M.B. Chan-Park, Q. Zhang, Advances in carbon-nanotube assembly, *Small* 3 (2007) 24–42.
- [21] N. Tian, Z.Y. Zhou, S.G. Sun, Y. Ding, Z.L. Wang, Synthesis of tetrahedral platinum nanocrystals with high-index facets and high electro-oxidation activity, *Science* 316 (2007) 732–735.
- [22] H. Weyhers, S. Ehlers, H. Hahn, E.B. Sout, R.H. Muller, Solid lipid nanoparticles (sln)—Effects of lipid composition on *in vitro* degradation and *in vivo* toxicity, *Pharmazie* 61 (2006) 539–544.
- [23] C. Emmenegger, P. Mauron, P. Sudan, P. Wenger, V. Hermann, R. Gallay, A. Zuttel, Investigation of electrochemical double-layer (ecd) capacitors electrodes based on carbon nanotubes and activated carbon materials, *J. Power Sources* 124 (2003) 321–329.
- [24] Z. Bing, Y. Yuan, Y. Wang, Z.W. Fu, Electrochemical characterization of a three dimensionally ordered macroporous anatase tio_2 electrode, *Electrochem. Solid State Lett.* 9 (2006) A101–A104.

- [25] C.G. Liu, H.T. Fang, F. Li, M. Liu, H.M. Cheng, Single-walled carbon nanotubes modified by electrochemical treatment for application in electrochemical capacitors, *J. Power Sources* 160 (2006) 758–761.
- [26] Q. Jiang, M.Z. Qu, G.M. Zhou, B.L. Zhang, Z.L. Yu, A study of activated carbon nanotubes as electrochemical super capacitors electrode materials, *Mater. Lett.* 57 (2002) 988–991.
- [27] W. Zheng, Y.F. Zheng, Gelatin-functionalized carbon nanotubes for the bioelectrochemistry of hemoglobin, *Electrochem. Commun.* 9 (2007) 1619–1623.
- [28] U. Yogeswaran, S. Thiagarajan, S.M. Chen, Nanocomposite of functional multiwall carbon nanotubes with nafion, nano platinum, and nano biosensing film for simultaneous determination of ascorbic acid, epinephrine, and uric acid, *Anal. Biochem.* 365 (2007) 122–131.
- [29] Y. Liu, S. Wu, H.X. Ju, L. Xu, Amperometric glucose biosensing of gold nanoparticles and carbon nanotube multilayer membranes, *Electroanalysis* 19 (2007) 986–992.
- [30] X.B. Yan, X.J. Chen, B.K. Tay, K.A. Khor, Transparent and flexible glucose biosensor via layer-by-layer assembly of multi-wall carbon nanotubes and glucose oxidase, *Electrochem. Commun.* 9 (2007) 1269–1275.
- [31] X.T. Zhang, W.H. Song, P.J.F. Harris, G.R. Mitchell, Electrodeposition of chiral polymer-carbon nanotube composite films, *ChemPhysChem* 8 (2007) 1766–1769.
- [32] S.Z. Zong, Y. Cao, H.X. Ju, Direct electron transfer of hemoglobin immobilized in multiwalled carbon nanotubes enhanced grafted collagen matrix for electrocatalytic detection of hydrogen peroxide, *Electroanalysis* 19 (2007) 841–846.
- [33] M.D. Rubianes, G.A. Rivas, Dispersion of multi-wall carbon nanotubes in polyethylenimine: A new alternative for preparing electrochemical sensors, *Electrochem. Commun.* 9 (2007) 480–484.
- [34] H.W. Zhang, Z.J. Zhang, J.J. Li, S.M. Cai, Effects of direct current bias voltages on supported bilayer lipid membranes on a glassy carbon electrode, *Electrochem. Commun.* 9 (2007) 605–609.
- [35] H. Yu, Q.L. Sheng, L. Li, J.B. Zheng, Rapid electrochemical preparation of a compact and thick prussian blue film on composite ceramic carbon electrode from single ferricyanide solution in the presence of HauCl_4 , *J. Electroanal. Chem.* 606 (2007) 55–62.
- [36] Y.Z. Xian, F. Liu, L.J. Feng, F.H. Wu, L.W. Wang, L.T. Jin, Nanoelectrode ensembles based on conductive polyaniline/poly(acrylic acid) using porous sol-gel films as template, *Electrochem. Commun.* 9 (2007) 773–780.
- [37] H.J. Wan, Q.L. Zou, R. Yan, F.Q. Zhao, B.Z. Zeng, Electrochemistry and voltammetric determination of tannic acid on a single-wall carbon nanotube-coated glassy carbon electrode, *Microchim. Acta.* 159 (2007) 109–115.
- [38] U.A. Kirgoz, S. Timur, D. Odaci, B. Perez, S. Alegret, A. Merkoci, Carbon nanotube composite as novel platform for microbial biosensor, *Electroanalysis* 19 (2007) 893–898.
- [39] J.F. Zhai, M.H. Huang, S.J. Dong, Electrochemical designing of au/pt core shell nanoparticles as nanostructured catalyst with tunable activity for oxygen reduction, *Electroanalysis* 19 (2007) 506–509.
- [40] R.A. Hatton, N.P. Blanchard, V. Stolojan, A.J. Miller, S.R.P. Silva, Nanostructured copper phthalocyanine-sensitized multiwall carbon nanotube films, *Langmuir* 23 (2007) 6424–6430.
- [41] D. Enders, T. Nagao, T. Nakayama, M. Aono, *In situ* surface-enhanced infrared absorption spectroscopy for the analysis of the adsorption and desorption process of au nanoparticles on the SiO_2/Si surface, *Langmuir* 23 (2007) 6119–6125.
- [42] W. Chen, X.L. Pan, X.H. Bao, Tuning of redox properties of iron and iron oxides via encapsulation within carbon nanotubes, *J. Am. Chem. Soc.* 129 (2007) 7421–7426.
- [43] T. Bordjiba, M. Mohamedi, L.H. Dao, B. Aissa, M.A. El Khakani, Enhanced physical and electrochemical properties of nanostructured carbon nanotubes coated microfibrillar carbon paper, *Chem. Phys. Lett.* 441 (2007) 88–93.
- [44] S. Bollo, N.F. Ferreyra, G.A. Rivas, Electrooxidation of DNA at glassy carbon electrodes modified with multiwall carbon nanotubes dispersed in chitosan, *Electroanalysis* 19 (2007) 833–840.
- [45] F.Q. Hu, S.P. Jiang, Y.Z. Du, H. Yuan, Y.Q. Ye, S. Zeng, Preparation and characteristics of monostearin nanostructured lipid carriers, *Int. J. Pharm.* 314 (2006) 83–89.

- [46] S.A. Yuan, Q.O. He, S.J. Yao, S.S. Hu, Mercury-free detection of europium (iii) at a glassy carbon electrode modified with carbon nanotubes by adsorptive stripping voltammetry, *Anal. Lett.* 39 (2006) 373–385.
- [47] X.Y. Yang, Y.H. Lu, Y.F. Ma, Y.J. Li, F. Du, Y.S. Chen, Noncovalent nanohybrid of ferrocene with single-walled carbon nanotubes and its enhanced electrochemical property, *Chem. Phys. Lett.* 420 (2006) 416–420.
- [48] W. Sugimoto, T. Saida, Y. Takasu, Co-catalytic effect of nanostructured ruthenium oxide towards electro-oxidation of methanol and carbon monoxide, *Electrochem. Commun.* 8 (2006) 411–415.
- [49] P.C. Ke, Fiddling the string of carbon nanotubes with amphiphiles, *Phys. Chem. Chem. Phys.* 9 (2007) 439–447.
- [50] W.J. Jin, X.F. Sun, Y. Wang, Solubilization and functionalization of carbon nanotubes, *New Carbon Mater.* 19 (2004) 312–318.
- [51] V. Georgakilas, K. Kordatos, M. Prato, D.M. Guldi, M. Holzinger, A. Hirsch, Organic functionalization of carbon nanotubes, *J. Am. Chem. Soc.* 124 (2002) 760–761.
- [52] D. Tasis, N. Tagmatarchis, A. Bianco, M. Prato, Chemistry of carbon nanotubes, *Chem. Rev.* 106 (2006) 1105–1136.
- [53] M. Kryszak, B. Parekh, T. Debies, R.A. Dileo, B.J. Landi, R.P. Raffaele, G.A. Takacs, Gas-phase surface functionalization of multi-walled carbon nanotubes with vacuum uv photo-oxidation, *J. Adhes. Sci. Technol.* 21 (2007) 999–1007.
- [54] B. Parekh, T. Debies, P. Knight, K.S.V. Santhanam, G.A. Takacs, Surface functionalization of multiwalled carbon nanotubes with UV and vacuum UV photo-oxidation, *J. Adhes. Sci. Technol.* 20(16) (2006) 1833–1846.
- [55] S. Nagasawa, M. Yudasaka, K. Hirahara, T. Ichihashi, S. Iijima, Effect of oxidation on single-wall carbon nanotubes, *Chem. Phys. Lett.* 328 (2000) 374–380.
- [56] N.O.V. Plank, R. Cheung, Functionalisation of carbon nanotubes for molecular electronics, *Microelectron. Eng.* 73–74 (2004) 578–582.
- [57] R. Verdejo, S. Lamoriniere, B. Cottam, A. Bismarck, M. Shaffer, Removal of oxidation debris from multi-walled carbon nanotubes, *Chem. Commun.* (2007) 513–515.
- [58] D.R.S. Jeykumari, S.S. Narayanan, Amperometric determination of hydrogen peroxide by functionalized carbon nanotubes through edc/nhs coupling chemistry, *J. Nanosci. Nanotechnol.* 7 (2007) 1824–1830.
- [59] Y. Chen, R.C. Haddon, S. Fang, A.M. Rao, W.H. Lee, E.C. Dickey, E.A. Grulke, J. C. Pendergrass, A. Chavan, B.E. Haley, R.E. Smalley, Chemical attachment of organic functional groups to single-walled carbon nanotube material, *J. Mater. Res.* 13 (1998) 2423–2431.
- [60] J. Chen, A.M. Rao, S. Lyuksyutov, M.E. Itkis, M.A. Hamon, H. Hu, R.W. Cohn, P.C. Eklund, D.T. Colbert, R.E. Smalley, R.C. Haddon, Dissolution of full-length single-walled carbon nanotubes, *J. Phys. Chem. B* 105 (2001) 2525–2528.
- [61] J. Chen, M.A. Hamon, H. Hu, Y.S. Chen, A.M. Rao, P.C. Eklund, R.C. Haddon, Solution properties of single-walled carbon nanotubes, *Science* 282 (1998) 95–98.
- [62] M. Holzinger, O. Vostrowsky, A. Hirsch, F. Hennrich, M. Kappes, R. Weiss, F. Jellen, Sidewall functionalization of carbon nanotubes, *Angew. Chem. Int. Ed.* 40 (2001) 4002–4005.
- [63] V. Georgakilas, D. Voulgaris, E. Vazquez, M. Prato, D.M. Guldi, A. Kukovec, H. Kuzmany, Purification of hipco carbon nanotubes via organic functionalization, *J. Am. Chem. Soc.* 124 (2002) 14318–14319.
- [64] L.M. Wei, Y.F. Zhang, Covalent sidewall functionalization of single-walled carbon nanotubes via one-electron reduction of benzophenone by potassium, *Chem. Phys. Lett.* 446 (2007) 142–144.
- [65] Y. Martinez-Rubi, J. Guan, S. Lin, C. Scriver, R.E. Sturgeon, B. Simard, Rapid and controllable covalent functionalization of single-walled carbon nanotubes at room temperature, *Chem. Commun.* (2007) 5146–5148.
- [66] R.J. Chen, S. Bangsaruntip, K.A. Drouvalakis, N.W.S. Kam, M. Shim, Y.M. Li, W. Kim, P. J. Utz, H.J. Dai, Noncovalent functionalization of carbon nanotubes for highly specific electronic biosensors, *Proc. Natl. Acad. Sci. USA.* 100 (2003) 4984–4989.

- [67] R.J. Chen, Y.G. Zhang, D.W. Wang, H.J. Dai, Noncovalent sidewall functionalization of single-walled carbon nanotubes for protein immobilization, *J. Am. Chem. Soc.* 123 (2001) 3838–3839.
- [68] B.R. Azamian, J.J. Davis, K.S. Coleman, C.B. Bagshaw, M.L.H. Green, Bioelectrochemical single-walled carbon nanotubes, *J. Am. Chem. Soc.* 124 (2002) 12664–12665.
- [69] K. Glasmastar, C. Larsson, F. Hook, B. Kasemo, Protein adsorption on supported phospholipid bilayers, *J. Colloid Interface Sci.* 246 (2002) 40–47.
- [70] J.J. Davis, K.S. Coleman, B.R. Azamian, C.B. Bagshaw, M.L.H. Green, Chemical and biochemical sensing with modified single walled carbon nanotubes, *Chem. – Eur. J.* 9 (2003) 3732–3739.
- [71] K. Masaharu, S. Takamasa, N. Naotoshi, Aqueous electrochemistry of c[sub 60] incorporated in artificial lipid thin-film on a p-type semiconductive diamond electrode, *J. Electrochem. Soc.* 149 (2002) E227–E232.
- [72] S.S. Karajanagi, H. Yang, P. Asuri, E. Sellitto, J.S. Dordick, R.S. Kane, Protein-assisted solubilization of single-walled carbon nanotubes, *Langmuir* 22 (2006) 1392–1395.
- [73] Z. Li, T. Hulderman, R. Salmen, R. Chapman, S.S. Leonard, S.H. Young, A. Shvedova, M. I. Luster, P.P. Simeonova, Cardiovascular effects of pulmonary exposure to single-wall carbon nanotubes, *Environ. Health Perspect.* 115 (2007) 377–382.
- [74] J.M. Bonard, T. Stora, J.P. Salvetat, F. Maier, T. Stockli, C. Duschl, L. Forro, W.A. deHeer, A. Chatelain, Purification and size-selection of carbon nanotubes, *Adv. Mater.* 9 (1997) 827–831.
- [75] P. Yu, J. Yan, J. Zhang, L.Q. Mao, Cost-effective electrodeposition of platinum nanoparticles with ionic liquid droplet confined onto electrode surface as micro-media, *Electrochem. Commun.* 9 (2007) 1139–1144.
- [76] Y.N. Jiang, H.Q. Luo, N.B. Li, Determination of nitrite with a nano-gold modified glassy carbon electrode by cyclic voltammetry, *Int. J. Environ. Anal. Chem.* 87 (2007) 295–306.
- [77] C. Richard, F. Balavoine, P. Schultz, T.W. Ebbesen, C. Mioskowski, Supramolecular self-assembly of lipid derivatives on carbon nanotubes, *Science* 300 (2003) 775–778.
- [78] B.L. Allen, P.D. Kichambare, A. Star, Carbon nanotube field-effect-transistor-based biosensors, *Adv. Mater.* 19 (2007) 1439–1451.
- [79] Y.L. Zhang, J. Dunlop, T. Phung, A. Ottova, H.T. Tien, Supported bilayer lipid membranes modified with a phosphate ionophore, *Biosens. Bioelectron.* 21 (2006) 2311–2314.
- [80] Y. Wu, J.S. Hudson, Q. Lu, J.M. Moore, A.S. Mount, A.M. Rao, E. Alexov, P.C. Ke, Coating single-walled carbon nanotubes with phospholipids, *J. Phys. Chem. B* 110 (2006) 2475–2478.
- [81] R. Qiao, P.C. Ke, Lipid-carbon nanotube self-assembly in aqueous solution, *J. Am. Chem. Soc.* 128 (2006) 13656–13657.
- [82] M.R.R. de Planque, N.C. Toledo, S.A. Contera, J.F. Ryan, Lipid bilayer functionalization of multiwalled carbon nanotubes, *Biophys. J.* (2007) 552A.
- [83] J.S. Ye, F.S. Sheu, Functionalization of cnts: New routes towards the development of novel electrochemical sensors, *Curr. Nanosci.* 2 (2006) 319–327.
- [84] O.V. Gerasimov, J.A. Boomer, M.M. Qualls, D.H. Thompson, Cytosolic drug delivery using ph- and light-sensitive liposomes, *Adv. Drug Deliv. Rev.* 38 (1999) 317–338.
- [85] Y. Amao, Y. Yamada, Photovoltaic conversion using zn chlorophyll derivative assembled in hydrophobic domain onto nanocrystalline TiO₂ electrode, *Biosens. Bioelectron.* 22 (2007) 1561–1565.
- [86] P.E. Jensen, R. Bassi, E.J. Boekema, J.P. Dekker, S. Jansson, D. Leister, C. Robinson, H. V. Scheller, Structure function and regulation of plant photosystem i, *Biochim. Biophys. Acta-Bioenerg.* 1767 (2007) 335–352.
- [87] J.R. Stromberg, A. Marton, H.L. Kee, C. Kirmaier, J.R. Diers, C. Muthiah, M. Taniguchi, J. S. Lindsey, D.F. Bocian, G.J. Meyer, D. Holten, Examination of tethered porphyrin chlorin and bacteriochlorin molecules in mesoporous metal-oxide solar cells, *J. Phys. Chem. C* 111 (2007) 15464–15478.
- [88] Q.B. Meng, K. Takahashi, X.T. Zhang, I. Sutanto, T.N. Rao, O. Sato, A. Fujishima, H. Watanabe, T. Nakamori, M. Uragami, Fabrication of an efficient solid-state dye-sensitized solar cell, *Langmuir* 19 (2003) 3572–3574.

- [89] P. Maruthamuthu, S. Fiechter, H. Tributsch, Lipid (detergent)-based composite-dye solar cell, *C. R. Chim.* 9 (2006) 684–690.
- [90] X. Li, Y.H. Peng, J.S. Ren, X.G. Qu, Carboxyl-modified single-walled carbon nanotubes selectively induce human telomeric i-motif formation, *Proc. Natl. Acad. Sci. USA* 103 (2006) 19658–19663.
- [91] T.A. Spurlin, A.A. Gewirth, Effect of C₆₀ on solid supported lipid bilayers, *Nano Lett.* 7 (2007) 531–535.
- [92] M.T. Swihart, Vapor-phase synthesis of nanoparticles, *Curr. Opin. Colloid Interface Sci.* 8 (2003) 127–133.
- [93] K. Furukawa, K. Sumitomo, H. Nakashima, Y. Kashimura, K. Torimitsu, Supported lipid bilayer self-spreading on a nanostructured silicon surface, *Langmuir* 23 (2007) 367–371.
- [94] A. Pantos, D. Tsiourvas, G. Nounesis, C.M. Paleos, Interaction of functional dendrimers with multilamellar liposomes: Design of a model system for studying drug delivery, *Langmuir* 21 (2005) 7483–7490.
- [95] A. Pantos, D. Tsiourvas, C.M. Paleos, G. Nounesis, Enhanced drug transport from unilamellar to multilamellar liposomes induced by molecular recognition of their lipid membranes, *Langmuir* 21 (2005) 6696–6702.
- [96] C. Yoshina-Ishii, Y.H.M. Chan, J.M. Johnson, L.A. Kung, P. Lenz, S.G. Boxer, Diffusive dynamics of vesicles tethered to a fluid supported bilayer by single-particle tracking, *Langmuir* 22 (2006) 5682–5689.
- [97] C. Yoshina-Ishii, G.P. Miller, M.L. Kraft, E.T. Kool, S.G. Boxer, General method for modification of liposomes for encoded assembly on supported bilayers, *J. Am. Chem. Soc.* 127 (2005) 1356–1357.
- [98] C. Yoshina-Ishii, S.G. Boxer, Arrays of mobile tethered vesicles on supported lipid bilayers, *J. Am. Chem. Soc.* 125 (2003) 3696–3697.
- [99] E. Boukobza, A. Sonnenfeld, G. Haran, Immobilization in surface-tethered lipid vesicles as a new tool for single biomolecule spectroscopy, *J. Phys. Chem. B* 105 (2001) 12165–12170.
- [100] J.B. Wu, J.P. Tu, T.A. Han, Y.Z. Yang, W.K. Zhang, X.B. Zhao, High-rate dischargeability enhancement of ni/mh rechargeable batteries by addition of nanoscale coo to positive electrodes, *J. Power Sources* 156 (2006) 667–672.
- [101] L.X. Zhang, X.P. Sun, Y.H. Song, X. Jiang, S.J. Dong, E.A. Wang, Didodecyltrimethylammonium bromide lipid bilayer-protected gold nanoparticles: Synthesis characterization and self-assembly, *Langmuir* 22 (2006) 2838–2843.
- [102] M.P. Aliste, S.C. Harvey, Lipid properties on nano-disc particles of apo a-i, *Abstr. Pap. Am. Chem. Soc.* 231 (2006) 189.
- [103] B. Angelov, A. Angelova, B. Papahadjopoulos-Stenberg, S. Lesieur, J.F. Sadoc, M. Ollivon, P. Couvreur, Detailed structure of diamond-type lipid cubic nanoparticles, *J. Am. Chem. Soc.* 128 (2006) 5813–5817.
- [104] R. Angius, S. Murgia, D. Berti, P. Baglioni, M. Monduzzi, Molecular recognition and controlled release in drug delivery systems based on nanostructured lipid surfactants, *J. Phys. Condes. Matter* 18 (2006) S2203–S2220.
- [105] N. Zhang, Q.N. Ping, G.H. Huang, W.F. Xu, Y.N. Cheng, X.Z. Han, Lectin-modified solid lipid nanoparticles as carriers for oral administration of insulin, *Int. J. Pharm.* 327 (2006) 153–159.
- [106] D. Anrather, M. Smetazko, M. Saba, Y. Alguel, T. Schalkhammer, Supported membrane nanodevices, *J. Nanosci. Nanotechnol.* 4 (2004) 1–22.
- [107] P. Sharrna, S. Brown, G. Walter, S. Santra, B. Moudgil, Nanoparticles for bioimaging, *Adv. Colloid Interface Sci.* 123 (2006) 471–485.
- [108] F. Pinaud, X. Michalet, E. Margeat, H.P. Moore, S. Weiss, Examining the lipid raft hypothesis in living cells using targeted quantum dots and single molecule imaging, *Eur. Biophys. J. Biophys. Lett.* 34 (2005) 704.
- [109] S. Ramachandran, N.E. Merrill, R.H. Blick, D.W. van der Weide, Colloidal quantum dots initiating current bursts in lipid bilayers, *Biosens. Bioelectron.* 20 (2005) 2173–2176.

- [110] G. Gopalakrishnan, C. Danelon, P. Izewska, M. Prummer, P.Y. Bolinger, I. Geissbuhler, D. Demurtas, J. Dubochet, H. Vogel, Multifunctional lipid/quantum dot hybrid nanocontainers for controlled targeting of live cells, *Angew. Chem. Int. Ed.* 45 (2006) 5478–5483.
- [111] K. Konopka, G.S. Harrison, P.L. Felgner, N. Duzgunes, Cationic liposome-mediated expression of HIV-regulated luciferase and diphtheria toxin genes in hela cells infected with or expressing HIV, *Biochim. Biophys. Acta – Mol. Cell Res.* 1356 (1997) 185–197.
- [112] D.J. Stephan, Z.Y. Yang, H. San, R.D. Simari, C.J. Wheeler, P.L. Felgner, D. Gordon, G. J. Nabel, E.G. Nabel, A new cationic liposome DNA complex enhances the efficiency of arterial gene transfer *in vivo*, *Hum. Gene Ther.* 7 (1996) 1803–1812.
- [113] Y.J. Gu, W.T. Wong, Nanostructure ptu/mwnts as anode catalysts prepared in a vacuum for direct methanol oxidation, *Langmuir* 22 (2006) 11447–11452.
- [114] O.C. Hibbitt, R.P. Harbottle, S.N. Waddington, C.A. Bursill, C. Coutelle, C. Keith, R. Wade-Martins, Delivery and long-term expression of a 135 kb ldlr genomic DNA locus *in vivo* by hydrodynamic tail vein injection, *J. Gene Med.* 9 (2007) 488–497.
- [115] Z.C. Neal, M.K. Bates, M.R. Albertini, H. Herweijer, Hydrodynamic limb vein delivery of a xenogeneic DNA cancer vaccine effectively induces antitumor immunity, *Mol. Ther.* 15 (2007) 422–430.
- [116] M.E. Hayes, D.C. Drummond, K. Hong, J.W. Park, J.D. Marks, D.B. Kirpotin, Assembly of nucleic acid-lipid nanoparticles from aqueous-organic monophases, *Biochim. Biophys. Acta-Biomembr.* 1758 (2006) 429–442.
- [117] M.E. Hayes, D.C. Drummond, D.B. Kirpotin, W.W. Zheng, C.O. Noble, J.W. Park, J. D. Marks, C.C. Benz, K. Hong, Genospheres: Self-assembling nucleic acid-lipid nanoparticles suitable for targeted gene delivery, *Gene Ther.* 13 (2006) 646–651.
- [118] W.J. Li, F.C. Szoka, Lipid-based nanoparticles for nucleic acid delivery, *Pharm. Res.* 24 (2007) 438–449.
- [119] V.V. Kumar, D. Chandrasekar, S. Ramakrishna, V. Kishan, Y.M. Rao, P.V. Diwan, Development and evaluation of nitrendipine loaded solid lipid nanoparticles: Influence of wax and glyceride lipids on plasma pharmacokinetics, *Int. J. Pharm.* 335 (2007) 167–175.
- [120] Y.C. Li, L. Dong, A. Jia, X.M. Chang, H. Xue, Preparation and characterization of solid lipid nanoparticles loaded traditional chinese medicine, *Int. J. Biol. Macromol.* 38 (2006) 296–299.
- [121] Y.Q. Li, N. Taulier, A.M. Rauth, X.Y. Wu, Screening of lipid carriers and characterization of drug-polymer-lipid interactions for the rational design of polymer-lipid hybrid nanoparticles (pln), *Pharm. Res.* 23 (2006) 1877–1887.
- [122] J. Liu, W. Hu, H.B. Chen, Q. Ni, H.B. Xu, X.L. Yang, Isotretinoin-loaded solid lipid nanoparticles with skin targeting for topical delivery, *Int. J. Pharm.* 328 (2007) 191–195.
- [123] K. Derakhshandeh, M. Erfan, S. Dadashzadeh, Encapsulation of 9-nitrocampthothecin, a novel anticancer drug, in biodegradable nanoparticles: Factorial design, characterization and release kinetics, *Eur. J. Pharm. Biopharm.* 66 (2007) 34–41.
- [124] B.A. Yegin, J.P. Benoit, A. Lamprecht, Paclitaxel-loaded lipid nanoparticles prepared by solvent injection or ultrasound emulsification, *Drug Dev. Ind. Pharm.* 32 (2006) 1089–1094.

USING LIPOSOMES TO OBSERVE THE INTERACTIONS OF AUTOIMMUNE ANTIBODIES

Marie Kelly-Worden^{1,*} and Sara Ghassemifar¹

Contents

1. Introduction	226
1.1. History of Liposomes	226
1.2. Preparation of Liposomes	226
1.3. Preparation of PC:PS Liposomes	228
2. Reconstitution	228
2.1. Reconstitution of Cellular Membrane Fragments into Liposomes (mCs)	228
2.2. Reconstitution of Vesicular Fragments (mVs)	229
3. Immunofluorescence and Liposomes	232
3.1. Immunofluorescence	232
3.2. Fluorescent Microscopy	233
3.3. Vesicle Plating	233
3.4. Confocal Microscopy	234
4. Autoimmune Antibodies	235
4.1. Antiphospholipid Antibodies	235
4.2. M6 Antibody	236
4.3. M6 Antibody Interacting with Synaptic Vesicles	236
4.4. M6 Antibody Interacting with Proteins	237
4.5. M6 and Liposomes	237
5. Discussion and Conclusions	238
6. Future Directions	239
7. Acknowledgements	239
References	239

Abstract

Artificial vesicles have been used for decades to examine reconstituted purified membrane proteins and reconstitution of pieces of cellular (mCs) or vesicular membranes (mVs). Reconstitution of vesicles into liposomes allows vesicular proteins to maintain a semi-natural environment. These mVs can then be incorporated into planar lipid bilayers either by direct brushing or by incorporating through the use of an osmotic gradient.

* Corresponding author. Tel.: +765 285 5997; Fax: +765 285 3210;
E-mail address: mlkellyworde@bsu.edu.

¹ Department of Physiology and Health Science, Ball State University, 2000 University Ave., Muncie, IN 47306, USA

Incorporation can be monitored by the nystatin/ergosterol technique or by observing capacitance change. Liposomes and mVs can also be used for examining autoimmune antibodies-vesicular membranes interaction using poly-D-lysine plated coverslips. Modified synaptic vesicles (mSVs) can be prepared and plated onto poly-D-lysine coated coverslips. The mSVs can be processed using primary antibodies against specific synaptic vesicular proteins (such as VAMP and Rabphilin-3A) and the appropriate secondary Alexa fluor antibody. Simultaneously the mSVs can be examined for the ability of autoimmune antibodies to bind with these vesicles, and any cross-reactivity can be observed by fluorescent microscopy. Here we describe fluorescent techniques for examining liposomes, synaptic vesicles, and mSVs as well as bilayer techniques for examining mSVs.

1. INTRODUCTION

1.1. History of Liposomes

Although every cell within our bodies is created out of lipids and proteins with other accessorized elements that vary according to the role of the individual cell, our ability to study the components of cells in artificial environments only began within the last half of the twentieth century. Liposomes were first observed by A.D. Bangham and R.W. Horne [1] close to the time the first bilayer experiment was performed by P. Mueller, D.O. Rudin, H.T. Tien, and W.C. Wescott in 1962 [2]. However, the use of the term “liposome” referring to artificially created lipid vesicles would not find its way into scientific vocabulary until 1968 when G. Sessa and G. Weissmann used the term for phospholipid spherules [3]. They reconstituted cytochrome *c* and albumin into their liposomes and discovered that different phospholipids had different properties such as the way the lipids interacted with ions. However, the most relevant accomplishment to this particular chapter was not that they discovered different ion interactions but that they prepared liposomes and discussed protein reconstitution. Similarly, we begin this chapter by discussing liposome preparation and protein reconstitution.

1.2. Preparation of Liposomes

Liposomes were first created from ovoidlecithin, a natural mixture of lipids in egg whites [3], because the early experiments were limited by the availability of purified lipids. Today, researches have a vast assortment of natural and synthetic lipids at their disposal. Hence, liposome preparation is no longer limited by what is available, but by the boundaries of the experiment being performed. Liposomes can be prepared from a single lipid or from multiple lipids; some lipid mixtures are used more commonly than others.

As liposomes must provide a suitable environment for incorporation, some researchers have addressed this problem by creating an environment similar to the natural environment provided by the membrane. For example, if one wanted to incorporate the membrane of a vesicle (such as synaptic vesicle membranes) into liposomes (mSVs), an ideal mixture of lipids for these liposomes would be equivalent to what is estimated to occur in the synaptic vesicle membrane: 25–32% phosphatidylcholine

(PC), 15–24% phosphatidylethanolamine (PE), 4–8% phosphatidylserine (PS), 3–8% sphingomyelin (SM), 2–3% phosphatidylinositol (PI), 0–1% phosphatidic acid (PA), and 33–38% cholesterol [4–6]. Indeed, preparation of mSVs has been achieved using purified or synthetic lipids in a ratio similar to what would be found in the vesicle membrane such as DOPC/DOPE/SM/CH/DOPS (32:25:15:20:8 molar ratio). This composition of lipids allows for the formation of vesicles with small diameters, which are highly curved like a synaptic vesicle [7].

However, a second criterion to consider when deciding to use a particular lipid composition is what is the purpose of the liposomes in a given experiment? Researchers commonly prepare mSVs for examining synaptic vesicle fusion—the process of neurotransmitter release from the vesicle through the formation of a pore connecting the cytosol of the vesicle to the extracellular fluid. *In vivo*, synaptic vesicles would remain docked at the presynaptic membrane to plasma membrane proteins, known as t-SNAREs. Docking occurs through the interaction of synaptic vesicle associated membrane protein, VAMP, and the plasma membrane protein, syntaxin. Once the signal for fusion occurs, these proteins form the fusion pore. *In vivo*, these events are observed as small changes in capacitance. In synaptic vesicle fusion assays *in vitro*, a planar lipid bilayer apparatus is commonly used. The bilayer serves either as an artificial vesicular membrane or as an artificial presynaptic membrane. The investigator compares the number of fusion events of the mSVs (observed as either changes in conductance or changes in capacitance) into the bilayer over a given period [8]. Thus, the ideal vesicles would be the ones that are like synaptic vesicles and that allow monitoring of fusion events.

Creating lipid-composed mSVs that not only promote fusion but also allow the observation of fusion events is not a difficult task. The DOPC/DOPE/SM/CH/DOPS mixture mentioned earlier produces highly curved vesicles promoting fusion *in vitro* and enabling these liposomes to be used for fusion assays to examine SNARE protein interactions. However, a composition of just PE:PC:PS will also work for this purpose and allows for the counting of individual fusion events [8,9].

Therefore, fusion assays do not require all the lipids in the synaptic vesicle membrane. Likewise, the entire synaptic vesicle membrane with all vesicle proteins is not necessary either. In fact, only the basic fusion proteins, the SNAREs, are necessary for fusion assays. The proteins responsible for interlocking with VAMP and docking the vesicle at the synaptic membrane are the t-SNAREs, syntaxin (mentioned earlier), and SNAP-25. Liposomes containing SNARE proteins (mSPVs) can be prepared using a mixture equivalent to that found in synaptic vesicle lipids, or a preparation of PE:PC:PS, or even a simpler composition of just PC:PS and all of these mixtures will allow for observation of fusion events. However, changing the ratio of PC and PS can affect the degree of fusion observed in the assay.

When working with purified proteins, there is a third factor to consider. The concentration of lipids within liposomes can be varied according to what is being incorporated and to the outcome desired. Certain membrane proteins could be incorporated into artificial liposomes with one liposome composition promoting incorporation of the protein better than another, and it must be determined whether the goal of the experiment is more to examine the protein in a natural environment or to increase the amount of protein within the liposomes. If proteins are to be incorporated

into the liposome for an assay, it is best to remember that what is observed *in vivo* is not always optimal for an *in vitro* assay. For example, liposomes may be prepared to examine the interactions of antibodies with membrane proteins. When working with autoimmune antibodies, using multiple lipids may not be in one's best interest. Alving *et al.* [10] began looking at the interaction of autoimmune antibodies produced by mice injected with a lipid mixture. They examined the anticoagulant activities of four monoclonal antibodies that interacted with phosphatidylinositol 4 monophosphate, PIP. They found that all four antibodies (numbered 1–4) showed anticoagulant activity in the presence of Thrombofax (a mixture of bovine brain phospholipids), and the fourth antibody showed a lower level of activity than the other antibodies. However, when only PC:PS liposomes were substituted for Thrombofax, the anticoagulant activity of the fourth antibody was no longer detectable. Not to mention, the action of the first antibody became intermediate. Therefore, when testing for the activity of autoimmune phospholipid antibodies a simple PC:PS liposome mixture may help to decrease false positive or less reactive readings.

1.3. Preparation of PC:PS Liposomes

Since mSVs used for fusion have previously been prepared using just PC and PS and this simple mixture of liposomes is less likely to give a false positive result, we decided to start with these two lipids. PC:PS at a concentration of 10 mg/ml chloroform can be combined in a ratio of 7:3, evaporated under nitrogen or argon gas, and resuspended by vortexing in a volume of either 150 mM NaCl or KCl sufficient to maintain lipid concentration at 10 mg/ml. These liposomes can be filtered to produce liposomes of a specific size or sonicated to produce vesicles within a specific size range. These liposomes may also be used to create mSVs or other liposomes.

2. RECONSTITUTION

The first modified liposomes were those containing reconstituted proteins. These proteoliposomes (mPVs) were created to examine the properties of the newly formed lipid spheres and not to examine the properties of the incorporated proteins [3]. Much has changed since these early experiments. Today, reconstitution is a method used primarily to study the properties of proteins or protein containing membranes that are being incorporated into the liposomes. Proteins may be incorporated individually or groups of interacting proteins can be incorporated. Groups of proteins may be used to create artificial systems (such as the bilayer system used to examine the incorporation of mSVs and mSPVs in the fusion assay).

2.1. Reconstitution of Cellular Membrane Fragments into Liposomes (mCs)

The process of creating liposomes containing cellular membrane fragments (mCs) appears in publication in 1980. Morris *et al.* decided to create the liposomes from a mixture of rat brain gangliosides, combining a rat brain synaptosome preparation with

a liposome preparation in order to study tetanus toxin [11]. Synaptosomal preparations are one of the earliest types of cellular membrane preparations in publication. The first cited synaptosomal preparation was that done in 1964 by Whittaker, Michaelson and Kirkland only two years after the first liposomal preparation [12].

The first step in creating mCs is the preparation of the plasma membrane of interest. This requires the removal of the specific tissue of interest. The first step is always to breakdown the tissue into small pieces, homogenization of the tissue sample, and removal of large pieces of debris by low speed centrifugation. The next steps involve removal of either supernate or loose pellet and resuspension in a buffer. This is often followed by a sucrose gradient spin in which the band containing the membrane fraction is removed.

2.2. Reconstitution of Vesicular Fragments (mVs)

For preparing liposomes containing organelles, the procedure is similar to that for the preparation of cellular membranes. There are some minor differences because the desire is now to leave the plasma membrane behind. First, the organelle must be purified and then the liposomes should be created for incorporation. We will begin by discussing the purification of rat brain synaptic vesicles as an example.

2.2.1. Preparation of rat brain synaptic vesicles

Approximately 14 frozen rat brains are fragmented in a mortar using a pistol while pouring liquid N₂ over the tissue. The brain fragments are added to 140 ml of 320 mM sucrose buffer in a homogenizer. AEBSF or PMSF can be added to eliminate protease activity. The suspension is then homogenized using five (up/down) strokes at 900 rpm in glass Teflon homogenizer. The suspension is then centrifuged at 1000 *g* for 10 min. The supernate is kept and the pellet discarded. The resulting supernatant is centrifuged at 15,000 *g* for 20 min. The pellet is saved and the supernate discarded. The pellet is resuspended in 120 ml of 320 mM sucrose buffer and centrifuged at 15,000 *g* for 20 min. The pellet is saved and the supernate discarded. The pellet is resuspended in 13 ml of 320 mM sucrose buffer. The solution is homogenized using a glass Teflon homogenizer with five (up/down) strokes at 900 rpm. Ice cold dH₂O is added (117 ml) and mixed as best as possible. Within one minute of adding the ice cold dH₂O, add 1 ml of 1M HEPES-NaOHⁱ (pH 7.4). Let the solution remain on ice for 30 min. The solution is then centrifuged at 15,000 × *g* for 20 min. The supernate is saved and the pellet discarded. The supernatant is centrifuged at 20,000 *g* for 2 hours. The pellet is resuspended in 6–8 (depending on consistency) mL of 40 mM sucrose and homogenized with 5 (up/down) strokes at 1200 rpm. A 200 mM sucrose/400 mM sucrose gradient is created. The suspension is added to the gradient and centrifuged at 65,000 *g* for 5 h. The 200 mM/400 mM interface band is removed using 10 cc syringe with a #20 × 1.5 needle (3–4 ml). The sample is sheered twice through the needle and run on an S-1000 column. Column fractions can then be tested for the presence of synaptic vesicles (by anti-VAMP antibody and/or other vesicular markers) and combined (current preparation by Dixon Woodbury, see [9] for Torpedo synaptic vesicle preparation).

2.2.2. Preparation of fusigenic vesicles

Synaptic vesicles are quite small, in the sub-micron range [13]. Observing individual fusion events would be quite challenging even with modern day optics. This is why planar lipid bilayers or a patch clamp setup are used for observing fusion events. Even with the use of a planar lipid bilayer setup, the vesicles do not possess large enough changes in membrane capacitance for direct observation due to the small amount of total membrane that is incorporating. Therefore, the creation of larger vesicles (mSVs) that contain vesicle membranes is desirable. We will discuss two techniques that allow for the direct electrical measurement of change upon incorporation of modified vesicles into the planar lipid bilayer membrane. These two techniques are the nystatin and ergosterol technique and the capacitance change technique.

2.2.3. The nystatin/ergosterol technique

The nystatin/ergosterol technique is based on the interaction of nystatin with ergosterol and cholesterol. Ergosterol is the plant equivalent of cholesterol. However, the two compounds vary in composition. This is what is responsible for the antifungal properties of nystatin. In the presence of ergosterol, nystatin forms non-specific cation channels. However, the same is not true for cholesterol. These cation pores breakdown the stability of the fungal membrane. Addition of nystatin and ergosterol into liposomes creates fusigenic artificial vesicles (AVs) with cation pores in the membrane. When these vesicles incorporate into lipid bilayers that do not contain nystatin, the channels collapse as the nystatin and ergosterol disperse into the membrane. The collapsing channels can be viewed as spikes. These vesicles can be prepared using a wide variety of lipid compositions. However, the general composition is a mixture of PE:PC:PS:Ergosterol and nystatin. The technique was originally developed by Woodbury and Miller in 1990 [14]. A modified procedure is presented here.

2.2.4. Preparation of nystatin ergosterol fusigenic vesicles

PE:PC:PS:Ergosterol at a ratio of 2.1/0.9/1/1 (by weight) can be dissolved in 10 mg/ml chloroform. Nystatin should be added with a final concentration 50 ng/ml. Evaporate the chloroform from the mixture using nitrogen or argon gas until a dry plaque can be seen on the bottom of a 13 × 100 mm test tube. After evaporation, add either NaCl or KCl solution (150 mM with 8–10 mM HEPES, pH 7.2) to the test tube to bring the final lipid concentration to 10 mg/ml. Vortex the mixture for 5 min until cloudy. Then, sonicate in a water bath sonicator (at room temperature) for a total of 90 s. After the first 60 s of sonication, the mixture should become translucent. Swirl the mixture before sonicating for the remaining 30 s. The liposomes can be quick frozen in liquid nitrogen or a dry ice/ethanol bath and stored until use [9].

The fusigenic liposomes are added to a bilayer chamber containing either a NaCl or KCl bath (depending on how the liposomes were reconstituted). A gradient is created across the bilayer membrane until a fusion event is observed. Fusion events are visible as spikes that represent the incorporation of nystatin channels in the membrane and the inevitable collapse of these channels that result from the lack of ergosterol in the bilayer membrane.

2.2.5. The jumping voltage capacitance change technique

Incorporation of large vesicles or granules can be observed by monitoring changes in capacitance that occur when the vesicle or granule membrane becomes continuous with the bilayer membrane. Since most protocols for bilayer fusion experiments require the individual to perform the experiment in voltage clamp mode to promote fusion, observing capacitance changes at the same time can become difficult. This can be overcome by programming the software on a bilayer setup to do repeated short capacitance measurements while holding the voltage in between measurements. This information can be saved by enabling the notebook function (using HEKA software) and saving the notebook file periodically or by programming a capacitance measurement followed by a holding voltage sequence (using p-CLAMP software in the save mode). Thus, capacitance change can be recorded alternately with membrane holding voltage. The information can be combined and plotted using a program such as EXCEL. This method is not ideal for small vesicles undergoing complete fusion where capacitance change may simply result in brief spikes or what appears to be increased noise.

Figure 1 demonstrates the incorporation of t-SNARE vesicles into a DOPC:DOPS phospholipid bilayer using HEKA 9 and pulse software. The mSPVs were created by incorporating purified syntaxin 1-A and SNAP-25 (25 $\mu\text{g}/\text{ml}$) into fusogenic liposomes. Nystatin/ergosterol liposomes were prepared as described in section 2.2.4 with the following exception. Instead of a PE:PC:PS mixture, an equivalent amount of just DOPC:DOPS in a 7:3 ratio was used. Nystatin and ergosterol were added to the vesicles only as a secondary way to observe fusion. Liposomes were resuspended in 150 mM KCl, 8 mM HEPES. Bilayer membranes were formed using VAMP containing lipids. VAMP containing lipids were 7:3 DOPC:DOPS (50–100 μl) with 1 μl of VAMP (625 ng/ml). The membrane was formed and allowed to stabilize prior to the addition of t-SNARE vesicles to

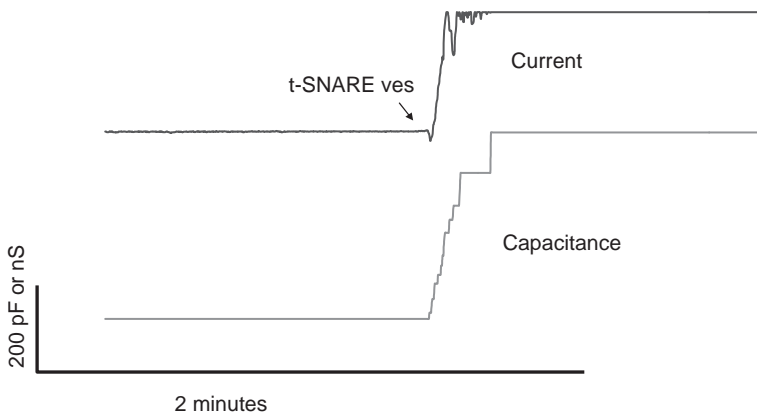


Figure 1 Vesicles containing t-SNARE proteins were added to a bilayer bath and stirred. The vesicles interact with the v-SNARE, VAMP, located in the bilayer membrane. The interaction is noted as step increases in capacitance and conductance demonstrating that the mSVs are docked and forming a fusion pore.

the bath. Interaction of t-SNARE vesicles with VAMP in the vesicular membrane is observed as step increases in capacitance and conductance [15].

3. IMMUNOFLUORESCENCE AND LIPOSOMES

In the 1970s, fluorescent probes began to be used to examine lipid bilayers [16, 17]. The initial questions were purely scientific looking at dynamics and binding properties of fluorescent probes to the lipids. By the late 1970s, fluorophore-quencher-loaded liposomes were being used to examine antibody mediated cell cytotoxicity [18] and by the early 1980s a fluorescence assay was developed to monitor vesicle fusion and lysis [19].

3.1. Immunofluorescence

Liposomes can be visualized using fluorescent lipids, creating the liposomes in fluorescent solutions or through the use of fluorescent antibodies. Multiple lipids including PE, PC and PS can be purchased in fluorescent forms. These include NBD bound (green), rhodamine bound (red), dansyl bound (blue), pyrene bound as well as fluorescence. Table 1 presents some of the fluorescent lipids that are available today.

Table 1 Immunofluorescent lipids

Lipid	Excitation (nm)	Emission (nm)	Area of label
PA (18:1–12:0 NBD)	464	531	Fatty acid
PC (18:1–6:0 NBD)	464	531	Fatty acid
PI (BIODIPY-FL)	505	513	Sn-acyl chain
PI (BIODIPY-TMR-X)	542	547	Sn-acyl chain
PI (BIODIPY-TR-X)	589	617	Sn-acyl chain
PE (18:1 Dansyl)	336	513	Head group
PE (18:1 Fluorescein)	440	515	Head group
PE (18:1 Lissamine Rodamine)	490	571	Head group
PE (18:1 Pyrene)	357	379	Head group
PS (18:1 Dansyl)	340	578	Head group
PS (18:1 NBD)	460	534	Head group
PS (16:0, 6:0-N-NBD) or (16:0, 12-N-NBD)	460	534	Fatty acid
PS (18:1, 6:0-N-NBD) or (18:1, 12-N-NBD)	460	534	Fatty acid

The table presents some of the fluorescent lipids available today for PA, PC, PI, PE, and PS. When deciding which fluorescent lipid to use or which combination of lipids to use, the excitation and emission of the fluorescence as well as the site of attachment are to be considered.

If the desire is to visualize a protein within the membrane of a liposome, an antibody against the incorporated protein can be used. The antibody can be labeled to be fluorescent or a secondary fluorescent antibody can be used. Using a secondary fluorescent antibody can increase the sensitivity of the assay and secondary fluorescent antibodies are available in a spectrum of colors with Alexa fluors being some of the brightest. When choosing a secondary antibody, make sure your secondary antibody is highly absorbed so that background fluorescence is eliminated. We have also discovered that a red fluorescent such as a 568 is better than a green fluorescent such as 488 when working with liposomes if using a fluorescent microscope.

3.2. Fluorescent Microscopy

Fluorescent microscopy can be used to examine fluorescent liposomes, fluorescent reconstituted membranes, fluorescently labeled membrane proteins, or interactions of fluorescent antibodies with the reconstituted liposomes. When working with liposomes, visualizing the interactions of the liposomes is one of the greatest challenges. Fluorescence makes these small structures, which are generally not clearly visible in a light microscope, become clearly visible. The mSVs created by reconstitution of synaptic vesicles into liposomes are still in the sub-micron range, at the limits of the optics for a normal light microscope. Labeling synaptic vesicle proteins allows one to visualize mSVs. [Figure 2](#) shows the fluorescent microscopic image of synaptic vesicles labeled using an anti-mouse Alexa fluor 488 secondary antibody (see [Section 4.3](#) for details).

3.3. Vesicle Plating

When plating liposomes, synaptic vesicles or mSVs, two methods have commonly been used. The difference is only in the plating material. A pre-made plating solution of poly-D-lysine or Cell-Tak will do. For the experiments described here,

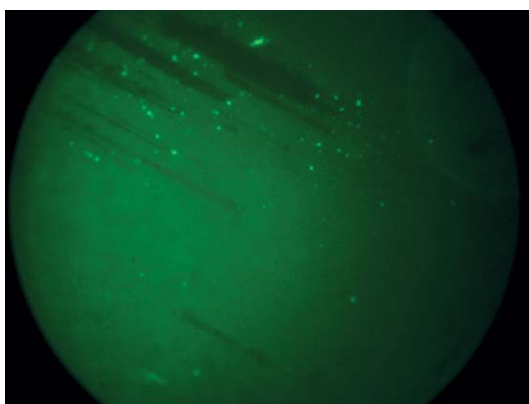


Figure 2 Synaptic vesicles were plated onto a poly-D-lysine coated coverslip and incubated with mAb10F5 in PBS within a Falcon 100B petri dish. The coverslip was washed three times with PBS before incubation with Alexa Fluor 488. Green fluorescent dots are actually clusters of synaptic vesicles at $10 \times$ gain.

a poly-D-lysine solution coated onto coverslips placed in a Falcon 100B petri dish or wells was performed. However, poly-D-lysine or Cell-Tak coated slides can be used as well. Plating is necessary for immunofluorescence studies in order to hold the vesicles or liposomes in place so that solution changes, washes, and different antibodies can easily be applied. Whether to use coverslips, slides or wells depends on the layout of the experimental design. If the desire is to simply look at the liposomes using a light microscope, then slides are fine. However, if the plan is to use immunofluorescence, coverslips or wells become a necessity. Coating coverslips poses different advantages and disadvantages. Coated coverslips can easily be removed. The coverslips can be placed in single well dishes such as falcon 100B or multi-well plates can be used. This allows for washing of the coverslip to be conducted in separate chambers and also allows for antibody treatments to be conducted in different chambers. However, there is a greater potential for vesicle removal during transferring of the coverslip.

When coating multi-well plates, one needs to remember that the lens objective must be able to enter the well and descend to a point where the liposomes are capable of being visualized. A six well plate will work. Higher number wells usually pose a problem. Using single well or multi-well plates allows for solutions to be changed more readily between antibody additions. [Figure 3](#) demonstrates liposomes plated onto poly-D-lysine coated wells.

3.4. Confocal Microscopy

Confocal microscopy offers several advantages over basic fluorescent microscopy. Using confocal microscopy allows one to have better control of the depth of field. One can eliminate “out-of-focus” information and can collect serial optical sections from thick specimens. This allows for extremely high-quality images to be obtained from specimens prepared for basic fluorescent microscopy.

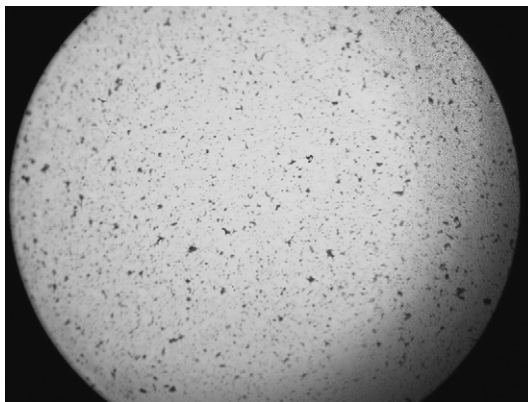


Figure 3 Liposomes made of PS and PC (10 mg/ml) in PBS were plated onto wells coated with poly-D-lysine for 2 h at 4 °C. The wells were gently washed three times with PBS. Black dots are actually clusters of liposomes at 10 × gain (×10 CP-ACHROMAT/0.25 NA).

Confocal imaging was created by Marvin Minsky, and patented in 1957. Confocal imaging is achieved by scanning one or more focused beams of light, usually from a laser or arc-discharge source, across the specimen. The point of illumination is brought to focus in the specimen by the objective lens, and laterally scanned. The sequences of points of light from the specimen are detected by a photomultiplier tube through a pinhole, and the output is built into an image displayed by the computer. An advantage of this technique is the clearer images that can be obtained and the ability to put together a 3-D image from the serial optical sections acquired [WR 1].

4. AUTOIMMUNE ANTIBODIES

When antibodies are produced that recognize constituents of our own bodies, referred to as *self*, we categorize these antibodies as autoreactive or autoimmune antibodies. These antibodies can be fairly harmless or result in the development of a disease state within the body. Any disease that results from the presence of autoimmune antibodies is classified as an autoimmune disease. Examples of autoimmune diseases include diabetes mellitus type 1 (IDDM), Sjögren's syndrome, Hashimoto's thyroiditis, Graves' disease, rheumatoid arthritis (RA) and Sydenham's chorea. The diseases that arise are generally the result of misidentification of the antibody that was originally produced against a viral or bacterial invader.

4.1. Antiphospholipid Antibodies

A classification of autoimmune antibodies exists that binds specifically to lipids. These antibodies are known as antiphospholipid antibodies or APLs. The autoreactivity of these antibodies can cause problems related to the heart, vascular system and the central nervous system. One way in which APLs affect the central nervous system is by decreasing blood flow to the brain. The blood supply to a particular part of the brain may be disrupted due to autoimmune vasculitis (blood vessel inflammation) or as the result of thrombi (blood clots) or emboli (freely moving clots) [20]. Formation of thrombi may be promoted by activation of endothelial cells by the antiphospholipid antibodies [21] or by interactions of these antibodies with platelets or other factors in the blood coagulation pathway [22]. The presence of these antibodies not only leads to arterial and/or venous thrombosis but also increases the risk of miscarriage in women. When antiphospholipid antibodies promote these symptoms the, patient is diagnosed with antiphospholipid syndrome (APS) or Hughes syndrome [21,23].

Antiphospholipid antibodies (APLs) are a family of immunoglobulins directed against negatively charged phospholipids such as cardiolipin and PS or against a phospholipid cofactor. Phospholipid cofactors include plasma membrane proteins such as β 2 glycoprotein I (β 2-GPI), prothrombin, protein C, protein S, and annexin V. During non-autoimmune disease state, the APLs bind antigens in the absence of a cofactor. During an autoimmune disease, the APLs actually require the

binding of a phospholipid cofactor. In fact, the production of thrombi can be associated with the presence of antibodies to just the β 2-GPI cofactor [24].

4.2. M6 Antibody

Group A streptococcal infection can lead to the development of autoimmune disorders that proceed pharyngitis [25–27]. These disorders include acute rheumatic fever (ARF), and pediatric autoimmune neuropsychiatric disorders associated with streptococcal infection, PANDAS [28], and Sydenham's chorea, a movement disorder that can be autoimmune mediated as a consequence of acute rheumatic fever [29]. The autoreactive antibodies generated in these disorders are intended to recognize the streptococcal M protein antigen. The M protein protects the streptococcal bacteria from phagocytosis by white blood cells.

Symptoms of Sydenham's chorea include involuntary, purposeless movements of the limbs and abnormal muscle contractions (known as chorea), and can be associated with obsessive compulsive behavior, other behavioral abnormalities and/or language disorders [30–32]. The development of obsessive compulsive behavior is an overlap between patients with Sydenham's chorea and individuals with PANDAS. These symptoms develop weeks to months after Group A streptococcal infection and are believed to be the result of an autoimmune-mediated process reacting within the basal ganglia [26]. The involvement of the basal ganglia is supported by the role of this region in controlling movements as well as controlling behavior.

It is interesting to note that patients with Sydenham's chorea and children with PANDAS possess larger basal ganglion regions (caudate, putamen and globus pallidus) than controls [33,34] and the same monoclonal antibody associated with rheumatic fever, D8/17, is more pronounced in children with Sydenham's chorea and PANDAS [35]. D8/17 is a cross-reactive antibody recognizing the streptococcal M protein. The specific M type that is recognized by D8/17 corresponds to group A streptococcal protein M6 [36].

4.3. M6 Antibody Interacting with Synaptic Vesicles

Antibodies generated against the M6 epitope have been produced in mouse. Figure 4 demonstrates the interaction of one of these autoreactive M6 antibodies, mAb10F5, with synaptic vesicles containing liposomes. Briefly, poly-D-lysine was plated onto 22 mm Corning coverslips placed in falcon 100B petri dishes and allowed to dry overnight at room temperature. Rat brain purified synaptic vesicles described earlier were diluted 1:200 in PBS (Fisher) and were allowed to settle on the poly-D-lysine coated coverslips for 2 h at 4 °C. The coverslip was submerged in Odyssey Blocking Buffer for 1 h. After 1 h, ~0.1–0.2% triton X-100 was added to the buffer and incubated for 30 mins. Streptococcal autoimmune antibody mAb10F5 was added to the solution (1:1250 in PBS) and incubated overnight at 20 °C. The coverslips were then washed two times with PBS and incubated for 1 h with Alexa Fluor 488 in blocking buffer (1:2000). The coverslip was rinsed with PBS 3X and examined for the presence of immunofluorescence using fluorescent microscopy.

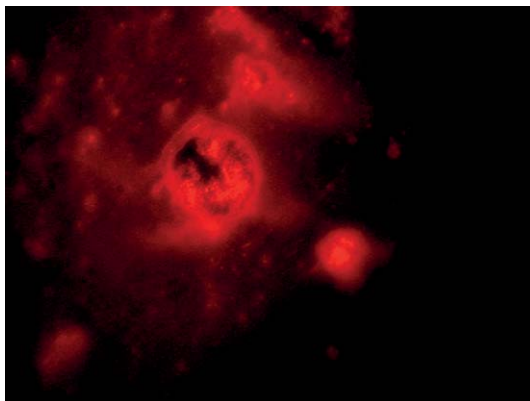


Figure 4 Modified synaptic vesicles (mSVs) were prepared and plated onto a poly-D-lysine coated coverslip placed in Falcon 100B petri dish. Liposomes were treated with blocking buffer and triton X-100 prior to incubating with streptococcal mAb10F5 overnight at 20 °C. The coverslips were then washed three times with PBS and incubated for 1 h with Alexa Fluor 568 diluted in blocking buffer. The coverslips were gently washed three times with PBS. Both larger liposomes and enclosed synaptic vesicles or mSVs within the center of the larger liposomes at 100 × magnification (×100 CP-ACHROMAT/1.25 NA oil) exhibited interaction with streptococcal mAb10F5.

4.4. M6 Antibody Interacting with Proteins

Since the M6 antibody interacted with synaptic vesicles, a question arose whether the antibody interacts with a protein within the vesicular membrane or with a lipid? Prime candidates for proteins targets are the vesicle associated membrane protein, VAMP, and rabphilin 3A. VAMP serves as the vesicular docking protein and is involved in pore formation during neurotransmitter release. Rabphilin 3A is a trafficking protein that promotes movement of vesicles in the reserve pool so that the vesicles can dock and release neurotransmitter. Interaction of the autoreactive antibody with either of these proteins would explain one possible mechanism for how a streptococcal antibody could promote a neurological disorder.

4.5. M6 and Liposomes

The M6 antibody bound the synaptic vesicles (Fig. 3) and the mSVs (Fig. 4). The question is would it bind the liposomes without vesicular protein present? Both synaptic vesicles and the mSVs we created contain PC and PS. If M6 is an antiphospholipid antibody it may also bind to PS. Figure 5 demonstrates the interaction of pure liposomes with the M6 antibody. Briefly, PC:PS liposomes were prepared as described in section 1.4. The liposomes were vortexed and sonicated then plated onto poly-D-lysine coated wells as described in section 3.3. Liposomes were allowed to settle on the poly-D-lysine coated coverslips for 2 h at 4 °C. The coverslip was submerged in Odyssey Blocking Buffer for 1 h. After 1 h, 0.1% triton X-100 was added to the buffer and incubated for 30 min. The liposomes were incubated overnight with mAb10F5 (1:1250). The samples were washed with PBS two times and incubated for 1 h with Alexa Fluor 568 in blocking buffer (1:2000). The samples were rinsed with PBS 3X then imaged using fluorescent microscopy (Fig. 5).

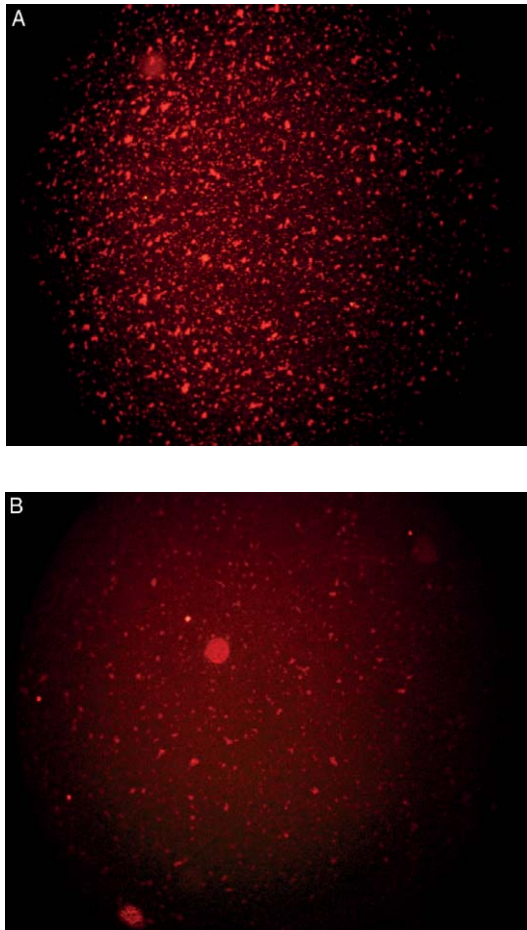


Figure 5 Interaction of mAb10f5 with PC:PS liposomes. (A) Liposomes made of 7:3 PS:PC were plated onto the wells coated with poly-D-lysine and were allowed to settle for 2 h at 4 °C. Liposomes were treated with blocking buffer and triton X-100 and incubated with streptococcal mAb10F5 overnight at 20 °C. The wells were then washed with PBS and incubated for 1 h with Alexa Fluor 568 antibody diluted in blocking buffer. The wells were gently washed with PBS prior to imaging. Red fluorescent dots are liposomes at 10 × gain (×10 CP-ACHROMAT/0.25 NA) which interacted with mAb10F5. (B) Liposomes made of 7:3 PS:PC were treated with only secondary Alexa Fluor 568 antibody as a control.

5. DISCUSSION AND CONCLUSIONS

Several techniques can be used to observe liposome structures once created and we have discussed only a few of them here. We can examine incorporation of membranes into other structures such as the incorporation of synaptic vesicles membranes into liposomes for conducting fusion assays using planar lipid bilayers and either the nystatin/ergosterol technique or the capacitance change technique.

We can use immunofluorescence to observe liposomal sub-microscopic structures directly and to even examine the level of interaction of antibodies with our liposomes. We can use liposomes to narrow the point of interaction of an autoimmune antibody by starting with reconstituted cellular membranes and working our way down to the proteins within the cellular or vesicular membrane. These advances in liposome research have allowed us to examine the sub-microscopic world around us.

Liposomes and the structures we can create with them open a door for observing the interactions of autoimmune antibodies not only with the proteins contained within the liposomes, but also with the lipids within the liposomes. The PC:PS liposomes described in [Section 4.5](#) were positive for M6 antibody, suggesting that the M6 antibody may act as an APL antibody on top of having interactions with *self* protein antigens such as myosin. The degree of APL activity of the antibody is under investigation.

However, anti-PS antibodies are not common. Even in disorders involving multi-system dysfunction, less than 20% of patients possess antiphospholipid antibodies [37]. When examining patients specifically with APL antibodies, the lipid bound by the antibody differs from patient to patient with only about 21% (3/14) of these patients possessing anti-PS antibodies [24]. Therefore, a high degree of interaction of the autoimmune antibody with the lipids could not be expected when using PC:PS containing liposomes. Thus, this combination of lipids can be used for examining specific autoimmune protein/antibody interactions as well as a way to test for potential APL activity.

6. FUTURE DIRECTIONS

We intend to continue studying the interactions of M6 antibodies with synaptic vesicle components and to determine which synaptic proteins interact with these antibodies. We will also be performing immunofluorescent assays to determine the specificity of the interaction of the mAb10F5 antibody with phospholipids.

7. ACKNOWLEDGEMENTS

We thank Dr. Dixon Woodbury for supplying the synaptic vesicles used in these experiments and for his helpful input. We also thank Dr. Vincent Fischetti for providing the M6 antibody, mAb10F5. Without the generosity of these individuals, this project would not have been accomplished. We also acknowledge Dr. Bhanu Jena for use of equipment that provided the data for [Fig. 1](#).

REFERENCES

- [1] A.D. Bangham, R.W. Horne, A correlation between surface charge and coagulant action of phospholipids, *J. Mol. Biol.* 8 (1964) 660–668.

- [2] P. Mueller, D.O. Rudin, H.T. Tien, W.C. Wescott, Reconstitution of cell membrane structure *in vitro* and its transformation into an excitable system, *Nature* 194 (1962) 979–980.
- [3] G. Sessa, G. Weissmann, Phospholipid spherules (liposomes) as a model for biological membranes, *J. Lipid. Res.* 9 (1968) 310–318.
- [4] W.S. Davidson, A. Jonas, D.F. Clayton, J.M. George, Stabilization of alpha-synuclein secondary structure upon binding to synthetic membranes, *J. Biol. Chem.* 273 (1998) 9443–9449.
- [5] D.M. Michaelson, G. Barkai, Y. Barenholz, Asymmetry of lipid organization in cholinergic synaptic vesicle membranes, *Biochem. J.* 211 (1983) 155–162.
- [6] E. Jo, J. McLaurin, C.M. Yip, P.S.t. George-Hyslop, alpha-Synuclein membrane interactions and lipid specificity, *J. Biol. Chem.* 275 (2000) 34328–34334.
- [7] S. Moses Dennison, M.E. Bowen, A.T. Brunger, B.R. Lentz, Neuronal SNAREs Do Not Trigger Fusion between Synthetic Membranes but Do Promote PEG-Mediated Membrane Fusion, *Biophys. J.* 90 (2006) 1661–1675.
- [8] M.L. Kelly, D.J. Woodbury, Ion Channels from Synaptic Vesicle Membrane Fragments Reconstituted into Lipid Bilayers, *Biophys. J.* 70 (1996) 2593–2599.
- [9] D.J. Woodbury, K. Rognlien, The t-SNARE syntaxin is sufficient for spontaneous fusion of synaptic vesicles to planar membranes, *Cell. Biol. Int.* 24 (2000) 809–818.
- [10] B.M. Alving, B. Banerji, W.E. Fogler, C.R. Alving, Lupus anticoagulant activities of murine monoclonal antibodies to liposomal phosphatidylinositol phosphate, *Clin. Exp. Immunol.* 69 (1987) 403–408.
- [11] N.P. Morris, E. Consiglio, L.D. Kohn, W.H. Habig, M.C. Hardegree, T.B. Helting, Interaction of fragments B and C of tetanus toxin with neural and thyroid membranes and with gangliosides, *J. Biol. Chem.* 10 (1980) 6071–6076.
- [12] V.P. Whittaker, I.A. Michaelson, R.J. Kirkland, The separation of synaptic vesicles from nerve-ending particles (“synaptosomes”), *Biochem. J.* 90 (1964) 293–303.
- [13] W.J. Betz, J.K. Angleson, The synaptic vesicle cycle, *Annu. Rev. Physiol.* 60 (1998) 347–363.
- [14] D.J. Woodbury, C. Miller, Nystatin-induced liposome fusion. A versatile approach to ion channel reconstitution into planar bilayers, *Biophys. J.* 58 (1990) 833–839.
- [15] M.L. Kelly, W.J. Cho, A. Jeremic, R.A. Hamdah, B.P. Jena, Vesicle swelling regulates content expulsion during secretion, *Cell Biol. Int.* 28 (2004) 709–716.
- [16] R.A. Badley, W.G. Martin, H. Schneider, Dynamic behavior of fluorescent probes in lipid bilayer model membranes, *Biochem.* 12 (1973) 268–275.
- [17] M.T. Flanagan, T.R. Hesketh, Electrostatic interactions in the binding of fluorescent probes to lipid membranes, *Biochim. Biophys. Acta.* 298 (1973) 535–545.
- [18] B. Geiger, A.D. Schreiber, The use of antibody-coated liposomes as a target cell model for antibody-dependent cell-mediated cytotoxicity, *Clin. Exp. Immunol.* 35 (1979) 149–154.
- [19] D.A. Kendall, R.C. MacDonald, A fluorescence assay to monitor vesicle fusion and lysis, *J. Biol. Chem.* 257 (1982) 13892–13895.
- [20] A. Farzaneh-Far, M.J. Roman, M.D. Lockshin, R.B. Devereux, S.A. Paget, M.K. Crow, A. Davis, L. Sammaritano, D.M. Levine, J.E. Salmon, Relationship of antiphospholipid antibodies to cardiovascular manifestations of systemic lupus erythematosus, *Arthritis Rheum.* 54 (2006) 3918–3925.
- [21] P. Chen, Y. Lin, K. Wu, J.H. Yen, T.T. Ou, C.C. Wu, H.W. Liu, W.C. Tsai, Activation of endothelial cells by antiphospholipid antibodies—a possible mechanism triggering thrombosis in patients with antiphospholipid syndrome, *Kaohsiung. J. Med. Sci.* 22 (2006) 484–490.
- [22] B. Giannakopoulos, F. Passam, S. Rahgozar, S. Krilis, Current concepts on the pathogenesis of the antiphospholipid syndrome, *Blood* 109 (2007) 422–430.
- [23] G. Hughes, Hughes Syndrome (the antiphospholipid syndrome) Ten clinical lessons, *Autoimmun. Rev.* 7 (2008) 262–266.
- [24] A. Parodi, M. Drosera, L. Barbieri, A. Rebor, Antiphospholipid antibody system in systemic sclerosis, *Rheumatology (Oxford)* 40 (2001) 111–112.
- [25] C.A. Kirvan, S.E. Swedo, *et al.* Streptococcal mimicry and antibody-mediated cell signaling in the pathogenesis of Sydenham’s chorea, *Autoimmunity* 39 (2006) 21–29.
- [26] R.C. Dale, Streptococcus pyogenes and the brain: living with the enemy, *Rev. Neurol.* 37 (2003) 92–97.

- [27] A. Quinn, K. Ward, V.A. Fischetti, M. Hemric, M.W. Cunningham, Immunological relationship between the class I epitope of streptococcal M protein and myosin, *Infect. Immun.* 66 (1998) 4418–4424.
- [28] S.J. Perlmutter, M.A. Garvey, X. Castellanos, B.B. Mittleman, J. Giedd, J.L. Rapoport, S.E. Swedo, A case of pediatric autoimmune neuropsychiatric disorders associated with streptococcal infections, *Am. J. Psychiatry* 155 (1998) 1592–1598.
- [29] E.M. Ayoub, L.W. Wannamaker, Streptococcal antibody titers in Sydenham's chorea, *Pediatrics* 38 (1966) 946–956.
- [30] M.C. Cunningham, D.P. Maia, A.L. Teixeira, Jr., F. Cardoso, Sydenham's chorea is associated with decreased verbal fluency, *Parkinsonism Relat. Disord.* 12(3) (2008) 165–167.
- [31] M.T. Mercadante, M.C. Campos, M.J. Marques-Dias, E.C. Miguel, Leckman, Vocal tics in Sydenham's chorea, *J. Am. Acad. Child. Adolesc. Psychiatry* 36 (1997) 305–306.
- [32] F. Ashbarh, A.B. Negrao, V. Gentil, D.M.T. Zanetta, J.A. da Paz, M.J. Marques-Dias, M.H. Kiss, Obsessive-compulsive and related symptoms in children and adolescents with rheumatic fever with and without chorea: A prospective 6-month study, *Am. J. Psychiatry* 155 (1998) 1122–1124.
- [33] A.J. Church, F. Cardoso, R.C. Dale, A.J. Lees, E.J. Thompson, G. Giovannoni, Anti-basal ganglia antibodies in acute and persistent Sydenham's chorea, *Neurology* 59 (2002) 227–231.
- [34] J.N. Giedd, J.L. Rapoport, M.J. Kruesi, C. Parker, M.B. Schapiro, A.J. Allen, H.L. Leonard, D. Kaysen, D.P. Dickstein, W.L. Marsh, Sydenham's chorea: Magnetic resonance imaging of the basal ganglia, *Neurology* 45 (1995) 2199–2202.
- [35] S.W. Swedo, H.L. Leonard, B.B. Mittleman, A.J. Allen, J.L. Rapoport, S.P. Dow, M.E. Kanter, F. Chapman, J. Zabriskie, Identification of children with pediatric autoimmune neuropsychiatric disorders associated with streptococcal infections by a marker associated with rheumatic fever, *Am. J. Psychiatry* 154 (1997) 110–112.
- [36] E. Kemeny, G. Husby, R.C. Williams, Jr., J.B. Zabriskie, Tissue distribution of antigen(s) defined by monoclonal antibody D8/17 reacting with B lymphocytes of patients with rheumatic heart disease, *Clin. Immunol. Immunopathol.* 72 (1994) 35–43.
- [37] M. Arbuckle, M. McClain, M. Rubertone, R.H. Scofield, G.J. Dennis, J.A. James, J.B. Harley, Development of autoantibodies before the clinical onset of systemic lupus erythematosus, *N. Engl. J. Med.* 349 (2003) 1526–1533.

INTERACTIONS OF PHOSPHOLIPID BINDING PROTEINS WITH NEGATIVELY CHARGED MEMBRANES: β_2 -GLYCOPROTEIN I AS A MODEL MECHANISM

Snežna Sodín-Šemrl,^{1,*} Mojca Frank,¹ Aleš Ambrožič,¹ Janez Pavlič,^{2,3} Vid Šuštar,⁴ Saša Čučnik,¹ Borut Božič,¹ Tanja Kveder,¹ and Blaž Rozman¹

Contents

1. Introduction	244
2. β_2 -Glycoprotein I, as an Example of Plasma Proteins	245
2.1. Structural Requirements of β_2 -GPI for Binding to Phospholipid Bilayers	246
2.2. Functional Similarities (and Structural Differences) Between β_2 -GPI and Apolipoproteins	247
2.3. Structural Similarities Between Human β_2 -GPI and Other Proteins	248
2.4. Different Forms of β_2 -GPI with Posttranslational and Other Modifications	249
3. Influence of the Phospholipid Membrane on β_2 -Glycoprotein I Binding (<i>In Vitro</i> Models)	254
3.1. Mechanism of β_2 -GPI Binding to Phospholipid Membrane	254
3.2. Changes in Membrane Properties Upon β_2 -GPI Binding	257
3.3. Binding of β_2 -GPI to the Membrane as a Function of β_2 -GPI Concentration	258
3.4. Phospholipid Membrane Properties Important for β_2 -GPI Binding	259
4. Influence of Environment or Millieu	261
4.1. The Influence of Ionic Strength and Divalent Ion Concentration on β_2 -GPI Membrane Binding	261
4.2. The Influence of pH on β_2 -GPI Membrane Insertion	263
4.3. The Influence of EDTA on β_2 -GPI Membrane Binding	264
4.4. The Influence of Albumin and γ -Globulin on β_2 -GPI Membrane Binding	264

* Corresponding author. Tel.: +383-1-522-5596; Fax: 386-1-522-5598;
E-mail address: ssodin1@yahoo.com.

¹ Department of Rheumatology, University Medical Centre, Vodnikova 62, SI-1000 Ljubljana, Slovenia

² College of Health Studies, University of Ljubljana, Poljanska 26, SI-1000 Ljubljana, Slovenia

³ Laboratory of Physics, Faculty of Electrical Engineering, University of Ljubljana, Trzaska 25, SI-1000 Ljubljana, Slovenia

⁴ Laboratory of Clinical Biophysics, Faculty of Medicine, University of Ljubljana, Lipiceva 2, SI-1000 Ljubljana, Slovenia

5. Implication of <i>In Vitro</i> Practical and Theoretical Models to the Clinical Setting	264
5.1. From <i>In Vitro</i> Vesiculation to Microparticles (in absence and presence of anti- β_2 -GPI antibodies)	264
5.2. Role of Phospholipids and β_2 -GPI in the Development and in Maintaining the Autoimmune Response	266
6. Concluding Remarks	268
References	268

Abstract

The way proteins associate with the lipid bilayer defines not only their function, but in autoimmune diseases, such as antiphospholipid syndrome (APS), also represents the conformational change of an antigen necessary for the exposure of critical epitopes recognized by potential autoantibodies. These interactions between the antigen (bound to phospholipid bilayers) and its antibodies could lead to clinical implications. Our aim was to review and characterize the requirements of the plasma protein β_2 -glycoprotein I (β_2 -GPI), one of the major proteins implicated in autoantibody development in APS for interactions with phospholipids, to provide primary sequence and secondary structure information of its Vth phospholipid binding domain, and to perform a NCBI search for comparison between homology of the Vth β_2 -GPI domain with other known proteins. The second part addresses the effects of phospholipid membrane composition, charge, and specifically, the mechanism of interaction with artificial negatively charged membranes as *in vitro* model systems (vesicle and other studies). The third part focuses on the influence of environmental factors on β_2 -GPI–phospholipid binding, and the fourth part addresses antibody binding to membrane-bound β_2 -GPI, exposure of its epitopes, recognition by its autoantibodies, and the functional (clinical) implications (specifically in APS). The development of antigenicity is addressed, with an emphasis on human studies and pathogenicity of antibodies. In the future, we plan to concentrate also on the numerous, important and critical reports centered on cell-specific and receptor-mediated studies, which we have omitted in the present compilation, since they are beyond the scope of this chapter.

1. INTRODUCTION

Membrane proteins are generally divided into integral membrane proteins (with tight interactions within the phospholipid bilayer, such as transmembrane amphipathic proteins) and peripheral membrane proteins (proteins that adhere only temporarily to their associated biological membranes and could be released from the membrane by gentle extraction procedures). To interact with phospholipid bilayers, peripheral membrane proteins (which are synthesized as water-soluble proteins and can be attached to either the outer or inner leaflet of the plasma membrane) can be modified by lipid-binding tails and are thus directed to the membrane. This covalent attachment is called lipidation or acylation and is possible with different lipid groups, such as prenyl, myristyl, and palmitoyl groups. Palmitoylation can often be reversible, allowing proteins to be recruited to the membrane when necessary [1]. Glycosylphosphatidylinositol anchors are added to certain proteins that have had their single transmembrane domain cleaved off, thus leaving the protein bound to the exterior

leaflet of the plasma membrane with only the glycosylphosphatidylinositol anchor. These proteins could be released from the membrane *in vitro* by phosphatidylinositol-specific phospholipase C.

The reversibility of membrane binding is also critical for plasma proteins, such as β_2 -glycoprotein I (β_2 -GPI), which can interact with the phospholipid layer by electrostatic interactions, hydrophobic loops, and alpha helices. The flexibility of conformational orientation and reversibility between soluble state and membrane-bound state of plasma proteins are key features contributing to their recognition also by autoantibodies in autoimmune diseases.

The focus of this chapter will be primarily on the review and characterization of *in vitro* chemical, physical, molecular, and biochemical properties influencing β_2 -GPI and its binding to phospholipid membranes, while omitting its receptor mediated protein-protein interactions.

To elucidate these properties, the following will be addressed:

- β_2 -GPI, as an example of plasma proteins (characterization through homology and analogy studies, β_2 -GPI structural implications for membrane binding, posttranslational modifications such as glycosylation, dimerization, potential for electrostatic, hydrophobic interactions, and α helical configuration)
- Influence of the phospholipid membrane (such as composition, charge, curvature, fluidity)
- Influence of environment or milieu (physical and chemical factors such as ionic strength, pH and divalent ion concentration)
- Implication of *in vitro* practical and theoretical models to the clinical setting (translating *in vitro* vesiculation to *in vivo* settings generating microparticles, in absence and presence of anti- β_2 -GPI antibodies, and characterizing the role of phospholipids and β_2 -GPI in the development and in maintaining the autoimmune response)

2. β_2 -GLYCOPROTEIN I, AS AN EXAMPLE OF PLASMA PROTEINS

Plasma is the clear, almost colorless supernatant left over following the centrifugation of whole blood (with suspended red and white blood cells and other cellular components). Plasma proteins are mainly albumins, globulins and also include antibodies and blood-clotting proteins (coagulation factors).

The questions of how, why, and when water-soluble plasma proteins (such as β_2 -GPI) that normally circulate in plasma bind to lipid bilayers has been raised repeatedly. Since antiphospholipid syndrome (APS) is an autoimmune disease characterized by the persistence of antiphospholipid antibodies (aPL, among them also anti- β_2 -GPI), recurrent arterial or venous thromboses, and/or fetal death, it is critical to address what stimulates binding of β_2 -GPI to the phospholipid membrane.

Since similar structural motifs are often prerequisites for common functions, and since the multiple physiological functions of β_2 -GPI have not been fully elucidated, our aim was to address the following:

- What are the structural requirements of β_2 -GPI for binding to phospholipid bilayers?
- Are there functional similarities between β_2 -GPI and other structurally similar proteins such as complement control proteins (CCP) domain family?
- Which structural similarities between β_2 -GPI and other functionally similar proteins exist?

2.1. Structural Requirements of β_2 -GPI for Binding to Phospholipid Bilayers

β_2 -GPI, also known as apolipoprotein H (apoH), circulates in human plasma in free form (60%) and in lipoprotein-bound form (30–40% reported). β_2 -GPI is a 326 amino acid glycoprotein generated after the cleavage of its 19 amino acid hydrophobic N-terminal signal peptide (for review see Ref. [2]). The isoelectric point of β_2 -GPI is 5–7 [3] so the protein is negatively charged under a pH of 7.4. β_2 -GPI will not preferentially insert into negatively charged phospholipid layers; however its interactions with phospholipids has been considered the mechanism responsible for its physiological and pathogenic functions [4]. On the basis of algorithms, β_2 -GPI was calculated to contain 45% β -sheet, 18% turns, and 37% alpha helix structures [5].

β_2 -GPI is composed of four domains (with around 60 amino acids each), which are structurally similar, whereas the fifth domain (82 amino acids) contains an extra C-terminal loop (Cys³⁰⁶-Cys³²⁶), which is susceptible to proteolytic cleavage and is necessary for phospholipid binding.

Wurm proposed early on that both ionic and hydrophobic interactions were important for β_2 -GPI to bind phospholipid membranes [6]; however it was not until reports indicating that cleavage of β_2 -GPI between Lys³¹⁷ and Thr³¹⁸ in the Vth domain abolished its binding to anionic phospholipids, indicating this region to be essential [7].

The highly positively charged region between Cys²⁸¹ and Cys²⁸⁸ (CKNKEKKC) is predicted to be highly conserved and is critical for phospholipid binding [8]. This surface-exposed turn provides for the electrostatic interaction between the Vth domain of β_2 -GPI and phospholipids (Fig. 1). The region of amino acids (AA) 311–317 facilitates the insertion of β_2 -GPI in lipid membranes [9]. The β_2 -GPI four highly conserved AA ³¹³LeuAlaPheTrp³¹⁶ sequence and particularly Trp³¹⁶ is essential for β_2 -GPI insertion into the phospholipid layer [10] (Fig. 1).

In addition to electrostatic interactions and hydrophobic loops, critical membrane binding motifs are alpha helices that function more than just membrane anchors. They can serve as autoinhibitory domains to suppress soluble protein presence or its activity in plasma, as sensors or modulators of membrane curvature. Alpha helices can respond to and change membrane properties [11]. Several amphitropic proteins that control budding or tubule formation in cells have alpha-helical motifs, which are the most ubiquitous helical secondary structure in proteins. The insertion of the hydrophobic part of these helices generates an asymmetry in the lateral pressure of the two leaflets and induces positive curvature [11]. β_2 -GPI also has one short alpha helix (AA 263–266) and one ₃₁₀ helical motif (AA 320–322) in its Vth domain, presumably involved in the earlier mentioned changes in membrane

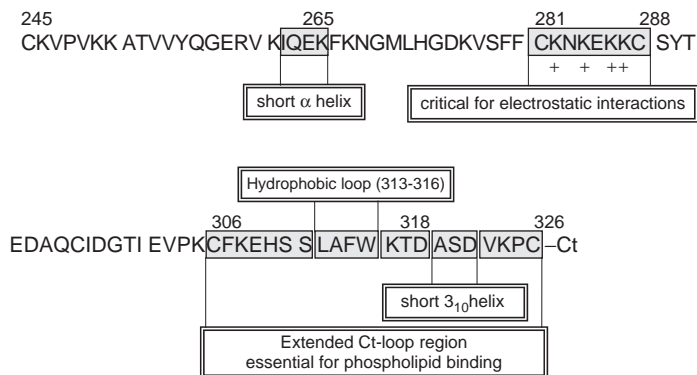


Figure 1 Schematic drawing of β_2 -GPI domain V primary amino acid sequence spanning from Cys²⁴⁵ to Cys³²⁶. The region between Cys²⁸¹ and Cys²⁸⁸ includes four Lys residues and is critical for phospholipid binding through electrostatic interactions, while the region between Cys³⁰⁶ and Cys³²⁶ contains a hydrophobic loop essential for phospholipid binding. There are three disulfide linkages in the Vth (Sushi-2) domain. Two helical motifs are found in the Vth domain of β_2 -GPI, a short α helix located between AA 263–266 and one 3_{10} helical turn motif (AA 320–322) located in the hydrophobic loop region close to the C-terminus [12]. The Vth domain is held together by three disulfide bonds.

properties [12] (Fig. 1). The general consensus from analysis of protein helices present in protein data bank is that 3_{10} helices comprise only 3–4% of all residues and are short, occurring frequently at the ends of α -helices and as connectors between two β -strands [13].

2.2. Functional Similarities (and Structural Differences) Between β_2 -GPI and Apolipoproteins

β_2 -GPI has been termed apoH [14], because around 30–40% of this protein is bound to lipoproteins, although it bears no structural similarities to other apolipoproteins [15]. In fact, β_2 -GPI significantly differs from other apolipoproteins in essential structural parameters, such as percentage of alpha-helical conformation and interaction with air-water interfaces [14]. Apolipoproteins A-I, A-II, C-I and E have a secondary structure with a much higher percentage of residues in alpha-helical configuration. Highly flexible proteins, such as Apo-A-I, A-II and C-I absorb rapidly and reversibly to air-water surfaces, whereas more rigid (classical globular proteins) interact more slowly and irreversibly. The surface activity of β_2 -GPI at neutral pH resembles that of globular proteins. Treatment with acid or base unfolds β_2 -GPI to such an extent that it becomes a more flexible protein and resembles more other loosely folded apolipoproteins. The secondary, tertiary and quaternary structure of β_2 -GPI is quite different from other apolipoproteins. This difference would be expected to affect protein–lipid interactions as well [14].

The conformation of apolipoproteins changes dramatically in presence of lipid, however the secondary and tertiary structures of β_2 -GPI may be quite similar in lipidated and lipid-free states, and it has been proposed that β_2 -GPI may associate

with plasma lipoproteins through protein–protein interactions rather than protein–lipid interactions [14]. The secondary structure of β_2 -GPI consists mainly of β pleated sheets and random coils with little α helices and is quite different from that of other well-characterized apolipoproteins. This difference in structure is true as well for the tertiary and quaternary structure of β_2 -GPI as determined by circular dichroism and would be expected to affect protein–protein and protein–lipid interactions [14]. In contrast to other apolipoproteins, lipid-free β_2 -GPI does not self-associate in aqueous solution [14].

2.3. Structural Similarities Between Human β_2 -GPI and Other Proteins

Structurally, β_2 -GPI is a noncomplement member of the CCP family [16]. Although β_2 -GPI belongs to the CCP family of proteins, its homology to CCP, to complement factor or to complement decay-accelerating factor, as determined by homology comparison using NCBI Basic local alignment search tool BLASTp, is below 35% identity. There are three other homologous proteins containing the first four consecutive CCP modules: vaccinia virus 35 kDa protein [17], measles virus-binding protein CD46 [18] and Hikaru genki protein and fragments of factor H [19]. Unlike other members of the CCP super-family that have been shown to be located on chromosome 1 in the human, β_2 -GPI has been assigned to chromosome 17 [20].

The amino acid sequence of β_2 -GPI is highly conserved in mammalian species, such as humans, primates, nonprimate monkeys and shows 84% homology to rat, bovine and mouse amino acid sequences, which also consist of five CCP domains. The first four domains similar to the ones of β_2 -GPI (around 60 amino acids each) function as protein–protein interaction domains in many different proteins (including cell surface proteins such as selectins, von Willebrand factor type D, complement regulatory proteins and others).

Based upon the predicted structure of the β_2 -GPI protein from the cDNA sequence, there are 22 Cys residues in human β_2 -GPI. These positions are conserved in bovine, rat, mouse and dog β_2 -GPI proteins. In contrast to bovine β_2 -GPI, where all 11 disulfide bonds have been mapped, the position of only six have been confirmed in humans, however it is reasonable to assume (based on the high homology between the two species) that the 11 disulfide bonds are identical in both species [21].

In 1984, Lozier *et al.* [22] performed a sequence homology search comparing β_2 -GPI to other known proteins (in a computerized data base »Atlas of protein sequence and structure«) and found it to be unique. There was no significant homology found over long segments with other known proteins. However, when the literature was checked further, they found that the amino terminal 20 amino acid residues of β_2 -GPI matched exactly the amino terminal sequence of a 54 kDa human serum protein with binding capability to human activated protein C, that was named »APC-binding protein« or »APC inhibitor« [23]. Purification of this APC-binding protein used heparin affinity chromatography and it is known that β_2 -GPI also binds heparin [24], indicating that there might be a tertiary similarity between both. β_2 -GPI is abundantly rich in proline (31 residues or 8.3%) and Cys

residues (22 residues or 6.2%) and there is tendency for the two (Cys-Pro) to appear together at regular intervals around 60 residues long. There are five Trp residues in β_2 -GPI, a high number, considering that Trp is the least abundant of the 20 amino acids in most proteins [22].

Domain V is also characterized by an unusual amino acid composition. The sequence is rich in Lys (18%) and the highest homology in NCBI BLASTp search performed found to be 76% identical to the human β_2 -GPI domain V was a protein similar to Chico protein from *Monodelphis domestica* (accession# XP_001370229). The same was also true for total human β_2 -GPI protein where the strongest similarity was found to be with a protein similar to Chico protein (75% identical). The Chico protein is a *Drosophila* protein homologue of vertebrate insulin receptor substrate proteins (IRS1-4) and is implicated in control of cell size, cell proliferation and overall body growth.

2.4. Different Forms of β_2 -GPI with Posttranslational and Other Modifications

There are many forms of posttranslational and other modifications (Fig. 2) that could influence the structure and function of the β_2 -GPI polypeptide molecule.

Each form reveals specific epitopes and different antibody binding sites many of which have been extensively and sometimes controversially described to be involved in the pathogenesis of APS [25].

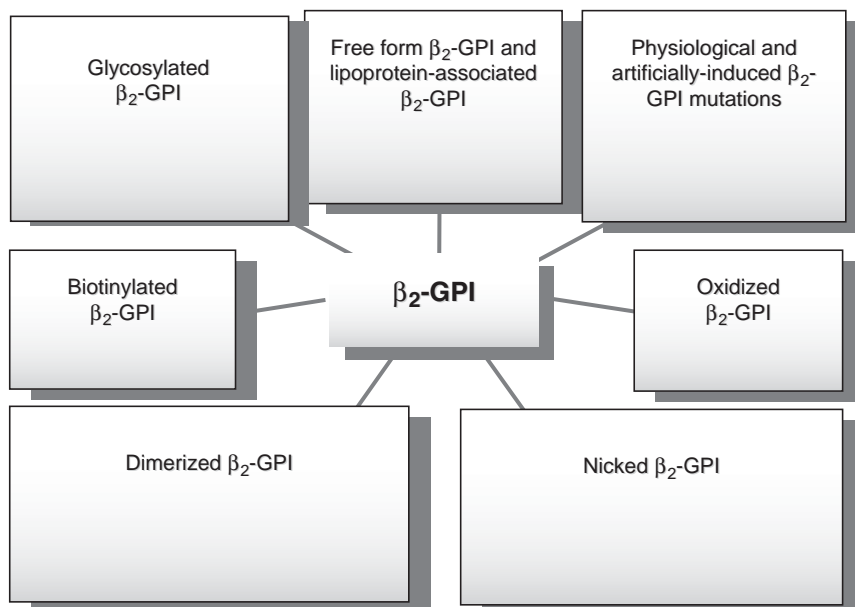


Figure 2 β_2 -GPI is found in many different forms, among them are: free-soluble form, lipoprotein-bound form (VLDL, LDL, HDL), oxidized-LDL-bound form, oxidized β_2 -GPI form, biotinylated β_2 -GPI, dimerized form, the nicked form, and the mutated β_2 -GPI.

2.4.1. Free Form and Lipoprotein-Associated β_2 -GPI

The structure of β_2 GPI in solution exhibits well defined spatial orientation and due to the flexibility of the interdomain linkers can adopt an optimal spatial and entropic conformation through bending [26]. Under nearly physiological conditions β_2 GPI is more bent and forms an averaged S-shaped solution structure with a tilt angle of $\sim 60^\circ$ between CCP2 and CCP3. Solution β_2 GPI structure represents the free, not immobilized structure, which is described as immunologically less active [26].

In general, apolipoproteins have a high degree of conformational flexibility and respond dramatically to relatively minor environmental changes. Lipid presence also causes major conformational changes in apolipoproteins. β_2 -GPI is an unusual apolipoprotein differing from others in its secondary, tertiary and quaternary structure. At pH extremes it is expected to unfold and generate a more flexible tertiary structure. β_2 -GPI is masked on lipoprotein surface and not recognized by the polyclonal anti- β_2 -GPI antibodies [27].

2.4.2. β_2 -GPI glycosylation

In 1989, β_2 -GPI was described to be highly glycosylated, with five attached glucosamine-containing oligosaccharides, located in domains III and IV, the variability of which was thought to account for at least five isoforms as judged by isoelectric focusing [28]. Neuraminidase treatment decreased the number of bands to two. The five reported glucosamine-attached oligosaccharide side chains are composed of galactose, mannose, *N*-acetylglucosamine, fucose and *N*-acetylneuraminic acid [29]. Carbohydrates are mainly linked to Asn residues (Asn-X-Ser/Thr); in β_2 -GPI to Asn residues at positions 143, 164, 169, 174, and 234. Mannose is organized in a N-linked structure [30]. N-linked glycosylation occurs cotranslationally [31] and may affect the course of polypeptide folding. β -GPI is also O-glycosylated (with sugar moieties bound to Ser or Thr) and O-linked chains are represented by sialic acid $\alpha(2-6)$ linked to galactose or *N*-acetylgalactosamine [30]. Galactose is also organized into O-linked chains.

The removal of a large portion of the carbohydrate moiety of β_2 -GPI did not alter the secondary structure, however after enzymatic cleavage of around 96% of the carbohydrate moiety, large significant changes were observed [32] resulting in an increase in the magnitude of molar ellipticity and the amount of beta-turns (accompanied by a reduction in random coil). Oligomannose N-glycans were indicated to ensure proper folding of β_2 -GPI polypeptide chains and may be a requirement for the biological activity of β_2 -GPI [32]. Digoxigenin-labelled lectins and Concanavalin A lectin affinity chromatography were used to analyze β_2 -GPI for its bound oligosaccharides [30, 33] and results showed that β_2 -GPI was rich in sialic acid linked to galactose or *N*-acetylgalactosamine. High mannose N-glycan chains are barely detectable. The carbohydrate content of β_2 -GPI is estimated at around 19% of the molecular weight [33], N-glycosidase F treatment (which cleaves all types of Asn bound N-glycans) reduced the molecular weight to 32.5 kDa and using biochemical analysis revealed that no specific carbohydrate complex is bound to a single isoform [30] and that each isoform may contain different glycosylation patterns. Glycosylation influences the conformation and antibody binding, but does not affect the β_2 -GPI binding capacity to lipid membranes [34].

2.4.3. β_2 -GPI oxidation

Diagnostic assays for anticardiolipin antibodies (aCL) detection are routinely performed on microtitre plates coated with cardiolipin (CL). Schlame *et al.* report that contact between CL and NUNC-Immuno plates leads to extensive oxidation, generating peroxy-CLs [35]. The group resolved CL into 12 molecular species, ranging from oxidized to nonoxidized with different degrees of unsaturation that all showed immuno-reactivity (under anaerobic conditions) with serum from APS patients.

β_2 -GPI is susceptible to oxidative modifications by the hydroxyl radical ($\star\text{OH}$) that may influence its lipid-binding and antigenic properties. Radiolytic $\star\text{OH}$ caused a dose-dependent loss of tryptophan, production of dityrosine and carbonyl groups and caused altered phospholipid binding and recognition by autoantibodies depending on their epitope specificities [36]. Twenty selected IgG anti- β_2 -GPI positive samples showed that prior exposure of human β_2 -GPI to increasing amounts of $\star\text{OH}$ lead to the categorization of antibodies into two groups based on their reactivity on a β_2 -GPI ELISA. The first group exhibited increased IgG binding (plateau at 20–40 nmol) then decrease, whereas the second group showed a steady marked decrease in binding affinity (dose-dependent loss). The first group also showed a correlation for the presence of lupus anticoagulant and APS features. It is of interest that the second group also showed negative results in the standard aCL test [36]. It has been proposed that this second subset of anti- β_2 -GPI antibodies recognized epitope/s located within or near the phospholipids binding site on native β_2 -GPI [37]. Oxidation of β_2 -GPI alters its amino acid composition, influences its phospholipid binding ability and modulates autoantibody recognition, thereby contributing to shaping epitope diversity.

2.4.4. β_2 -GPI biotinylation

When β_2 -GPI was labeled with biotin-hydrazide after oxidation of its glycan chains (β_2 -GPI-bh), it bound to apoptotic cells, thus confirming that β_2 -GPI-bh had a greater apparent affinity for anionic phospholipids than native β_2 -GPI. In presence of monoclonal anti- β_2 -GPI antibody (8C3), the ability of native β_2 -GPI to bind anionic phospholipids was increased, whereas the binding of β_2 -GPI-bh was barely affected by the addition of 8C3 [38].

Oxidation and biotinylation of β_2 -GPI glycan chains induce an increase in its affinity for anionic phospholipids and if such oxidative processes occur naturally, they could participate in enhancing aPL formation [38]. In order to determine why biotinylation of β_2 -GPI increased both its affinity and its recognition by aCL, electrophoretic analysis was performed and revealed that oxidation and biotinylation of glycan chains of β_2 -GPI induce the formation of covalent high molecular weight polymers (corresponding to dimeric and trimeric forms), which are absent in native β_2 -GPI [39]. In solution, as studied by static and dynamic light scattering, β_2 -GPI-bh was dimeric at 1 μM in PBS, whereas native and oxidized β_2 -GPI were both monomeric. The ability of high molecular weight β_2 -GPI-bh to bind to phosphatidylserine (PS)-coated microtitre plates was determined not to be greater than that of monomeric β_2 -GPI-bh. Anti- β_2 -GPI monoclonal antibody 9G1 (known to bind β_2 -GPI in solution and to be directed against domain I of β_2 -GPI) recognized high

molecular weight β_2 -GPI-bh better than 50 kDa β_2 -GPI. The group postulates that oxidation and biotinylation lead to the autoassociation of the β_2 -GPI molecule and that this induces the conformational change necessary to expose cryptic epitopes recognized by aCL. Autoassociation could also increase epitope density and if the binding site is created by the association of at least two β_2 -GPI molecules, autoassociation may create this particular site [39].

2.4.5. β_2 -GPI dimerization

Dimerization has been shown to provide avidity-affinity changes in recognition to aPL autoantibodies. As reported already in 1995 [40] experiments had been performed in order to determine whether phospholipid membranes were necessary for aCL- β_2 -GPI recognition and whether certain neo-antigen epitopes were created as a consequence of β_2 -GPI-phospholipid interaction. The result of these early studies showed that when standard polystyrene immunoassay plates were used in the ELISA no antibody-antigen binding was detected, however when gamma-irradiated (high binding) plates were used significant specific binding was detected and this difference attributed to the higher density of β_2 -GPI immobilized on the high binding plates and antibody bivalency. This report supports the hypothesis that phospholipid-bound β_2 -GPI is the physiologic target of aCL. The role of bivalent high affinity binding of aCL- β_2 -GPI complexes to lipid planar membranes, composed of phosphatidylcholine (PC) and PS, was confirmed by Willems *et al.* [34]. Affinity decreased greatly with decreasing PS content. At physiologic conditions (10 mol% PS, 120 mM NaCl and 3 mM CaCl₂), a K_d of 14 μ M was observed. In the absence of β_2 -GPI, the binding of aCL was negligible. The initial monovalent association of aCL- β_2 -GPI is rapidly followed by formation of bivalent aCL-(β_2 -GPI)₂ complexes. These initial studies had been followed by the confirmation that a similar sequence of events is occurring for the interactions between anti- β_2 -GPI antibodies and β_2 -GPI as a consequence of a conformational change of β_2 -GPI. The influence of different binding conditions was evident when studying the interaction between high or low avidity IgG anti- β_2 -GPI and β_2 -GPI antigen, which was either free in solution or bound to microtitre plates or nitrocellulose membranes. The density of β_2 -GPI, which was 20–30 times higher on the nitrocellulose membrane than on the surface of ELISA plates, was not sufficient for the recognition of the antigen by anti- β_2 -GPI antibodies. Some high avidity samples reacted only with nonreduced β_2 -GPI and minority of low-avidity samples recognized only denatured and reduced β_2 -GPI. These results suggest that neither high density of the antigen nor high avidity of the antibodies (Fab fragments) alone was sufficient for the binding of anti- β_2 -GPI antibodies to β_2 -GPI. Some conformational changes and consequently exposed neo-epitopes are required for the recognition of β_2 -GPI by polyclonal anti- β_2 -GPI antibodies [41].

Using site-directed mutagenesis, β_2 -GPI mutants were formed [42] and the role of β_2 -GPI dimerization and higher antibody affinity was strengthened, however in this study, the dimerization forming mutants indicated that binding occurs already in fluid phase and that the neo-epitope formation (following binding to phospholipids) is not required for binding. In 2001, both covalent and noncovalent chimeric fusion proteins composed of the dimerization- β_2 domain (apple 4) of factor XI and β_2 -GPI

were constructed and used in a phospholipid binding assay [43] and indicated that both dimeric chimera bound to the phospholipids with much stronger affinity as compared to their counterparts (either plasma derived β_2 -GPI or apple2- β_2 -GPI) and also had the longest clotting times in the coagulation assays.

2.4.6. Nicked β_2 -GPI

The Cys³⁰⁶-Cys³²⁰ loop of β_2 -GPI domain V is surface exposed and susceptible to proteolytic cleavage. Two cleavage sites in domain V were found in the commercial human protein, one major site at Lys³¹⁷-Thr³¹⁸ and another minor at Ala³¹⁴-Phe³¹⁵ [7].

Hoshino *et al.* [44] presented the model of the fifth domain by heteronuclear multidimensional nuclear magnetic resonance supporting the suggestion that the effects of cleaving Lys³¹⁷-Thr³¹⁸ are very local and exclusively restricted within several residues around the nick, however resulting in a large decrease of affinity for negatively charged phospholipids.

Characterization of plasmin-cleaved β_2 -GPI with a nick between Lys³¹⁷ and Thr³¹⁸ revealed that this form of β_2 -GPI has neutral phospholipids, notably PC and sphingomyelin (SM) bound to the molecule. The protein was crystallized and PC moiety was found to be bound in a groove present in the large positive patch that is involved in phospholipid binding. It was suggested that the loss of phospholipid binding ability of nicked β_2 -GPI might be due to the binding of neutral lipids [45].

Hagihara *et al.* [46] produced a nicked form of β_2 -GPI at Lys³¹⁷-Thr³¹⁸ by either a long incubation with bovine factor Xa or with a shorter incubation by plasmin [47]. Recently this was also reported by factor XIa [48].

The nicked form was found in plasma of healthy subjects [49]. However, patients with disseminated intravascular coagulation had particularly high levels of nicked β_2 -GPI [47]. In this pathologic condition the cleaved β_2 -GPI was found in plasma in concentrations up to 12 $\mu\text{g}/\text{ml}$ and the intact protein decreased for 70% [50]. Additional conditions for the elevated nicked form include treatment with streptokinase [50], lupus anticoagulant positive patients [47] and patients with leukemia [51]. Recently an elevated ratio nicked/intact protein was found in patients with ischemic stroke and lacunar infarcts demonstrated by magnetic resonance imaging [49].

One of the important features of the nicked form represents a lower or even absent affinity for phospholipids, particularly CL [7, 46, 51]. The Vth domain of various β_2 -GPI preparations (from 9.2–50.3% of cleaved protein between Lys³¹⁷-Thr³¹⁸ and Ala³¹⁴ and Phe³¹⁵) had little influence on the affinity for the vesicular, but not the immobilized, phospholipids [52].

The conformational changes in the nicked form resulted in novel hydrophobic and electrostatic interactions. Such a change may have important implications for exposure of cryptic epitopes located in domain IV [53], but resulting in loss of antigenicity in routine tests.

2.4.7. β_2 -GPI mutations

The naturally occurring missense mutation substituting Trp³¹⁶ with Gly disrupts the integrity of Leu³¹³Ala Phe Trp³¹⁶ hydrophobic loop and abolishes the CL binding of β_2 -GPI in CL ELISA [10, 21]. In contrast mutated β_2 -GPI still retains its ability to bind to negatively charged heparin, the binding of which is primarily electrostatic [45, 54].

There were some conflicting results regarding the importance of domain configuration and disulphide bond integrity in β_2 -GPI phospholipid binding. Mutagenesis studies [10, 21] reported that disulphide bond between Cys²⁸¹ and Cys³⁰⁶ within domain V is essential for β_2 -GPI binding to CL in CL ELISA assay. The missense mutation substituting Cys³⁰⁶ with Gly³⁰⁶ disrupted the disulphide bond between Cys²⁸¹ and Cys³⁰⁶ rendering β_2 -GPI incapable of binding in CL ELISA assay. The mutation affects the normal configuration of the domain V that appears to be critical for clustering of positively charged amino acids along with the hydrophobic loop AA 313–316 [10, 21]. In contrast, Wang *et al.* reported that the ability of β_2 -GPI to insert into the DP (dipalmitoyl) PS monolayers is independent of three dimensional as well as domain structure of β_2 -GPI, since heat inactivated and reduced/alkylated β_2 -GPI was still able to insert into DPPS monolayer [4, 55].

3. INFLUENCE OF THE PHOSPHOLIPID MEMBRANE ON β_2 -GLYCOPROTEIN I BINDING (*IN VITRO* MODELS)

The interactions of β_2 -GPI with phospholipids have been considered as a basic mechanism related to its physiological and pathogenic functions [4]. In contrast to binding of β_2 -GPI to natural membranes (not focused on in this chapter), several studies reported on β_2 -GPI's interaction with artificial phospholipid membranes such as liposomes, supported planar lipid bilayers and phospholipid monolayers that serve as cell membrane *in vitro* models. Binding of β_2 -GPI to artificial membranes will be reviewed in this part of the chapter. The mechanism of β_2 -GPI binding regarding β_2 -GPI structure and phospholipid membrane properties, conformational changes and oligomerization of β_2 -GPI upon phospholipid binding, as well as environmental factors (pH, ionic strength, the presence of divalent ions Ca²⁺, Mg²⁺) that potentially influence the interaction of β_2 -GPI with phospholipid membrane will be discussed.

3.1. Mechanism of β_2 -GPI Binding to Phospholipid Membrane

The structural and biochemical data indicate a relatively simple membrane binding mechanism of β_2 -GPI. The positively charged multilycine rich region on domain V interacts with negatively charged phospholipid headgroups and hydrophobic flexible loop ³¹³LeuAlaPheTrp³¹⁶ putatively inserts into the lipid layer [9,12,55,56]. This positions Trp³¹⁶ at the interface region between the acyl chains and phosphate headgroups thereby anchoring the protein to the membrane [9, 45]. The ability of β_2 -GPI to insert into the phospholipid membrane was studied using the phospholipid monolayer technique, which was shown to be a powerful technique in membrane insertion analysis (reviewed in [4]). Monolayers were prepared by spreading the lipid solution (DPPS; DPPC; DPPG (phosphatidylglycerol); CL; dioleoyl (DO) PS and DOPC) onto the subphase buffer surface to the desired initial monolayer surface pressure. An increase in the monolayer surface pressure upon the addition of β_2 -GPI (isolated from human serum, final concentration of

β_2 -GPI 50 nM) was interpreted as a consequence of the protein's insertion into the phospholipid layer. The insertion of β_2 -GPI into phospholipid membrane was further investigated using electron spin resonance spectroscopy [56,57]. The spectra of spin labeled CL molecules, which are sensitive to the changes in lipid order depending on the depth of a label location, were recorded. A restriction of the CL side chain mobility upon β_2 -GPI addition was limited to the outer region of the bilayer indicating that the protein penetrated into the interfacial surface-headgroup membrane region. No deeper penetration into the hydrophobic membrane core was observed. The flexible hydrophobic loop composed of AA 313–316 in domain V was suggested to anchor β_2 -GPI in the interfacial phospholipid headgroup region of CL-containing large unilamellar vesicles (LUVs), probably with the indole ring of Trp³¹⁶ positioned close to the carbonyl residues [56].

3.1.1. Conformational change of β_2 -GPI upon phospholipid binding

It is heavily discussed whether a conformational change of β_2 -GPI upon β_2 -GPI membrane binding with exposure of cryptic epitopes or clustering of β_2 -GPI molecules on the surface of negatively charged membrane forming a bivalent/multivalent antigen is important for aPL binding.

Solution structure of β_2 -GPI reveals an inherent interdomain flexibility indicating that β_2 -GPI might adopt a number of different conformations by reorienting the flexible domains in response to different environmental conditions and phospholipid membrane binding [26]. Destabilization of the protein and partial loss of tertiary structural elements were assumed to take place upon β_2 -GPI association with lipids [56]. Hamdan *et al.* showed that binding of domain V is essential for β_2 -GPI interaction with target membrane and that large scale structural changes are initiated upon the initial binding of domain V to the PS small unilamellar vesicles (SUVs) [58]. Circular dichroism spectroscopy revealed that β_2 -GPI (purified from human serum) undergoes a remarkable conformational change in the secondary protein structure when interacting with negatively charged DM (dimyristoyl) PG or CL-containing SUVs at low ionic strengths [59]. Upon the addition of negatively charged SUVs a considerable increase in the α -helix content (6.8% and 12.6% for DMPG or CL-SUVs, respectively) was observed [59]. The conformational change was slightly different upon β_2 -GPI interaction with DMPG and CL-containing SUVs. DMPG-induced conformational change of β_2 -GPI might be explained in context of distinct microenvironment near the membrane surface, suggesting that DMPG does not serve as a specific binding site for β_2 -GPI [55,59]. In contrast, CL binding induced a more specific conformational change of β_2 -GPI with an additional decrease in β sheet content that cannot be simply ascribed to the microenvironment at the membrane surface [59]. No conformational change was observed when neutral DMPC SUVs were added indicating that β_2 -GPI did not associate with neutral DMPC SUVs [59]. Fluorescence microscopy techniques were widely used in investigation of the conformations adopted by membrane-bound β_2 -GPI, taking advantage of the intrinsic fluorescence signal of the native β_2 -GPI, which is mainly derived from its five Trp residues, one in each domain. With the exception of water exposed Trp³¹⁶, which was suggested to contribute most to the emission spectrum of the native β_2 -GPI, all the other Trp residues are embedded in the

hydrophobic domain interior [56]. The addition of increasing amounts of negatively charged CL or DMPG (but not neutral DMPC) vesicles (SUVs; LUVs) to the solution containing β_2 -GPI induced a large blue shift of the β_2 -GPI fluorescence emission maximum [55, 56]. The blue shift reflects an increase in the hydrophobicity of β_2 -GPI's Trp environment probably due to the transfer of the water exposed Trp³¹⁶ to the lipophilic environment of vesicle bilayer [56]. Phospholipid binding of domain V of β_2 -GPI was suggested to induce the adsorption of domains I-IV along the plane of the negatively charged membrane surface [55,60]. Hamdan *et al.* investigated the contribution of individual domains to the binding of β_2 -GPI to PS-containing SUVs using different fluorescence techniques. Individual β_2 -GPI domains exhibited ionic strength-dependent water-soluble and membrane-bound states [58].

It was hypothesized that β_2 -GPI can adopt at least two conformations upon binding to PS-containing membranes depending on the ionic strength [55]. At low ionic strengths the protein assumes conformation, in which both the C- and N-termini are oriented along the plane of the lipid bilayer with each domain acquiring its specific membrane interaction (domain V is bound to membrane, likely juxtaposing Trp³¹⁶ to the charged PS headgroups, domain IV associates with membrane, domain III is tightly embedded in the bilayer, domain II resides in the aqueous phase and domain I is bound to membrane) [58]. At physiologic ionic strength, domain I detaches from the membrane surface while other domains still maintain their association with membrane. Conformationally altered domain I projects away from the membrane surface being able to interact with other proteins and/or cell surface ligands/receptors [58,60].

3.1.2. Oligomerization of β_2 -GPI upon phospholipid binding

In addition to exposure of cryptic epitopes in the CCP domains, the conformational change observed upon β_2 -GPI binding to CL-containing LUVs was proposed to induce the oligomerization of membrane-bound β_2 -GPI molecules via their hydrophobic interface on CCP domains I-III [56]. Clustering of β_2 -GPI on the surface of negatively charged membranes may be essential for autoantibody binding determining the role of β_2 -GPI in autoimmune diseases. Atomic force microscopy was applied to directly visualize the binding of β_2 -GPI (purified from human plasma) to planar-supported lipid bilayers composed of palmitoyl-oleyl (PO) PC and varying degrees of POPS (0–20 mol%) at physiological ionic strengths in the presence or absence of Ca²⁺ [57]. The partially cohesive protein agglomerates with a height of approximately 3.3 nm, indicating horizontal-like orientation of protein molecules, that spread laterally up to 500 nm were resolved on the surface of POPS/POPC bilayers [57]. Time resolved atomic force microscopy showed the formation of new protein clusters and the growth of pre-existing clusters. No binding of β_2 -GPI to pure POPC bilayer was observed. Two state reaction model of β_2 -GPI membrane binding using atomic force microscopy and surface plasmon resonance was proposed [57]. Fast step of β_2 -GPI binding to negatively charged lipids, mainly based on the electrostatic interactions, is followed by a slower phase of the protein agglomeration on the bilayer surface accompanied by a protein-induced rigidification of the membrane [57]. Fast reaction step strongly depended on POPS content and was modulated by the presence of Ca²⁺.

3.2. Changes in Membrane Properties Upon β_2 -GPI Binding

In mixed liposomes composed of neutral and negatively charged phospholipids β_2 -GPI (isolated from bovine plasma) interacted only with negatively charged phospholipids, suggesting that β_2 -GPI might segregate negatively charged phospholipids [61]. Similarly, lateral clustering of β_2 -GPI molecules on PS-containing planar lipid bilayers might be accompanied by a locally limited segregation of lipids [57].

The insertion of β_2 -GPI into the negatively charged phospholipid membrane caused the restriction of the phospholipid acyl chain mobility in the outer (interfacial headgroup) region of the bilayer [56,57].

3.2.1. Precipitation and adhesion of membranes

Binding of β_2 -GPI to membranes of negatively charged liposomes in low ionic strength buffers resulted in their agglutination and subsequent precipitation [6, 60]. Low-salt-dependent multiple protein membrane cross-linking interactions between adjacent negatively charged membranes might take place upon β_2 -GPI binding [55, 56, 62, 63]. Hagihara *et al.* have shown that in addition to the relatively high affinity binding of domain V to lipids, domain I also exhibits lipid-binding properties, although of relative low affinity [61]. Domain I of β_2 -GPI was implicated in the aggregation and subsequent precipitation of negatively charged phospholipid membranes under low ionic strength conditions [58]. Hamdan *et al.* reported that only the full length recombinant protein (but not domain-deleted β_2 -GPI fragments, lacking either domain V or domain I) could precipitate PS-containing SUVs [58]. Binding of domain I to PS SUVs is ionic strength-dependent and was observed only under low ionic strength conditions [58]. Under physiologic conditions domain I was released from the membrane. Therefore it was suggested that through domain V and domain I β_2 -GPI binds multiple lipid residues on juxtaposed vesicle membranes inducing intervesicular aggregation and precipitation [58].

β_2 -GPI was shown to induce the adhesion of CL-containing giant phospholipid vesicles (GPVs) [62,63]. β_2 -GPI-induced adhesion (cross-linking) of negatively charged GPVs under low ionic strength conditions can be explained in the context of electric double layer theory, taking into account the specific spatial distribution of charge within the membrane attached β_2 -GPI molecules [63,64].

Alternatively, global (low-salt) high-affinity alterations of target membranes induced by β_2 -GPI binding at two distinct membrane sites within the same vesicle might occur resulting in increased hydrophobicity and subsequent membrane precipitation from the aqueous phase [60]. The conformation assumed by β_2 -GPI in low ionic strength conditions with both the C- and N-termini oriented along the plane of the lipid bilayer was suggested to facilitate such intravesicle binding of β_2 -GPI to the membrane [60].

3.2.2. Budding of membranes

The budding of membranes of negatively charged unilamellar GPVs, containing 10 mol% of POPS was observed in the presence of β_2 -GPI (purified from human plasma) at low ionic strength conditions. The budding of GPVs was explained by the insertion of the hydrophobic loop of β_2 -GPI into the outer phospholipid layer

resulting in increased spontaneous curvature as well as increased surface area of the outer phospholipid layer with respect to the inner phospholipid layer of GPV membrane, favoring vesicle shape transformation [65]. However, no vesiculation of the budding membrane of PS-containing GPVs could be observed in the presence of β_2 -GPI [65]. The (temperature-induced) budding of negatively charged GPVs in the presence of β_2 -GPI in the outer solution was studied both experimentally and theoretically. The attachment of positively charged β_2 -GPI to the negatively charged surface of GPV caused coalescence of the spherical membrane bud with the parent vesicle before the bud could vesiculate (detach) from the parent vesicle (Fig. 3) [64].

3.3. Binding of β_2 -GPI to the Membrane as a Function of β_2 -GPI Concentration

Binding of β_2 -GPI to the negatively charged lipids is stoichiometric; as long as the vesicle surface was not totally covered by the protein, a linear decrease in the wavelength of the emission maximum, which is proportional to the amount of the bound protein, was observed [55]. Ellipsometric measurement of β_2 -GPI adsorption

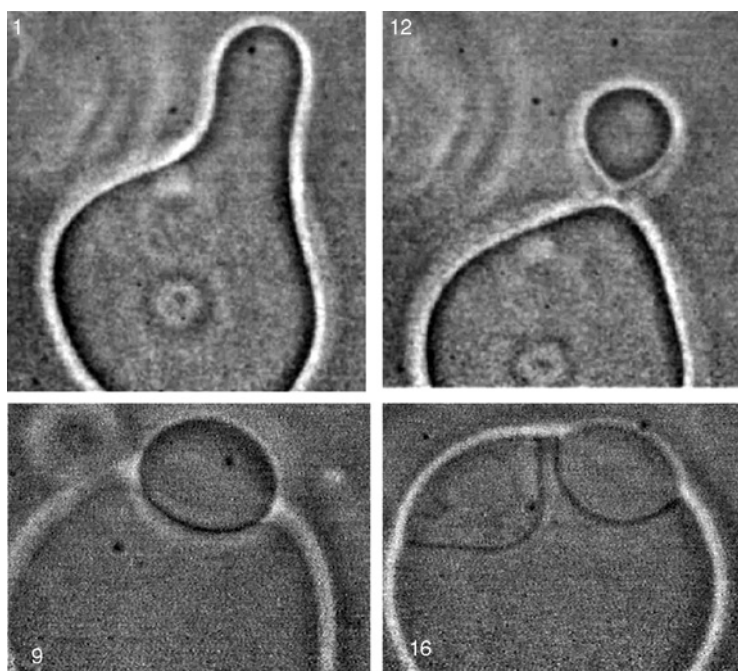


Figure 3 Adhesion of the daughter vesicle to the outer surface of the mother membrane of POPC-CL-cholesterol vesicle following temperature-induced budding of the GPV in the presence of β_2 -GPI in the solution. Adapted from Ref. [64]. The numbers on the upper panels (1,12) represent the sequential micrographs of the bud formation process, while the numbers on the lower panels (9,16) represent the sequential micrographs of the adhesion process.

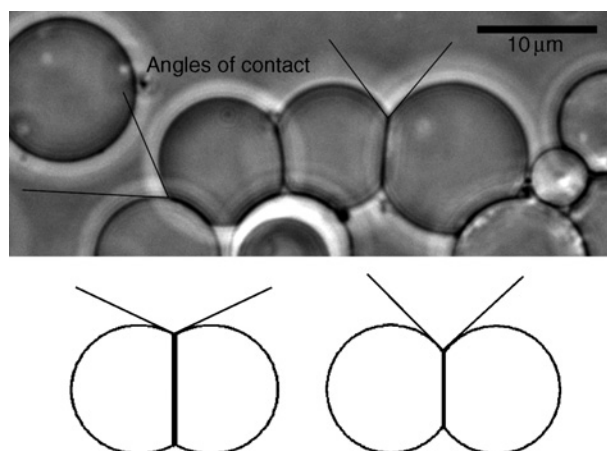


Figure 4 Adhesion of CL-containing GPVs with indicated effective angles of contact between GPVs. Larger effective angles of contact—stronger adhesion; smaller effective angles of contact—weaker adhesion. Adapted from Ref. [66].

onto planar 20 mol% PS-containing phospholipid bilayers at near physiologic ionic strength showed that amount of protein bound to membrane is proportional to its concentration, approaching the plateau at β_2 -GPI concentrations above 1 μM [34].

Similarly, the influence of β_2 -GPI concentration on precipitation/adhesion of phospholipid membranes was investigated. Lee *et al.* [60] examined the precipitation of PS-containing SUVs in the presence of increasing amounts of β_2 -GPI in low ionic strength conditions using fluorescent technique. The precipitation of PS-containing SUVs increased with increasing β_2 -GPI concentration, reaching the maximum at 200 nM [60]. The influence of increasing β_2 -GPI concentration on the adhesion of 10 mol% CL-containing GPVs was studied under low ionic strength conditions. The strength of adhesion was determined by measuring effective angles of contact between adhered GPVs (Fig. 4, top panel) 25–30 min after the addition of β_2 -GPI, using Image J software [66]. A larger (smaller) effective angle of contact between adhered GPVs was interpreted as indicating a stronger (weaker) adhesion between membranes (Fig. 4, bottom panel).

An average effective angle of contact at different β_2 -GPI concentrations was then calculated. Fig. 5 (Frank *et al.*, in preparation) [67] depicts the dependence of the average effective angle of contact between CL-containing GPVs on the concentration of β_2 -GPI. The angle approaches the plateau as β_2 -GPI concentration raises above 2 μM .

3.4. Phospholipid Membrane Properties Important for β_2 -GPI Binding

3.4.1. Membrane charge and composition

It has been shown by different *in vitro* membrane models (large multilamellar vesicles, SUVs, LUVs, planar lipid bilayers) that negatively charged phospholipids are essential for the interaction of β_2 -GPI with phospholipid membranes

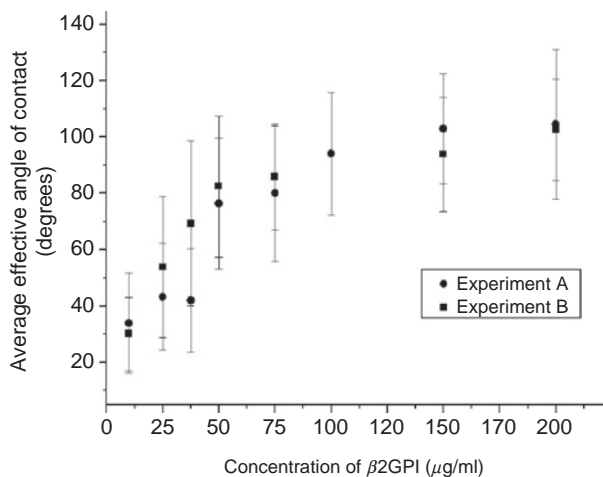


Figure 5 Dependence of the average angle of contact between GPVs containing 10 mol% of cardiolipin on the concentration of β_2 -GPI. Adapted from Ref. [67].

[6,34,56,57,58,61,68]. No binding of β_2 -GPI to neutral phospholipid membranes containing PC, SM and phosphatidylethanolamine, with an exception of Harper *et al.* [68], who found similar K_d values for β_2 -GPI interaction with phosphatidylethanolamine and PS SUVs, could be observed in these models. Similarly, the insertion of β_2 -GPI was reported to be significantly stronger into negatively charged DPPS, DPPG or CL phospholipid monolayers than into neutral DPPC monolayers [4]. Interestingly, neutral DPPC monolayers were shown to bind β_2 -GPI [69] and the adhesion of neutral POPC/cholesterol GPVs was induced in the presence of β_2 -GPI [63].

Binding of β_2 -GPI to negatively charged phospholipid membrane is saturable [6] and reversible [34]. The affinity of β_2 -GPI binding to negatively charged membranes increases with the increasing molar fraction of negatively charged phospholipids [34, 55, 70]. Low K_d values (10^{-8} to 10^{-7} M) obtained for β_2 -GPI binding to phospholipid membranes that contain 50–100 mol% of negatively charged phospholipids (CL, PS, PG, phosphatidylinositol (PI), phosphatidic acid (PA)) at low and high ionic strengths indicated the high affinity of β_2 -GPI–membrane interaction [6,61]. However considerably higher K_d values were observed for β_2 -GPI binding to membranes containing more physiological (5–20 mol%) concentrations of negatively charged phospholipids at high ionic strength conditions [34,57,68,70]. This suggests that under physiological conditions binding of β_2 -GPI to phospholipid membranes is rather weak. Therefore, β_2 -GPI does not appear to possess the necessary phospholipid binding affinity to displace prothrombin and other coagulation factors from negatively charged membrane surface despite its high plasma concentration. This raises a doubt about the physiological function of β_2 -GPI as a natural anticoagulant [68]. Some authors reported that the affinity of β_2 -GPI for negatively charged phospholipid bilayers under near physiological conditions (5–20 mol% of negatively charged phospholipid, high ionic strength) is independent

of chemical composition of the negatively charged polar phospholipid headgroup (PS, PG or CL) [34, 55]. Others showed that the interaction of β_2 -GPI with SUVs containing 20% of PS is slightly more favorable than with SUVs composed of 20 mol % of either CL, PA or PI [68]. For membranes with high anionic phospholipid content (50–100 mol%) the differences in K_d values between different anionic phospholipid species were more pronounced—binding of β_2 -GPI to CL, PG, PS, and PA containing membranes was 10-times stronger with respect to PI containing membranes [6, 61]. It was also noted that there are some differences in the ability of β_2 -GPI to insert into negatively charged monolayers composed of CL, DPPS or DPPG [69]. Similarly, maximal binding of β_2 -GPI to negatively charged membranes under near physiological conditions (corresponding to 160 lipid molecules per protein binding site) was not sensitive to the membrane composition regarding the species of an anionic phospholipid (PS, PG, or CL) [34], rather it was determined by the steric hindrance between the protein molecules on the membrane surface [34]. The effect of chemical membrane composition on the stoichiometry of β_2 -GPI (isolated from bovine plasma) binding was more pronounced with membranes containing more than 50% of negatively charged phospholipids (20 vs 70 lipid molecules per binding site with 50 mol% containing CL vs 67 mol% containing PS liposomes) [61].

3.4.2. Membrane lipid phase and lipid acyl chain saturation

The dependence of the spatial orientation of β_2 -GPI on neutral and negatively charged monolayers on the phase state of a lipid monolayer was studied [69]. On neutral DPPC monolayers β_2 -GPI assumed an upright orientation, which was insensitive to the phase state of the monolayer. In contrast, two different spatial orientations were observed with β_2 -GPI bound to negatively charged DPPS monolayer—an upright orientation in the liquid phase state and a flat orientation with β_2 -GPI lying on the membrane surface in the condensed phase state [69]. Since phase separation exists within biological membranes, different spatial orientations of membrane-bound β_2 -GPI might be found also *in vivo* influencing its physiological and pathogenic roles [69].

The insertion of β_2 -GPI might be influenced by the saturation of phospholipid acyl chains. The enhanced insertion of β_2 -GPI was observed into monolayers containing unsaturated phospholipids (DOPC or DOPS) when compared to monolayers composed of saturated phospholipids (DPPC or DPPS) [4].

4. INFLUENCE OF ENVIRONMENT OR MILLIEU

4.1. The Influence of Ionic Strength and Divalent Ion Concentration on β_2 -GPI Membrane Binding

Protein/phospholipid electrostatic interactions are sensitive to the changes of environmental pH, ionic strength and divalent cation concentration. The changes in bulk solution pH and ionic strength may affect the degree of the ionization of protein and lipid molecules thereby modifying protein/phospholipid interaction [4].

Surface potential of the membrane is strongly influenced by the concentration of monovalent and divalent ions in the buffer [34]. Divalent ions (Ca^{2+} , Mg^{2+}) shield the negative charge of the membrane even more effectively than monovalent ions as they can directly affect intermolecular electrostatic repulsion by binding to the lipid headgroups and bridging a pair of lipid molecules [4].

The affinity of β_2 -GPI for negatively charged phospholipid membranes is strongly influenced by ionic strength and concentration of divalent cations (Ca^{2+} , Mg^{2+}) [6,34,55,57,68,70]. This further supports the notion that the primary mechanism of β_2 -GPI membrane binding is based on electrostatic interactions.

Wurm *et al.* studied the effect of increasing NaCl and divalent cation (Ca^{2+} , Mg^{2+}) concentration on the binding of β_2 -GPI on large multilamellar vesicles containing 100 mol% PS. Maximal binding was observed at 0.025 M NaCl, followed by a steady decrease of binding capacity with increasing salt concentration and nearly zero membrane binding of β_2 -GPI at 0.5 M NaCl [6]. The binding capacity reduced slightly with increasing molarity of divalent ions, the effect being a little more pronounced for Ca^{2+} [6]. K_d values for binding of bovine β_2 -GPI to LUVs containing more than 50% of negatively charged phospholipid were reported to be in the 10^{-8} and 10^{-7} M range under low and high ionic strength conditions, respectively [61].

The influence of environmental ionic conditions on β_2 -GPI binding to phospholipid membranes containing physiologically more relevant levels of negatively charged phospholipids (5–20 mol%) was investigated. A relatively high affinity of β_2 -GPI for membranes containing 20 mol% PS were reported at low ionic strength (60 mM NaCl, no Ca^{2+}) conditions [34]. Increasing the concentration of NaCl from 25 to 200 mM resulted in an approximately 10-fold increase of apparent K_d values for β_2 -GPI binding to 20 mol% containing SUVs. Addition of Ca^{2+} was shown to strongly decrease the affinity of β_2 -GPI for phospholipid membranes containing 20 mol% of PS [55, 57, 68, 70]. Raising the concentration of CaCl_2 from 0 to 20 mM yielded an 8-fold increase in apparent K_d values for β_2 -GPI binding to 20 mol% PS-containing SUVs [68]. Under near physiological conditions (120 mM NaCl, 3 mM CaCl_2) reported K_d values for β_2 -GPI binding on 10 and 20 mol% PS-containing membranes were 14 μM [68, 70] and 3.9 μM [68], respectively. This suggests that at plasma concentrations of β_2 -GPI (4 μM) less than 25% of maximal binding of β_2 -GPI to 10 mol% PS containing membranes could be expected [68,70].

The effect of ionic strength (50–1000 mM NaCl or KCl) and divalent cations (Ca^{2+} or Mg^{2+}) on the detachment of β_2 -GPI from the membrane surface of DMPC containing SUVs was investigated using fluorescence techniques [55]. The blue shift of fluorescence emission maximum of β_2 -GPI as well as doxyl-PC quenching extent (measuring insertion of β_2 -GPI) were reduced in the presence of increasing ionic strength and divalent cation concentration indicating the detachment of β_2 -GPI from membrane surface of DMPC vesicles. However, the effect of cations on the blue shift of β_2 -GPI was remarkably different from that on the doxyl-PC quenching extent. The blue shift of β_2 -GPI decreased significantly by increasing ionic strength to 100 mM and Ca^{2+} (Mg^{2+}) concentration to 0.5 mM. In contrast, fluorescence quenching data were significantly reduced only at much higher ionic

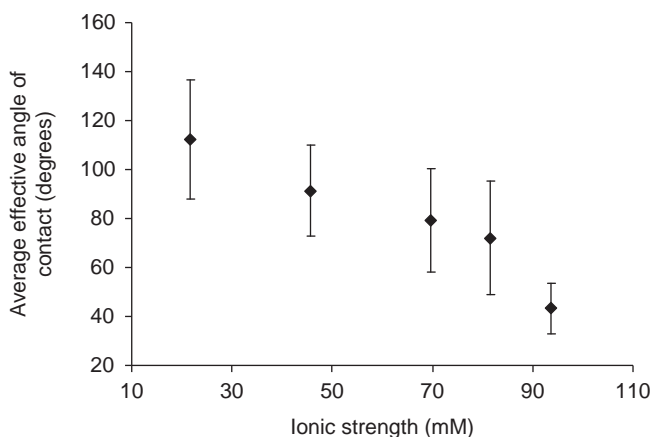


Figure 6 Dependence of the average angle of contact between GPVs in the presence of β_2 -GPI (178 $\mu\text{g}/\text{ml}$) on the ionic strength of solution. Adapted from Ref. [67].

strength (200 mM) and Ca^{2+} (Mg^{2+}) concentration (2.5 mM) [55]. Similar results were obtained from studying the insertion ability of β_2 -GPI using the monolayer approach. Increasing subphase concentration of Na^+ as well as Ca^{2+} (Mg^{2+}) induced a partial detachment of β_2 -GPI from DPPS monolayer [4]. However, even at very high subphase Na^+ and Ca^{2+} (Mg^{2+}) concentrations (0.5 M) increase in the DPPS monolayer surface pressure remained as high as 60% of the maximal value [4]. Membrane insertion of β_2 -GPI cannot be weakened much by raising buffer's ionic strength and divalent cation concentration suggesting that hydrophobic interaction is strongly involved in the insertion process of β_2 -GPI [4, 55].

Membrane binding of β_2 -GPI under low ionic strength conditions was shown to induce phospholipid vesicle precipitation/adhesion. At low ionic strengths β_2 -GPI is supposed to bind target membrane(s) at two distinct sites through domains V and I facilitating intravesicle or intervesicle interaction. No precipitation could be observed at high ionic strength (150 mM NaCl) [60]. The influence of increasing ionic strengths (22–94 mM) on β_2 -GPI induced adhesion of 10 mol% PS-containing GPVs was studied. The strength of adhesion between adhered GPVs was determined as depicted in Fig. 4. Increasing the ionic strength from 22 to 94 mM resulted in a decrease of an average effective angle of contact between adhered PS-containing GPVs from 112° to 43° (Fig. 6, Frank *et al.*, in preparation)[67]. This suggests the weakening of adhesion between GPVs probably due to the gradual, ionic strength sensitive decrease in binding of domain I of β_2 -GPI to the membrane surface of GPVs as well as due to ionic-strength modulated attractive interactions between GPV like-charged membranes.

4.2. The Influence of pH on β_2 -GPI Membrane Insertion

The influence of pH on the insertion ability of β_2 -GPI was studied using the monolayer approach [4]. Decreasing subphase pH from 10.7 to 5.0 increased the ability of β_2 -GPI to insert into DPPS monolayer probably reflecting an increase in

net positive charge on the protein surface. At pH values below 5.0 the insertion ability of β_2 -GPI weakened probably because of the loss of negative charge in the lipid headgroups.

4.3. The Influence of EDTA on β_2 -GPI Membrane Binding

A sharp decrease in the binding capacity of β_2 -GPI to large multilamellar PS vesicles was observed already at very low concentrations of EDTA with no influence on the binding capacity by further increasing EDTA concentration [6].

4.4. The Influence of Albumin and γ -Globulin on β_2 -GPI Membrane Binding

Binding of β_2 -GPI on large PS-containing multilamellar vesicles remarkably decreased in the presence of bovine serum albumin, human serum albumin and horse γ -globulin in a concentration dependent manner [6]. The effect was most pronounced with the latter. At physiological albumin and horse γ -globulin concentrations very low binding of β_2 -GPI on PS-containing vesicles was observed [6].

5. IMPLICATION OF *IN VITRO* PRACTICAL AND THEORETICAL MODELS TO THE CLINICAL SETTING

β_2 -GPI is the principle antigenic target for aPL in patients with APS, which is characterized by recurrent thromboses, pregnancy loss and presence of aPL. There is a significant correlation between the presence of anti- β_2 -GPI autoantibodies and thrombotic manifestations, however the pathophysiological mechanisms by which the anti- β_2 -GPI autoantibodies exert their pathological effects remain to be elucidated.

From *in vitro* studies and calculated K_d for β_2 -GPI binding to anionic phospholipids it is clear, that about half of plasma β_2 -GPI would be in the free form. Same experiments also showed clear reversibility of membrane binding [70]. These properties of β_2 -GPI seem very important for the binding to anionic phospholipids and promoting vesiculation as a proposed physiologic function of β_2 -GPI.

5.1. From *In Vitro* Vesiculation to Microparticles (in absence and presence of anti- β_2 -GPI antibodies)

Human studies on β_2 -GPI-phospholipid membrane interaction focused mainly on changes of biological membranes. A general feature of activated cells is that they can shed fragments of their plasma membranes into the extracellular space [71]. Such fragments, resulting from an exocytotic budding process, are colloquially known as microparticles (MPs). MPs are fragments released from stimulated or apoptotic cells after plasma membrane remodeling and are usually referred to as 0.1 to 1 μ m membrane particles. They include cytoplasmic components and membrane-derived

elements such as negatively charged phospholipids, most commonly PS, or cell-surface receptors. MPs constitute reliable hallmarks of cell damage while the cells, from which they stem, remain sequestered in tissues or are promptly submitted to phagocytic clearance. MPs contribute to hemostatic and inflammatory responses, vascular remodeling and angiogenesis, cell survival, and apoptosis, well-known processes involved in atherothrombosis [72,73]. Hardly detectable in the peripheral blood of healthy individuals, procoagulant MPs circulating at elevated levels are often associated with thrombotic propensity [73]. The mechanisms involved in generation of MPs have not been revealed yet. Loss of membrane lipid asymmetry might be accompanied by blebbing and subsequent shedding of lipid-symmetric microvesicles from the cell surface [74–77]. However, insuperable shape changes would be produced by the large mass-imbalance generated if outward transport of phospholipids would not be compensated by inward transport of other lipids since less than 1% of a mass imbalance between outer and inner phospholipid layer produces large shape changes in giant unilamellar liposomes [78]. Although the cell might be able to compensate for bilayer imbalances by releasing microvesicles, PS exposure in platelets can occur without microvesicle release rendering this mechanism of vesiculation less probable [79].

In studies of membrane traffic processes it was already demonstrated that direct interactions between proteins and lipid bilayers are important in the acquisition of high membrane curvature of membrane transport carriers such as tubules and vesicles [80]. A variety of proteins have been identified that directly bind and deform membranes [80]. Budding of GPVs observed in the presence of β_2 -GPI suggest that β_2 -GPI could also be involved in processes of budding and vesiculation of cellular membranes [65]. Since β_2 -GPI is an abundant plasma protein, it binds to virtually every cell expressing negatively charged phospholipids in the outer layer of the cell membrane. Therefore, the involvement of β_2 -GPI in the budding and vesiculation of biological membranes is likely to be one of its physiologic functions, governing the curvature enhancement of lipid membranes as the basis of some cellular processes [81]. One possible example of β_2 -GPI involvement in cellular processes is the formation of apoptotic blebs on the cells losing transmembrane lipid asymmetry at the beginning of apoptosis, where abundant quantities of β_2 -GPI were detected [82]. The budding of phospholipid vesicles could be explained by the insertion of the C-terminal loop of β_2 -GPI into the outer layer of a phospholipid membrane, which increases the area of the outer layer of the phospholipid bilayer. The change in the area of one membrane monolayer results according to the bilayer couple hypothesis [83,84], in the transformation of the vesicles' shape. It was shown by experimental models that if the area of the outer monolayer became larger than the area of the inner one with a relative difference of about 1% or more, a small vesicle budded off a large vesicle [78,85]. Additionally, C-terminal loop of β_2 -GPI is relatively short and after insertion into a membrane it does not expand through the whole width of the outer layer of the membrane. Its insertion into an external portion of outer layer of the membrane thus necessarily causes also an increase of the spontaneous curvature of the membrane [86,87].

Simultaneous addition of β_2 -GPI and anti- β_2 -GPI antibodies triggered more pronounced budding of GPVs than in experiments with β_2 -GPI alone [65].

Additionally, when β_2 -GPI and anti- β_2 -GPI antibodies were simultaneously present in the solution, small daughter vesicles were formed on some GPVs [65]. Enhanced budding and vesiculation was the result of simultaneous action of β_2 -GPI and anti- β_2 -GPI antibodies and it could be explained by enhanced binding of β_2 -GPI to phospholipid membranes in the presence of anti- β_2 -GPI antibodies. Since β_2 -GPI is an abundant plasma protein, the same situation can be present also in patients with anti- β_2 -GPI antibodies. Evidence suggests that more pronounced budding of membranes and formation of daughter vesicles is a feasible pathogenic action of anti- β_2 -GPI antibodies. It is reasonable to conclude that this pathogenic action of anti- β_2 -GPI antibodies might be the cause for increased number of MPs with procoagulant properties derived from endothelial cells, platelets, and other blood cells as detected in patients with APS.

5.2. Role of Phospholipids and β_2 -GPI in the Development and in Maintaining the Autoimmune Response

Although different pathogenic actions of anti- β_2 -GPI antibodies have been described by now [88,89], their role in promoting blood coagulation in APS patients is not yet fully understood.

A part of the pathogenic actions is very likely associated with anti- β_2 -GPI antibody/ β_2 -GPI phospholipid binding which is greatly enhanced due to the formation of stable complexes formed by two β_2 -GPI molecules adsorbed to a negatively charged membrane and one molecule of anti- β_2 -GPI antibody bound to epitopes on β_2 -GPI [34].

From lessons learned on the many models of β_2 -GPI interactions with the phospholipid bilayers starting from Wurm [6] and the antigenicity of hepatitis B surface antigen proteins bound to phospholipids [90], we hypothesize that similar events could be occurring. What might be happening *in vivo* is that the antigenic activity of β_2 -GPI is dependent on the membrane fluidity for optimal conformation. Once this conformation is in place, additional interactions by the various phospholipid groups give different patterns of antigenicity. The antigenic determinants closest to the lipid-protein interface could change upon direct interaction with the phospholipids, the rest would depend on the »correct« protein conformation determined by the appropriate phospholipid composition [90].

In vitro studies suggest that the primary T-cell autoimmune response is directed against the epitope located on the Vth domain of β_2 -GPI. A recent model has been proposed whereby autoreactive CD4⁺ T cells to β_2 -GPI that promote aPL production were identified in patients with APS [91–93]. At least four distinct T-cell epitopes were identified, but the majority of the β_2 -GPI-specific T-cell clones responded to a peptide encompassing AA 276 to 290 (KVSFFCKNKEKKCSY) of β_2 -GPI that contains the phospholipid-binding site critical for electrostatic interactions [94, 95]. Most of β_2 -GPI-specific T-cell clones were able to stimulate autologous peripheral blood B cells to promote anti- β_2 -GPI antibody production in the presence of recombinant β_2 -GPI [91]. These results indicate that β_2 -GPI-specific CD4⁺ T cells in patients with APS preferentially recognize the antigenic peptide containing the major phospholipid-binding site (AA281–288) and have the capacity

to stimulate B cells to produce anti- β_2 -GPI antibodies. Dendritic cells or macrophages pulsed with β_2 -GPI-bound PS liposome induced a response of T-cell clones specific for a peptide encoding AA 276–290 in HLA-DR–restricted and antigen-processing–dependent manners. In contrast, those pulsed with β_2 -GPI or PS liposome alone failed to induce a response [96]. Together these findings indicate that specialized antigen-presenting cells capturing β_2 -GPI-coated anionic phospholipids efficiently present a disease-relevant cryptic T-cell determinant of β_2 -GPI as a result of antigen processing. As described previously, aPL induce a release of increased number of MPs providing the positive feedback necessary for sustained aPL production.

Additionally, Yamaguchi *et al.* demonstrated that efficient presentation of cryptic determinants recognized by β_2 -GPI-reactive T cells is achieved by monocytes undergoing Fc γ RI-mediated uptake of β_2 -GPI/PS opsonized by IgG anti- β_2 -GPI antibodies [97]. High avidity IgG anti- β_2 -GPI antibodies, which were reported to possess high pathogenicity [98] would also have enhanced the capacity to promote this process. A model by which a pathogenic loop maintains sustained anti- β_2 -GPI autoantibody production in patients with APS was proposed [97].

We speculate that this model could also be connected with epitope spreading observed in patients with APS, where anti- β_2 -GPI antibodies associated strongest with thrombosis were reported to recognize the I_{st} domain [99].

An intriguing finding of a high frequency (42%) of IgG anti- β_2 -GPI antibodies in children with atopic dermatitis (AD) [89] might give us at least a partial answer to the question about the mechanism triggering the anti- β_2 -GPI antibody response. By contrast to antibodies from the APS patients, whose major epitope proved to reside within domains I to IV [100] and only a minority of antibodies bound to domain V [101,102], the sera from the children with AD showed a reactivity restricted to domain V of β_2 -GPI [89]. The proteolytic cleavage of the C-terminal loop between Lys-317 and Thr-318 by plasmin abolished the binding of anti- β_2 -GPI antibodies from the children with AD [89]. The lack of binding to cleaved β_2 -GPI could be attributed to either a conformational change of β_2 -GPI [53] or direct disruption of the epitopic site in domain V [7, 94, 95]. The failure of anti- β_2 -GPI antibodies from children with AD to bind cleaved β_2 -GPI or β_2 -GPI associated with CL further supported hypothesis that their epitopes were located at or at least in close vicinity of the phospholipid binding site in domain V. The mechanisms responsible for the occurrence of IgG anti- β_2 -GPI antibodies in AD are not clear. Several interdependent factors are probably involved. In virtually all sera from children with AD having antibodies against human β_2 -GPI we found also a similar reactivity to bovine β_2 -GPI [89]. An important factor responsible for the occurrence of antibodies against bovine β_2 -GPI might be repeated exposure to nutritional β_2 -GPI early in life, when the intestinal mucosa is more permissive for large molecules [103]. It is conceivable that in infancy the ingested bovine or some other type of β_2 -GPI (from dietary products) could act as a peroral immunization agent inducing a transient production of species specific anti- β_2 -GPI antibodies. In children with AD this humoral immune response may spread also to human β_2 -GPI. The properties of anti- β_2 -GPI response in early childhood point to similar epitope as revealed for T-cell epitopes in patients with APS indicating an immunodominant region of β_2 -GPI, which is close to phospholipid binding site.

In the peripheral blood of healthy subjects, low levels of MPs are detected. Mean levels of circulating MPs appear stable in adulthood, whereas a 2-fold elevation is characteristic of childhood [104]. These data together with the location of the epitope of anti- β_2 -GPI in children with AD indicate that β_2 -GPI-phospholipid interaction plays a role also in triggering an immune response to β_2 -GPI.

6. CONCLUDING REMARKS

The roles of either β_2 -GPI or anti- β_2 -GPI antibodies, despite numerous articles, remain obscure. This review allowed us to conclude that concerning the artificial membrane studies there have been many publications concentrating on β_2 -GPI-phospholipid interactions; however there is significantly less information regarding β_2 -GPI and biological, natural membrane associations. β_2 -GPI-phospholipid binding seems to be a crucial step in the *in vitro* systems for antigenicity generation. This needs to be further addressed to better understand the *in vivo* mechanisms that prime the autoimmune loop.

REFERENCES

- [1] J.Y. Lu, S.L. Hofmann, Thematic review series: Lipid posttranslational modifications. Lysosomal metabolism of lipid-modified proteins, *J. Lipid Res.* 47 (2006) 1352–1357.
- [2] S. Sodin-Semrl, B. Rozman, Beta2-glycoprotein I and its clinical significance: From gene sequence to protein levels, *Autoimmun. Rev.* 6 (2007) 547–552.
- [3] A. Richter, H. Cleve, Genetic variations of human serum beta2-glycoprotein I demonstrated by isoelectric focusing, *Electrophoresis* 9 (1988) 317–322.
- [4] S.X. Wang, G.P. Cai, S.F. Sui, The insertion of human apolipoprotein H into phospholipid membranes: A monolayer study, *Biochem. J.* 335(Pt 2), (1998) 225–232.
- [5] D. Borchman, E.N. Harris, S.S. Pierangeli, O.P. Lamba, Interactions and molecular structure of cardiolipin and beta 2-glycoprotein 1 (beta 2-GP1), *Clin. Exp. Immunol.* 102 (1995) 373–378.
- [6] H. Wurm, Beta 2-glycoprotein I (apolipoprotein H) interactions with phospholipid vesicles, *Int. J. Biochem.* 16 (1984) 511–515.
- [7] J.E. Hunt, R.J. Simpson, S.A. Krilis, Identification of a Region of beta2-Glycoprotein I Critical for Lipid Binding and Anti-Cardiolipin Antibody Cofactor Activity, *Proc. Natl. Acad. Sci. USA.* 90 (1993) 2141–2145.
- [8] A. Steinkasserer, C. Estaller, E.H. Weiss, R.B. Sim, A.J. Day, Complete nucleotide and deduced amino acid sequence of human beta 2-glycoprotein I, *Biochem. J.* 277(Pt 2), (1991) 387–391.
- [9] B. Bouma, P.G. de Groot, J.M. van den Elsen, R.B. Ravelli, A. Schouten, M.J. Simmelink, R. H. Derksen, J. Kroon, P. Gros, Adhesion mechanism of human β_2 -glycoprotein I to phospholipids based on its crystal structure, *EMBO J* 18 (1999) 5166–5174.
- [10] H. Mehdi, A. Naqvi, M.I. Kamboh, A hydrophobic sequence at position 313–316 (Leu-Ala-Phe-Trp) in the fifth domain of apolipoprotein H (beta2-glycoprotein I) is crucial for cardiolipin binding, *Eur. J. Biochem.* 267 (2000) 1770–1776.
- [11] R.B. Cornell, S.G. Taneva, Amphipathic helices as mediators of the membrane interaction of amphitropic proteins and as modulators of bilayer physical properties, *Curr. Protein Pept. Sci.* 7 (2006) 539–552.
- [12] R. Schwarzenbacher, K. Zeth, K. Diederichs, A. Gries, G.M. Kostner, P. Laggner, R. Prassl, Crystal structure of human beta2-glycoprotein I: Implications for phospholipid binding and the antiphospholipid syndrome, *EMBO J* 18 (1999) 6228–6239.

- [13] L. Pal, G. Basu, Novel protein structural motifs containing two-turn and longer 3_{10} -helices, *Protein Eng. Des. Sel.* 12 (1999) 811–814.
- [14] N.S. Lee, H.B. Brewer Jr, J.C. Osborne Jr., Beta 2-Glycoprotein I. Molecular properties of an unusual apolipoprotein H, *J. Biol. Chem.* 258 (1983) 4765–4770.
- [15] R.A. Roubey, Autoantibodies to phospholipid-binding plasma proteins: A new view of lupus anticoagulants and other “antiphospholipid” autoantibodies, *Blood* 84 (1994) 2854–2867.
- [16] L.P. Chung, D.R. Bentley, K.B. Reid, Molecular cloning and characterization of the cDNA coding for C4b-binding protein, a regulatory protein of the classical pathway of the human complement system, *Biochem. J.* 230 (1985) 133–141.
- [17] A.P. Wiles, G. Shaw, J. Bright, A. Perczel, I.D. Campbell, P.N. Barlow, NMR studies of a viral protein that mimics the regulators of complement activation, *J. Mol. Biol.* 272 (1997) 253–265.
- [18] J.M. Casasnovas, M. Larvie, T. Stehle, Crystal structure of two CD46 domains reveals an extended measles virus-binding surface, *EMBO. J* 18 (1999) 2911–2922.
- [19] P.N. Barlow, A. Steinkasserer, D.G. Norman, B. Kieffer, A.P. Wiles, R.B. Sim, I.D. Campbell, Solution structure of a pair of complement modules by nuclear magnetic resonance, *J. Mol. Biol.* 232 (1993) 268–284.
- [20] Y. Sheng, D.A. Kandiah, S.A. Krilis, Beta2-glycoprotein I: Target antigen for “antiphospholipid” antibodies. Immunological and molecular aspects, *Lupus* 7(Suppl. 2), (1998) S5–S9.
- [21] D.K. Sanghera, D.R. Wagenknecht, J.A. McIntyre, M.I. Kamboh, Identification of structural mutations in the fifth domain of apolipoprotein H (beta 2-glycoprotein I) which affect phospholipid binding, *Hum. Mol. Genet.* 6 (1997) 311–316.
- [22] J. Lozier, N. Takahashi, F.W. Putnam, Complete amino acid sequence of human plasma beta 2-glycoprotein I, *Proc. Natl. Acad. Sci. USA* 81 (1984) 3640–3644.
- [23] W.M. Canfield, W. Kiesel, Evidence of normal functional levels of activated protein C inhibitor in combined Factor V/VIII deficiency disease, *J. Clin. Invest.* 70 (1982) 1260–1272.
- [24] H.G. Schwick, H. Haupt, Chemistry and function of human plasma proteins, *Angew. Chem. Int. Ed. Engl.* 19 (1980) 87–99.
- [25] Z. Li, S.A. Krilis, Anti- β_2 -glycoprotein I antibodies and the antiphospholipid syndrome, *Autoimmun. Rev.* 2 (2003) 229–234.
- [26] M. Hammel, M. Kriechbaum, A. Gries, G.M. Kostner, P. Laggner, R. Prassl, Solution structure of human and bovine β_2 -glycoprotein I revealed by small-angle X-ray scattering, *J. Mol. Biol.* 321 (2002) 85–97.
- [27] R. Gambino, G. Ruiu, G. Pagano, M. Cassader, The binding of apolipoprotein H (beta2-Glycoprotein I) to lipoproteins, *Prostag. Oth. Lipid M.* 57 (1999) 351–359.
- [28] A. Gries, J. Nimpf, H. Wurm, G.M. Kostner, T. Kenner, Characterization of isoelectric subspecies of asialo-beta 2-glycoprotein I, *Biochem. J.* 260 (1989) 531–534.
- [29] M.I. Kamboh, R.E. Ferrell, B. Sepehrnia, Genetic studies of human apolipoproteins. IV. Structural heterogeneity of apolipoprotein H (beta 2-glycoprotein I), *Am. J. Hum. Genet.* 42 (1988) 452–457.
- [30] R. Gambino, G. Ruiu, G. Pagano, M. Cassader, Qualitative analysis of the carbohydrate composition of apolipoprotein H, *J. Protein Chem.* 16 (1997) 205–212.
- [31] M.L. Kiely, G.S. McKnight, R.T. Schimke, Studies on the attachment of carbohydrate to ovalbumin nascent chains in hen oviduct, *J. Biol. Chem.* 251 (1976) 5490–5495.
- [32] M.T. Walsh, H. Watzlawick, F.W. Putnam, K. Schmid, R. Brossmer, Effect of the carbohydrate moiety on the secondary structure of beta 2-glycoprotein. I. Implications for the biosynthesis and folding of glycoproteins, *Biochemistry* 29 (1990) 6250–6257.
- [33] R. Gambino, G. Ruiu, G. Pagano, M. Cassader, Characterization of the carbohydrate structures of apolipoprotein H through concanavalin A affinity chromatography, *J. Lipid Mediat. Cell Signal.* 16 (1997) 11–21.
- [34] G.M. Willems, M.P. Janssen, M.M. Pelsers, P. Comfurius, M. Galli, R.F. Zwaal, E.M. Bevers, Role of divalency in the high-affinity binding of anticardiolipin antibody-beta 2-glycoprotein I complexes to lipid membranes, *Biochemistry* 35 (1996) 13833–13842.
- [35] M. Schlame, I. Haller, L.R. Sammaritano, T.J. Blanck, Effect of cardiolipin oxidation on solid-phase immunoassay for antiphospholipid antibodies, *Thromb. Haemost.* 86 (2001) 1475–1482.

- [36] J. Arvieux, V. Regnault, E. Hachulla, L. Darnige, F. Berthou, P. Youinou, Oxidation of beta2-glycoprotein I (beta2GPI) by the hydroxyl radical alters phospholipid binding and modulates recognition by anti-beta2GPI autoantibodies, *Thromb. Haemost.* 86 (2001) 1070–1076.
- [37] J. Arvieux, V. Regnault, E. Hachulla, L. Darnige, B. Roussel, J.C. Bensa, Heterogeneity and immunochemical properties of anti-beta2-glycoprotein I autoantibodies, *Thromb. Haemost.* 80 (1998) 393–398.
- [38] A.D. d'Angeac, I. Stefas, C. Duperray, M. Rucheton, H. Graafland, J.L. Montero, R. Chicheportiche, Oxidation and biotinylation of beta 2 glycoprotein I glycan chains induce an increase in its affinity for anionic phospholipids similar to that obtained by the addition of anti-beta 2 glycoprotein I or anti-cardiolipin antibodies, *J. Immunol. Methods* 300 (2005) 160–178.
- [39] A.D. d'Angeac, I. Stefas, H. Graafland, F. De Lamotte, M. Rucheton, C. Palais, A.K. Eriksson, P. Bosc, C. Rose, R. Chicheportiche, Biotinylation of glycan chains in beta2 glycoprotein I induces dimerization of the molecule and its detection by the human autoimmune anti-cardiolipin antibody EY2C9, *Biochem. J.* 393 (2006) 117–127.
- [40] R.A. Roubey, R.A. Eisenberg, M.F. Harper, J.B. Winfield, "Anticardiolipin" autoantibodies recognize beta 2-glycoprotein I in the absence of phospholipid. Importance of Ag density and bivalent binding, *J. Immunol.* 154 (1995) 954–960.
- [41] S. Cucnik, T. Kveder, B. Rozman, B. Bozic, Binding of high-avidity anti-beta2-glycoprotein I antibodies, *Rheumatology (Oxford)* 43 (2004) 1353–1356.
- [42] Y. Sheng, D.A. Kandiah, S.A. Krilis, Anti-beta 2-glycoprotein I autoantibodies from patients with the "antiphospholipid" syndrome bind to beta 2-glycoprotein I with low affinity: Dimerization of beta 2-glycoprotein I induces a significant increase in anti-beta 2-glycoprotein I antibody affinity, *J. Immunol.* 161 (1998) 2038–2043.
- [43] B.C. Lutters, J.C. Meijers, R.H. Derksen, J. Arnout, P.G. de Groot, Dimers of beta 2-glycoprotein I mimic the in vitro effects of beta 2-glycoprotein I-anti-beta 2-glycoprotein I antibody complexes, *J. Biol. Chem.* 276 (2001) 3060–3067.
- [44] M. Hoshino, Y. Hagihara, I. Nishii, T. Yamazaki, H. Kato, Y. Goto, Identification of the phospholipid-binding site of human β_2 -glycoprotein I domain V by heteronuclear magnetic resonance, *J. Mol. Biol.* 304 (2000) 927–939.
- [45] G.P. de Groot, B. Bouma, B.C. Lutters, M.J. Simmelink, R.H. Derksen, P. Gros, Structure-function studies on beta 2-glycoprotein I, *J. Autoimmun.* 15 (2000) 87–89.
- [46] Y. Hagihara, K. Enjyoji, T. Omasa, Y. Katakura, K. Suga, M. Igarashi, E. Matsuura, H. Kato, T. Yoshimura, Y. Goto, Structure and function of the recombinant fifth domain of human beta 2-glycoprotein I: Effects of specific cleavage between Lys77 and Thr78, *J. Biochem.* 121 (1997) 128–137.
- [47] N. Ohkura, Y. Hagihara, T. Yoshimura, Y. Goto, H. Kato, Plasmin can reduce the function of human beta2 glycoprotein I by cleaving domain V into a nicked form, *Blood* 91 (1998) 4173–4179.
- [48] T. Shi, B. Giannakopoulos, G.M. Iverson, K.A. Cockerill, M.D. Linnik, S.A. Krilis, Domain V of beta2-glycoprotein I binds factor XI/XIa and is cleaved at Lys317-Thr318, *J. Biol. Chem.* 280 (2005) 907–912.
- [49] S. Yasuda, T. Atsumi, M. Ieko, E. Matsuura, K. Kobayashi, J. Inagaki, H. Kato, H. Tanaka, M. Yamakado, M. Akino, H. Saitou, Y. Amasaki, *et al.*, Nicked beta2-glycoprotein I: A marker of cerebral infarct and a novel role in the negative feedback pathway of extrinsic fibrinolysis, *Blood* 103 (2004) 3766–3772.
- [50] D.A. Horbach, E. van Oort, T. Lisman, J.C. Meijers, R.H. Derksen, P.G. de Groot, Beta2-glycoprotein I is proteolytically cleaved in vivo upon activation of fibrinolysis, *Thromb. Haemost.* 81 (1999) 87–95.
- [51] Y. Itoh, K. Inuzuka, I. Kohno, H. Wada, H. Shiku, N. Ohkura, H. Kato, Highly increased plasma concentrations of the nicked form of β_2 glycoprotein I in patients with leukemia and with lupus anticoagulant: Measurement with a monoclonal antibody specific for a nicked form of domain V, *J. Biochem.* 128 (2000) 1017–1024.
- [52] T.A. Brighton, Y.P. Dai, P.J. Hogg, C.N. Chesterman, Microheterogeneity of beta-2 glycoprotein I: Implications for binding to anionic phospholipids, *Biochem. J.* 340(Pt 1), (1999) 59–67.

- [53] E. Matsuura, J. Inagaki, H. Kasahara, D. Yamamoto, T. Atsumi, K. Kobayashi, K. Kaihara, D. Zhao, K. Ichikawa, A. Tsutsumi, T. Yasuda, D.A. Triplett, *et al.*, Proteolytic cleavage of β_2 -glycoprotein I: Reduction of antigenicity and the structural relationship, *Int. Immunol.* 12 (2000) 1183–1192.
- [54] J. Guerin, Y. Sheng, S. Reddel, G.M. Iverson, M.G. Chapman, S.A. Krilis, Heparin inhibits the binding of beta 2-glycoprotein I to phospholipids and promotes the plasmin-mediated inactivation of this blood protein. Elucidation of the consequences of the two biological events in patients with the anti-phospholipid syndrome, *J. Biol. Chem.* 277 (2002) 2644–2649.
- [55] S.X. Wang, G. Cai, S. Sui, Intrinsic fluorescence study of the interaction of human apolipoprotein H with phospholipid vesicles, *Biochemistry* 38 (1999) 9477–9484.
- [56] M. Hammel, R. Schwarzenbacher, A. Gries, G.M. Kostner, P. Lagner, R. Prassl, Mechanism of the interaction of β_2 -glycoprotein I with negatively charged phospholipid membranes, *Biochemistry* 40 (2001) 14173–14181.
- [57] R. Gamsjaeger, A. Johs, A. Gries, H.J. Gruber, C. Romanin, R. Prassl, P. Hinterdorfer, Membrane binding of beta2-glycoprotein I can be described by a two-state reaction model: An atomic force microscopy and surface plasmon resonance study, *Biochem. J.* 389 (2005) 665–673.
- [58] R. Hamdan, S.N. Maiti, A.J. Schroit, Interaction of beta2-glycoprotein I with phosphatidylserine-containing membranes: Ligand-dependent conformational alterations initiate bivalent binding, *Biochemistry* 46 (2007) 10612–10620.
- [59] S.X. Wang, Y.T. Sun, S.F. Sui, Membrane-induced conformational change in human apolipoprotein H, *Biochem. J.* 348(Pt 1), (2000) 103–106.
- [60] A.T. Lee, K. Balasubramanian, A.J. Schroit, β_2 -glycoprotein I-dependent alterations in membrane properties, *Biochim. Biophys. Acta* 1509 (2000) 475–484.
- [61] Y. Hagihara, Y. Goto, H. Kato, T. Yoshimura, Structure and function of beta 2-glycoprotein I: With special reference to the interaction with phospholipid, *Lupus* 4(Suppl. 1), (1995) S3–S5.
- [62] A. Ambrožič, S. Čučnik, N. Tomšič, J. Urbanija, M. Lokar, B. Babnik, B. Rozman, A. Igljič, V. Kralj-Igljič, Interaction of giant phospholipid vesicles containing cardiolipin and cholesterol with beta2-glycoprotein-I and anti-beta2-glycoprotein-I antibodies, *Autoimmun. Rev.* 6 (2006) 10–15.
- [63] J. Urbanija, N. Tomšič, M. Lokar, A. Ambrožič, S. Čučnik, B. Rozman, M. Kanduser, A. Igljič, V. Kralj-Igljič, Coalescence of phospholipid membranes as a possible origin of anticoagulant effect of serum proteins, *Chem. Phys. Lipids* 150 (2007) 49–57.
- [64] J. Urbanija, B. Babnik, M. Frank, N. Tomšič, B. Rozman, V. Kralj-Igljič, A. Igljič, Attachment of β_2 -glycoprotein I to negatively charged liposomes may prevent the release of daughter vesicles from the parent membrane, *Eur. Biophys. J.* (2008).
- [65] A. Ambrožič, B. Božič, T. Kveder, J. Majhenc, V. Arrigler, S. Svetina, B. Rozman, Budding, vesiculation and permeabilization of phospholipid membranes—evidence for a feasible physiologic role of beta2-glycoprotein I and pathogenic actions of anti-beta2-glycoprotein I antibodies, *Biochim. Biophys. Acta* 1740 (2005) 38–44.
- [66] M. Frank, M. Manček-Keber, M. Kržan, S. Sodin-Semrl, R. Jerala, A. Igljič, B. Rozman, V. Kralj-Igljič, Prevention of microvesiculation by adhesion of buds to the mother cell membrane—a possible anticoagulant effect of healthy donor plasma, *Autoimmun. Rev.* 7 (2008) 240–245.
- [67] M. Frank, J. Pavlič, K. Bohinc, B. Rozman, V. Kralj-Igljič, A. Igljič, Influence of ionic strength on agglutination of like-charged phospholipid membranes induced by beta2-GPI (in preparation).
- [68] M.F. Harper, P.M. Hayes, B.R. Lentz, R.A. Roubey, Characterization of beta2-glycoprotein I binding to phospholipid membranes, *Thromb. Haemost.* 80 (1998) 610–614.
- [69] F. Wang, X.F. Xia, S.F. Sui, Human apolipoprotein H may have various orientations when attached to lipid layer, *Biophys. J.* 83 (2002) 985–993.
- [70] E.M. Bevers, R.F. Zwaal, G.M. Willems, The effect of phospholipids on the formation of immune complexes between autoantibodies and beta2-glycoprotein I or prothrombin, *Clin. Immunol.* 112 (2004) 150–160.
- [71] R.F. Zwaal, A.J. Schroit, Pathophysiologic implications of membrane phospholipid asymmetry in blood cells, *Blood* 89 (1997) 1121–1132.
- [72] O. Morel, F. Toti, B. Hugel, J.M. Freyssinet, Cellular microparticles: A disseminated storage pool of bioactive vascular effectors, *Curr. Opin. Hematol.* 11 (2004) 156–164.

- [73] M.J. VanWijk, E. VanBavel, A. Sturk, R. Nieuwland, Microparticles in cardiovascular diseases, *Cardiovasc. Res.* 59 (2003) 277–287.
- [74] P. Comfurius, J.M. Senden, R.H. Tilly, A.J. Schroit, E.M. Bevers, R.F. Zwaal, Loss of membrane phospholipid asymmetry in platelets and red cells may be associated with calcium-induced shedding of plasma membrane and inhibition of aminophospholipid translocase, *Biochim. Biophys. Acta* 1026 (1990) 153–160.
- [75] P.J. Sims, T. Wiedmer, C.T. Esmon, H.J. Weiss, S.J. Shattil, Assembly of the platelet prothrombinase complex is linked to vesiculation of the platelet plasma membrane. Studies in Scott syndrome: An isolated defect in platelet procoagulant activity, *J. Biol. Chem.* 264 (1989) 17049–17057.
- [76] T. Wiedmer, S.J. Shattil, M. Cunningham, P.J. Sims, Role of calcium and calpain in complement-induced vesiculation of the platelet plasma membrane and in the exposure of the platelet factor Va receptor, *Biochemistry* 29 (1990) 623–632.
- [77] R.F. Zwaal, P. Comfurius, E.M. Bevers, Platelet procoagulant activity and microvesicle formation. Its putative role in hemostasis and thrombosis, *Biochim. Biophys. Acta* 1180 (1992) 1–8.
- [78] E. Farge, P.F. Devaux, Shape changes of giant liposomes induced by an asymmetric transmembrane distribution of phospholipids, *Biophys. J.* 61 (1992) 347–357.
- [79] J. Dachary-Prigent, J.M. Pasquet, J.M. Freyssinet, A.T. Nurden, Calcium involvement in aminophospholipid exposure and microparticle formation during platelet activation: A study using Ca^{2+} -ATPase inhibitors, *Biochemistry* 34 (1995) 11625–11634.
- [80] F. Khashayar, P. De Camilli, Mechanisms of membrane deformation, *Curr. Opin. Cell Biol.* 15 (2003) 372–381.
- [81] S. Svetina, B. Žekš, Shape behavior of lipid vesicles as the basis of some cellular processes, *Anat. Rec.* 268 (2002) 215–225.
- [82] L. Casciola-Rosen, A. Rosen, M. Petri, M. Schlissel, Surface blebs on apoptotic cells are sites of enhanced procoagulant activity: Implications for coagulation events and antigenic spread in systemic lupus erythematosus, *Proc. Natl. Acad. Sci. USA.* 93 (1996) 1624–1629.
- [83] M.P. Sheetz, S.J. Singer, Biological membranes as bilayer couples - molecular mechanism of drug erythrocyte interaction, *Proc. Natl. Acad. Sci. USA.* 71 (1974) 4457–4461.
- [84] S. Svetina, B. Žekš, Membrane bending energy and shape determination of phospholipid vesicles and red blood cells, *Eur. Biophys. J.* 17 (1989) 101–111.
- [85] K. Berndt, J. Käs, R. Lipowsky, E. Sackmann, U. Seifert, Shape transformations of giant vesicles: Extreme sensitivity to bilayer asymmetry, *Europhys. Lett.* 13 (1990) 659–664.
- [86] L. Miao, U. Seifert, M. Wortis, H.G. Dobereiner, Budding transitions of fluid-bilayer vesicles: The effect of area-difference elasticity, *Phys. Rev. E.* 49 (1994) 5389–5407.
- [87] S. Svetina, B. Žekš, Bilayer couple as a possible mechanism of biological shape formation, *Biomed. Biochim. Acta* 44 (1985) 979–986.
- [88] P.L. Meroni, P. Riboldi, Pathogenic mechanisms mediating antiphospholipid syndrome, *Curr. Opin. Rheumatol.* 13 (2001) 377–382.
- [89] A. Ambrožič, T. Avičin, K. Ichikawa, T. Kveder, E. Matsuura, M. Hojnik, T. Atsumi, B. Rozman, T. Koike, Anti- β_2 -glycoprotein I antibodies in children with atopic dermatitis, *Int. Immunol.* 14 (2002) 823–830.
- [90] J. Gomez-Gutierrez, I. Rodriguez-Crespo, D.L. Peterson, F. Gavilanes, Antigenicity of hepatitis B surface antigen proteins reconstituted with phospholipids, *Biochim. Biophys. Acta* 1233 (1995) 205–212.
- [91] T. Arai, K. Yoshida, J. Kaburaki, H. Inoko, Y. Ikeda, Y. Kawakami, M. Kuwana, Autoreactive CD4^+ T-cell clones to β_2 -glycoprotein I in patients with antiphospholipid syndrome: Preferential recognition of the major phospholipid-binding site, *Blood* 98 (2001) 1889–1896.
- [92] N. Hattori, M. Kuwana, J. Kaburaki, T. Mimori, Y. Ikeda, Y. Kawakami, T cells that are autoreactive to β_2 -glycoprotein I in patients with antiphospholipid syndrome and healthy individuals, *Arthritis Rheum.* 43 (2000) 65–75.
- [93] K. Yoshida, T. Arai, J. Kaburaki, Y. Ikeda, Y. Kawakami, M. Kuwana, Restricted T-cell receptor beta-chain usage by T cells autoreactive to β_2 -glycoprotein I in patients with antiphospholipid syndrome, *Blood* 99 (2002) 2499–2504.

- [94] J. Hunt, S. Krilis, The fifth domain of beta 2-glycoprotein I contains a phospholipid binding site (Cys281–Cys288) and a region recognized by anticardiolipin antibodies, *J. Immunol.* 152 (1994) 653–659.
- [95] Y. Sheng, A. Sali, H. Herzog, J. Lahnstein, S.A. Krilis, Site-directed mutagenesis of recombinant human beta 2-glycoprotein I identifies a cluster of lysine residues that are critical for phospholipid binding and anti-cardiolipin antibody activity, *J. Immunol.* 157 (1996) 3744–3751.
- [96] M. Kuwana, E. Matsuura, K. Kobayashi, Y. Okazaki, J. Kaburaki, Y. Ikeda, Y. Kawakami, Binding of β_2 -glycoprotein I to anionic phospholipids facilitates processing and presentation of a cryptic epitope that activates pathogenic autoreactive T cells, *Blood* 105 (2005) 1552–1557.
- [97] Y. Yamaguchi, N. Seta, J. Kaburaki, K. Kobayashi, E. Matsuura, M. Kuwana, Excessive exposure to anionic surfaces maintains autoantibody response to 2-glycoprotein I in patients with antiphospholipid syndrome, *Blood* 110 (2007) 4312–4318.
- [98] B. Božič, S. Čučnik, T. Kveder, B. Rozman, Avidity of anti-beta-2-glycoprotein I antibodies, *Autoimmun. Rev.* 4 (2005) 303–308.
- [99] B. de Laat, R. H.W.M. Derksen, R.T. Urbanus, P.G. de Groot, IgG antibodies that recognize epitope Gly40–Arg43 in domain I of β_2 -glycoprotein I cause LAC, and their presence correlates strongly with thrombosis, *Blood* 105 (2005) 1540–1545.
- [100] M. Igarashi, E. Matsuura, Y. Igarashi, H. Nagae, K. Ichikawa, D.A. Triplett, T. Koike, Human beta2-glycoprotein I as an anticardiolipin cofactor determined using mutants expressed by a baculovirus system, *Blood* 87 (1996) 3262–3270.
- [101] J. George, B. Gilburd, M. Hojnik, Y. Levy, P. Langevitz, E. Matsuura, T. Koike, Y. Shoenfeld, Target recognition of beta2-glycoprotein I (beta2GPI)-dependent anticardiolipin antibodies: Evidence for involvement of the fourth domain of beta2GPI in antibody binding, *J. Immunol.* 160 (1998) 3917–3923.
- [102] G.M. Iverson, E.J. Victoria, D.M. Marquis, Anti-beta2 glycoprotein I (beta2GPI) autoantibodies recognize an epitope on the first domain of beta2GPI, *Proc. Natl. Acad. Sci. USA* 95 (1998) 15542–15546.
- [103] M. Kuitunen, E. Savilahti, A. Sarnesto, Human alpha-lactalbumin and bovine beta-lactoglobulin absorption in infants, *Allergy* 49 (1994) 354–360.
- [104] V. Proulle, B. Hugel, B. Guillet, L. Grunebaum, T. Lambert, J.M. Freyssinet, M. Dreyfus, Circulating microparticles are elevated in haemophiliacs and non-haemophilic individuals aged <18 years, *Br. J. Haematol.* 131 (2005) 487–489.

SUBJECT INDEX

- Active transport, 156
Antibodies, 228, 232–236, 239
Antifungal agent, 60
Antiphospholipid, 235, 237, 239
Antiphospholipid antibodies
 antigenicity, 266, 268
 autoimmunity, 245, 256, 266–268
 biotinylation, 251–252
 BLASTp search, 249
 conformational changes, 250, 252, 254
 dimerization, 252–253
 glycosylation, 245, 250
 lipids, 246–248, 250–253, 255–258, 261, 264–265
 membrane budding, 258
 membrane charge and composition, 259–261
 microparticles, 245, 264–266
 mutations, 253–254
 oxidation, 251–252
 pH, 246–247, 263–264
 posttranslational modifications, 249–254
 sequence homology, 248
 thrombosis, 267
Antiphospholipid syndrome, 245, 249, 251, 264, 266–267
Antonov's rule, 174
Apolipoprotein, 246–248, 250
Artificial bilayer lipid membrane
 dipole potential
 dipole-modifying agent, 84
 membrane surface charge, 72, 86, 88–89, 100
Artificial vesicles, 230
Autoimmune, 228, 235–236, 239
Autoimmune response, 245, 266
- Bell's model, 184
Bilayer techniques, 226–228
Bilayer thickness, 160, 185
Biolabelling, 215
Biosensor, 203–204, 208–210, 213, 215
BLM permeability, 156–160, 191–192
Born energy, 155, 157–159
Born model, 165–170
- Capacitance measurements, 231
Carbon nanotubes, 203–204, 208–209, 212
Cellular imaging, 215–216
Charge recombination kinetics, 28
Counterions, 110, 131
- Debye length, 129, 131, 133–134, 142, 151
Dipolar ordering, 110, 145–151
Dipolar potential, 180–183, 194
Dipole-dipole specific interactions, 181, 194
Dipole moment, 184–185
- Dipole partition, 183–187
Drug delivery, 208, 212–213, 215, 217–218
- Electric double layer, 107–151
Electrostatic effect, 161, 176–177, 179–181, 184, 194
Embedded vesicles, 3, 12, 14–15, 18–20
Excluded volume, 107–109, 112, 119, 127, 129, 137, 150
- Fluorescent lipids, 232
Functionalization, 203–208, 213–216, 218
Fusigenic vesicles, 230
- Gene delivery, 216–217
Gibbs energy, 156, 161, 165–169, 172–177, 179–181, 184–185, 189
Gibbs energy of partitioning or resolution, 161
 β 2-Glycoprotein I, 244–245, 254
Grothuss mechanism, 190, 192, 195
- Hydrated transient defects, 158
Hydrocarbon chain, 157, 190
Hydrogen bond, 161, 165, 171–173, 177, 179, 185, 190–192, 194–195
Hydrophilic defect, 188
Hydrophobic defect, 188
Hydrophobic effect, 172, 174–177, 179, 181
Hydrophobic interaction, 157, 174
Hyperosmotic stress, 28, 35–38
- Image force, 179–181, 184–185, 194
Ion and dipole transport, 156
Ion-dipole specific interactions, 161, 177, 194
Ionic flux, 157, 190, 195
Ion radius, 166, 169–171, 177–178, 180, 195
Ion resolution, 161–162, 165, 177
Ion transfer, 161–162, 165–167, 169, 179–182
- Lipid bilayers, 155–160, 177, 187–188, 190, 192, 194
Lipids(s), 27–29, 31–36, 38–43, 45, 48–52, 155–160, 177, 180, 185, 187–190, 192, 194, 202–203, 208–218
Liposome(s), 156, 158–159, 190, 192, 225–234, 236–239
- M6 antibody, 236–237, 239
Mass spectrometry, 38
mCs, 225, 228–229
Mediated attraction, 151
Membrane, 107–151
Membrane binding, 245–246, 254–256, 261–264
Membrane permeability, 155–195

- Modified synaptic vesicles (mSVs), 226–228, 230–231, 233, 237
- Multi-wall carbon nanotube, 204–205, 208, 210
- Nanomaterials, 203, 207–210, 213–214
- Nanoparticles, 108, 110, 112, 114, 116, 118–119, 123, 140–153, 203, 208, 211, 213–218
- Non-local electrostatics, 168
- Nystatin, 226, 230–231
- Partition coefficient, 157, 169, 175–177, 182
- Partitioning, 155, 157–158, 160–161, 190–195
- Passive transport, 156–157, 187–190
- Permeability, 155–159, 176, 182–183, 185, 187–192
- Permeability coefficient, 157, 182, 185, 187, 190, 192, 195
- Phospholipid(s), 156–157, 181, 190–192, 244–247, 251–268,
- Photosynthetic membrane proteins, 31–34
- Plasma protein, 245, 265–266
- Poisson–Boltzmann, 109–110, 123, 127, 129–131, 133, 136–137, 142
- Polyelectrolyte multilayer films, 2–3, 7–20
- Pore mechanism, 155, 157, 187–190, 195
- Pore structure, 188
- Proton fluxes, 159–160, 190–191
- Proton wire, 190, 192
- Quadrupolar ordering, 110, 138, 140–145, 151
- Reconstitution, 226, 228–229, 233
- Self-assembled lipid membranes, 202–203
- Self-assembly, 202–203, 206, 208, 210, 213–214
- Sensor, 209–211, 213
- Single-wall carbon nanotube, 204–210, 212
- Solubility–diffusion mechanism, 155, 157–158, 192, 194–195
- Solvation, 161–162, 169, 173
- Solvation energy, 161–165, 168–170, 172, 174, 177–179
- Solvophobic effect, 156, 161, 167, 174, 177, 180, 194
- Solvophobic equation, 174–176, 180
- Streptococcus, 240
- Supported lipid bilayers, 2–7, 12, 20
- Surface potential, 156, 181, 194
- Synaptic vesicles, 226–227, 229–230, 233, 236–237
- Syngomyacin E
- SRE channel forming activity
 - actin, 60
 - polymers, 94–100
 - sphingolipids, 63–64
 - sterols, 63–64
 - SRE channels
 - clusters, 60, 68, 78–80, 86, 89–92
 - conductance, 60, 63–65, 67–74, 79, 92–94
 - gating charge, 60, 79–86, 95, 100
 - lifetime, 60, 77, 91–92
 - mean number of small channels in cluster, 88–89
 - polyethylene glycols (PEGs), 67–68, 70
 - pore radius, 64, 68
 - selectivity, 60, 65–68
 - small (elementary) channels, 60, 70–74, 85–86
 - voltage-dependent properties, 89
- Thermal fluctuations, 158, 188–189, 191
- Transient fluctuations, 191
- Transient hydrogen bonded chains, 190–191
- Transient pore mechanism, 155, 187–190, 195
- Transmembrane potential, 183
- Vesicle plating, 233–234
- Vesiculation, 245, 258, 264–266
- Water concentration, 185–186
- Water permeability coefficient, 185